Controls on pore systems and surfaces of the carbonate-rich Eagle Ford Formation

GAIANI, ILARIA

Controls on pore systems and surfaces of the carbonate-rich Eagle Ford Formation

Ilaria Gaiani

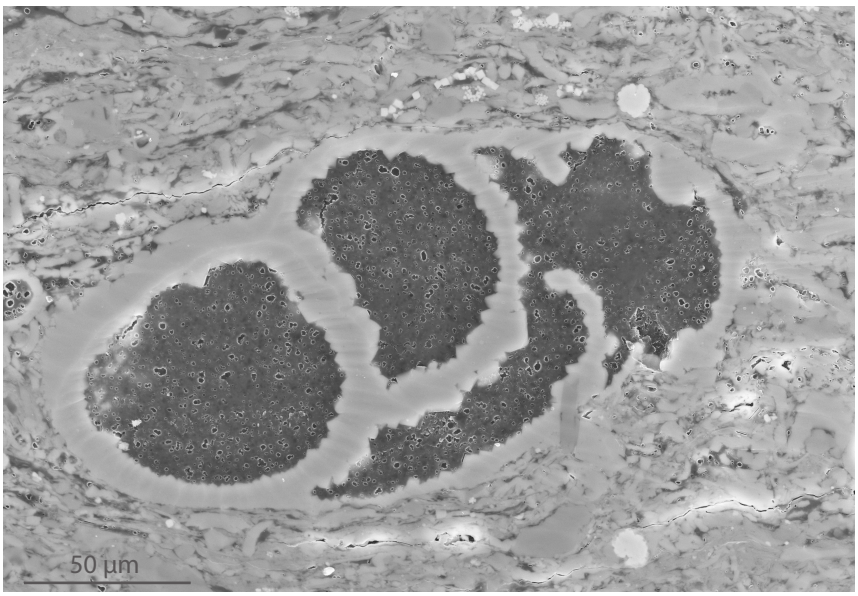

A Thesis presented for the degree of

Doctor of Philosophy

Durham University

Department of Earth Sciences
University of Durham
England

2019

Abstract

In all types of reservoirs, understanding the pore system is crucial to quantifying and predicting multiphase fluid storage and flow. The prediction of the fluid storage and flow helps to decipher the volume of the reservoir of interest, how easily accessible it is and how recoverable its reserves are. In the hydrocarbon industry, the focus of many recent studies is towards reserves in tight reservoirs. Improvements in the extraction methods such as the introduction of horizontal wells and hydraulic fracturing have indeed rendered these reserves economically viable.

However, quantifying the pore system of fine-grained reservoirs is hugely challenging due to the mineralogical and textural heterogeneity at the microscale and the sub-nanometer to micrometer size of pores. In this work, the pore system and pore surfaces of the Cretaceous Eagle Ford Formation are characterised by analysing a set of 25 samples from outcrops and six wells with maturities of R_0 0.4-0.5%, 0.9% and 1.2%. The aim of this work is to establish an analytical workflow for the characterisation of the pore system in tight reservoirs, also by highlighting the importance of a multi-disciplinary approach, often neglected.

The set of samples was analysed using a varied range of techniques; X-Ray Diffraction, optical microscopy, Energy Dispersion X-ray spectroscopy (EDS), Scanning Electron Microscopy (SEM) and micro-CT scans were used to reconstruct the mineralogical and textural framework in which porosities occur. Petrographic studies show that the organic matter (OM) is a marine type II kerogen and that microfacies vary from finely laminated foraminiferal mudstones to packstones. SEM-EDS and Cathodo-luminescence (CL) techniques were used to reconstruct mineral paragenesis and OM evolution. SEM and Backscattered-SEM (BSEM) high resolution maps identified different pore types and showed how pores change with maturity. At R_0 0.4-0.5% the main porosity types are interparticle, enclosed within the coccolithic matrix, whereas at R_0 1.2% spherical OM pores smaller than 20 nm are more frequent, related to the thermal maturation of the OM. Pore sizes were calculated using a combination of SEM, N_2 and CO_2 gas adsorption and Mercury injection Porosimetry (MICP). Immature and oil window samples present pores larger (~2-100 nm) than samples in the gas maturity window(~1-40 nm). MICP analyses indicate a connected pore system in all the samples. Focussed Ion Beam (FIB)-SEM

volumes show that at R_0 0.4 to 0.9%, the pore system is connected through interparticle pores, whereas at R_0 1.2%, the connectivity occurs through pore throats < 10 nm. Environmental SEM (ESEM) observations and Chemical Force Microscopy (CFM) studies at the nanoscale show that surface wettability depends on chemical variations of the fluid interacting with the pore surfaces, also validated with AFM-IR analyses, and on the pore surface mineralogy. AFM-IR studies also identified *in situ* chemical changes between different organic molecules and between the same organic molecules at increasing maturities. In summary, this work brings to light the necessity to use a combination of physical and chemical methods to define the parameters affecting the pore system and its evolution with time. Moreover, the use of state-of-the-art methods such as the AFM-IR has allowed to validate previous theories on the organic molecules behaviour and to suggest a new approach for further studies at the nanoscale of rock surfaces.

Declaration

I declare that this thesis, which I submit for the degree of Doctor of Philosophy at Durham University, is my own work and not substantially the same as any which has previously been submitted at this or any other university.

Ilaria Gaiani

Copyright

Acknowledgements

I would like to thank my supervisor, Professor Andrew Aplin, for all the constructive scientific discussions and for always finding the time to meet. Thank you, Andy, for the constant support and for providing me with the right amount of research freedom and guidance.

Thank you to my second supervisor, Professor Chris Greenwell, for guiding me through the chemistry part of my PhD and for the insightful discussions. I am extremely grateful to Dr Pablo Cubillas, for the vital help in the development of the project and for all the time spent together doing experiments in the lab. A special mention to my external supervisor, Dr Ruarri Day-Stirrat, for making this project possible and the time to me dedicated throughout this PhD and during my visit in the Shell offices in Houston. Thank you to Shell for sponsoring my project and allowing me to conduct state-of-the-art experiments around the world.

Thank you to the NERC CDT in Oil and Gas, my other sponsor, for the high-quality 20 weeks and more of trainings. These trainings have been an incredible opportunity to learn science, network with world-class energy experts, see amazing geology, meet long-time friends and travel around Europe. Thank you, Lorna and Anna for the spotless organisation.

Particular mention to everyone that helped me during the experimental part of the program: Dr Jim Buckman in Edinburgh, Dr Kate Dobson and Leon Bowen in Durham, the AFM lab group in Nebraska, Dr Martin Smith and Philip Green in Newcastle, Dr Miriam Unger and Bruker in Karlsruhe and Dr Pieter Bertier in Aachen.

Thank you also to all the people met in the department during these four years, without whom I certainly couldn't have made it. Thank you to Ali, Aylin, Pierre-Yves, Ines, Giacomo and Telemaco for all the fun evenings. Thank you Vili, for the great friendship born during the coffee breaks. A special thanks to all the friends that supported me during the last year; I couldn't thank Alex enough, for all the moments shared together and for taking care of me in the last months of the PhD. Thank you, Eloïse, for always brightening

my days with your positivity. Thank you to "the Greeks", Dimitrios, Pavlos and Nikos, for all the passionate discussions about the Mediterranean spirit. Thank you to Kate, for being the "BBB" and to Simon for making me love the French humour. Thank you, Nico, for your daily dose of support and affection. Thank you, CJ and Marie Anne for making every break more pleasant and Sean, for always being ready to help.

Many thanks to my housemates Valentina, Emma, Devin, Guillaume and to my almost-housemates Giulia and Maria, for really making me feel at home.

I am grateful to all my friends back home and around the world for always rooting for me.

Finally, thank you to my close and extended family, for the ceaseless support and for always looking out for me.

Table of Contents

Chapter 1

Introduction

1.1. Pore system characterization

In all types of underground reservoirs, an understanding of pore systems is essential to determine where resources are stored, how they are connected and how they can be extracted. In hydrocarbon reservoirs, deciphering the pore system is a fundamental step in the generation of reliable volume estimations and fluid flow models. Once the potential profitability of the reservoir is established, these models can help to maximise well performance and enhance the productivity of the reservoir.

1.2. Aims and objectives

The final aim of this study is to provide a comprehensive understanding of the pore system and of the pore surfaces of the Eagle Ford reservoir by integrating geological, physical and chemical principles. This multi-disciplinary approach is often neglected, as it requires systematically different background competencies, but this work demonstrates that it is essential in order to make quantitative statements regarding the pore system of the Eagle Ford pore system and, in general, of tight reservoirs. Moreover, this work offers a new, reliable workflow for the characterisation from the nano-scale to the micro-scale of a complex pore-system. Once the system has been characterised at the nano and micro-scale, the reservoir properties can be upscaled, taking into account the variabilities of the pore systems in function of the textural framework.

In particular, this work allowed to answer the following questions:

- How do diagenesis and burial history affect the pore system?
- How does the pore system change with the change in thermal maturity?
- Which microfacies contain the best pore system?
- How does the chemistry of the oil affect the pore surfaces?
- Is porosity influenced by the OM type?
- How does the surface chemistry of the pores vary and what controls it?
- How do the surface chemistry variations influence wettability?

The integration of the quantitative physical and geological analysis of the pores with a methodical reconstruction of their surface chemistry has also allowed the validation of completely novel testing methods (chapters 5 and 6). These testing methods have permitted to:

- Quantify and observe the surface chemistry variabilities of pure calcite crystals in contact with different oil compounds.
- Provide a new approach into the characterization of the nanometric surface chemistry variabilities of a mudstone reservoir.
- Examine and chemically analyse in situ the chemical variations of the organic molecules with progressively increasing thermal maturities.

1.3. Unconventional resources

In the last two decades, the advent of new technologies such as horizontal drilling and multistage hydraulic fracturing stimulation has rendered economically viable many hydrocarbon resources that were previously unrecoverable with conventional extraction methods (Grafton et al., 2016; Ríos et al., 2016; Slatt and O'Brien, 2011). Nowadays, unconventional hydrocarbons make up to more than 20% of the total worldwide resources (Aminzadeh and Dasgupta, 2013), indicating the need for detailed characterisation. The investigation of these resources is complicated by the fact that they are formed by nanometre to micrometre grain-size (< 62.5μm) sediments and are minerally and texturally heterogeneous (Algré and Legrand, 2014; Aplin et al., 2011; Bryndzia and Braunsdorf, 2014; Macquaker and Gawthorpe, 1993; Macquaker et al., 2007; Passey et al., 2010; Saidian et al., 2014). Due to their fine-grained and heterogeneous texture, unconventional reservoirs also present a diverse pore system formed by pores

from the sub-nanometre to the micron scale size. This tight, heterogeneous pore system produces a network with permeabilities in the range of sub nanodarcies to microdarcies (Merriman et al., 2003).

1.4. The Eagle Ford Formation

This work aims to characterise the pore system of the Eagle Ford Formation. The Eagle Ford is a carbonate-rich unconventional reservoir, that was targeted as productive by the hydrocarbon industry in 2008, when hydraulic fracturing and horizontal drilling were here employed for the first time. In less than six years after the first discovery well, its production grew from virtually zero to more than 1 million barrels of oil equivalent per day (boe/d), and 7 billion cubic feet of gas equivalent (bcfe/d) per day. Its most recent production is of 1.4 boe/d and 4.9 bcf/d (U.S. EIA, 2019), making it the second-best unconventional play in the United States following the Marcellus Formation in terms of productivity. Due to the heterogeneity and complexity of this reservoir, assessing the pore system and understanding how it varies through time requires a detailed analysis of the controlling factors affecting the pores. This detailed analysis can be only done by using a multi-scale, multi-disciplinary approach. The combination of these techniques allows to place the pore system of the Eagle Ford Formation in a petrological framework, to quantify the pore sizes, volumes and connectivity, to analyse the surface chemistry characteristics of the pores and to understand how the system evolves through time.

1.5. Depositional environment and diagenesis

The first factor that is being considered in this study is the petrological framework of the Eagle Ford samples and its relationship with the pore system. A porous network cannot be understood without considering the solid framework that encases it. The mineral and organic constituents of the rock, together with the rock fabric and texture, determine the nature of the porosities and therefore control the whole flow system network (Dawson and Almon, 2010; Katsube and Williamson, 1994). In turn, the microfacies and the mineralogical composition of the sediments are a function of their depositional and palaeoceanographic settings (Bjorlykke, 1998). Textural and compositional analyses can give important insights into the interpretation of the depositional environment and the

burial history of the samples (Bathurst, 1974; Bjorlykke, 1998; Macquaker and Gawthorpe, 1993; Macquaker et al., 2007; Folk, 1959). Unravelling the diagenetic history of the sediments also has important implications in the assessment of reservoir properties of petroleum systems (Aplin and Macquaker, 2011; McAllister et al., 2015; Taylor and Macquaker, 2014). During burial, the sediments undergo a series of mechanical and chemical reactions that modify the pore network, the fluid properties as well as the mineral precipitates (Aplin et al., 2006; Bjorlykke, 1998). Mechanical compaction occurs at shallow depths (<2 km) and low temperatures (<60-80^{0}C), and it is mainly a function of the effective stress and grain strength and size (Bjorlykke, 1998; Goulty, 1998). Chemical compaction, on the other hand, mainly depends on the chemical kinetics controlling the dissolution and precipitation of minerals (Aplin and Macquaker, 2011; Bjorlykke, 1998; Peltonen et al., 2009). Evidence of mechanical compaction can be sought, for example, in the reduction of porosity and in overpressure signals (e.g. expansion seams by pressure solution) and in the re-alignment of the mineral grains perpendicular to the stress direction. By looking for petrographical evidence of specific depositional patterns and diagenetic modification through time, it is possible to gain information on how these controls affect the pore system.

1.6. Thermal evolution of organic matter

Understanding how organic matter is transformed at progressively higher burial stresses and temperatures is a vital step to the assessment of hydrocarbon resources in unconventional reservoirs (Chalmers and Bustin, 2017; Hackley et al., 2017; Schito et al., 2017; Teichmüller, 1986). In addition, organic matter maturation significantly modifies the pore system, so that understanding its composition and retention helps in the overall comprehension of the nature and surface chemistry of the pore system. During thermal maturation, the organic matter generates oil, which migrates through the reservoir in the pore network of the unconventional source rock (Berg, 1999; Jia et al., 2014). The generated bitumen can modify the connectivity and the chemistry of the pore network (Anderson, 1986; Morrow, 1990).

In the gas window, thermal cracking of kerogen induces the formation of a large amount of organic nanoporosity (Chalmers et al., 2012; Curtis et al., 2011; Loucks et al., 2012, 2011,

2009). These nanopores play an important role in the overall pore volume, as, due to their large surface areas, they are able to adsorb and store large amounts of gas (Chalmers et al., 2017; Curtis et al., 2011; Loucks et al., 2010, 2009; Ross and Marc Bustin, 2009; Wang and Reed, 2009). Moreover, several studies on mudstones have indicated that the connectivity of the pore system is associated to the narrow pore throats formed by the clay-rich matrix and the organic matter nanopores (Aplin and Moore, 2016; Clarkson et al., 2013a; Klaver et al., 2016; Mathia et al., 2019; Wang et al., 2016).

1.7. Pore systems in mudstones

Given the relevance into the understanding of the pore system network in tight reservoirs, many studies have been made on the quantitative characterization of porosities in mudstones and chalk reservoirs (Aplin and Moore, 2016; Bernard et al., 2013; Busch et al., 2017; Chalmers et al., 2012; Chalmers and Bustin, 2015; Fishman et al., 2012; Javadpour, 2009; Klaver et al., 2015; Kuila, 2013; Liu et al., 2017; Loucks et al., 2012; Loucks and Reed, 2014; Ma et al., 2016; Mathia et al., 2019; Peng et al., 2014; Saidian et al., 2014; Tian et al., 2015; Wang et al., 2015). All the studies concluded that the pore system evolution is dictated by the primary rock texture and mineralogy, as well as by burial processes. Reduction of the available pore spaces is driven by compaction processes, precipitation of mineral phases in the form of cements, and migration of bitumen (Aplin et al., 2011; Chalmers and Bustin, 2015; Milliken and Day-Stirrat, 2013; Tiab and Donaldson, 2004). In contrast, an increase in the pore volumes can be given by chemical dissolution of mineral phases (Baruch et al., 2015; Loucks et al., 2010; Schieber, 2013) and, as previously mentioned, the maturation of the organic matter. In the gas window, the high surface areas of generated organic nanopores are found to be critical for the adsorbtion and storage of large amounts of gas (Chalmers et al., 2017; Curtis et al., 2011; Loucks et al., 2010, 2009; Ross and Bustin, 2009; Wang and Reed, 2009). It was also observed that the migration of hydrocarbons, by migrating through the pore network, coats the mineral surfaces and inhibits the precipitation of further mineral phases by reducing the number of possible nucleation sites for cements (van Duin and Larter, 2001; Worden et al., 1998).

1.8. Pore surface wettability variations

Apart from inhibiting the cementation of new mineral phases, the migration of hydrocarbons also affects the wettability of mineral surfaces (Anderson, 1986; Basu and Sharma, 1997; Tölke et al., 2010). The wettability, in turn, strongly influences the productivity and the distribution of the hydrocarbons in a reservoir (Abdallah et al., 2007; Anderson, 1986; Mirchi et al., 2014). When a reservoir is oil-wet, pore surfaces retain more oil and the recovery rates are lower compared to a more water-wet reservoir. Unravelling the driving mechanisms that alters the wettability, therefore, contributes to the interpretation of the whole pore system behaviour and evolution. Wettability studies on hydrocarbon reservoirs brought to light that wetting behaviours can change at the nanometre scale and can evolve through time (Brown and Fatt, 1956; Buckley, 1998; Holbrook and Bernard, 1958). Many wettability studies focus on rendering an oil-wet reservoir more water-wet, increasing in this way the productivity; the alteration of the wettability and can be done by adding surfactants to the system or by reducing the overall salinity of the brine (Acevedo et al., 1992; Ahmadi et al., 2018; Alvarez et al., 2014; Andersen et al., 2016; Austad et al., 1997; Ayirala et al., 2006; Bryant et al., 1991; Feng and Xu, 2015; Kumar et al., 2005a; Penny et al., 2012; Standnes and Austad, 2000; Zhang and Somasundaran, 2006). Before adding surfactants in the production phase, however, it is necessary to understand how wettability changes depending on different properties. Previous works observed that wetting behaviours depend on many factors, such as the physiochemical conditions, the brine chemistry, the capillary pressure, the oil chemistry, the surface chemistry and surface roughness (Hiorth et al., 2010). Given the number of parameters that the wettability depends on, it is only possible to observe how they affect the system by analysing them separately. In the work done in this thesis, the factors that are considered are the chemistry of the oil interacting with the surface and the surface chemistry.

1.9. The Eagle Ford pore system

Despite the success of this formation, further work needs to be done in order to better decipher the pore system and its controlling factors, especially considering future requirements to effectively manage the resources in a mature field. Several studies in the

recent years have analysed the porosity of the Eagle Ford (Anovitz et al., 2014; Chalmers et al., 2017; Ko et al., 2017; Ojha et al., 2017; Pommer et al., 2014; Schieber et al., 2016). In particular, Anovitz et al. (2014) studied the evolution of porosities with maturity combining SEM imaging and small angle neutron scattering (SANS). The data showed that the porosity of the system is highly dependent on the mineralogy and thermal maturity of the samples. However, the study does not give a detailed analysis of the samples and the pores. Ko et al. (2017), using a multi-technique approach, investigated the Eagle Ford pores and pore network in a quantitative way. Their samples, however, did not consider the evolution of the pore system as a function of maturity. Chalmers et al. (2017) took into account the thermal maturity of the samples, but the study only analysed the evolution of the organic matter without considering the impacts of the burial diagenesis on the rest of the porosity. Schieber et al. (2016) offered a detailed, but not quantitative investigation of the pore types and their evolution with burial diagenesis. However, none of these studies offers a quantitative analysis of the pore system in terms of changes in thermal maturity, and none has integrated a surface chemistry study to the petrological and physical characterisation of the pore system. Therefore, this thesis aims to cover all the points that have been neglected by previous works.

1.10.The multi-scale, multi-technique approach

Quantifying pore properties such as distribution, shape and surface chemistry can ultimately enhance well performance and production. However, the porosity assessment requires a methodical approach and the combination of several techniques (Bustin et al., 2008; Saidian et al., 2014). It is essential to determine the factors that influence pore structure and connectivity, specifically the rock texture, the mineralogy and the diagenetic processes that have occurred in the formation. Here, bulk rock analytical techniques, namely X-ray powder diffraction, Rock Eval and TOC measurements, have identified the bulk mineral composition of the samples, their organic matter content and hydrocarbon generation potential. Petrological studies as transmitted and reflected optical microscopy and scanning electron microscope (SEM) imaging have allowed the identification of the main components of the samples and to distinguish the microfacies and the depositional settings. Interpretation of diagenetic processes and textural

variability is performed through the integration of bulk mineralogy analyses, optical and electron microscope imaging, as well as Energy Dispersive X-ray spectroscopy (EDS) and cathodoluminescence (CL) mapping and X-ray computed tomography (XR-CT). Once the framework in which the pores were formed and evolved is reconstructed, quantification of the porosity and of the pore system connectivity is assessed. This is done using a multi-technique approach; SEM and EDS high magnification and high-resolution analyses measured the quantity, shapes and area fraction of pores as well as distinguished the pores in different types depending on their relationship with the bulk rock. N_2 and CO_2 gas adsorption and Mercury Injection Capillary Pressure (MICP) were used to assess the pore size distribution, the pore connectivity and pore volumes. Focused Ion Beam (FIB) reconstructed volumes distinguished the organic matter pores and helped to visualise and quantify the connectivity of the organic and non-organic pores. Given the different scales at which sample properties vary, a combination of these techniques was necessary in order to provide an accurate understanding of the pore system. Moreover, samples from the immature, oil and gas window were analysed and compared to decipher the pore system evolution with maturity.

Pure calcite crystals are also used to test how different oil compounds changed the surface wetting properties at the nanoscale, by using Chemical Force Microscope (CFM) analyses and Atomic Force Microscope (AFM) combined with a nano-infrared (IR) source. Chips of Eagle Ford samples were then studied using the CFM methodology combined with EDS chemical mapping of the same areas. This tested the variability of the wetting behaviour at the nanoscale and its variability on different mineral surfaces. AFM-IR analyses were also performed for the first time on rock chips to test the methodology and to target nano-chemical variations on the same mineral surface given by organic compounds. Finally, AFM-IR was used on organic compounds on polished rock samples. This allowed the chemical variations of different organic matter types with maturity to be understood and to place these variations into a wetting behaviour context.Thesis layout

This thesis is presented in forms of journal-style chapters. Each of the four data chapters (chapters 3-6) contains an introduction, a methodology, a result, a discussion and a conclusion paragraph. Some repetitions may occur in terms of methodology and concepts. The data chapters are preceded by an introduction and proceeded by a final

discussion and conclusion chapter that binds together the main findings of this work (Chapter 6). The data chapters contain some contributions to existing studies and mostly novel data and are therefore intended to be submitted in relevant academic journals in the near future. The data, apart from the XRD, Rock Eval and MICP analyses, were all collected by myself. The processing and interpretation of the data was completed by myself with the guidance of my supervisors.

Chapter 2: *Reconstruction of diagenetic processes in the Eagle Ford Formation based on petrographical studies across a maturity gradient.*

This chapter is a petrographical study of the samples. It aims to describe the samples in terms of composition, domains and microfacies. Through a qualitative and quantitative analysis of the samples, the main diagenetic processes were identified and placed in a precise thermal window. Different pore types were also distinguished and positioned in the microfacies and burial history context.

Chapter 3: *Characterization of the porosity system of the Eagle Ford Formation as a function of diagenesis and maturity*.

This chapter is a characterisation of the pore system of the Eagle Ford samples, taking into account the framework in which the pores formed and evolved. It quantitatively describes the pore properties, volumes and pore system connectivity by combining observations from different techniques. Moreover, it integrates the pore system attributes and thermal history evolution with the petrographical study of chapter 2.

Chapter 4: *AFM study of adhesion forces on calcite surfaces aged in different oil compounds.*

Chapter 4 focuses on the surface chemistry variations in relation to the exposure of the surfaces to different oil fractions. Pure calcite surfaces first aged in brine and then in oil compounds with variable molecular weight aim to represent the carbonate-rich Eagle Ford rock surfaces. Variations of quantitative measurements at the nanoscale are translated into wetting changes. Changes in measurements from sample to sample are then correlated to the chemical changes of the oil compounds. This experimental study also aims to test and validate the Chemical Force Microscope (CFM) methodology that was used on rock chips in chapter 6.

Chapter 5: *Nanoscale variations in surface chemistry and implications for wettability in the Eagle Ford Formation.*

In this chapter the surface chemistry variations at the micro and nanoscale in relation to the mineralogy of the samples are described. State-of-the-art workflows for the wettability measurements at the nanoscale are tested; the combination of different techniques allowed to associate the relative changes in wettability to different mineral compounds. Moreover, nanometric chemical changes were also detected on the surfaces of coccolithic debris and associated to the presence or absence of certain organic compounds. Finally, chemical variations of the different organic matter types at different maturities were observed and associated to the wettability changes.

Chapter 2

Reconstruction of diagenetic processes in the Eagle Ford Formation based on petrographical studies across a maturity gradient

2.1. Introduction

Studying organic-rich mudstones from a petrographical point of view is a crucial step in the assessment of the resources and in the understanding how these resources can be extracted. Detailed description of diagenetical and textural variations has important implications in the prediction of lateral distribution and of reservoir properties such as porosity, permeability and rock strength (Schieber et al., 2016).

However, interpretation of the depositional and diagenetic history of mudstones is complicated by their textural and mineralogical heterogeneity and by their typical micrometre grain-size. Mudstones can be deposited in a large variety of environments and throughout their depositional history undergo a series of physical and chemical processes, which can be reconstructed by means of petrographical and geochemical studies.

2.1.1. Mudstone heterogeneity

Variations in mineralogy and texture at the micron-scale are determined by sediment supply, sea-bottom conditions during deposition, the nature of the depositional environment and the chemical and mechanical changes through time (Macquaker and

Bohacs, 2007; Schieber, 1991). In turn, the mineral and organic constituents of the rocks, as well as their diagenetic history, control the pore system (Allen et al., 2014; Aplin and Moore, 2016; Bernard et al., 2013a, 2012a; Chalmers et al., 2012; Clarkson et al., 2013b; Czerniakowski et al., 1984; Hemes et al., 2016; Higgs et al., 2007; Houben, 2013; Jennings and Antia, 2013; Katsube and Williamson, 1994;. Klaver et al., 2015a; Kuila et al., 2014; Loucks et al., 2009; Mathia, 2014; Milliken et al., 2013; Pommer et al., 2015; Ross and Marc Bustin, 2009; Rutter et al., 2017; Wang and Reed, 2009; Worden and Morad, 2000; Yang et al., 2015). Both mechanical and chemical processes affect pore size distributions, permeability and the capability of the rock to be fracked during the production phase (Aplin et al., 2011; Bernard et al., 2010; Dawson and Almon, 2010; Jarvie et al., 2007; Katsube and Williamson, 1994; McAllister et al., 2015; Taylor et al., 2014).

2.1.2. Mechanical and chemical compaction

Mechanical compaction occurs at shallow depths (< 2.0 km) and low temperatures (< 60-80 ^{0}C) and is mainly a function of the effective stress and grain strength and size (Aplin et al., 2006; Bjorlykke, 1998; Fabricius, 2003; Goulty, 1998). Evidence of mechanical compaction can be observed in the reduction of porosity and in the re-alignment of the mineral grains perpendicular to the stress direction. Chemical compaction, on the other hand, mainly depends on the chemical kinetics controlling the dissolution and precipitation of the minerals (Aplin and Macquaker, 2011; Bjorlykke, 1998; Fabricius, 2007; Gorniak, 2016; Mallon and Swarbrick, 2008; Peltonen et al., 2009). Common evidences for chemical compaction in mudstones are dissolution of mineral grains and cements, replacement of mineral phases and pressure-solution stylolites (Fishman et al., 2012; Jason E Heath et al., 2011; Rashid et al., 2015). These reactions begin during the deposition and continue throughout the burial history of the sediments, progressively modifying the porosity and the pore system (Dewhurst et al., 1998; Gorniak, 2016).

2.1.3. Sedimentology and diagenesis of fine-grained, organic-matter rich carbonates

This study is an effort to understand the sedimentology and diagenesis of a carbonate and organic-matter rich formation, the Eagle Ford. This formation is often defined generally

as a mudstone or, in industry terms, as a shale (Dawson, 2000; Hsu and Nelson, 2002; Jennings and Antia, 2013; Jiang et al., 2013; Mullen, 2010; Rylander et al., 2013; Tian et al., 2018; Workman, 2013). Nonetheless, these terms are geologically inaccurate due to the presence of large amounts of carbonates, which outdistance the Eagle Ford from a characteristical mudstone. Previous studies on the Eagle Ford (Driskill et al., 2012; Ergene, 2014; Pommer et al., 2015) and, more in general, on carbonate-rich tight reservoirs (Lønøy, 2006; Mathia et al., 2016; Pahnke, 2014) show that large amounts of carbonates (> 50%) have also large impact on the sedimentology, the diagenesis, and consequently the whole pore system evolution; the rigid carbonatic structure is believed to prevent high degrees of compaction as it would occur in clay-rich formations, which are more ductile and prone to be deformed and compacted when exposed to mechanical stresses (Bennett et al., 1991). As previously mentioned, prevention of compaction also determines preservation of interparticle and intraparticle pores (Loucks et al., 2012; Milliken and Day-Stirrat, 2013; Ohiara et al., 2017; Schieber, 2010). On the other hand, carbonates are highly affected by chemical compaction processes. In other studies on carbonate-rich tight formations, carbonates are found to undergo dissolution and reprecipitation processes throughout the whole maturity sequence (Czerniakowski et al., 1984; Jennings and Antia, 2013; Mathia et al., 2016; McAllister et al., 2015). Moreover, high amounts of faecal pellets and foraminifera are often found to play an important role in the whole pore system and pore connectivity (Ergene, 2014; Laughrey and Ruble, 2013; Mcallister, 2017; Ríos et al., 2016; Slatt, 2011). In this study, the role of the carbonates and the bioclasts, as well as the whole interpretation of sedimentological and diagenetic processes that have taken place in the pore system origin and evolution, is assessed.

2.1.4. Eagle Ford petrography

Various authors have already analysed the Eagle Ford Formation from a petrographic point of view (Driskill et al., 2012; Ergene, 2014; Mcallister, 2017; Milliken et al., 2016; Pommer and Milliken, 2015), but given the high lithological heterogeneities, this sample set is unique. Moreover, in previous studies, either the analysed microfacies were not equivalent (Ergene, 2014), or the samples did not cover the whole maturity range (Driskill et al., 2012; Mcallister, 2017; Schaiberger, 2016). Pommer (2014) and Pommer and Milliken

(2015) analysed a very similar sample set to the one used in this thesis. However, the petrographic studies are mainly focused on the evolution of pore types with thermal maturity and were only performed by means of Scanning Electron Microscope (SEM) analyses.

2.1.5. Samples from different maturities

As the samples analysed in this present study were collected from outcrops and wells at different depths in south-west Texas, changes in fabric and mineralogy with increasing maturity can be examined. These samples range from thermal maturities of R_0 0.4% to 1.2%, corresponding to temperatures between ~50° and 120° C respectively. This thermal range constitutes the range in which most of the chemical reactions take place. Moreover, having samples of the same lithostratigraphy at different maturities is crucial to determine at which temperature and under which conditions hydrocarbon migration and trapping have occurred (Chen et al., 2016). The large range of burial depths and thermal maturities also allows the identification of the specific time and temperature frames at which the diagenetic processes and the porosity evolutions have taken place. As previously mentioned, the lithological heterogeneity of the samples at multiple scales, together with the variations in mineralogy, burial history and depositional environments, strongly controls the reservoir properties (Dawson et al., 2008). The work presented in this chapter is an effort to define the organic matter content and type, the presence of sedimentary structures, the mineral replacements and the horizontal lithological variations, which are amongst the factors that can influence the reservoir characteristics.

2.2. Materials and methodology

2.2.1. A multi-technique approach

The samples in this present study were examined with a varied range of techniques: XRD data provided information on the mineralogy of the samples and Rock-Eval® and TOC give insights into the nature of organic matter and on the hydrocarbon generation potential. The petrology and textural analysis were performed by transmitted and reflected optical microscopy and by X-ray computed tomography (CT). Ar-ion milled samples were also analysed with an SEM, enabling the different components and pore

types to be examined at the nanometre scale. In addition, cathodoluminescence (CL) and Energy Dispersive X-ray analysis (EDS) data were taken to help reconstruct the paragenesis and depositional setting of the samples. The different resolutions and scales (nanometer to the centimetre sizes) at which the samples were analysed provide a more general understanding of the whole sedimentology and diagenetic sequence of the Eagle Ford formation.

2.2.2. Depositional environment

The understanding of the depositional environment changes leads to decipher paleoenvironmental changes such as sea-level fluctuations, uplift and burial. These changes, in turn, have important implications for reservoir quality. For instance, they can provide information on the lateral continuity or vertical heterogeneity of the sediments. Until recently, it was generally thought that fine-grained sediments enriched in organic carbon were deposited in low-energy settings with persistent anoxic levels in bottom water (Potter et al., 2005). However, new findings have brought to light that mudstones are deposited at different sedimentation rates, levels of oxygen and energy environments (Abbott, 2000; Aplin and Macquaker, 2011; Macquaker et al., 2010; Macquaker and Bohacs, 2007; Schieber, 2011, 2003; Schieber and Southard, 2009; Wignall et al., 1994). The preservation of organic matter, vital for the creation of good quality source rocks, is dictated by factors like primary production rate, water column depth and depletion of oxygen from the sediments (Hedges and Keil, 1995). Moreover, the seabed depositional environment also affects the bacterial reduction of sulphate to sulphide, which is responsible for the precipitation of pyrite and the degradation of organic matter (Jørgensen, 1982).

2.2.3. Geological background

2.2.3.1. Study area

The Eagle Ford Formation is widespread across South and East Texas, attaining approximately a width of 80 km (50 mi) and a length of 650 km (400 mi) (Figure 2.1) The sets of samples that are investigated in this thesis were taken from outcrops and six different wells (Figure 2.2).

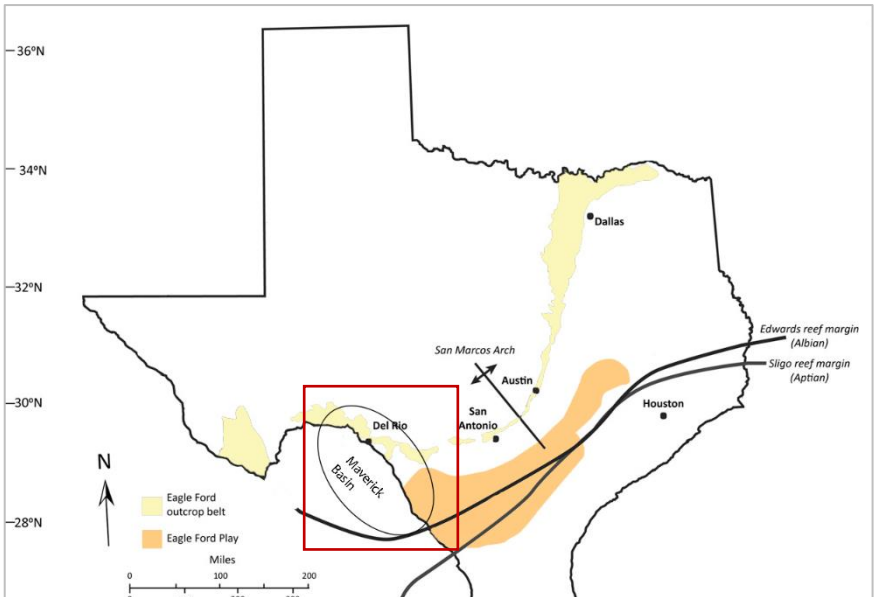

Figure 2.1. Map of Texas showing modern location of the Eagle Ford outcrops and play (modified after Lowery et al. 2012). The red square indicates the study area.

2.2.3.2. Regional stratigraphy

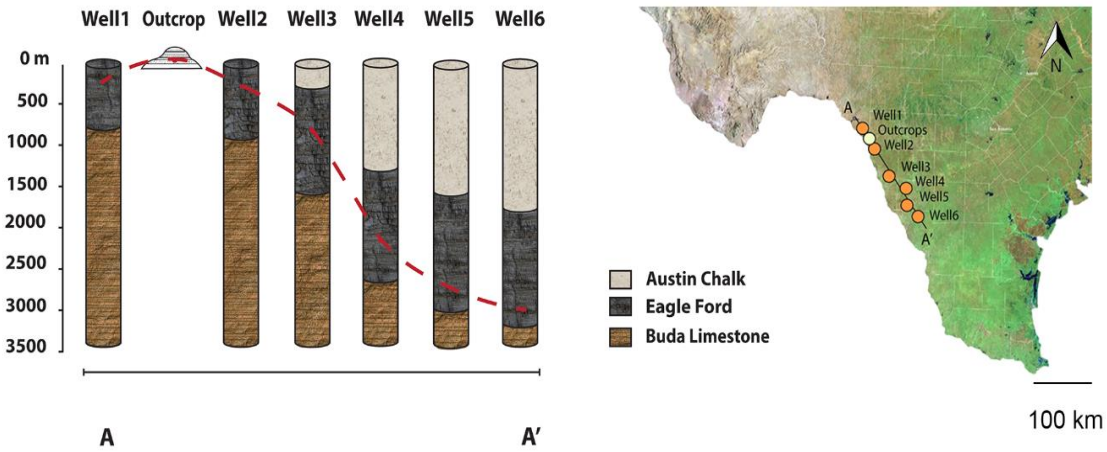

Figure 2.2. On the left, schematic diagram of the wells and the depths at which the samples were taken. On the right, a map of Texas with the samples locations.

The formation deepens and dips southwards and thickens towards the South-East (Donovan et al., 2012; Pathak et al., 2014). It is indeed found in outcrops, in the North-West part of Texas as well as in the subsurface, up to ~4,755 m (~15,600 ft) deep at the Sligo shelf margin (Figure 2.3). Lithologically, the formation overlies the Buda Limestone and underlies the Austin Chalk, and can be distinguished in two units. The Lower Eagle Ford is a carbonate-rich (40-90% CaCO3) source rock with TOC% values of ~6% and HI of ~500mgHC, while the Upper Eagle Ford is less organic-rich (1-3% TOC) and presents a higher carbonate content (50-100%) (Liro et al., 1994b; McAllister et al., 2015). As it becomes deeper towards the southeast, the temperature and thermal maturity increase and the formation gradually transitions three different maturity windows: oil, wet gas and finally dry gas (Figure 2.3).

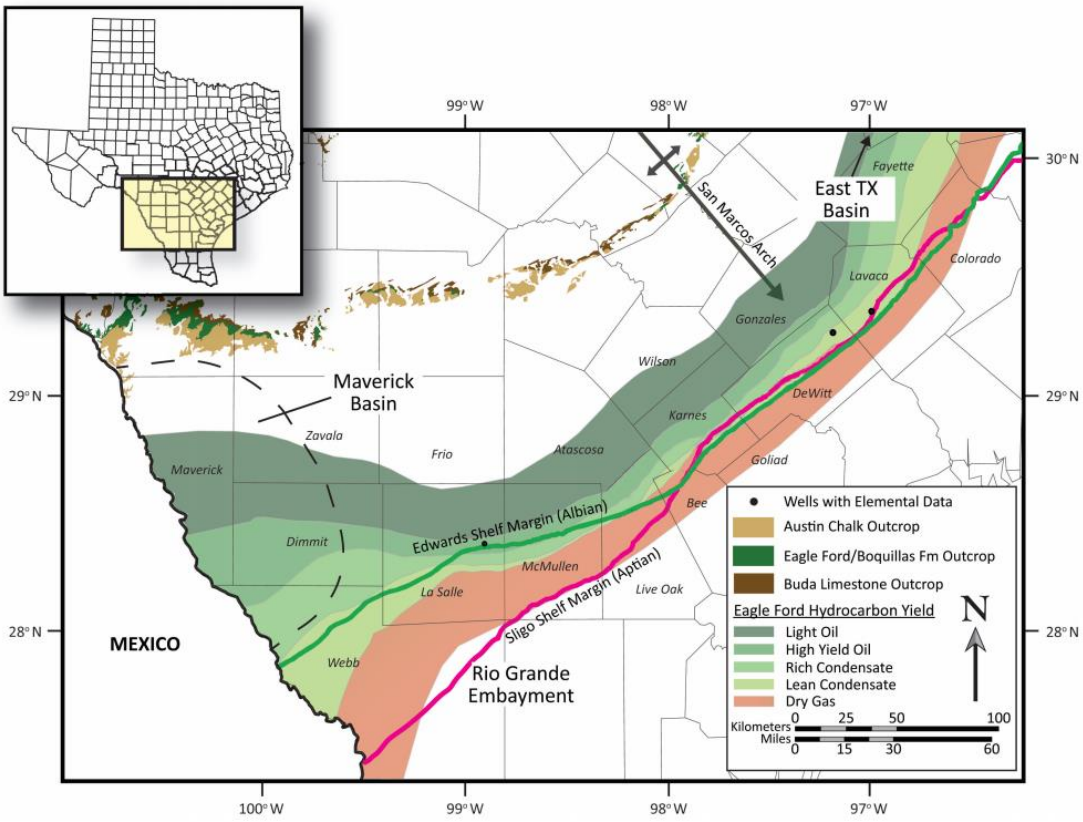

Figure 2.3: Eagle Ford location map with the different maturity windows. In green: oil, in light green condensate and in red dry gas (modified after Tinnin and Darmaoen, 2016).

2.2.3.1. Geological setting

In the studied area, the Eagle Ford Shale was deposited during the Upper Cretaceous on the Commanche Platform (Figure 2.4). This late Jurassic-Early Cretaceous platform resulted as an amalgamation of a carbonate shelf complex developed between the proto-Gulf of Mexico and the Western Interior Seaway (KWIS) of North America (Lowery et al., 2014) (Figure 2.2).

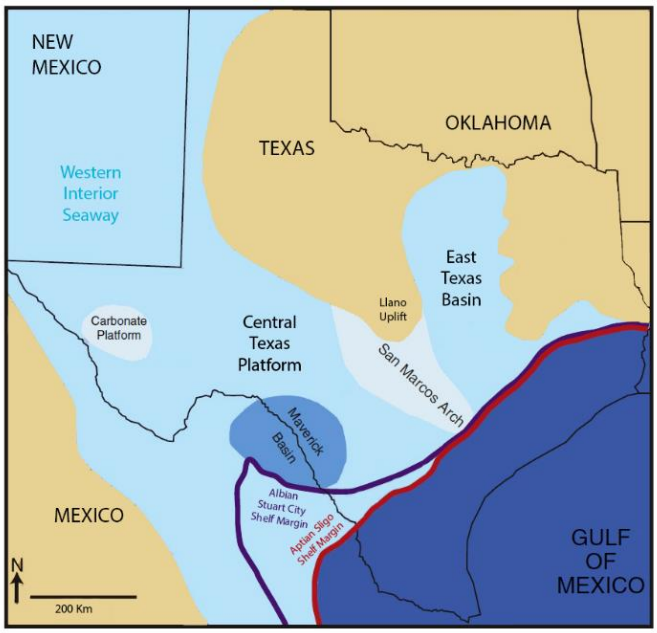

Figure 2.4: . Paleogeography map of Texas modified after Denne et al. (2014).

Eagle Ford sedimentation began as part of a major transgression that drove the sediment deposition from a shelf margin towards intrashelf depocenters (Galloway, 2008). The sediments overlie the Buda Limestone and were deposited irregularly along the play according to its bathymetric and structural features such as the San Marcos Arch and the shelf margins Sligo and Stuart City (Hentz and Ruppel, 2010). These topographic highs experienced lesser subsidence compared to the confining basinal environments, resulting in a considerable variation of the sea depth through the Seaway (50 to 300 meters) (Driskill et al., 2012; Eldrett et al., 2014; Harbor, 2011). As a result, the formation thinned abruptly at the top of the topographic highs with respect to the basinal areas (Harbor and Ruppel, 2011), reaching the maximum thickness of 63 m and 146 m for the Lower and Upper Eagle Ford in the Maverick intra-shelf basin (Hentz and Ruppel, 2010)

Moreover, the San Marcos Arch divided the Texas carbonate platform into two major environments, discerned by the different sediment type. The East Texas basin is characterised by a larger amount of siliciclastic influx (quartz and plagioclase) coming from the river-dominated deltas that prograded from the North and ended in the marine shelf of East Texas (Jennings and Anthia, 2013). The river input is blocked by the San Marcos Arch that renders the West Basinal area more carbonate-rich and less clay and siliciclastic-rich.

The deposition of the Eagle Ford formation occurred between 98 and 91 Ma, covering the transition from Cenomanian to Turonian. This boundary also corresponds to the triggering of the OAE2, a global phenomenon characterised by a worldwide Carbon Isotope positive excursion (CIE) and global anoxic greenhouse conditions (Eldrett et al., 2014). The OAE2 in South Texas is manifested with a shallow sea where the circulation patterns created areas of upwelling along the shelf margin that resulted in the proliferation of microorganisms and to the abundance of organic matter on the seafloor (Denne et al., 2014). The scarcity of oxygen in the bottom-waters permitted high amounts of organic matter to be preserved and buried along with the fine-grained sediments, originating the Eagle Ford mudstones (Lowery et al., 2014). The sediments in the Cretaceous Western Interior Seaway, in particular within the Lower Eagle Ford Formation, were deposited as rhythmically interbedded limestones and marls. Thin layers of bentonites, rich in kaolinite and smectite clay minerals are also found, testifying a sporadic volcanic activity in the inland (Denne et al., 2014; Donovan et al., 2012). Recent studies have interpreted the driving mechanism of these sequences as a combination of astronomic forcing cycles (Eldrett et al., 2015). According to Eldrett et al. (2015), the marls are associated with insolation minima, stratified waters, reduced carbonate and silica production and high organic matter preservation (TOC 2-13 wt. %). On the other hand, the limestone beds are linked to insolation maxima, that led to the destratification of the water column and therefore to less effective preservation of the organic matter (TOC < 1.5wt. %) (Eldrett et al., 2015). Carbonates are mainly composed of coccoliths, benthic and planktonic foraminifera and in less abundance of echinoids and bivalves. Biogenic silica is interpreted to be produced by siliceous plankton (i.e. radiolaria) (Denne et al., 2014; Driskill et al., 2012; Lowery et al., 2014).

In turn, the Lower and Upper Eagle Ford sediments are distinguished by a decrease in gamma-ray values, given by thorium and uranium components, from the Lower to the Upper Eagle Ford. The decrease in gamma-ray values is attributed to the increase in carbonate content and a decrease in organic matter and bentonites (Denne et al., 2014). On an outcrop, the sediments can be distinguished by the dark-grey colour of the lower Eagle Ford mudrocks and the interbedded dark and light-grey mudrocks in the upper Eagle Ford (Figure 2.5).

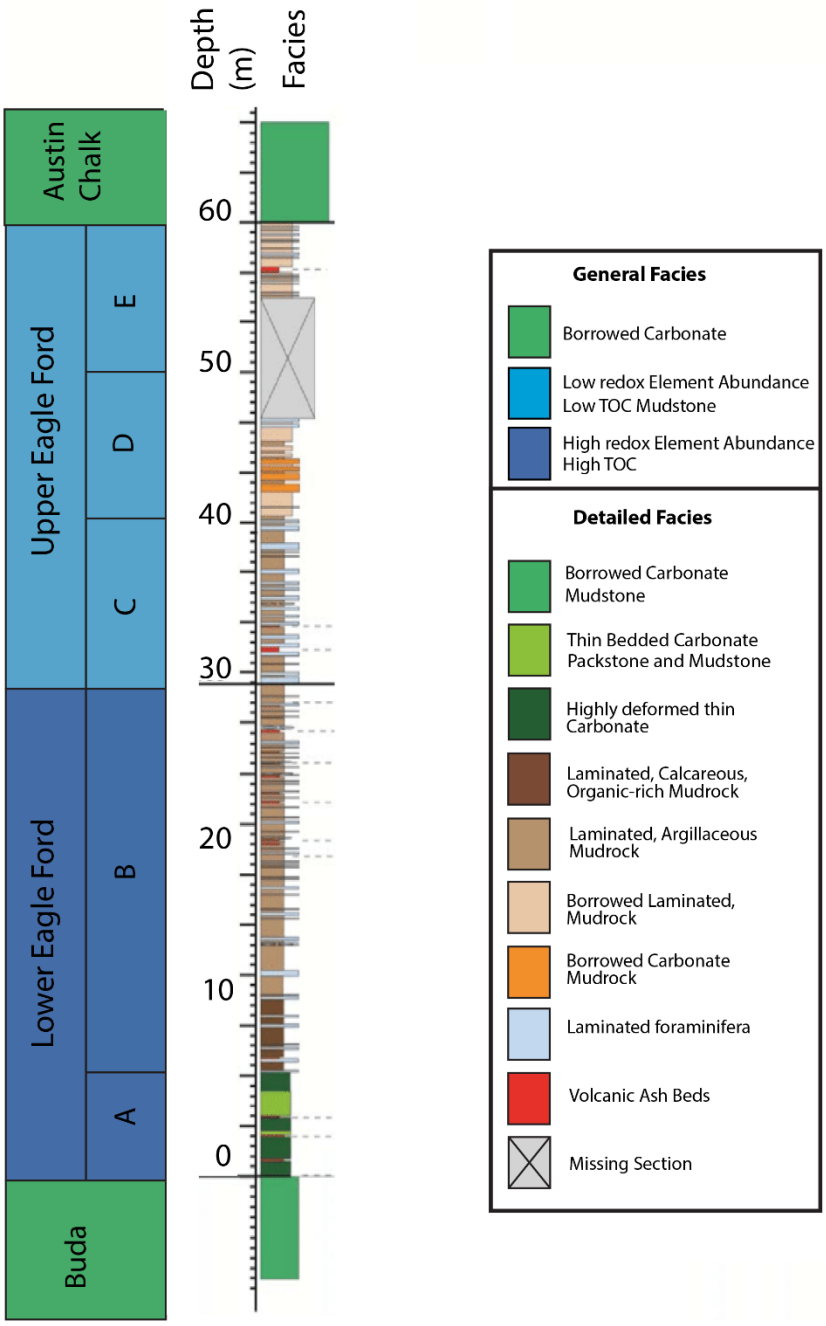

Figure 2.5: : Stratigraphic column of an outcrop location of the study area (after Pierce et al. 2016).

2.2.4. Samples and techniques

The samples analysed were collected from outcrops in Val Verde County, Texas, and from six different wells in South-West Texas (**Error! Reference source not found.**2). The samples were taken at depths ranging between 400 m above mean sea level (AMSL) to -4500 m AMSL, resulting in samples from three different thermal maturity windows: R_0 0.4-0.5%, R_0 0.9% and R_0 1.2% (immature, oil and gas window). This allows us to study lithological and diagenetic changes with an increase in temperature.

2.2.4.1. Mineralogy and bulk characterization

A set of 25 rock samples from outcrops and 6 wells at a range of maturities was provided by Shell. The bulk composition of the samples was determined in 17 of these samples using XRD at the James Hutton Institute, Aberdeen, UK. The whole rock analysis was performed on randomly-oriented powders. The samples were wet ground in ethanol using a McCrone micronizing mill and then spray-dried to produce the necessary random powder (Hillier, 2000). The powder X-ray diffraction (XRD) patterns were recorded from 4° to 70° 2θ using Copper Kα radiation. Along with the XRD data, the cation exchange capacity (CEC) of the samples was provided. The CEC is used to quantify the cations that a clay mineral can accommodate on its negatively charged surface (expressed in milli-equivalent per 100 grams). In particular, the measured CEC value is used to quantify the smectitic percentage in the Illite/Smectite (I/S) clay mineral group present in the bulk rock and to estimate a virtual I-S expandability of the group. Rock-Eval® and TOC analyses were performed by APT, Norway, using, respectively, a LECO SC-632 and a Rock-Eval-6 instrument. Prior to the analyses the samples were ground using a mortar and carbonate was removed by adding diluted HCl. The measurements were taken by heating the samples from 300 °C to 650 °C at a rate of 25 °C per minute.

2.2.4.2. Optical microscopy

12 thin sections (30 μm thick) were provided by the Shell Technology Centre laboratories, TX, US. Two sets of 17 thin sections from the available rock samples were also prepared

at Wagner Petrographic, US. The first set of thin sections was cut 30 μm thick and parallel to bedding and the other set, 100 μm thick, was cut perpendicular to the bedding.

For the optical microscopy analyses, a Leica DM2500P transmitted light petrography microscope was used for the 30 μm thin sections and a Leica DM1750M reflected light microscope was used for the 100 μm thin sections. The organic petrology analyses were completed at Newcastle University using a Leica DM2700P incident light microscope. The oil immersion technique with white and blue light was used, with a magnification of 50 ×. Point counting analyses were carried on the 30 μm thick thin sections using JMicrovision™ software. The point counting was based on 300 points at a magnification of 10 ×.

2.2.4.3. Scanning Electron Microscopy (SEM)

SEM images at high resolution were collected at Durham University using a Hitachi SU-70 FEG SEM, with a voltage of 10 kV, a working distance of 15 mm and a variable magnification of 500x to 10k x. The samples were 3 mm diameter cores cut using a Gatan ultrasonic cutter from 100 μm thick thin sections and Ar-ion polished using a Gatan Precision Ion Polishing system for 5 hrs at a beam angle 3° and 5 kV. The thin sections were all cut perpendicular to bedding. After polishing, the samples were carbon-coated to avoid charging, to reduce thermal damage and to improve the secondary electron signal. Backscattered (BSE) and secondary electron (SE) images were taken simultaneously in order to analyse both solid phases and porosities respectively. By qualitatively looking at the samples under the SEM, all the samples exhibit recurring components that can be distinguished in 5 groups: fossils and microfossils (in order of abundancy foraminifera, bivalves, calcispheres, radiolaria, fish bones), faecal pellets, pyrite, organic matter and matrix. These groups, called here domains, have distinctive characteristics in terms of pore types or mineralogy. In order to distinguish and quantify the domains, high resolution (4096 × 3349 pixels) SEM images for areas of 1 mm × 1mm at a magnification of 600 × were taken on all the 18 analysed samples. In the same areas, using the Oxford Instruments EDX system (X-MaxN 50 Silicon Drift Detector) attached to the Hitachi SU-70 FEG SEM, elemental identification was also conducted. The EDX maps were taken at a resolution of 1024 × 884 pixels, an energy range of 20 keV and a

dwell time of 250 μs. In order to identify and quantify the pore types, 4 areas of 50μm × 50μm were randomly chosen on each sample. The areas were chemically analysed with the EDX system of the Hitachi SEM, that allowed the pore types to be distinguished, and with an FEI Helios Nanolab 600, that allowed segmentation of the pores. This instrument has the advantage of producing more stable, better quality high magnification secondary electron images compared to the Hitachi SU70. Each area consisted of a montage of 20 high resolution (4096 × 3349 pixels) and high magnification (10 kx) images measuring 12.74 μm in width and 10.3 μm in height. The pixel size for the high magnification pictures was 3.1 nm, but the smallest pore was defined by 6 pixels (i.e. ~ 18 nm diameter). The images were taken using the instrument immersion mode, at 1.50 kV, 4.0 mm working distance and a dwell time of 10 μs. On the same samples, CL work was also performed using the Gatan Mono-CL system associated with the SEM. Areas of magnification of 600 to 1 k x were analysed using a panchromatic filter.

2.2.4.4. X-ray Computed Tomography (XRCT)

Five samples were scanned using the Xradia Zeiss Versa XRM-410 instrument at Durham University. Two samples (IM1_3 and GW6) were cores of 2.6 cm diameter and 1.2 cm height, whereas the other three cores were 5 mm in diameter and ~0.8 cm height. All the scans were performed using a standard LEI filter, and the scans were performed with a pixel size of 2.8 μm/pixel. The 3D volume and the processing of the data were performed using the software Avizo™ version 9.4 and a non-local means filter was applied to the raw data. In all the samples a cylindrical subvolume was extracted using the *Volume edit* function in Avizo™. The different greyscales in the scanned volumes correspond to different densities, and therefore different materials. The contrast between the greyscale led to the segmentation of five different phases. As the densities for some materials are similar, the greyscale contrast is too low to discriminate all the materials. In this case, a combination of phases is used in the segmentation. From the brightest (denser) to the darkest (less dense), the discriminated materials were: pyrite, carbonates, carbonates mixed with clay minerals, clay minerals and OM combined with pores. The segmentations were then, where available, validated using the XRD data (Table 2.1).

Sample Name	Maturity (R_0%)	Microfacies Type	Total Carbonates (%)	Total Silicates (%)	Total Clays (%)	TOC (wt %)
OW2	0.9	A	43.2	8.0	42.1	2.6
GW6	1.2	B	77.9	14.3	3.2	2.4
IM1_3	0.5	A	25.5	21.0	45.5	NA
IM2_3	0.4	A	50.1	24.2	9.0	7.9
IM2_5	0.4	A	NA	NA	NA	NA

Table 2.1: Samples of different maturities and microfacies analysed by XR-CT with the corresponding XRD data. NA = not available data.

In order to calculate the heterogeneities of the samples, the area fraction % of each phase was calculated for each slice parallel and perpendicular to the bedding (Figure 2.6). For this, the *Volume Fraction in xy* tool in Avizo™ was used. The average value of each phase was calculated by measuring the whole volume fraction in 3D.

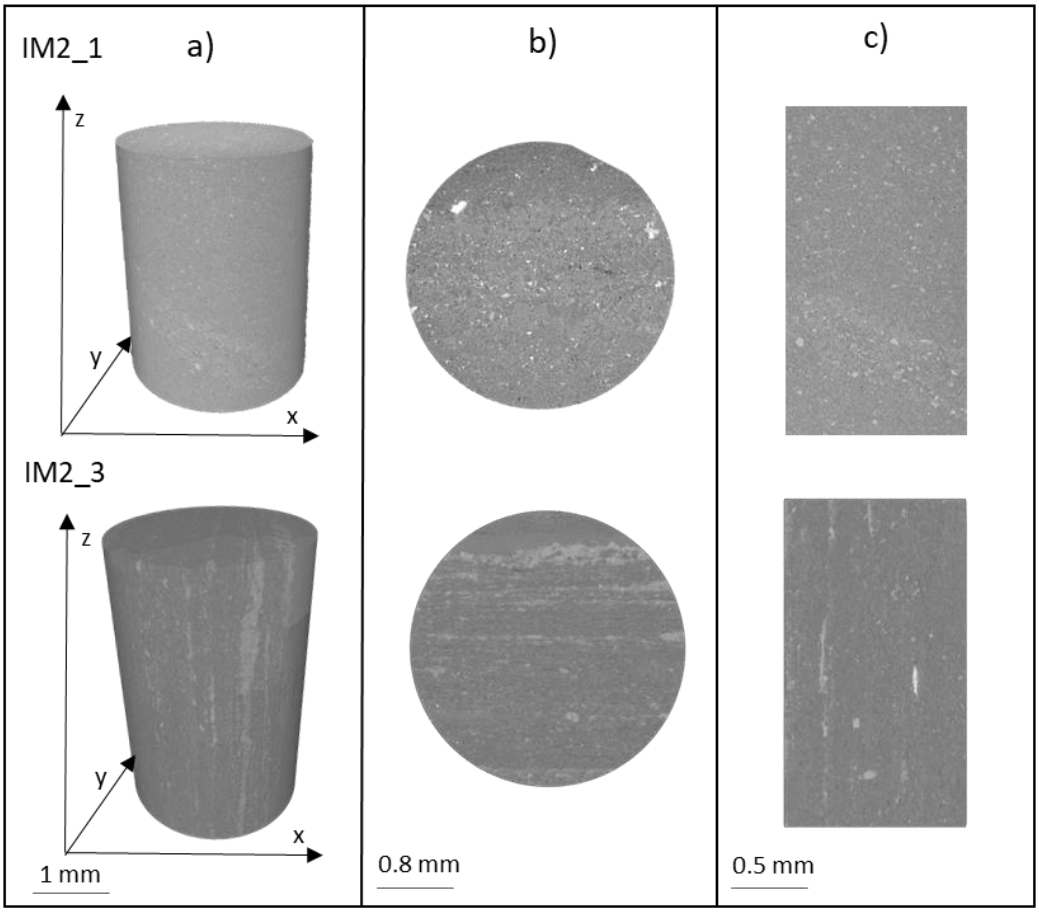

Figure 2.6: XRCT scans for samples IM2_1 (microfacies B, R_0 0.5%) and IM2_3 (microfacies A, R_0 0.5%). a) is the whole cylindrical masked volume in which the heterogeneity percentages were calculated. b) is a slice perpendicular to the bedding. The heterogeneity ca lculated on these slices (along the z plane) will be called along bedding. c) is a slice taken parallel to the bedding. The heterogeneity calculated on these slices will be called across bedding.

2.3. Results:

2.3.1. Bulk rock composition

XRD compositional analyses reveal significant vertical and lateral mineralogical variability. The most common mineralogical constituents are, in decreasing average volume content: calcite (59.6%), quartz (16.3%) and the clay mineral phases mixed illite/smectite (7.3%) and kaolinite (5.7%) followed by organic matter (3.4%) and pyrite (1.5%) (Table 2.2). Secondary minerals are plagioclase, k-feldspar, dolomite, ankerite, gypsum, apatite and marcasite. A variation with thermal maturity in the mineralogical content is observed for quartz and kaolinite, that decrease with the increase in maturity (Figure 2.7). Quartz content is on average ~24% in the immature window and ~11% in the oil and gas window. Kaolinite decreases from an average of ~13% in the immature and oil window to an average of ~1% in the gas window. Mixed I/S and calcite, on the other hand, starts to increase from the oil maturity window, from an average of 6% for the immature window to an average of ~10% for the oil and gas window. Na-plagioclase also increases, from 0% to 2%. K-feldspar is only present in the immature and oil window samples (on average ~1% of the bulk mineral content). Gypsum occurs only in the outcrop samples. TOC varies from 0.4% to 7.9%, reflecting the variable but sometimes high amount of organic matter in these samples and shows a general decrease with the increase in maturity (**Error! Reference source not found.**). Along with the bulk mineralogy of the samples, the CEC of the clays was also measured (Table 3.0). The CEC values for these samples range between 0.5 and 9.1 meq/100 g and is positively correlated to the amount of mixed I/S (Figure 2.8).

Sample Names	Microfacies Type	V. Reflectance (R_{o} %)	Well number	Depth (m)	Calcite (%)	Dolomite (%)	Ankerite (%)	Siderite (%)	Pyrite (%)	Quartz (%)	K feldspar (%)	Plagioclase (%)	Kaolinite (%)	I/S (%)	TOC (wt %)	Total clays (%)	Total carbonates (%)	Total Si-licates (%)	CEC
OC1	A	0.4	Outcrop	outcrop	50.5	1.3	0.6	0.1	1.1	30.6	1.5	0.4	3.3	4.4	4.4	7.7	52.5	32.5	1.6
OC2	A	0.4	Outcrop	outcrop	57.8	0.0	0.4	0.0	1.2	19.3	0.6	0.1	5.6	3.4	6.6	9.0	58.2	20.0	0.7
OC3	A	0.4	Outcrop	outcrop	49.8	0.2	0.3	0.0	1.3	23	1.2	0.1	6.6	5.0	5.5	11.6	50.3	24.3	0.8
IM1_1	A	0.4	1	71.8	45.2	0.0	0.6	0.5	2.2	21.7	2.6	0.4	8.1	9.8	4.5	17.9	46.3	24.7	5.5
IM1_2	A	0.4	1	74.9	33.8	1.3	1.5	0.5	2	30.2	0.8	0.2	25.8	1.6	6.3	27.4	37.1	31.2	4
IM1_3	A	0.4	1	94.5	24.8	0.3	0.0	0.4	5.1	20.7	0.0	0.3	43.0	2.5	N/A	45.5	25.5	21.0	N/A
IM2_1	A	0.5	2	73.73	34.9	0.0	1.4	0.0	2.2	31.5	1.6	0.1	12.9	6.6	5.8	19.5	36.3	33.2	2.1
IM2_2	B	0.5	2	73.53	75.4	0.0	0.7	0.1	0.2	18.4	0.4	0.0	3.9	0.8	1.9	4.7	76.2	18.8	1.2
IM2_3	A	0.5	2	148.4	50.1	0.0	0.0	0.0	2.2	22.4	1.5	0.3	1.8	7.2	7.9	9.0	50.1	24.2	3.8
OW1	A	0.9	3	973.2	56.6	0.6	0.0	0.3	1.6	18.9	0.6	4.1	3.6	12.6	5.0	16.2	57.5	23.6	N/A
OW2	A	0.9	3	961.8	41.6	0.6	0.9	0.1	2.2	3.6	0.1	4.3	24.0	18.1	4.5	42.1	43.2	8.0	9.1
GW1	A	1.2	4	2556.3	56.8	0.0	0.1	0.3	2	13.6	0.1	0.9	1.9	18.5	3.5	20.4	57.2	14.6	8.2
GW5	B	1.2	4	2556.7	64.7	0.0	0.1	2.4	0.6	8.9	0.5	0.7	1.0	12.5	1.6	13.5	67.2	11.3	5.8
GW4	B	1.2	4	2532.5	61.0	10.3	1.6	0.1	1	12.7	0.2	2.7	0.0	8.3	1.0	8.3	73	15.6	1

Sample Names	Microfacies Type	V. Reflectance (R_{o} %)	Well number	Depth (m)	Calcite (%)	Dolomite (%)	Ankerite (%)	Siderite (%)	Pyrite (%)	Quartz (%)	K feldspar (%)	Plagioclase (%)	Kaolinite (%)	I/S (%)	TOC (wt %)	Total clays (%)	Total carbonates (%)	Total Silicates (%)	CEC
GW3	B	1.2	4	2547.9	83.4	0.0	0.3	0.1	0.5	5.4	0.1	1.4	0.0	4.4	0.7	4.4	83.7	6.9	2.2
H3A 1	B	1.2	4	2526.2	79.5	0.4	0.0	0.1	0.3	15.4	0.0	1.5	0.2	2.5	1.0	2.7	79.9	15.4	N/A
H3A 2	A	1.2	4	2527.8	58.4	0.3	0.0	0.1	1	25.7	0.5	3.9	0.4	9.2	3.0	9.6	58.7	25.7	N/A
H3A 3	A	1.2	4	2547.4	44.5	0.0	0.0	0.2	2.8	13.5	0.6	5.2	3.3	28.5	5.4	31.8	44.5	13.5	N/A
H3A 4	B	1.2	4	2547.9	90.7	0.0	0.0	0.0	0.4	5.4	0.0	1.3	0	1.4	0.7	1.4	90.7	5.4	N/A
H3A 5	A	1.2	4	2548.6	50.7	0.0	0.1	0.2	3.9	10.6	0.6	7.4	1.3	21.8	6.0	23.1	50.7	10.6	N/A
H3A 6	B	1.2	4	2558.3	95.7	0.0	0.0	0.0	0.1	4.1	0.0	0.1	0	0	0.2	0.0	95.7	4.1	N/A
GW6	B	1.2	5	2797.9	71.0	6.4	0.4	0.1	0.2	13	0.5	0.8	0.0	3.2	2.4	3.2	77.9	14.3	N/A
GW2	B	1.2	5	2802.2	79.5	2.7	0.4	0.3	0.4	12.3	0.1	0.7	1.6	1.4	2.3	3.0	82.9	13.1	0.5
GW7	C	1.2	6	3014.5	73.7	0.0	0.2	0.7	2.1	6.2	0	0.5	0.0	12.2	0.7	12.2	74.6	6.7	2.9
GW8	C	1.2	6	3014.8	83.8	0.1	0.3	0.2	1.2	3.9	0.1	0.5	0.0	7.0	0.5	7.0	84.4	4.5	1.3

Table 2.2: Bulk mineralogy data, microfacies type and CEC. The N/A sign indicates that the data are not available, as the sample was not analysed.

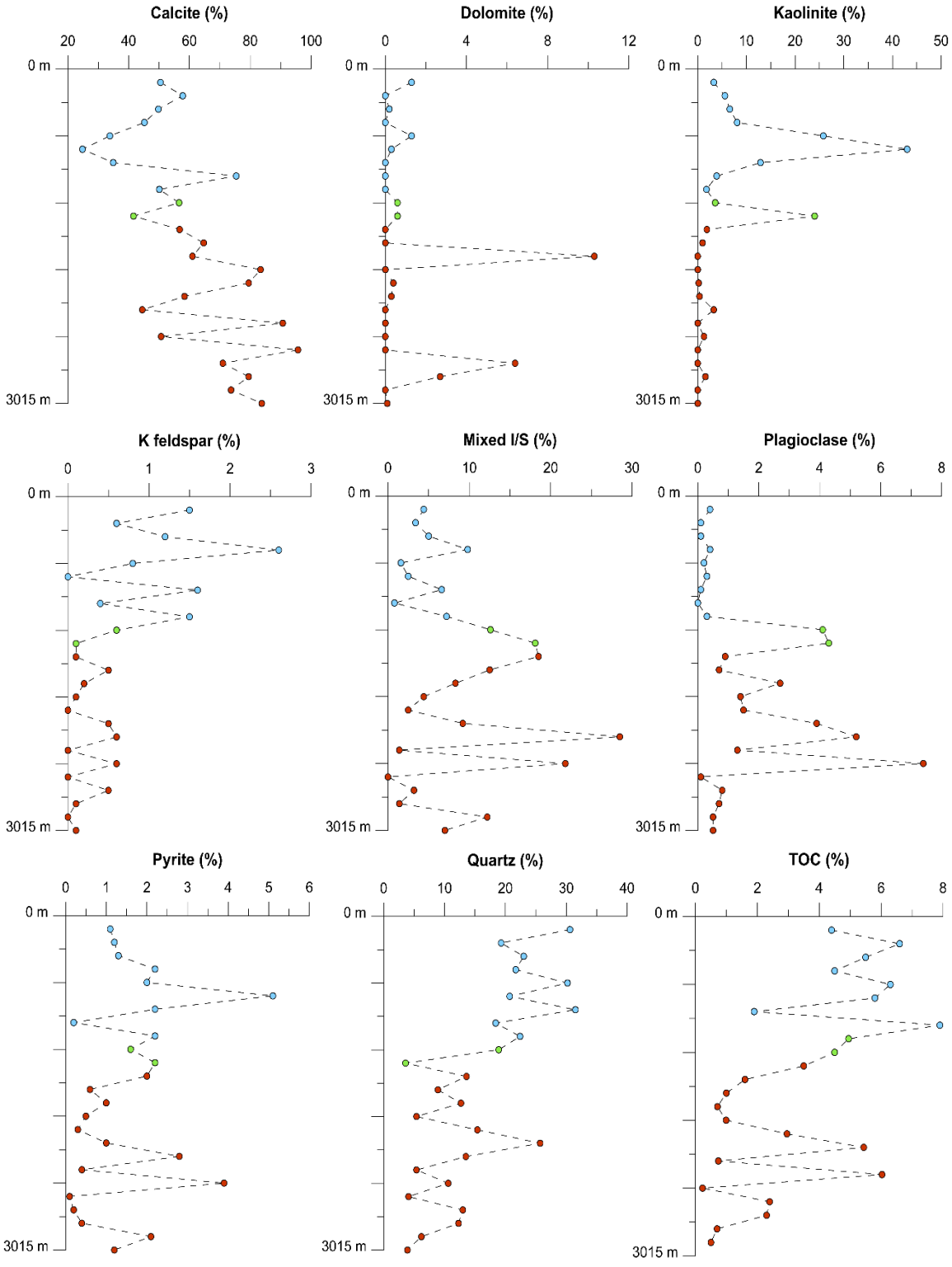

Figure 2.7: Plots of the most common minerals vs depth for all the samples analysed with XRD in all microfacies. Each point corresponds to a sample, and the colours represent the different maturities (blue, R_0 0.5%; green, , R_0 0.9%; red, , R_0 1.2%).

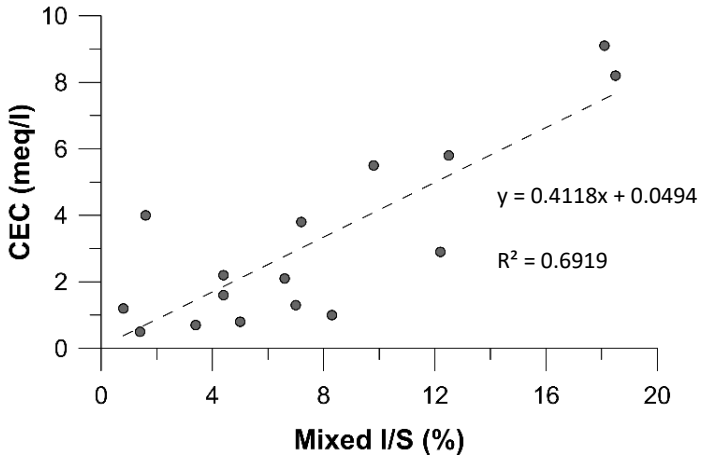

Figure 2.8: CEC (meq/l) vs mixed-layer I/S (%) plot for the samples analysed (see table 3.0 for more details).

2.3.2. Rock-Eval

Rock-Eval analyses are reported in Table 2.3. The Van Krevelen diagram (Hydrogen Index vs Oxygen Index) underlines two families of samples (Table 2.3).

Sample Names	LECO TOC (wt%)	S1 (mg HC/g)	S2 (mg HC/g)	S3 (mg CO2/g)	Tmax (°C)	Hydrogen Index (S2x100/TOC)	Oxygen Index (S3x100/TOC)	S1/TOC Norm. Oil	Production Index (S1/(S1+S2)
OC1	4.4	3.0	22.4	0.5	435	507	10	68	0.12
OC2	6.1	2.2	36.6	0.7	426	602	12	36	0.06
OC3	4.6	2.0	34.8	0.9	428	761	19	44	0.06
IM2_1	5.8	2.7	32.5	0.4	433	562	7	46	0.08
IM2_2	2.1	1.1	15.2	0.3	433	723	13	53	0.07
IM2_3	6.3	3.0	46.6	0.9	433	736	13	48	0.06
OW1	5.0	5.4	27.1	0.5	445	547	11	108	0.17
OW2	3.6	2.8	13.8	0.4	444	383	11	78	0.17
GW1	3.9	3.3	2.7	0.6	475	69	16	86	0.55
GW3	0.7	0.6	0.7	0.4	425	98	53	89	0.47
GW4	1.0	0.8	0.8	0.3	449	80	32	75	0.48
GW7	0.4	0.5	0.8	0.3	441	195	78	115	0.37
GW8	0.6	0.3	0.4	0.3	432	66	49	53	0.45
H3A 1	1.0	0.8	0.6	0.4	468	63	35	82	0.57
H3A 2	3.0	2.0	1.3	1.1	469	44	36	68	0.61
H3A 3	5.4	6.5	4.8	1.2	477	87	22	119	0.58
H3A 4	0.7	0.7	0.5	0.4	431	72	47	96	0.57
H3A 5	6.0	5.7	3.5	1.1	473	58	18	95	0.62
H3A 6	0.2	0.1	0.2	1.1	440	78	483	57	0.42

Table 2.3: Rock Eval Data. The Hydrogen, Oxygen and Production Index were also calculated for each sample analysed.

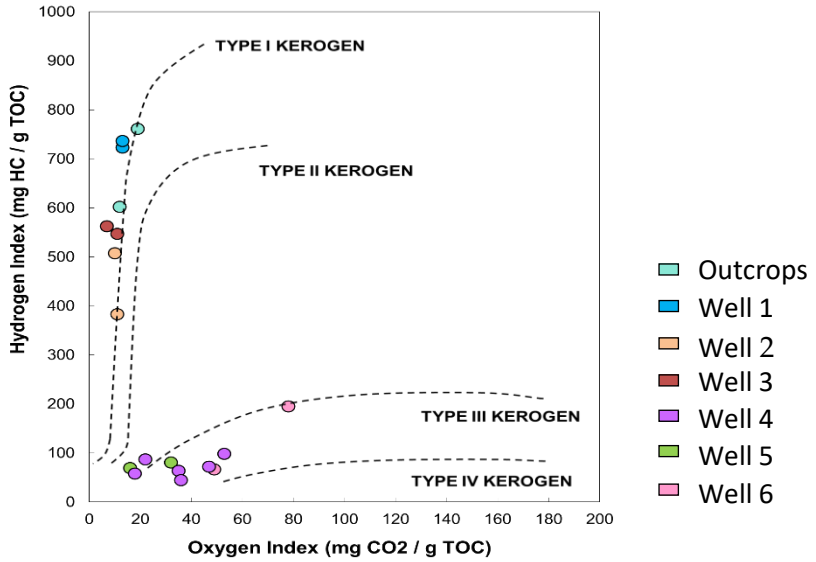

Figure 2.9: Van Krevelen diagram showing two families of samples. The immature samples (outcrops, wells 1, 2) have a high Hydrogen index and a low Oxygen Index. The samples in the oil and gas window (well 3, 4, 5) have a low Hydrogen index.

The immature samples (R0 0.4%-05%) have a high Hydrogen Index (between 383 and 761 mg HC/g TOC) and a low Oxygen Index (7 to 19 mg CO2/g TOC), whereas the oil and gas maturity samples present a low (<200 mg HC/g TOC) Hydrogen Index and higher (between 16 and 78 mg CO2/g TOC) Oxygen Index. The plot also shows the original kerogen type (i.e. the kerogen that has not generated any hydrocarbons) is a type I-II oil-prone marine kerogen. The temperature of maximum S2 generation, Tmax, ranges between 425 °C and 477 °C and confirms that the samples are situated within the oil window generation range, except for samples GW1, H3A1, H3A2, H3A3 and H3A5 that have a Tmax higher than 465 °C and lie instead within the gas window maturity (Figure 2.10). The S2 peaks (mg HC/g) decrease significantly from the immature samples, with a maximum of 46.6 mg HC/g (IM2_3, Ro 0.5%) to the gas window, with a minimum of 0.2 mg HC/g (H3A6 R0 1.2%). However, caution must be taken when interpreting the data for the mature samples with low TOC values (i.e. samples GW3, GW7 and GW8). For these samples, the data collected are poor as S2 peaks are too small to be meaningful.

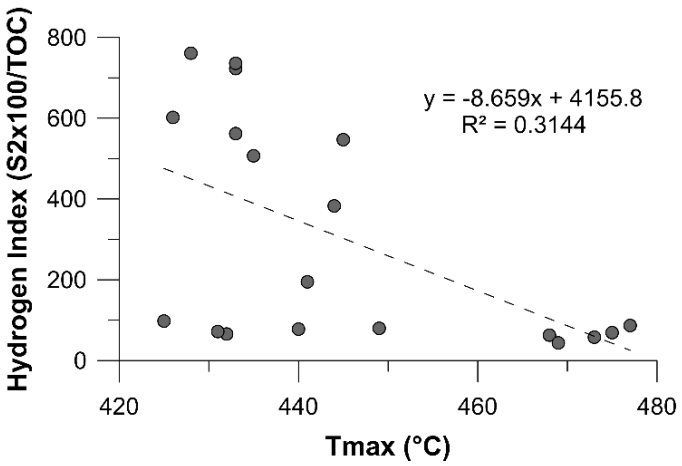

Figure 2.10: Hydrogen Index (S2x100/TOC vs Tmax (°C) for all the samples analysed using the Rock Eval method, at all maturities.

2.3.3. Petrographic studies

2.3.3.1. Domains

Five domains were distinguished in these samples: fossils, matrix, faecal pellets, pyrite and organic matter (Figure 2.11).

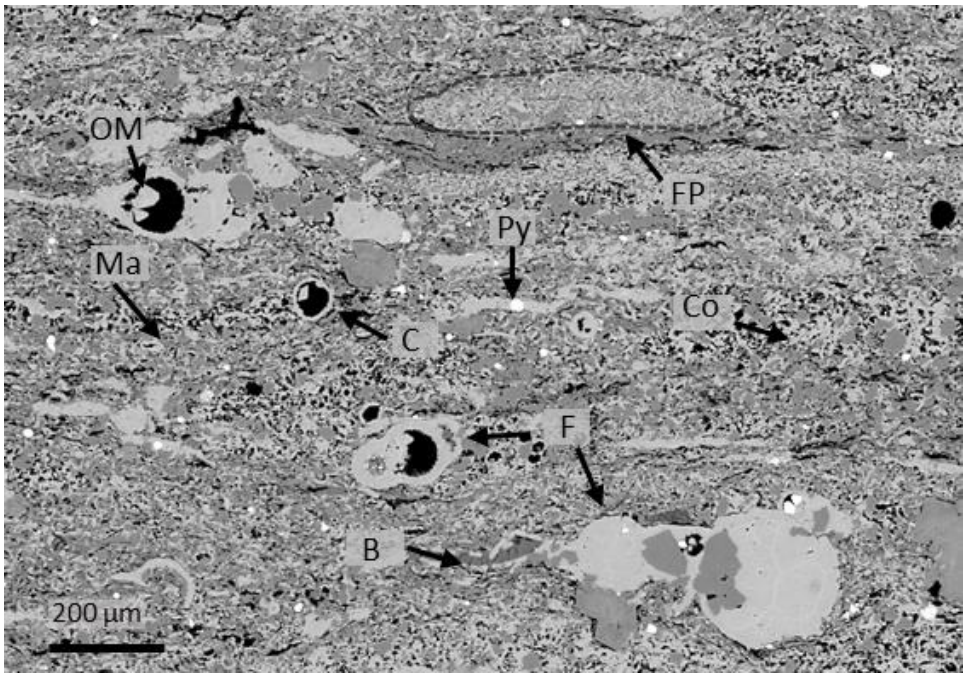

Figure 2.11: SEM BSE image of sample IM1_2 (R_0 0.5%), highlighting the domains present in the samples: Faecal Pellets (FP), Matrix (Ma), Organic matter (OM), Pyrite (Py) and Fossils: Coccoliths (Co), Bivalve Shells (B), Foraminifera (F).

For the organic matter, the organic petrology results are also included. The thin sections analysed and the corresponding maturity and microfacies types are the samples listed in Table 2.3.

Table 2.3

2.3.3.2. Microfossils

Sample Names	LECO TOC (wt%)	S1 (mg HC/g)	S2 (mg HC/g)	S3 (mg CO2/g)	Tmax (°C)	Hydrogen Index (S2x100/TOC)	Oxygen Index (S3x100/TOC)	S1/TOC Norm. Oil	Production Index (S1/(S1+S2)
OC1	4.4	3.0	22.4	0.5	435	507	10	68	0.12
OC2	6.1	2.2	36.6	0.7	426	602	12	36	0.06
OC3	4.6	2.0	34.8	0.9	428	761	19	44	0.06
IM2_1	5.8	2.7	32.5	0.4	433	562	7	46	0.08
IM2_2	2.1	1.1	15.2	0.3	433	723	13	53	0.07
IM2_3	6.3	3.0	46.6	0.9	433	736	13	48	0.06
OW1	5.0	5.4	27.1	0.5	445	547	11	108	0.17
OW2	3.6	2.8	13.8	0.4	444	383	11	78	0.17
GW1	3.9	3.3	2.7	0.6	475	69	16	86	0.55
GW3	0.7	0.6	0.7	0.4	425	98	53	89	0.47
GW4	1.0	0.8	0.8	0.3	449	80	32	75	0.48
GW7	0.4	0.5	0.8	0.3	441	195	78	115	0.37
GW8	0.6	0.3	0.4	0.3	432	66	49	53	0.45
H3A 1	1.0	0.8	0.6	0.4	468	63	35	82	0.57
H3A 2	3.0	2.0	1.3	1.1	469	44	36	68	0.61
H3A 3	5.4	6.5	4.8	1.2	477	87	22	119	0.58
H3A 4	0.7	0.7	0.5	0.4	431	72	47	96	0.57
H3A 5	6.0	5.7	3.5	1.1	473	58	18	95	0.62
H3A 6	0.2	0.1	0.2	1.1	440	78	483	57	0.42

The fossils can be either carbonatic (foraminifera, calcispheres, coccoliths, bivalves, inoceramids, pelecypods, ostracods, sponges and corals, echinoderm and crinoid plates and spiculae), silicic (radiolarians) or phosphatic (fish bones). The pelecypods are thin-shelled filaments of shells, thought to be at the larval or juvenile stage. They are occasionally found clustered in micrometric-size laminations. The calcispheres are interpreted to belong to the *Pithonella* species. The foraminifera can be in turn be distinguished as planktonic (*Globorotalia*, *Globotruncana*, *Heterolix Striata*) and, in minor abundances, benthic (*Bulimina*) or agglutinates (Figure 2.12). These interpretations are in accordance with the work by Denne et al. (2014). As the size of foraminifera can

potentially provide insights on the depositional environment, for each sample 100 foraminifera were measured along their long axis analysing the thin sections (Table 2.4). For the samples analysed, the smaller foraminifera average size is observed in sample IM1_3 (39 μm) and the largest in sample IM2_5 (106 μm). No correlation between size and maturity was found. The fossil percentages were also calculated by point counting (Table 2.4). The fossils were distinguished between bivalves, phosphatic shells, foraminifera, radiolaria, echinoids and calcispheres. In the point counting, euhedral calcite crystals were also taken into account. Foraminifera are the most common fossil type and vary between an average of 61% for microfacies A, 46% for microfacies B and 24% for microfacies C (Table 2.5). The foraminifera were also distinguished between the most common four classes (Table 2.6). In all wells and at all maturities, the majority of the foraminifera studied are Heterolix and Globorotalia. Calcispheres are also common at all depths. They reach 34% of the total most frequent fossil types in sample GW4 (R_0 1.2%).

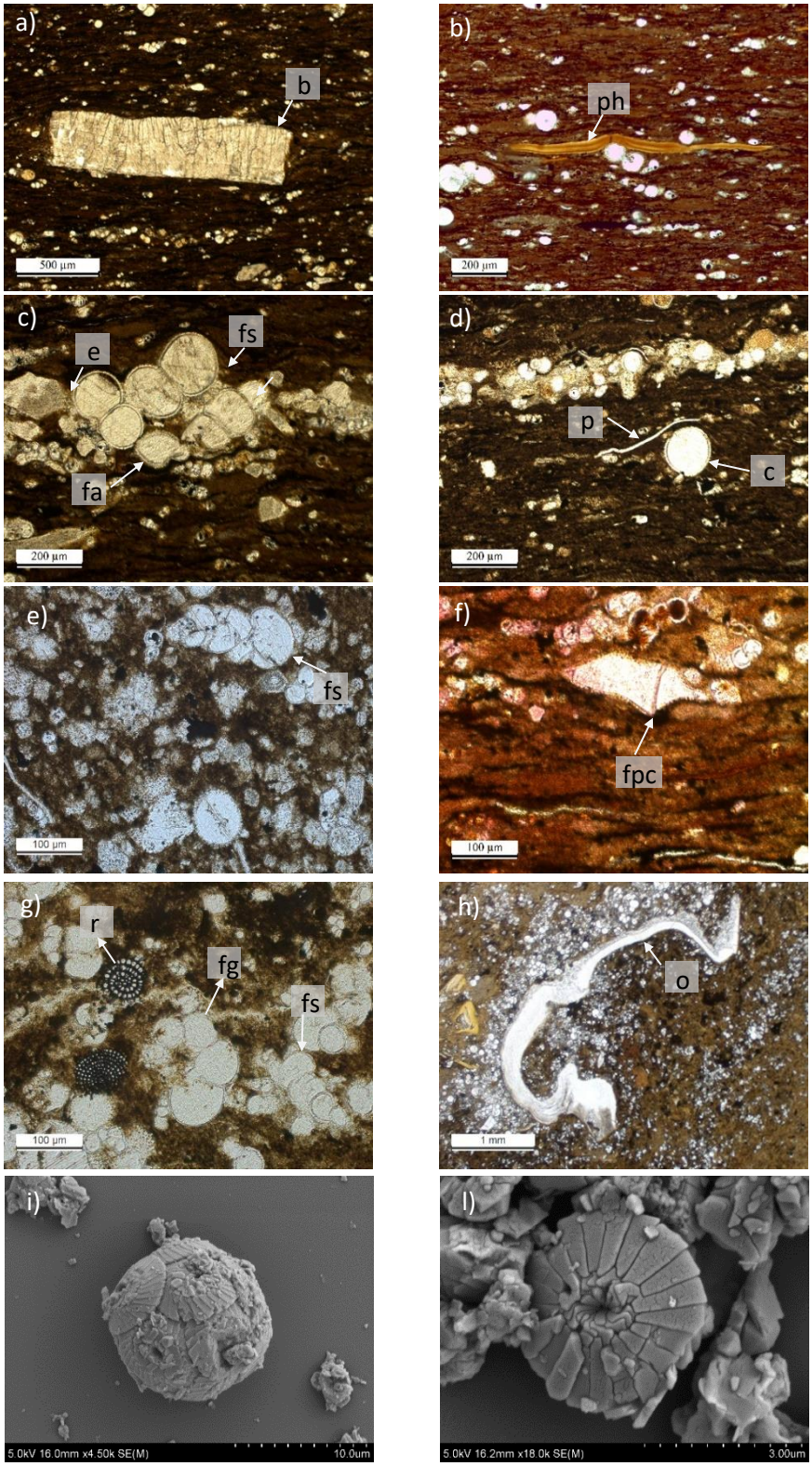

Figure 2.12: Images of fossils under thin section and SEM SE light (i and l) a) calcitic bivalve shell (b); b) phosphatic shell (fh); c) echinoderm plates (e), serial foraminifer (Heterolix striata) (fs), agglutinated foraminifer (fa); f) foraminifer with polygonal chambers (Globotruncana) (fpc); g) foraminifer with rounded chambers (Globorotalia) (fg), pyritised radiolaria (r); h) oyster shell (o); i) intact coccollitosphere l) intact coccolith

Sample Name	OC6	OC7	0C2	IM1_2	IM1_3	OC1	OC2	OC3	IM2_4	IM2_3	IM2_7	IM2_5	IM2_3	IM2_2	OW7	OW8	OW2	OW1	GW1	GW4	GW9	GW2	GW6
V.Reflectance (R_0 %)	0.4	0.4	0.4	0.4	0.4	0.4	0.4	0.4	0.5	0.5	0.5	0.5	0.5	0.5	0.9	0.9	0.9	0.9	1.2	1.2	1.2	1.2	1.2
Foram size (μm)	73.4	84.2	42.1	59.0	39.4	60.5	96.3	93.5	40.2	67.7	50.9	105.6	55.7	48.9	50.9	69.2	53.3	100.2	42.1	68.6	42.6	52.3	91.9

Table 2.4: Average foraminifera size (μm) for the samples analysed and corresponding vitrinite reflectance (R_0 %).

Samples names	Microfacies Types	V. Reflectance (R_0 %)	Depth (m)	Bivalves (%)	Phosphatic shells (%)	Foraminifera (%)	Calcite euedral crystals (%)	Echinoids (%)	Calcispheres (%)	Radiolaria (%)
OC1	A	0.4	outcrop	8	7	71	3	1	10	0
OC2	A	0.4	outcrop	9	9	62	6	4	8	0
OC3	A	0.4	outcrop	5	3	65	20	2	5	0
IM1_1	A	0.4	74.9	9	0	81	0	0	10	0
IM1_2	A	0.4	94.5	55	0	42	3	0	0	0
IM2_1	A	0.5	73.7	2	5	51	10	29	3	0
IM2_2	B	0.5	73.5	0	3	1	96	0	0	0
IM2_3	A	0.5	148.4	12	14	54	10	0	7	0
OW1	A	0.9	973.2	7	9	70	5	0	9	0
OW2	A	0.9	961.8	5	0	76	4	5	10	0
GW1	A	1.2	2556.3	4	0	71	2	12	11	0
GW5	B	1.2	2556.7	8	0	56	8	3	25	0
GW4	B	1.2	2532.5	19	1	54	9	0	10	7
GW2	B	1.2	2802.2	12	0	39	2	0	34	3
GW6	B	1.2	2797.9	18	0	45	2	0	26	0
GW7	C	1.2	3014.5	0	5	23	13	27	30	2
GW8	C	1.2	3014.8	23	4	24	7	26	16	0

Table 2.5: Percentages of the different fossil types distinguished in the samples. The calcite euhedral crystals are also taken into account.

Samples names	Microfacies Types	V. Reflectance (R_0 %)	Depth (m)	Serial (*Heterolix*) (%)	Rounded chambers (*Globorotalia*) (%)	Polygonal chambers (*Globotruncana*) (%)	Agglutinated (%)
OC1	A	0.4	outcrop	37	53	6	4
OC2	A	0.4	outcrop	41	49	7	3
OC3	A	0.4	outcrop	63	37	0	0
IM1_1	A	0.4	74.9	58	35	4	3
IM1_2	A	0.4	94.5	42	36	8	14
IM2_1	A	0.5	73.7	93	7	0	0
IM2_2	B	0.5	73.5	0	2	0	0
IM2_3	A	0.5	148.4	35	60	3	2
OW1	A	0.9	973.2	17	50	30	3
OW2	A	0.9	961.8	26	45	9	20
GW1	A	1.2	2556.3	80	20	0	0
GW5	B	1.2	2556.7	60	30	10	0
GW4	B	1.2	2532.5	38	62	0	0
GW2	B	1.2	2802.2	32	68	0	0
GW6	B	1.2	2797.9	41	59	0	0
GW7	C	1.2	3014.5	88	12	0	0
GW8	C	1.2	3014.8	98	2	0	0

Table 2.6: Percentage of the different foraminifera types distinguished in the samples.

2.3.3.3. Matrix

In thin section under transmitted light, the matrix appears as a micritic compound, whereas under the SEM, the different components forming the matrix can be distinguished. On average, the matrix is composed of micron-sized coccolithic debris (by more than 40%), carbonates (~5%), pyrite (~2-3%), clay minerals (~20%), silicates (~15%) and organic matter (~15%) (Figure 2.11).

2.3.3.4. Faecal pellets

Faecal pellets are a major rock-forming constituent. They are carbonate aggregates formed by zooplanktons (copepods) (Hattin, 1975). On average, they measure between 70 μm to 200 μm and in the samples analysed reach up to 800 μm. The faecal pellets are considered a separate domain from the matrix as they are formed predominantly by coccolithic debris (~90%) and organic matter, whereas the clay minerals and the silicates are in very minor

abundance (~5%). They can be very common: on a 1mm x 1mm area, for example, in samples OC2 and OC3 ~50 specimens were recognised, occupying ~24% of the sample surface (Figure 2.13).

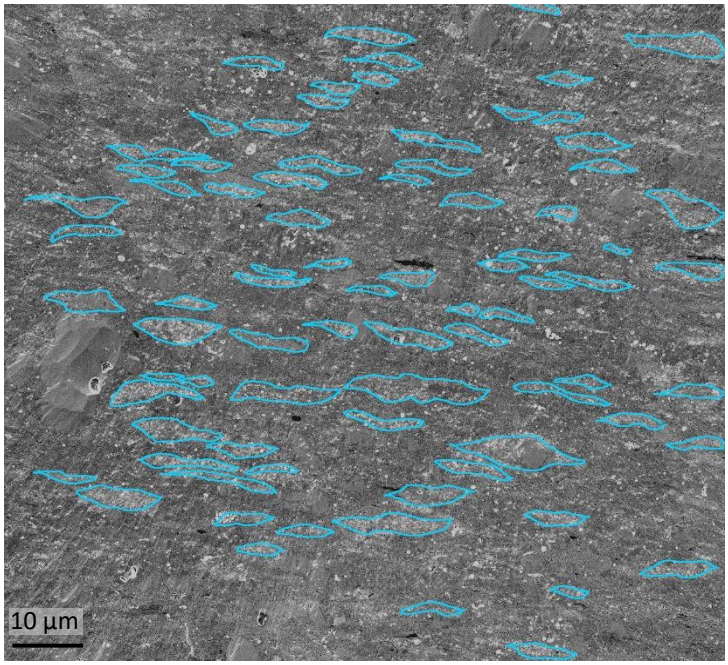

Figure 2.13: SEM SE image of an area 1 mm x 1 mm sample OC2 (R_0 0.5%), highlighting the fecal pellets (blue), which are recognised by their ellipsoidal shape.

2.3.3.5. Organic Matter

Organic matter is present at all maturities in the form of kerogen and migrated bitumen. Organic petrology analyses were performed to distinguish the various maceral types (Figure 2.14). The main macerals are liptinite (mostly alginite, sporinite, cutinite, resinite, bituminite) followed by inertinite and vitrinite. Macerals from the liptinite group are considered algal materials and bacterial lipids (Type I marine kerogen) (Ma, 2016). The alginites can be either lamellar masses (lamalginites) or discrete bodies (telalginites, such as *Tasmanites* or *Leiosphaeridia*) (Neto et al., 1992). The high-intensity yellow fluorescence in the immature samples (Figure 2.14 e) is indicative of high remaining hydrocarbon potential. The liptinite group also includes amorphous organic material that is derived from algae or bacterial precursors (Hackley and Cardott, 2016). The inertinite represents small fragments of oxidized plant tissue and has very low oil/gas potential (kerogen Type IV) (Edman and Pitman, 2010). Evidence for this is also the weak fluorescence compared to the liptinite macerals. Vitrinite is associated with Type II or III kerogen (Tissot and

Welte, 1978) and refers to organic matter derived from the woody tissue of vascular plants (Hackley and Cardott, 2016). The organics are generally aligned parallel to bedding, and change colour with increasing maturity (from brownish to grey-black in white light optical microscopy). Although vitrinite reflectance analysis was not performed, the macerals that were found are in line with the Rock-Eval experiments, which show a predominant Type I-II marine kerogen (Figure 2.14).

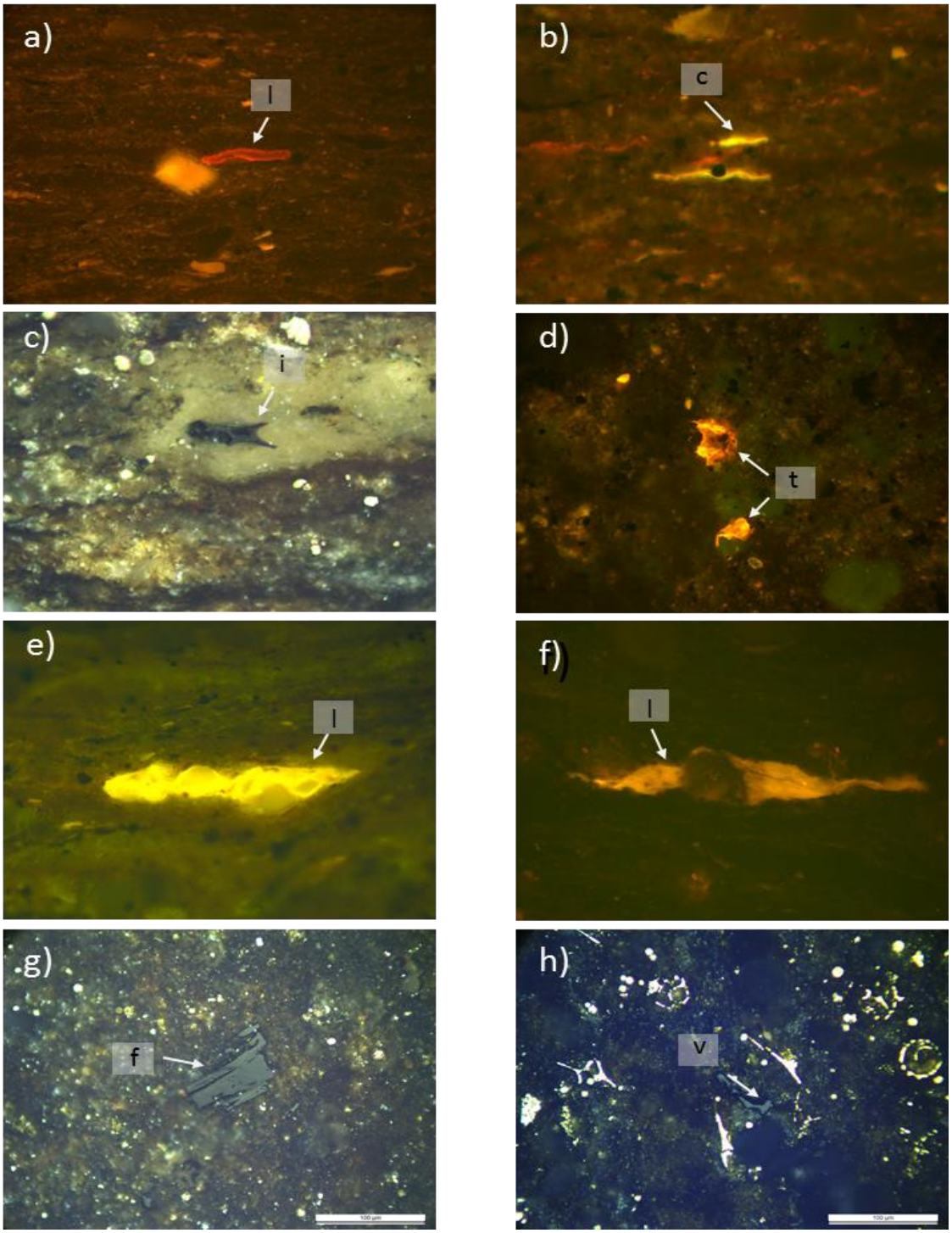

Figure 2.14: a) Blue light fluorescence, oil immersion photomicrograph of a lamalginite (l) (sample OW4, R_0 0.5%); Blue light fluorescence, oil immersion photomicrograph of cutinites (c) (sample OC6, R_0 0.5%); c) White incident light, oil immersion photomicrograph of inertinite (i) (sample OC7, R_0 0.5%); d) Blue light fluorescence, oil immersion photomicrograph of a telalginite (t) (sample OC1, R_0 0.4%); e) Blue light fluorescence, oil immersion photomicrograph of a lamalginite (l) (sample OC3, R_0 0.4%); f) Blue light fluorescence, oil immersion photomicrograph of a lamalginite (l) (sample GW10, R_0 1.2%); g) White incident light, oil immersion photomicrograph of a fusinite (f) (sample GW10, R_0 1.2%); h) White incident light, oil immersion photomicrograph of a vitrinite (v) and pyritised sponge spiculae (sample OW2, R_0 0.9%). The white bar represents a scale of 100 μm.

2.3.3.6. Mineral compounds

The mineral compounds that constitute the sample were deposited as flocs (<~ 10 μm) or as single particles (>~ 10 μm) (Aplin and Moore, 2016) (Figure 2.15).

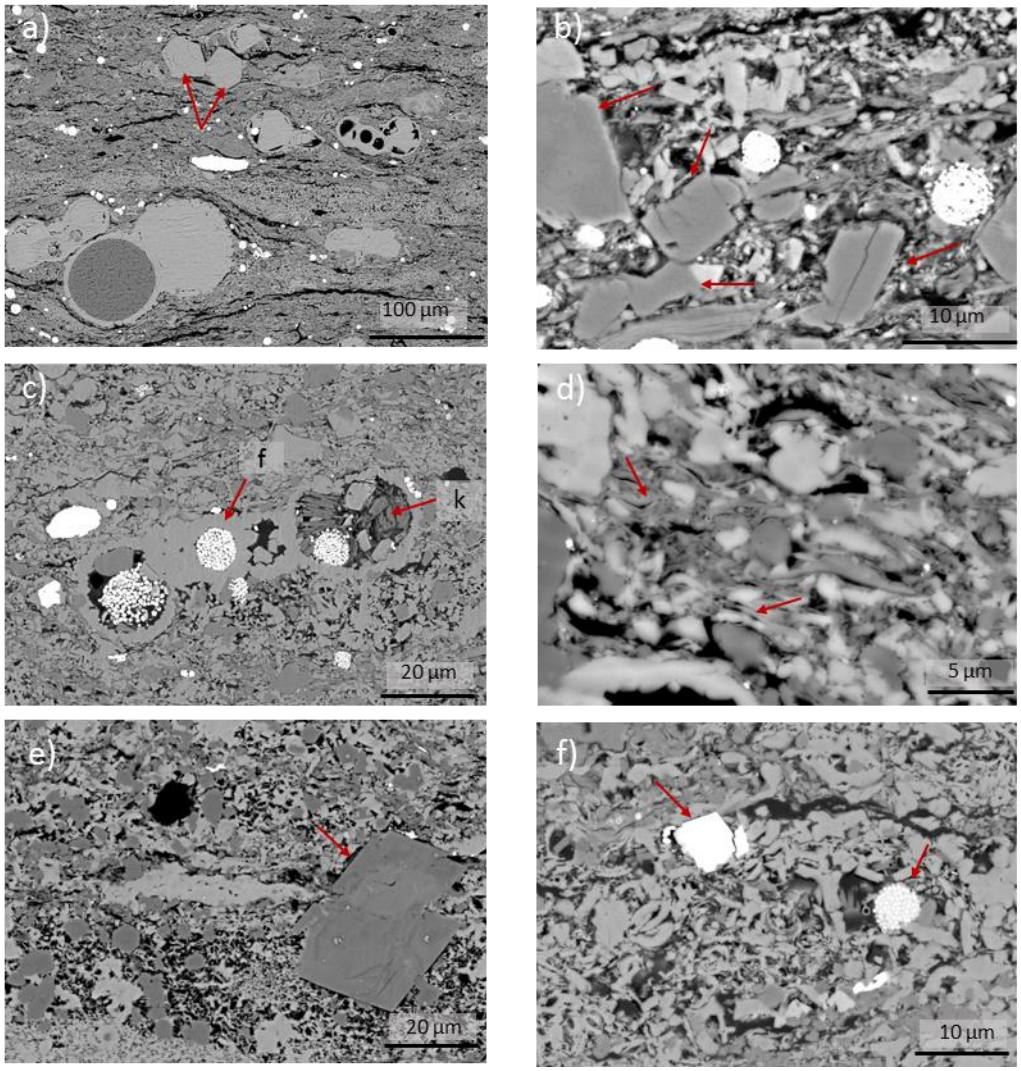

Figure 2.15: SEM images of the different mineral compouds indicated by the red arrows. a) calcite subhedral particles (sample OC2, R_0 0.4%); b) quartz subhedral particles (sample OC1, R_0 0.4%); c) framboidal pyrite (f) and kaolinite booklets (k) in foraminifera chambers (sample IM1_1, R_0 0.5%); d) mixed illite/smectite (sample H3A2, R_0 1.2%); e) euhedral dolomite (sample GW4, R_0 1.2%); f) on the left, euhedral pyrite, on the right, a framboidal pyrite (sample H3A5, R_0 1.2%).

The minerals do not account for the cements that fill the primary pores. Therefore, correlations between the minerals and the mineralogy content cannot strictly be made. As the point counting was made to quantitatively estimate the domains, differentiation between the types of minerals in the point counting was not made. The minerals are found within the matrix and are classified into:

a) Carbonates

Carbonates are ubiquitous and can be distinguished as calcite, dolomite, ankerite and siderite phases. The calcite is present as sub-euhedral crystals smaller than 30 μm. The smaller minerals (< 5 μm) are also a key component of the micritic matrix. CL studies allowed differentiation of the dual origin of the carbonate minerals, which is either detrital or authigenic, formed as reprecipitated mineral phases. Dolomite cements are a minor constituent of the overall mineralogy of the samples (<3% in all the samples except in samples GW4, GW2 and GW6). They are large (20-50 μm) crystals formed by replacement of existing calcite crystals, as testified by the nanometric crystals of calcite within rhombohedral dolomites (Figure 2.15e). Ankerite and siderite account for less than 2% of the total mineralogy and therefore are not considered.

b) Silicates

Silicate crystals found in the samples are quartz and, in minor amounts, K-feldspar and plagioclase. Quartz is usually less than 3 μm in diameter, euhedral and generally occurs as filling the pore spaces between the coccolithic matrix (see paragraph 2.3.3.3). For this reason, the origin of this micro-crystalline euhedral quartz is considered authigenic.

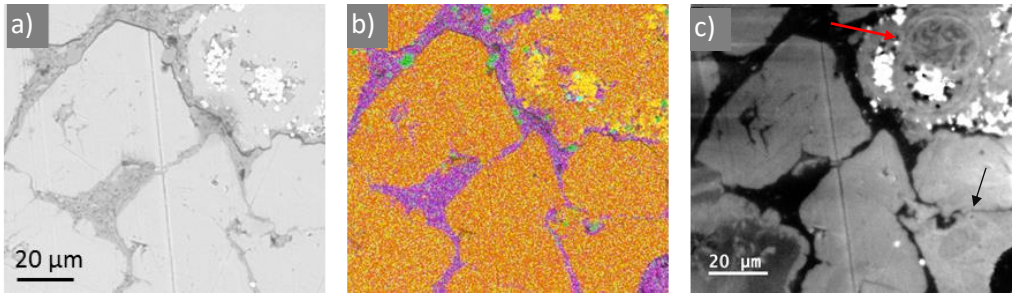

Figure 2.16: Sample GW7 (R_0 1.2%), microfacies C. a) SEM BSE image; b) elemental map of the same area; c) corresponding area in panchromatic CL. In the elemental map, the orange colour corresponds to calcite, the green is quartz, the purple is mixed clays (kaolinite + I/S) and the yellow is apatite. The red arrow on the panchromatic CL image indicates a recrystallised foraminifer. The black arrow indicates dissolution at a contact between two carbonatecrystals. The microquartz is too small to reveal any information about its origin.

Sub-angular, irregular, larger (5-10 μm) quartz is also present in minor quantities (Figure 2.15 b), and their angular shape could be an indication of a detrital origin (Milliken and Olson, 2017; Pommer, 2014; Pommer et al., 2014). Cathodoluminescence analyses and the

distinction between detrital and authigenic quartz are complicated by the small sizes of the grains (Figure 2.16), and by the relatively small abundance compared to the carbonates (Pommer, 2014) (Table 2.2).

Minor K-feldspar crystals are also found, exclusively in the immature and oil window (R_o 0.4% to 0.9%). Their origin is not unequivocal, but their angular shapes are indicative of detrital origin. The plagioclase, i.e. albite, appears as angular dispersed in the matrix. XRD data show that these grains are only found in the gas maturity window (R_0 1.2%). EDX maps show calcite crystals being replaced by albite, which is indicative of an authigenic origin.

c) Clay Minerals

The predominant clays are kaolinite and mixed-layer illite/smectite. Kaolinite sheets are common in the matrix and are variable in size, usually smaller than 5 μm. Their shape is variable; they can have sub-angular or rounded borders and their texture is commonly in the form of flaky booklets (Figure 2.15 c and d). Due to their ductile behaviour, they can be affected by compaction. They mainly occur in the immature (R_0 0.4-0.5%) and oil (R_0 0.9%) window samples and are often associated with the replacement of other minerals such as calcite. For this reason, kaolinite tactoids were interpreted as authigenic by many authors (Driskill et al., 2012; Jennings and Antia, 2013; Pommer, 2014).

Mixed Illite/smectite particles are found at all maturities, but in major abundances in the high maturity window (R_0 1.2%). They appear in forms of very small (<4 μm) fibres and sheets and for this reason, it is hard to determine whether their origin is allogenic or authigenic (Milliken et al., 2016).

d) Pyrite

Pyrite occur in the form of single subhedral crystals or as framboids. They are found dispersed within the matrix, within organic matter, or precipitated within foraminifera tests (Figure 2.15 f). The pyrite crystals and framboids have variable sizes (50 nm to 30 μm). The subhedral grains are interpreted to be mainly marcasite, a dimorph of pyrite. Other minerals, occurring in minor abundances are ankerite, siderite and apatite.

2.3.3.7. Microfacies

Transmitted light optical microscopy allowed the microfacies to be discerned by observing the fabric and texture of the rocks and to understand their microstructures. The microfacies were defined observing the mineralogy, the presence of fossils and the crystal types and sizes, the amount of matrix and its relationship with the crystals, the presence or absence, shape and thickness of laminae and the various microstructures. The three microfacies identified were: laminated foraminiferal mudstones, wackestones and packstones. From now on, in this and in the following chapters, these facies will be called A, B and C respectively (Figure 2.17).

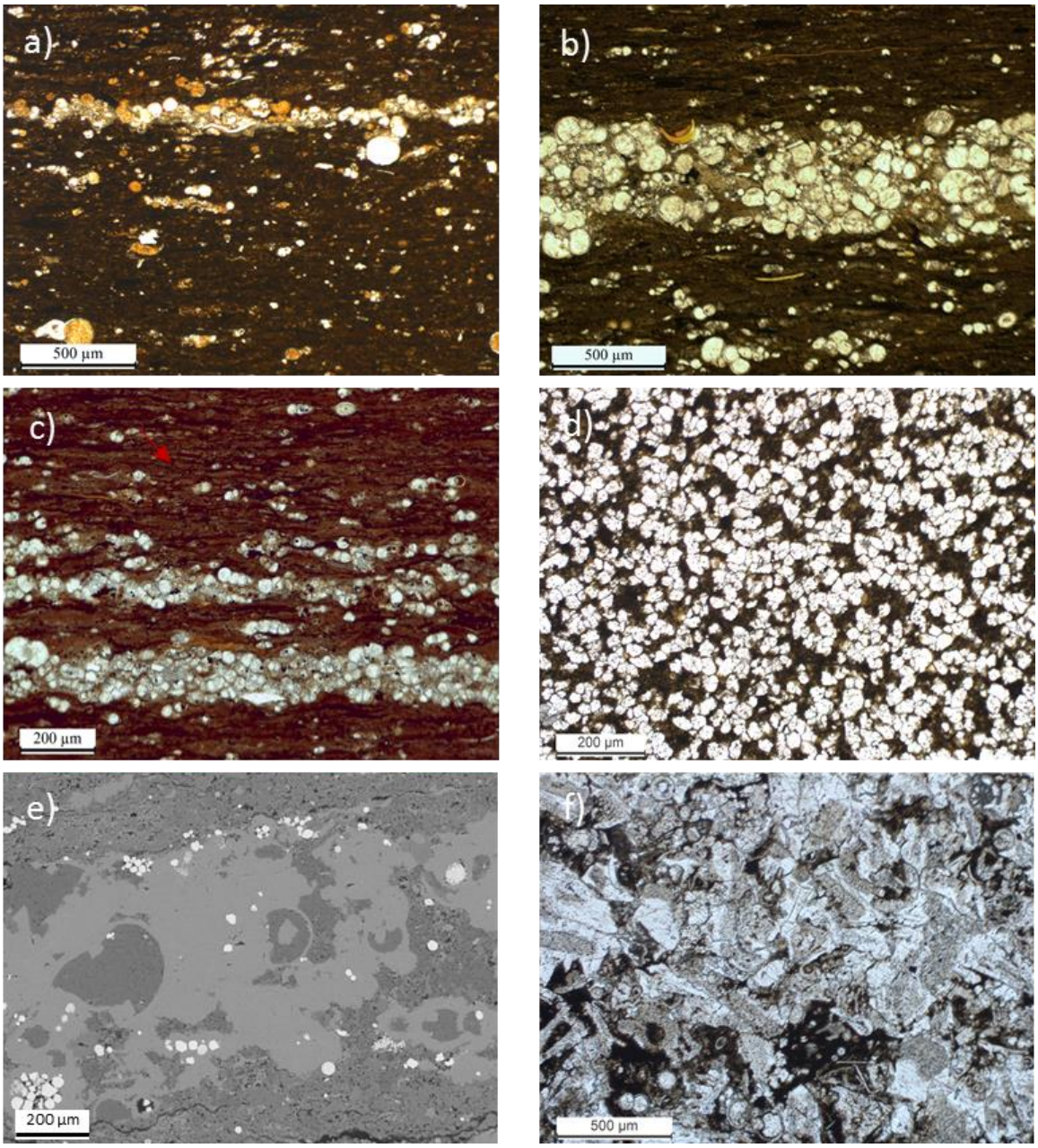

Figure 2.17: Thin section and SEM images of the microfacies types. a) laminated foraminiferal silt-rich mudstone (microfacies A, sample IM2_6 (R_0 0.5%)); b) laminated foraminiferal clay-rich mudstone (microfacies A, sample OW4 (R_0 0.9%)); c) laminated foraminiferal-calcite rich mudstone (microfacies A, sample IM2_3 (R_0 0.5%)). The red arrow indicates wavy and inclined laminae within the matrix; d) recrystallised sparry wackestone (microfacies B, sample IM2_2 (R_0 0.5%)); e) wackestone (microfacies B, sample IM1_2 (R_0 0.5%)); f) packstone (microfacies C, sample GW7 (R_0 1.2%)).

a) Microfacies A: laminated foraminiferal mudstone

A mudstone is described as a rock that comprises particles predominantly smaller than 62.5 μm. A laminated foraminiferal mudstone is a mudstone containing micrometric (100 to 600 μm) foraminiferal-rich levels. The mineralogical content of the laminated foraminiferal mudstones is varied, and are primarily formed by clays, carbonates, silicates and feldspars (Aplin and Macquaker, 2011). The mudstones present in these samples are mainly carbonate-rich (47.6% on average), with minor contents of silicates (23.2% on average) and clays (20.6% on average). The TOC content ranges between 3 wt % and 7.9%, with an average of 5.2 wt. %. These samples can be sub-divided into three types:

a) Laminated foraminiferal, silt-rich mudstones containing more than 30% silicates. The thin sections appear light brown in colour. Samples OC1, IM2_1 and H3A2 are laminated foraminiferal silt-rich mudstones (Figure 2.17 a).

b) Laminated foraminiferal, clay-rich mudstones: XRD data show that foraminiferal clay-rich mudstones contain at least 27% of clays and 36% of carbonates. Under transmitted light, the thin sections appear as light-brown to red-brown. Samples IM1_2, IM1_3, OW2 and H3A3 are classified as clay-rich mudstones (Figure 2.17 b).

c) Laminated foraminiferal, carbonate-rich mudstones: these contain at least 50% of carbonates and appear dark to light brown in thin section. They mostly contain faecal pellets and foraminifera. Samples OC2, OC3, IM2_3, OW1 and H3A5 are classified as laminated foraminiferal carbonate-rich mudstones (Figure 2.17 c).

In all the foraminiferal mudstone types, the laminae appear as horizontal and parallel-laminated at the centimetre scale. The laminations are caused by alternations of foraminiferal-rich layers (white-pale colours) with more clay and organic-matter rich laminae, that form the matrix.

The foraminifera-rich layers are formed by at least 90% of foraminifera held together by calcite cements. The foraminifera tests within these beds and dispersed in the matrix are either hollow or filled with cements (mainly blocky calcite and in minor amounts also quartz or kaolinite), occasional minerals (pyrite) or organic matter. The foraminiferal laminae exhibit a sharp erosive contact derived from the contact between the hard fossils

on a softer micritic substrate (Figure 2.17 a). Weak forms of wave ripples and inclined laminae are also present (Figure 2.17 c). Signs of compaction and loading can be seen in the flattened faecal pellets, the deformed particles surrounding the foraminifera and the crushed tests of foraminifera or other fossils perpendicular to the burial stress direction (Figure 2.18 b). Dispersed within the matrix are different types of fossils such as foraminifera, phosphatic shells and fish bones, coccospheres, bivalves, inoceramids, pelecypods, ostracods, radiolaria, spiculae, echinoderms. There are also frequent faecal pellets and detrital silicate compounds (quartz, plagioclase, K feldspar) and carbonates (mainly calcite and dolomite). Amongst the fossils, the foraminifera are the most common and constitute at least 10% of the whole microfacies, measuring between 20 μm up to 400 μm. On average, they are larger than 62.5 μm (silt-size). Pyrite is common (between 1% and 5.1%) within the matrix and in the foraminifera tests in the forms of framboids or euhedral crystals. Less common is the presence of plagioclase (average 2%) and dolomite (average 0.3%). Intergranular pores dominate the pore system in the samples from microfacies A. At increasing maturities (form R_0 0.4% to R_0 1.2%), an increase in organic matter pores at the expense of intergranular pores (-44%) is observed.

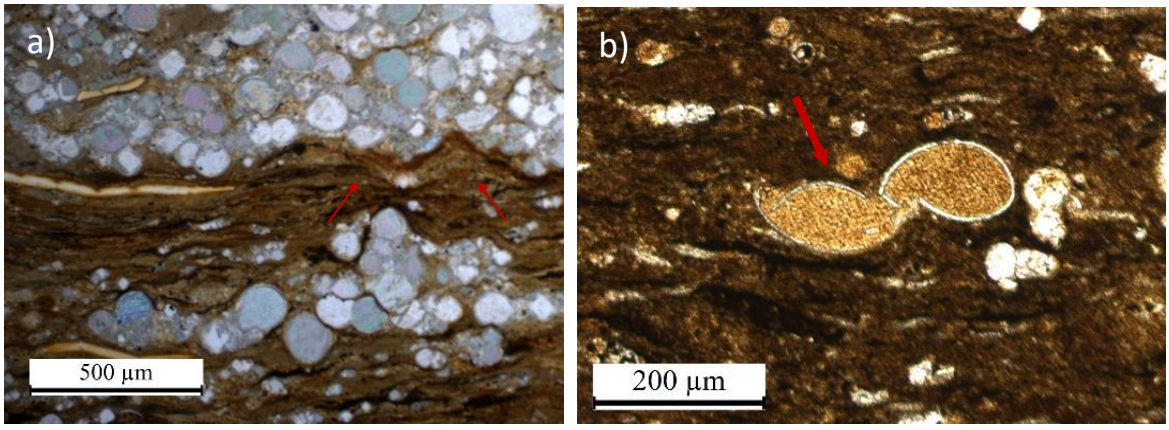

Figure 2.18: a) Thin section photomicrograph of sample IM2_5 (microfacies A, R_0 0.5%). The red arrows indicate a sharp contact between the hard foraminiferal layer and the ductile clay-rich matrix on the bottom. b) Thin section photomicrograph of sample OW8 (R_0 0.5%). The red arrow indicates a foraminifer with chambers collapsed from the burial stress.

b) Microfacies B: wackestone

Wackestones are defined as a mud-supported carbonate rock that contains > 10% grains (Dunham, 1962). The wackestones in the samples analysed here are formed by laminae, apart from sample IM2_1 (R_0 0.4%), which is a pervasively recrystallised, sparry

wackestone. This type of sample was classified as concretionary by McAllister (2017). The crystals are formed by large (> 50 μm) sub-angular to angular calcite crystals. Surrounded by angular calcite particles are occasional intact planktonic foraminifera which suggests the angular granules did not have a biogenic origin. Further evidence for this are the CL images, in which the grains do not reveal any overgrowth from original biogenic carbonates (i.e. fossils, shell fragments or coccoliths). The matrix is formed by a mixture of micro and nanograins of quartz, carbonates, clays and organic matter. For this sample, the TOC content is 1.9%. (Figure 2.17 d).

On the other hand, in the laminated wackestone samples (GW3, GW4, GW5, H3A4, H3A6, GW2, GW6 at R_0 1.2%), CL images show that the coarse (> 60 μm) sub-angular or rounded calcite crystals are reprecipitated cements around fossils (foraminifera, calcispheres and radiolaria) and faecal pellets (Figure 2.19). Where still visible and preserved, the constituents filling the foraminifera are predominantly calcitic cements and organic matter. The most common pores are interparticle matrix pores (on average, 57%), like in microfacies A. However, by a qualitative analysis, it can be seen that the abundant calcite cement within the foraminifera and the matrix has significantly reduced the number of interparticle and intraparticle pores (see Chapter 3). Weak forms of wave ripples and inclined laminae are present but usually disrupted by the pervasive cementation.

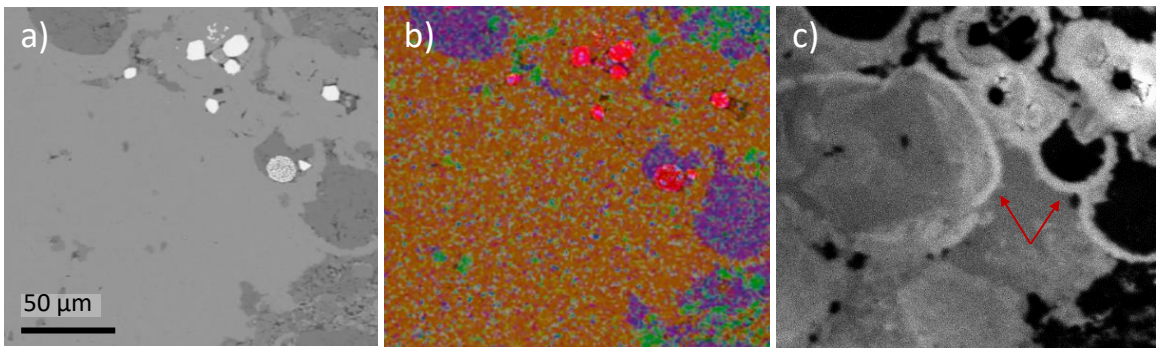

Figure 2.19: Calcite grain overgrowth in sample GW3 (microfacies B, R_0 1.2%). a) is an SEM BSE image, b) is the elemental map of the same area and c) is the corresponding area in panchromatic. On the elemental map, the orange colour corresponds to calcite, purple is kaolinite, green is quartz and pink is pyrite. The red arrow on the panchromatic image indicates a primary biogenic calcite foraminifera, around which the calcite cements have reprecipitated in different phases, which correspond to different greyscales.

c) Microfacies C: packstones

Packstones are defined as grain-supported carbonate rocks that contain 1% or more of the mud-grade size fraction (Dunham, 1962). The two packstone samples GW7 and GW8 are formed by high percentages of carbonates (75% and 84%) and low amounts of mixed-layer illite/smectite (12% and 7%) and TOC (0.5 wt % and 0.7 wt %). The packstones have a massive texture with no clear sedimentary structures. The carbonates comprise foraminifera, sponge spicules, bivalves and oyster fragments, calcispheres and echinoderm plates and spines. The samples, analysed under the CL, show evidence of dissolution and reprecipitation of calcite, that grows on the surfaces of the fossil shells and masks the original fabric (Figure 2.20).

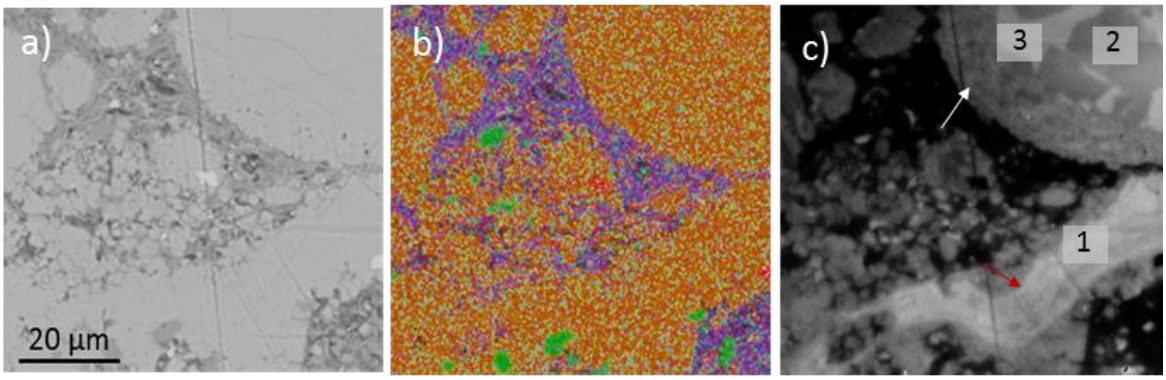

Figure 2.20: Sample GW7 (microfacies C, R_0 1.2%). a) SEM BSE image; b) elemental map of the same area; c) corresponding area in panchromatic CL. In the elemental map, the orange colour corresponds to calcite, the green is quartz, the purple is mixed clays (kaolinite + I/S) and the red is pyrite. The red and white arrow on the panchromatic CL image indicates recrystallised bioclasts, possibly an oyster shell (red) and an agglutinated foraminifera (white). The numbers indicate the different calcite precipitation phases.

They are white to light brown in thin section (Figure 2.17 f). The most common pore types for this microfacies are interparticle matrix pores, which constitute on average 60% of the overall pore types. Since organic matter contents are low, the organic matter pores account for only ~5% of the overall porosity. Dissolution pores, on the other hand, are more abundant than in the other microfacies and constitute up to 31% of total number of visible pores, compared to an average of 3.7% in microfacies A and an average of 7.3% in microfacies B. The intraparticle fossil and mineral pores are a minority (< 5%).

2.3.3.8. Pore types

The high resolution and high magnification SEM maps allowed the identification and differentiation of pores as small as 18 nm in diameter. The classification of the different pore types was modified after Loucks et al. (2012). Interparticle matrix pores, interparticle mineral pores, intraparticle fossil pores, intraparticle dissolution pores and organic-matter pores were discerned (Figure 2.21). The pore types were also quantified by analysing the SEM SE maps overlain with the EDX chemical maps (Table 2.7).

Samples names	V. Reflectance (R_o%)	Microfacies Type	OM pores (%)	Interparticle matrix pores (%)	Intraparticle mineral pores (%)	Intraparticle fossil pores (%)	Intraparticle dissolution pores (%)
OUT1	0.4	A	6	68	15	11	0
OUT2	0.4	A	8	69	13	7	3
OUT3	0.4	A	10	64	18	8	0
IM1_1	0.4	A	7	71	8	13	1
IM2_2	0.5	B	4	69	9	6	12
IM2_3	0.5	A	4	77	13	2	4
OW1	0.9	A	5	74	9	10	2
OW2	0.9	A	12	65	8	3	12
GW5	1.2	B	13	65	15	6	1
GW4	1.2	B	13	64	17	2	4
GW2	1.2	B	18	47	19	4	12
H3A2	1.2	A	47	41	2	0	10
H3A3	1.2	A	41	38	16	2	3
H3A4	1.2	B	29	57	10	3	1
H3A5	1.2	A	43	37	18	0	2
GW6	1.2	B	27	37	19	3	14
GW7	1.2	C	5	61	4	2	28
GW8	1.2	C	4	59	1	5	31

Table 2.7: Percentage of the different pore types relative percentages measured by observing the SEM and EDX maps.

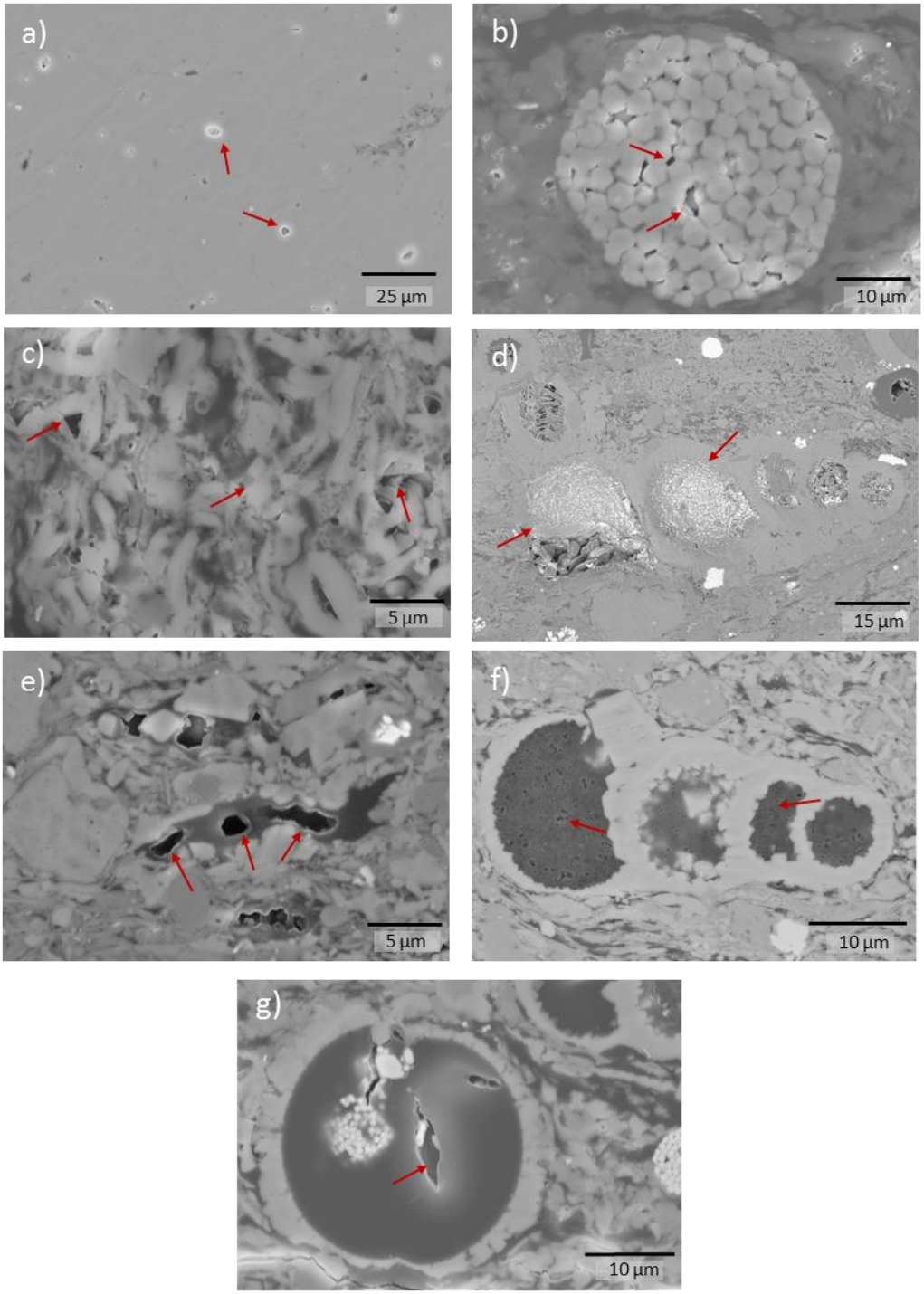

Figure 2.21: SEM images of the different pore types indicated by the red arrows. a) dissolution pores (sample H3A2, R_0 1.2%); b) interparticle mineral pores in framboidal pyrite (sample IM1_3, R_0 0.4%); c) interparticle matrix pores (sample IM1_2, R_0 0.5%); d) OM fracture pores in bitumen filling a foraminifer-coccosphere chamber (sample OW2, R_0 0.9%); e) pendular pores in an organic matter filament within the matrix (sample OW2, R_0 0.9%); f) OM sponge pores in bitumen filling foraminifer chambers

a) Interparticle matrix pores

Interparticle matrix pores are pores that occur between particles. In these samples, they are found as intra-aggregate porosities between clays and carbonates, between the coccolithic debris in the matrix and in the faecal pellets (Figure 2.21 c). For the 18 samples analysed, the interparticle matrix pores are the most frequent type, occurring at all maturities (37 to 77% of the overall number of pore types), apart from samples H3A2, H3A3 and H3A5 where the OM pores are slightly more abundant. Relatively to the rest of the pore types, the highest percentages of interparticle matrix pores are found at lowest maturities (R_0 0.4-0.5%).

b) Intraparticle mineral pores

The intraparticle mineral pores reflect the abundance of framboidal pyrite and kaolinite, whose structure often allows intraparticle pores to form. In general, they range between 1% and 19% of the overall pore types and do not follow a specific trend with increasing maturity, nor with microfacies type (Figure 2.21 b).

c) Intraparticle dissolution pores

Intraparticle dissolution pores can be identified by their elliptical shape within precipitated carbonate minerals and, to a lower extent, K-feldspar and plagioclase minerals. They are found at all maturities, but they become more abundant in the oil and gas maturity window samples. They are mainly found in microfacies B and C. In the two samples from microfacies C, at the highest maturity, they reach 31% of the overall visible pore volume (Figure 2.21 a).

d) Intraparticle fossil pores

Intraparticle fossil pores occur within well-preserved foraminifera tests and coccolithophorids and are most common in the least mature samples (R_0 0.4-0.5%). Intraparticle dissolution pores have a more elliptical shape and are found within precipitated carbonates and, to a lesser extent, plagioclase minerals. They range between

0% and 31% and are found at all maturities, but most commonly in the highest maturity samples (R_0 1.2%).

e) Organic matter pores

Organic matter pores are pores found in the organic matter and can be distinguished in 3 types: pendular, spongy and fracture-like OM pores (Walls and Sinclair, 2011) (Figure 2.21 e,f,g). Pendular and fracture-like OM pores are generally larger, more elongated and have a higher aspect ratio compared to spongy OM pores. Pendular and fracture-like pores are present at all maturities but begin to be more common in the oil window. From qualitative observations, spongy OM pores are the most abundant pore type; they have a circular or semi-circular shape and are usually smaller than 10 nm. The spongy OM pore type is only found in the highest maturity samples (R_0 1.2%), where OM that has not developed a spongy texture can also be present. The pendular and fracture-like OM pores are rare (< 10% of the overall porosity) and are found in the immature and oil window samples. SEM images show that not all the organic matter that is present in the gas window has generated pores. This is indicative of the presence of different organic matter types (Löhr et al., 2015). Loucks et al. (2012) suggest that, for example, Type II kerogen is more prone to generate OM pores than Type III kerogen. Several authors suggest instead that the OM pores are generated only in bitumen after the secondary cracking in the gas window (Löhr et al., 2015; Milliken et al., 2013; J Schieber, 2013). Organic matter pores reach 41% of the overall pore types in sample H3A2 (microfacies A, R_0 1.2%).

2.3.4. Diagenetic processes and interpretation

2.3.4.1. Cements and mineral replacements

Cements and mineral replacements are two different processes. A cement is defined as a mineral phase that has precipitated from an aqueous solution into primary void space whereas a mineral replacement involves the dissolution of a primary mineral phase and precipitation of a new, authigenic mineral phase (Maliva and Siever, 1988). However, in limestones, the two concepts are rarely distinguishable and only the authigenic minerals that do not show any clear precipitation into an open space are termed replacements

(Milliken and Day-Stirrat, 2013). In this study, the term replacement will only be used where the process is evidently a replacement and not cementation.

The fact that the majority of the bioclasts are intact and filled with cements, implies that a phase of cementation has occurred at relatively shallow burial depths, in the early stages of diagenesis (Heydari, William and Wade, 2002; Hentz and Ruppel, 2010; Mcallister, 2017). Diagenesis in these samples is very complex and consists of multiple phases of cementation (Figure 2.20) as well as multiple cement types. In particular, observations of the infills of the foraminifera chambers allow us to infer the nature of the cements as well as the sequence of precipitation (Table 2.8). The foraminifera tests have large (> 50 μm) chambers and are the most obvious sites in which cements precipitate. As the XRD data only provide the bulk composition of the samples, in order to have a better insight on the cements that are present, the foraminifera infills were quantified by means of point counting studies in 17 samples from different maturities.

Sample Names	V. Reflectance (R_o%)	Microfacies Types	Calcite cement (%)	Quartz cement (%)	OM fill (%)	Clay cement (%)	TOC (wt %)	Total clays (%)	Total carbonates (%)	Total Silicates (%)
OC1	0.4	A	64	13	10	13	4.4	7.7	52.5	32.5
OC2	0.4	A	55	5	12	28	6.6	9.0	58.2	20.0
OC3	0.4	A	59	8	9	24	5.5	11.6	50.3	24.3
IM1_2	0.4	A	54	2	21	23	6.3	27.4	37.1	31.2
IM1_3	0.4	A	69	4	18	9	N/A	45.5	25.5	21.0
IM2_1	0.5	A	87	7	6	0	5.8	19.5	36.3	33.2
IM2_2	0.5	B	100	0	0	0	1.9	4.7	76.2	18.8
IM2_3	0.5	A	57	7	10	26	7.9	9.0	50.1	24.2
OW1	0.9	A	29	15	17	39	5.0	16.2	57.5	23.6
OW2	0.9	A	29	5	4	62	4.5	42.1	43.2	8.0
GW1	1.2	A	56	4	13	27	3.5	20.4	57.2	14.6
GW5	1.2	B	67	5	7	20	1.6	13.5	67.2	11.3
GW4	1.2	B	78	12	10	0	1.0	8.3	73	15.6
GW2	1.2	B	80	4	9	7	2.3	3.0	82.9	13.1
GW6	1.2	B	100	0	0	0	2.4	3.2	77.9	14.3
GW7	1.2	C	80	7	6	7	0.7	12.2	74.6	6.7
GW8	1.2	C	96	2	0	2	0.5	7.0	84.4	4.5

Table 2.8: Percentage of the relative percentages of different cement types within the foraminifera tests and the corresponding XRD bulk rock results. For more detaild bulk mineralogy refer to chapter 3. OM = organic matter, N/A = not available data.

2.3.4.2. Calcite and Dolomite

The most common type of cement is calcite, which precipitates in the intrafossil porosity and within the matrix debris. Especially within the fossil tests that are partially filled with cements, the cements can be identified by their angular shape (Figure 2.22).

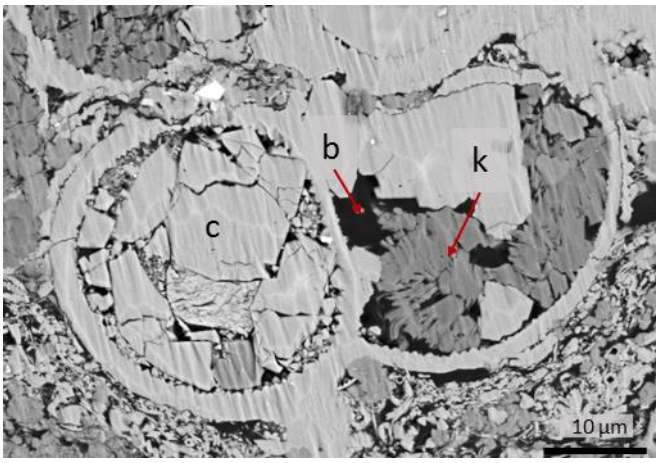

Figure 2.22: Foraminifera chambers in sample IM2_4 (R_0 0.5%) filled with cements of calcite (c), kaolinite (k) and infill of bitumen infill (b).

Figure 2.23 shows that there is no apparent trend between the increase in depth and maturity and the increase in calcite cement in the foraminifera chambers.

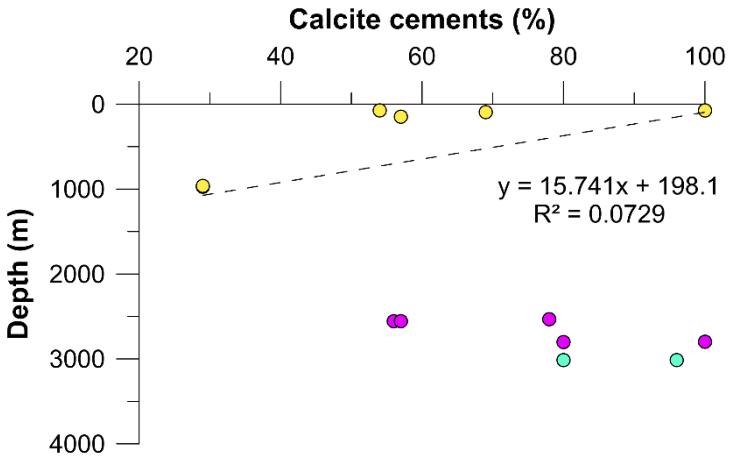

Figure 2.23: Total calcite cements (%) vs depth plot. Yellow dots correspond to the laminated foraminiferal mudstone samples, purple dots to the wackestone samples and the light blue dots to the packstone samples. There is no clear correlation between the cements filling the foraminifera and the depth at which the samples are found.

The foraminifera chambers filled with cements are extremely common (> 90 % of the chambers), and amongst those, calcite is the most frequent cement. On average, cements are more frequent in microfacies B and C (83% and 88% respectively) compared to microfacies A (57.2%). However, an increase in cement and authigenic calcite within the matrix and the faecal pellets with increasing maturity can be noticed. In particular, the cements begin to fill the faecal pellets and matrix interparticle pores in the oil window (R_0 0.9%) and become pervasive in the gas window (R_0 1.2%) (Figure 2.24).

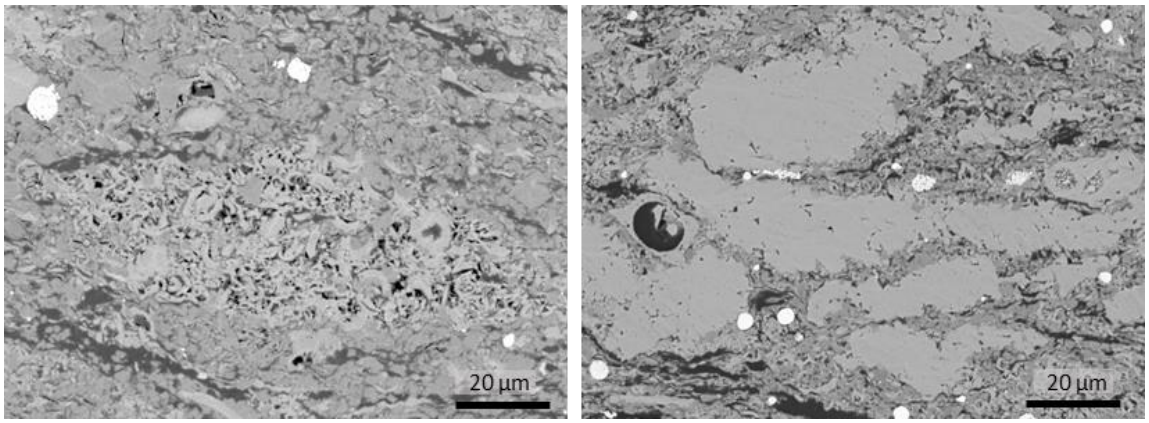

Figure 2.24: On the left, a fecal pellet in an immature sample (sample IM1_1, R_0 0.5%). On the right, faecal pellets in a gas window sample (sample H3A1, R_0 1.2%).

In the gas window, calcite overgrowths surrounding the primary calcite minerals and fossils are also common. Microfacies B, in particular, shows extensive calcite cements around the original detrital calcites and around the fossils. The cements are better observed in CL, which enables the visualisation of the various episodes of calcite precipitation. As seen in Figure 2.20, calcite cements are interpreted to have formed in at least 3 different episodes. The CL also shows that microfacies B is in fact originally very similar to microfacies A. However, in microfacies B the calcite cements have entirely masked the faecal pellets and foraminifera, which appear here as massive calcite crystals (Figure 2.26). The two samples from microfacies C instead present a massive structure in which the fossil debris, mainly formed by shells and spiculae, is held together by calcite cement (Figure 2.25). A previous phase of calcite cement is also observed in forms of overgrowth around the debris. Previous studies using carbon isotopes (Mcallister, 2017 and references therein) have demonstrated that the carbonate cements were precipitated from a marine inorganic source and not from microbial processes. Moreover, the presence of zonations in the calcite (Figure 2.27) suggests existing very small chemical variations

in the calcite-saturated fluid, which are interpreted as changes in the microbial oxidation of organic matter (McAllister et al., 2015).

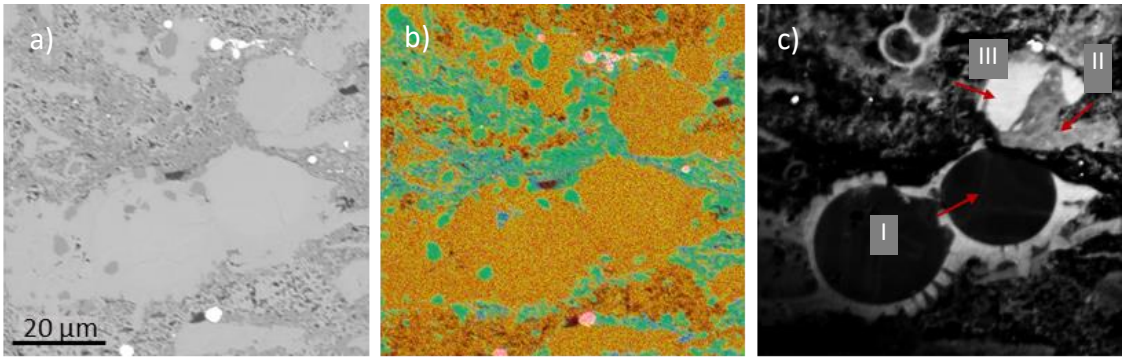

Figure 2.27: Sample H3A2 (R_0 1.2%). a) is an SEM BSE image, b) is the elemental map of the same area and c) is the corresponding area in panchromatic CL. On the elemental map, the orange colour corresponds to calcite, green is quartz and pink is pyrite. The red arrows indicate the three calcite cement phases, which have a different greyscale compared to the foraminifera shell.

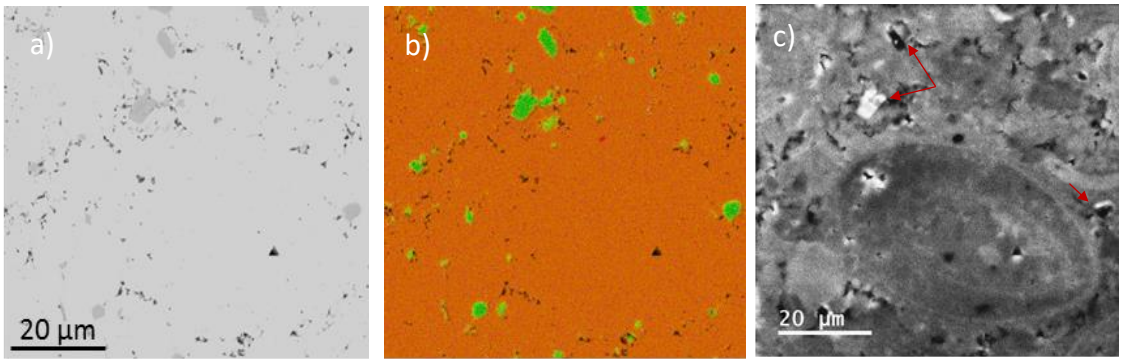

Figure 2.25: Sample H3A6 (R_0 1.2%), microfacies B. a) SEM BSE image; b) elemental map of the same area; c) corresponding area in panchromatic CL. In the elemental map, the orange colour corresponds to calcite and green is quartz. The red arrows on the panchromatic CL image indicate the microquartz cements, which have different greyscales and suggest a different timing of deposition. The white rim on the black paticle on the right suggests that the white particle was deposited on a later stage. The structure of an original bioclast completely recrystallised is also visible.

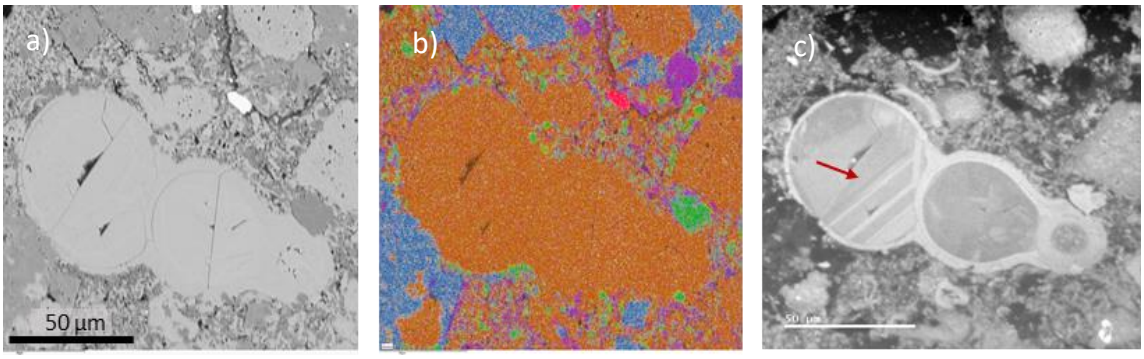

Figure 2.26: Sample GW4 (R_0 1.2%). a) is an SEM BSE image, b) is the elemental map of the same area and c) is the corresponding area in panchromatic CL. On the elemental map, the orange colour corresponds to calcite, green is quartz, purple is kaolinite, blue is dolomite and pink is pyrite. The red arrow indicates the cement growth zonations.

2.3.4.3. Dolomite

Crystals of dolomite are observed around foraminifera shells or scattered in the matrix (Figure 2.28). CL analyses show the existence of micro-crystals of calcite within the dolomite crystals, which indicates that the dolomite is authigenic. Magnesium is probably derived from the dissolution of other mineral phases (ie. feldspars, clays). The large dimensions of the dolomite crystals suggest an early diagenetic origin, when there was still sufficient pore space for the precipitation of large crystals, but could be also formed as a replacement of other carbonate phases (i.e. calcite).

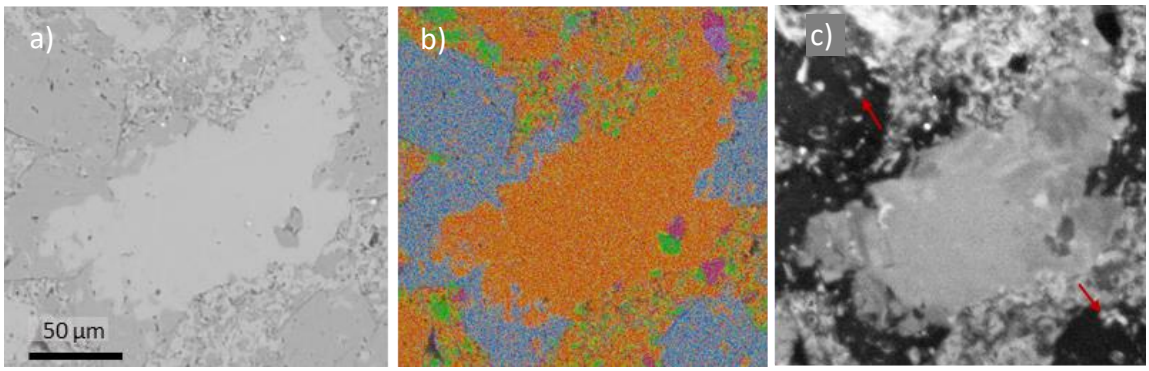

Figure 2.28: Calcite mineral overgrowth in sample IM2_1 (R_0 0.5%) surrounded by dolomite cements. a) is an SEM BSE image, b) is the elemental map of the same area and c) is the corresponding area in panchromatic. On the elemental map, the orange colour corresponds to calcite, purple is kaolinite, green is quartz and blue is dolomite. The red arrows on the panchromatic image indicate the calcite remnants on which the dolomite has precipitated, suggesting an authigenic origin.

2.3.4.4. Quartz

Quartz cements are commonly found in the Eagle Ford samples in all the microfacies types. They are observed in forms of subangular granules (5-10 µm) precipitated in the intraparticle pores within the allochems, or as micro-crystals (<3 µm), filling the pores within the coccolithic matrix (**Error! Reference source not found.**). The sub-angular granules within the fossils seen in thin section are a minor cement constituent (< 15%), occurring at all maturities. There is no apparent relationship between the sub-angular cements and the fossils. The micro-crystals, instead, have generally smoothed borders and occur at all maturities, increasing in gas window (R_0 1.2%) samples. However, XRD data show that the quartz bulk percentage does not have any direct relationship with the increase in thermal maturity (Table 2.2). This suggests that the quartz precipitation

process starts early with the precipitation of sub-angular cements and micro-crystals in primary pores and continues at higher maturities as a micro-grain replacement in the matrix. Milliken et al. (2016) have studied the origins of the silica in the Upper Eagle Ford and have concluded that the majority of the quartz that is found is authigenic and most likely originated from the alteration of original biogenic opal derived from radiolarian microfossils and sponge spicules. The radiolarian microfossils are composed by opal-A, which, being unstable transforms into a more stable phase opal-CT as lepispheres which in turn transform into quartz (Fishman et al., 2014; Kastner et al., 1977; Peltonen et al., 2009). The samples in this study were taken from the Lower Eagle Ford intervals, but the micro-quartz origin can be inferred as the same as for the one described by Milliken et al., 2016 for the Upper Eagle Ford.

Another possible origin for the micro-quartz precipitation at higher maturities is explained by the release of Si from illitization reactions during late diagenesis (T > 90°) (Thyberg and Jahren, 2011; Worden and Morad, 2003). However, the XRD analyses do not allow us to differentiate illite from smectite, and therefore it is not possible to determine whether illitization has occurred. The fact that bulk quartz does not increase in the oil and gas window compared to the low maturity window samples can be explained with the fact that the Si becomes available for the precipitation of quartz as well as other minerals such as Na-rich plagioclase (albite), the abundance of which increases in the gas maturity window (from an average of 1% to an average of 2%) (Table 2.2).

2.3.4.5. Clays

Kaolinite and mixed illite/smectite are common cements in these samples. The kaolinite appears in forms of micrometric (<3 μm) booklets within the allochems and in the matrix. Within the foraminifera tests, it usually fills the space that is not occupied by calcitic cements, and therefore it is interpreted as post-dating calcite (Figure 2.29). The kaolinite in the matrix usually occurs as single booklets, whereas in the forams it is commonly found in the form of aggregates. In the matrix, the distinction between the kaolinite, the mixed illite/smectite and the other mineral grains is only possible under the SEM. On the contrary, to differentiate the clay cements from the OM infill and the quartz and calcite cements, an optical microscope is sufficient. Point counting of the cements shows that the clay cements within the foraminifera tests are more common in microfacies A than in microfacies B and C (on average, 25% vs 5% and 4.5% respectively). There is no apparent trend between the clay cements within the allochems and the increase in maturity nor the ratio of clays. This can be explained by the fact that the clays are present in large amounts in the matrix and that kaolinite and mixed-layer illite/smectite cannot be differentiated by point counting. Considering the origin of the clays to be authigenic, relationships between the clay mineralogy and cements can be made.

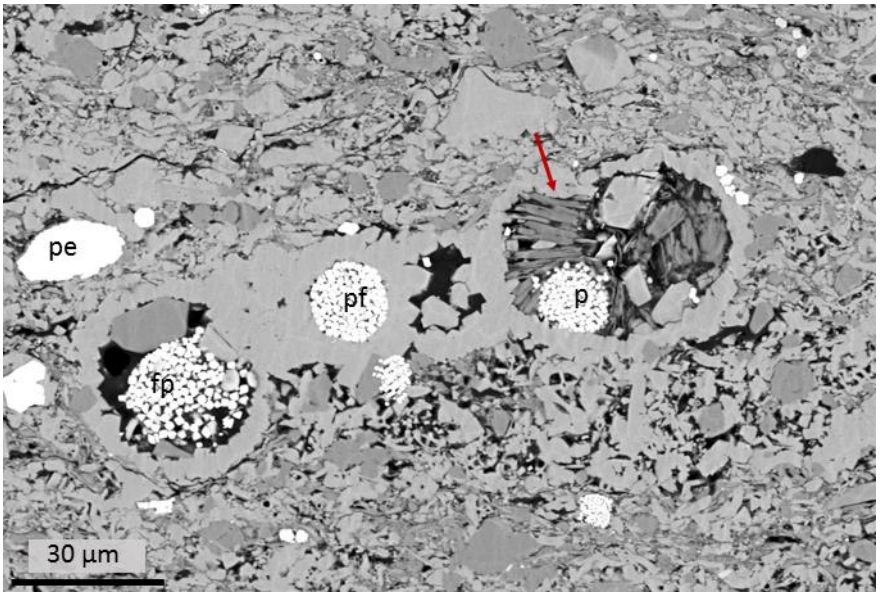

Figure 2.29: Sample H3A5 (R_0 1.2%). Foraminifera with different cements filling the chambers. The red arrow indicates the kaolinite booklets filling the space left free by the calcite (*c*) and the pyrite (*p*). The pyrite occurs as framboidal (pf) and euhedral (pe).

As seen in the bulk rock composition Paragraph (2.3.1), the bulk mineralogy data show an abrupt decrease in kaolinite amounts from the oil to the gas window. On average the kaolinite at R_0 < 0.9% is ~13%, whereas at higher maturities (R_0=1.2%) is ~1%. In contrast, the I/S bulk ratio increases from an average of ~7% at R_0 < 0.9% to an average of ~9% in the gas window samples (Figure 2.7).

Differences in the bulk mineralogy of the samples can be due to 1) diagenetic processes or 2) variations in sediment supply at individual locations. The abrupt decrease in kaolinite at thermal maturities > R_0 0.9%, suggests that diagenetic processes are predominant. The major clay diagenetic process occurring at temperatures > 90° is illitization, which modifies kaolinite and K-feldspar, mobilising Al, K and Si in the system, producing illite and micro-quartz. A simplified equation of the reaction is: Kaolinite + K-feldspar ➔ Illite + Albite + H_2O. In turn, the origin of kaolinite and I/S is interpreted as related to the dissolution and alteration of detrital aluminium oxides and clay minerals delivered to the basin as ash (Jennings and Antia, 2013; Taylor et al., 2014; Wilson et al., 2016). The alteration of plagioclase mobilizes Al in the porewaters, which becomes available for the precipitation of the kaolinite and I/S.

2.3.4.6. Albite

Euhedral crystals of albite are commonly observed in the BSE images, replacing the calcite (Figure 2.30). They are common in oil and gas window samples, whereas they are rare in immature samples. Bulk mineralogy data are in accordance with the observations, and the average albite content at R_0 < 0.9% is ~1%, whereas at R_0 ≥ 0.9% ~2%. Albite is common in microfacies A and B, whereas in microfacies C it only represents 0.5% of the bulk mineralogical content. The precipitation of albite is thought to be derived from the mobilization of Na and Al occurring in the early phases of diagenesis, because of the alteration and dissolution of detrital aluminium oxides (Jennings and Antia, 2013; Taylor et al., 2014; Wilson et al., 2016).

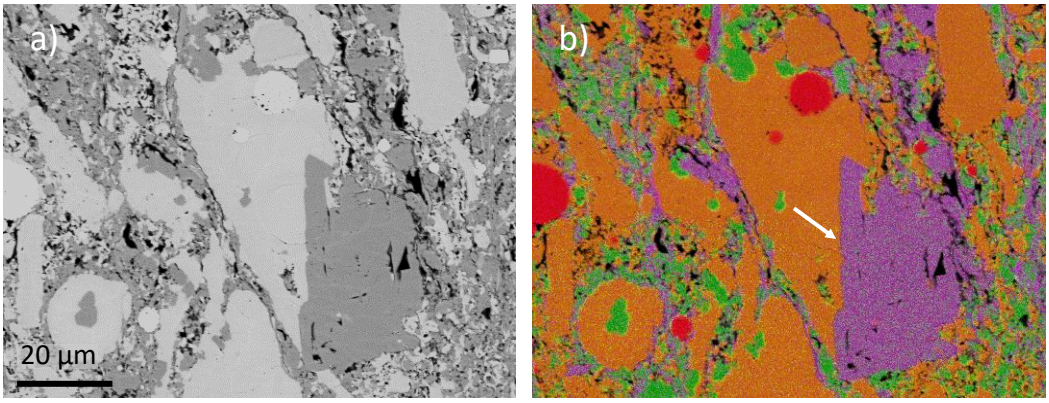

Figure 2.30: Sample GW4 (R_0 1.2%). a) is an SEM BSE image, b) is the elemental map of the same area. On the elemental map, the orange colour corresponds to calcite, green is quartz, purple is albite, and red is pyrite. The black arrow indicates the intergrowing between the albite and the calcite cement.

2.3.4.7. Pyrite

Pyrite is scattered through the matrix and occurs in minor amounts as a cement in the foraminifera chambers. As mentioned above, it is mainly seen in the oil window and gas window, but it is also frequent in the immature window. The average pyrite content is 1.5%, with no correlations with microfacies nor maturity. The presence of pyrite within the foraminifera chambers was not quantified, as the crystals can be too small to be seen and it appears opaque in transmitted light, making it difficult to differentiate with other opaque minerals. Under the SEM it appears as framboidal or euhedral. It has variable dimensions (< 30 µm) and is also seen filling fractures. Its occurrence is associated with the sulphate reduction during early burial diagenesis (Dawson, 2000).

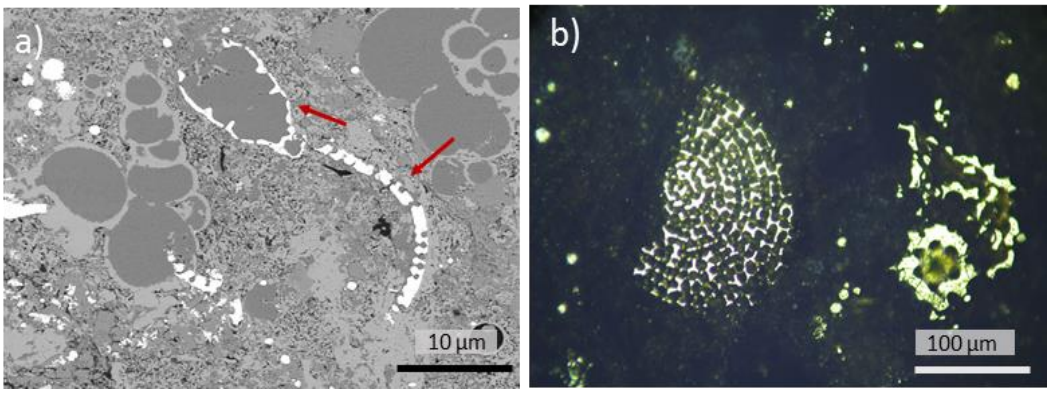

Figure 2.31: a) SEM BSE image of pyrite replacing calcitic foraminifera shells (sample IM2_1, R_0 0.5%); Reflected light photomicrograph of a thin section showing pyrite replacing radiolaria (red arrow) and siliceous sponges (white arrow) (IM2_1, R_0 0.5%);

Pyrite cements juxtapose early phase cements in the foraminifera, indicating an early phase cement which coincides in time with the precipitation of the other mineral phases that fill the tests. Replacive pyrite, usually at the expenses of calcite cements or bioclasts, is also found as scattered throughout the matrix and within the allochems (Figure 2.31).

2.3.4.8. OM infill

OM occurs as infill in the intraparticle fossil and mineral pores and in the interparticle matrix pores (Figure 2.32). Bitumen can be distinguished from the kerogen in the cases where it fills intraparticle porosity and when it coats mineral crystals. The OM that occurs as an infill of primary or secondary pores, is indicative of a hydrocarbon phase that has been generated and has migrated through the pore system, being trapped in free spaces (i.e. the pores).

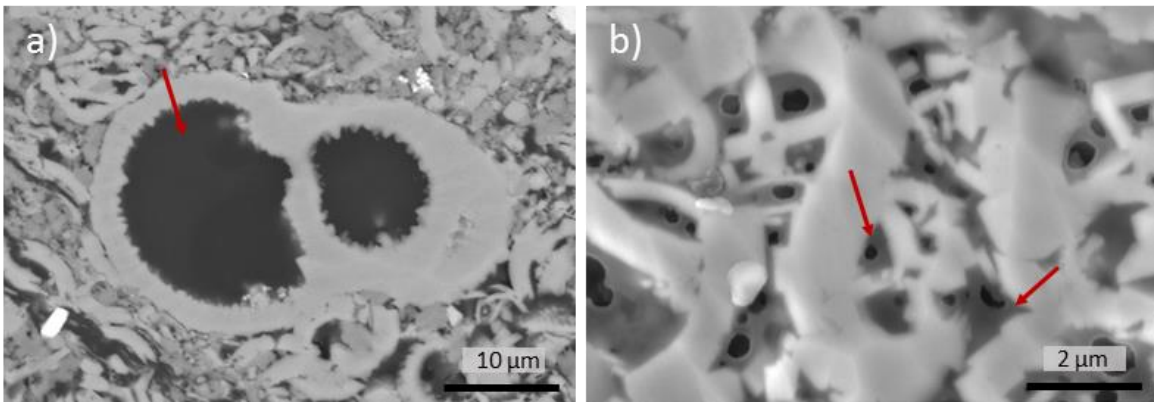

Figure 2.32: a) Bitumen filling the chambers of a foraminifer (sample OC2, R_0 0.5%). b) Bitumen filling the coccolithic matrix (sample H3A1, R_0 1.2%). In b) some spaces between the coccolith plates are completely filled with bitumen, whereas others present porosities within the bitumen.

The decomposition of organic matter was studied by Lewan (1991), who suggested that it produces an increase in volume, causing a pressure differential and the migration of the organic matter (Loucks and Reed, 2014). When the organic matter is clearly considered as migrated, for example the one present in the foraminifera tests, it is named bitumen. The OM in the foraminifera tests is common and is also seen under transmitted light. Point counting indicates that the OM fill is present at all maturities, which supports the hypothesis that the OM migration begins at the very early stages of diagenesis (at $R_0 \leq$

0.4%). The presence of OM infills in the low-maturity samples is consistent with generation from a sulfur-rich kerogen (Sun et al., 2015). In the foraminifera tests where other cement phases have precipitated, OM fills the remaining pore space. This implies that the organic matter migration post-dates the other early phase cements. Pyrite is commonly seen as a replacement or on the top of OM or other cements, which suggests that some pyrite precipitates also at a later stage (Figure 2.31). Organic matter infills are also commonly found within faecal pellets and within the matrix, filling pore spaces or fractures. Point counting results from the foraminifera chamber fills also show that Microfacies A samples present the major occurrence of OM infills (average value of 11.4%), which decrease in microfacies B and C (average values of 8.4 and 3 % respectively) (Table 2.8).

In the oil and gas window, as seen in the pore section, the bitumen infills, exhibit OM pendular and sponge-like pores, which are indicative of a continuous hydrocarbon generation and migration. XRD data show that the TOC (wt %) content is higher in the samples from microfacies A, which is also the microfacies with a lower average calcite content compared to microfacies B and microfacies C (47%, 78% and 79% respectively) (Figure 2.33).

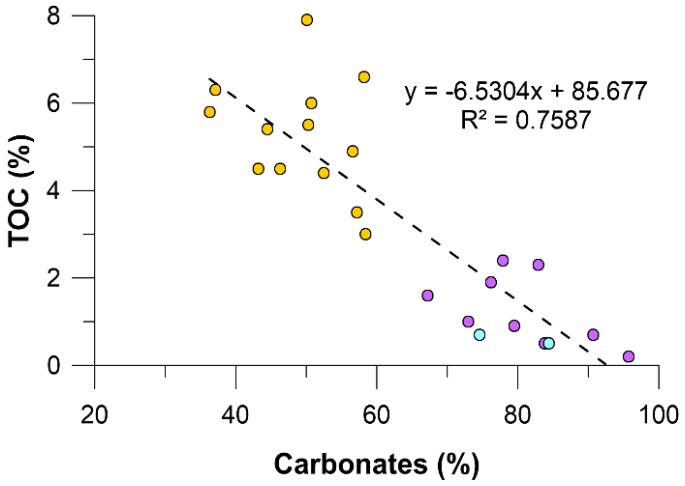

Figure 2.33: TOC wt. % vs carbonates (%) for all the samples analysed, from all maturities. The yellow colour corresponds to microfacies A samples, purple to microfacies B samples and light blue to microfacies C samples. There is a clear trend between the carbonates and the TOC (%), and between the carbonates and OM content and the microfacies types.

This suggests that carbonate cementation was hindered by the migration of bitumen in the TOC rich samples. However, as the carbonate cementation is more pervasive at high maturities and the organic matter migration occurs at an earlier stage, the inverse correlation is more indicative of primary depositional process controls (Pommer and Milliken, 2015).

2.3.4.9. Gypsum veins

Gypsum veins are very rare and are only observed in the outcrop samples (Figure 2.34). They can be as thick as 30 μm and they completely cut through the existing texture. Due to their occurrence only on outcrop samples, they are interpreted as weathering products, caused by the infiltration of meteoric waters saturated by $CaSO_4$. Gypsum veins commonly present shrinkage cracks, which are caused by the dehydration of the gypsum to its hemihydrate form (Schieber et al., 2016).

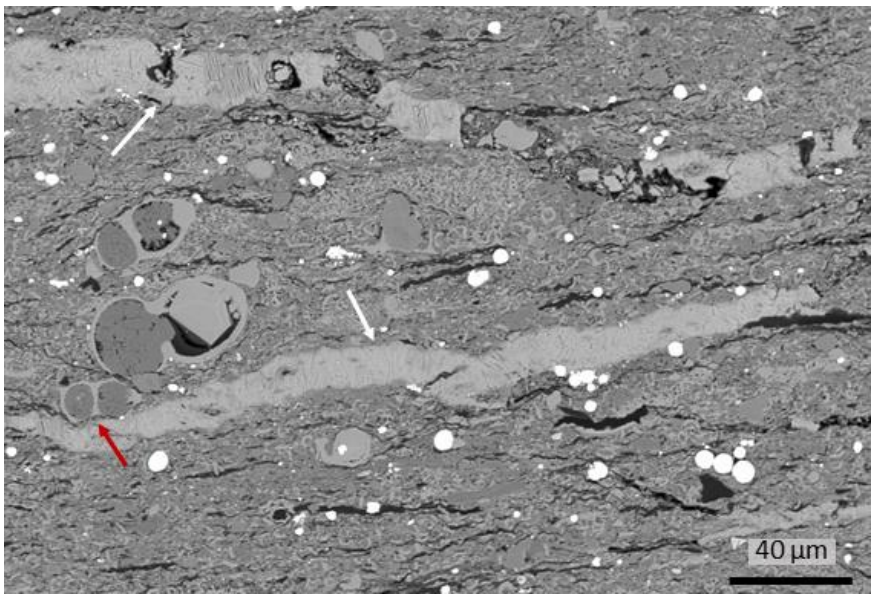

Figure 2.34: SEM BSE image. Gypsum veins (white arrows) in an outcrop sample (sample OC1, R_0 0.5%). The veins cut through the original texture. The red arrow indicates a foraminifera shell partially destroyed by the gypsum vein.

2.3.4.10. Compactional features

Compaction is indicated by the presence of collapse features, such as collapsed foraminifera chambers or fragmented shells (Figure 2.35 c and d). The foraminifera

usually remain intact, probably because of the early phase cements that infill the chambers rendering the allochems more resistant to the burial stress. However, when the tests are not completely filled with cements, they are subject to the compactional stress normal to bedding, and therefore prone to collapse and destruction (Figure 2.35 d). Other signs of compaction can be seen around the rigid grains. The ductile material (i.e. clays and OM) compacts around rigid grains (Figure 2.35 a). The lensoidal faecal pellets also appear flattened perpendicular to the burial stress (Figure 2.35 b).

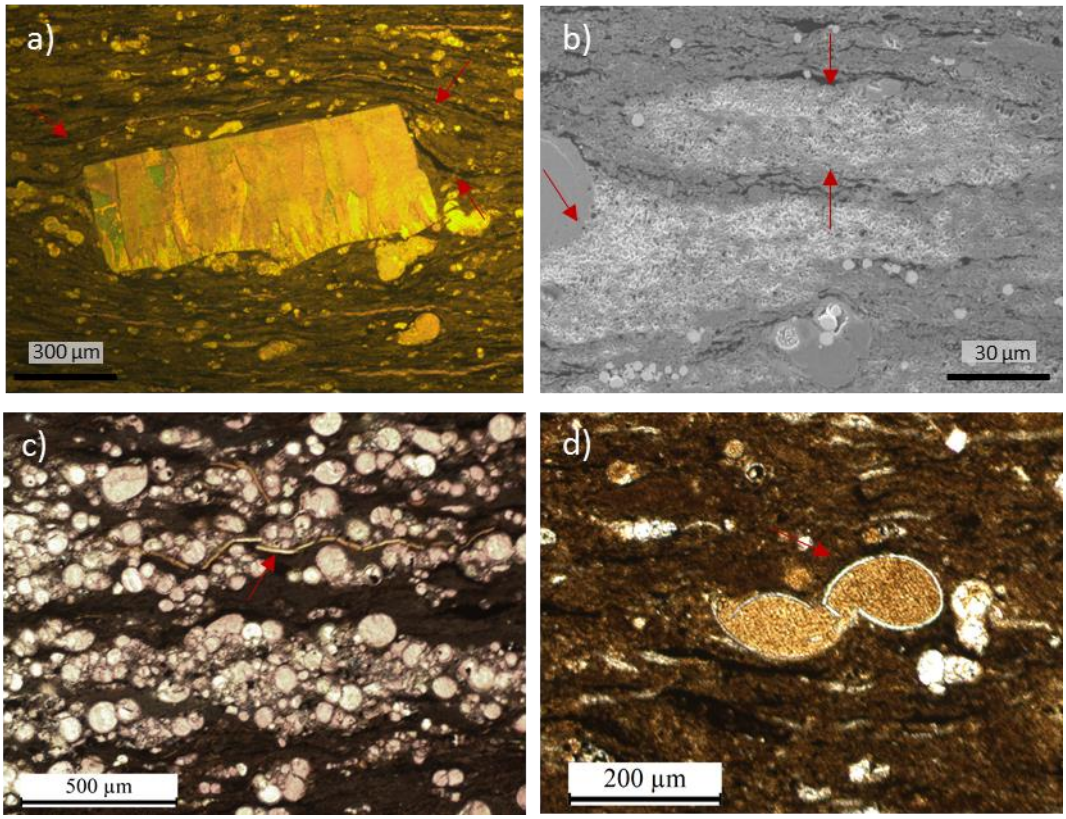

Figure 2.35: a) Thin section photomicrograph. The red arrows indicating ductile sediment compacting the hard bivalve shell (sample OC7, R_0 0.5%); b) SEM mixed SEM BSE image of a faecal pellets stressed in the direction of the bedding. On the left, a harder grain is compressing a faecal pellet (sample OC2, R_0 0.5%); c) Thin section photomicrograph of a thin bivalve shell broken by the foraminifera (pelecypod) (sample IM2_5, R_0 0.5%); d) Thin section photomicrograph of collapsed tests of a foraminifer (sample OW8, R_0 0.9%);

2.3.4.11. Dissolution

Evidence of dissolution of the mineral components is found in the contacts between the more cohesive particles or bioclasts. In some samples, pressure solution micro-stylolites have also formed. Dissolution is also present in minerals such as carbonates or K-feldspar and produces intraparticle dissolution pores. Intraparticle dissolution pores are mainly

present in the oil and gas window. The fact that dissolution pores begin to widely occur in the oil window, correlates them to the decarboxylation of kerogen that generally occurs between 80°C and 120°C and generates carboxylic and phenolic acids (Leggett and Zuffa, 1987; MacGowan and Surdam, 1993; Schieber et al., 2010; G. Yuan et al., 2019). These acids dissolve the mineral phases starting from the discontinuities in the mineral lattice, which generate the pores within the minerals (Figure 2.36).

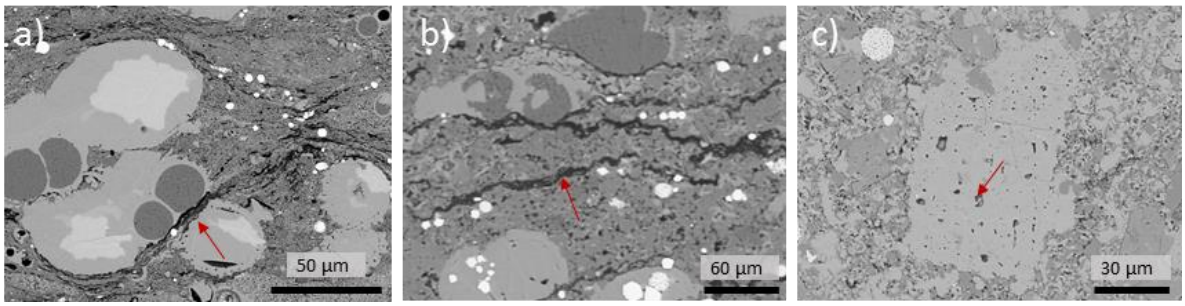

Figure 2.36: a) SEM BSE image. The red arrow indicates a contact between two tests. Where the contact has occurred, the two tests are partially dissolved. (sample OW8, R_0 0.5%); b) SEM BSE image. The red arrow indicates a pressure solution vein filled with organic matter (sample OW8, R_0 0.5%); c) SEM BSE image. The red arrow indicates dissolution pores within a carbonate crystal.

2.3.4.12. Fractures

The original texture of the samples can be overprinted by fractures (Figure 2.37). Where present, fractures can significantly contribute to the increase of permeability and act as pathways for the hydrocarbons (Loucks et al., 2012). The fractures are generally a few (<5 µm) thick. Identification of lateral extent is impeded by the limited size of the samples, but fractures are commonly observed to run from one side of the thin section to the other (~1 cm wide). The fractures generally run parallel to the laminations, but cross-cutting perpendicular fractures also occur. As observed by Ríos et al. (2016), microfractures can develop parallel to the bedding along the contact between the foraminifera-rich layers and the clays, by differences in mechanical strength. Fractures can be either empty or filled with cements.

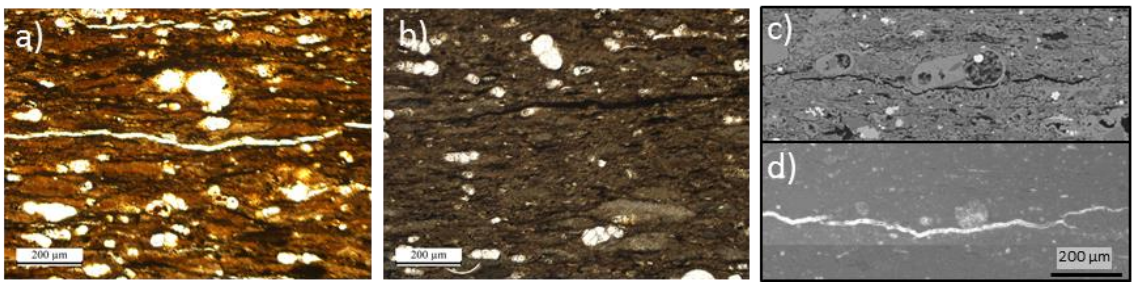

Figure 2.37: a) Thin section photomicrograph of sample IM2_7, R_0 0.5%; b) thin section photomicrograph of sample OW8, R_0 0.9%; c) SEM BSE and d) SEM SE images of a void fracture.

The most common cement is fibrous calcite. Pyrite cement is also common, especially in sample IM1_2. In many cases they cross-cut the existing texture as well as cement infills in the allochems. This indicates that they were formed in a late phase of burial diagenesis, and probably caused by the volume increase during the hydrocarbon generation processes (Bernard et al., 2013b; Blood and Lash, 2015). As explained in Chapter 3, caution must be taken when observing the fractures that are not filled with cements, as they can be induced by releasing stress from well recovery (Antrett et al., 2011; Flügel, 2004; Gregg et al., 1982) or by mishandling during sample preparation (see Chapter 3).

2.3.5. Interpretation of the samples paragenesis

The wide maturity range of the sample set (R_0 0.4 to 1.2%) provides a unique opportunity to investigate the diagenesis of the samples through time. Petrographic analyses by means of optical microscope, SEM and CL provide a relative timescale of the mechanical and chemical processes these sediments have gone through (Figure 2.38).

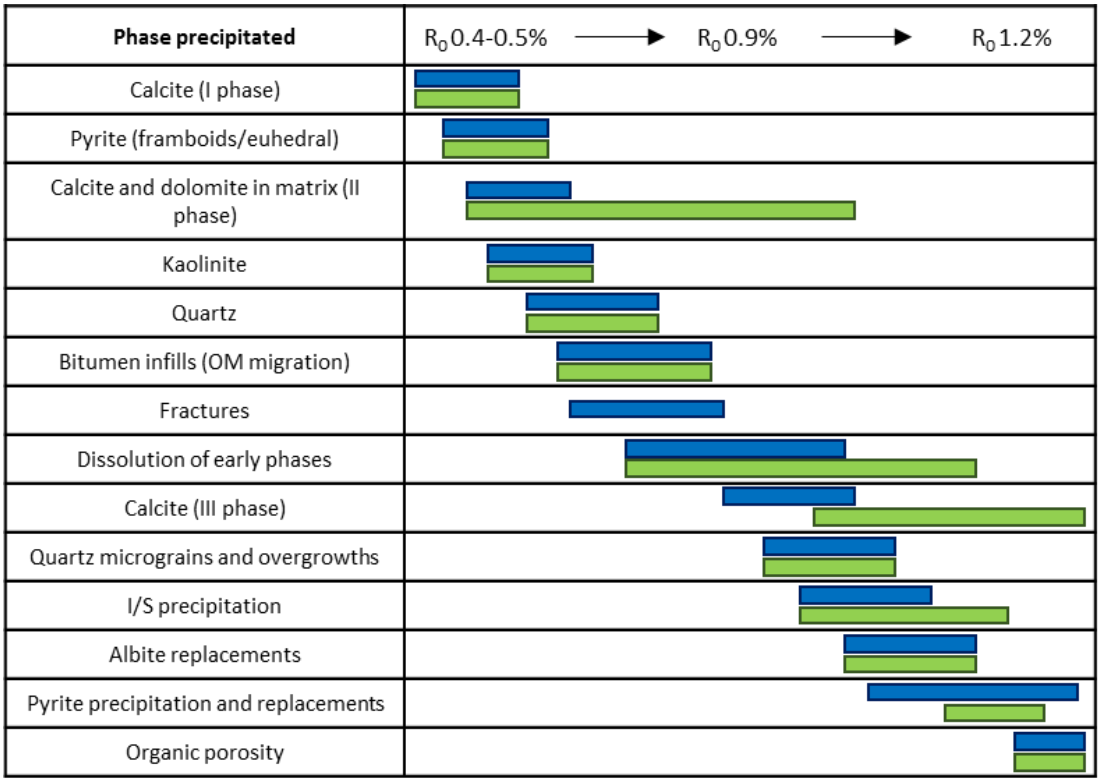

Figure 2.38: Reconstructed paragenesis sequence with the chemical processes occurred in microfacies A (blue) and microfacies B and C (green).

2.3.5.1. Compaction

The first process to modify the sediments deposited on the subsurface is mechanical compaction. Compactional processes begin in the early phases of diagenesis and continue during the burial history of the samples. Pommer (2014) suggests that at low maturities, the lack of extensive cementation and the presence of inter- and intraparticle pores within the allochems and the coccolithic debris is indicative of a porosity loss that has occurred primarily via compactional processes. Compaction is observed in the flattening of faecal pellets, in the rearrangement of ductile particles around more rigid and large particles and bioclasts, in the collapse of the foraminifera chambers and in the fragmentation of

thin shells. However, the large skeletal framework has allowed for the preservation of many micro- and nano- primary pores. Other authors (Fabricius, 2003; Gorniak, 2016; Mallon and Swarbrick, 2008; Pahnke, 2014; Pollastro, 1986), by studying the porosity evolution in chalk, have concluded that compaction associated to initial burial reduces porosities by up to 50%, and that further compaction is hindered by the rigidity of the carbonates and by the presence of cement phases. Mechanical compaction in the early phase of diagenesis is juxtaposed by chemical processes.

2.3.5.2. Immature window processes

The first chemical reaction is the precipitation of euhedral calcite cement. This cement is commonly observed in microfacies A in the foraminifera chambers and is thought to have preserved the tests during compaction (Pommer et al., 2014). The origin of this first generation of calcite cement is probably caused by the calcite-saturated marine waters and bacterial sulphate reduction processes (Irwin et al., 1977; Macquaker, 1997; McAllister et al., 2015; Scotchman, 1987). Sulphate reduction at $R_0 \leq 0.4\%$ is also responsible for the release of H_2S which, reacting with detrital iron minerals present in the system, causes the precipitation of pyrite (Berner, 1984). Pyrite cement occurs as euhedral and framboidal and is observed as filling the pores in the foraminifera with calcite and kaolinite and is thus considered synchronous with these mineral phases. Kaolinite, in fact, is also considered to be precipitated at $R_0 \leq 0.4\%$. This mineral generally fills the spaces in the intra-fossil pores that are not filled with calcite and it is also commonly observed filling completely the foraminifera chambers. Kaolinite is therefore interpreted as slightly post-dating the calcite cement precipitation. The presence of an early kaolinite phase is linked to the instability of other mineral phases (i.e. plagioclase), which dissolve and reprecipitate as more stable minerals. This was suggested for mudstone plays by several authors (Jennings and Antia, 2013; Taylor et al., 2014; Wilson et al., 2016), and also by Fabricius (2007), in North Sea chalk reservoirs. Quartz precipitation and replacements are also observed at $R_0 < 0.4\%$. Quartz derives from the precipitation of opal-A and appears in form of equant partcles and in form of micro-crystals (< 3 μm). At temperatures < 50° C, opal-A transforms in the more stable phase opal-CT, which in turns, at temperatures < 100° C, transforms into quartz (Kastner et al., 1977; Maliva and Siever, 1988). The equant

quartz and the micro-crystals begin to be present at $R_0 \leq 0.4\%$ and become abundant after the oil window. First stage quartz is thought to derive from the radiolaria shells, that are already almost completely dissolved during early diagenesis (if not replaced by other minerals, i.e. pyrite), and to replace early diagenesis phases (i.e.calcite, kaolinite). The fact that the micro-crystals overlie other minerals and fill the inter and intraparticle pores suggests that they were precipitated at $R_0 \leq 0.4\%$, after the calcite, the kaolinite and the pyrite cements. Dolomite is also observed replacing the calcite, and given the large dimensions of the crystals, is thought to have formed at $R_0 \leq 0.4\%$, when there was sufficient pore space for the mineral to form and precipitate. Quartz, dolomite, kaolinite and calcite cements in microfacies B and C samples are also considered to have formed at this stage. However, differently from microfacies B and C samples, in microfacies A the presence of high percentages of TOC (%) results in higher bitumen volumes. The presence of OM infills in the immature microfacies A samples suggests that the OM migration begins at $R_0 \leq 0.4\%$. The fact that the organic matter fills large intra-mineral and fossil pore spaces in microfacies A and B samples left unoccupied by pyrite, calcite, quartz or kaolinite, suggests that this phase postdates the other mineral phases and continues during the oil maturity stage. The filling and coating of organic matter in the immature samples is thought to inhibit the formation of further cement phases in the oil and gas window. Microfacies B and C samples, indeed, contain less TOC (%) and are more prone to secondary calcite reprecipitation compared to microfacies A samples.

2.3.5.3. Oil window processes

In the oil window, other phases increase in abundance such as albite and mixed I/S, whereas kaolinite becomes less abundant. Albite replacements and mixed-layer I/S are thought to have formed by the alteration of kaolinite and detrital K-feldspar (Bjørlykke, 2014). Illitization also releases Si, wich reprecipitates in form of micro quartz in the nano and micropores within the matrix.

In microfacies A, at R_0 ~0.9%, the bitumen fills or borders the minerals, modifying the wettability of the reservoir and potentially inhibiting further calcite precipitation (Scholle, 1977). In these samples, the carbonate cement continues to precipitate but is not pervasive as in microfacies B and C samples in the high maturity window (R_0 1.2%). The reason for

this is the low abundance of organic matter in these microfacies. The organic matter content is not enough to generate significant oil and alter the wetting state of the rock from water-wet to oil-wet, and therefore it does not suppress the diagenesis. Calcite cement, where possible, continued to precipitate throughout the burial history as seen in CL.

2.3.5.4. Dissolution and mineral precipitation

Dissolution associated with OM maturation is mainly observed in the creation of etched pores within the minerals, whereas dissolution derived by pressure-solution is observed between the rigid clasts and in pressure-solution veins (Figure 2.36). Dissolution also continues during late burial diagenesis, when the samples enter the gas window maturity. Fe redox reactions and the dissolution of radiolarians and of K-feldspar, calcite and I/S minerals allows for the availability in solution of elements such as Ca, Fe, Al, Si and Mg and the reprecipitation or the replacement of other minerals. Calcite reprecipitation is mainly observed in the faecal pellets, where the interparticle pores are in most cases occluded by calcite cements. Pyrite, for example, precipitates in this late stage in the organic matter or within mineral crystals. Textural heterogeneities observed with XR-CT

XR-CT analyses show that the samples are heterogeneous at the millimetre scale (Figure 2.39). Considering that each of the ~1000 slices analysed is one pixel wide (2.8 μm), the variations are measured along a ~2.8 mm thick volume. In the 5 samples analysed, the heterogeneities occur in all the samples, independently from their maturity and the microfacies type (A or B). Heterogeneities across the bedding are more pronounced and demonstrate mineralogical changes caused by environmental variations and sediment input over time. Along the bedding, the variations are less visible, especially for samples OW2, GW6 and IM2_1. This means that, at the millimetre-scale, in the same depositional event, the sediment input on the seafloor was deposited homogeneously. Both across and along the bedding, the carbonate variations are inversely correlated to the clay and mixed silicates-clays-carbonates variations, similarly to what observed from the XRD analyses. The abundances of the OM-pores and pyrite phases are too low to identify any variation at this resolution. The variabilities across the bedding in some cases exceed 100% of the

average values calculated for the total volume of rock analysed, whereas along the bedding on average they exceed the mean values by ~40%.

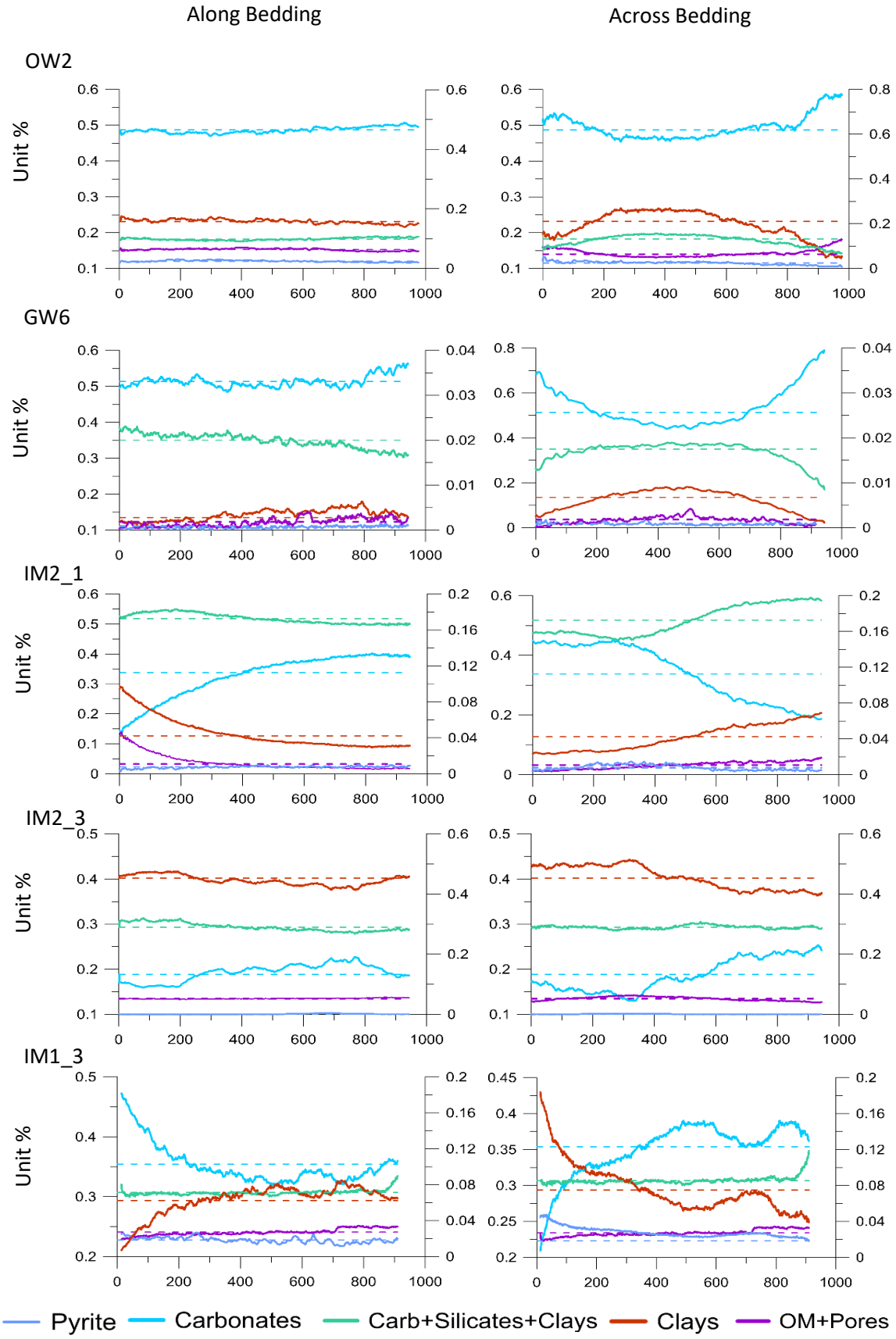

Figure 2.39: Calculated heterogeneities from XRCT scans. The x axis corresponds to the slice number, the y axis to the percentage of each mineral. The y axis on the right of each plot is the relative percentage for the OM and the pyrite phases, in minor abundances compared to the other phases (represented on the left y axis). The dotted lines correspond to the average value of each phase for the whole sample.

2.4. Discussion

Petrographic studies of the Eagle Ford samples allow the identification of diagenetic changes as a function of lithology and maturity. These changes are determined by specific mechanical and chemical factors, the understanding of which leads to a predictive model for reservoir quality (Ali et al., 2010; Driskill et al., 2009). Bulk mineralogical results show that the samples are carbonate and organic-matter-rich and contain clays, quartz, K-feldspar, pyrite and other minerals in minor abundances. Petrographic analyses show that the samples undergo mechanical and chemical changes as a function of thermal maturity.

2.4.1. Depositional environment

The mineral composition and the mechanical and chemical changes are strictly related to the depositional environment (Ali et al., 2010; Schieber, 2011). The low detrital quartz component in the Eagle Ford, for example, is caused by the presence of the San Marcos Arch, which blocked the clastic input from the North-East (Pommer, 2014) (Figure 2.1). Mineral composition differences are the main reason for the dissimilarities between microfacies A and B: microfacies A samples contain more TOC, more silicates and less carbonate compared to microfacies B samples. Moreover, the analogies in the texture, i.e. the laminations, and the presence of recrystallized foraminifera in the oil window wackestones, suggests that the depositional environment for the two microfacies was similar. In particular, the organic matter type (I-II marine kerogen), the very fine grain size of the sediments (< 62.5 μm), the scarcity of benthic fauna and the occurrence of laminations suggest deposition in deep (~100 m), dysoxic to intermittently anoxic environments (Bernhard, 1986; Denne et al., 2014; Donovan et al., 2012; Robison, 1997). Incomplete anoxia is suggested by the presence of sharp erosional contacts, wave laminations and ripples (Macquaker et al., 2007; Schieber, 2010; Schieber et al., 1998), which point to a depositional environment where bottom water currents occurred. Moreover, the high vertical heterogeneities and the condensed millimetric layers of planktonic fossils have been linked to periods of increased fertility and high primary productivity. This suggests that stratified waters and euxinic bottom water conditions alternated with times of mixed surface waters and suboxic to anoxic conditions, where

primary productivity was enhanced (Denne et al., 2016; Frébourg et al., 2016; Wendler et al., 2002; Wever et al., 2014).

2.4.2. The three microfacies: depositional context

The differences between the mudstone and the wackestone samples are shown by the large volume of carbonates in the wackestone samples, juxtaposed with a low TOC wt %. These two elements are linked to primary depositional processes. The low (average 1.3%) TOC values for the wackestone microfacies are related to aerobic oxidation of organic matter, which, as McAllister (2014) has suggested, it is likely to have occurred at the sediment-water interface. Changes in TOC values can also be related to differences in sediment input or to enhanced primary productivity, which can cause dilution (Arthur et al., 1986; Elderbak et al., 2014; Gamero Diaz et al., 2013; Macquaker and Bohacs, 2007). This is also shown by the $\delta^{13}C$ data taken on similar samples by McAllister (2017). $\delta^{13}C$ values indicate that carbonate cements are mainly derived from a marine source and not from microbial processes (McAllister, 2017 and references therein), which is in accordance to the fact that the system is dominated by marine, biogenic calcite. The lack of organic matter characterises also the two packstone samples (R_0 1.2%, ~0.5% wt TOC). Despite this similarity with the wackestone samples, the packstones display a coarser grained texture formed by bioclasts. The massive texture and the presence of large (> 20 μm), reworked bioclasts is indicative of a different environmental setting compared to the mudstones and the wackestones. The inclusion of echinoderms, bivalves and other reworked bioclasts suggests high energy event sedimentation (Harbor, 2011), with greater exposure to oxygenated environments and carbonate-saturated marine waters, which lithify the sediments.

2.4.3. Variations in time and space

The fact that mudstones, wackestones and packstones are present in the same sample set and in the same wells, is associated with a change in the depositional conditions. However, the absence of a complete dataset from each core and the absence of well correlations impedes to discriminate whether this is due to sea-level rise, or to the location of deposition of the samples. Many studies (Schieber et al., 1998; Wignall et al., 1994) have

highlighted the vertical and lateral variations in mudrocks and tied them to different depositional settings in time and space. In this specific case, studies from other authors with more complete datasets than this one propose that the Lower Eagle Ford Formation was deposited during a transgressive system tract (Donovan et al., 2012; Driskill et al., 2012; Liro et al., 1994a), which would lean towards the relative sea-level rise hypothesis. Nonetheless, the map of the sample locations (Figure 2.1) also shows that the samples were deposited in different parts of the Maverick basin, related to different paleoenvironments and paleobathymetries, which would favour the location hypothesis. However, results from the calculations of foraminifera dimensions show that there is no clear variation in the foraminifera lengths from one size of the Maverick basin to the other (well 1 to well 6). This could indicate that the surface water conditions and chemistry were the same all over the basin, and therefore that the microfacies were laterally continuous (Driskill et al., 2012). Therefore, changes in microfacies are more likely to be related to a change in sediment input through time and to the nature of biological productivity rather than a change between the depositional locations.

2.4.4. Diagenesis

Studying the diagenesis and reconstructing the depositional environment is also imperativee to determine how reservoir properties, such as porosity and permeability, vary within the samples, between the samples and between the microfacies. The porosity and the connectivity of the system are highly dependant on the mineral framework and on the diagenetic processes the samples have undergone. Many studies show that mechanical compaction in mudrocks and fine-grained carbonates reduces the porosity (Aplin et al., 2006; Milliken and Day-Stirrat, 2013; Pahnke, 2014; Scholle, 1977; Pollastro, 1986). In the samples from this study, pores are categorised as organic matter pores, interparticle matrix pores, intraparticle fossil pores and intraparticle mineral pores. The pores analysed with the SEM in this study are > 18 nm, but not necessarily the smallest pore sizes for these samples (see Chapter 4). Lønøy (2006), describing the pore system in Cretaceous and Tertiary chalk sediments, suggested that most of the carbonate-related pores were pores < 10 nm, occurring between grains of planktonic coccoliths (Pahnke, 2014). Given the large amounts of coccoliths in these samples, the presence of pores < 10

nm can be assumed as well. As the laminated foraminiferal mudstone microfacies is the only one in this dataset for which samples from the immature to the gas window are found, the evolution of the mineral and pore system with thermal maturity can be established.

2.4.5. Calcitic framework

In the mudstone microfacies, in the immature window, the rigid structure allows the preservation of the pores within the matrix, within the faecal pellets and within the fossils and inhibits the compaction of ductile grains (Loucks et al., 2012; Milliken and Day-Stirrat, 2013; Schieber, 2010). Particularly important are the faecal pellets, which can measure over 100 μm (Table 2.4), shelter more interparticle pores than the rest of the matrix due to a lack of clay laths clogging the porosities. They can account for as much as 25% of the total rock components and can provide a location where oil may reside. Moreover, faecal pellets have also been considered a possible source of hydrocarbons in chalk reservoirs (Moussa, 1988; Torres et al., 2017), and could potentially explain the source of some of the hydrocarbons in the Eagle Ford Formation as well. The abundant foraminifera, on the other hand, provide pores as large as 60 μm, in which liquid hydrocarbons can be trapped (Slatt et al., 2012). The interparticle matrix pores are on average the most abundant pore type at all maturities and in all microfacies (Table 2.7). This signifies that the calcitic skeletal framework, and consequently the diagenesis the samples are subject to, strongly affected the pore system and connectivity (Pommer and Milliken, 2015; Pommer, 2014). In microfacies B and C samples the carbonates are more abundant and the grain sizes are generally larger compared to microfacies A. Given the low amounts of the other components, microfacies B and C samples present a relatively higher amount of interparticle matrix pores compared to the other pore types (Table 2.8). In these microfacies (R_0 1.2%) faecal pellets and most of the intraparticle porosity results completely cemented. The fact that a reduced amount of foraminifera chambers are filled with bitumen compared to microfacies A (on average 11.4% in microfacies A compared to 8.4 and 3% respectively for microfacies B and C respectively), also indicates that microfacies B and C samples have generated and store fewer amounts of hydrocarbons compared to microfacies A.

2.4.6. Porosity reduction processes

The presence of calcite, kaolinite, pyrite and quartz cements in the immature samples indicates that porosity reduction processes occurred at $R_0 \leq 0.4\%$, even before significant compaction. Affected by the cementation are the interparticle matrix pores, in which kaolinite and micro quartz crystals precipitate. Around 90% of the large intraparticle fossil pores, on the other hand, are in the samples filled with cements. The pores are filled sequentially by the secondary minerals calcite, pyrite, kaolinite and quartz, with a predominance of calcite cement (on average in all the samples analysed ~68%). Subsequently to the precipitation of these cements, but always at $R_0 \leq 0.4\%$, the OM starts to migrate into the available pore spaces, further reducing the porosity. Even though the studied samples from microfacies B and C all come from the gas window, evidence suggests that the pore system for these samples already changed in the immature window as well. Highly pervasive cementation processes, in fact, are not hindered by the migrated organic matter as in microfacies A samples. Microfacies B and C do not contain enough organic matter to impede the pervasive calcite cementation. Because of this, many of the inter- and intraparticle pores that can be seen in microfacies A (i.e. within the faecal pellets, in the matrix and in the foraminifera) are not present in microfacies B and C. However, micro migration from local OM-richer microfacies (A) would be expected to trap hydrocarbons in the microfacies with lower contents of OM (microfacies B and C). This could be explained by the fact that perhaps, in the early stages the amounts of bitumen generated in the OM-rich layers is not enough for expulsion. When the samples enter the oil window, in all the microfacies types, minerals start to dissolve as a result of physical processes, chemically unstable phases and acidic fluids formed by organic matter degradation (Figure 2.36). This causes chemical changes in the system and the reprecipitation of minerals in form of cements, mainly calcite, kaolinite, I/S and quartz. The cements precipitate in the available remaining spaces, which are primary and secondary pores in the matrix, in the faecal pellets, in the fossils, or in fractures caused by the fluid pressure generated during burial (Gottardi and Mason, 2018). In particular, the small (< 3 μm) crystals of quartz and clays are responsible for the reduction of the interparticle matrix pores. Overall, qualitatively speaking, the cementation of the skeletal framework produces a decrease in the bulk porosity and a decrease in the pore sizes

(Milliken and Day-Stirrat, 2013) (see chapter 4 for more details). Indeed, the interparticle and intraparticle fossil and mineral pores, which are affected by higher degrees of compaction and diagenesis compared to the immature window samples, begin to close up or completely disappear.

2.4.7. Porosity generation

The processes responsible for porosity decreases are partly compensated by processes that increase porosity.

2.4.7.1. Thermal maturation of organic matter

In the gas window, the organic matter pores increase due to thermal cracking and gas generation (Chen and Xiao, 2014; Löhr et al., 2015). Organic matter pores are more common in the microfacies where there is more TOC, i.e. in microfacies A samples. In microfacies B, even if the OM is not abundant, their relative abundance compared to the other pore types, is between 10 and 30%. The reason for this is that, in general, the other pore types decrease in abundance. In microfacies C samples, the amount of TOC is so low that the organic matter generated pores are < 5% of the pore types. The OM pores, which are relatively smaller compared to the other pore types, form within the organic matter infills and stringers, creating the spongy aspect in the OM. However, merely from 2D image analyses, little can be said about the connectivity and permeability of the system and on the hydrocarbon flow. The fact that the generated organic matter found the path to migrate in the pores suggests that the system was connected at least at $R_0 \leq 0.4\%$. Further insights on the pore system require integration of the petrography data with measurements on the pore system, which is undertaken in the next chapter.

2.4.7.2. Dissolution

Dissolution caused by acidic fluids produces intraparticle dissolution pores, which appear especially in calcite and feldspar minerals (Baruch et al., 2015; Löhr et al., 2015). The dissolution pores, however, are at most 14% of the overall pore types in the mudstones and in the wackestones. In the packstones, they reach 31% of the total pore types. However, in microfacies B and C the system is affected by pervasive cementation,

which reduces the total porosity (Milliken and Day-Stirrat, 2013). The dissolution in the grains might be due to the higher depth at which the samples are found, or to the intrinsic nature of the clasts. Perhaps, shell fragments and echinoderms already present structural mineralogical defects that allow the acids to etch the grains more effectively. The dissolution of primary mineral components caused by acid generation and pressure dissolution thus produces a redistribution of the porosities, with formation of dissolution intraparticle pores and the reprecipitation of the phases in a more buffered system.

2.4.7.3. Fractures

Reservoir properties also require an adequate fracture characterization. Natural fracture porosities, when present, can increase the vertical and lateral connectivity and provide fluid pathways throughout the formation (Ramirez and Aguilera, 2016). In these samples, fractures are common and range from the micrometric to centimetric scale. Fractures are found filled with hydrocarbons, which validates the hypothesis that fluids exploited these channels as migration pathways during the expulsion phase. Also, they can be found filled with cements, and in particular with calcite, which suggests that the fluids were calcite-saturated. Despite acting as baffles in the sediments, it has been suggested that fractures with cements can play an important role in the production phase, as they can be reactivated during hydraulic fracturing and serve as fluid pathways (Aplin and Macquaker, 2011; Cho et al., 2013; Gale and Holder, 2010; Ghanizadeh et al., 2015; Loucks et al., 2012). Furthermore, in these samples, empty fractures are also frequently found. Many authors (Clarkson et al., 2012; Gottardi and Mason, 2018; Ramiro-Ramirez, 2016) have highlighted the presence of a wide natural fracture system in the Eagle Ford Formation at many scales (nm to km). The fractures pores observed in these samples could have contributed to the migration of hydrocarbons and overall fluid flow. However, fracture pores, especially at this scale, are likely to be caused partly by stress release or by sample preparation and therefore caution must be taken in assessing the permeability and connectivity of the system by considering the fractures in the calculations (Clarkson et al., 2012; Ramiro-Ramirez, 2016).

2.4.7.4. Brittleness of the rock

Although not considered in this study, another important property to take into account is the brittleness of the rock. The three microfacies, being carbonate-rich, are brittle and likely to propagate fractures during hydraulic fracturing (Davies et al., 2012; Mcallister, 2017). The presence of laminations in the mudstone and wackestone samples provides planes of weakness where the fractures can nucleate and propagate. Moreover, the low values of CEC in all the microfacies (< 10 meq/l) allow hydrocarbon extraction with a reduced risk of clay mineral swelling (Mc Allister, 2017).

2.5. Concluding comments

Carbonate and organic-rich samples from the Lower-Eagle Ford Formation (Texas, USA) were examined to gain a better understanding of the sedimentology and diagenetic history of the Formation and to evaluate the factors that influence its reservoir characteristics. Namely, the petrographical analysis presented in this chapter allowed the determination of the organic matter content and type, to evaluate the hydrocarbon generation potential and to observe the changes in fabric and mineralogy with increasing temperature and maturity. All these factors also allow to better understand the pore system and its evolution during burial diagenesis.

The key outcomes of this study are:

1. The formation is highly heterogeneous, and three different microfacies can be distinguished: laminated foraminiferal mudstones, wackestones and packstones. The laminated foraminiferal mudstones are carbonate-rich (47.6% on average) with an average TOC content of 5.2 wt. %. The wackestone samples are interpreted to have been formed in similar depositional settings as the laminated foraminiferal mudstones but present higher carbonate and lower TOC content. This facies presents extensive calcite precipitation, that occludes or reduces the pores in the system. The packstones are formed by large bioclasts fragments held together by carbonate cements. They are highly carbonatic (~80%), with an average TOC value of 0.6 wt %.
2. Types of pores were identified: interparticle matrix pores, intraparticle pores (fossil, dissolution and mineral) and organic matter pores. Interparticle matrix pores are the dominant pore type, but with the increase in maturity, organic matter pores are found to increase relative to the other pore types up to becoming the prevailing pore type in the samples in the gas window, but only in some samples in the laminated foraminiferal mudstones. Changes in pore types with changes in maturities and lithofacies underline how the pore system is interconnected with the diagenesis and mineralogy of the samples. Organic matter pores, when the TOC wt % is sufficiently high, can play an important role in the whole pore system development.

3. Five domains were identified in these samples; fossils, matrix, faecal pellets and organic matter. Foraminifera are the most common fossil type in all microfacies. The matrix is mainly composed of micron-sized coccolithic debris (~40%) and clay minerals (~20%). The faecal pellets are formed predominantly by coccolithic debris (~90%), hence they are considered a separate domain from the matrix.
4. Petrographic analyses show that the laminated foraminiferal mudstones and wackestones were deposited in an intermittently dysoxic environment in which weak bottom water currents occurred. This depositional environment allowed for the preservation of the organic matter and for the formation of vertical heterogeneities. In the laminated foraminiferal mudstones, millimetric condensed layers of planktonic fossils are alternated to more clay and organic-matter rich laminae. In the wackestones, the original laminated texture has been disrupted by pervasive cementation. In the packstones instead, the massive texture suggests a more oxygenated and a higher energy depositional environment compared to the other two microfacies.
5. The presence of high degrees of heterogeneities, especially in the laminated foraminiferal mudstones, implies that the Eagle Ford are probably characterised by high degrees of vertical anisotropy, which impacts the permeability and fluid flow properties of the system (Yang and Aplin, 1998).
6. The organic matter is a type I-II marine kerogen. The main macerals are liptinite followed by inertinite and vitrinite. In the immature window, the samples also show a high hydrogen index (between 390 and 790 mg HC/g TOC). Both the organic matter type and the high hydrogen index are indicative of organic matter with high hydrocarbon generation potential, implying the Eagle Ford is a good source rock.
7. The samples belong to three maturity ranges (R_0 0.4-0.5%, R_0 0.9% and R_0 1.2%). This allows correlation of the different diagenetic processes to the different thermal windows. Cementation starts to occur in the immature window with the precipitation of early calcite and pyrite cements and subsequently kaolinite and quartz. In the mudstones, the cements mainly fill the intraparticle fossil pores within the foraminifera chambers and the interparticle matrix pores in the matrix

and in the faecal pellets. As burial stresses increase, dissolution of mineral components and pressure-solution features start to appear in the oil and in the gas window (T > 80 ^{0}C). Intraparticle dissolution pores in carbonate and K-feldspar minerals also appear in the oil window and are linked to the acid production caused by the decarboxylation of the organic matter. The dissolution of mineral components prompts the availability of chemical components in the system, which reprecipitate in forms of cements. The cements increase in the oil and gas window maturity, especially in the wackestones and in the packstones microfacies samples. The different cementation processes between the microfacies have here been linked to different depositional environments as well as to the bitumen migration. Since the generation of hydrocarbons and their initial migration at $R_0 \leq$ 0.4%, bitumen infilling pores is thought to inhibit carbonate cementation. At $R_0 \geq$ 1.2% (~120 ^{0}C) the organic matter starts generating gas, which creates sponge-like pores within the organic matter. This process occurs in all the microfacies, but given the low amounts of TOC wt % in the wackestones and the packstones, it is more evident in the laminated mudstone samples. The amount of TOC wt % in the system is considered crucial in the interpretation of the pore system, both because more organic matter inhibits cementation and preserves the primary pores and because in the gas window the organic matter generates porosities.

8. The pore system in the laminated foraminiferal mudstone microfacies is believed to host the best reservoir characteristics; the lower cementation and the higher amount of TOC wt % help to preserve the primary mineral pores and to generate more hydrocarbons. The presence of laminations in the system also provides important planes of weakness where fractures can nucleate and propagate during hydraulic fracturing.

Chapter 3

Characterization of the porosity system of the Eagle Ford Formation as a function of diagenesis and maturity

3.1. Introduction

In the petroleum industry, evaluating the quality of a reservoir is essential to understand its production potential (Birdwell and Washburn, 2015; Chalmers et al., 2017). In particular, in unconventional reservoirs, the mineral and textural heterogeneity combined with the small size (nano to microscale) of the pores require a thorough characterization of the system (Aplin and Macquaker, 2011; Bryndzia and Braunsdorf, 2014; Macquaker et al., 2007). Indeed, the quality of unconventional reservoirs is defined by a combination of rock properties, such as available fluid storage, effective permeability, organic matter content and organic matter type (Shim et al., 2011). The available fluid storage and the effective permeability of a reservoir are determined by the pore system (Clarkson et al., 2012), which in unconventional reservoirs is constrained by narrow, irregular pores. In particular, in these reservoirs the permeability ranges from sub-nD to tens of μD (Bustin et al., 2008; Wang and Reed, 2009), impeding a free-state fluid flow as in conventional reservoirs and therefore a hydrocarbon extraction by conventional methods (Clarkson et al., 2012).

3.1.1. Pore system controlling factors

3.1.1.1. Mineralogy

Rock textures, together with the mineralogical and organic matter content of the rocks, are fundamental controls of the pore system (Bjorlykke, 1998; Javadpour et al., 2012; Milliken, 2014; Wilkinson et al., 2001). Textural and mineralogical variations reflect both temporal and lateral variabilities of the depositional environment and diagenetic processes (Macquaker and Gawthorpe, 1993; Macquaker et al., 2007). Therefore, the bulk rock framework and its transformation with diagenesis must be studied in relation to the differences in pore space geometries and their evolution during thermal maturation (Houben et al., 2014; Jennings and Antia, 2013; Philipp et al., 2017). In mudstones, for example, when platy minerals are present (i.e. clays and micas), the pore structures within these minerals are complex and formed by pores smaller than 50 nm (Chalmers and Bustin, 2015). These pores, given the ductile behaviour of clays and micas, evolve with an increase in burial stress, temperature and compaction (Aplin et al., 2006; Aplin and Moore, 2016; Dewhurst et al., 1998; Rutter and Wanten, 2000; Yang and Aplin, 2010). More mechanically competent particles, instead, such as calcite and quartz, are able to shelter interparticle pores larger than 50 nm at increasing burial stresses (Schieber, 2013). During diagenesis, precipitation of mineral phases in form of cements in the available pore spaces is believed to induce the reduction of pore volumes (Aplin et al., 2011; Chalmers and Bustin, 2015; Milliken and Day-Stirrat, 2013; Tiab and Donaldson, 2004) and the hindrance in the flow of hydrocarbons during primary migration. In contrast, chemical dissolution of mineral phases can develop porosity within minerals (Baruch et al., 2015; Loucks et al., 2010; Schieber, 2013).

3.1.1.2. Organic matter content

Another component that is often positively correlated to the increase in pore volume is organic matter (OM) content (Loucks et al., 2009; Wang and Reed, 2009). Many studies have shown that maturation of kerogen and bitumen in the gas window induces the formation of organic nanopores which, due to their large surface areas, are able to adsorb

and store large amounts of gas (Chalmers et al., 2017; Curtis et al., 2011; Loucks et al., 2010, 2009; Ross and Marc Bustin, 2009; Wang and Reed, 2009). Moreover, Bernard et al. (2013), Driskill et al. (2012); Löhr et al. (2015) and Milliken et al. (2014) observed a correlation between the shape of the organic pores and the maceral type, concluding that porosity and pore-size distribution is also influenced by the OM nature. Coating of minerals with migrated hydrocarbons is also considered responsible for the inhibition of the precipitation of further mineral phases (Bukar, 2013; Worden et al., 1998). This favours the preservation of porosity, also explaining the positive relationship between the organic matter content and the pore volumes, even at low maturities (Chalmers et al., 2017; Sun et al., 2017).

3.1.1.3. Rock texture and microfacies

Along with the mineralogical content and the diagenetic modifications, rock texture and facies types are also responsible for pore system changes (Bathurst, 1974; McAllister et al., 2015; Mcgarity, 2013; Taylor and Macquaker, 2014). In laminated mudstones, for example, the horizontal parallel bedding provides preferential pathways for fluid flow, rendering the horizontal permeability over 10^3 times higher than the vertical permeability (Armitage et al., 2011; Chandler et al., 2016; Mullen, 2010; Philipp et al., 2017; Rutter et al., 2017; Tiab and Donaldson, 2004; Yang and Aplin, 1998).

Mineralogy and facies types are also responsible for changes in rock mechanical parameters (Busch et al., 2017; Philipp et al., 2017; Rutter et al., 2017). Mechanical parameters are important during the completion phase, as they determine the "frackability" of the rocks and the productivity potential of the reservoir (Josh et al., 2012; Shim et al., 2011). Geomechanical studies demonstrated that Young's elastic modulus decreases with increasing clay and TOC content and increases with increasing carbonate and silica (Hornby, 1998; Jarvie et al., 2007; Rutter et al., 2017; Rybacki et al., 2016; Sone and Zoback, 2013). Therefore, the presence of calcite, dolomite and quartz or feldspar over more ductile materials (i.e. clays, micas, organics), increases the brittleness of the rocks, facilitating the fracturing process and increasing borehole stability (Gamero Diaz et al., 2013; Jarvie et al., 2007; Josh et al., 2012; Li et al., 2018; Peters et al., 2015; Rutter et al., 2017; Slatt, 2011; Wang and Reed, 2009). Being relatively brittle and more resistant to

compaction compared to clay-rich systems, carbonate-rich mudstones are particularly attractive to the energy industry.

3.1.1.4. Aim of the study

This study aims to:

1) Analyse how the pore system relates to the rock fabric. Quantitatively measure the pore types and pore shapes.
2) Quantify the pore numbers and pore volumes.
3) Determine the connectivity of the pore system and the type of pores the system is composed of.
4) Determine the pore system changes in relation to the petrographic background, and infer how the thermal maturity and diagenesis changes impact the pore system and connectivity.

Given the heterogeneity of the formation, implementing a multi-scale, multi-techniques approach leads to a thorough understanding of the pore system. The robust workflow of techniques and methods enables to have a detailed characterization of the pore network, which will eventually be of aid in the well performance and production phase. In addition, the produced data can be implemented in fluid flow models in order to minimise the uncertainties regarding the volume of hydrocarbons present, their location and accessibility. Deciphering how the pore system relates to the microfacies type also helps to upscale the micrometre and centimetre scale rock properties to entire reservoir sections where similar fabrics and textures are detected.

Combination of the detailed petrography study in chapter 2 and the extensive quantitative analysis in this chapter add further rigor and in-depth analysis to previous studies on porosity characterisation in mudrock reservoirs and highlight the importance of a holistic approach.

3.1.1.5. The samples analysed

In this study, samples ranging from the lower oil maturity window (R_0 0.44%) to the gas window (R_0 1.22%) of the Lower Eagle Ford Formation were analysed. The Eagle Ford is

a carbonate- and organic matter-rich formation that was deposited in the proto-Gulf of Mexico between 91 to 98 Ma. At present, this formation extends from East to West Texas, producing 1.3 million bo and 4.9 tcf of gas per day (U.S. EIA, 2019), making it the second-best US unconventional play, after the Marcellus basin play. The formation is characterised by limestones and marlstones rich in foraminifera and coccoliths, which affect the heterogeneity of the pore system and the behaviour of the fluid flow (Denne et al., 2014; McAllister et al., 2015; Pahnke, 2014). As the porosity system is heterogeneous and characterised by nanometric to micrometric pore sizes, a multi-scale and multi-technique approach is needed to develop a comprehensive understanding of its structure (Bustin et al., 2008; C.R. Clarkson et al., 2013; Mastalerz et al., 2008; Schmitt et al., 2013). Bulk chemistry and petrography data provide information on the mineralogy of the rocks and on the microfacies and domains constituting the rocks. Imaging techniques such as electron microscopy allow the quantification of the pore types, shapes, orientation, sizes and the monitoring of sediment transformations occurring during diagenesis (Chalmers and Bustin, 2015; Shao et al., 2017). Gas adsorption and mercury injection data bring essential information to the reservoir porosity characterization, namely the size of the pore bodies and throats as well as their volume and specific surface area. However, to have a better understanding of the 3D pore structure, direct visualization of the rock structure is advantageous. For this, X-Ray Computed Tomography (XRCT) and Focused Ion Beam (FIB) slicing are routinely used methods (Desbois et al., 2011, 2009; Hemes et al., 2015; Klaver et al., 2016, 2012; Zhou et al., 2016). For rocks as tight as these, the FIB technique is preferred, as it enables the visualisation of pores as small as 20 nm, in contrary to the XRCT that is not able to distinguish pores smaller than 1μm.

3.1.1.6. Previous works on the Eagle Ford Pore system

Several studies have previously analysed the pore system of the Eagle Ford in an effort to better determine the reservoir properties (Anovitz et al., 2014; Chalmers et al., 2017; Ko et al., 2017a; Ojha et al., 2017; Pommer et al., 2014; Schieber et al., 2016). However, no work has been carried out on the evolution of the pore systems during thermal maturation, merging petrographic data with the analytical techniques and analysing the porosities of samples in 3D. Pommer (2014) analysed in detail the porosity evolution, but only using

SEM analyses. Chalmers et al. (2017) adopted a multidisciplinary approach, taking into account the framework and the thermal maturity of the samples. In their study, however, only the evolution of the organic matter was analysed and not the substantial porosity associated with mineral phases. Ko et al. (2017) investigated the Eagle Ford pores and pore network in a quantitative way using various techniques. Nevertheless, the samples examined were all taken from two oil-producing wells, ruling out the possibility of understanding the evolution of the porosities as a function of burial diagenesis.

3.2. Methodology

25 samples from the Lower Eagle Ford Formation were taken from 6 different wells and 2 outcrop locations from the immature, oil and gas window in West Texas, US (Figure 2.1).

To characterise the porosities, the following techniques and parameters were used:

3.2.1. Helium Pycnometer

Grain density measurements were carried out by using a Micromeritics AccuPyc II 1340 Pycnometer at Durham University. The gas chosen for the analyses was helium, as it is chemically inert and with a smaller kinetic radius (260 ppm) compared to other gases. The experiments were performed on volumes of rock smaller than 1 cm^3, dried for 24 h at 105° C. The total porosities were then calculated using the following equation:

$$\Phi = \left(1 - \frac{\rho b}{\rho_{gr}}\right) \cdot 100\%$$

Where ρb is the bulk density measured of a calculated volume and mass and ρ_{gr} is the measured grain density for each sample.

3.2.2. SEM and FIB-SEM

SEM images at high resolution (4096 × 3349 pixels) were collected at Durham University using a Hitachi SU-70 FEG SEM, with a voltage of 10 KV, a working distance of 15 mm and a variable magnification of 500 × to 10k ×.

The 20 samples analysed were 3 mm diameter cores drilled using a Gatan ultrasonic cutter from 100 μm thick thin sections and Ar-ion polished using a Gatan precision ion polishing system with beam energies of 0.1 to 0.3 kV and an angle of 5^0. The thin sections were all cut perpendicular to the bedding of the lithologies. After polishing, the samples were carbon-coated to avoid charging, reduce thermal damage as well as improve the secondary electron signal. Backscattered and secondary electron images were taken simultaneously in order to analyse the samples components as well as the porosities in the samples respectively. As described in chapter 3, by a qualitative observation of the variations in the porosity parameters and values relative to the different constituents, five

different domains were chosen: fossils and microfossils, faecal pellets, pyrite, organic matter and matrix. The distinction of the domains allows inferences about which domains contribute the most to the overall porosity.

In order to distinguish and quantify the domains, high resolution (4096 × 3349 pixels) SEM images for areas of 1mm x 1mm at a magnification of 600 × were taken for all the samples. In the same areas, chemical element identification was also carried out by producing EDX maps with an Oxford Instruments EDX system (X-MaxN 50 Silicon Drift Detector) provided in the Hitachi SU-70 FEG SEM. The maps were taken at a resolution of 1024 × 884 pixels, a voltage of 20 kV and a dwell time of 250 μs.

The same areas were also analysed using a FEI Helios Nanolab 600 at Durham University. This instrument has the advantage of producing more stable, better quality high magnification secondary electron images compared to the Hitachi SU70. However, since the Nanolab microscope does not have an EDX or a backscattered detector, the porosity images taken with this instrument had to be correlated to the chemical and domain studies performed with the Hitachi SU70 microscope.

In order to remove any uncertainty derived from the heterogeneities in the samples, for each sample four areas of 50 μm × 50 μm were randomly chosen in order to provide a reliable 2D representation of each sample. Each area consisted of a montage of 20 high resolution (4096 x 3349 pixels) and high magnification (10 k ×) images measuring 12.74 μm in width and 10.3 μm in height (Figure 3.1). The pixel size for these images was 3.1 nm/pixel, and the smallest pores identified had a diameter of 18.8 nm. The images were taken using the instrument immersion mode, at 1.50 kV, 4.0 mm working distance and a dwell time of 10 μs. The overlay of the latter images with the corresponding EDX maps allowed to discern five main porosity types and quantify the respective percentages: matrix interparticle pores, mineral intraparticle pores, fossil intraparticle pores and organic matter pores.

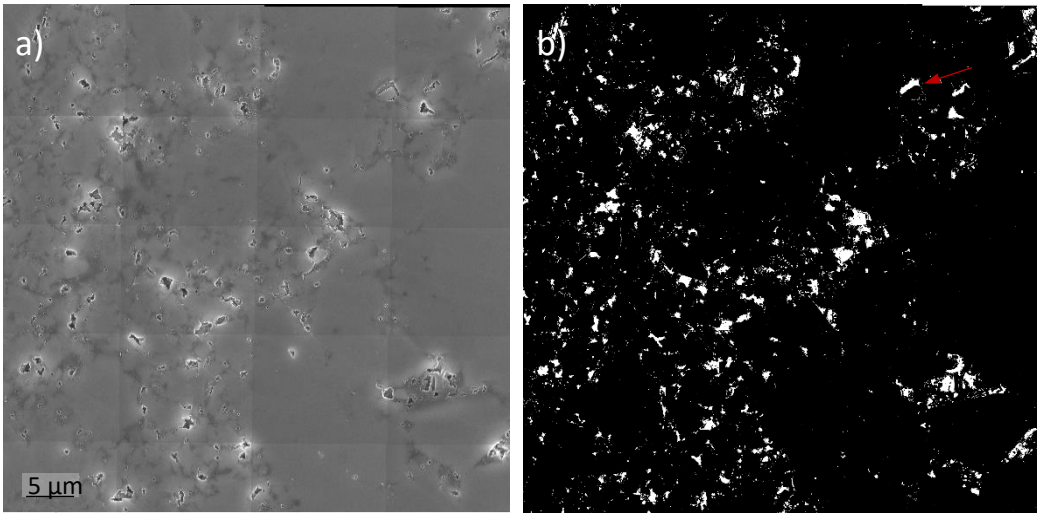

Figure 3.1: a) Example of an SEM-SE 50 µm x 50 µm map (area 2, sample GW2, R_0 1.2%) b) example of a Matlab binary image porosity thresholding of the same area. The red arrow indicates a pore were the Matlab code has not detected the pore boundary correctly. After manually correcting the pores, for each pore the different parameters were extracted and analysed separately.

The quantification of the area percentage of the porosities and other parameters of each image and area was carried out by means of the software MATLAB™ provided with the Image Processing Toolbox™. Each pore was segmented and separated from the rest of the image by means of specific algorithms. To do so, the Canny method was used. This consists of a multi-step algorithm that reduces the image noise by means of a Gaussian filter, computes an image gradient and thresholds the output. The result is an image with only the thresholded edges of the objects, in this case, the pores (Canny, 1986). To have better edge detection results, dilation, eroding and greyscale segmentation processes were implemented to the Canny method. If the pores visible to the naked eye were not all automatically detected, the images were manually edited using Photoshop™ (Figure 3.1).

For each pore in every image, different parameters were analysed:

Area: the number of pixels in the region converted in nm^2.

Perimeter: the boundary of each porosity in pixels converted in nm.

Equivalent diameter: is calculated as the diameter of a circular pore with the same area, in nm. It is calculated as $2 \cdot \sqrt{\frac{Area}{\pi}}$.

Equivalent radius: is calculated as the radius of a circular pore with the same area, in nm. It is calculated as $\sqrt{\frac{Area}{\pi}}$.

Minor Axis: is the length (in nm) of the minor axis of the ellipse.

Major Axis: is the length (in nm) of the major axis of the ellipse.

The calculated shape factors were elongation, circularity and orientation:

Elongation: is calculated as $1 - aspect\ ratio\ \left(\frac{minor\ axis\ length}{major\ axis\ lentgh}\right)$. It is a dimensionless value ranging from 1, for the most elongated pores to 0 for the circular pores.

Orientation: is the angle (in degrees) between the x-axis and the major axis of the ellipse that has the same second-moments as the region.

Circularity: is the degree to which porosities are similar to a circle and is a function of the form of the pore as well as of the smoothness of the perimeter. It is a dimensionless value, defined as: $\frac{4\pi Area}{Perimeter^2}$. The values range from 0 to 1, with 1 indicating a perfect circle and values approaching to 0 indicating an increasingly elongated polygon.

3.2.3. Mercury injection capillary pressure (MICP)

23 samples were analysed using the Micrometrics Autopore II 9920 at Newcastle University. The samples were cut to 1 cm^3 and freeze-dried at -50° for 10 hours prior to the analysis.

The equivalent pore throat sizes were obtained by converting the intruding pressures using the Washburn equation (Washburn, 1921), which, assuming cylindrical pores, states that the size of a pore is inversely proportional to the amount of pressure that is required to intrude a pore The equation was used assuming a contact angle of 140^0 and a surface tension of 0.485 N/m. The analyses consisted of calculating the total intruded volume of mercury for 57 pressure points between 3 and 39000 psi, by measuring the volume of mercury remaining in the penetrometer stem. The maximum applied pressure allowed to detect pores as small as 5.6 nm in diameter. In order to avoid experimental errors and artefacts induced by drying and destressing, conformance and compaction corrections were applied and a cut-off radius was chosen for all the samples. The corrections were

applied following the method proposed by Comisky et al., (2011). The pore volume compressibility for each pressure step and plotting it against the mercury pressure Comisky et al., (2011) and references therein. Any deviation at low pressures from the linear portion of the curve corresponds to the pore throat radius in which the mercury is starting to be intruded (Comisky et al., 2011 and references therein). The total porosity was calculated by using the bulk grain density extracted from the XRD data, assigning to the organic matter a density a value of 1.1 g/cm^3 for the immature samples, 1.2 g/cm^3 for the oil and 1.3 g/cm^3 for the gas maturity window samples (Okiongbo et al., 2005). To have an idea on the heterogeneity of the observed porosities, fractal dimensions were calculated by using the expression D = 3-A, where A is the slope parameter in the linear trendline intersecting the data in the $\log -\frac{dv}{dr}$ vs $\log dv$ plot (Friesen and Mikula, 1988; S. Liu et al., 2017). Values of fractal dimensions may vary between 2 and 3, with 2 corresponding to a perfectly smooth surface and 3 to a completely irregular surface (Wang et al. 2015).

The mean radius was calculated after applying the conformance and compaction corrections by selecting the radius corresponding to the average accumulated porosity values.

Most samples were also run in drainage, which corresponds to an extrusion curve in the pressure/cumulative volume diagram (Figure 3.2). Apart from acquiring information on the pore throat sizes from the intrusion data, the measurement of the mercury extruded from the sample at decreasing pressure steps can also yield details on how much mercury has been retained inside the pores, and therefore on the pore system and capillarity of the samples (Klaver et al., 2015).

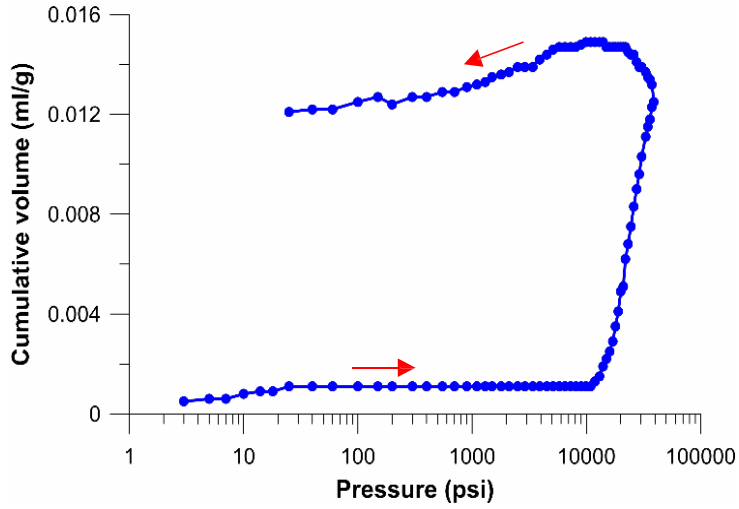

Figure 3.2: Example of MICP pressure (psi) vs cumulative volume (ml/g) plot (GW5 sample, R_0 1.2%). The arrows indicate the imbibition and drainage paths.

Initial pore entry pressure was also identified by plotting the Hg intrusion pressure (psi) vs. the Hg intrusion percentage and selecting the inflection point on the curve. This point indicates the first mercury that enters the largest pore throats that control the sample pore volume. It enables us to have information on the pore throat distribution and on the connectivity of the pores (Shafer and Neasham, 2000; Tian et al., 2018). Another factor to consider is the compressibility of the samples. Some authors (Friesen and Mikula, 1988; Mathia, 2014; Shafer and Neasham, 2000) have linked the amount of carbonates and more soft components (i.e. clays, organic matter) to the strength of the material, and hence to the hysteresis shape.

3.2.3.1. Gas Adsorption

N_2 gas adsorption measurements were executed on 12 samples at Aachen University. Additionally, CO_2 gas was also employed for 6 of the samples. Temperatures of 72° K for N_2 and of 0°C for CO_2 were used for the analyses. The samples were crushed manually using a pestle and mortar and sieved to a grain fraction between 63 and 375 μm. All 12 samples were outgassed and then heated for 20 hours at a temperature of 105 °C to remove any adsorbed capillary water. The quantity of gas adsorbed was measured at 64 manually selected increasing pressure steps from 0 kPa to 100 kPa, with an equilibration time of 10 s for every pressure step and an evacuation pressure of 133 kPa.

The specific surface area was calculated using the BET method, that assumes a multilayer gas molecule adsorption model (Brame and Griggs, 2016). The total specific pore volume was measured using the Gurvitsch rule, the pore size distribution using the Barret-Joyner-Jalenda (BJH) approach and the surface area analysis using the Brunauer-Emett-Teller (BET) method (Gregg and Sing 1982). Both adsorption and desorption curves were measured as the hysteresis pattern formed between the adsorption and desorption branches provides information on the types of pores present in the samples (Sing, 1985). The pore size distributions, the pore volumes and the BET surface area of the samples were extracted from the adsorption curves. The technique allowed to analyse porosities ranging from 2 nm up to 200 nm in diameter with N_2 and from 1.25 nm to 2 nm using CO_2.

3.2.3.2. FIB slice and view

FIB-SEM tomography volumes of 5 samples (Table 3.1) were produced slicing the samples using the FEI Helios Nanolab 600 (Curtis et al., 2010) using the FEI Slice and View G2 software.

Sample Names	Well number	Ro (%)	TOC (wt%)	Sum Carbonates (%)	Sum Clays (%)	Sum silicates (%)
IM2_1	2	0.5	5.8	36.3	19.5	33.2
IM2_3	2	0.5	7.9	50.1	9.0	24.2
OW1	3	0.9	4.9	56.6	16.2	23.6
GW11	4	1.2	3.4	N/A	N/A	N/A
H3A5	4	1.2	6.5	50.7	23.1	18.6

Table 3.1: Samples analysed using the FIB- slice and view technique.

In order to avoid curtain effects (Curtis et al., 2010), the area was platinum coated before being milled. The milling was performed using the ion beam (30 kV voltage, beam current of 9 nA at a working distance of 4 mm) and a total of 300 slices 12.74 μm wide and 10.3 μm high and were taken at intervals of 10.25 nm. The overall measured volume was 12.74

μm x 10.3 μm x 3.1 μm. The images were taken using the electron beam at 20 kV of voltage, a beam current of 1.4 nA and a magnification of 12 kx. The images were collected at a resolution of 1024 x 884 pixels and 6 μm of dwell beam time.

The images were saved in sequence and stacked in order to reconstruct a volume by means of the FIB *Stack Wizard Tool* in the software Avizo™, also considering the drift occurring during the sample slicing in the FEI.

The 5 samples were chosen in order to cover the whole maturity sequence, by accounting for similar mineralogy and TOC values. The selection of the location of the slicing was made accounting for the areas having a good balance between OM content and mineralogy and was therefore not completely random.

For each sample, the organic matter and the porosity were segmented and quantified in Avizo. The segmentation was done by using a greyscale thresholding. The pores in the SEM images have a darker greyscale compared to the organic matter. As at times the automatic greyscale thresholding does not select the edge of the pores automatically, the pore segmentation was corrected manually. As the resolution for this technique was 12.4 nm/pixel, the smallest pore sizes were identified in pores of ~ 25nm of diameter. The connectivity of the pores and of the OM particles was also analysed by means of the Axis *Connectivity tool* in Avizo, and the connectivity of the two phases is calculated by dividing the volume fraction of the connected pores or OM particles over the volume fraction of the total amount of pores or OM. To test which pore sizes have more relevance on the overall pore network, the connectivity of the pores was also measured by analysing only the pores smaller than 100 nm. The total porosity of the samples was also measured by dividing the pore volume fraction by the total volume fraction.

Each pore and OM particle were analysed using the material statistics and label analysis tool in Avizo™. The distinction between OM-related pores and non-OM related pores was calculated by analysing the slices separately. The parameters analysed as a 3D volume were:

Area: is defined as the number of non-zero pixels in a binary image, converted to nm^2 by multiplying it by the area of a single pixel.

Perimeter: it estimates the number of points that lie on the object boundary.

Volume: is the volume of the object, calculated by summing the number of voxels occupied by the object.

Equivalent Diameter: is given by the formula $\sqrt[3]{\frac{6 \times Volume3d}{\pi}}$.

Orientation: is the theta orientation of the particle in degrees [-180,180], computed with the inertia moments.

Feret diameter: is defined as the distance between two parallel tangents of the particle at an arbitrary angle.

Length: calculated as the maximum of the Feret diameters, in 3D.

Width: calculated as the minimum of the Feret Diameters in 3D.

Sphericity: it indicates how spherical an object is in 3D, is expressed as the ratio of the surface area of a sphere to the surface area of a particle. It is calculated as: $\frac{\pi^{\frac{1}{3}}(6V)^{\frac{2}{3}}}{A}$ where V is the volume of a particle and A is its surface area. It varies between 0 and 1, with 1 being a perfectly spherical object.

Shape_3D: is a factor defined as; $\frac{Area\ 3D}{36pixelscvolume3D^2}^3$, in which 1 equals to a perfect sphere.

3.3. Results

Before quantifying the porosities and the pore structure, the samples were also studied by means of bulk analysis methods (XRD, TOC wt% and Rock-Eval) and optical and electron microscopy (see Chapter 2) (Table 3.2).

Sample names	Well Number	R_0%	TOC%	Carbonates (%)	Silicates (%)	Kaolinite (%)	I/S (%)	Microfacies Type	Φ % (Helium)	Φ% (MICP)	Φ % FIB- SEM	Φ% FIB	Φ volume N_2(cm^3/g)
OC1	Outcrop	0.4	4.4	52.5	32.5	3.3	4.4	A	16.9	8.9	2.5	N/A	0.009
OC2	Outcrop	0.4	6.6	58.2	20	5.6	3.4	A	15.0	11.6	1.35	N/A	0.027
OC3	Outcrop	0.4	5.5	50.3	24.3	6.6	5	A	18.9	16.3	0.73	N/A	0.039
IM1_1	1	0.4	4.5	46.3	24.7	8.1	9.8	A	14.2	8.5	N/A	N/A	N/A
IM1_2	1	0.4	6.3	37.1	31.2	25.8	1.6	A	N/A	N/A	N/A	N/A	N/A
IM1_3	1	0.4	N/A	25.1	21	43	2.5	A	13.3	N/A	1.2	N/A	N/A
IM2_1	2	0.5	5.8	36.3	33.2	12.9	6.6	A	8.5	8.4	2.9	1.8	0.014
IM2_2	2	0.5	1.9	76.2	18.8	3.9	0.8	B	8.3	1.7	1.02	N/A	0.006
IM2_3	2	0.5	7.9	50.1	24.2	1.8	7.2	A	17.1	14.8	1.32	4.1	N/A
OW1	3	0.9	4.9	56.6	23.6	3.6	12.6	A	16.5	10.6	0.4	5.7	N/A
OW2	3	0.9	4.5	43.2	8	24	18.1	A	14.8	10.7	0.75	N/A	N/A
GW1	4	1.2	3.5	57.2	14.6	1.9	18.5	A	16.7	12.1	N/A	N/A	N/A
GW3	4	1.2	0.5	83.8	6.9	0	4.4	B	10.1	N/A	0.25	N/A	0.022
GW4	4	1.2	1	73	15.6	0	8.3	B	11.2	5.6	1.4	N/A	0.024
GW5	4	1.2	1.6	67.2	11.3	1	12.5	B	13.5	11.2	1.17	N/A	N/A
H3A 1	4	1.2	0.9	79.5	16.9	0.2	2.5	B	12.0	7.9	2.5	N/A	0.017
H3A 2	4	1.2	3	58.4	30.2	0.4	9.2	A	12.5	7.2	0.35	N/A	0.023
H3A 3	4	1.2	5.4	44.5	19.3	1.6	28.5	A	18.2	13.0	3.93	N/A	N/A
H3A 4	4	1.2	0.7	90.7	6.7	0	1.4	B	6.5	6.1	0.27	N/A	0.012
H3A 5	4	1.2	6	50.7	18.6	1.3	21.8	A	15.0	12.9	3.62	4.5	N/A
H3A 6	4	1.2	0.2	95.7	4.2	0	0	B	17.9	6.8	N/A	N/A	N/A
GW6	5	1.2	2.4	77.9	14.3	0	3.2	B	14.7	6.6	N/A	N/A	N/A
GW2	5	1.2	2.3	82.9	13.1	1.6	1.4	B	15.8	6.7	2.93	N/A	N/A
GW7	6	1.2	0.7	74.6	6.7	0	12.2	C	10.0	3.9	0.13	N/A	0.008
GW8	6	1.2	0.5	84.4	4.5	0	7	C	7.4	4.5	2.37	N/A	0.010

Table 3.2: List of the samples analysed, subdivided by outcrop and well names, maturity and microfacies type. The mineralogical composition measured by means of XRD is also listed, as well as the TOC (wt %) results. Carbonates comprise calcite, dolomite and ankerite, whereas silicates include quartz, K-feldspar and plagioclase. For more detailed XRD results, refer to chapter 3. The total porosity values measured by means of He-pycnometer, MICP, FIB-SEM image processing and FIB, and the total pore volumes for N_2 and MICP are listed. N/A = not measured.

The samples are carbonate-rich (37-84%), with minor components of other minerals such as quartz, clays (mixed illite/smectite and kaolinite), plagioclase and pyrite. TOC (wt %) values range from 0.5 to 7.9% and decrease with increasing maturity, whereas carbonate values slightly increase with increasing maturity (Table 3.2). Rock-Eval studies show that

the sample maturity range is between R_0 0.4% and R_0 1.2% and that organic matter is mainly marine Type I and II (Table 2.3). Petrographic analyses validate the marine origin of the organic matter and show that the terrigenous sedimentary input is low relative to the marine and allochthonous input (Paragraph 2.2.3).

As seen in Chapter 2, optical and electron microscope analyses allowed the subdivision of samples into three categories according to the different microfacies: microfacies A, corresponding to laminated foraminiferal mudstone samples, microfacies B, corresponding to the wackestone samples, and microfacies C corresponding to the packstone samples (Figure 2.7). All the samples from microfacies B and C, apart from microfacies B sample IM2_1, R_0 0.5%, have a maturity of R_0 1.2%, and therefore a detailed study of the porosity evolution with the increase of thermal maturity and burial is only possible for samples belonging to microfacies A (Table 2.3). An increase in the maturity sequence determines an intensification of mechanical and chemical compaction processes, which affect the properties and mineralogy of the rocks. In these samples, the most relevant diagenetic processes are, in sequence: carbonate and clay cements precipitation, oil emplacement that partly fills inter and intraparticle pores, framboidal pyrite formation, dissolution and reprecipitation of carbonates and other phases (quartz, feldspar, clays), organic matter thermal cracking and calcite and plagioclase dissolution. A detailed description of all the petrographic results can be found in Chapter 2.

3.3.1. Total porosity

The porosity percentages were calculated for all of the samples by means of SEM, FIB-SEM, Helium porosimeter and MICP methods (Table 3.2). FIB-SEM pore volumes were calculated only for 4 samples (sample GW11, lacking the analyses with the other techniques, is not considered). The FIB-SEM porosities range from 1.8% to 5.7%. SEM pore area calculations were carried out on 18 samples and range between 0.1% (sample GW7) and 3.9% (sample H3A3). However, these image processing techniques do not allow the measurement of pores smaller than 18 nm, and therefore the total porosity values are not representative of the bulk porosities of the samples. The helium pycnometer calculated porosity, on the other hand, represents the overall porosity of the samples, as the size of its kinetic diameter (260 pm) allows it to enter all pores, in contrast to the other techniques

used here. The total porosity values range from 6.5% (sample H3A4) to 18.9% (sample OC3). MICP values (between 1.7% and 16.3%) are always lower than the helium porosity values, as generally the mercury cannot enter pores smaller than 5.6 nm of diameter.

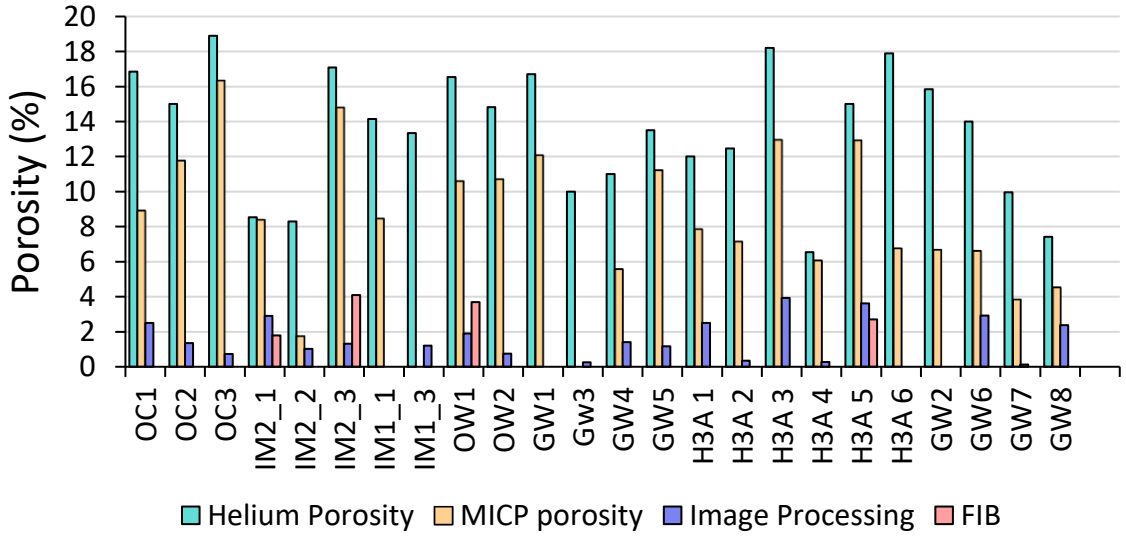

Figure 3.3: Chart showing the total porosity measured using various techniques (Helium Porosity, MICP, image Processing using FIB-SEM and FIB). The total porosities display different results depending on the technique used. The results depend on the resolutions of each technique. The helium porosimeter and the MICP allow displaying a larger pore range compared to the Image processing FIB-SEM and FIB techniques. However, the Helium porosimeter results will not be used n this work as considered less reliable compared to the MICP bulk porosity values (see text for more detail).

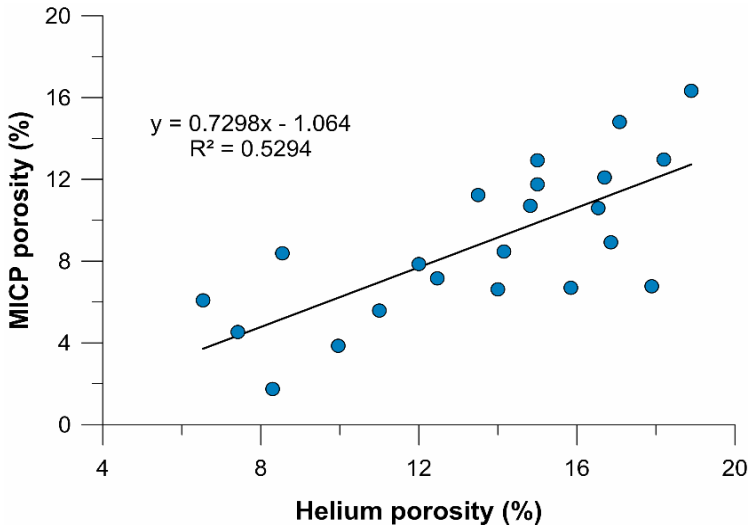

Figure 3.3: MICP porosity (%) vs Helium porosity (%).

However, helium porosity data is reasonably well correlated (R^2 = 0.53) with the MICP results (Figure 3.). As helium porosities were calculated on very small (<0.5 mm) rock chips, it is believed that the measured bulk volumes and densities could be affected by experimental errors (Bustin et al., 2008). For this reason, for any correlation between porosities and mineralogy, microfacies or maturity, the MICP data were considered more reliable.

The lowest porosity value (1.7%) is found in sample IM2_2 (R_0 0.5%). This sample is highly recrystallised and, as explained in Chapter 2, no trace of bio-carbonate compounds can be seen, in contrast to the rest of the microfacies B samples. The two microfacies C samples, GW7 and GW8, yield a porosity of 3.9% and 4.5% respectively whereas the high maturity microfacies B samples yield a porosity range between 5.6% and 11.2%. In microfacies A samples, the porosity values range between 7.2% and 16.3%. The MICP porosity values are found to be related to the mineral composition of the samples and to diagenetic processes, rather than decreasing gradually with maturity (Figure 3.4).

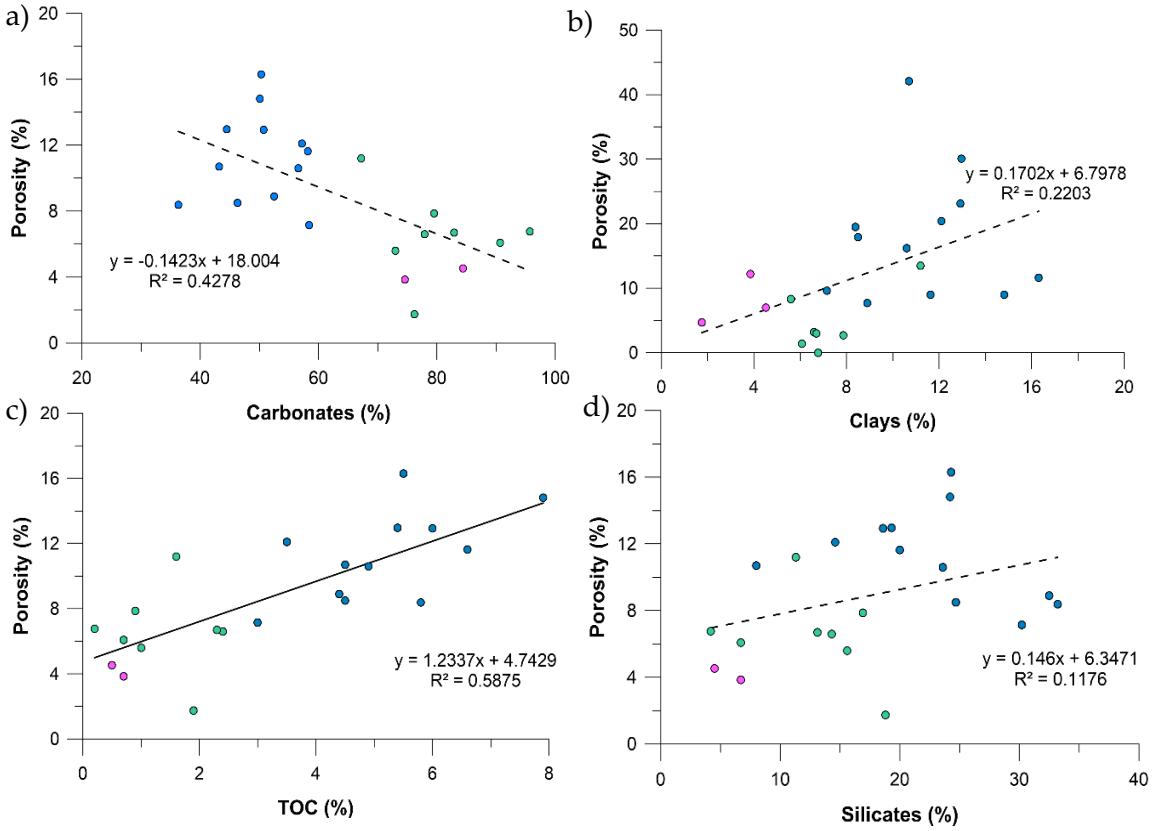

Figure 3.4: MICP porosity (%) vs mineralogical contents for all samples at all maturities. A) carbonates (calcite, dolomite and ankerite) (%), b) TOC (wt%), c) clays (%) and d) silicates (K-feldspar, plagioclase and quartz) (%). The different colours correspond to the differen microfacies: microfacies A (blue), microfacies B (green) and microfacies C (purple).

A good (R^2=0.51) negative relationship between the carbonate percentage and the porosity values can be seen (Figure 3.4 a). Indeed, the lowest porosity values are found in samples from microfacies B and C, where the reprecipitation of carbonate minerals (calcite and dolomite) is more common (Figure 3.5). In agreement with other studies (Kuila et al., 2014; Milliken et al., 2013; Passey et al., 2010), the TOC (wt%) versus porosity (%) plot shows there is a positive correlation between the abundance of organic matter and porosity (Figure 3.4 b). There is no apparent trend between the porosity values and clay or silicates (quartz and feldspar) fractions (the R^2 values are 0.22 and 0.12 respectively) (Figure 3.4 c and d).

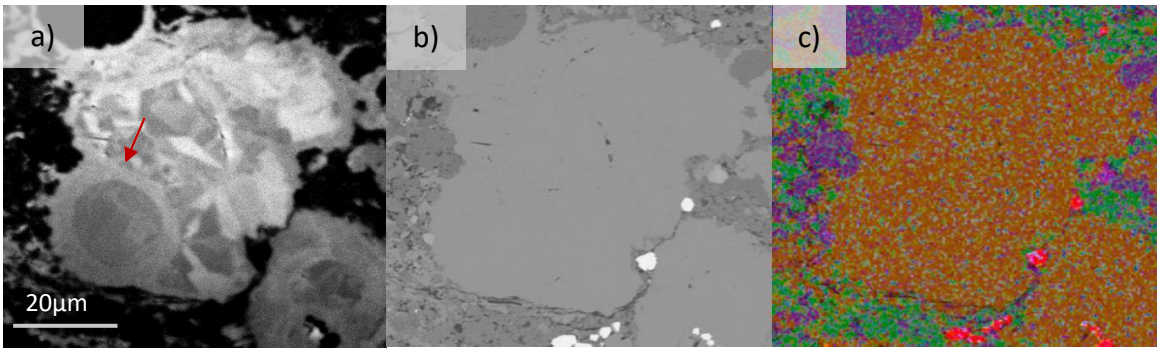

Figure 3.5: Example of calcite reprecipitation around a calcitic bioclast, probably a foraminifera (sample GW3, R_0 1.2%). a) is a CL panchromatic image, b) is a SEM-BSE image and c) is the corresponding SEM-EDS elemental map. On the elemental map, the orange colour corresponds to calcite, purple is kaolinite, green is quartz and pink is pyrite. The red arrow on the panchromatic image indicates a primary calcitic crystal, around which the calcite has reprecipitated in different phases corresponding to different greyscales.

3.3.1.1. Porosity from SEM observations

The combined EDX-SEM maps along with the FIB 3D models were used to distinguish the different pore types and shape factors. The classification of the different kinds of porosities was modified after Loucks et al. (2012).

3.3.2. Pore types

Interparticle matrix pores, intraparticle mineral pores, intraparticle fossil pores, intraparticle dissolution pores and organic-matter pores were identified using the high resolution (10k ×) 50 µm x 50 µm maps (Figure 3.6 and Figure 3.7, Table 3.3).

3.3.2.1. Intraparticle dissolution pores

Intraparticle dissolution pores have a more elliptical shape and are found within precipitated carbonates and, at a lower extent, plagioclase minerals. They range between 0% and 31% and are found at all maturities, but most abundantly in the highest maturity window samples, in microfacies C (R_0 1.2%) (Figure 3.6 a).

3.3.2.2. Intraparticle mineral pores

Intraparticle mineral pores reflect the abundance of framboidal pyrite and kaolinitic clays, whose structure often allows intraplate pores to form (Figure 3.6 b). They range between 1% and 19% of the overall pore types, and they don't follow a specific trend with increasing maturities, nor with the microfacies type.

3.3.2.3. Interparticle matrix pores

Interparticle matrix pores are described as pores that occur between particles. In these samples, they are found as intra-aggregate porosities between clays and carbonates, between the coccolithic debris in the matrix and in the faecal pellets (Figure 3.6 c). For the 18 samples analysed, the interparticle matrix pores appear as the most frequently type occurring at all maturities (37 to 77% of the overall pore types), apart from samples H3A2, H3A3 and H3A5 where the OM pores are slightly more abundant. Relatively to the rest of the pore types, the highest percentages of interparticle matrix pores are observed at the lowest maturities (R_0 0.4-0.5%).

3.3.2.4. Intraparticle fossil pores

Intraparticle fossil pores occur primarily within well-preserved foraminifera hollow tests or coccolithophorides, and they are more common in the least mature samples (R_0 0.4-0.5%) (Figure 3.6 d).

3.3.2.5. Intraparticle organic matter pores

Organic matter pores are pores found in the organic matter and can be distinguished as 3 types: pendular, spongy and fracture-like OM pores (Walls and Sinclair, 2011) (Figure

3.6 e-g). Pendular and fracture-like OM pores are generally larger, more elongated and have a higher aspect ratio compared to spongy OM pores. Spongy OM pores are the most abundant, are circular or semi-circular and are usually smaller than 10 nm. The spongy OM pore type is only found in the highest maturity samples (R_0 1.2%) and at high maturities, OM that has not developed a spongy texture is also present. Pendular and fracture-like OM pores are rare (<10% of the overall porosity) and are found in immature and oil window samples.

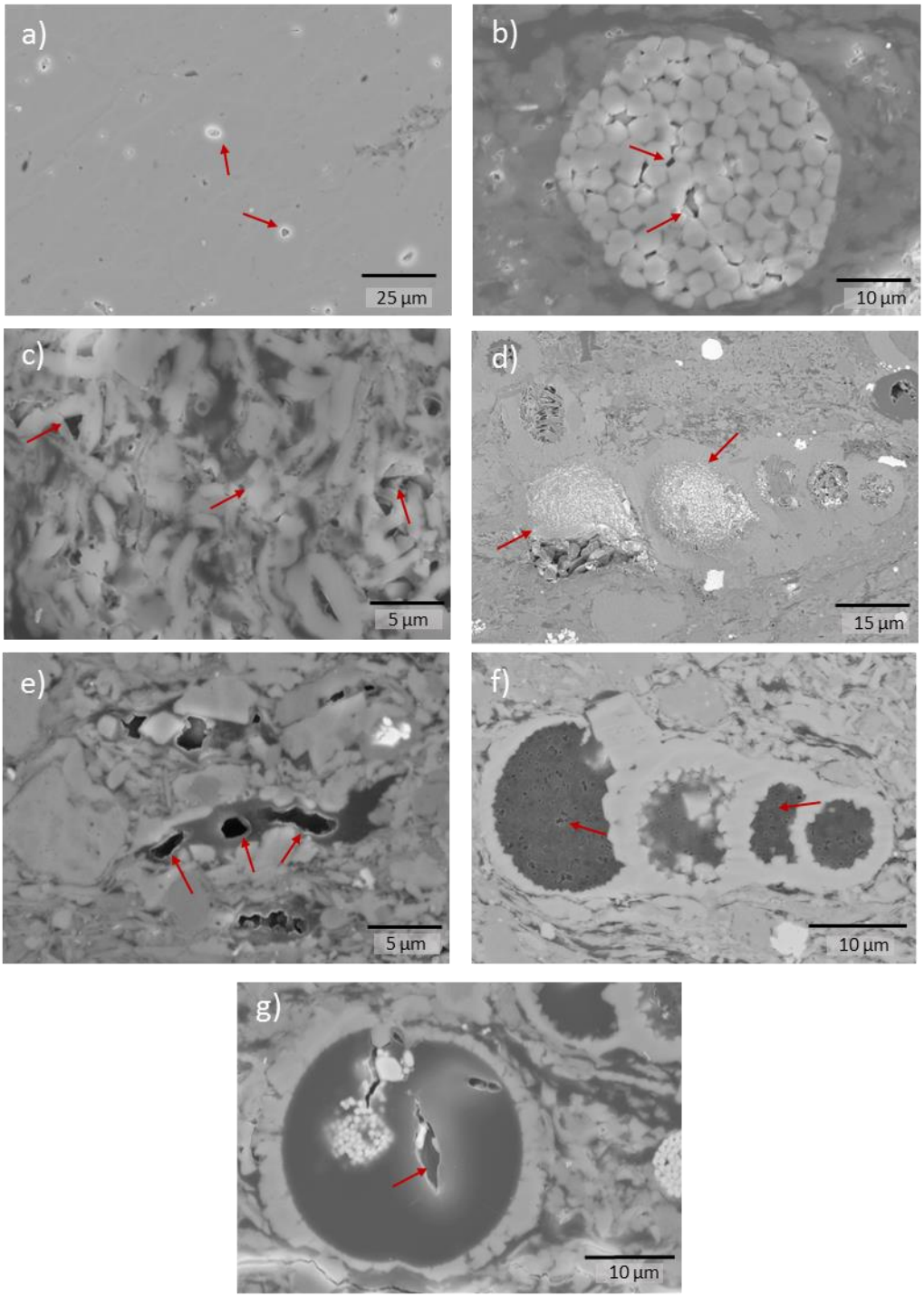

Figure 3.6: SEM images of the different pore types indicated by the red arrows. a) dissolution pores (sample H3A2, R_0 1.2%); b) interparticle mineral pores in framboidal pyrite (sample IM1_3, R_0 0.4%); c) interparticle matrix pores (sample IM1_2, R_0 0.5%); d) OM fracture pores in bitumen filling a foraminifer-coccosphere chamber (sample OW2, R_0 0.9%); e) pendular pores in an organic matter filament within the matrix (sample OW2, R_0 0.9%); f) OM sponge pores in bitumen filling foraminifer chambers

3.3.2.6. Pore types as a function of maturity

Considering the different microfacies, in microfacies A the pore types follow a trend with increasing maturity; in general, the most abundant pores are the interparticle matrix porosities, which range from an average of 60% in the immature and oil window samples to an average of 39% in the gas window samples (Figure 3.7). The foraminifera can be several hundred nanometers wide, and during diagenesis they are often only partially filled with authigenic cements such as calcite, quartz and kaolinite (Figure 2.29). Another component that increases the intraparticle matrix pores in microfacies A samples is the large abundance of faecal pellets amid the matrix (see Chapter 2). The porosity of OM increases from an average of 7% in the immature and oil window samples to an average of 30% for the gas window samples. In this microfacies, the intraparticle mineral pores are ~13% in the immature window, ~9% in the oil window and ~12% in the gas window.

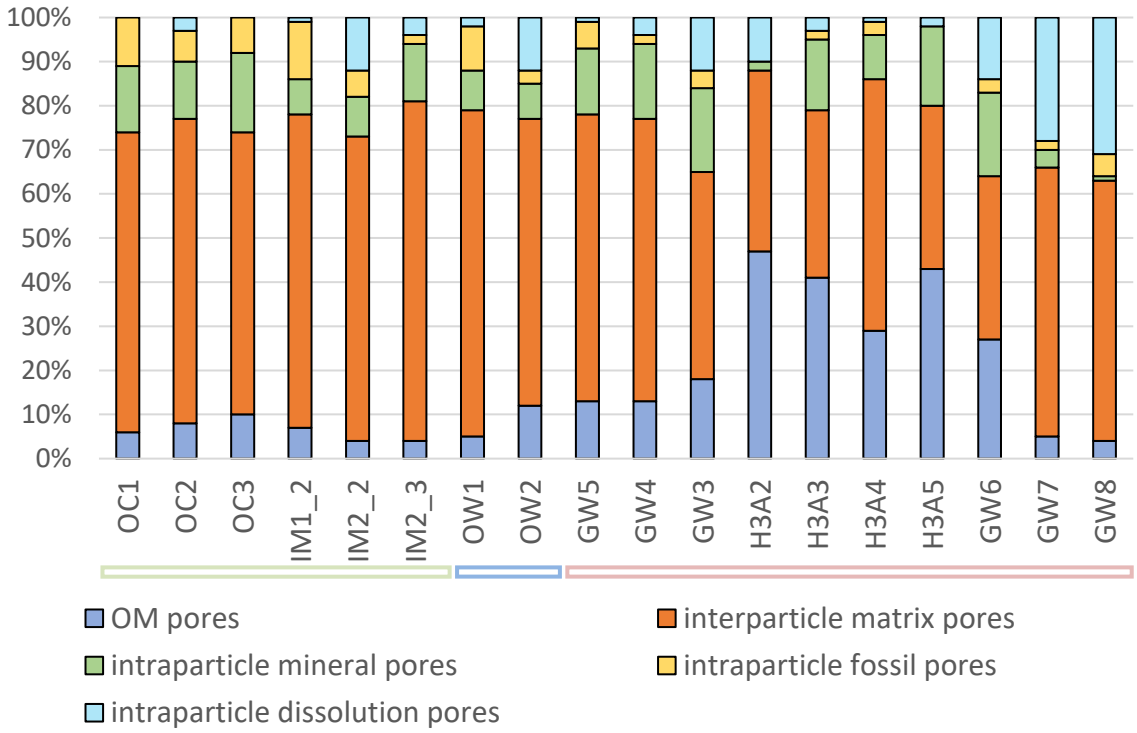

Figure 3.7: Chart displaying the relative pore type area percentages measured by analysing FIB-SEM maps overlapped to EDX maps of the same areas. The colour contour boxes indicate the different maturity windows. Green corresponds to immature samples, blue corresponds to the oil samples (R_0 0.9%) and red corresponds to the gas window samples (R_0 1.2%). Interparticle matrix pores are significantly high at all maturities. Intraparticle mineral pores are present at all maturities. Intraparticle dissolution pores are mainly present in the gas window (R_0 1.2%), especially in the microfacies C samples (GW7 and GW8). See chapter 3 for more details.

In addition, the hollow chambers of the foraminifera constitute a significant portion of the overall pore types as well (up to 13%, in sample IM2_3).

Microfacies B and C samples (except for sample IM2_2, R_0 0.5%) all belong to the gas window maturity. In these samples, the most common pores are interparticle matrix pores, with an average of 54% in microfacies B and 60% in microfacies C. Following the interparticle matrix pores, in the microfacies B samples, with an average of 16%, are the intraparticle mineral pores. In microfacies C samples and in sample IM2_2, their average relative percentage is ~5%. In microfacies C and in sample IM2_2, more common are the dissolution intraparticle pores, with a pore type percentage average of 24%. OM-related pores in microfacies B and C are also found. In microfacies B, the OM-pore types are on average 17%, compared to ~4% in microfacies C. However, the TOC wt% of the two microfacies C samples is < 1%, which also explains the low quantity of OM-related pores.

Sample names	V. Reflectance (R_0%)	Microfacies Type	Interparticle matrix pores	Intraparticle mineral pores	Intraparticle fossil pores	Intraparticle dissolution pores
OC1	0.4	A	68	15	11	0
OC2	0.4	A	69	13	7	3
OC3	0.4	A	64	18	8	0
IM1_2	0.4	A	71	8	13	1
IM2_2	0.5	B	69	9	6	12
IM2_3	0.5	A	77	13	2	4
OW1	0.9	A	74	9	10	2
OW2	0.9	A	65	8	3	12
GW5	1.2	B	65	15	6	1
GW4	1.2	B	64	17	2	4
GW3	1.2	B	47	19	4	12
H3A2	1.2	A	41	2	0	10
H3A3	1.2	A	38	16	2	3
H3A4	1.2	B	57	10	3	1
H3A5	1.2	A	37	18	0	2
GW6	1.2	B	37	19	3	14
GW7	1.2	C	71	4	2	18
GW8	1.2	C	77	1	5	13

Table 3.3: Pore types and corresponding microfacies and maturity.

3.3.2.7. Shape factors

The elongation, orientation and circularity were the calculated shape factors (Figure 3.8). In microfacies A, at increasing maturities the elongation tends towards higher values (from a peak average of 0.65 to a peak average of 0.85 in the most mature samples), denoting more elongated pores in the gas window samples. The circularity, on the other hand, measures the smoothness and the shape form and increases for samples in the oil and gas window (from a peak average of 0.12 to a peak average of 0.25). The fine stringers of OM are aligned with the laminations and in the gas window, where the stress is also higher, present circular or semi-circular pores. These pores are also often aligned to the organic matter laminae and therefore aligned with the laminations (Figure 3.9).

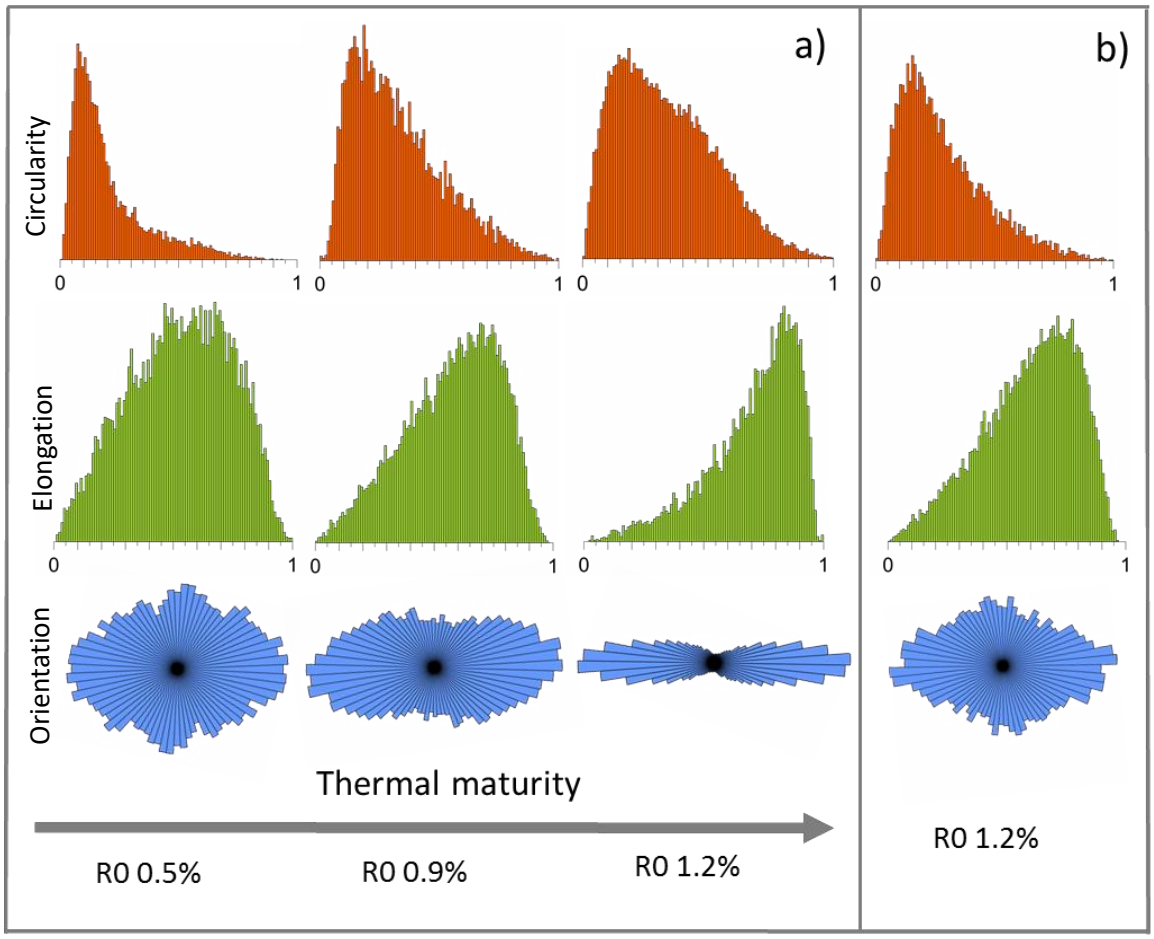

Figure 3.8: Shape factors of circularity, elongation and orientation for all pore types in relation to the maturity and the microfacies for example samples. The y axis for the circularity and the elongation in frequency. The x axis varies from 0 to 1, with 1 being the most circular/elongated pores. The diagram for the orientation is a 360⁰ rose diagram and displays the orientation of the longest axis of each pore. a) Microfacies A and B samples at increasing maturities and b) Microfacies C samples in the gas window. In microfacies A, the samples exhibit more circular, more elongated and more well oriented parallel to the bedding pores. In microfacies C, the samples, despite being in the gas window, show similar shape factors to the immature and gas window samples.

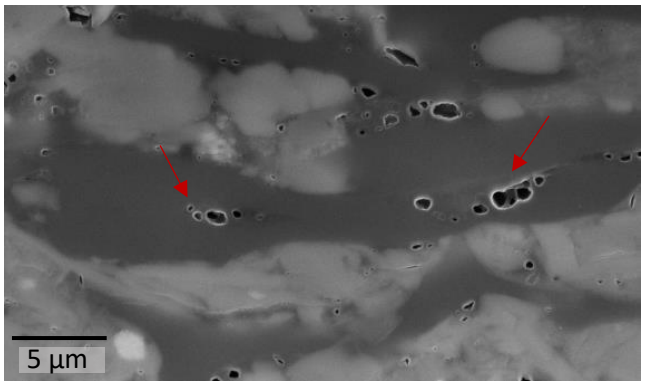

Figure 3.9: Organic matter in sample GW4 (R0 1.2%) containing OM elongated pores in the direction of the OM lamination (red arrows).

Samples from the gas window of microfacies B are characterised by significantly elongated and mixed circular and acicular pores. The acicular pores are related to the high percentages of interparticle matrix pores and intraparticle mineral pores, which are formed by the pore spaces between euhedral minerals. The circular and semi-circular pores are instead related to the organic matter, which generates gas, producing bubble-like pores. In microfacies C, the pores are not strongly oriented in one direction and are mostly acicular. The majority of pores comprise interparticle matrix pores, which have generally angular edges.

3.3.2.8. Pore areas and PSD

The pore areas calculated in the image processing analyses range between 0.1% for sample GW7 and 3.9% for sample H3A3 (Figure 3.10: left) (Table 3.4).

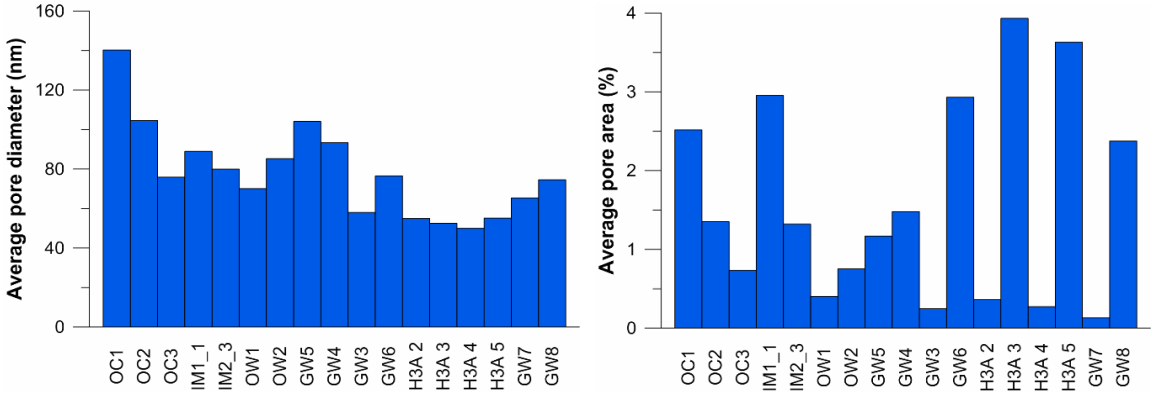

Figure 3.10: left) average pore diameter (nm) and right) average pore area (%) for all the samples from the 10 k x SEM-SE image processing analyses.

There is no clear correlation between pore area percentages and maturity, but correlations can be found with the pore area percentages and the microfacies. In microfacies A samples, the precipitation of calcite in the highest maturity window (R_0 1.2%) has in some cases (samples GW3, H3A2, H3A5) significantly reduced the number of interparticle pores within the faecal pellets and the matrix. Comparing samples from the same maturity and microfacies with similar mineralogy (i.e. samples H3A2 and sample H3A3), the total porosity drops by up to 85% between a sample with and a sample without calcite reprecipitation.

Samples names	V. Reflectance (R_0%)	Microfacies Type	TOC (wt %)	Average pore area (%)	Average pore diameter (nm)
OC1	0.4	A	4.4	2.5	140.3
OC2	0.4	A	6.6	1.4	104.7
OC3	0.4	A	5.5	0.7	75.9
IM1_1	0.4	A	6.9	3.0	89.0
IM2_3	0.5	A	7.9	1.3	79.9
OW1	0.9	A	5.0	0.4	70.1
OW2	0.9	A	4.5	0.8	85.3
GW5	1.2	B	1.6	1.2	104.1
GW4	1.2	B	5.6	1.5	93.4
GW3	1.2	B	0.5	0.2	58.0
GW6	1.2	A	2.4	2.9	76.5
H3A 2	1.2	A	3.0	0.4	55.0
H3A 3	1.2	A	5.4	3.9	52.5
H3A 4	1.2	B	0.7	0.3	50.0
H3A 5	1.2	A	6.0	3.6	55.2
GW7	1.2	C	0.7	0.1	65.4
GW8	1.2	C	0.5	2.4	74.6

Table 3.4: Average pore area (%) and average pore diameter (nm) from the SEM-SE image processing analyses.

The SEM-SE pore size analyses show that there is a trend with microfacies type as well as with maturity. Calculated average pore size distributions for the different thermal maturities show that the pore diameter decreases in size with the increase in maturity (Table 3.4). Typical values are 99 nm for the low maturity window, 78 nm for the oil window samples and 68 nm for the gas maturity samples. In microfacies A, the average diameter ranges between 140 nm for sample OC1 (R_0 0.44%), decreasing to 50 nm for sample H3A4 (R_0 1.22%). For microfacies C samples (GW7 and GW8) the pore radius is comprised between 65 and 74nm, whereas in microfacies B samples (IM2_2, GW3, GW4, GW5, H3A1, H3A4, H3A6, GW6 and GW2) it ranges between 50 and 58 nm (Figure 3.10: right). The pore areas and pore size distributions were also compared (Figure 3.11).

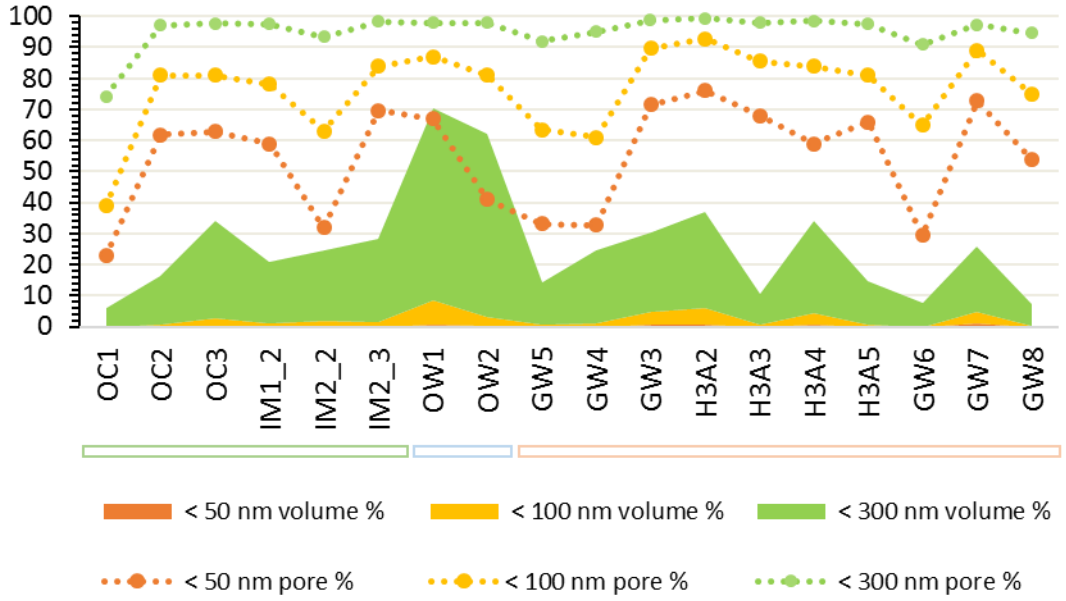

Figure 3.11: Relative percentages of the pore areas as a function of the pore sizes (straight line) and the number of pores smaller than 50, 100 and 300 nm (dotted line). The colours behind the sample names indicate the different maturities. Green corresponds to immature samples, blue corresponds to the oil samples (R_0 0.9%) and red corresponds to the gas samples (R_0 1.2%%). The difference between the pore areas and the number of pores under a certain value is considerable: for pores smaller than 50 nm, which account for 21% up to 76% of the total pores, their total pore area is always less than 2%.

Pore area and pore size distributions show that, although for all the samples analysed between 40 and 93% of the pore diameter sizes are smaller than 100 nm, these pores account for only up to 7% of the overall pore area. For pore sizes smaller than 50 nm, which comprise up to 76% of the overall number of pores, the input to the pore area decreases to less than 2%. In general, in these samples with this technique, the overall contribution of pores larger than 300 nm to the total area is always higher than 40%, even if they account for only an average of 9% of the overall porosity.

3.3.3. Gas adsorption

3.3.3.1. N_2 Isotherm types

The 12 samples analysed using nitrogen indicate a typical type IV isotherm, suggesting multilayer adsorption (Brunauer et al., 1938). All the isotherms show a sharp increase in the quantity of gas adsorbed around 0.9 P/P0, indicating multilayer adsorption followed

by a capillary condensation in the range of the meso- and macroporosities (Rouquerolt et al., 1994; Thommes et al., 2015) (Figure 3.12. For more results see Figure A.1-Figure A.4).

3.3.3.2. N_2 hysteresis shapes

The adsorption/desorption curves present a hysteresis in all the samples, signifying the process is not reversible. For all the samples, the hysteresis loop closure point is found around a pressure of 0.42 P/P0, which corresponds to the lower limit of capillary condensation hysteresis (Gregg et al., 1967). However, the shape of the hysteresis varies as a function of maturity and of the microfacies analysed. In the samples belonging to microfacies A, the hysteresis changes shape and increases with the increase in maturity. The narrow hysteresis shape found at low maturities (Figure 3.12a) indicates the dominance of a meso and macroporous system network, in which the gas can easily flow through the pores and pore throats. The larger hysteresis at the higher maturities (Figure 3.12 b) suggests instead the presence of both micro and mesopore volumes, indicative of a more complex, yet connected pore system formed by narrower pore throats in which the gas cannot easily pass through, causing a delay in the desorption. Similar behaviour to the low maturity samples of microfacies A is seen in microfacies B and C samples, but with a lower adsorption capacity (Figure 3.12 c; d). According to the IUPAC classification, the shape also suggests a geometry of the pore types (IUPAC, 1985). Samples from the high maturities of microfacies A present an H2 shape type loop, which is typically associated with ink bottle-shaped pores (narrow mouths and larger bodies). In the low maturity samples of microfacies A and in the microfacies B and C samples the hysteresis curves resemble more an H3-H4 type, which is interpreted as a pore system formed by slit-shaped porosities.

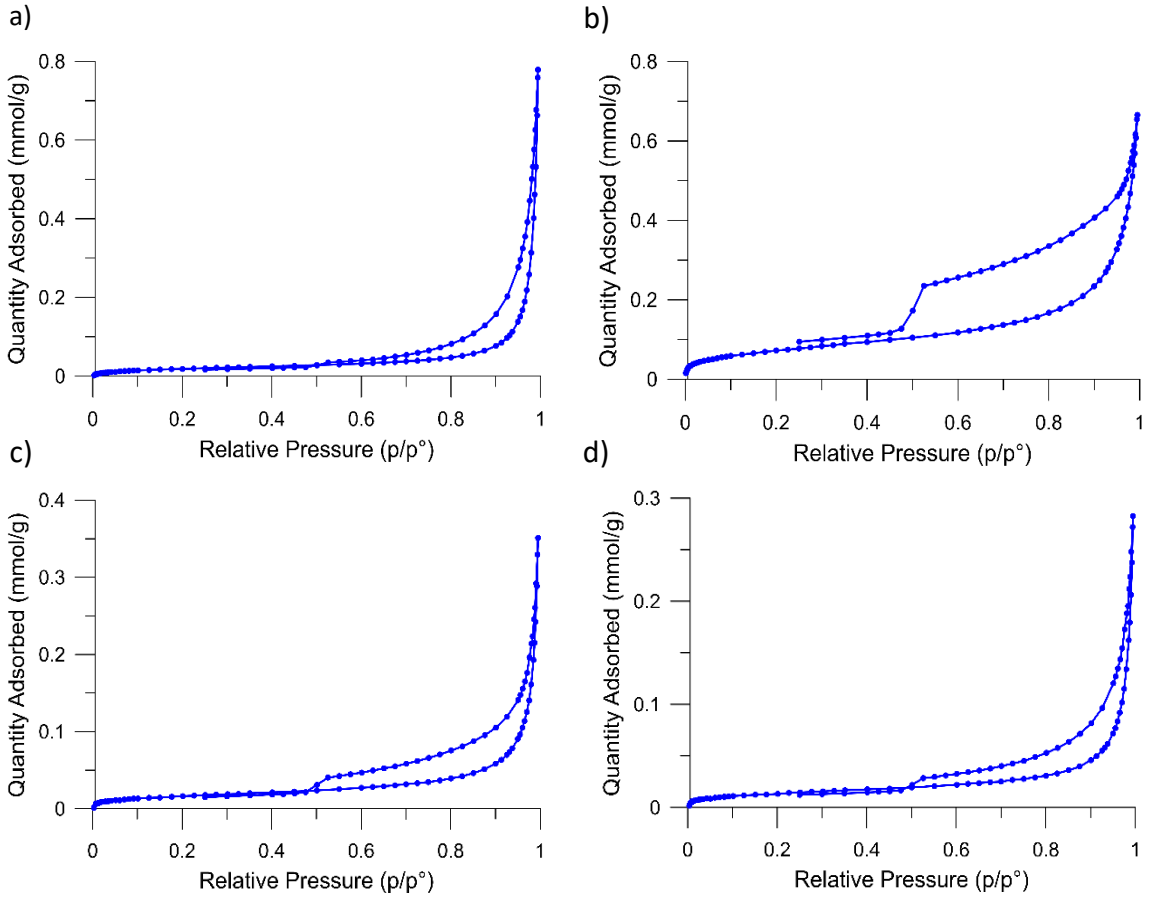

Figure 3.12: Gas adsorption N_2 measurements for two samples from microfacies A in the a) immature (OC1) and b) gas window (H3A5), c) a microfacies B (R_0 1.2%) sample (GW4), and d) microfacies C (R_0 1.2%) sample (GW7). The sample in microfacies A in the gas window exhibits a larger hysteresis, signifying that the pore system is more complex and that the pore throats are narrower.

3.3.3.3. Pore volumes

The pore volumes of the samples analysed range from 0.01 cm^3/g (sample IM2_2) to 0.04 cm^3/g (sample OC3) (Table 3.5). These values are in accordance with the porosity values measured with the MICP, that shows that sample IM2_2 and sample OC3 yield the lowest and highest total porosities, respectively. BET surface areas range from 0.32 m^2/g (sample IM2_2) to 5.80 m^2/g (sample H3A2) and the BET values show a strong correlation (R^2=0.91) with the TOC wt% values (Figure 3.13 a). Although there is no clear trend between the mineral content of the samples and the pore volume or the BET specific surface area, the samples exhibit an inverse relationship between the average pore diameter and the micro

and mesopore volumes, and between the BET specific surface area and the micro and mesopore volume (Figure 3.13b).

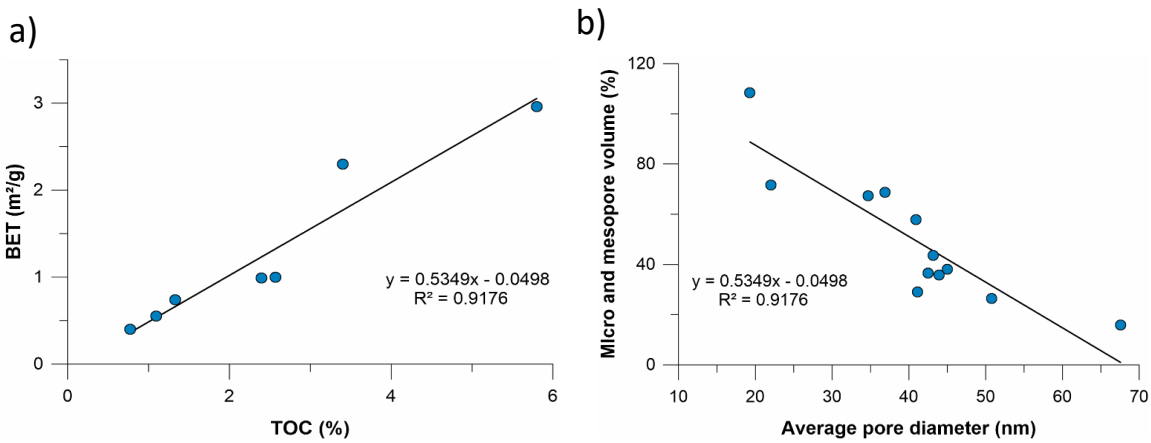

Figure 3.13: Gas adsorption N_2 measurements of a) BET specific surface area (m^2/g) vs TOC (wt %) and b) average pore diameter (nm) vs micro and mesopore volume.

Also, the pore volume analyses indicate that most of the pore volume (59.8 to 89.7%) is within the macropores (pores > 50 nm) for all the samples except for sample H3A2 (32.4% of the pore volume) (Table 3.5). Positive correlations with the maturity of the samples start to be seen for pore volumes of pores smaller than 20 nm normalised to the TOC values (average of 1.2% for samples with R_0 0.5% to an average of 19.7% for samples at R_0 1.2%) (Table 3.5).

Sample Names	Well names	R_0 (%)	TOC (wt %)	BET surf area (m^2/g)	CO_2 surf. area (m^2/g)	Average Pore Diameter (nm)	Cumulative volume N_2 (cm^3/g)	Volume macropores N_2 (cm^3/g)	Volume mesopores N_2 (cm^3/g)	Volume micropores CO_2 (cm^3/g)	Macropore volume N_2 (%)	Mesopore volume N_2 (%)	Pore volume < 20nm N_2 (%)	Pore Volume/ TOC (cm^3/g)
OC1	outcrop	0.5	4.4	0.557	1.6	67.3	0.009	0.007	0.003	0.134	74.5	27.7	8.2	0.002
OC2	outcrop	0.5	6.6	1.572	2.9	68.7	0.027	0.021	0.006	0.134	77.8	23.3	8.0	1.219
OC3	outcrop	0.5	5.5	2.721	3.7	57.8	0.039	0.028	0.011	0.157	71.7	28.2	12.0	2.189
IM2_1	2	0.5	5.8	0.522	NA	108.5	0.014	0.013	0.001	N/A	89.7	9.9	2.5	0.430
IM2_2	2	0.5	1.9	0.321	NA	71.6	0.006	0.005	0.001	N/A	86.8	10.4	3.9	2.055
H3A1	5	1.2	1.0	2.398	NA	29.0	0.017	0.012	0.005	0.10	69.6	29.0	19.1	19.338
H3A2	5	1.2	3.0	5.799	NA	15.9	0.023	0.010	0.013	N/A	43.3	56.6	36.5	12.335
H3A4_	5	1.2	0.7	1.331	4.1	36.6	0.012	0.008	0.004	N/A	65.8	32.9	15.4	20.874
GW2	4	1.2	2.3	3.399	2.1	26.4	0.022	0.013	0.009	0.14	59.8	40.2	23.6	10.251
GW4	4	1.2	1.0	2.571	1.9	38.2	0.024	0.017	0.008	0.12	69.5	32.7	14.3	14.294
GW7	6	1.2	0.4	0.771	NA	43.6	0.008	0.006	0.002	N/A	71.2	23.7	13.8	34.519
GW8	6	1.2	0.6	1.094	NA	35.8	0.010	0.007	0.003	N/A	71.8	30.8	14.4	26.236

Table 3.5: Gas adsorption measurements (N_2 and CO_2) of surface areas, average pore diameters, macro-, meso- and micropore volumes and calculated pore volumes for pores < 20 nm. To see how the presence of organic matter influences the total pore volume, the pore volumes were also normalised to the TOC values. The percentages of each pore volume fraction compared to the total pore volumes was also calculated

3.3.3.4. Pore size distributions

Combined CO_2/N_2 adsorption data cover a pore-size distribution that ranges from 1 nm to 250 nm, with the data exhibiting a good transition between the two gases. From the PSD vs dv/dw pore volume cumulative plots, it is possible to notice a variation in pore sizes with the microfacies type. Microfacies A and B samples mainly exhibit pores in the mesopore range. CO_2 analyses in these samples also display the presence of pores < 2nm. Cumulative pore sizes plots (Figure 3.14) also show that in the gas window samples the porosity is held within pores smaller than 10 nm, whereas in the immature window it is mostly between 10 and 100 nm.

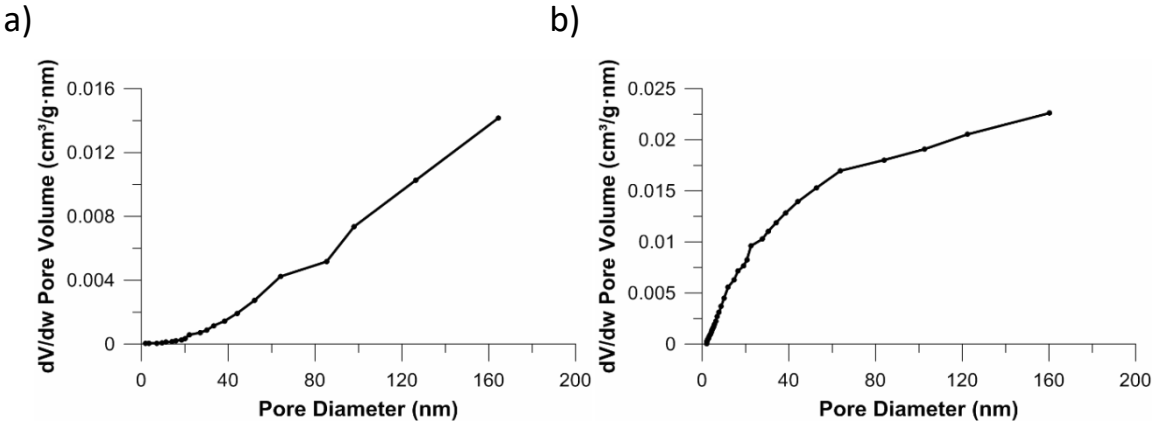

Figure 3.14: Cumulative plots of pore size distributions vs dV/dw Pore Volume (cm³/g·nm) for a) an immature sample (OC3) and b) a gas window sample (H3A2) from microfacies A.

The pore sizes for microfacies A and B decrease with increasing in maturity, from an average of 75 nm to an average of ~ 30 nm. Samples from microfacies C exhibit larger pore diameters (on average ~ 40 nm) compared to samples from microfacies A and B at the same maturity (R_0 1.2%) (on average ~ 30 nm). dv/dlogr plots imply a bimodal distribution of pore sizes for samples from microfacies A and sample H3A4 from microfacies B (Figure 3.15a and b) and a unimodal distribution for samples from microfacies B and C (Figure 3.15 c and d).

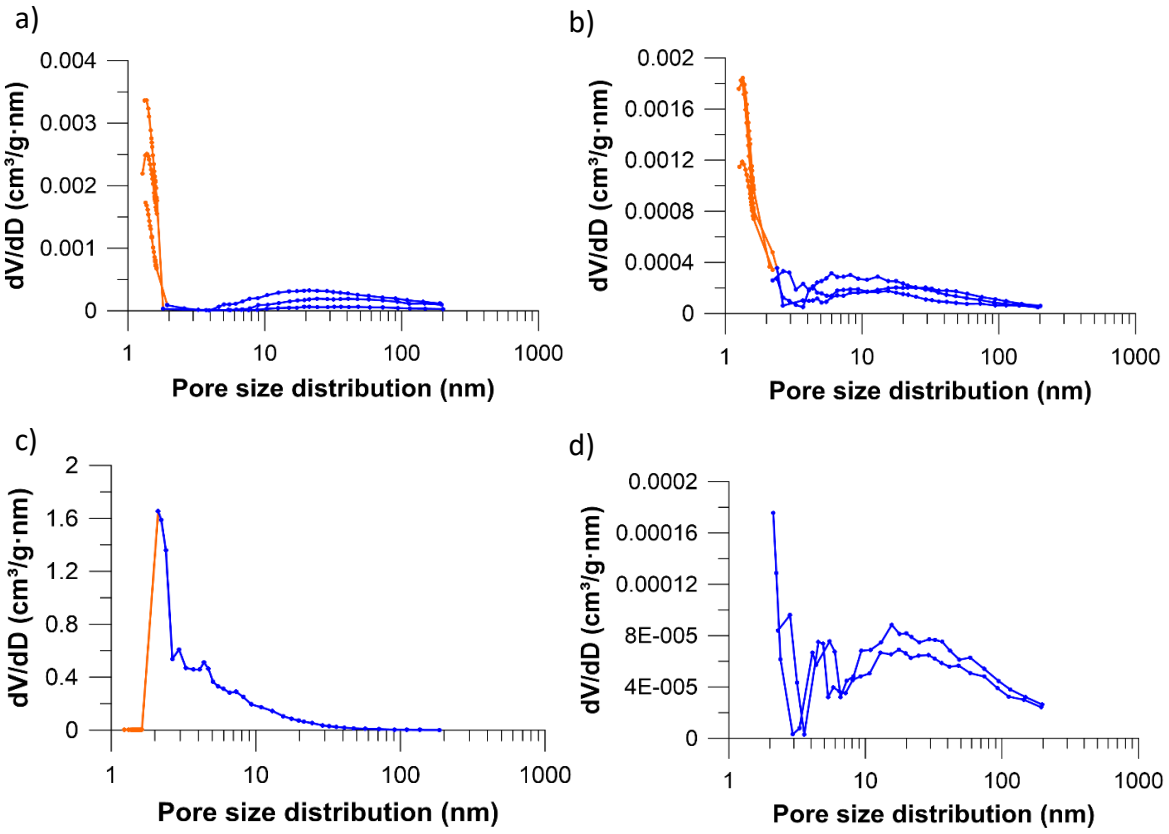

Figure 3.15: Pore size distributions using the gas adsorption technique (CO_2, orange and N_2, blue) for a) OC1, OC2 and OC3 samples (R_0 0.5%, microfacies A), b) H3A2, H3A3 and H3A5 (R_0 1.2%, microfacies A), c) sample H3A1 (R_0 1.2%, microfacies B) and d) samples GW7 and GW8, R_0 1.2%, microfacies C). The distributions are bimodal for samples from microfacies A and shift to lower values in the gas maturity samples. They pore sizes appear instead unimodal for samples from microfacies B. Microfacies C samples present pores between 10 and 100 nm as well as pores < 4 nm. However, no CO_2 data is available to quantify the pores smaller than 2 nm.

3.3.4. Mercury injection capillary pressure (MICP)

Before the analyses of the data, all curves were corrected for conformance and compaction errors. By plotting the pore throat sizes versus the pore volume fraction, the pore throat distribution can be analysed (Figure 3.16). The samples present a unimodal pore size distribution for the pore size range analysed, and the pore size ranges depend strictly on the microfacies type and on the maturity of the samples.

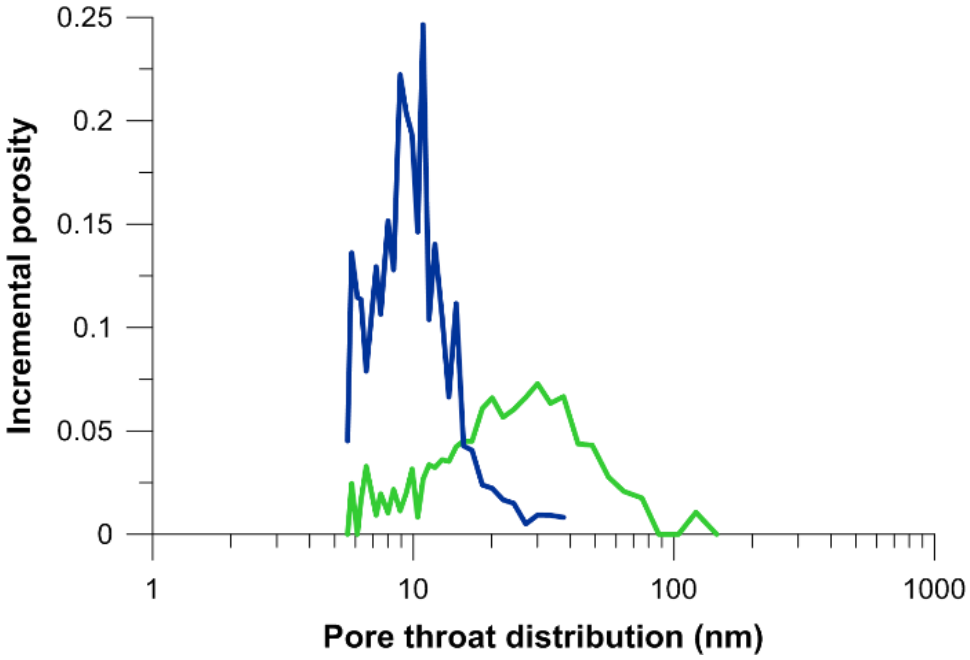

Figure 3.16: Pore size distributions for two exemplary samples from microfacies A in the immature window (blue) and the gas window (green).

3.3.4.1. Pore-throat size distribution

In microfacies A, an increase in maturity determines a shift in the pore throat diameters from an average of 23 nm for the immature samples (R_0 0.4%), to an average of 16 nm for the highest maturity samples (R_0 1.2%). Moreover, the pore throat distribution presents a broader spectrum in the low maturities, covering the meso- and macropore sizes, to a narrower spectrum at high maturities, restricted to micro and mesopores smaller than 20 nm (Table 3.7). For additional data, refer to Figure A.5Figure A.6 in the appendix.

Sample Names	Well Names	Ro (%)	TOC (wt%)	Microfacies	Average pore diameter sizes (nm)	Fractal Dimensions	MICP Porosity (%)	Entry Pressures	MICP porosity Volume (cm^3/g)	Retained Hg Volume (%)
OC1	Outcrop	~0.4	4.4	A	7.2	2.27	8.9	20000	0.005	10.2
OC2	Outcrop	~0.4	6.6	A	27.6	2.39	11.8	1500	0.027	43.4
OC3	Outcrop	~0.4	5.5	A	43.4	2.19	16.3	700	0.197	42.6
IM1_1	1.0	~0.5	4.5	A	NA	2.84	8.4	NA	0.001	NA
IM2_1	2.0	~0.5	5.8	B	8.4	2.26	1.7	17000	0.001	NA
IM2_2	2.0	~0.5	1.9	A	NA	2.41	14.8	NA	0.001	NA
IM2_3	2.0	~0.5	7.9	A	27.8	2.48	8.5	1300	0.001	32.3
OW1	3.0	~0.9	4.9	A	38.4	2.28	10.6	900	0.026	43.9
OW2	3.0	~0.9	2.6	A	27.6	2.31	10.7	1500	0.022	NA
GW1	4.0	~1.2	3.5	A	10.7	2.75	12.1	9900	0.021	NA
GW5	4.0	~1.2	1.6	B	10.3	2.34	6.7	10900	0.025	39.8
GW4	4.0	~1.2	1.0	B	10.3	2.32	NA	10900	0.012	NA
GW3	4.0	~1.2	0.5	B	16.5	2.28	5.6	3900	0.006	3.2
H3A1	4.0	~1.2	1.0	B	15.5	2.33	11.2	4500	0.011	28.4
H3A2	4.0	~1.2	3.0	A	8.9	2.33	6.6	15000	0.010	25.6
H3A3	4.0	~1.2	5.4	A	12.3	2.37	3.9	7300	0.006	46.6
H3A4	4.0	~1.2	0.7	B	17.8	2.33	4.5	3400	0.006	21.6
H3A5	4.0	~1.2	6.0	A	13.7	2.39	7.9	5800	0.034	47.1
H3A6	4.0	~1.2	0.2	B	13.7	2.28	7.2	5800	0.008	26.1
GW6	5.0	~1.2	2.4	B	11.7	2.90	13.0	8100	0.013	53.0
GW2	5.0	~1.2	2.3	B	12.3	2.31	6.1	7300	0.016	44.7
GW7	6.0	~1.2	0.7	C	34.2	2.20	12.9	1100	0.006	NA
GW8	6.0	~1.2	0.5	C	49.8	2.28	6.8	550	0.012	NA

Table 3.6: MICP results for the samples analysed: average pore diameter sizes calculated by intruded volume (nm), fractal dimensions and MICP measured porosity, entry pressures, porosity volumes and retained Hg volume values (%). NA = data not available.

In samples from microfacies B, the pore throat size distribution is composed only of mesopores and the average pore throat diameter is 18 nm. In the two microfacies C samples, the pore throat size distribution is delimited between 10 and 100 nm, with no variations in frequency values. The average pore throat diameter in these two samples is 42 nm.

3.3.4.2. Hg saturation

Plotted diagrams of pressures (psi) vs mercury saturation (%) (Figure 3.17) give insights on the connected porosity, and therefore on the permeability of the samples. In most of the samples (except for samples OC3, GW8 and H3A3), the volume percentage in the steep side of the curve is below 10%, indicative of a tight, yet connected, pore network. The inflection point, which corresponds to the pressure at which the saturation of mercury increases abruptly, is situated above 1000 psi in all the samples except for sample GW8, sample OW1 and sample OC3. This pressure, which is the pressure at which the mercury is starting to enter the system, corresponds to a pore throat radius of ca. 100 nm, meaning that most of the samples the pore throats have sizes in the mesopore or micropore range (Figure 3.17).

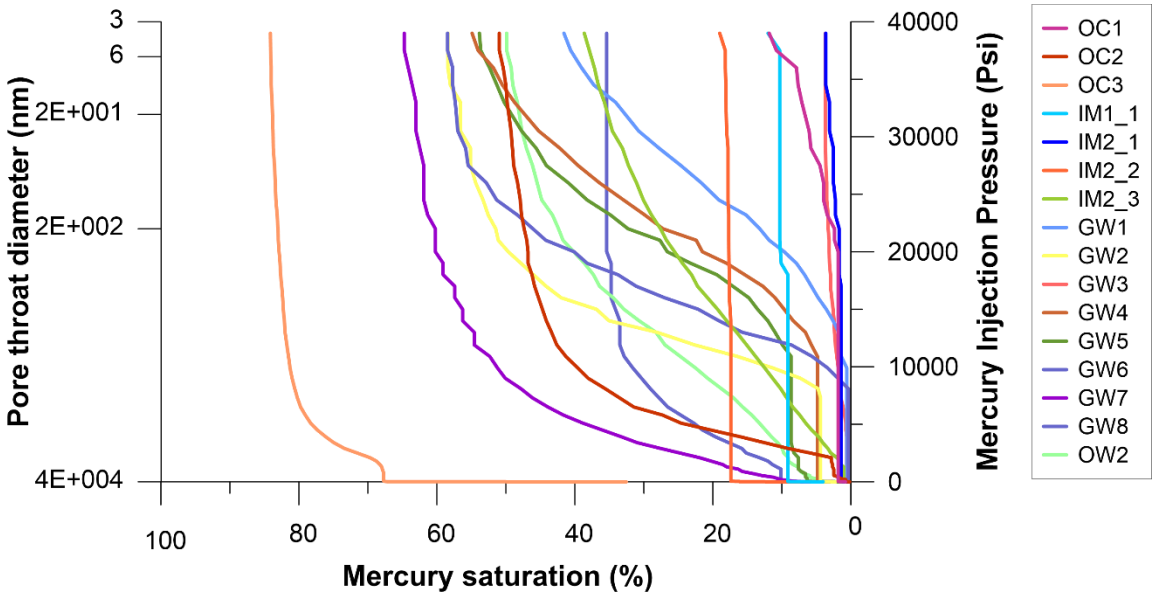

Figure 3.17: Mercury saturation (%) vs Mercury pressure (psi) plots. Each mercury pressure is correlated to a pore throat size. In all the samples except for samples GW8, OW1 and OC3, the inflection point, i.e. the first mercury entering the pore system, is situated above 1000 psi.

3.3.4.3. Hysteresis

The extrusion curve can provide information on the quantity of mercury that is retained in the pore system during the pressure reduction and on the nature of connectivity of the pores (Figure 3.2). The more "snap-off" of mercury occurs, the more the system is heterogeneous and formed by small pore-throats connecting larger pore bodies (Klaver et al., 2015). The small pore throats, indeed, cause the mercury to remain trapped in the

samples during the drainage phase. In the samples, no clear trend occurs between the retained mercury and maturity, mineralogy or microfacies. However, the lower retained mercury volume values (10.2%) and the higher (53%) are found in a low maturity (sample OC1) and a high maturity sample respectively (sample GW2) (Table 3.7). Overall, the average retained volume is more than one third (36.1%). Sample OC3 has the lowest inflection point (700 psi) and a corresponding high porosity fraction (12.2%). Comparing the total pore volumes from the gas adsorption and the MICP analyses, cumulative volumes measured with the MICP method are in the same range as the ones measured with the BET method. Generally, the MICP values are slightly lower (except for sample OC3 ad sample GW8); moreover, the MICP displays more pore volumes in the range of the micro and mesopores compared to macropores: on average, ~54% over ~28% for the MICP data and ~29% over 71% for the gas adsorption data respectively (Table 3.7).

3.3.4.4. Fractal dimensions

To measure the complexity of the pore medium, fractal dimensions (Df) were calculated using a $\log -\frac{dv}{dr}$ vs $\log dv$ plot (Figure 3.18). The more the value is high, the more the system is complex. In the sample datasets, Df values range between 2.19 (sample IM2_2) and 2.9 (sample GW6). The average fractal dimension is 2.38. In microfacies A high maturity samples, a good relationship exists between the TOC wt% values (R^2=0.52) and the fractal dimensions (Figure 3.19). Also, a good (R^2=0.58) inverse correlation is found between the carbonate (%) and the fractal dimensions (Figure 3.20 a) and a positive correlation between % silicates and the fractal dimensions in the immature window (Figure 3.20 b).

Sample Names	Well names	R_0 (%)	TOC (wt %)	Average Pore Diameter (nm)	Pore Volume/ TOC (cm^3/g)	Cumulative volume MICP (cm^3/g)	Cumulative volume macropores MICP (cm^3/g)	Cumulative volume mesopores MICP (cm^3/g)	Cumulative voume micropores MICP (cm^3/g)	Macropore volume MICP (%)	Mesopore volume MICP(%)	Micropore volume MICP (%)
OC1	outcrop	0.5	4.4	67.3	0.0	0.005	0.001	0.001	0.003	15.6	22.2	62.2
OC2	outcrop	0.5	6.6	68.7	1.2	0.027	0.001	0.025	0.001	4.8	91.1	4.1
OC3	outcrop	0.5	5.5	57.8	2.2	0.197	0.159	0.037	0.001	80.9	18.6	0.7
IM2_1	2	0.5	5.8	108.5	0.4	0.001	0.001	0.000	0.000	38.5	30.8	30.8
IM2_2	2	0.5	1.9	71.6	2.1	0.001	0.001	0.000	0.000	100.0	0.0	0.0
H3A1	5	1.2	1.0	29.0	19.3	0.011	0.001	0.008	0.002	11.5	72.6	15.9
H3A2	5	1.2	3.0	15.9	12.3	0.010	0.001	0.004	0.005	10.4	41.7	47.9
H3A4_	5	1.2	0.7	36.6	20.9	0.006	0.001	0.005	0.000	10.7	82.1	7.1
GW2	4	1.2	2.3	26.4	10.3	0.016	0.001	0.014	0.001	7.5	86.9	5.6
GW4	4	1.2	1.0	38.2	14.3	0.013	0.001	0.008	0.004	8.8	63.2	28.0
GW7	6	1.2	0.4	43.6	34.5	0.006	0.002	0.004	0.000	28.6	71.4	0.0
GW8	6	1.2	0.6	35.8	26.2	0.012	0.003	0.008	0.001	25.2	70.4	4.3

Table 3.7: MICP pore volume measurements and calculated micro, meso and macropore volume from MICP data (%).

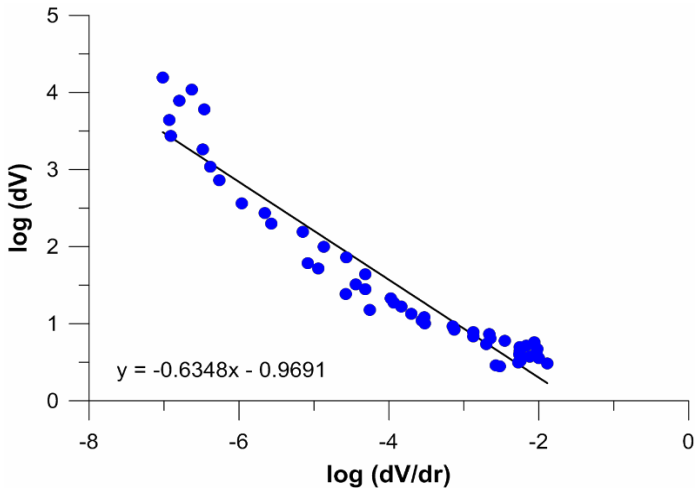

Figure 3.18: Example of a fractal dimension plot calculation based on MICP analyses (sample GW5, R_0 1.2%). The slope of the fitting line in the double logarithmic plot can be used to calculate the fractal dimension (in this case, D*f* = 3-0.63).

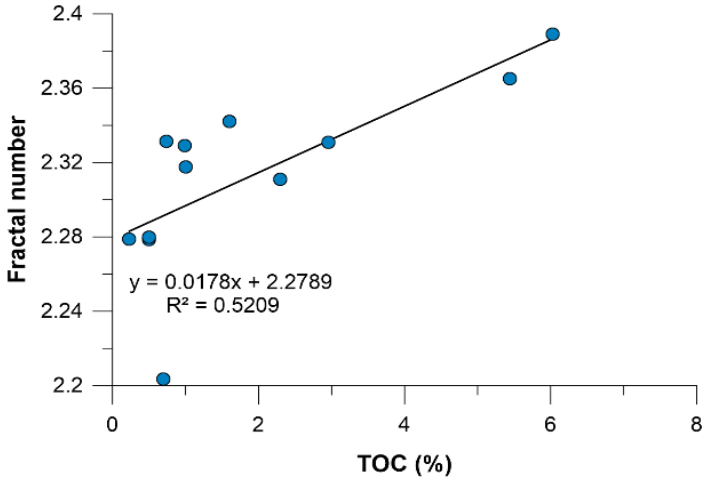

Figure 3.19: Fractal dimension vs TOC (wt %) plot for the high maturity (Ro 1.2%) samples.

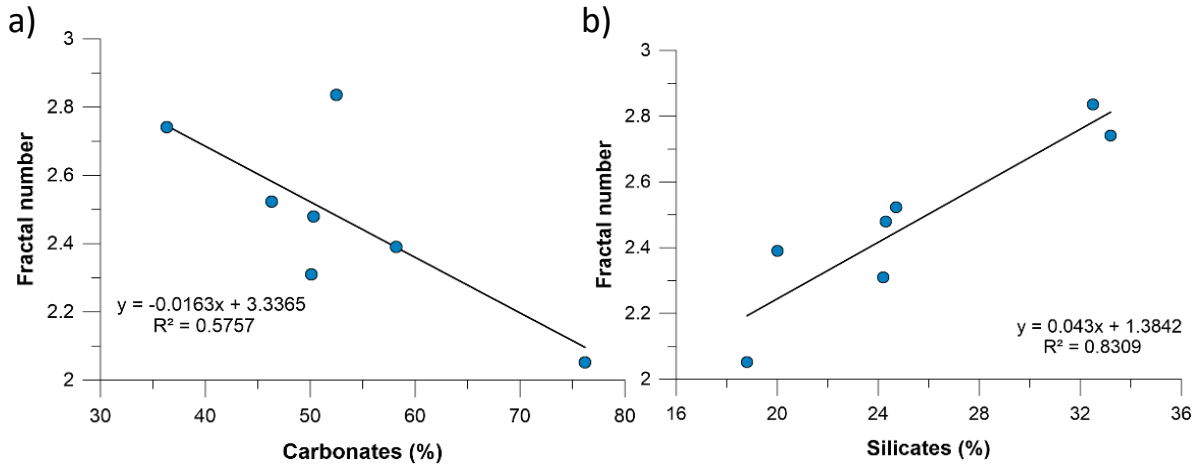

Figure 3.20: Fractal dimension vs a) carbonates (calcite, dolomite and ankerite) (%) and b) silicates (quartz, K-feldspar, plagioclase) for samples at low maturities (R_0 0.5%).

3.3.5. Focused Ion Beam (FIB)

3.3.5.1. Porosity and OM volume fractions

In order to visualise and measure in 3D, variations in the nature of the pore system, only samples from microfacies A were selected for this technique (Figure 3.21). To calculate the OM volumes, a kerogen density of 1.1 g cm^{-3} for the immature samples, 1.2 g cm^{-3} and of 1.35 g cm^{-3} for the most mature samples were used, as suggested by Okiongbo et al. (2005).

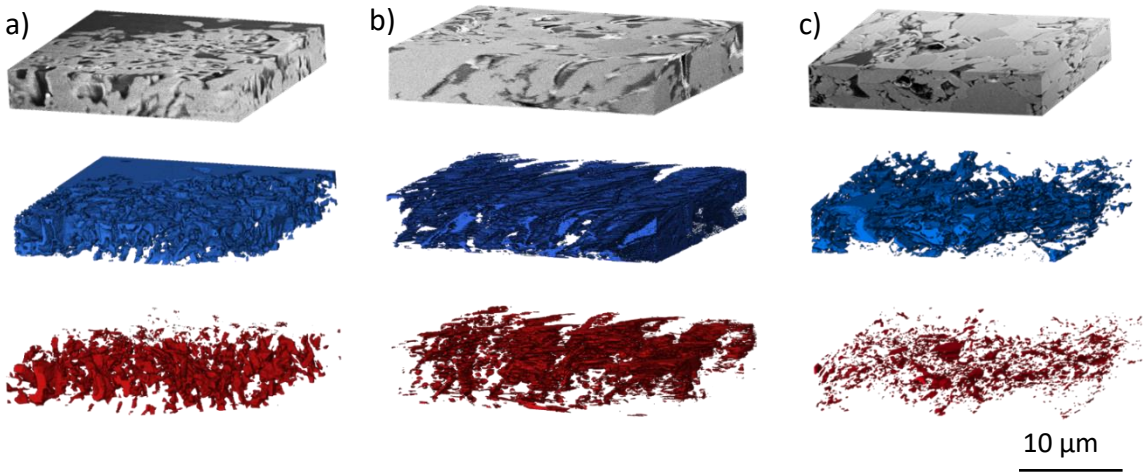

Figure 3.21: 3D FIB volume renders at increasing maturities of samples a) IM2_1 (R0 0.5%), b) OW1 (R0 0.9%) and c) H3A5 (R0 1.2%). The blue colour represents for the three samples the segmented 3D volume of OM and the red colour represents the segmented 3D volume of pores.

The bulk density, typically close to 2.7 g cm^{-1}, was calculated using the bulk mineralogy and TOC wt% values. The calculated porosity values range from 1.8% for sample IM2_1 to 4.5% for sample H3A5. The organic matter volume fractions observed in the samples vary between 11.4% for sample H3A5 to 24.6% for sample IM2_3. The OM volumes measured after the 3D thresholding in Avizo are in all the samples very similar, but slightly larger than the OM volumes calculated from the TOC% values (Table 3.8). The reasons behind the discrepancy between the FIB and XRD values could be due to the volume of the sample chosen for the FIB not being representative, or the greyscale thresholding not being accurate.

The 2D slices give an insight into where the porosity is situated. For the samples analysed, most of the porosity is situated in the matrix for the low maturity and oil window samples (IM1_1, IM1_3, OW1) and in the OM in the higher maturity (R_0 1.2%) samples (H3A5, GW11). The amount of porosity within the OM was calculated by filling the void spaces within the OM using the *fill* function in Avizo and subtracting the actual OM volume to the result (Figure 3.23). This method is not accurate, as it does not consider the porosity within the OM in the case of the presence of open voids. However, similarly to the FIB-SEM pore type calculations, results show that samples at high maturities exhibit larger (up to 80% more in sample H3A5) portions of porosity within the OM volume compared to the samples at low maturities (up to 54% in sample OW1).

Sample names	OM volume (%)	Porosity volume (%)	Con-nected OM (%)	Total con-nected porosity (%)	No. of pores analysed	Average pore sizes (nm)	OM pores (calculated by	Carbonates (%)	Silicates (%)	Clays (%)	TOC (wt %)	Calculated volumes from TOC	Con-nected porosity for pores <
IM2_1	13.5	1.8	84.6	6.2	587	127	0.4	36.3	33	19.5	5.8	13.4	2.4
IM2_3	24.6	4.2	97.7	26	1159	118	2.3	50.1	24	9	7.9	18.3	8.9
OW1	11.4	3.7	72.3	13.7	4942	72	2.1	56.6	19	3.6	4.9	10.6	4.3
GW11	16.7	2.7	94.1	1.4	8391	58	2.0	NA	NA	NA	3.4	6.3	1.0
H3A5	14.1	4.5	94.3	13.6	3466	39	3.6	50.7	10.6	23.1	6.5	12.5	8.0

Table 3.8: Results from FIB analysis. The OM is always well connected, whereas the porosity connectivity varies from sample to sample. The connected pores < 100 nm increase relative to the overall connected pores at increasing maturities. The volumes of organic matter calculated from the TOC values are similar to the volumes calculated from the FIB method. GW11 sample was only analysed using the FIB technique, and therefore no XRD or other data was available apart from TOC (wt %). NA= not available data.

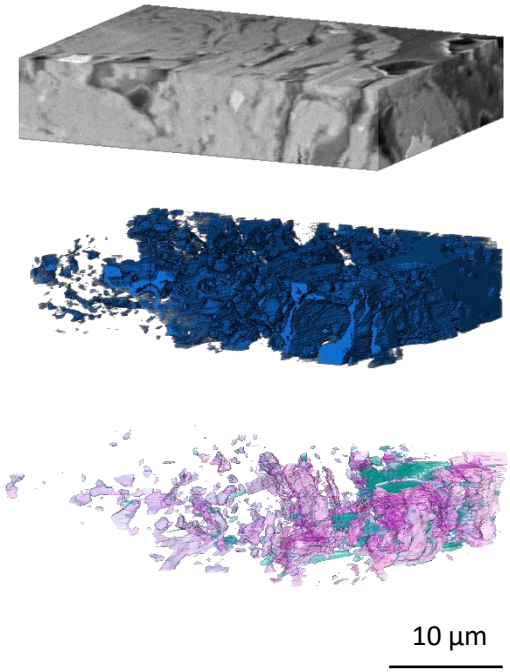

Figure 3.23: FIB 3D volume rendering for sample IM2_3. In blue, the segmented OM volume. In pink, the non- OM pores and in celeste the OM pores obtained using the *fill* function. This function consists in filling the void spaces in the OM and then subtracting the OM volume to the result.

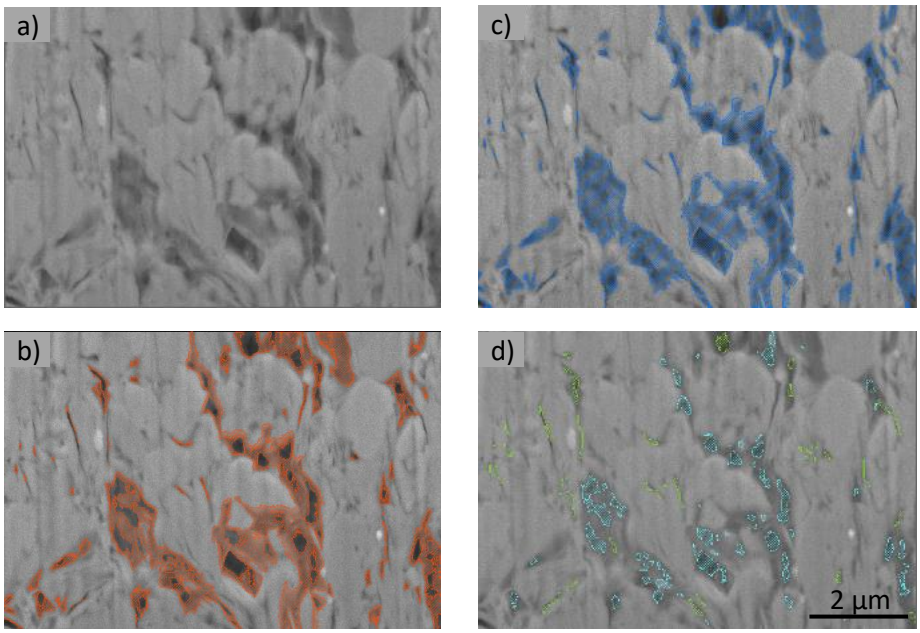

Figure 3.223: Example of the Avizo fill function on one slice of sample H3A5 (R_0 1.2%). a) is the unprocessed sample, in b) the orange colour corresponds to the segmented OM, in c) the blue colour corresponds to the segmented OM together with the segmented pores. In d) in the light blue are the pores obtained by subtracting slice b) to slice c). In light green, the non-OM pores.

3.3.6. Pore size distributions and connectivity

Pore size distributions display a decrease in pore size from the lowest to the highest maturity sample analysed (Table 3.9); the mean diameter pore size values range from 126.9 nm for sample IM1_1 to 39.5 nm for sample H3A5. Measuring the connected OM and porosity, the data show how the connectivity of the OM within the samples is always high (between 72% and 98%), whereas the connectivity of the porosities varies from sample to sample (between 1.4% for sample GW11 to 26% for sample IM2_3). The connected OM do not show a direct relationship with the TOC (wt %) content, but the TOC wt % is high (> 3.4 %) in all the samples analysed.

Sample Names	Pore volume < 45 nm (%)	Number of pores < 45 nm (%)	Pore volumes < 95 nm (%)	Number of pores < 95 nm (%)	Pore volumes < 250 nm (%)	Number of pores < 250 nm (%)
IM2_1	0	24	1.9	48	39.9	95.0
IM2_3	0.04	26.9	3.25	65.8	36.9	93.0
OW1	0	40.4	1.1	72	12.4	66.7
GW11	0.039	57.2	20.3	90.1	66.8	99.6
H3A5	0.04	49.5	19.4	82.8	66.8	99.7

Table 3.9: FIB cumulative pore volume analysis from a volume of 12.7 μm x 10.3 μm x 3.1 μm in size. The most distinct difference between the pore volumes of samples from the immature and oil window and samples from the gas window samples is seen at the pore size threshold of 95nm.

The connected pores, although they do not show any trend with the increase in maturity, appear to vary depending on the dimensions of the pores. By filtering the pores smaller than 100 nm, the connected porosity values decrease to less than 34% of the overall connectivity values in the immature and oil window samples, and to at least 70% in the most mature samples. However, the smaller pores visible with this technique have a diameter of 25 nm, suggesting that even more pores could be connected through non-visible, smaller pores. In all the samples, the pore volume distributions do not match the distribution of numbers of pores relative to pore sizes: there is a larger number of pores

with small diameters, but they contribute relatively little to the total pore volumes (Figure 3.23).

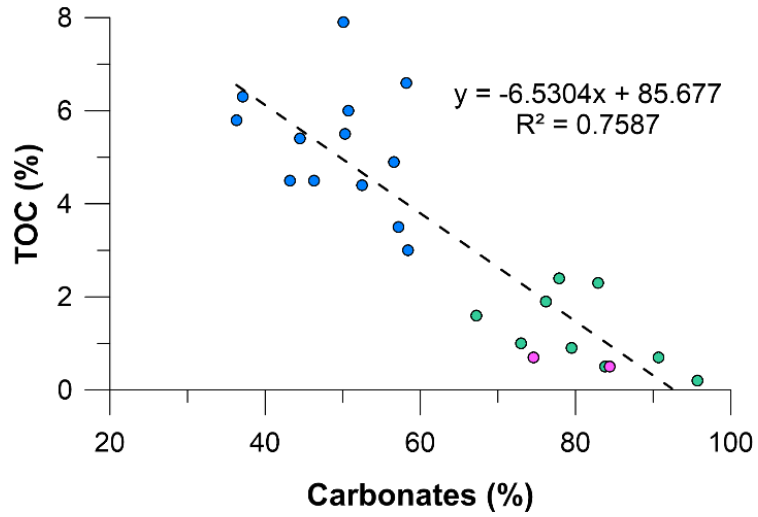

Figure 3.24: TOC (wt%) vs carbonate content (%) from the XRD analyses. The plot highlights a strong negative correlation.

In sample OW1, the pore volume for pores with a diameter larger than 250 nm, accounts for 87.6% of the total pore volume even though the pores smaller than 250 nm correspond to the 66.7% of the total number of pores. In sample IM2_1, the pore volume for pore sizes larger than 95 nm accounts for 95% of the total pore volume. The pore size distribution is bimodal, with 19% of the pores having a diameter between 30 and 40 nm and the rest of the pores a diameter between 95 and 350 nm. Sample IM2_3 presents a bimodal distribution of pore sizes (25nm to 95nm and 150 to 350 nm). The pore volumes compared to the pore sizes have similar values to sample IM2_1, with pores larger than 250 nm accounting for 63.1% of the total pore volume with 93.0% of the pores smaller than 250 nm. In sample GW11 and sample H3A5, 99.6% and 99.7% respectively of the porosities is associated with pores smaller than 250 nm. In both of the high maturity samples, the accumulated pore volume for pores with a diameter smaller than 250 nm is 66.8%, whereas in the immature and oil window samples the cumulative pore volume below pore sizes of 250 nm does not exceed 40% (Table 3.9).

For pore sizes smaller than 95 nm, in the two gas window samples, 20.3% and 19.4% of the pore volumes are situated in pores smaller than 95 nm, whereas in the immature and oil window samples, in pores smaller than 95 nm the pore volume values range between

1.1% and 3.25%. This is consistent with the results obtained in the SEM image processing interpretations and in the MICP pore volume estimates (Figure A.7).

3.4. Discussion

Deciphering all the factors and processes that lead to such a complex network is essential to bring to light the intrinsic nature of this heterogeneous reservoir. A comprehensive understanding of the pore sizes, shapes and connectivity can be achieved only by a combination of all the methodologies described in this chapter and the bulk rock analyses described in Chapter 2.

Microfacies classification and mineralogy analyses are essential for the FIB-SEM and FIB observations, as they provide information on the evolution of the pore types in terms of maturity and facies type. The classification of the pore types in five groups, combined with the analysis of the overall porosity and connectivity by means of FIB-SEM, FIB, Gas Adsorption and Mercury Injection Porosimeter data, allows the most relevant processes occurring in the three microfacies to be inferred. The merging of the observations is aimed to provide an overall understanding of the pore system in terms of hydrocarbon storage and flow potential.

3.4.1. Mineralogy

The mineralogy of the samples impacts the total porosity; TOC wt% values present a strong positive correlation with the total porosity, whereas the carbonates (calcite, dolomite and ankerite) show an inverse relationship. Clays (kaolinite and mixed illite-smectite) and silicates (quartz and feldspars), present but in minor abundances, might play a role as assemblage grains in the compaction phase and show weak correlations with the maturities analysed. Quartz occurs as microgranules and its content increases from the oil to the gas window. The micro quartz, as seen in Chapter 2, precipitates in the pore spaces within the matrix, decreasing the overall porosity. Previous studies have shown that pores associated with the clay-rich matrix are common and usually < 10 nm (Mark E Curtis et al., 2012; Javadpour, 2009; Kuila et al., 2014; Loucks et al., 2009; Milliken et al., 2013; Passey et al., 2010; Schieber et al., 2010; Walls and Sinclair, 2011). In this work, however, clay minerals are always less than 30% of the overall mineralogy and clay-hosted pores account for up to 19% of the overall porosity with no clear variation with maturity or microfacies. The pore system observed in these samples resembles more the

one of a chalk reservoir rather than a clastic mudstones one. The similarity is due to the abundance of inter- and intra-particle porosities within the coccolithic debris, as well as the diagenetic processes linked to carbonates and organic matter (Fabricius, 2003; Martin et al., 2011). The system is mainly controlled by a tight, rigid, carbonate framework surrounded by a more ductile organic matter phase.

3.4.2. Carbonates and organic matter

Carbonates in these samples are both primary and authigenic. Primary carbonates include biogenic foraminifera, coccoliths or other fossil debris, whilst authigenic carbonates derive from mineral precipitation from oversaturated marine waters (McAllister et al., 2015; Moore, 2001). As seen in chapter 2, carbonate cements start to occur in the immature window ($R_0 \leq 0.5\%$) and continue to precipitate at $R_0 \geq 1.2\%$ occluding the primary intraparticle and interparticle pores. The availability of carbonate-saturated fluids was interpreted to derive from the increase in dissolution of the primary calcite crystals. Calcite crystals dissolve because of increasing burial stresses and increasing acidification of connate waters due to organic matter maturation processes. Evidence in dissolution from pressure-solution is present at all maturities, but dissolution intraparticle pores start to be abundant in the oil and gas maturity window (Figure 2.36). Reprecipitation processes are also frequently observed and testified by means of cathodoluminescence analyses at all maturities, although they are more common in the oil and gas window compared to the immature window ($R_0 \geq 0.9\%$) (Figure 2.19). Organic matter, on the other hand, is classified as either marine or terrigenous kerogen or a secondary migrated bitumen (Dawson, 2000; Denne et al., 2016; Ergene, 2014; Fishman et al., 2012; Mcgarity, 2013).

Organic matter (TOC wt%) and carbonate minerals (calcite, dolomite and ankerite) percentages are also negatively correlated (Figure 3.24). This negative relationship can be explained by the fact that often the carbonate skeletal structure is filled or rimmed with organic matter, which, as in other studies (Scholle, 1977), is here thought to inhibit the precipitation of further calcite cement. The more the organic matter there is, the least carbonate cements precipitate (Figure 3.25).

Despite being mainly associated only to the carbonates and to the organic matter, this formation is highly heterogeneous and complex. The complexity of the formation is governed by a series of processes that are linked to the origin and evolution of the play, which also determine the storage and fluid flow capacity of these rocks.

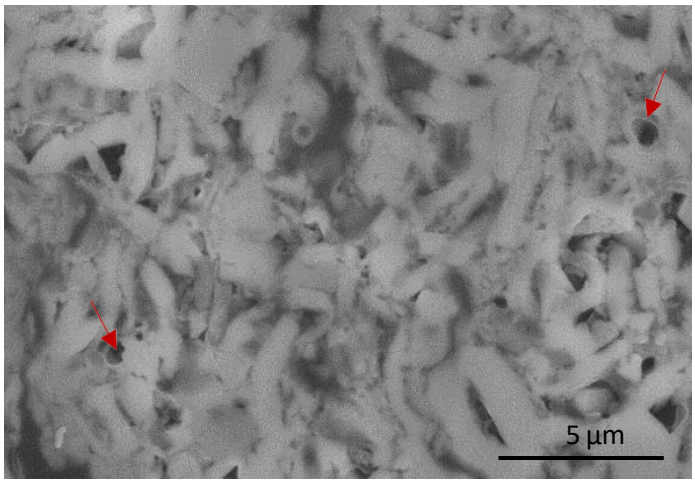

Figure 3.25: SEM-BSE image of sample IM2_3 (R0 0.5%) overlapped with a SE image of the same area. The arrows indicate pores bordered with OM within the carbonate matrix. The pores are not entirely within the OM, but between the carbonate particles and the OM. For this reason, they were classified as interparticle matrix pores in the pore types quantification.

3.4.3. Early-stage compaction

As observed in other petrographic studies on the Eagle Ford (Ergene, 2014; Mcallister, 2017; Pommer and Milliken, 2015), the first process occurring at the early stages of sediment burial is mechanical compaction. Early mechanical compaction in these samples is testified by grain fracturing, pressure solution and re-alignment processes (Figure 2.35). Porosity reduction due to compaction is believed to be primarily affected by the most ductile components, such as clays and kerogen (Loucks et al., 2012; Milliken et al., 2014; Pommer et al., 2014). However, as seen in Chapter 2, in the Eagle Ford, the presence of a solid skeletal framework formed by carbonates and, in minor abundances, silicates, is thought to have mitigated the compaction processes and fracturing, hence preserving primary porosity (Ko et al., 2017 and references therein) (Figure 3.25). As observed in other works (McAllister et al., 2015; Pommer et al., 2014), the large foraminifera chambers are here usually only partly filled by early-stage cements, allowing for the retention of

intraparticle fossil primary pores. Nonetheless, even if the presence of mechanical compaction is undoubted and testified by deformation and re-alignment processes (see Chapter 2), the degree to which it has affected the porosity system cannot be inferred.

3.4.4. Dissolution processes

Evidence of dissolution processes is commonly observed in these samples. Dissolution derived by mechanical compaction is testified in the contact within rigid clasts (Figure 2.36) and in pressure-solution veins. Dissolution also continues during late diagenesis, at temperatures > 80 ^{0}C. At these temperatures, the organic matter decarboxylation causes the expulsion of acidic fluids, which unbalance the pH conditions at which the minerals are stable. The acidification of the connate waters is believed by many authors to cause the dissolution of mineral phases such as calcite, feldspar and clay minerals (Er et al., 2016; Loucks et al., 2012; Leggett and Zuffa, 1987; MacGowan and Surdam, 1993; Schieber et al., 2010). In this study, in the samples analysed, SEM image processing shows evidence of the dissolution of minerals. Starting from the oil window, an increase in corroded seams in noticed (Figure 2.36 a), as well as the formation of new intraparticle mineral pores mainly within the carbonates and feldspar minerals (Figure 2.36 c). Intraparticle dissolution pores can be as small as 20 nm and are more common, compared to other types of porosities, in microfacies C (R0 1.2%) (Table 3.3). Biogenic products such as faecal pellets, on the other hand, appear well preserved even at high maturities. Their preservation could be related to early OM migration into the pores or to the same mucillagineous coating that also preserves the original porosities within the coccoliths (Porter and Robbins, 1981). In general terms, when mineral phases dissolve, they release in the fluids elements that favour the precipitation of other mineral phases in forms of cements.

3.4.5. Cementation processes

When mineral phases precipitate producing cements, these newly formed components impact the pore system as well as the overall structure of the affected area. As seen in Chapter 2, the different depositional environment in which the microfacies have formed causes the samples to have distinct diagenetic patterns relative to the microfacies type.

Cathodoluminescence studies indicate that there is a greater abundance of authigenic carbonates in microfacies B and C compared to the microfacies A samples (see Chapter 2). Moreover, if the cements in microfacies A mainly impact the intraparticle primary fossil pores, in microfacies B and C cements are found around the minerals, also affecting the interparticle matrix pores (Figure 3.7). In chapter 3 it is observed how, by looking at a whole maturity sequence from the same microfacies (microfacies A samples), the increase in burial stress and temperature produces the dissolution and reprecipitation of new phases (Figure 3.5), which are believed to affect the bulk porosity and the pore system (Mastalerz et al., 2013; Mathia et al., 2016).

3.4.6. Total porosity and microfacies types

Total porosities calculated with different techniques show that FIB and FIB-SEM values are ~ 10 times or lower compared to the bulk MICP measurements. As stated in Klaver (2014), this difference is mainly caused by the different resolution of the techniques, which is also the reason why the MICP measurements are the most reliable in terms of bulk porosity. Indeed, the Hg porosimetry can measure pores as small as 2.8 nm in diameter whereas the FIB-SEM and the FIB techniques cannot detect pores smaller than ~18 nm in diameter. The different values suggest that the samples present a large number of pores smaller than 18 nm.

Total porosities also vary between the three microfacies. Samples from microfacies A have on average higher total porosities than samples from microfacies B and C. In microfacies A samples, the calcite percentage is lower compared to the microfacies B and C samples and overall, the total porosity exhibits a negative relationship with the carbonates component. This negative correlation is linked to the reprecipitation of calcite cement phases within the available pores within the minerals, the fossils and the matrix. Cementation and reprecipitation processes, as seen in chapter 2, occured earlier in the burial hisotry and in more abundance in microfacies B and C samples, causing a higher decrease in porosity (-40% and -60% respectively) compared to microfacies A samples at similar maturities (R_0 1.2%). Particularly noteworthy in microfacies A samples is the presence of faecal pellets, in which intraparticle pores can account for more than 40% of the total area percentage and for more than 60% of the interparticle matrix pores (see

Chapter 2). In microfacies B samples, faecal pellets are also present, but their pores are filled with calcite cements (Figure 2.24). Microfacies C samples differ from microfacies A and B samples also for the nature of their fossil components, which are mainly broken fossil bioclasts held together by calcite cements.

3.4.7. Influence of organic matter on bulk porosity

As previously mentioned, in the gas window, along with the cementation processes that fill the pores, pores are also generated both by dissolution processes and by the thermal maturation of the organic matter. In the gas window, organic matter pores are mainly present in the form of sponge-like pores. They are typically smaller than 20 nm (King et al., 2015; Liu et al., 2017), and the positive correlation between the TOC and bulk porosity also suggests that many of the organic matter generated pores are not visible with the image processing techniques used in this work (Kuila, 2013; Milliken et al., 2013). In the gas window, the organic matter pores are not observed in all the organic moieties, but appear to be confined within the bitumen phase (Figure 3.26).

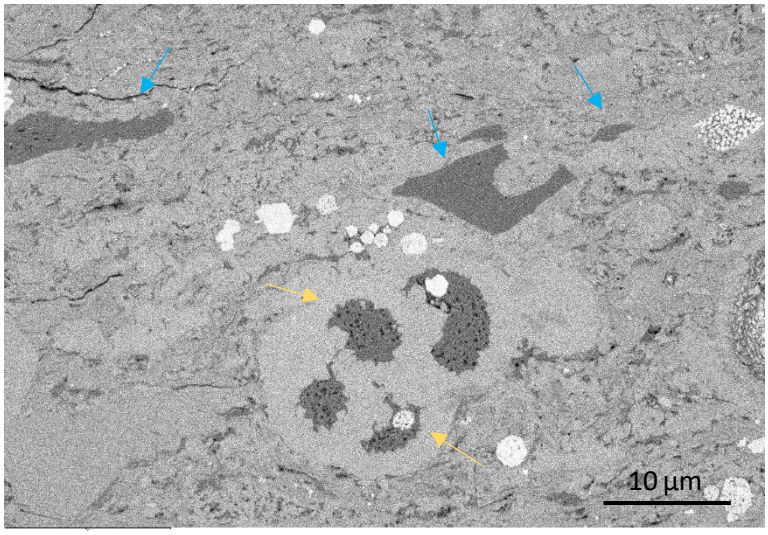

Figure 3.26: SEM-BSE image of sample H3A3 (R_0 1.2%) overlapped with a SE image of the same area. The yellow arrows indicate porous organic matter, whereas the blue arrows non-porous organic matter. Porous and non-porous organic matter coexist in samples at gas maturities.

These observations are in line with the previous works by Bernard et al., (2013, 2012); Ko et al., (2017), Milliken et al., (2013) which attest that different organic matter types can

have significant variations in pore generation from pyrolysis. In particular, the same authors consider the bitumen phase extremely important for the organic matter pore formation related to the gas generation in the gas window. Other authors believe instead that the organic matter porosity differences are already present in the immature window and caused by the textural differences, but are masked by compaction during burial (Fishman et al., 2012; Milliken et al., 2013) and by bitumen migration (Löhr et al., 2015). Given that migrated bitumen is also present in the immature samples (Paragraph 2.3.4), it is not here possible to attest whether the kerogen structure presents primary pores. Therefore, both the hypothesis can be considered valid.

Organic matter is also often found to fill or rim the intraparticle fossil pores and the carbonate skeletal structure. When filled, the overall porosity decreases. When rimmed, the porosity decreases with reference to the skeletal carbonate framework, but it also prevents the reprecipitation of authigenic minerals, such as calcite or quartz, within the minerals. In the analysed faecal pellets from all maturities, the coccolithic structure presents pores rimmed with OM (Figure 3.25). It is still unclear whether this OM is related to the oil migration and trapping, or to the polysaccharides-derived coating of the coccolithic faecal pellets as suggested by Slatt and O'Brien, (2011) and Spain and McLin, (2013). At low maturities, oil emplacement in the reservoir, as well as the faecal pellet copepod-derived coating, would have favourable effects on the overall matrix porosity, inhibiting mineral dissolution and precipitation of other mineral phases (Bukar, 2013). In support of this hypothesis, it is the strong negative correlation between TOC (wt %) and carbonates (%) (Figure 3.24).

3.4.8. Total porosity and thermal maturity

Contrarily to what was observed by other authors (Klaver et al., 2016; Mastalerz et al., 2013; Mathia et al., 2016), however, total porosity analyses with the MICP technique show that there is no direct correlation with burial depth. This suggests that organic matter maturation, dissolution and reprecipitation processes cause a porosity redistribution in the system. New pores are formed by the maturation of organic matter and due to the etching of the minerals (Figure 3.6 f and a respectively), whereas primary pores are totally or partially occluded by the reprecipitation of secondary mineral phases. The dissolution

and reprecipitation phenomenon is common and has been observed in many types of reservoirs (Cao et al., 2014; Dayal, 2017; Fowler and Yang, 2003; Giles and de Boer, 1990; Gorniak, 2016; Worden and Morad, 2003; Yuan et al., 2019). No variation was also noticed with the increase in maturity between the immature (R_0 0.4-0.5%) and the oil window samples (R_0 0.9%), as observed by other authors (e.g. Klaver et al., 2016 and Mathia et al., 2016). Generally, the decrease in bulk porosity between the immature and oil window maturity is explained by the migration of hydrocarbons that flow through the available paths and obstruct the pores and pore throats. However, in the Eagle Ford Formation, hydrocarbon generation occurs at a lower maturity than in clastic source rocks, probably due to the high sulphur content of the kerogen (Sun et al., 2016). If OM pores associated to depositional texture of the organic matter are present, the clogging of primary OM pores cannot be observed for this dataset (Curtis et al., 2012; Ko et al., 2017; Löhr et al., 2015a; Loucks et al., 2012, 2012; Milliken et al., 2013). The lowest maturity samples analysed already present migrated OM. Moreover, in the oil window, no significant change in pore types compared to the immature window is noticed. In the shift between the oil and the gas window, however, from what is visible by the image processing techniques, the dissolution intraparticle pores and the organic matter pores increase by up to +200%. Matrix-related pores instead decrease by up to -61% in relation to the immature and the gas window maturities (Figure 3.7). The values support the redistribution of porosity correlated to dissolution, reprecipitation and gas maturation processes.

3.4.9. Pore shapes

Along with variations in pore types, the pore shapes also suggest a change in the pore system between the immature and gas maturity samples and between the samples from the three microfacies. In the immature window samples, where the interparticle pores related to the carbonate and silt aggregates are more abundant, the pores are angular, not significantly elongated and not oriented in one direction (Figure 3.8). This is in contrast to clay-rich mudstone studies, in which the pores are mainly related to the clay particles and are relatively flat at all maturities (Aplin and Moore, 2016; Desbois et al., 2009; Heath et al., 2011; Hemes et al., 2016; Houben, 2013). With the increase in maturity, in the gas

window samples from microfacies A and B, pores are significantly more elongated and oriented, similarly to what was observed by Bernard et al. (2012) in the Posidonia shale. Moreover, in the gas window, the samples exhibit a range of more circular pores along with the non-circular pores. This variation is caused by a systematic change in the pore system: interparticle matrix pores and intraparticle fossil and mineral pores become less abundant due to the increase in compaction and cementation of mineral phases in the primary pores (Aplin et al., 2006; Dewhurst et al., 1998). On the other hand, dissolution and organic matter pores, which have a spherical or ellipsoidal shape, start to form. In microfacies C samples the most abundant pore types are the interparticle matrix pores. In fact, the pore shapes are similar to the ones for the immature samples of microfacies A and B. Many other shale studies have observed the formation of organic matter pores at high maturities (Bernard et al., 2013b; Mark E. Curtis et al., 2012; Jason E. Heath et al., 2011; Loucks et al., 2009; Mathia, 2014; Milliken et al., 2014; Passey et al., 2010; S. Wang et al., 2016) and their spherical or ellipsoidal shapes compared with the other pore types (Alcantar-Lopez and Chipera, n.d.; Busch et al., 2017; Jiao et al., 2014; King et al., 2015; Löhr et al., 2015; L. Ma et al., 2016). However, the sphericity of the pores is not indicative of a simple pore system. The fractal dimensions calculated from the MICP technique, indeed, also indicate that at increasing TOC values in the most mature samples, the fractal dimensions become higher. This implies that the more organic matter is present, the more the system evolves into a complex, possibly tortuous pore system.

3.4.10. Pore size distributions and maturity

The complexity of the pore system is also related to the pore size distribution differences between the samples at low maturity and at high maturities, and the samples from the different microfacies. MICP and gas adsorption show very similar trends in the pore size distributions (Table 3.5, 3.6, 3.7). However, the MICP average diameter values are slightly smaller (-40%). This is because MICP measures pore throats, whereas gas adsorption measures pore bodies (Gregg et al., 1967). In addition, despite following the same maturity and microfacies trend, the two image processing techniques are unable to detect pores < 18 nm, which MICP and gas adsorption analyses indicate as abundant. Moreover, advances in imaging techniques, such as the use of He-ion microscopy, have allowed

visualisation of these small (< 10 nm) pores within the organic matter of several other mudstone reservoirs (Cavanaugh and Walls, 2015; Dong and Harris, 2013; King et al., 2015; Wang et al., 2016). By merging all the techniques implemented in this study, it is possible to conclude that the bimodal distribution for microfacies A samples (Figure 3.15) is given by large intraparticle fossil and mineral pores and by the micro and meso interparticle matrix pores, which are formed by the spaces between coccolithic fragments, organic matter and minerals or precipitates (i.e. clays, quartz, feldspars, pyrite framboids and carbonates). In the gas maturity window, the pores become smaller (between ~3 and ~30 nm) and have a narrower pore size distribution, similarly to the microfacies B samples. This is here interpreted to be caused by the organic matter maturation, compaction and reprecipitation processes discussed before. Microfacies C samples have instead slightly larger pores sizes (~40 nm on average) given by the bioclasts interlocked with cements. In this case, as seen Chapter 2 (paragraph 2.3.2.3) the bioclasts are constituted by large (> 50 μm) shell fragments, sponges and foraminifera.

3.4.11. Pore volumes and maturities

The pore volume distributions data from the various techniques, show discrepancies in the calculations of the contributions between micro, meso and macroporosities (Table 3.5, 3.6). In general, incongruities between the techniques are explained by the different resolutions and measurement methods (Klaver et al., 2015a). In particular, it must be taken into account that the MICP technique measures the pore throats, whereas the gas adsorption the pore bodies. Therefore, larger pore sizes can be expected in the gas adsorption measurements. These large pores usually match the large foraminifera tests, or the intraparticle pores within the coccoliths in the faecal pellets or in the matrix (Mathia et al., 2016).)High pore volume percentages found at larger pore sizes in this study differ from previous works, in which much of the porosity consists of micro and mesopores associated with organic pores as well as clay minerals (Allen et al., 2014; Liu et al., 2017; Mathia et al., 2019; Sondergeld et al., 2010). In these samples, clays are not believed to be playing a major role. In microfacies A, the meso and micropores measured with the MICP and gas adsorption techniques show an increase in pore volume from the oil to the gas window. This suggests that in the gas window, smaller pores also contribute to the

hydrocarbon storage potential. This is also testified by the increase in BET surface area in the gas window. Moreover, the correlation between the BET surface areas (m^2/g) and TOC (%) at high maturities indicates that the small pores are mainly associated with organic matter. In fact, as many authors have observed, the TOC content is a key factor in the gas storage capacity (Chen et al., 2016; Sondergeld et al., 2010; Wang et al., 2016). This is because the organic matter generates pores at high maturities and organic micropores, presenting larger surface areas, are able to adsorb more methane (Bustin et al., 2008; Chen et al., 2016; Rexer et al., 2013; Ross and Bustin, 2009). The organic matter pore volume contribution to the overall pore volume is shown to increase from the immature to the gas window; this is shown in the increase in OM pore voumes in the gas window in the FIB analyses, in the increase in organic matter pores seen in the SEM images and in the increase in pores smaller than 20 nm in the gas window measured with the gas adsorption technique. However, pore volume quantifications also show that meso and macropores contribute at a greater extent to the total pore volumes (Figure 3.24). Therefore, it can be concluded that organic matter pores at high maturities certainly contribute to the connectivity and gas storage, transforming the whole pore system, but macropores play a key role even in the gas window.

Change in pore systems can be observed as a function of increasing thermal maturity, but also between the different microfacies. Microfacies A, which contains less carbonate and more organic matter compared to the other two microfacies, displays a system governed by pores linked to the carbonate skeletal fraction. As seen before, at increasing maturities, interparticle and intraparticle pores relatively decrease compared to the organic matter pores. Microfacies B and C samples, instead, do not yield high amounts of TOC (wt%), rendering the pore system more carbonate-related. Lower pore volumes in microfacies B and C suggest that these facies have a tighter network compared to microfacies A in both the immature and gas maturity windows, which is probably related to their higher cementation factors relative to the microfacies A samples.

3.4.12. Pore Connectivity and microfacies types

As the pore shapes, sizes and types change with an increase in maturity and variations in microfacies types, the connectivity of the pore system also changes. Variations in

connectivity are noticed in the gas adsorption analyses, with the different hysteresis shapes between the microfacies A samples at low maturities and high maturities and in the microfacies B and C samples (Figure 3.12). The almost complete overlap between the adsorption and desorption curve in the low maturity samples of microfacies A samples suggests that the interparticle and intraparticle pores are well connected through relatively large (> 10 nm) pore throats that mainly reside between the matrix heterogeneous framework and the large foraminifera tests. The microfacies C pore network, instead, consists in a connected, yet tighter, carbonate and only partly OM-related system. Microfacies B samples also present low adsorption values, but the hysteresis is slightly larger compared to the microfacies C samples. In the mature samples of microfacies A instead, the hysteresis curves are large. This is indicative of a connected, yet more complex pore system formed by ink-bottle shaped pores (i.e. large pore bodies and narrow pore throats). The narrow pore throats impede the experimental CO_2 and N_2 gases to easily flow out of the pores thus forming the large hysteresis. As previously mentioned, the origin of these pore networks is tightly associated with the mineralogy and fabric of the different microfacies and to compaction and cementation processes. MICP drainage curves are in accordance with the gas adsorption data, as the snap-off percentages increase in the gas window maturities. Increasing snap-off values are indicative of larger amounts of mercury being retained in the samples after the measurements, meaning the pore throats are too small to allow a smooth flow of a non-wetting fluid (Tsakiroglou et al., 1997). To support these statements are also the FIB data, which, by analysing the connectivity of microfacies A samples in pores < 100 nm, suggest an increase in connectivity in the high maturity samples. However, FIB results show that the OM results almost entirely connected whereas the pores are connected for less than 26%. This suggests that, in the gas window, the smaller pores are not visible with the FIB-SEM technique and that the system is connected mainly through OM pore throats smaller than 25 nm. It can be concluded that in the laminated foraminiferal microfacies, organic matter micropores, although not being the main contributors in the whole pore storage capacity, have a pivotal role in the overall connectivity of the pore system (Liu et al., 2017; Passey et al., 2010).

In the gas window of the laminated foraminiferal mudstones pores result to be mainly OM related, but they can also be associated with inter and intraparticle pores within and in the carbonates, clays and silt.

The influence of the microfabrics in the connectivity of the pore network and in the pore structure profile in tight reservoirs was also testified in other works (Comisky et al., 2011b; Curtis et al., 2010; Dawson and Almon, 2010; Wang and Yu, 2017). However, most of the studies are centred on clay and silicate-rich mudstones. It is indeed commonly accepted that silt-rich mudstones are generally more permeable than clay-rich mudstones, as the nano-sized clays tend to obstruct the pores (Aplin and Moore, 2016; Dewhurst et al., 1998; Sun et al., 2016; Yang and Aplin, 2010). Carbonate-dominated mudstones have intrinsically different properties compared to silt and clay-rich mudstones, which juxtapose these fine-grained carbonate reservoirs to chalk reservoirs. However, authors (Dawson, 2010, Katsube) noticed that even in this reservoir, silt content increases the permeability of the system. By observing the mineralogy content, microfacies A yields a more connected pore network and larger pore volumes and it is also the microfacies with more silt content (Table 3.2). Despite not being directly correlated with the overall porosity percentages (Figure 3.4 d), silicates might play an important role in the connectivity and consequently in the permeability of the facies.

3.4.13. Pore connectivity and fluid flow

Based on Yang and Aplin's (2010) model, Mathia et al. (2019) estimated that the permeability of a pore network dominated by OM pores to be around 10 nD. For this formation, it can be inferred that in mature (R_0 1.2%) microfacies A samples the fluid pathways are too narrow to allow fluid transport at production timescales. Similarly, the entry pressures and the gas adsorption hysteresis for the calcite pathways in samples of microfacies B and C suggest very low permeability values. Immature microfacies A samples present a carbonate pathway consisting of larger pore bodies and larger pore throats compared to samples belonging to other microfacies and maturities, which is indicative of higher permeabilities. Potential pathways can also be the fracture-related pores, as they can provide a potential network for hydrocarbon migration and also enhance oil and gas recovery (Loucks et al., 2012 and references therein). The

microlaminations present in microfacies A samples are believed to favour the creation of fractures parallel to the laminae as well as to lead to an overall anisotropy, which is also reflected in the permeability (Mokhtari, 2014; Yang and Aplin, 1998). However, in this work, the fracture-related pores were not quantified thoroughly. Particular attention must be taken in the quantification of the fractures, as in samples as small as the ones analysed (from the millimetre to the centimetre scale) fractures can be caused by pressure release during the recovery phase as well as by mishandling during the sample preparation (Heath et al., 2011).

3.5. Concluding comments

The integration of different methodologies has allowed the quantitative characterisation of pores and the pore network, as well as identification of the primary factors affecting the increase and decrease in pore space and the connectivity of the pore system.

1. Pores can be classified into 5 types: interparticle matrix pores, intraparticle mineral pores, intraparticle fossil pores, intraparticle dissolution pores and organic matter pores. The interparticle matrix pores and the organic matter pores are the dominant pore types.
2. Pores in the laminated foraminiferal microfacies samples exhibit a clear evolution with increasing maturity. From the oil window (R_0 0.9%) to the gas window (R_0 1.2%) pores become smaller, more circular and more oriented parallel to the laminae. The interparticle matrix pores continue to play a major role, but the organic matter pores relative increase as a result of gas generation (from an average of 7% to an average of 30%).
3. Pores in samples belonging to the wackestone and limestone lithofacies are almost exclusively interparticle matrix pores, organic matter pores and intraparticle dissolution pores. The pore system is controlled by reprecipitation processes that start in immature ($R_0 \leq 0.4\%$) samples and become significant in the gas maturity window (R_0 1.2%), reducing both total porosity and pore sizes in comparison to the foraminiferal laminated mudstone samples at the same maturities.
4. Pore networks in immature samples of the laminated foraminiferal mudstones and in the wackestone and packstone microfacies are dominated by interconnected pores associated with the rigid carbonate skeleton (interparticle matrix pores).
5. Pore size distribution measurements by means of gas adsorption, MICP and image processing analyses suggest that, in all microfacies, the pore bodies and throats are predominantly within the mesopore range.
6. Pore volume analyses indicate that, although the system is dominated by mesopores, the macropores are the major contributor in the overall pore volumes for all samples at all microfacies. Image processing analyses and gas adsorption data normalised to the total pore volume suggest that, in the gas window maturity

(R_o 1.2%), the organic matter generated pores contribute to the overall pore volumes due to their high surface areas.

7. At gas window maturities (R_o 1.2%), in the laminated foraminiferal mudstone samples, the pore system undergoes a transformation. The organic matter starts to generate gas and spongy organic pores are formed. Petrographic evidence suggest that the whole pore system is affected by an increase in mechanical and chemical compaction and reprecipitation processes, which reduce the interparticle pore bodies and pore throat sizes. The pore network becomes more complex, formed by pore bodies connected through narrow (< 20 nm) pore throats within the OM and the interparticle matrix pores.
8. Samples in all microfacies result connected. However, laminated foraminiferal mudstones exhibit a pore system formed by higher pore volumes and higher connectivity values compared to the wackestones and the packstones.

Chapter 4

AFM study of adhesion forces on calcite surfaces aged in different oil compounds

4.1. Introduction

In tight reservoirs, oil is held in the nano and micropores in the system through strong capillary forces. These strong capillary forces, i.e. the interfacial tensions between the pore surfaces, the brine and the oil, are reflected by the relative wettability. Knowing the wettability and what affects it is essential for hydrocarbon recovery. The recovery is facilitated by the reduction of the capillary pressures, which occurs by the alteration of the interfacial tensions by using specific types of surfactants (or other chemistries) depending on the system (Mirchi et al., 2014). Wettability alteration is also believed to influence reservoir quality by halting diagenesis (van Duin and Larter, 2001; Worden et al., 1998). Therefore, an understanding of the wettability processes is related to both oil recovery and reservoir quality.

4.1.1. Wettability

Wettability is the tendency for a solid to cover itself with a certain fluid in reference than another competing one (Abdallah et al., 2007; Hassenkam et al., 2009). Wetting characteristics are related to interfacial energies. In a reservoir, interfacial tensions occur between the two immiscible liquid phases oil and water and the mineral surfaces. When a rock is water-wet, the interfacial tensions between water and oil are low and the rock surface prefer initially to be in contact with water and oil is the mobile phase. When a rock

is oil-wet, the rock surface is preferably in contact with oil (Abdallah et al., 2007; Anderson, 1986) (Figure 4.1).

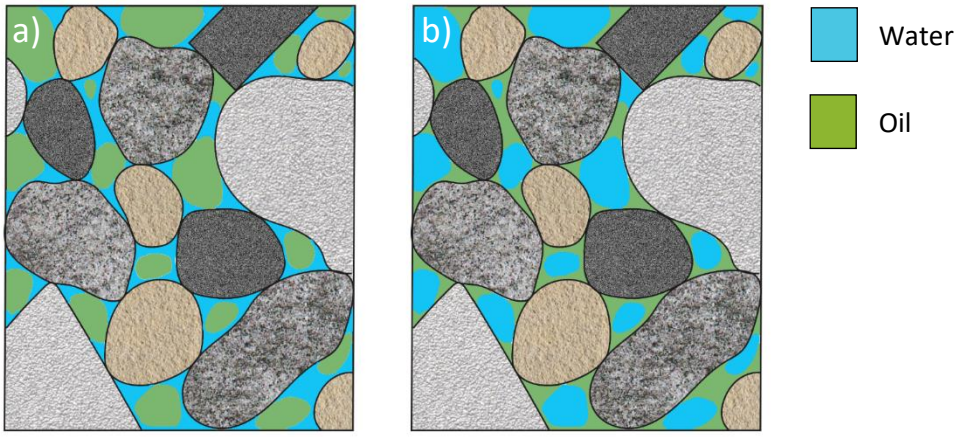

Figure 4.1: Simplified a) water-wet and b) oil-wet system. In a) the water preferentially adheres to the rock surfaces. In b) the oil preferentially adheres to the surfaces.

The measurement of the degree of oil or water wetting is essential during the production and recovery phase. For instance, a reservoir with strongly oil-wet pore surfaces will have lower recovery rates compared to a more water-wet or mixed-wet reservoir. Consequently, studying the wettability at the pore-scale helps to understand the reservoir-scale behaviours and, hence, to improve the reservoir productivity (Abdallah et al., 2007; Anderson, 1986; Mirchi et al., 2014). However, despite reservoirs being often described as either oil-wet or water-wet, the wetting behaviour of a pore system varies, and a reservoir can also present a complex, mixed wettability (Morrow, 1990). The concept of mixed wettability was first suggested by Salathiel (1973), who stated that during oil migration the smaller pores, due to the higher capillary pressures required to enter the small pore spaces, remain water wet, whereas the largest pores are more prone to be oil-wet. Moreover, it has been proved that the wettability can also vary from area to area, within the reservoir, giving rise to the so-called fractional wettability (Brown and Fatt, 1956; Holbrook and Bernard, 1958). Mixed and fractional wettability are thought to originate from an initial water-wet system. The wettability in a reservoir can evolve through time, becoming increasingly more oil-wet when the mineral surfaces are exposed to crude oil during thermal maturation (Buckley et al., 1998). At a fundamental level the wettability is determined by the interaction of Van Der Waals, electrostatic double layer

and steric forces between oil, water, brine and the minerals within the porous system (Hirasaki and Zhang, 2004; Thyne, 2015). As it is not possible to distinguish the three forces, only the net force between the solid-water and the water-oil interfaces, i.e. the disjoining pressure, is considered (Basu and Sharma, 1997; Hirasaki and Zhang, 2004; Shi et al., 2016). Therefore, the disjoining pressure determines the wettability of a reservoir (Basu and Sharma, 1997). When the disjoining pressure is sufficiently high, the water film that is coating the surfaces destabilizes and the low-molecular-weight polar compounds (e.g. phenols and acetic acid) can penetrate these coatings and cause part of the surface to be more oil-wet compared to the rest (Abdallah et al., 2007; Aplin and Larter, 2005; Larter et al., 1997; Larter and Aplin, 1995; van Duin and Larter, 2001).

Wettability can be altered from oil-wet to water-wet in order to improve oil recovery. When the capillary pressure is too low, spontaneous imbibition is not possible. However, by adding surfactants to the brine, spontaneous imbibition takes place displacing the oil in the pores to the surface of the reservoir (Austad et al., 2010, 1997; Ayirala et al., 2006; Standnes and Austad, 2000). The alteration of the wetting state can be done by reducing the overall salinity as well as by adding surfactants to the system (Acevedo et al., 1992; Ahmadi et al., 2018; Alvarez et al., 2014; Andersen et al., 2016; Austad et al., 1997; Ayirala et al., 2006; Bryant et al., 1991; Feng and Xu, 2015; Kumar et al., 2005a; Penny et al., 2012; Standnes and Austad, 2000; Zhang and Somasundaran, 2006). In this way, the recovery of the oil is eased and enhanced (i.e. enhanced oil recovery, EOR methods) (Tang and Morrow, 1999).

4.1.2. Surface charges

The alteration of the wettability state in the reservoir is possible because the interactions between a mineral surface and the oil's molecules depend on the electric potential and charge distribution. When the force is overall attractive, the polar functional group from the oil will cause rupture of the water layer on the mineral surface and adhere to the charged mineral surface (Salathiel, 1973; Yang et al., 2002). When the double layer force is repulsive, the layer remains stable (Yang et al., 2002). For this reason, the electrical charges on the surfaces are in many studies (Al Mahrouqi et al., 2017; Alvarez and Schechter, 2016; Kasha et al., 2015; Purswani et al., 2017; Sanaei et al., 2019; Zhang et al.,

2007) characterised by means of zeta potential calculations. From these studies, it emerges that the original calcite surface, being under-bond saturated, presents an overall positive charge and that the partially positive charge acts as an anchor point for the negatively charged species present in the oil. The oil molecules that are found to have more affinity to the calcite surfaces are negatively charged polar oil particles (Buckley et al., 1998; Karimi et al., 2015; Morrow and Mason, 2001). Nevertheless, the total surface charge of calcite has been reported to be a function of a series of factors, including the pH, the temperature and the type of fluid the surface enters in contact with (Borysenko, Polson, Arif, Anderson, 1986). Initial low pH conditions affect the calcite surface charge and increase the oil-wettability (Aksulu et al., 2012; Awolayo et al., 2018; Burgos et al., 2002), and temperatures higher than 100°C increase the diffusion rate and, in terms of oil recovery, the sweep efficiency (Austad et al., 1997; Standnes and Austad, 2000). The ions present in the brine are also able to affect the wettability by interacting with the ions complexating the calcite surface (Austad et al., 1997; Sakuma et al., 2014).

4.1.3. Previous studies on chemical interactions on calcite surfaces

Several authors have studied the chemical interactions of oil with carbonate surfaces by means of molecular dynamics simulation techniques (Chen et al., 2019; Prabhakar and Melnik, 2017; Sakuma et al., 2014; Sedghi et al., 2016; van Duin and Larter, 2001; Xin et al., 2019; Yu et al., 2009) and laboratory experiments such as contact angle measurement (Abdallah and Gmira, 2014; Hansen et al., 2000; Hirasaki and Zhang, 2004; Karoussi and Hamouda, 2008; McCaffery and Mungan, 1970; Xin et al., 2019), imbibition (Hirasaki and Zhang, 2004; Kumar et al., 2005b; Standnes and Austad, 2000), ESEM (Al Mahri et al., 2017) or AFM (Abdallah and Gmira, 2014; Basu and Sharma, 1997; Hassenkam et al., 2009; Karoussi et al., 2008; Karoussi and Hamouda, 2008; Seiedi et al., 2010; Skovbjerg et al., 2012). Buckley et al. (2003) list the advantages and disadvantages of each technique, concluding that the AFM is the best method to obtain information on organic material present on the surfaces and on its location and coverage on the mineral surface. At the same time, the AFM is also capable of measuring the wettability of the mineral surfaces at the nanoscale. This can be done by means of the measurement of adhesion forces between specific functional groups (molecules) and mineral surfaces. To measure the

adhesion forces, the AFM tip must be functionalised with a monolayer of the chemical group that is desired to be measured, in this case, the technique is referred as chemical force microscopy (CFM) (Noy et al., 1997). In the particular case of petroleum science, the most commonly used functional groups are -CH_3 and -COO(H), as methyl and carboxyl are commonly present in oil and are therefore representative of oil-mineral surfaces interactions (Hassenkam et al., 2015; Hilner et al., 2015; Sand et al., 2017).

4.1.4. Chemical Force Microscopy (CFM) on calcite surfaces

In these works, the CFM method with a -CH_3 functionalised tip was used. The non-polar tip can be used as a proxy of an oil molecule to determine the wettability of a surface by measuring its adhesion to a mineral surface. In the same way, it can also be used to study the wettability of oil-aged surfaces. This helps to understand adhesion changes on calcite surfaces exposed to different fluids and oil fractions. The calcite surfaces are intended to reproduce the pore surfaces of a carbonate-rich reservoir. As the wettability depends on many parameters, in this study only the type of oil in which the samples were aged was changed. To reproduce a carbonate-rich reservoir, freshly cleaved calcite crystals were first aged at a set temperature in a calcite-saturated brine (70 °C), and then in compounds with progressively increasing molecular weights (dodecane, decanoic acid in dodecane 0.1 M, decanoic acid in dodecane 1M, maltene C_5, maltene C_8, asphaltene, crude oil. This study, apart from providing insights on how the pore surfaces of a carbonate reservoir behave when in contact with different fluids, also sheds light on which oil fractions have greater effects on the wettability changes on calcite surfaces.

Over the years, several studies using different techniques have shown that crude oil alters the wettability of mineral surfaces, mainly due to the sorption of asphaltenes and resin fractions (Anderson, 1986; Buckley and Recovery, 1995; Drummond and Israelachvili, 2002; Ese et al., 2000; Karimi et al., 2015; Kumar et al., 2005a; Morrow, 1990; H Toulhoat et al., 1994; Vargas and Tavakkoli, 2018). Aged mineral particles have also been examined using AFM to confirm the precipitation of oil fractions on the surface (Abdallah et al., 2007; Basu and Sharma, 1997; Buckley and Lord, 2003; Karoussi et al., 2008; Kumar et al., 2005a). In addition, authors have reported on the use of CFM to investigate the wettability alteration of calcite (Chandrasekhar and Mohanty, 2018; Rezaei and Firoozabadi, 2014;

Standnes and Austad, 2003) or chalk particles (Hassenkam et al., 2015, 2009; Henriksen et al., 2004; Hirasaki and Zhang, 2004; Hopkins et al., 2017; Skovbjerg et al., 2013).

However, most CFM studies on calcite and chalk have aimed to investigate the most efficient recovery methods and not the differences in adhesion forces resulting from the interaction of different oils and oil fractions. Hassenkam et al. (2009), instead, investigated non-treated chalk surfaces and concluded that the mixed wettability residing in chalk reservoirs derives from the inherent heterogeneity of the chalk surfaces, and not from the migrating oil in the pore system. Skovbjerg et al. (2013) suggested, in contrast, that the differences in wettability were caused by nanometric clay laths attached to the coccoliths forming the chalk. A more similar working procedure to the one applied in this work was performed by Kumar et al. (2005). In their experiments, Kumar et al. (2005) investigated the effects of different Saturates-Aromatics-Resins-Asphaltenes (SARA) fractions on mica and silicon surfaces by ageing the crystals first in brine and then in oil. In their work, the measurements were performed using the standard contact angle procedure (Washburn, 1921) and AFM was only used as an imaging and adhesion measurement tool by means of a functionalised carboxyl tip. Contrarily to this work, the force measurements were conducted on single point locations and not on whole regions (mapping).

To validate the analyses and prove that the change in adhesion forces are caused by the different materials on the surface, the AFM-IR methodology was used. Since its development, the AFM-IR has been widely used in biological and polymer studies (Dazzi et al., 2012; Dazzi and Prater, 2017). From a geochemical point of view, however, this technique has for now only been applied to study the different organic matter types on shale rocks (Eoghan et al., 2016; Jakob et al., 2019; Yang et al., 2017).

The combination of CFM and AFM-IR studies offers a robust analysis at the nanometer scale of the wettability distribution, and its variation, on calcite surfaces exposed to fluids with different molecular weights. From a geological point of view, understanding the calcite surface behaviour when in contact with different fluids is crucial for the effective oil recovery from carbonate reservoirs as well as for CO_2 sequestration studies (Sand et al., 2008).

4.2. Methodology

4.2.1. Samples

d) All the surfaces examined were of samples prepared from Iceland Spar calcite crystals. To avoid contamination, all crystals (~4 × 5 × 1 mm) were freshly cleaved and immediately immersed in ageing solutions. The surface studied in all cases was the $\{10\bar{1}4\}$ calcite cleavage planes.

4.2.2. Brine

The brine used for the experiments was produced following the composition of an existing Gulf of Mexico seawater. The starting solution was a Milli-Q water, in which constituents were dissolved by calculating the molar fractions of each compound. The concentrations of the dissolved constituents are listed in Table 4.1. Calcite crystals were added to the brine to ensure the solution was carbonate saturated.

Brine constituents	**mg/L**
Na	29500
K	144
Mg	620
Ca	2080
Cl	48250
SiO_2	51
SO_4	21

Table 4.1: List and quantity of dissolved constituents in the artificially created brine. The starting liquid was distilled water. The grams to add to the distilled water were calculated taking into account the molar weight of each compound.

4.2.3. Oil compounds

The oil-based compounds used for this study were: dodecane, 0.1 M decanoic acid dissolved in dodecane, 1 M decanoic acid dissolved in dodecane, maltene C_5, maltene C_8, asphaltene and oil. The maltene C_5 and C_8 differ for the *n*-alkane (*n*-C_5 and *n*-C_8) used in the separation.

For the model oil solutions, a *n*-dodecane, 99% Fisher Scientific pure was used. The decanoic acid solutions were made by adding 0.1 M and 1.0 M 99% pure decanoic acid to the *n*-dodecane. The crude oil chosen for the analyses is a standard oil RM8505 acquired from the National Institute of Standards and Technology (NIST). The maltene C_5, maltene C_8 and asphaltene fractions were extracted from the crude oil by *n*-heptane addition (Liu, 2017). As the extracted oil fractions were solid, to maintain the sample in solution, toluene was added to the fractions in a 5 mg to 1 ml proportion.

4.2.4. Ageing procedure

To reproduce reservoir conditions, the cleaved samples were aged in brine for one month at 70° C. The pH of the brine was measured using a pH meter and probe (pH 7.3). In order to avoid the precipitation of salts on the crystal's surface during the ageing phase, the brine was calcite-saturated and no extra HCO_3 was added. The samples were then removed from the brine and placed in the different oil compounds for another month at 70° C. Prior to the AFM analysis, the samples were extracted from the oil solutions and washed in brine. Care was taken not to dry the surfaces, as this has been shown to induce organic precipitation (Kumar 2005). The calcite crystals were then glued on a glass surface using epoxy glue and were placed in a fluid cell. The fluid cell was created by placing an O-ring (polypropylene) around the crystal. The fluid cell was then filled with the brine solution to maintain equilibrium conditions inside the cell during imaging. To test the wettability variation on an initially oil-wet surface, analysis of calcite surfaces directly exposed to dodecane with no brine ageing were also carried out.

4.2.5. AFM tip functionalisation procedure

Gold coated (PNP-Tr-Au) AFM probes from Nanoworld (spring constant 0.08 N/m) were bought. For this type, the gold coating included both the backside of the cantilever and the probe itself, to facilitate the functionalisation. The functionalisation was performed using thiol-chemistry, in a procedure very similar to that described by Skovbjerg et al. (2012) and Hassenkam et al. (2016). The gold tips were first exposed to ozone in a UV/ozone cleaner (Love et al., 2005) for 10 minutes to remove any possible organic contaminants. Then, they were immediately submerged in ethanol for 10 minutes. The tips were then introduced in an ethanol solution of 0.05 mM of $HS(CH_2)_{10}CH_3$ (obtained from Sigma-Aldrich) for at least 24 hours. Before use, the tips were washed in ethanol and mounted on the AFM cantilever holder. Because of the strong reaction between the thiol group (HS) in the molecule and the gold coating the probe, this procedure results in AFM tips functionalised with CH_3 non-polar functional group molecules that can then interact with the sample's surface (**Error! Reference source not found.**).

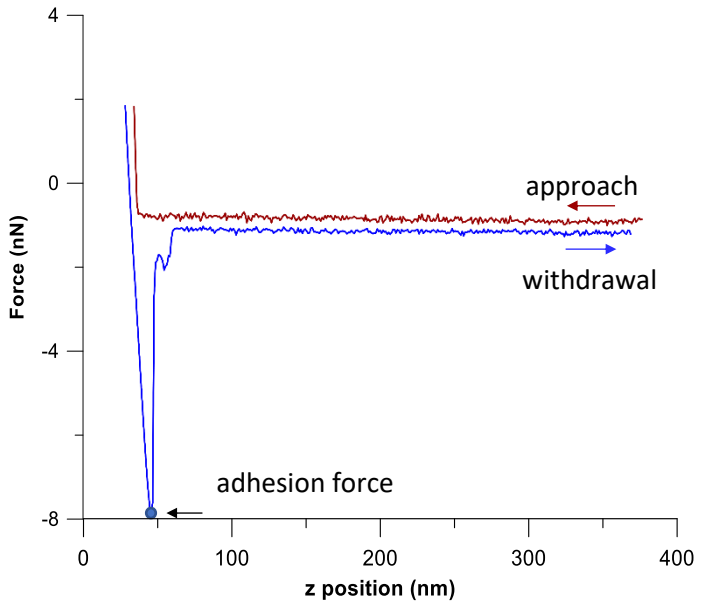

Figure 4.2: Typical force-distance curve resulting from the functionalised –CH3 tip approaching the surface (red) and then retracting (blue). The force of adhesion is calculated by analysing the minimum distance between the equilibrium position and the maximum deflection during retraction (in this case 6.9 nN). The force-distance curve was extracted from a map of a surface of a calcite crystal aged in asphaltene.

4.2.6. CFM setup

For the CFM analyses, a Nanowizard 3 AFM (JPK Instruments) was used. The data were collected on by theJPK instruments software and then converted to an ASCII file to be processed in Matlab. All the experiments were carried out at standard conditions (20^0 C and 1 atm). The AFM adhesion maps were collected in force mapping mode in at least 5 randomly chosen areas on the crystal surfaces of 30 x 30 μm^2 in size and a resolution of 25 x 25 pixels. This mode allows the cantilever to create, at each pixel point, a so-called force-distance curve (Figure 4.2). These curves represent the measured force (between sample and probe) as a function of the distance between the tip and the sample surface. These curves enable calculation of adhesion forces and to infer the mechanical properties of the sample in the measured location (Cappella and Dietler, 1999). The force of adhesion is defined as the force needed to disengage the tip from the surface during retraction (Hassenkam et al. 2009) and is calculated by analysing the minimum distance between the equilibrium position and the maximum deflection during retraction (Figure 4.2).

For the adhesion force measurements, the approach speed (of the probe against the sample) was kept at 10 μm/s, after contact a dwell time of 1 second was applied, before retracting the probe, to allow for the "formation" of bonds and therefore to obtain a consistent adhesion measurement. Retraction rate was also of 10 μm/s. Approach and retract speed were kept constant through all measurements, as this parameter has been shown to influence the measured adhesion (Cappella and Dietler, 1999; Kumar et al., 2005a). A tip-sample travel distance, *z*, of 0.7 μm was kept for all the experiments. The total force (or setpoint) used during the scans, was of 0.7 N) Maps of various area sizes at 128 x 128 or 256 x 256 pixels were also collected using the same speed and delay settings. However, these maps were only used for imaging purposes, as small pixel sizes cannot be representative of the adhesion forces of the area, as they may be smaller than the actual tip radius. (Tao and Bhushan, 2006).

To verify that the topographic heights on the surfaces were oil droplets, measurements using the quantitative imaging (QI) mode were also performed on the samples aged in the different oil compounds. The QI mode is similar to force volume mode but it can be performed at much faster scanning speeds, therefore reducing the time needed to perform

the imaging, and allowing for higher resolution scans. (Chopinet et al., 2013). For reproducibility reasons, at least two calcite crystals were aged for each experiment and the data collection was repeated in all the samples following the same procedure. A minimum of 10 areas 30 × 30 μm were mapped for the calcite aged only in brine and in each oil compound. whole duration of the experiment the tip was kept wet. Excess oil on the surface was removed by thoroughly washing the surface with brine using a syringe.

4.2.7. AFM data processing

The data were collected using the JPK software tool. To compute an automated analysis and to extract the adhesion forces and topography parameters, the raw data were extracted and processed using Python and Matlab. Topography and adhesion maps were plotted and tables with topography and adhesion forces parameters were created. The maximum value for the adhesion forces was set to 9 nN. Higher values imply that the cantilever remains attached to the surface, without registering the real adhesion force. Looking at the different force curves, 9 nN is established as the maximum upper value and a good threshold between the real and the fictitious values.

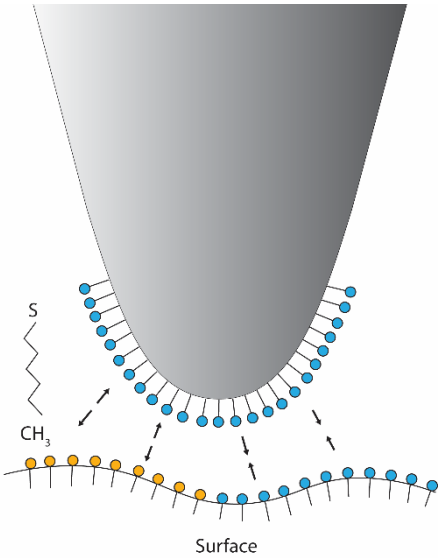

Figure 4.3: Schematic representation of gold tip functionalised using a $HS(CH_2)10CH_3$ thiol solution. The $-CH_3$ polar groups at the end of the molecule are hydrophobic (blue) and able to bond with polar hydrophobic molecules present on the surface (yellow), whereas repulsive forces occur between the $-CH_3$ groups and the hydrophilic molecules on the surface.

The agreement between topography and adhesion force maps can be visualised by correlating the topography and the adhesion cross plots of the same region and by creating linear regression models between the topography and adhesion force pixel values (Figure 4.4).

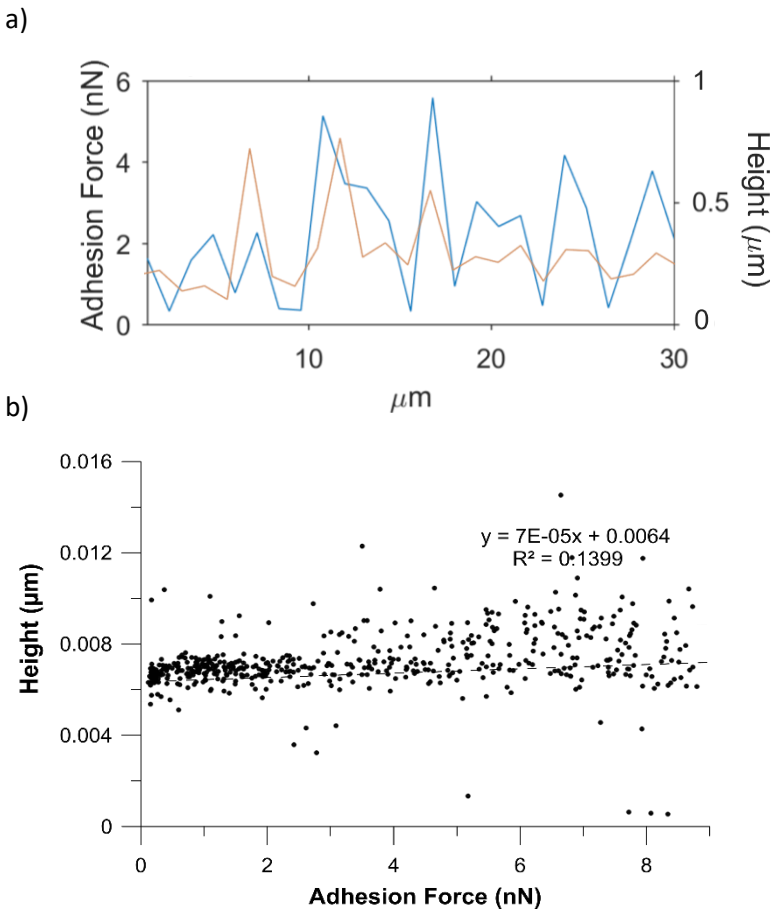

Figure 4.4: a) Example of cross correlation between a topography (blue) and an adhesion plot (red) and b) linear regression plot for the same area (area 2 of sample n. 1 aged in dodecane).

4.2.8. Infrared spectroscopy (IR spectroscopy)

IR spectroscopy is a technique used to give information on the vibrational bands present in a chemical compound (El-Saleh, 1996). IR spectroscopy involves the use of infrared radiation on a material. When the IR laser interacts with the material, the photons are absorbed by molecules within the material, which then vibrate. Molecules can have different degrees of vibrational modes, meaning that every molecule can vibrate in different ways. The vibrational modes correspond to particular bond types, which are

associated with specific energies and therefore frequency of the vibrations. The combination of the vibration types at specific frequencies creates a specific fingerprint for each measured compound. The possible vibrational modes are represented in Figure 4.5. The fingerprint is a function of the frequency (or wavelength) of the light absorbed. The most studied infrared region is between 4000 cm^{-1} and 400 cm^{-1}, as most of the vibrational frequencies are in that range. However, the absorption of the electromagnetic IR radiation only occurs when the molecule presents a dipole moment, i.e. areas of partially positive and negative charge (Fifield and Kealey, 1991; Harvey, 2000; Pavia et al., 2009; Smith, 2011). In Fourier-Transform Infrared (FT-IR) analyses, after the IR source has hit the sample and excited the molecules, the vibrations will be detected in forms of frequencies by means of a photoconductive detector. The AFM-IR methodology utilises the same IR principles, but the setting and sensitivity of the instrument differ from the original FT-IR.

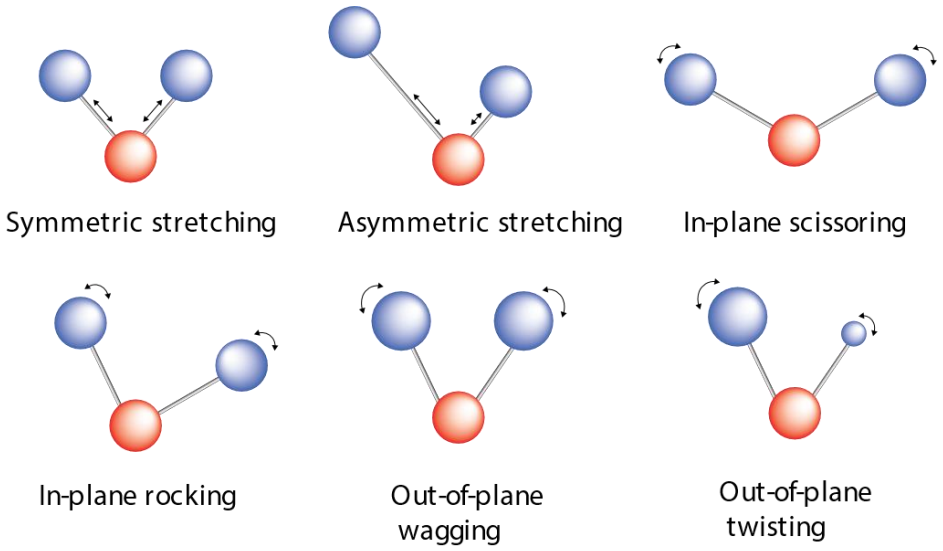

Figure 4.5: Possible vibrational modes identified with the IR spectroscopy.

4.2.9. AFM-IR

AFM-IR is an analytical technique that combines the nanoscale resolution of the AFM and the chemical analysis of IR spectroscopy. By employing the AFM tip as an IR detector, the AFM-IR can be applied to detect the chemical molecules present on the surface at a spatial resolution below 50 nm, in contrast to the ~2 μm of the FT-IR technique (Dazzi et al., 2012).

The configuration of the instrument is represented in Figure 4.6 and consists of a classic AFM setting, to which a tunable IR source is added.

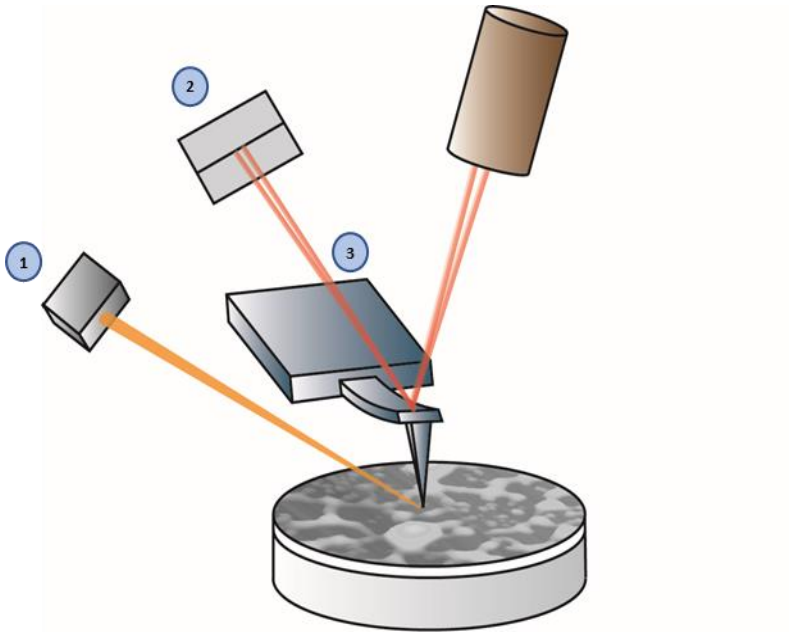

Figure 4.6: Schematic representation of an AFM-IR configuration. The IR laser (1) intersects the tip of the AFM (2) and, when the molecules on the surface are excited, produces contact resonant frequencies, which are tracked by the detector (3) and converted into specific wavenumbers.

The detection of chemical molecules on the surface is achieved by pointing the IR laser to the tip of the AFM. Once the IR laser is tuned into a wavelength the sample absorbs, the molecules on the surface will be excited and absorb light. In turns, the absorbed light converts into heat which causes thermal expansion. The thermal expansion excites the oscillations of the AFM probe, which are detected in the form of contact resonant frequencies. The frequency of the vibrations can be associated with a molecular bond type. Therefore, by measuring the responses of the AFM cantilever tip to the IR absorption, it is possible to create an IR spectrum, which is characteristic of a certain compound. The measurements can be done on single points of the surface, or also by tuning the laser to a fixed wavelength and creating a chemical map to detect the distribution of chemical species over a region on the sample surface (Bondy et al., 2017; Dazzi et al., 2012; Eoghan et al., 2016). For reproducibility reasons, at least 5 point-IR spectra were collected in each area.

4.2.10. AFM -IR experiments setup

A nanoIR2 and a nano IR3 system (Anasys Instruments, Santa Barbara, CA) were used to test the presence of chemical components on the calcite surfaces. The results from the two versions of the instrument are comparable, as the instruments operate in the same way. For the analyses, two IR tunable laser sources with different wavelength ranges were chosen. For the 2700-4000 cm^{-1} wavenumber range (high-range), a Fastspectra OPO laser was used and for wavenumbers comprised between 900 and 1900 cm^{-1} (mid-range), a PointSpectra QCL laser was used.

To calibrate the instrument and test the working method, a pmma (polymethyl methacrylate) test sample was first used. After the collection of the background spectra, the IR laser was tuned in four different spectra ranges between 900 and 1900 cm^{-1}, and in one spectrum range for wavelengths between 2700 and 4000 cm^{-1}. This provides more accurate results. As the IR sources are different, the data with the two lasers must be acquired at separate moments. The background spectra collection and the frequency tuning was performed before examining every sample. All the IR spectra were smoothed in the Anasys instruments software Analysis studio and the two laser spectra were plotted in the same diagram, normalising the frequency to the corresponding incident power. The acquisition interval is 4 cm^{-1} for the mid-range wavelength interval and 10 cm^{-1} for the high-range. For the chemical mapping of one area at a specific frequency, the 1630 cm^{-1} and the 2920 cm^{-1} wavelengths were chosen. These wavelengths correspond to the C=C aromatic vibration and to the CH_2 aliphatic stretching respectively. These absorbance bands were chosen as they are commonly found in organic compounds. The mapped areas were selected randomly on the calcite surfaces. For each sample, one area of 20 × 20 μm and one area of 2 × 2 μm were mapped. The point laser measurements were taken 5 times in different points of the surface in order to assure the repeatability of the measurement. A gold-contact mode tip was used. The metal coating allows the generation of an electric field on the tip, which intensifies the incident radiation (Dazzi and Prater, 2017).

4.3. Results

4.3.1. Topography and adhesion forces

Topography and adhesion force maps were plotted for each scanned area. For each scan, the maximum, minimum and average values were also calculated. For the adhesion plots, the average values, the area percentage covered by adhesion forces higher than 0.5 nN, 1 nN, 2 nN, 3 nN and 4 nN value of the average of the adhesion forces and of the forces higher than 0.5 nN, 1 nN, 2 nN, 3 nN and 4 nN was also calculated and plotted (Figure 4.7 and Table A.1).

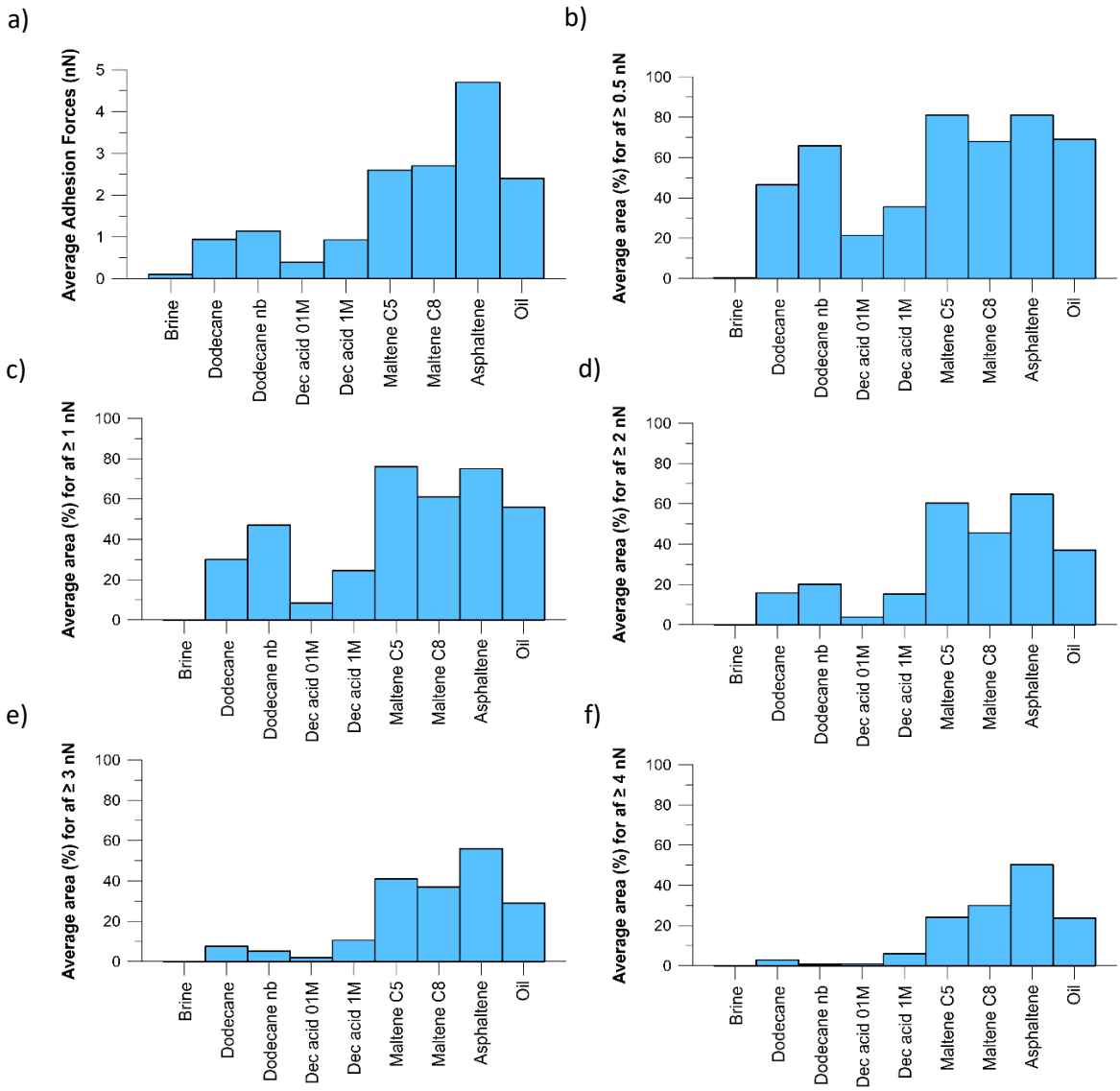

Figure 4.7: Average plots of a) average of adhesion forces (nN) in each area for the different aging experiments and percentages for the average areas covered by adhesion forces (af) higher than b) 0.5 nN, c) 1 nN, d) 2 nN, e) 3nN and f) 4 nN.

Two areas of 30 × 30 μm² each were used to underline any correlation between the topography and the adhesion forces in the oil compounds. The R^2 values for this correlation are plotted in Table 4.2.

Oil compound	**R^2 Linear Regression (area 1)**	**R^2 Linear Regression (area 2)**
Dodecane	0.079	0.1399
Decanoic Acid 0.1 M	0.4589	0.3827
Decanoic Acid 1 M	0.3746	0.2598
Maltene C5	0.0368	0.0207
Maltene C8	0.2015	0.0104
Asphaltene	0.0008	0.2804
Crude Oil	0.0129	0.1487

Table 4.2: R-squared (R^2) calculated for two areas from linear regression plots for each oil compound. The linear regression plots were made by plotting the topography values against the corresponding adhesion force values. A discrete agreement between the topography and the adhesion forces is noticed mainly in the model oil compound experiments.

4.3.1.1. Calcite in brine

a) Topography

High resolution (64 × 64 pixels to 128 × 128 pixels) maps at a scale of 10 × 10 μm² or 5 × 5 μm were used to analyse the topography. Topography maps indicate the surfaces aged in brine presents several randomly located asperity peaks of variable dimensions. The peaks are caused by semi-circular shaped asperities on the surfaces (Figure 4.8 a). On the images analysed, they reach 350 nm in height and measure up to 2.5 μm in diameter but are typically less than 100 nm high and have diameters between 20 and 50 nm.

No specific patterns on the surfaces are noticed. In some cases, it is possible to see calcite cleavage steps (Figure 4.8 b) which typically measure 100 – 300 nm in height drop.

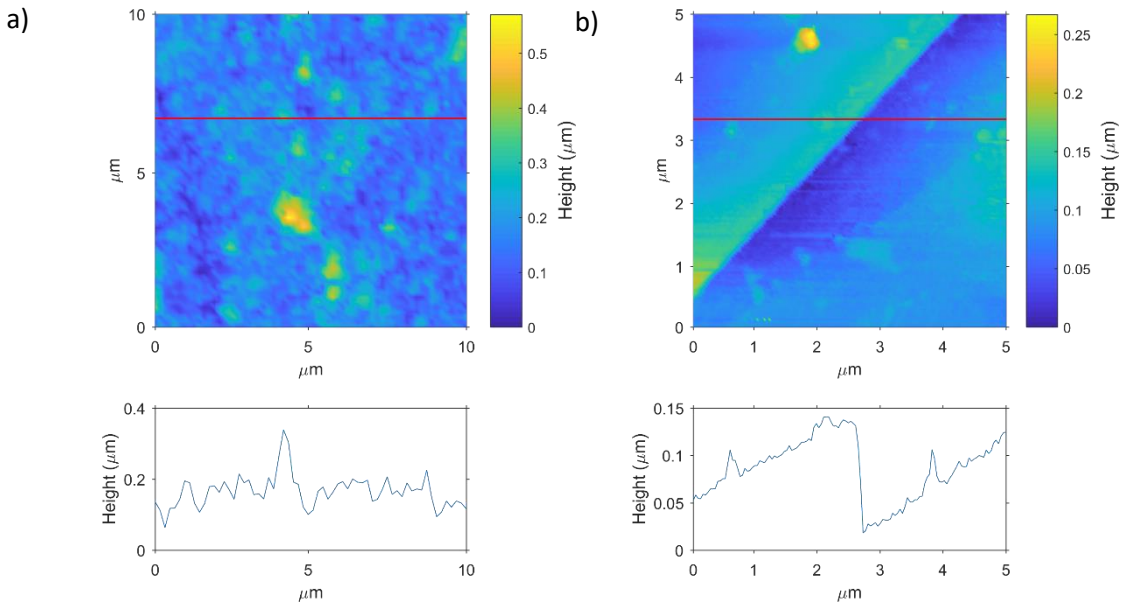

Figure 4.8: 128 x 128 pixels topography maps of a calcite surface aged in brine. a) area of surface roughness. The highest peak in this area measures 480 nm and the average topography is 165 nm. In b) a calcite step measuring 136 nm is present. The surface in this area appears smoother than in region a).

b) Adhesion forces

Adhesion forces vary from 11 pN to a maximum of 673 pN. In the 30 × 30 μm² regions, the adhesion forces vary from 20 nN to 470 pN (Figure 4.9). The area percentage covered by adhesion forces higher than 500 pN reaches a maximum of 3.7% and is less than 1% for 13 of the 15 areas analysed. In all the samples, no adhesion forces ≥1 nN were measured (Figure 4.7). The cross-sections at the same scan lines in the height maps and in the adhesion forces maps do not show any clear correlation between height and adhesion values, suggesting that the particles/droplets on the surfaces are not responsible for an adhesion increase.

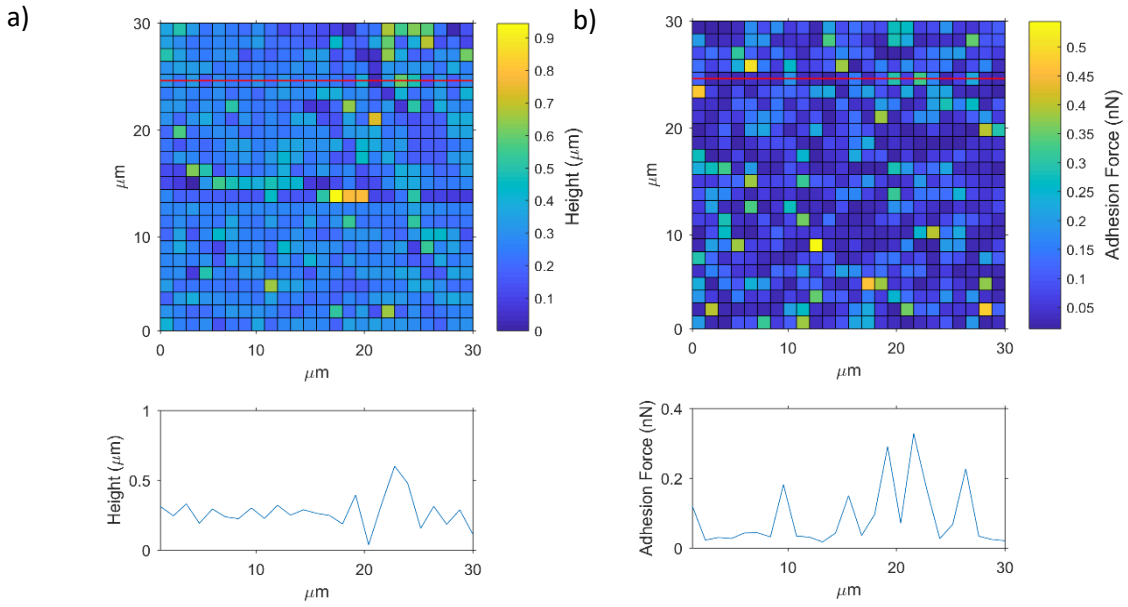

Figure 4.9: a) Topography and b) corresponding adhesion map of area 04 on calcite surfaces aged in brine. At the bottom of each map, the cross-section profile taken across the red line in the maps.

4.3.1.2. Calcite in dodecane

a) Topography

For the samples aged in dodecane, a maximum height difference of 722 nm was measured between two cleavage steps (Figure 12 a). Higher topography points corresponding to 1-3 pixels on the 25 × 25 pixels areas are randomly distributed on the surfaces. Mapped areas of 2 × 2 μm² show semi-circular topography highs of 180 to 230 nm (Figure 4.10).

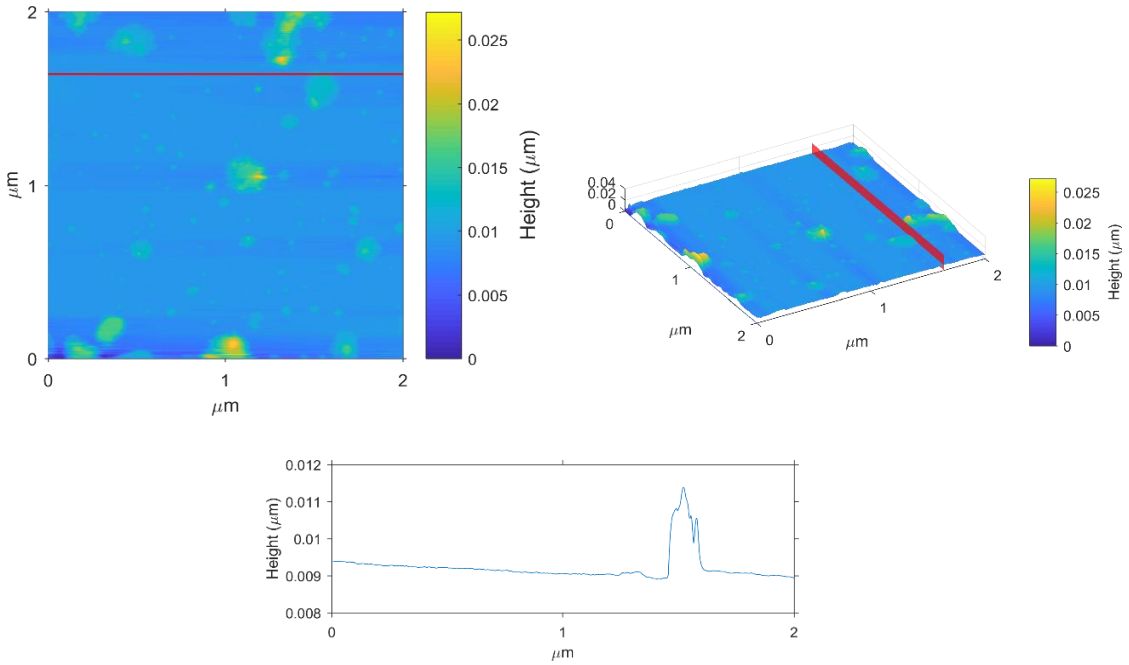

Figure 4.10: Topography in 2D nd 3D of an area of a calcite surface aged in dodecane.

b) Adhesion forces

Adhesion forces on calcite surfaces aged in dodecane vary from 0.1 nN to 9 nN. Average values of the adhesion forces calculated for each pixel point in each 30 × 30 μm² map vary between 160 pN to 2 nN. The area percentage covered by adhesion forces higher than 500 pN varies from 9.2% to 84.8%, with an average of 44.5%.

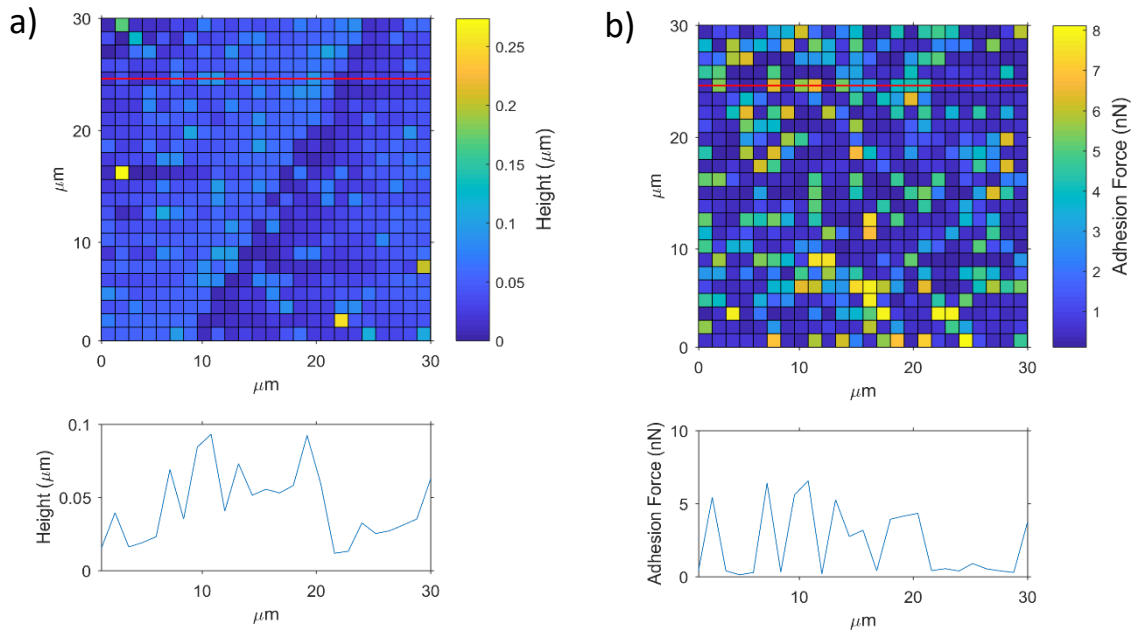

Figure 4.11: a) Topography and b) corresponding adhesion map of area 01 on calcite surfaces aged in dodecane. At the bottom of each map, the cross-section profile taken across the red line in the maps.

Areas covered by adhesion forces higher than 1 nN vary from 2.3% to 62% with an average of 30.2%, whereas percentages of areas of 30 × 30 μm² that present adhesion forces higher than 2 nN range between 0 and 47 %. For adhesion forces higher than 3 nN the maximum surface coverage is 27%, whereas adhesion forces higher than 4 nN cover up to 19.4% of a 30 × 30 μm² area, with an average of 3% of coverage (Figure 4.7).

In most cases, adhesion highs show discrete agreements with the topography highs (Figure 4.12), but the R^2 values (Table 4.2) indicate that the correlation is limited to some areas.

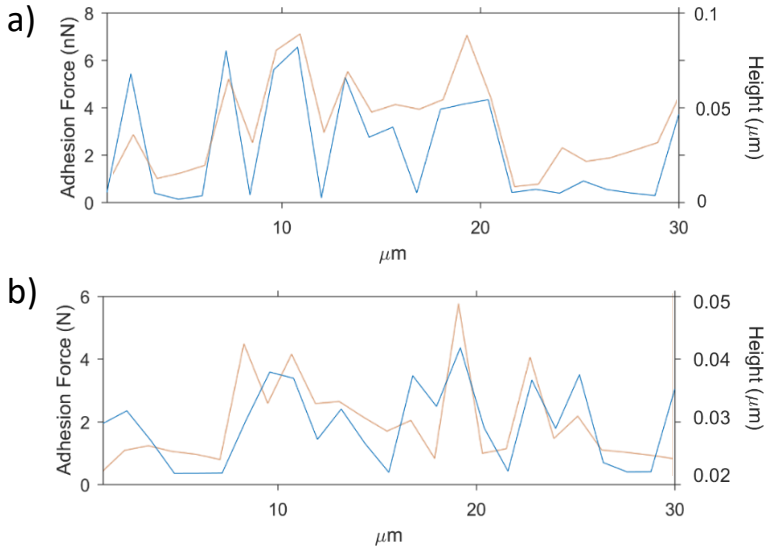

Figure 4.12: Overlapped cross-plots of the same points in a) area 01 and b) area 04 of the surface of calcite aged in brine and in dodecane. The topography (red) and the adhesion forces (blue) lines show a moderate correlation.

4.3.1.3. Dodecane with decanoic acid 01M

a) Topography

In the calcite surfaces aged in decanoic acid, 0.1 M, the highest topographic feature measured is 212 nm. In this case, surface features resembling droplets were clearly identified on the topographic scans. Therefore, the reported surface roughness is a combination of the actual topography of the calcite surface as well as by the particles and droplets deposited on its surface. The particle sizes are clear on the 128 × 128 pixel size maps, which show the random distribution of the droplets. At increasing magnifications, in 5 × 5 μm² or smaller areas, in some cases a "ramification" of ~ 20-30 nm high droplets on the surface can be seen (Figure 4.13).

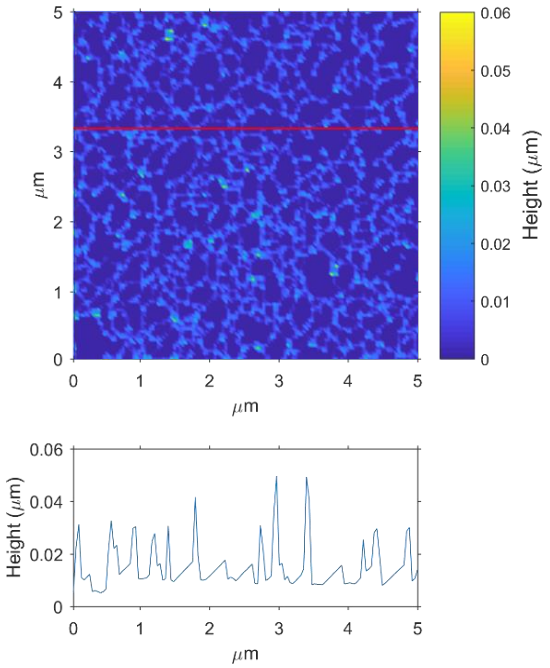

Figure 4.13: 5 x 5 μm wide topography map of a calcite surface aged in a decanoic acid solution 0.1 M. The droplets on the surface show ramifications and are on average 20 nm high.

b) Adhesion forces

Adhesion forces show a minimum of 7 pN and a maximum of 9 nN, with an average adhesion force of 410 pN in the 30 × 30 μm areas. The percentage of adhesion forces ≥ 0.5 nN for 30 × 30 μm² areas varies from 9.5% to 38.3%.

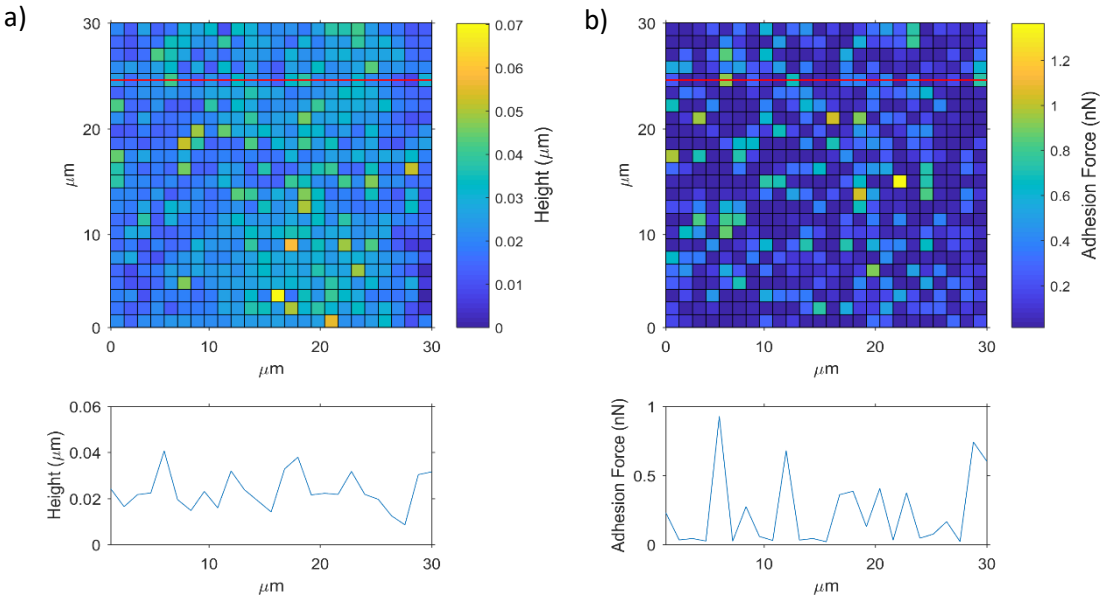

Figure 4.14: a) Topography and b) corresponding adhesion map of area 02 on calcite surfaces aged in brine and in decanoic acid 0.1 M. At the bottom of each map, the cross-section profile taken across the red line in the maps.

For adhesion forces ≥1 nN, the surface percentages drop to a minimum of 0.2% to a maximum of 29.7%, whereas adhesion forces ≥2 nN cover up to 13.3% of the measured areas. Adhesion forces higher than 3 nN and 4 nN cover a maximum of 7.7 and 4.8%, with an average of 2.4 and 1.1% respectively. By the overlapped cross-plots and the R^2 values (Table 4.2), a good agreement between the topography and the adhesion forces is observed (Figure 4.15).

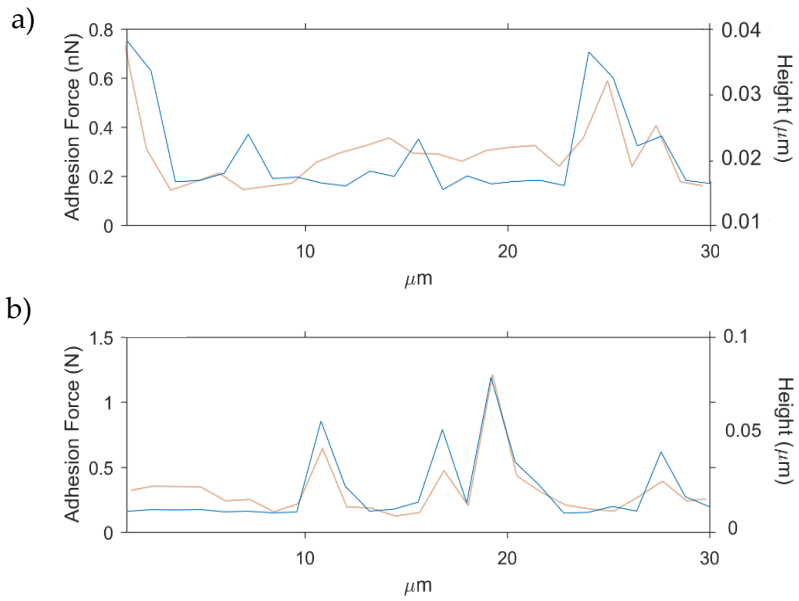

Figure 4.15: Overlapped crossplots of the same points in a) area 01 and b) area 05 of the surface of calcite aged in brine and in decanoic acid 0.1 M. The topography (red) and the adhesion forces (blue) lines show a moderate correlation

4.3.1.4. Dodecane with decanoic acid 1M

a) Topography

The peak to valley roughness in the topographic scans is 811 nm. Cleavage steps of variable height drops (~40 to ~600 nm) are present in the analysed areas. Topography highs are also formed by particles or droplets deposited on the surfaces. High resolution (128 × 128 nm^2) maps show particles-droplets of several micrometres on the surfaces as well as nanometer-sized particles-droplets. The distribution of the particle-droplets is random, both in a single region and between different regions (Figure 4.16).

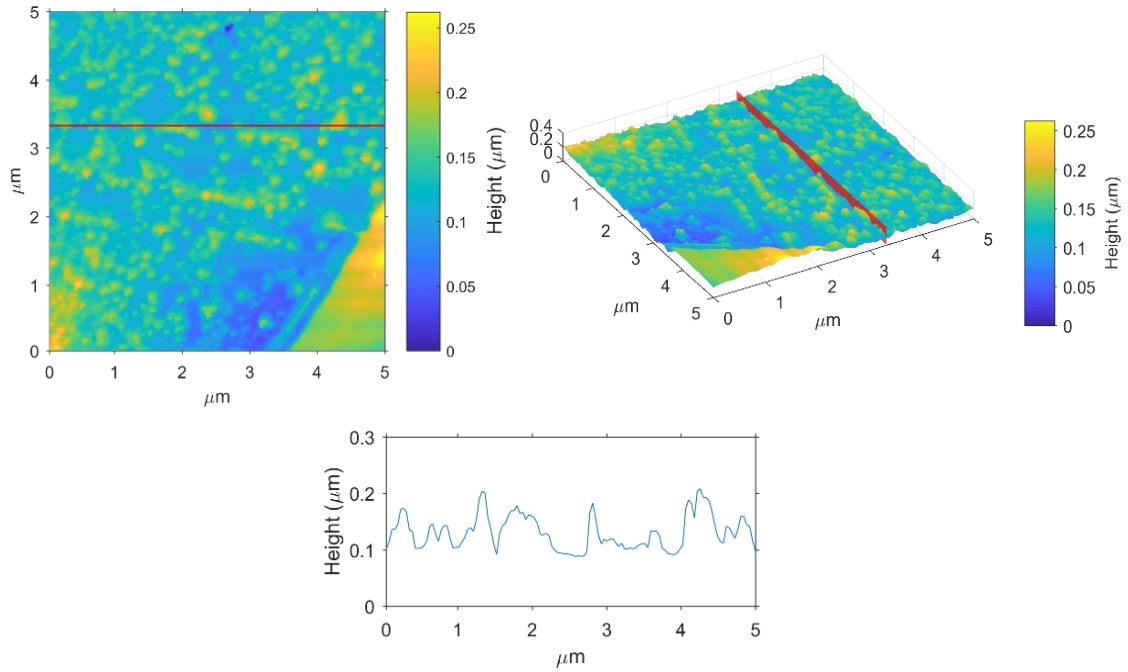

Figure 4.16: 5 x 5 μm² area of a calcite surface aged in a decanoic acid solution 1 M. In this area, the droplets on the surface are up to 200 nm high.

b) Adhesion forces values

Adhesion forces range from a minimum of 0 to a maximum of 9 nN, with an average of 1.1 nN. The average values range between 29 pN and 6.4 nN. The calculated percentage of the area in which the adhesion force is equal or higher than 0.5 nN and 1 nN is comprised between 0 and 99.6% and 0 and 98.3% respectively. When the adhesion forces are ≥ 4 nN the percentage of the area covered by these adhesion forces ranges between 0 and 81.4%. The average forces are 35.5% of the total 30 x 30 μm measured areas when ≥ 0.5 nN, 24.3% when ≥ 1 nN, 15.3% when ≥ 2 nN, 10.6% when ≥ 3 nN and 6.1% when ≥ 4 nN. There is a moderate match between the calcite surface topography and the adhesion forces (Figure 4.17 and Table 4.2). The cleavage steps act as entrapments for the dodecane and decanoic acid solution, making the distribution of the droplets on the surface non-ununiform. high adhesion forces are mainly present along the cleavage steps as well as associated with the irregularly shaped droplets randomly distributed on the surfaces.

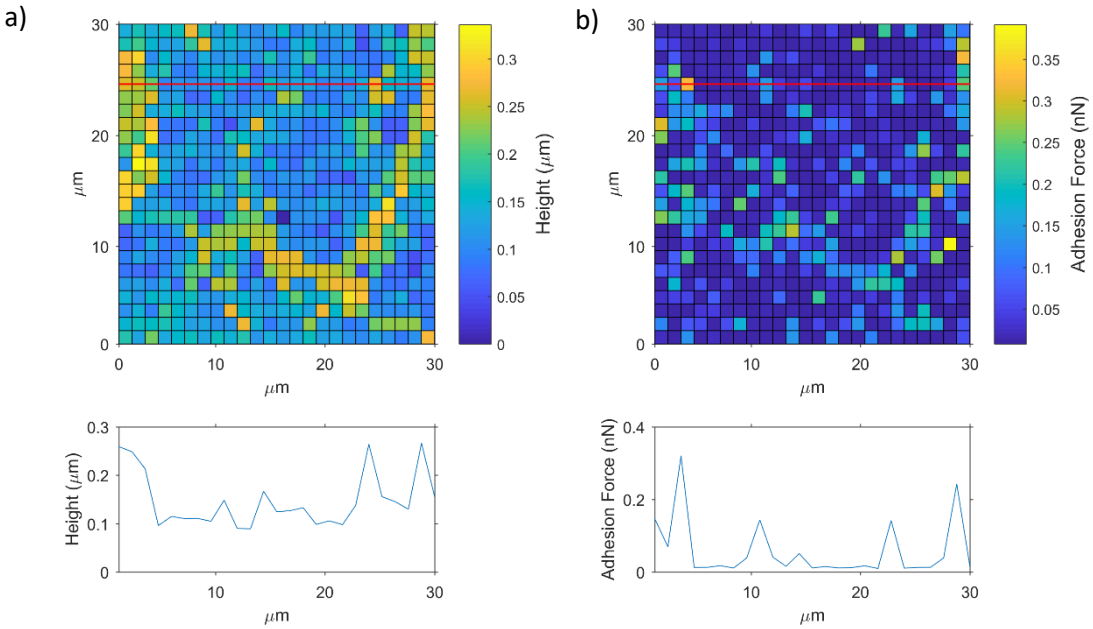

Figure 4.17: a) Topography and b) corresponding adhesion map of area 07 on calcite surfaces aged in brine and in decanoic acid 1 M. At the bottom of each map, the cross-section profile taken across the red line in the maps.

4.3.1.5. Maltene C5

a) Topography

The topography of calcite samples aged in maltene C_5 appears rougher compared to the previous solutions analysed. The peak to valley roughness reaches 4.7 μm, whereas the average measured roughness for the samples analysed is ~ 720 nm. The roughness is given by agglomerated blobs localised randomly on the surface of the samples and no cleavage plane is visible. The blobs measure on average 1 to 2 μm in diameter and are present on all the regions of the samples analysed.

b) Adhesion Force values

adhesion force values range between 0 and 9 nN, with an average value of 5.3 nN (Figure 21). The calculated average percentage of adhesion forces higher than 0.5 nN and 1 nN on a 30 × 30 μm surface is 75.6 and 72.6% respectively. For forces higher than 2nN, 3 nN and 4 nN, the average area percentages are 67.4%, 62% and 57% respectively. In some areas,

the adhesion forces are high in almost the whole surface of the samples, without reflecting the surface roughness of the area (Figure 4.18, Figure 4.19 and Table 4.2).

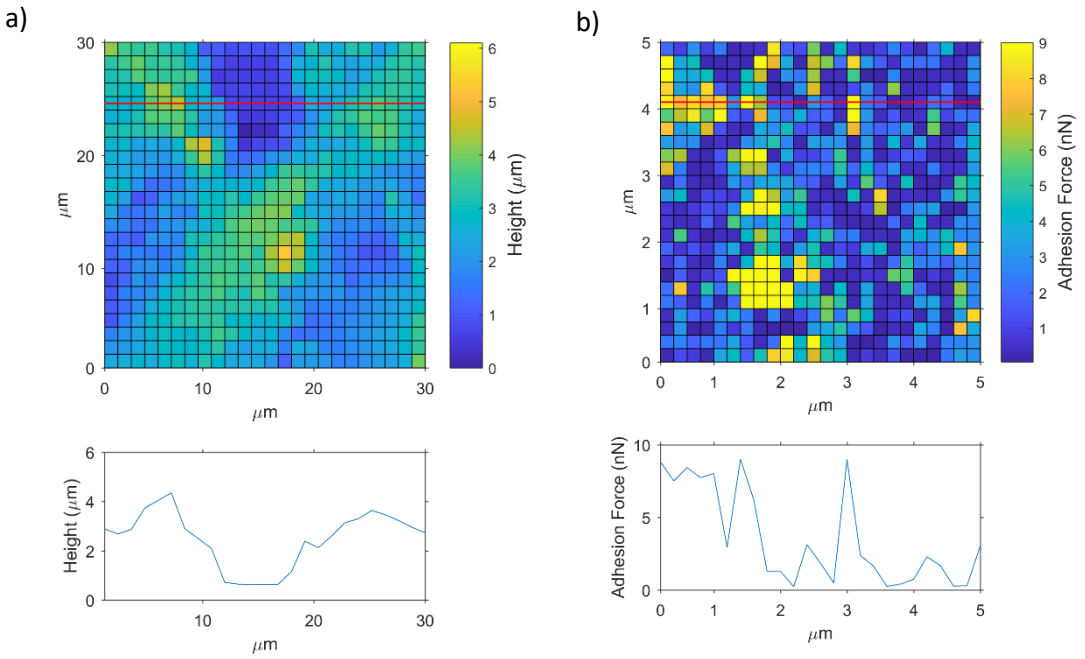

Figure 4.18: a) Topography and b) corresponding adhesion map of area 07 on calcite surfaces aged in brine and in maltene C5. At the bottom of each map, the cross-section profile taken across the red line in the maps.

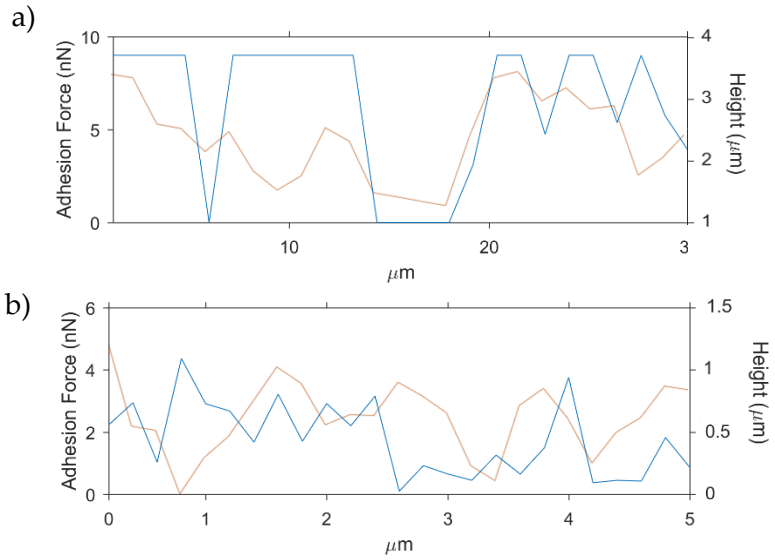

Figure 4.19: Overlapped crossplots of the same points in a) area 05 and b) area 06 of calcite surface aged in brine and in maltene C_5. The topography (red) and the adhesion forces (blue) lines show no correlation.

4.3.1.6. Maltene C8

a) Topography

The maximum peak-to-valley surface roughness observed in the samples is 2.1 μm, with an average roughness of 480 nm. Agglomerated blobs are present in all the scanned regions (Figure 4.20). In QI mode, these calcite surfaces of 2.5 × 2.5 μm² result to be completely covered by maltene C_8 (Figure 4.20). In this case, the topography results smoother with average roughness values of ~5 nm. In other 2.5 × 2.5 μm areas, the calcite surface is visible and 4-6 μm diameter wide particle/droplets are adhering to the surface (Figure 4.20).

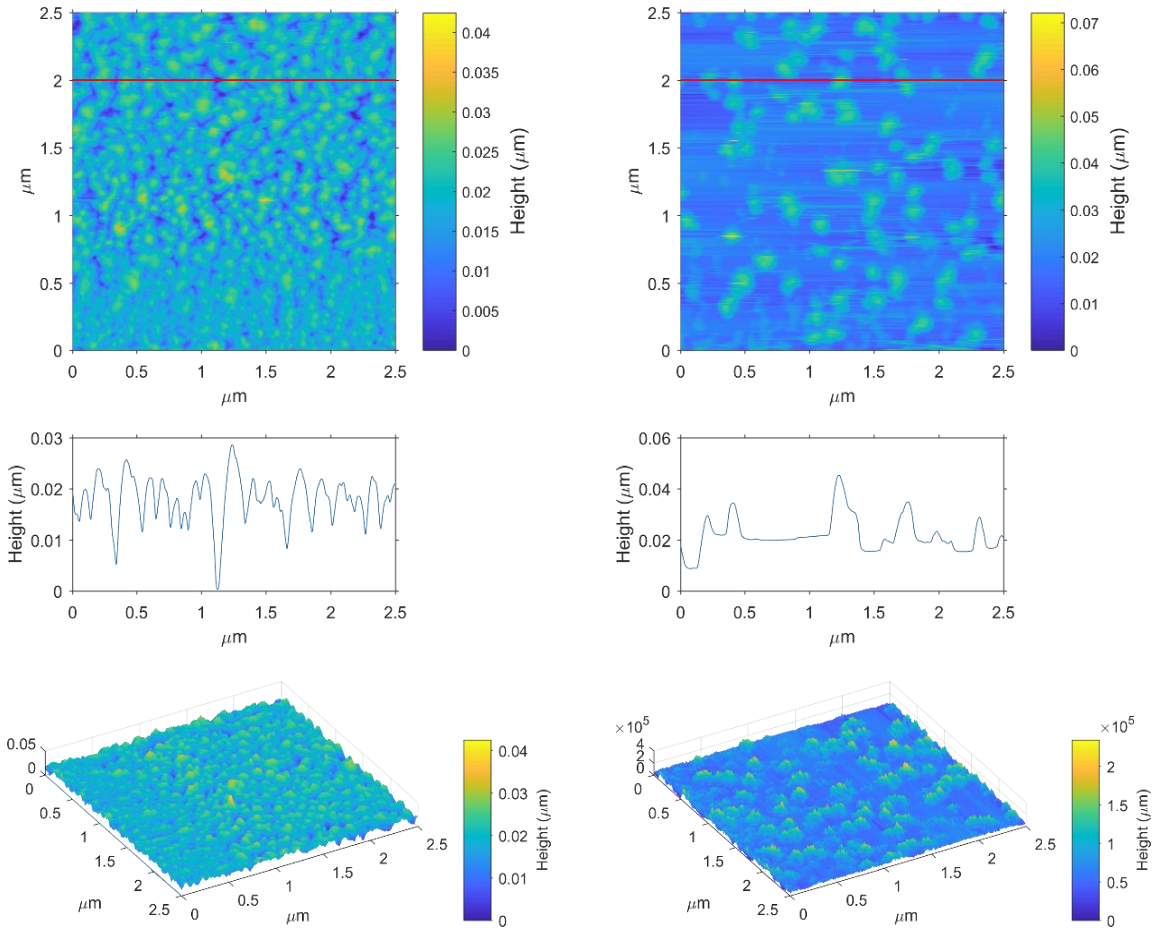

Figure 4.20: Topography maps in 2D and 3D (taken in QI mode) of calcite surfaces aged in maltene C_8. The surface roughness and the density of the particle/droplets varies from area to area.

b) Adhesion forces

Adhesion forces range between 10 pN and 7.5 nN, with average values across the samples of 2.7 nN. The percentage of adhesion forces ≥ 0.5 nN is on average 69%. For adhesion forces ≥1 nN, the surface percentages are on average 59%, whereas adhesion forces ≥2 nN cover up to 46% of the measured areas. Adhesion forces higher than 3 nN and 4 nN cover a maximum of 79% and 75%, with an average of 37and 30% respectively. The topography and adhesion forces cross plots of the same areas display a discrete positive relationship between the topography and the adhesion forces (Figure 4.21). However, despite being higher than the maltene C_5 values, the R^2 values do not display a significant correlation (Figure 4.22).

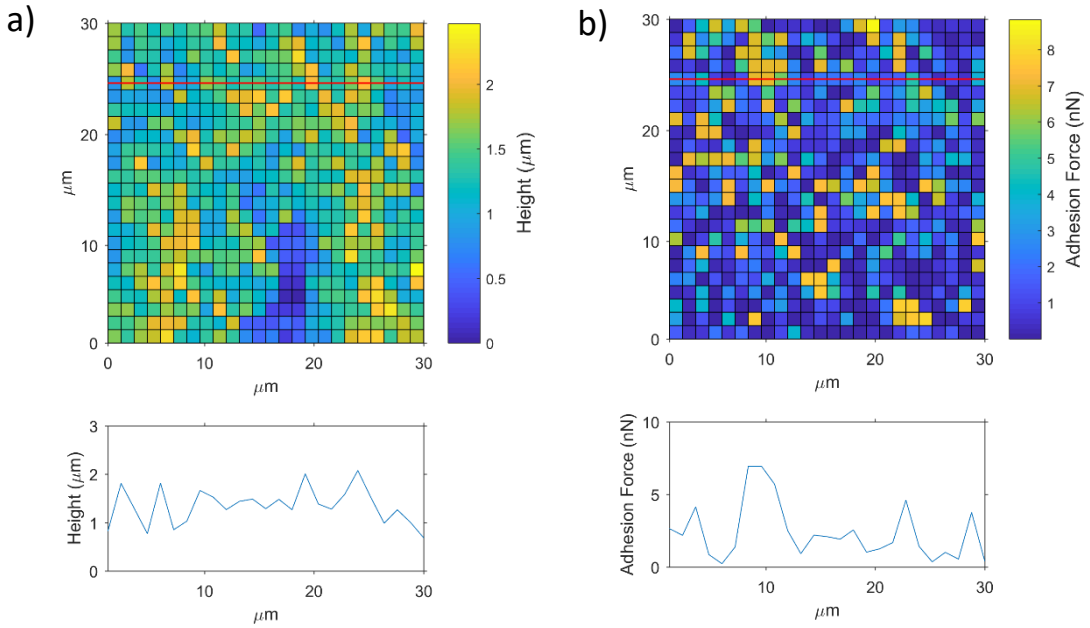

Figure 4.21: a) Topography and b) corresponding adhesion map of area 07 on calcite surfaces aged in brine and in maltene C_8. At the bottom of each map, the cross-section profile taken across the red line in the maps.

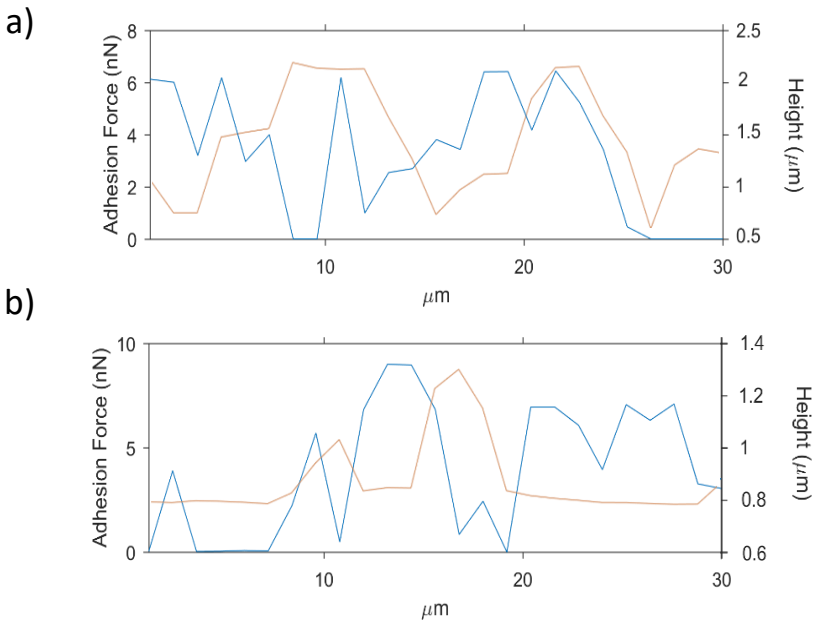

Figure 4.22: Overlapped crossplots of the same points in a) area 02 and b) area 11 of the surface of calcite aged in brine and in maltene C8. The topography (red) and the adhesion forces (blue) lines show no correlation.

4.3.1.7. Asphaltene

a) Topography

Areas analysed in QI mode show a microstructure formed by distinct blobs adhering to the surface. The blobs are either elongated, with rounded borders, or circular, ring-shaped. The maximum valley to peak value is 412 nm, and on average the surface roughness is 130 nm. The ring-shaped structures and the blobs observed adhering on the surfaces in the 2 × 2 μm areas have a typical diameter of 0.9-1 μm and are 50 to 230 nm high. Calcite cleavage steps, which measure ~ 1 μm in height are also visible (Figure 4.23 a).

Other areas exhibit patches of uniform calcite surface in between a rougher (~30 nm of average roughness against ~10 nm) layer of material, which is presumably the asphaltene deposited on the surface. The layer deposition is not uniform and is predominantly visible in areas of 5 × 5 μm or below scanned in QI mode. At smaller scan sizes, it is also possible to see the calcite surface and single droplets adhering to the surface (Figure 4.23 b).

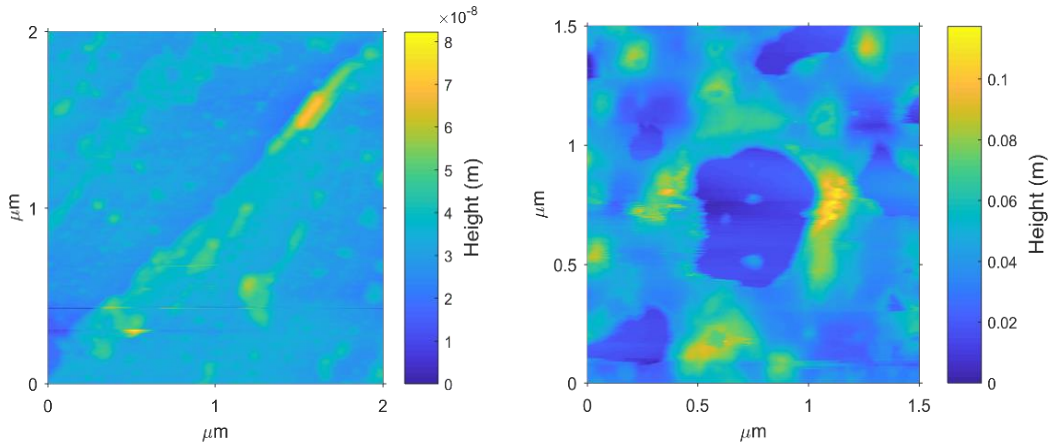

Figure 4.23: Topography maps taken in QI mode of regions of calcite surfaces aged in asphaltene. The distribution of the asphaltene is variable. In a blobs and ring-shaped structures are visible. In a a calcite step is also present, and the aspaltene appears more concentrated at the boundary between the step and on minor parallel surface cleavages. In b the calcite surface is exposed only in minor areas. In b small (~50 nm) single droplets are also visible.

b) Adhesion forces

The average minimum adhesion force is 60 pN and the average maximum of 8.2 nN. Considering the whole 30 × 30 μm areas, the average calculated adhesion force is 2.9 nN. The calculated average adhesion force percentages for forces ≥ 0.5 nN is 81%. For forces ≥ 1 nN is 73.3% and for forces ≥ 2 nN 58%. The percentage of surface covered by adhesion

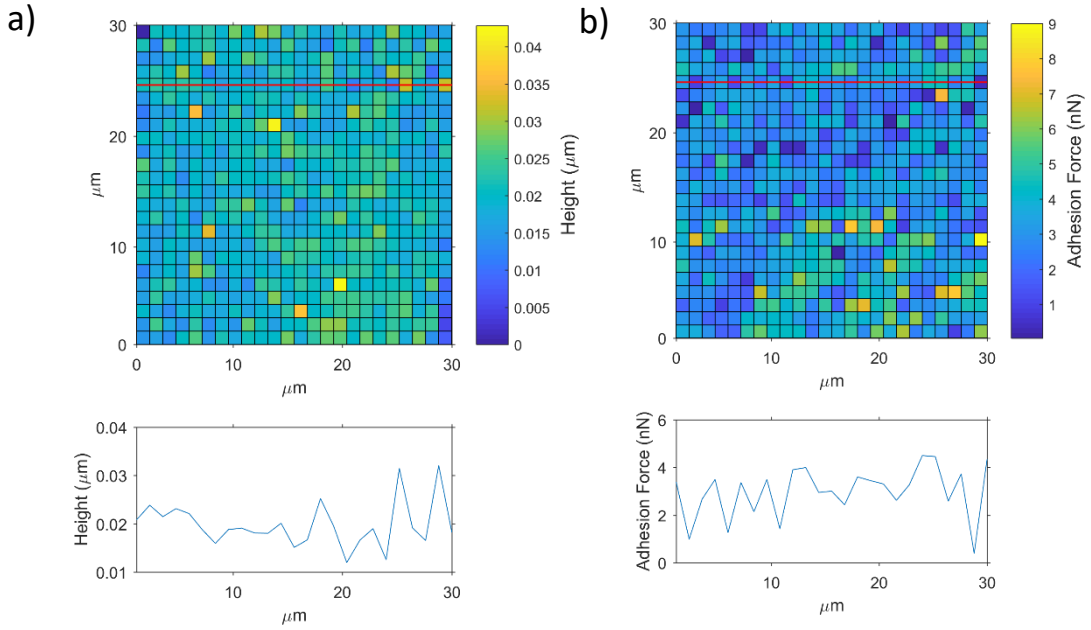

Figure 4.24: a) Topography and b) corresponding adhesion map of area 03 on calcite surfaces aged in brine and in asphaltene. At the bottom of each map, the cross-section profile taken across the red line in the maps.

forces equal or larger than 3 nN ≥decreases instead to 41% and for forces ≥ 4 nN to 27.8%. By observing the cross plots (Figure 4.25) and the R^2 values (Table 4.2) of the topography maps and the adhesion maps no clear relationship between the topography highs and the high adhesion forces is noticeable.

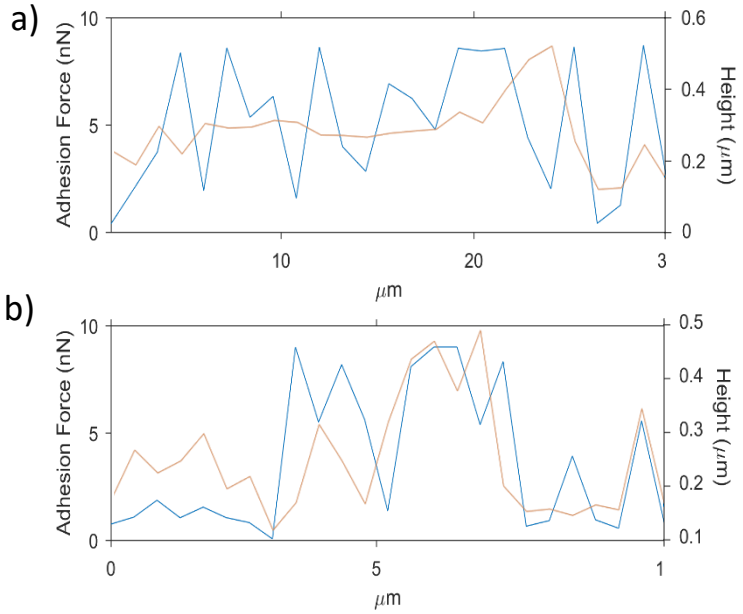

Figure 4.25: Overlapped crossplots of the same points in a) area 05 and b) area 03 of the surface of calcite aged in brine and in asphaltene. The topography (red) and the adhesion forces (blue) lines show discrete correlation.

4.3.1.8. Oil

a) Topography

Calcite aged in oil presents average surface roughness variations between the tops and the bottoms of the asperities of 230 nm, with a maximum of 510 nm. QI mode data highlighted a ramified distribution of the oil droplets, which reach ~ 200 nm in height (Figure 4.26). The distribution of the oil droplets is highly variable, consisting of connected droplets as well as single, round-shaped droplets. Maps at lower magnifications (Figure 4.26) highlight the high density of droplets on the surface.

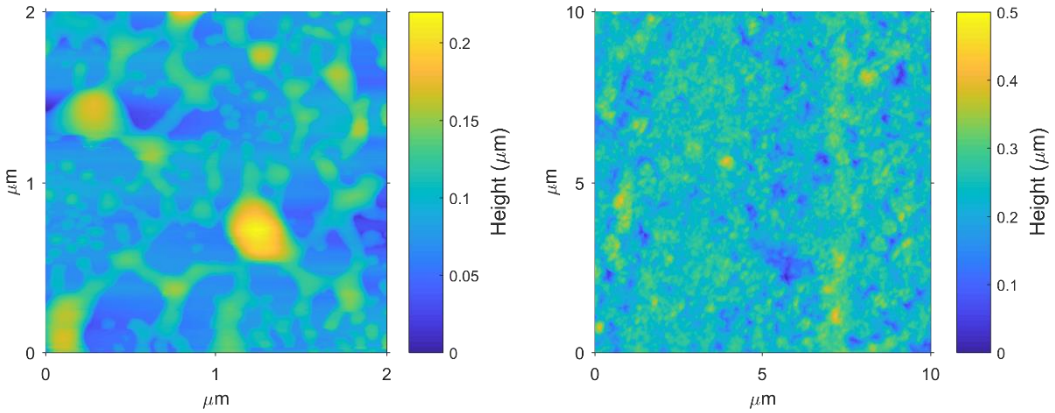

Figure 4.26: Topography maps taken in QI mode of regions of calcite surfaces aged in oil. The distribution of the oil is highly variable.

b) Adhesion forces

Adhesion forces on calcite crystals aged in oil range between a minimum average of 10 pN and a maximum average of 8.5 nN. On average, between all the areas analysed, the adhesion forces are 2.4 nN. 70% of the 30 x 30 μm surfaces are covered by adhesion forces ≥ 0.5 nN and a 56% by forces ≥ 1 nN. For adhesion forces ≥ 2 nN, the surface covered drops to 37% and for forces ≥ 3 nN 29.1%. adhesion forces ≥ 4 nN account for an average of 23% of the scanned regions. By cross-correlating the topography and the adhesion maps, no clear association is noticed between the two, signifying that the topography highs do not necessarily correspond to high adhesion forces (Figure 4.27 andFigure 4.28 and Table 4.2).

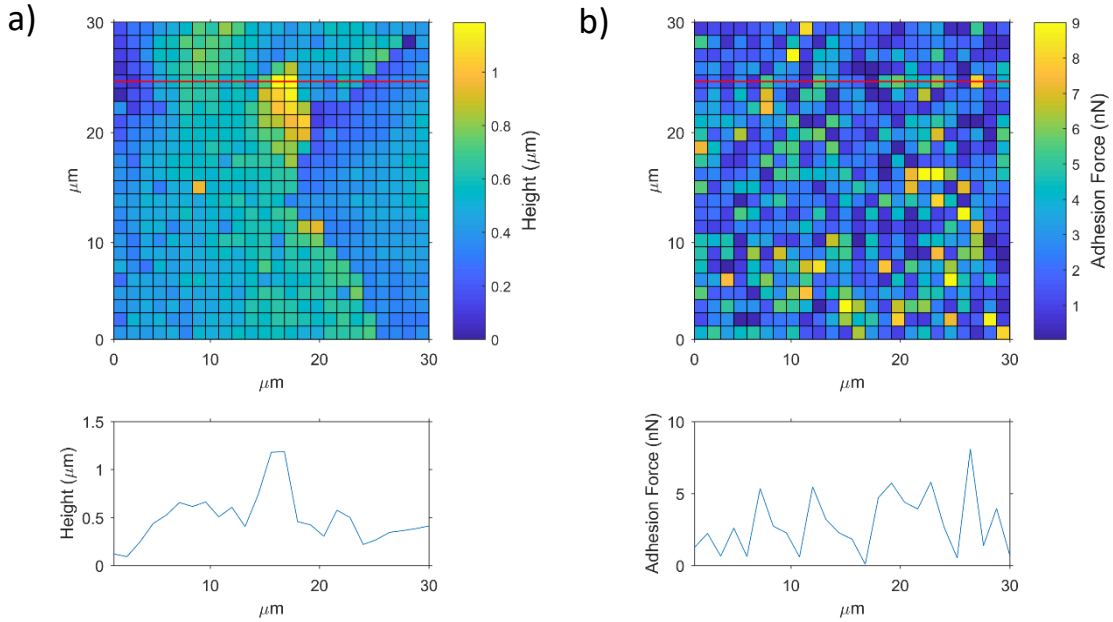

Figure 4.27: a) Topography and b) corresponding adhesion map of area 03 on calcite surfaces aged in brine and in asphaltene. At the bottom of each map, the cross-section profile taken across the red line shown in the maps.

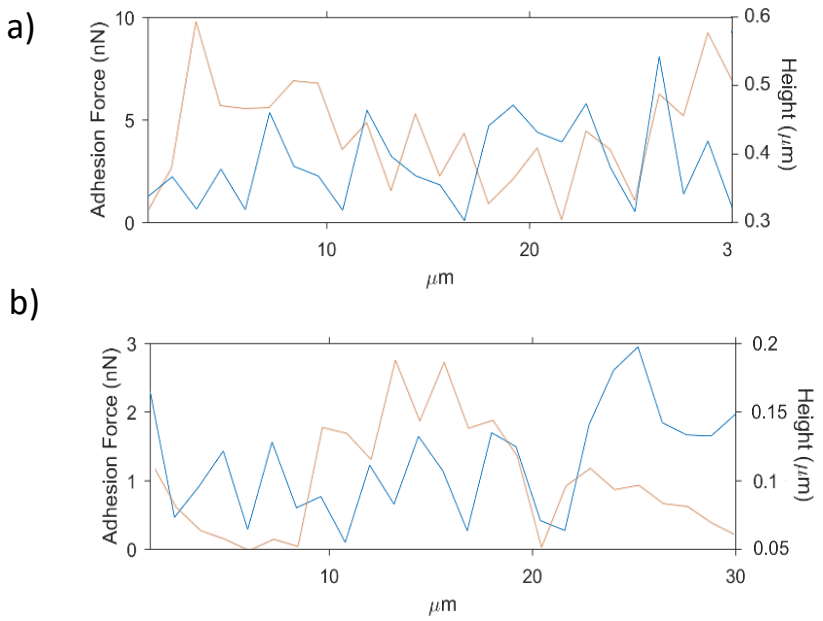

Figure 4.28: Overlapped crossplots of the same points in a) area 02 and b) area 04 of the surface of calcite aged in brine and in asphaltene. The topography (red) and the adhesion forces (blue) lines do not show a clear correlation.

4.3.1.9. Aged calcite dodecane with no brine

To test any variability in the adhesion behaviour and force measurements between calcite subject to a water-wetting phase before being affected by oil compounds, surfaces of calcite aged in brine and then dodecane were correlated to surfaces aged in only dodecane.

a) Topography

Calcite steps measuring up to 250 nm are visible on the surface. A maximum height variation of 650 nm is noticed and on average, on 30 × 30 mm areas, the peak to valley height is ~ 100 nm. QI mode scans highlight that the surface roughness is given by semi-circular or irregularly shaped droplets/particles which are randomly distributed on the calcite surfaces (Figure 4.29).

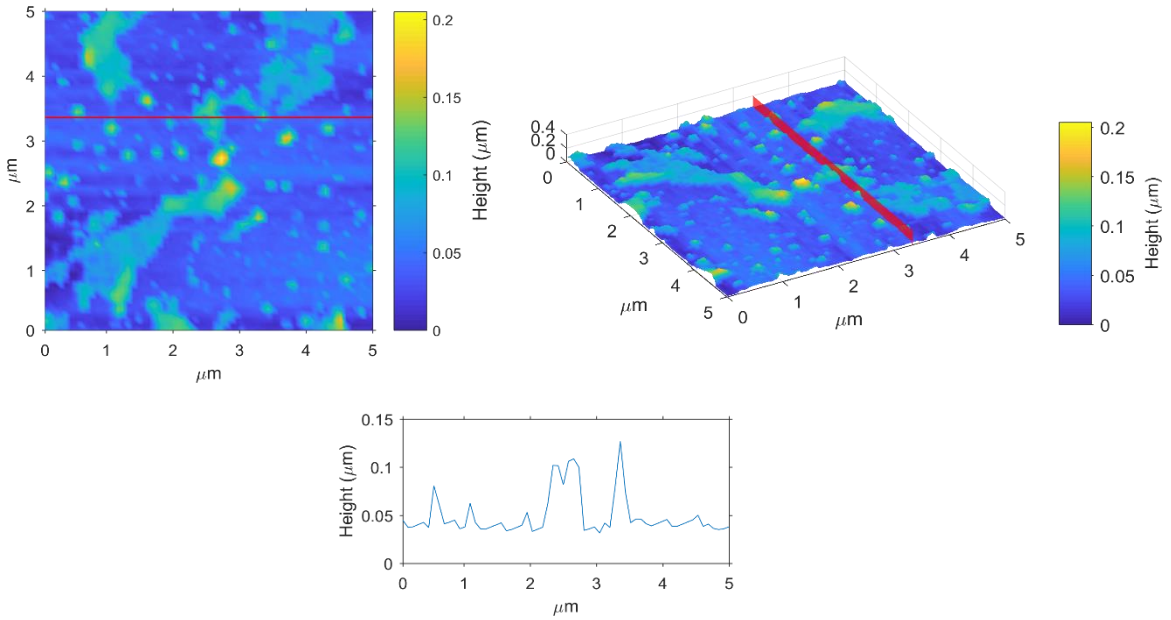

Figure 4.29: Topography maps in 2D and 3D of calcite surfaces aged only in dodecane. The droplets on the surface vary in dimension and in shape.

b) Adhesion Forces

Adhesion forces in calcite aged only in dodecane vary between a minimum of 150 pN and a maximum average of 4.3 nN. On average, the adhesion force on the 30 × 30 μm surfaces is 1.1 nN and forces ≥ 0.5 nN cover 66% of the surfaces. An average of 46.7% of the surface is occupied by adhesion forces ≥ 1 nN, whereas an average of 20% by forces ≥ 2 nN. Adhesion forces ≥ 3 nN occupy 5.1% of the surfaces, whereas the forces ≥ 4 nN occupy 0.8% of the whole surface areas. Cross correlating the adhesion maps with the topography maps, a discrete correlation can be found (Figure 4.30, Figure 4.31).

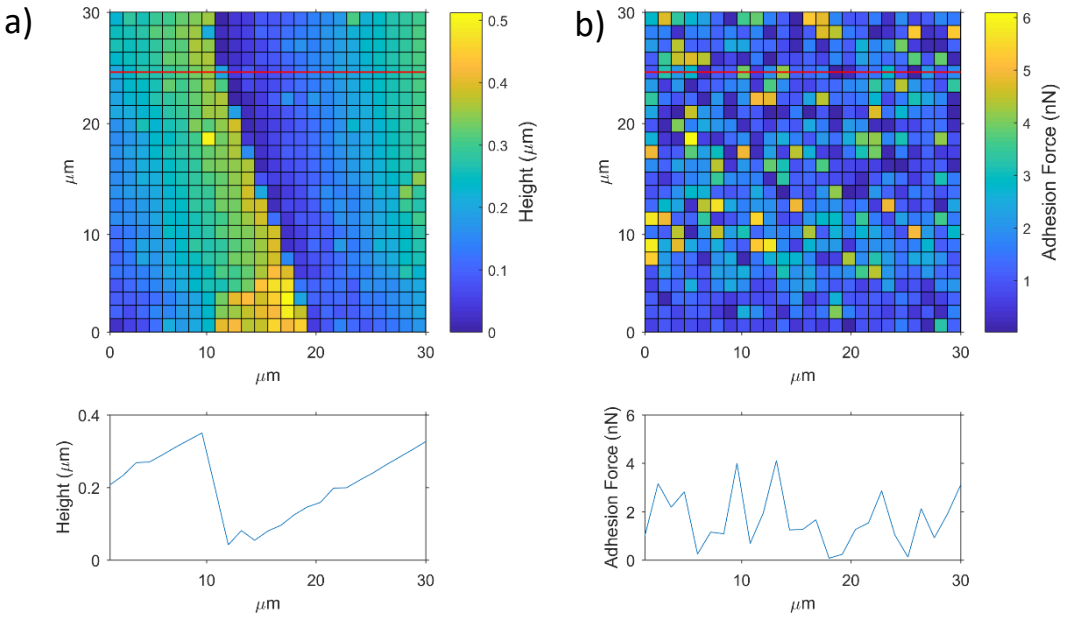

Figure 4.30: a) Topography and b) corresponding adhesion map of area 02 on calcite surfaces aged only in dodecane. At the bottom of each map, the cross-section profile taken across the red line in the maps.

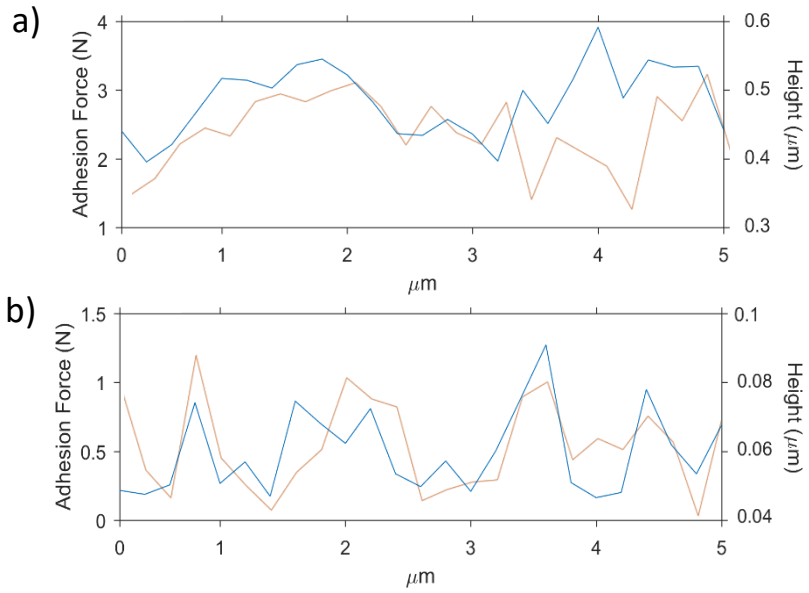

Figure 4.31: Overlapped crossplots of the same points in a) area 05 and b) area 06 of the surface of calcite aged only in dodecane. The topography (red) and the adhesion forces (blue) lines show a good correlation.

4.3.1.10.Summary of results

a) Average adhesion forces values:

Figure 35 displays the average adhesion force values measured for all the areas analysed with the different solutions/oil compounds. The lowest average adhesion forces are observed in the calcite aged in brine. The addition of model oil (dodecane and decanoic acid compounds) increases the overall average adhesion force on the 30 × 30 μm surfaces. Calcite surfaces aged in dodecane without brine have a larger average adhesion force value compared to the calcite aged first in brine and then in dodecane. Addition of decanoic acid to the dodecane produces an increase in the adhesion forces at concentrations of 1M, but for concentrations of 0.1 M no significant differences are noticed. Crude oil fractions exhibit higher (+360% increase) average adhesion values compared to the model oil compounds (Figure 4.7**Error! Reference source not found.**). The main differences are noticed in the minimum average adhesion values, which are always above 1 nN in the crude oil fractions. The average adhesion force in the crude oil is lower (2.4 nN) compared to the average adhesion force for the oil fraction asphaltene

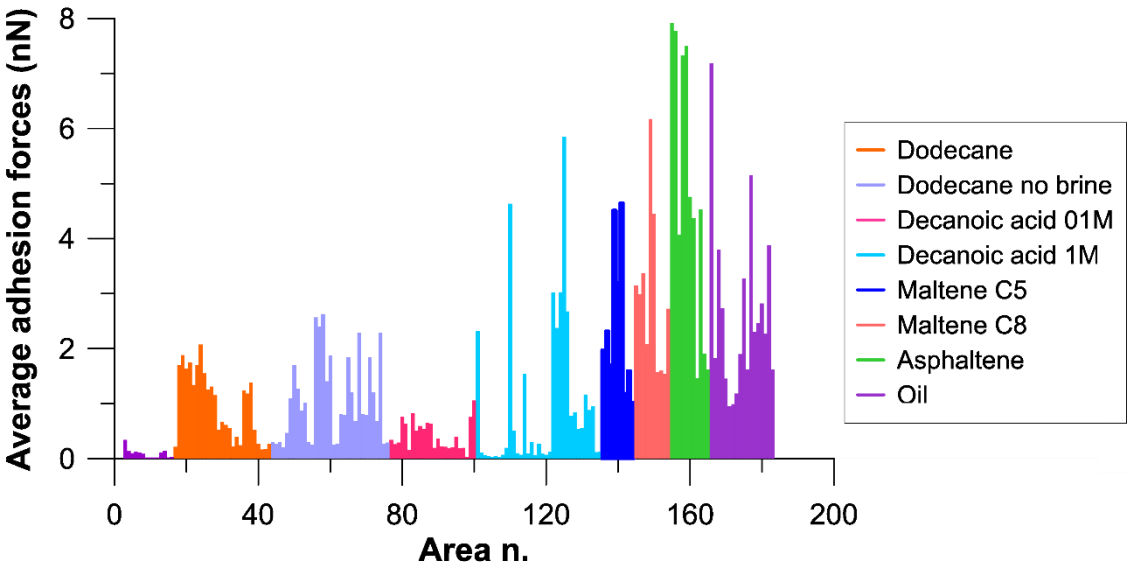

Figure 4.32: Average adhesion forces for all the calcite areas analysed. The colours correspond to the different aging experiments. Each column in the diagrams corresponds to an area analysed (Area n.).

(4.7 nN).

b) Surface area percentages of adhesion forces

Surface area percentages covered by adhesion forces reflect the same trend as the average adhesion force values. The percentage of 30 × 30 µm areas covered by adhesion forces larger than 0.5 nN is higher with the increase of heavy oil compounds in the solutions (Figure 4.33 a). Significant differences are noticed between the crude oil fractions and the model oil solutions at increasing adhesion forces: for adhesion forces higher than 4 nN, the average area percentages on the surfaces aged in crude oil fractions are 32% against 3% for the surfaces aged in model oil compounds (dodecane and decanoic acid). The area covered by adhesion forces ≥ 4 nN is lower (24%) in the oil compared to the area for the oil fraction asphaltene (50%) (Figure 4.7 and Figure 4.33).

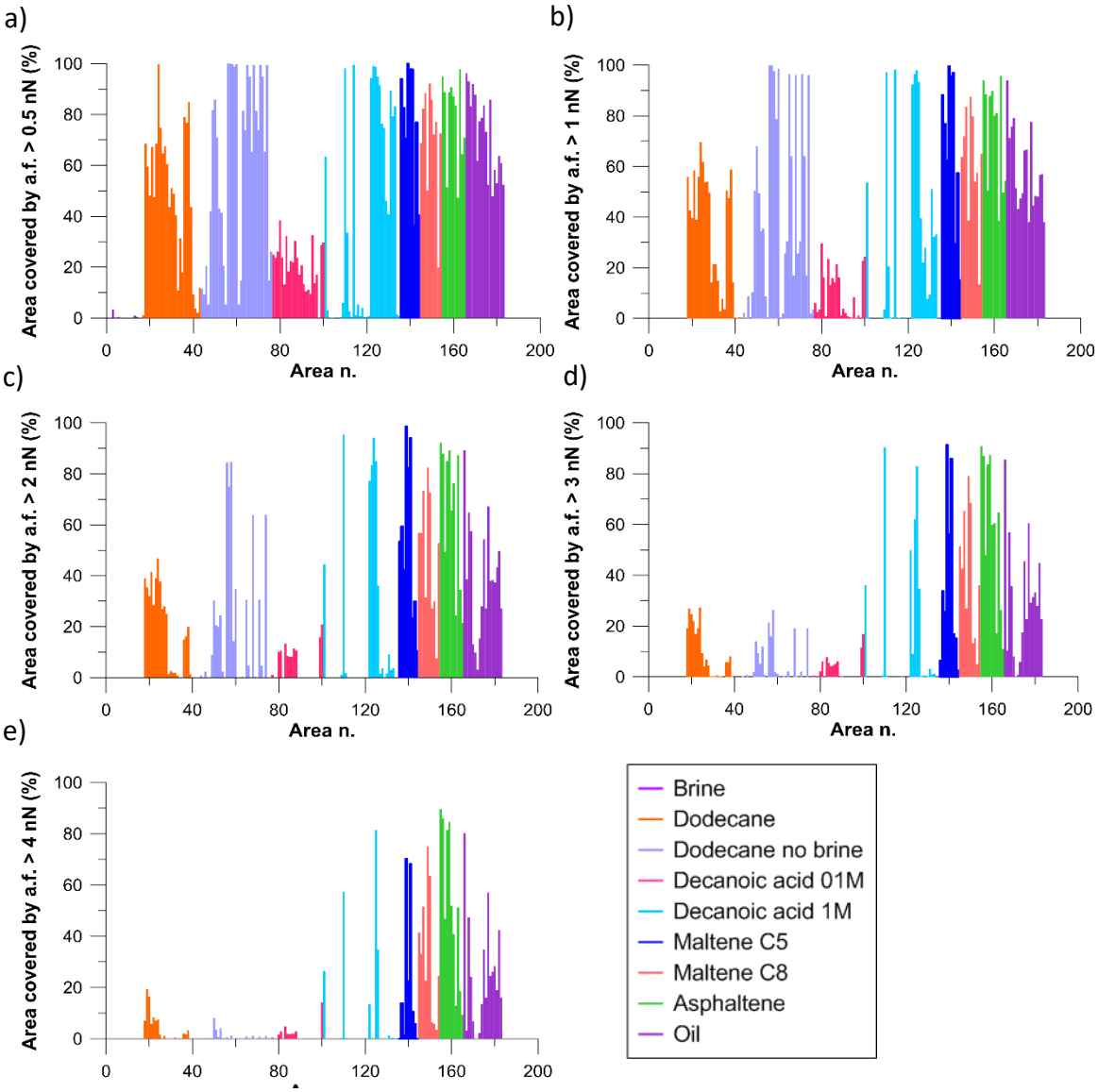

Figure 4.33: Percentages of the area coverage by adhesion forces (a.f.) larger than a) 0.5 nN, b) 1 nN, c) 2 nN, d) 3 nN, e) 4 nN. The colours correspond to the different aging experiments. Each column in the diagrams corresponds to an area analysed (Area n.).

c) Surface testing

To test the nature of the surface roughness, different surface areas of calcite crystals aged in decanoic acid 1M, asphaltene and oil were scanned in QI mode at a variable setpoint. The setpoint defines the magnitude of the tip-sample interaction and allows direct visualization of the compressibility of the particles/droplets on the surfaces. When the setpoint is gradually increased (0.2 to 5.2), the particles on the surface deform and contract. However, restoring the setpoint to the initial value, the particles return to the original shape (Figure 4.34). This behaviour rules out the possibility that these particles are solid crystal deposits on the surfaces and suggests that the asperities are instead compressible oil droplets adhering to the surfaces.

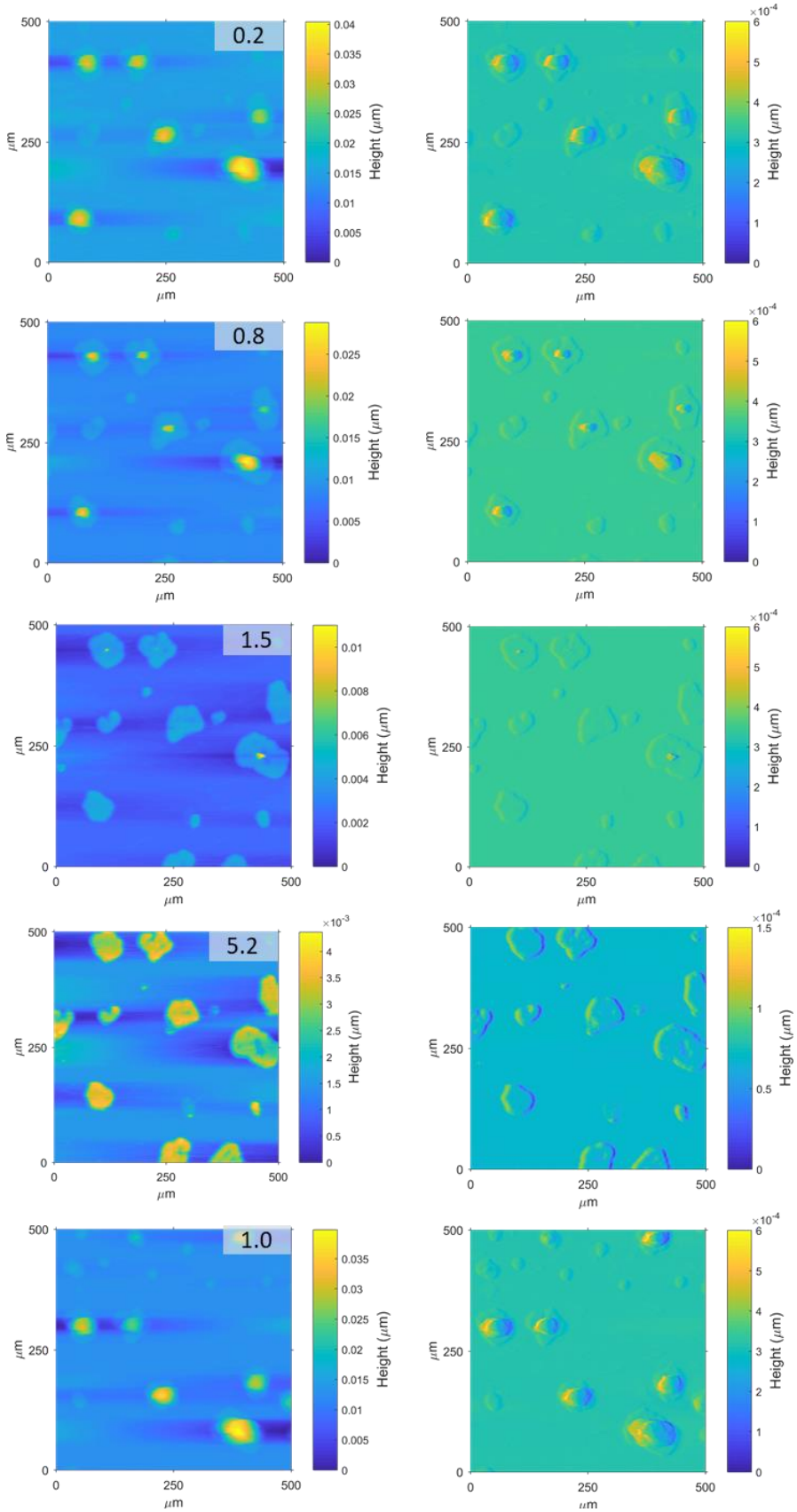

Figure 4.34: The same area of a calcite surface aged in decanoic acid 1 M scanned at different setpoint. At increasing setpoints (i.e. the force applied to the tip) the droplets are "squeezed" on the surface. When the setpoint decreases in the last row, the droplets return to their original aspect. The images on the left column are topography maps, whereas the ones on the right are deflection maps, used to better visualise the droplets.

4.3.2. Results: AFM-IR

4.3.2.1. AFM-IR chemical maps

The validation of the CFM data was performed by means of AFM-IR analyses. AFM-IR chemical maps at a wavelength of 2920 cm^{-1} were produced for all the samples aged in oil compounds (Figures 4.37 to 4.47 a and b). The 2920 cm^{-1} wavelength was chosen as it represents a CH_2 bond, indicative of organic molecules. The contrast of the colours in the chemical maps indicates areas where the variation in the amplitude-frequency of the peaks is located. All the samples show a heterogeneous distribution of the oil compounds on the surfaces. In all the samples, the chemical absorbance of the 2920 cm^{-1} peak is well correlated to the topography of the same area; the lowest absorption occurs in low topography areas. The most common vibrational groups were identified as in Table 4.3:

IR wavenumber (cm^{-1})	Bond	Type of compound
900-1000	C=H bend	alkenes
	O-H bend	carboxyls
1040	Si-O stretch	silicates, clays
1050	C-O stretch	alcohols
	C-N stretch	amines
1110	C-N stretch	aliphatics/amines
	C-O stretch	esters, ethers, alcohols
1200-1350	C-O stretch	carboxyls
1370	S=O stretch	sulfonates
1395-1440	O-H bend	carboxyls
1400-1500	C-O stretch	carbonates
1410	C-H bend	alkene
1430	C-H bend	aliphatic
1510- 1610	C=C stretch	aromatics
1620	N-H stretch	amines
1710	C=O stretches	carboxyls
2860	C-H stretches	aliphatic
3000-3100	C-H stretches	aromatics
>3000	O-H stretches	carboxyls, hydroxyls
3360-3440	N-H stretch	amines

Table 4.3: IR wavenumbers and assigned molecular motion and functional group.

4.3.2.2. AFM-IR point spectroscopy

a) Calcite in brine

Pure calcite nano-IR spectra analysis shows a small peak at 1310 cm^{-1}, one at 1420 cm^{-1} and a broad peak around 1585 cm^{-1}. The 1420 cm^{-1} peak represents the carbonate absorption band, while the 1585 cm^{-1} peak is assigned to the -OH stretching band. Other low absorption bands are present around 980 cm^{-1}, 1160 cm^{-1}, 1700 cm^{-1} and the peak at 2950 cm^{-1} are fingerprints related to organic compounds (i.e. O-H esters and carboxylic acid bends, C-H aliphatic stretches and C=O alcohols stretch). In the highest laser range, peaks at ~3250 cm^{-1} are also observed (Figure 4.35). The broad 3250 cm^{-1}, together with the 1585 cm-1 peak are within the water -OH group stretch region (Figure 4.35). Although extreme precaution has been taken for not contaminating the samples with organic material, on the surface low absorbance peaks of organic molecules were observed. The presence of small amounts of organic molecules can be explained by the contamination on the surface by "adventitious carbon". It is extremely rare not find any contamination-derived organic compound or water moisture from the atmosphere on a freshly cleaved mineral surface (Bovet et al., 2013; Stipp and Hochella, 1991).

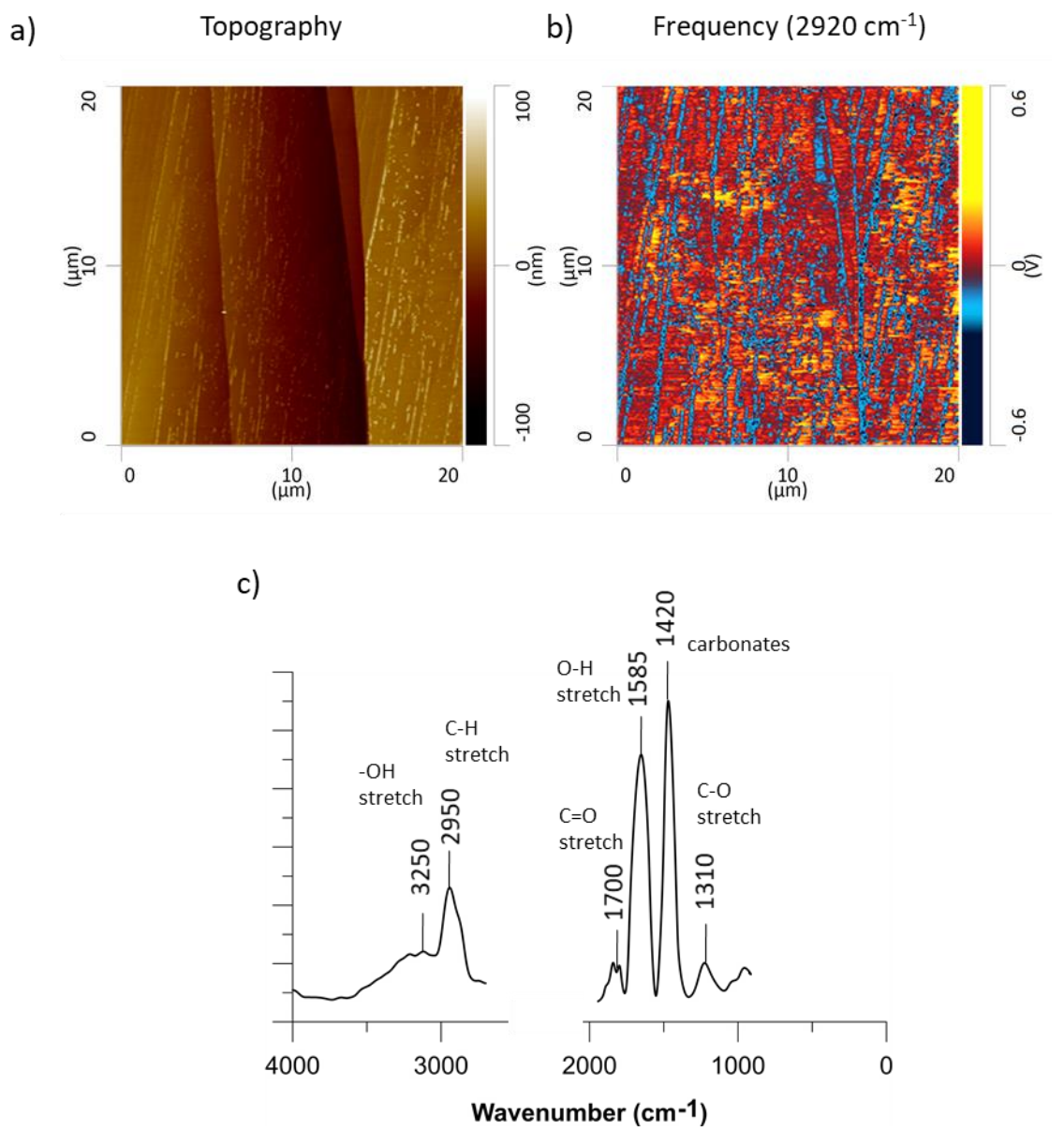

Figure 4.35: a) Topography and b) frequency map at the set wavenumber 2920 cm^{-1} of a 20 x 20 µm area and c) a nano-IR spectrum reconstruction of a point on the calcite surface aged in brine. The y axis on the spectrum is the absorbance, normalised as the two spectra were taken with different lasers.

b) Dodecane

The spectroscopy of the calcite surface covered in dodecane presents peaks in the low-range laser at 980 cm^{-1}, 1160 cm^{-1}, 1458 cm^{-1}, 1473 cm^{-1} and 1628 cm^{-1}. The 980 cm-1 is interpreted as a C-H bend and the 1160 cm^{-1} is assigned to a CH_2 twist or to a C-O stretch, the 1473 cm^{-1} and 1458 cm^{-1} are respectively assigned to methylene (CH_2) and methyl (CH_3) bends and overlap with the carbonate surface background peaks. The 2740 cm^{-1} and

the 2925 cm^{-1} peaks are assigned to aliphatic CH_2 and CH_3 stretches, whereas the 1628 cm^{-1} and the 3360 cm^{-1} absorbance bands are associated with the brine solution and correspond respectively to the O-H scissors and the O-H bond stretching.

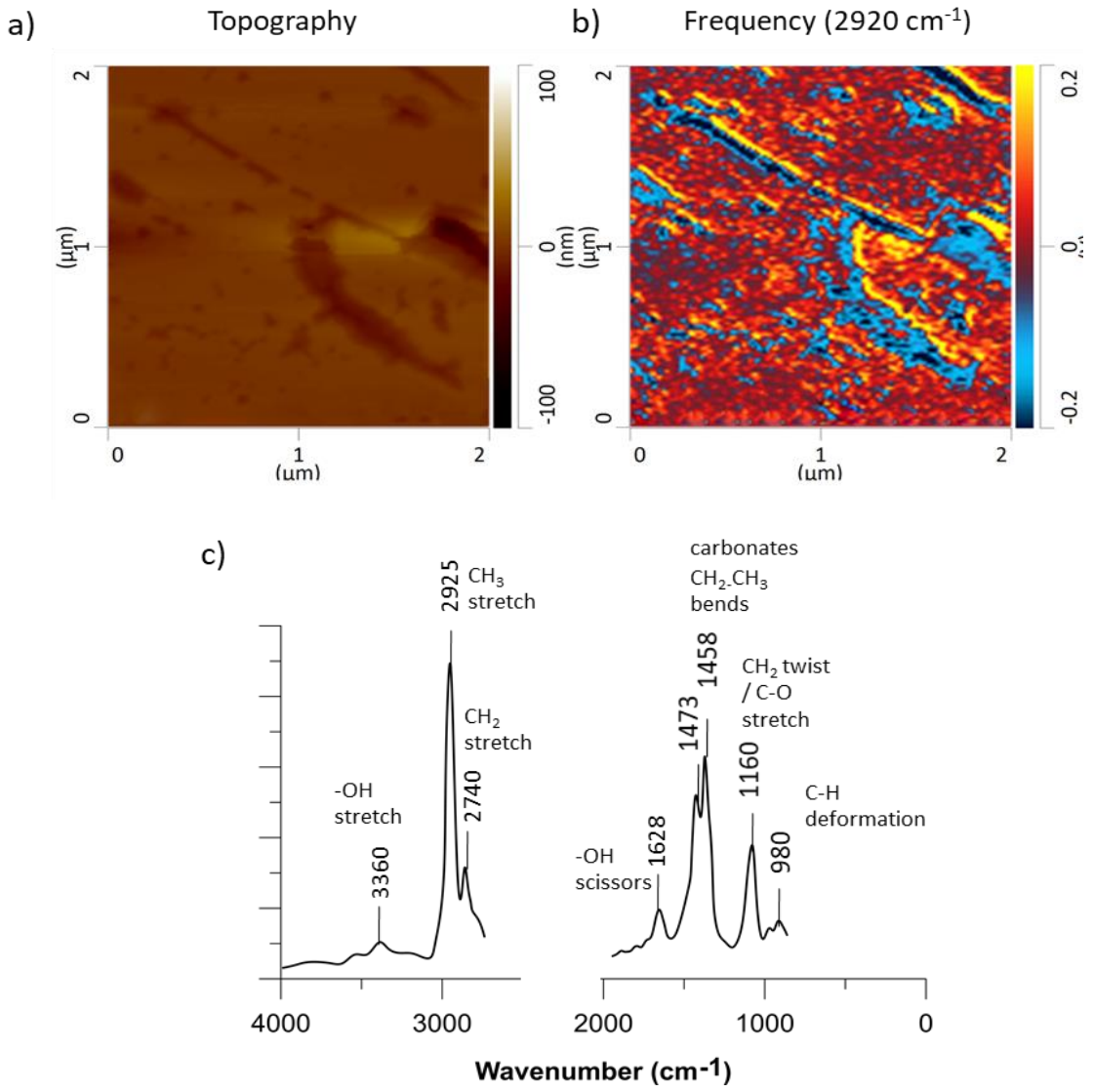

Figure 4.36: a) Topography and b) frequency map at the set wavenumber 2920 cm^{-1} of a 2 x 2 µm area and c) a nano-IR spectrum point reconstruction on the calcite surface aged in dodecane. The y axis on the spectrum is the absorbance, normalised as the two spectra were taken with different lasers.

c) Decanoic acid dissolved in dodecane

The dissolution of decanoic acid into the dodecane adds to the spectrum a peak at 1063 cm^{-1} and a peak at 1738 cm^{-1}, both corresponding to C=O stretches of the carboxylic acid groups. In the decanoic acid 1.0 M aged calcite, the 1738 cm^{-1} peak absorbs more compared to the decanoic acid 0.1 M aged calcite, indicating that the carboxylic acids are more

abundant in the high molarity of the decanoic acid solution. The CH_2 peak present at 1160 cm^{-1} in the dodecane appears at 1167 cm^{-1} in the decanoic acid 0.1 M and at 1152 cm^{-1} in the decanoic acid 1.0 M aged calcite surface. The region of the CH_2 peaks (1167 cm^{-1}) also overlaps to the C-O carboxylic acid stretch region. The CH_2 and CH_3 stretches caused by the presence of alkanes are seen here at the 1630 cm^{-1} peak. In the decanoic acid 0.1 M, at wavenumbers between 2700 cm^{-1} and 4000 cm^{-1}, the CH_2 and CH_3 stretches (2870 cm^{-1}) and the O-H stretch band (2982 cm^{-1}) are present. In the decanoic acid 1.0 M, the same bands are present at slightly different wavenumbers: the CH_2-CH_3 stretches at 2842 cm^{-1}, 2970 cm^{-1} and the O-H bond stretching around 3350 cm^{-1}. The O-H bends in these ranges are interpreted as being caused both by the carboxylic acids and by the brine solution (Figure 4.37Figure 4.39).

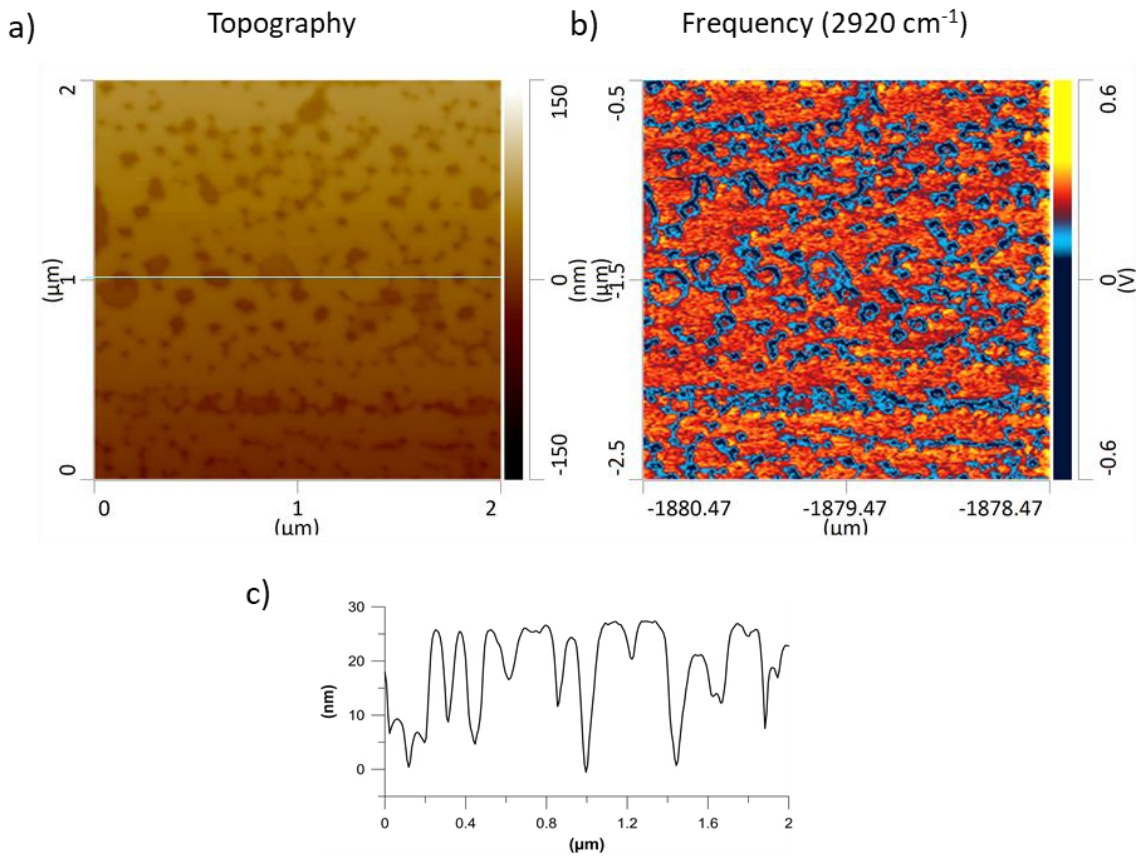

Figure 4.37: a) Topography and b) frequency map at the set wavenumber 2920 cm^{-1} of a 2 x 2 µm area and c) cross-plot profile of the blue line on the topography map of an area on the calcite surface aged in decanoic acid 0.1.

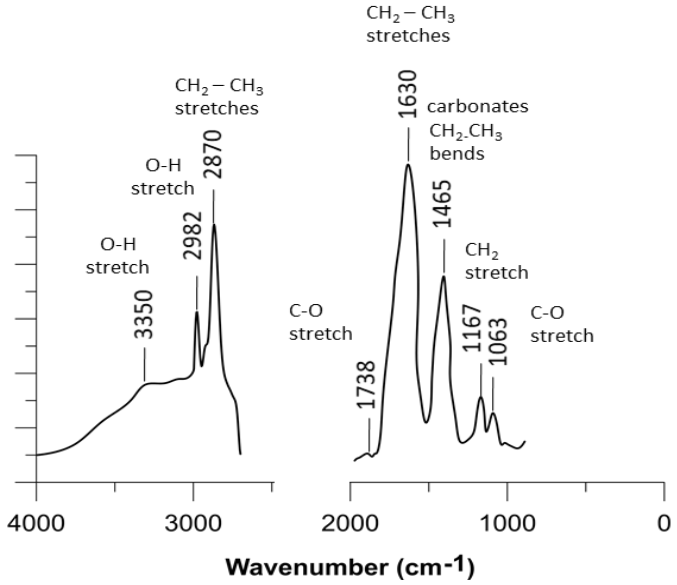

Figure 4.38 : a nano-IR spectrum point reconstruction of a point on the calcite surface aged in decanoic acid 0.1 M. The y axis on the spectrum is the absorbance, normalised as the two spectra were taken with different lasers.

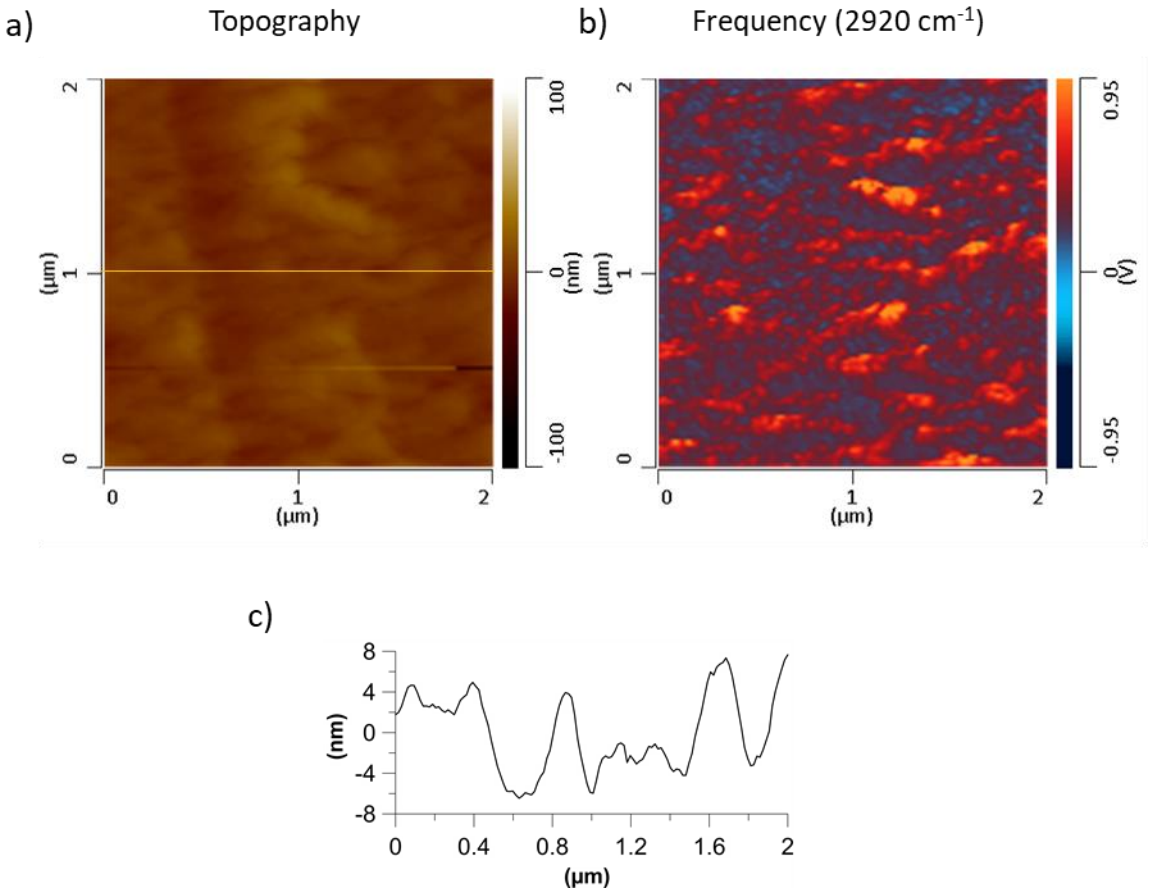

Figure 4.39: a) Topography and b) Frequency map at the set wavenumber 2920 cm^{-1} of a 2 x 2 µm area and c) a profile of the surface roughness (<10 nm) of the oil film coating the calcite surface.

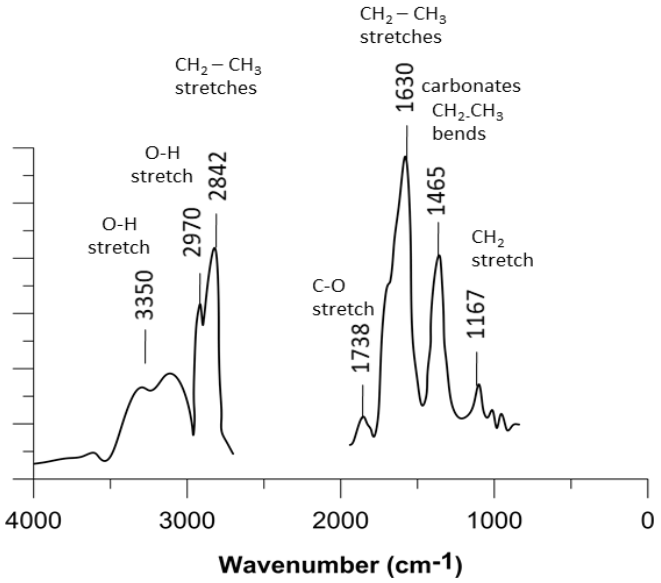

Figure 4.40: is a nano-IR spectrum reconstruction of a point on the calcite surface aged in decanoic acid 1 M. The y axis on the spectrum is the absorbance, normalised as the two spectra were taken with different lasers.

d) Calcite in maltene C_5

Calcite in maltene C_5 exhibits peaks at 1045 cm^{-1}, 1110 cm^{-1},1380 cm^{-1}, 1463 cm^{-1}, 1496 cm^{-1} and 1605 cm^{-1} for the low laser range. At wavenumbers between 4000 cm^{-1} and 2700 cm^{-1}, the surface absorbs at 2740 cm^{-1}, 2854 cm^{-1} and 3092 cm^{-1}. The 1045 cm^{-1} and the 1110 cm^{-1} peaks correspond to the CH_2 twist band of alkanes and to the C-O ester stretch band. The 1110 cm^{-1} peak also overlaps with the C-N stretch in aliphatics and amines. The 1380 cm^{-1} peak is assigned to the C-H alkane bend (CH_3) and to the inorganic carbonate peak. The 1462 cm^{-1}, 1496 cm^{-1} are given by the methyl CH_2 and CH_3 bending vibrations. The peak at 1605 cm^{-1} is associated with a C=C stretch present in aromatics. The 2740 cm^{-1} and the 2854 cm^{-1} are assigned to the CH_2 and CH_3 carboxylic acids stretchings and the 3092 cm^{-1} to the O-H stretch in alcohols or carboxylic acids. The absence of a 1710 cm^{-1} peak, which is a C=O stretch, could indicate a low abundance of carboxylic acids (Figure 4.41).

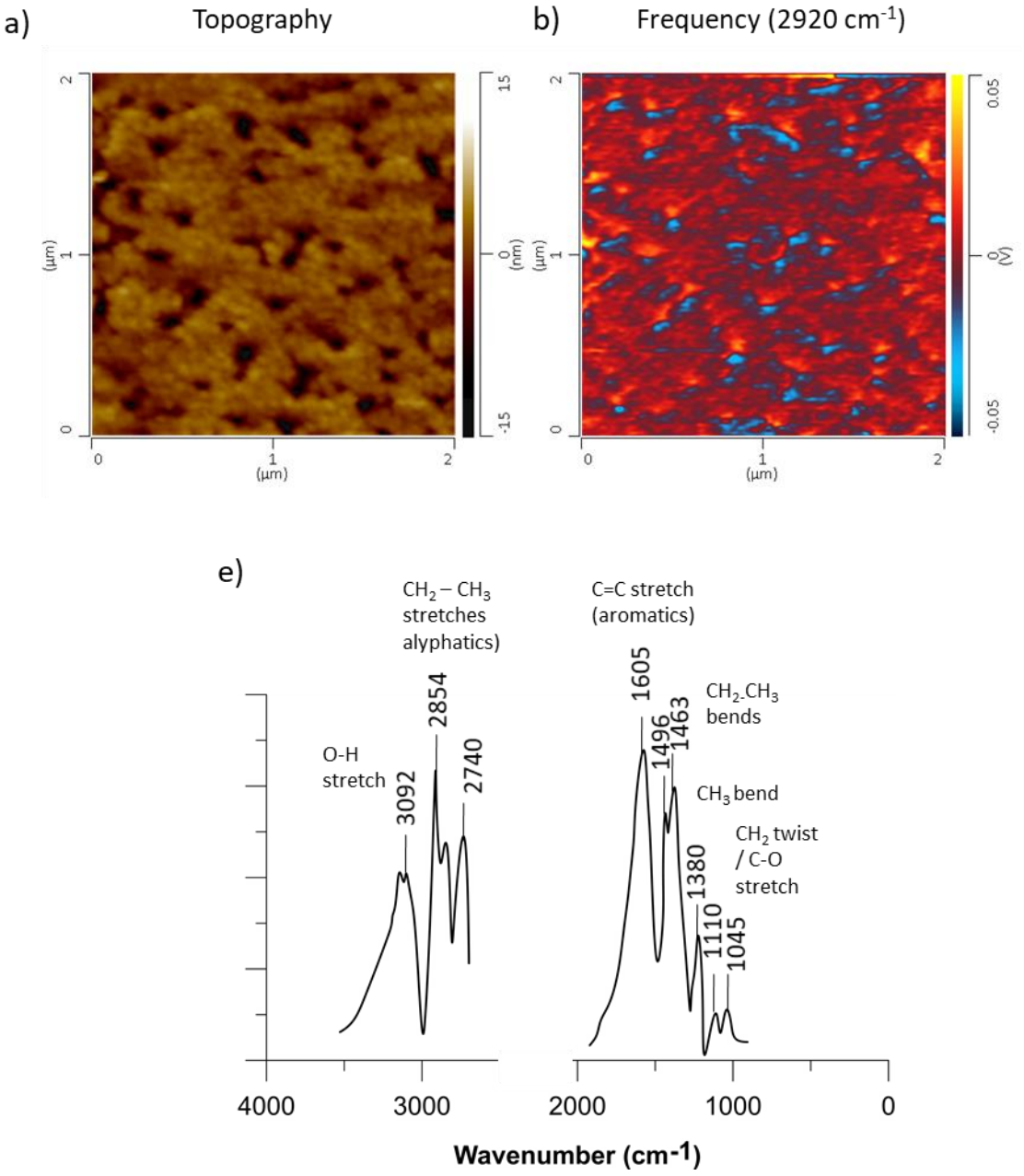

Figure 4.41: a) Topography and b) Frequency maps (b and d) at the set wavenumber 2920 cm^{-1} of a 20 x20 µm 2 x 2 µm area and d) a nano-IR spectrum reconstruction of a point on the calcite surface aged in maltene C_5. The y axis on the spectrum is the absorbance, normalised as the two spectra were taken with different lasers.

e) Calcite in maltene C_8

Calcite aged in maltene C_8 has a similar fingerprint to the calcite aged in maltene C_5. The assigned peaks are at 1040 cm^{-1}, 1120 cm^{-1}, 1459 cm^{-1}, 1602 cm^{-1} and 1710 cm^{-1} for the 912-1900 cm^{-1} laser range. In the higher range, the fingerprint is formed by peaks at 2750 cm^{-1}, 2894 cm^{-1} and a broad O-H stretch above 3100 cm^{-1} caused by the brine. The 1040 cm^{-1} and the 1120 cm^{-1} peaks are assigned to the C-O stretch band due to the presence of esters. The peak at 1459 cm^{-1} is given by the CH_2 aromatics or methylene vibrational bending, as well by the carbonate surface, and the 1602 cm^{-1} to the C=C aromatic stretching.

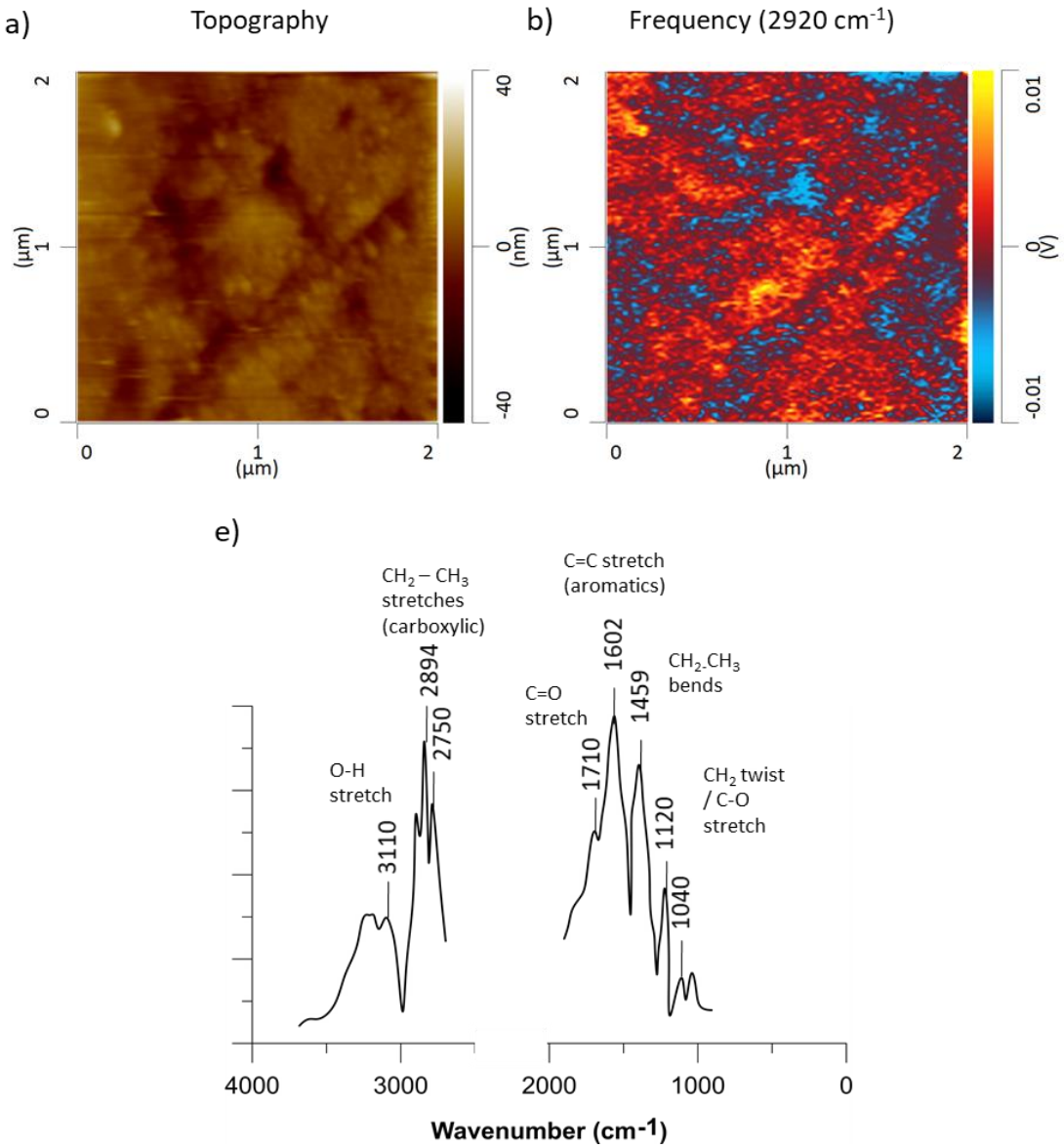

Figure 4.42: a) Topography and c) and b) Frequency map at the set wavenumber 2920 cm^{-1} of a 2 x 2 µm area and d) a nano-IR spectrum reconstruction of a point on the calcite surface aged in maltene C_8. The y axis on the spectrum is the absorbance, normalised as the two spectra were taken with different lasers.

The 1710 cm^{-1} peak is assigned to a C=O stretch typical of esters. The 2750 cm^{-1} and the 2894 cm^{-1} are assigned respectively to the CH_2-CH_3 aliphatic vibrational stretchings. Compared to the maltene c_5, the maltene C_8 presents a higher ~1490 cm^{-1} peak and lower values in the 2700 to 4000 cm^{-1} range, suggesting that the maltene C_8 is slightly richer in aromatics and depleted in aliphatics Figure 4.42.

f) Calcite in asphaltene

The fingerprint for the calcite aged in the asphaltene compound is similar to the maltene C_5 and C_8 fingerprints. The absorption peaks are seen at 994 cm^{-1}, 1110 cm^{-1}, 1430 cm^{-1}, 1595 cm^{-1}, 2866 cm^{-1}, 2960 cm^{-1} and 3060 cm^{-1}. A broad, low absorption peak caused by the acid hydroxyl group is also present between 3200 cm^{-1} and 3500 cm^{-1}. The absorption peaks at 994 cm^{-1} and at 1110 cm^{-1} are associated with the C-O stretch ester or carboxylic acids bands and the 1110 cm^{-1} peak also overlaps with the range of the functional group S=O. The 1430 cm^{-1} peak is related to the CH_2-CH_3 vibrational bend and the 1595 cm^{-1} to the C=C aromatic stretching or to N-H amines bend. The 2866 cm^{-1} and 2960 cm^{-1} peaks are assigned to the CH_2 and CH_3 aliphatic vibration groups. Compared to the maltene fractions, the asphaltene presents lower absorptions in the 2800-3000 cm^{-1} range, indicative of a lesser presence of aliphatic compounds, and a higher absorption in the 1100 cm^{-1} range, indicative of a higher presence of carboxylic acids (Figure 4.43Figure 4.44).

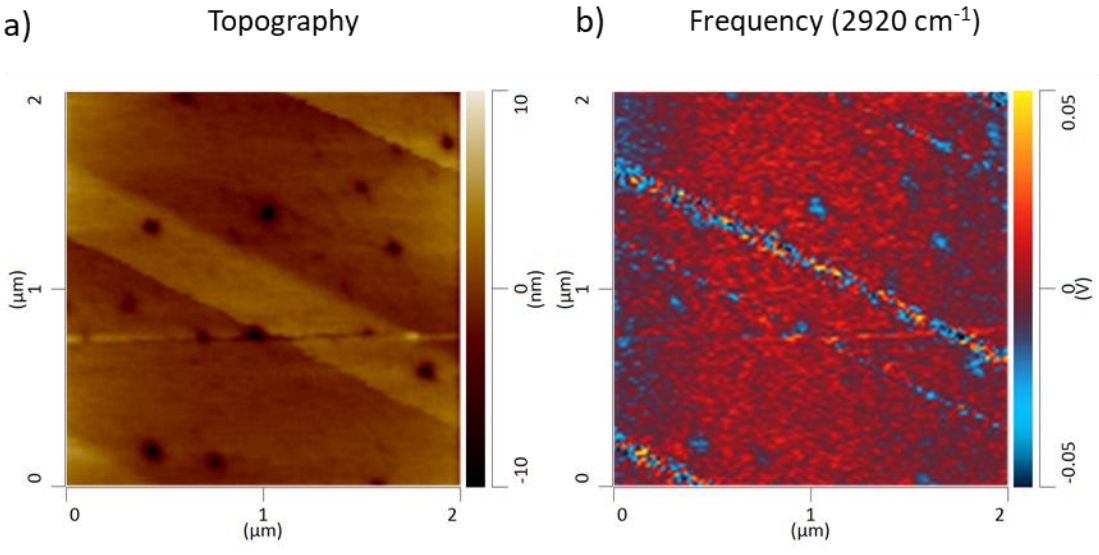

Figure 4.43: a) Topography and b) frequency map at the set wavenumber 2920 cm^{-1} of a 2 x 2 µm area.

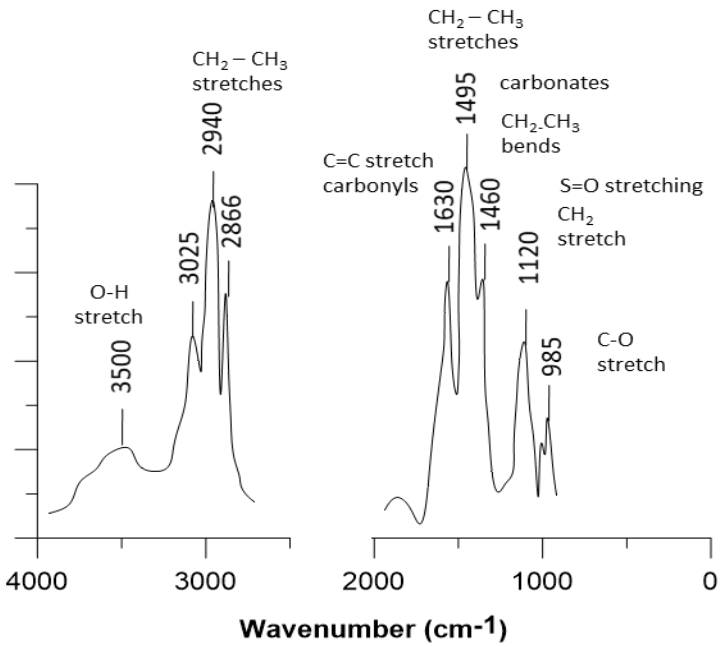

Figure 4.44: Nano-IR spectrum reconstruction of a point on the calcite surface aged in oil. The y axis on the spectrum is the absorbance, normalised as the two spectra were taken with different lasers.

g) Calcite in oil

The samples aged in calcite with unfractionated crude oil present peaks at 1040 cm^{-1}, 1120 cm^{-1}, 1377 cm^{-1}, 1460 cm^{-1}, 1494 cm^{-1}, 1622 cm^{-1}. The 1040 cm^{-1} and the 1120 cm^{-1} peaks are assigned to C-O stretch bands formed by esters or carboxylic acids bands. The latter also overlaps with the S=0 stretching in sulfonates/sulfones and to the C-N stretch in aliphatics/amines. In the high-IR laser range, absorption peaks are detected at 2866 cm^{-1}, 2940 cm^{-1}, 3025 cm^{-1} and 3200 cm^{-1}. As in the maltenes and asphaltenes, the 2866 cm^{-1} and the 2940 cm^{-1} peaks are associated with CH_2 and CH_3 aliphatic vibration groups, whereas the higher frequency peaks are assigned to the O-H stretching given by alcohols/carboxylic acids or water. Compared to the crystals aged in maltene and asphaltene, the crystals aged in oil have slightly higher transmittance relative values in the CH_2 - CH_3 bendings and stretches (~2860 cm^{-1}, 2940 cm^{-1} and ~1460 cm^{-1}) (Figure 4.45).

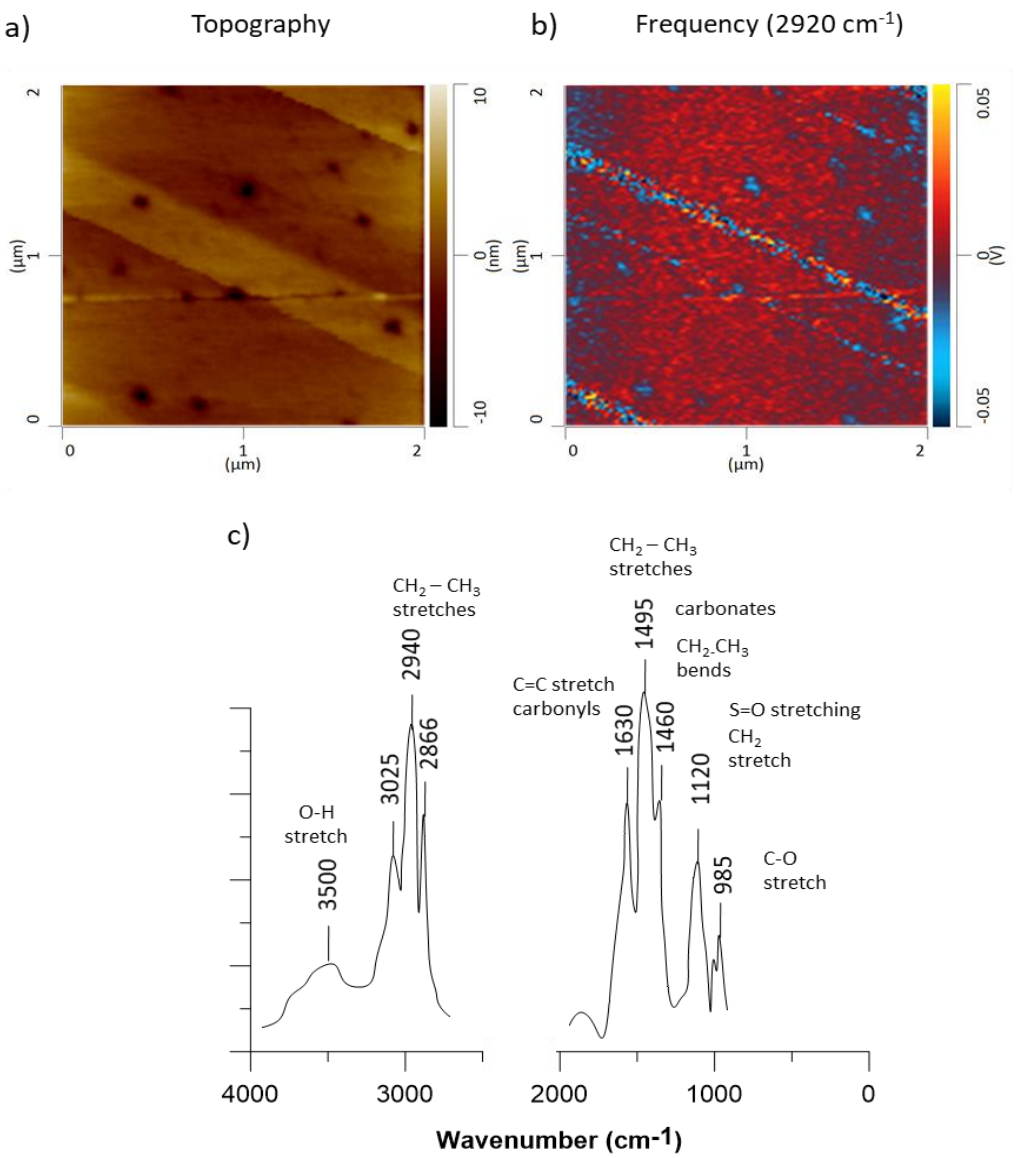

Figure 4.45: a) Topography and b) frequency map at the set wavenumber 2920 cm^{-1} of a 2 x 2 µm area and c) a nano-IR spectrum reconstruction of a point on the calcite surface aged in oil. The y axis on the spectrum is the absorbance, normalised as the two spectra were taken with different lasers.

4.4. Discussion

4.4.1. Calcite surface in contact with brine

The surface sites that can interact with species in aqueous solution or in oil are CO_3Ca^+, $CaOH_2^+$ and $CaCO_3^-$. When the calcite surface is within brine, the surface sites can interact with the ions in the solution, modifying the electrostatic potential and consequently the wettability of the mineral surface.

The solutions at which the mineral surfaces are exposed to in the reservoir are considered an important aspect in the wettability of the surfaces and also in the wettability alteration processes (Alvarez et al., 2014; Austad et al., 1997; Kumar et al., 2005b). The brine in which the samples were aged is a model Gulf of Mexico reservoir brine, containing Na^+, K^+, Mg^{2+}, Ca^{2+}, Cl^-, Si, SO_4^{2-} and CO_3^- ions. Buckley (1998), by analysing the surface zeta potential of calcite in contact with fluids, has concluded that the ions in the solution that most interact and bond with the surface ions are Na^{2+}, Ca^{2+}, Mg^{2+} and SO_4^{2-}. In particular, the presence of SO_4^{2-} is found to have a high affinity with the positive charges on the surface. When it is adsorbed on the surfaces, it lowers the positive charges and therefore also the electrostatic repulsion on the surface (Austad et al., 2010, 2005; Karoussi and Hamouda, 2008; Sakuma et al., 2014; Zhang and Somasundaran, 2006).

4.4.2. Adsorption of oil on the calcite surface

When oil is added to the system, calcite surface sites can interact with the oil polar groups (Anderson, 1986; Bennett et al., 2002; Buckley and Recovery, 1995; Kakati and Sangwai, 2018; Sand et al., 2017; Subramanian et al., 2017; Wu et al., 2017; Yang et al., 2002). There is still a debate on which oil compounds are responsible for wetting state changes. Many authors (Ese et al., 2000; Gonzalez and Travalloni-Louvisse, 1993; Langevin and Argillier, 2016; Lord and Buckley, 2002; Morrow, 1990; Mullins, 2011; Herve Toulhoat et al., 1994) have observed the most oil-wetting capacities in asphaltene-based compounds. Hoeiland et al. (2001), based also on other studies (Bennett et al., 2002; Larter et al., 2000; Larter and Aplin, 1995; Skauge et al., 1999; Takamura and Chow, 1983; Taylor et al., 1997; van Duin and Larter, 2001) suggest that it is not the oil fraction, but the number of certain kinds of molecules that is important for wetting behaviours. These authors observed that oil

compounds rich in phenols (Bennett et al., 2002; Kim et al., 2019; Larter et al., 2000; Larter and Aplin, 1995; Taylor et al., 1997; van Duin and Larter, 2001) or in organic acids (Hoeiland et al., 2001; Skauge et al., 1999) affect the wetting state changes more than high-molecular ring-structured acids. The phenols are small compounds characterised by a hydroxyl group attached to an aromatic group. The acid species are instead fatty acids, resins, or asphaltenes with a −COOH functionality. These polar molecules have enough water solubility to be able to penetrate into the water film and adsorb on the mineral surface, making the surface accessible to other, more complex, oil compounds. This is also the reason why, in the recovery phase, cationic and non-ionic surfactants are preferred to anionic surfactants as they can desorb the acidic components from the surface by forming an ion pair, favouring the oil mobility and thus wettability alterations (Heydari et al., 2018; Kumar et al., 2005; Standnes and Austad, 2003, 2000; Totland and Lewis, 2016; Wang et al., 2012).

4.4.3. Oil compound adhesion forces

e) As mentioned above, the carboxyl groups ($R\text{-}COO^-$) and the hydroxyl groups in phenol compounds are considered the "anchor" molecules for other surface-active components in the oil (Standnes and Austad, 2003; Zhang et al., 2007). The adsorption of the organic acids onto calcite occurs primarily through electrostatic attraction (Sørgård et al., 2017), whereas the other polar molecules are attracted by the carboxylic bonding onto the surface mostly through hydrophobic and dipole-dipole interactions. The more polar molecules are adsorbed to the surface, the more the surface will be oil-wet (Standnes and Austad, 2003). Therefore, the more carboxyl groups and/or phenols are present in the oil, the more the calcite surface will transition from water-wet to oil-wet. Many works have observed that asphaltenes are the oil fraction that most affects the wettability of the calcite surfaces (Buckley and Wang, 2002; Mahmoudvand et al., 2019; Mullins, 2011; Herve Toulhoat et al., 1994). Here, the adhesion values on the surfaces exposed to the maltene C_5, C_8 and the crude oil are lower (2.6, 2.7 and 2.4 nN respectively) than the adhesion forces on the calcite surfaces aged in asphaltene (4.7 nN). However, other studies (Kumar et al., 2005) have observed similarities in the adhesion forces on the asphaltene fraction and the crude oil aged mineral surfaces. The

crude oils used during the experiments, however, vary. It is possible that the difference in this case is caused by the high amounts of neutral oil fraction, which does not react as much as other polar molecules; analysing equal amounts of asphaltene and crude oil, the quantity of polar groups binding to the polar groups on the surface will thus be lower in the crude oil in respect of the asphaltene fraction. The adsorption also depends on the surface charges, which in turn depend on the chemical and thermodynamic conditions of the system (Buckley, 1998) and on the mineral surfaces analysed. Moreover, Natarajan et al., (2014) and Wang et al., (2010) suggest that the adsorption of asphaltenes onto mineral surfaces strongly depends on the concentration of asphaltenes in solution and on the time the surface was exposed to the oil fraction. In the work presented in this thesis, the adhesion forces did not show a linear increase or decrease during the same experimental session, which corresponded to the analysis of multiple areas on one sample. This provides evidence to the fact that the adhesion measured comes from the original functionalisation of the tip with the surface, and not from oil compounds stuck on the tip during the experiments.

4.4.4. The influence of brine

To test the influence of the brine on the wettability of the samples, the adhesion forces on the calcite surfaces aged in brine and then in dodecane were compared with the calcite surfaces directly aged in dodecane. The adhesion forces for the samples where the brine was in the system only during the experimental analyses slightly increase: from an average adhesion force of 0.9 nN in the samples aged in brine before, the samples aged without any brine present an average adhesion force of 1.2 nN (Figure 4.7). We here interpret the overall increase in wettability to be caused by the layer of brine between the surface and the oil compounds. This brine film contains cations and anions (i.e., Na^{2+}, Ca^{2+}, Mg^{2+} and SO_4^{2-}) that can directly be exchanged with the calcite surface and with the oil molecules, modifying the overall surface charge and reducing the available domains of adhesion for the oil to the surface (Karoussi and Hamouda, 2008; Austad et al., 2010, 2005; Sakuma et al., 2014; Zhang and Somasundaran, 2006). To consider this hypothesis, we assume that the groups in the oil interacting the most with the brine and with the mineral surfaces are polar carboxyls and phenols, (Bennett et al., 2002; Kim et al., 2019;

Larter et al., 2000; Larter and Aplin, 1995; Taylor et al., 1997; van Duin and Larter, 2001; Hoeiland et al., 2001; Skauge et al., 1999). The negative ends of the carboxyl acids can either be associated with the ions in the water film or, if the water film is discontinuous, interact with the cations on the calcite surface (Mirchi et al., 2014). Lager et al. (2008), Purswani et al. (2017), Zhang et al. (2007) established that, in presence of a brine film, the carboxylic material in the oil and the surface has weaker bonds compared to the ligand bonds between the brine and the carboxylic material. This possibly explains the difference in adhesion between the calcite aged in brine first and the calcite directly placed to age in dodecane. Figure 4.46 is a representation of possible case scenarios.

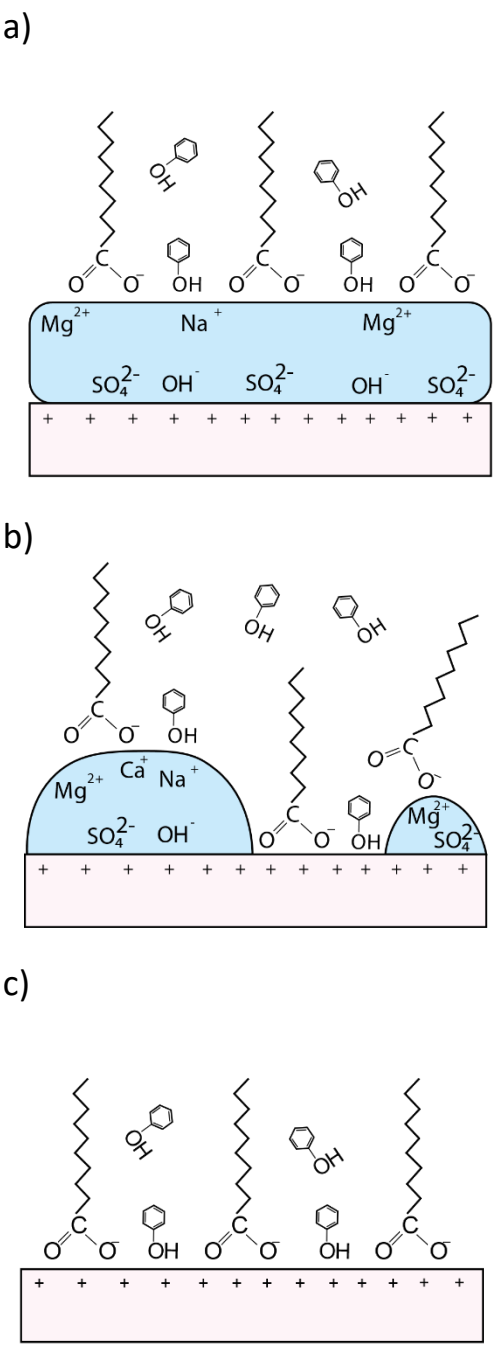

Figure 4.46: Stages of oil-wetting of a calcite surface (pink) in brine (blue). In a) the positively charged surface attracts the anions in the brine, which forms a uniform layer on the calcite surface. The oil molecules interact with the cations in the brine. In b) the phenols and the carboxyl acids in the oil break through the brine film and the polar ends form bondings with the calcite surface, rendering the surface mixed-wet. In c) the surface is completely covered by the oil. The oil molecules form robust interactions with the calcite surface and are able to displace the water layer.

4.4.5. IR spectra

The IR spectra confirm the presence of different compound classes on the surfaces of the calcite crystals. Starting from the calcite in brine and proceeding with the model oil compounds, we notice an increase in peaks associated with the increase in organic groups (Figure 4.35 andFigure 4.45). The presence of dodecane is associated to the alkane-related C-H groups. When decanoic acid is added to dodecane, fatty acid C-O and O-H bonds appear on the IR spectra. The surfaces aged in crude oil fractions are associated with an increase in C-O, O-H, C=C and C-H chemical bonds compared to the model oil compounds. These oil fractions are attributed to the presence of alkanes, aromatics and phenols. The asphaltene spectrum is similar to the maltenes spectrum but presents higher absorbances in the C-O and O-H groups peaks, associated with phenols, alcohols, paraffins and fatty acids. As seen before, the end groups in the phenols and in the fatty acids have a high affinity with the calcite surface molecules (Standnes and Austad, 2003; Zhang et al., 2007). The affinity is reflected in higher interactions with the calcite surface, and therefore in a greater destabilisation of the bonds between the water film and the calcite surface molecules. The more molecules in the oil interact with the calcite surfaces, the more the surfaces become oil-wet. In this work, the high affinity of carboxylic acids and phenols with the calcite surface polar groups is attested by the higher average adhesion forces in the asphaltenes compared to the other oil compounds. Therefore, IR confirms the presence of either individual compounds or compounds classes on the calcite surface.

4.4.6. Surface roughness

By observing the roughness of the surfaces affected by the different oil fractions, we gain important information regarding the way the oil fractions interact with the surface and the homogeneity of the oil film on the surfaces.

Both the linear regression measurements and the cross plots have highlighted in some areas a certain degree (for the 10 areas measured, an average of R^2= 0.2) of agreement between the topography and the corresponding adhesion values. The cross-correlation underlines that the topography roughness is caused by the oil droplets sticking on the

surfaces. Also, applying a high setpoint (i.e. the force applied to the tip scanning the surface), the droplets are seen to be dragged along the surface. If an area is scanned multiple times, the oil film is gradually removed from the surface, similarly to what was observed by Buckley and Lord (2003) (Figure A.8). The QI mode offered further confirmation on the presence of the oil compounds on the surfaces and provided information on the texture and distribution of the oil compounds. The same surface scanned at different setpoints also proved the compressibility of the material, with a semi-circular shape, lying directly on the completely smooth calcite surface (Figure 4.34). The existence of oil films on the calcite samples exposed to different oil compounds is also proven, for the first time, in this study by AFM-IR analyses. The AFM-IR frequency maps display a difference in absorption at a certain frequency. In this case, the 2920 cm^{-1} peak was chosen. Although the calcite surface can absorb at this wavenumber as well, the 2920 cm^{-1} peak intensity is greater in experiments in which organics interacted with the surface. This makes it possible, on a frequency map at the 2920 cm^{-1} peak, to locate the surface as opposed to the organic compounds. The frequency maps compared with the topography maps indicate that the calcite surface is coated by a ~20 to 30 nm layer of oil compounds (e.g., Figure 4.37 c), which is of variable thickness and discontinuous (i.e. Figure 4.36 a and b). The peak to valley roughness of this layer is on average of a few nanometers (<10 nm) (Figure 4.39 c). The roughness and thickness of the film coat are not found to have any correlation with the type of oil fraction analysed.

Some calcite regions, independent of the compound in which they were aged, present areas of higher adhesion close to topography features such as calcite steps. Higher adhesions along the step planes compared to the {1014} surfaces can be topography related, with more oil remaining entrapped between two steps, or also caused by the different distribution of surface charges between the calcite planes. Kim et al. (2019) observed that, when a plane contains more Ca^{2+} ions, for example, the electrostatic interactions between the surface and the oil compounds are larger, and the calcite attracts more polar anions to the surface. The negatively charged molecules are responsible for increasing adhesion forces, corresponding to more oil-wet surfaces.

4.4.7. Distribution of oil on the surface

In the samples analysed, the distribution of the oil fractions is very variable, producing a mixed wettability behaviour at the microscale. The surfaces present a complete oil coverage in some areas and scattered oil droplets in other areas of the same crystal (asphaltene sample 1.5 x1.5 μm). There are also areas on the surface where large (1-2 μm) oil droplets coexist with a continuous oil film formed by nanometric size (~10 nm high) droplets. Bertrand et al. (2002), observed a similar behaviour on alkanes absorbed on water and called this state frustrated-complete wetting. Where the film is discontinuous, the water-wetting areas can either be islands on a semi-continuous film, continuous except for some areas where droplets are present, or spread but discontinuous, producing a "branched' system of oil droplets (Figure 4.13). The latter was observed to occur in some areas in the model oil compound fractions, and it is known as the Ouzo effect. The Ouzo effect refers to a phenomenon in which the droplet formation occurs when an organic phase is diluted in water (Lu et al., 2017). Further studies must be made to understand what alters the wettability on the surface at the micro and nanoscale. Bertrand et al. (2002) suggested that the connectivity of the oil on the surfaces depends on many factors, such as the initial geometry of the surface, the surface charges, the exposure the surface has to the brine and other thermodynamic conditions. Other possible reasons are related to the attractive capillary forces between the oil molecules, i.e. the strength of the lateral interactions between the oil molecules in the interfacial film (Buckley, 1998; Buckley and Wang, 2002; Wang et al., 2017). In this work, the surface coverage percentage by means of the ~20-30 nm thick oil film increases with the increase in heavy oil fraction components (Figure 4.7). In model oil compound aged surfaces, the presence of oil droplets, as opposed to a homogeneous film, is common (Figure 4.10). The surfaces aged with crude oil and with asphaltene and maltene fractions show a higher density of droplets on the surfaces or a more uniform layer of oil compared to the model oil fractions (Figure 4.20).

In conclusion, the increase of surface coverage agrees with the increase in adhesion forces, suggesting a positive correlation between the oil fraction components and the oil-wetting behaviour in calcite surfaces. Many papers (Drummond and Israelachvili, 2002; Hassenkam et al., 2009; Mirchi et al., 2014; Yang et al., 2002) quantify the relationship

between adhesion forces and contact angle by using the relationship $W_a = \gamma_L (1+ \cos \theta)$, where W_a is the work of adhesion, γ_L is the surface tension between the fluids and θ is the contact angle at the solid surface. However, despite having quantified the adhesion forces, in this work, no relationship between adhesion forces and contact angle was made. Further work needs to be done to quantify the exact wettability of the samples.

4.5. Concluding comments

This work has provided evidence of the importance of the type of oil compounds in wettability changes and has provided a solid base for the study of the fluid migration and hydrocarbon recovery in a tight carbonate reservoir system. In particular, from this study, it can be inferred that:

1. The organic layer, independently from the compound in which the calcite was aged into, forms a heterogeneous organic film on the surface; it is possible to observe single droplets, complete or incomplete coverage of the organic film as well as an organic film with droplets on the top. The organic layer can reach up to 30 nm of thickness. Single droplets vary in size, with the smaller detectable droplet being around ~ 10 nm wide to ~ 2-3 μm wide. The height of the droplets varies from a few nm (~10 nm) to ~200 nm.
2. Oil compounds have the tendency to concentrate along the calcite steps by forming elongated and parallel droplets.
3. IR spectra confirm the presence of the oil compounds on the surface. The adding of decanoic acid to the dodecane is indicated in the IR by the presence of fatty acid vibrations. The crude oil fractions are characterised by vibrational groups typical of aromatics, fatty acids, esters and alcohols.
4. Adhesion force measurements indicate an increase in the adhesion forces in the crude oil fractions compared to the model oils. The lower values are registered in the calcite aged in brine, whereas the highest average adhesion forces are given by the asphaltene fraction (4.7 nN).
5. The percentage of surface covered by progressively higher adhesion forces increase in the crude oil and crude oil fractions compared to the model oil compounds. In particular, the highest average area percentages covered by adhesion forces higher than 4 nN is found on calcite surfaces aged in asphaltene (~ 50 %) This is also in line with the topography observations, which indicate that the number of droplets per unit area is higher in the crude oil fractions relatively to the model oil compounds.
6. The AFM-IR frequency maps validate the results given by the adhesion forces and the topography maps. The AFM-IR maps show that the oil compound forms a layer on the

surface which is sometimes disrupted, allowing for the visualisation of the calcite surface.

7. The adhesion forces are indicative of the wetting state of a surface. The calcite aged in brine, with an average adhesion force of 0.1 nN and a percentage of surface covered by adhesion forces higher than 0.5 nN of 0.4 %, displays a completely water-wet surface. The calcite aged in asphaltene, with an average adhesion fore of 4.7 nN and a percentage of surface covered by adhesion forces higher than 4 nN of 81%, is indicative of a nearly completely to completely oil-wet surface.
8. Higher adhesion forces in the asphaltene fraction are related to higher interactions between the oil groups and the surface molecules. IR data indicate that asphaltenes yield many polar groups, such as alcohols, phenols and fatty acids, which are considered responsible for the increase in adhesion forces.

Chapter 5

Nanoscale variations in surface chemistry and implications for wettability in the Eagle Ford formation

5.1. Introduction

Wettability plays a crucial role in the fluid displacement in porous media, and therefore understanding the wettability behaviour of a reservoir is essential for the full understanding of the oil recovery dynamics (Brady et al., 2016; Rabbani et al., 2018). When a reservoir is predominantly water-wet, the oil is concentrated in the larger pores and, depending on the permeability of the reservoir, it is easily displaced by the aqueous solution. However, when a reservoir is oil-wet, the oil is present in small pores and adheres onto the surfaces, rendering the displacement more difficult (Basu and Sharma, 1997). On the other hand, the emplacement of oil in the smaller pores creates a connected organic network and possible migration pathways (Basu and Sharma, 1997; Cardott et al., 2015; Hackley and Cardott, 2016). It has been established that all reservoirs, before being filled with oil, are initially water-saturated and therefore water-wet (Basu and Sharma, 1997; Hiorth et al., 2010; Salathiel, 1973; Tiab and Donaldson, 2004). After the oil enters the system, the water film covering the surfaces can be completely or partially ruptured depending on several factors, such as the physicochemical conditions, the brine chemistry, the capillary pressure, the oil chemistry and the surface chemistry and surface roughness (Hiorth et al., 2010). The effects regarding the nature of the oil have been highlighted in Chapter 4, concluding that, in accordance with other studies (Buckley, 2001; Kumar et al., 2005; Radke et al., 1992), a calcite system is more prone to become oil-

wet when the oil contains many short aromatic molecules or carboxylic acids. In this chapter, the factor that will be considered is the nature of the mineral surfaces interacting with the oil molecules. Previous works (Borysenko et al., 2009; Drummond and Israelachvili, 2002; Peng et al., 2015; Siddiqui et al., 2018) inferred that mineral surfaces present different surface properties and electrical attributes, which cause variations in the wetting behaviour of the surfaces.

5.1.1. Mineral and organic surfaces

Many studies on wettability changes caused by the mineral surfaces regard the clay mineral phase (Hilner et al., 2015; Purswani et al., 2017; Rezaei Gomari et al., 2006; Skovbjerg et al., 2013; Zhang and Somasundaran, 2006). Clay mineral surfaces are characterised by a high surface area and high surface charges, able to bear a high degree of interaction with the aqueous solution and with the oil polar groups, rendering the pore surfaces more oil-wet (Tang and Morrow, 1999). Differences between the type of clays were also observed. Borysenko et al. (2009), measuring two shale samples with different clay values, noticed that the sample with more illite was more hydrophilic than the sample bearing more kaolinite, consistent with the fact that kaolinite clays have fewer substitution sites than the illite–smectite ones (Bantignies et al., 1997; Skovbjerg et al., 2012). Silicate surfaces, on the other hand, have an acidic interface between the surface and the water layer (Tiab and Donaldson, 2004) that make the surfaces able to adsorb the basic oil constituents (i.e. nitrogen-bearing compounds). Carbonate surfaces are instead more basic, and able to adsorb more acidic compounds such as carboxyls and phenols (Buckley, 2001; Tiab and Donaldson, 2004). Since the oil compounds are generally more acidic, the carbonate-rich reservoirs have a higher tendency to be oil-wet. Apart from the mineralogical content, the wettability in a reservoir also depends on the organic matter values. Higher TOC values are typically correlated with more oil-wet surfaces (Siddiqui et al., 2018, Lan et al 2015). The higher the total organic carbon, the higher the concentrations of organic matter, which can migrate and coat the mineral compounds, altering the wettability of the system.

5.1.2. Wettability in unconventional reservoirs

The mineralogical heterogeneity at the microscale of unconventional reservoirs leads to a more complex characterization of the wettability compared to the more uniform conventional reservoirs (Alvarez and Schechter, 2016; Siddiqui et al., 2018). In general, the coexistence of different minerals and the organic matter renders the wettability mixed-wet. As stated in the previous chapters, being carbonate-rich, the Eagle Ford is not a shale play *sensu stricto*. The richness in carbonates and the presence of high amounts of coccolithic debris can juxtapose this reservoir to a chalk reservoir (Figure 5.1).

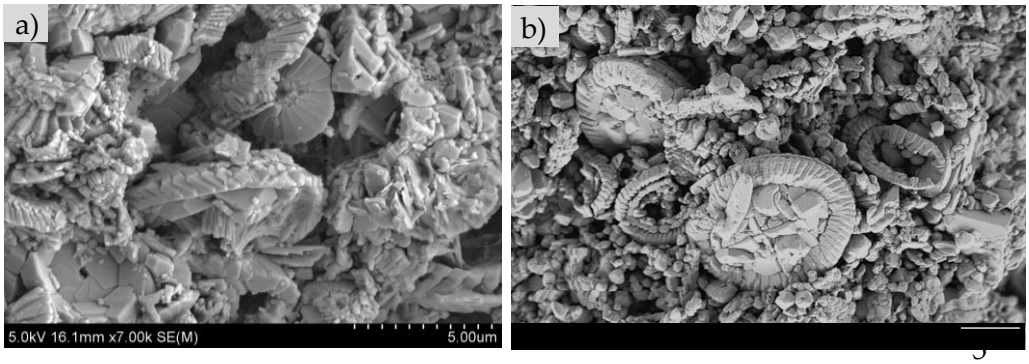

Figure 5.1: SEM micrographs of a) a zoom in the matrix of Eagle Ford sample IM2_3 (R0 0.5%) and b) Stevns Klint chalk (from Strand et al. 2007). The coccolithic debris present in the Eagle Ford is very similar to the one of the chalk sample.

Chalk systems are considered hydrophobic at the large scale (Chilingar and Yen, 1983; Strand et al., 2007), but recent studies have shown that many chalk surfaces have a nonuniform wetting behaviour (Hassenkam et al., 2009; Skovbjerg et al., 2012, 2013). It was suggested the hydrophobic patches could derive from the polysaccharides coating on the coccoliths or from nanometer-size authigenic clays attached to the coccoliths. Skovbjerg et al., (2013a, 2012) infer that both the organic film and the clays could serve as anchor points for the absorption of more organic compounds.

5.1.3. A wettability study at the nanoscale

This work is an effort to quantify the wettability at the nanoscale and to understand how the wettability varies with the variations in mineralogy and organic matter content. In characterising the wettability of shale reservoirs, several techniques have been employed such as the NMR (Odusina et al., 2011) the imbibition method (Jadhunandan and Morrow, 1991) and the contact angle method (Bai et al., 2013; Basu and Sharma, 1997; Hirasaki and Zhang, 2004; Siddiqui et al., 2018). To examine the wettability of a reservoir at the micron scale, it is also possible to use the Environmental Scanning Electron Microscope (Bennett et al., 2002; Buckman et al., 2016). However, despite providing information at the microscale on an actual rock chip surface, the ESEM does not provide quantitative results. In this study, apart from the ESEM, the Atomic Force Microscopy (AFM) will be used to quantitatively analyse fresh rock chips surfaces from the Eagle Ford Formation. The wettability is here analysed by functionalising the cantilever tip with -CH_3 groups and calculating the adhesion forces. This Chemical Force Microscopy (CFM) study, combined with ESEM preliminary examinations and SEM and chemical mapping analyses, provides a solid evaluation of the wettability and nano-surface chemistry behaviour in a heterogeneous system.

5.1.4. Wettability changes with the organic matter type

The presence of hydrocarbons migrating into a tight reservoir also raises some questions regarding the origin of the oil (Bernard et al., 2012), and whether it is the oil that has migrated the responsible for the wettability alteration. Despite many studies have been carried out in the origin of the oil, the origins of the hydrocarbons and the storage and migration of the hydrocarbons in source rocks are still not comprehensively known (Xie et al., 2005). As seen in Chapter 2, Ar-Ion polished samples analysed under the SEM, combined with bulk geochemical analyses can provide preliminary information into the understanding of the maturities at which the hydrocarbons have migrated and generated (Curtis and Ambrose, 2011; Loucks et al., 2012; Milner et al., 2010; Taheri et al., 2013). Many studies have also examined how the kerogen of an immature sample evolves if

heated at progressively higher temperatures (Horsfield et al., 1989; McCarthy et al., 2011). However, due to the micrometre-size of the organic particles in unconventional reservoirs, these studies are performed on extracted kerogen samples and not on the actual rock chips. In the recent years, the advancement of novel, high-resolution techniques, have allowed for the investigation of the geochemical composition of the organic matter in place (Bernard et al., 2012; Yang et al., 2017). Bernard et al. (2012) investigated the organic constituents of the Barnett Shale by using transmission electron microscopy (TEM) and synchrotron-based scanning transmission X-ray microscopy (STXM) nanoscale experiments. In the work of this thesis, the geochemistry of the compounds on the surface was analysed at the nanoscale with a novel approach. In a first moment, the surfaces of fresh rock chips were scanned using the AFM-IR combined with SEM-EDS chemical mapping. This to examine the variability of the organic compounds on the surface in relation to the mineralogy variability. In a second moment, polished rock surfaces were investigated, and the organic matter types identified by SEM analyses were correlated with AFM-IR analyses, similar to the work of Yang et al. (2017). The latter study was made to determine which organic matter type had generated pores and evolved during thermal maturity.

5.2. Materials and Methods

5.2.1. Samples

The samples analysed were taken from the Lower Eagle Ford Formation in South-West Texas. Prior petrographic and geochemistry analyses (see Chapter 2) have assigned to these samples 3 maturity windows: R_0 0.4-0.5%, R_0 0.9% and R_0 1.2% (respectively immature, oil and gas window).

5.2.2. Environmental Scanning Electron Microscope (ESEM)

As a qualitative analysis of the wettability behaviour on the surfaces, surfaces of Eagle Ford Formation rock chips were analysed using an Environmental Scanning Electron Microscope (ESEM).

The Philips XL30 ESEM with LAB6 gun facility at Heriot Watt University was used for the analyses. The images were collected at increasing pressures of 0.5 torr intervals up to a pressure of 6.5 torr (0.87 KPa). Around 6.5 Torr (0.87 KPa), the water humidity in the chamber reaches 100%, allowing water droplets to condensate on the surface of the samples. A voltage of 20 kV and a working distance of 6.5-7.5 mm was kept during the analyses. The magnification values during the analyses varied between 250 × and 3500 ×. The samples analysed were sample IM2_1 and sample IM2_3 from the lower maturity window (R_0 0.5%), sample OW2 from the oil window (R_0 0.9%) and sample GW6 from the gas window (R_0 1.2%) (Table 5.1). To avoid any kind of contamination, the samples were broken immediately prior to the analyses into rock chips ~ 2-3 mm thick and ~ 10 mm long. The procedure for the images collection was created by following Wei et al (2002), as in Bennett et al. (2004) and Buckman et al. (2016).

Sample Names	R_0%	TOC (wt %)	Total Silicates (%)	Total carbonates (%)	Total I/S (%)	Total Kaolinite (%)
OC2	~0.44	6.6	58.2	2.9	3.4	5.6
IM2_3	~0.55	7.9	24.2	50.1	7.2	1.8
OW2	~0.9	2.6	8.0	43.2	18.1	24.0
GW7	~1.25	0.5	4.5	84.4	12.2	0

Table 5.1: Samples analysed with the ESEM technique. Rock-Eval, TOC (wt %) and XRD data are listed (for more detail, see chapter 3). The samples were selected from different maturities, from an outcrop and from three different wells.

5.2.3. Chemical Force Microscopy (CFM)

5.2.3.1. Sample preparation

For the CFM analysis, the samples were broken in millimetre-sized rock chips. In order to study the adhesion force of the pore surfaces in the samples, rock chips were freshly cleaved. The cleavage plane corresponds to the surface of major weakness (King et al., 2015).

As the surface topography in rock chips is extremely rough (>1000 nm), before the analyses the samples were Ar-Ion polished using a Gatan precision Ion Polishing system. In order to visualise the actual surfaces, the samples were only partially polished for 30 minutes at a beam angle of 3° and a voltage of 5kV. In this way, only the highest asperities were removed and the cantilever tip was able to cover the whole z-height distance (up to ~800 nm) (Figure 5.2). Being careful not to contaminate the freshly cleaved surface, the samples were then glued on a glass surface using an epoxy glue and, positioned in a fluid cell. The fluid cell was created by placing a glass O-ring onto the glass surface surrounding the sample. For the CFM analyses, the fluid cell was then filled with a calcite saturated solution, prepared by adding calcite crystals into distilled water.

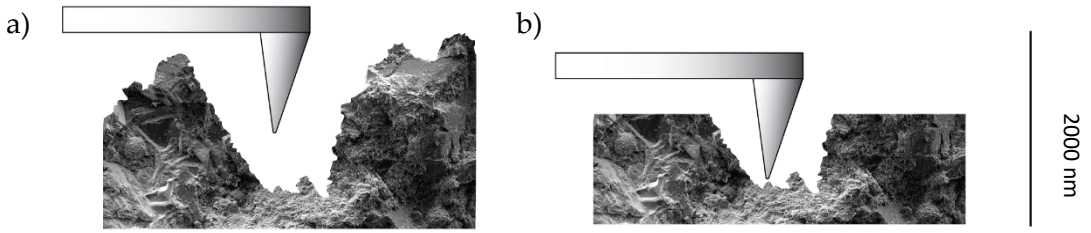

Figure 5.2: Schematic representation of the surface roughness of a rock chip a) before and b) after the Ar-Ion polishing.

5.2.3.2. Tip preparation

As described in Paragraph 4.2.5, the tips were gold coated (PNP-Tr-Au) probes from Nanoworld (spring constant 0.08 N/m). The functionalisation was performed similarly to the procedure described by Skovbjerg et al. (2012) and Hassenkam et al. (2016). The gold tips were first exposed to UV irradiation in a UV/ozone cleaner (Love et al., 2005) for 10 minutes and then immediately submerged in ethanol for 10 minutes. The tips were then submersed in an ethanol solution of 0.05 mM of $HS(CH_2)10CH_3$ for at least 24 hours. Before use, the tips were washed in ethanol and mounted on the AFM holder. This procedure leaves AFM tips functionalised with CH_3 non-polar functional group molecules that can interact with the surface (Figure 5.3).

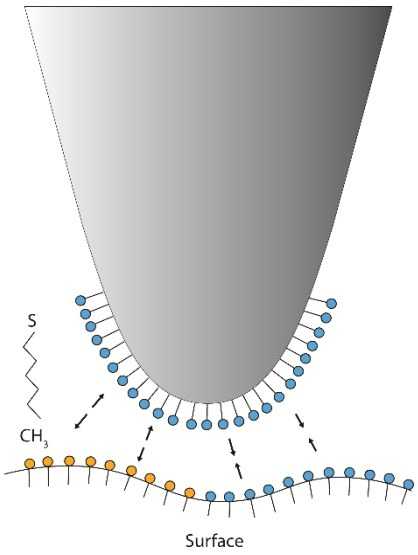

Figure 5.3: Schematic representation of gold tip functionalised using a $HS(CH_2)10CH_3$ thiol solution. The $-CH_3$ polar groups at the end of the molecule are hydrophobic (blue) and able to bond with polar hydrophobic molecules present on the surface (yellow), whereas repulsive forces occur between the $-CH_3$ groups and the hydrophilic molecules on the surface

5.2.3.3. Data collection

Before the data collection, the tip was calibrated using the calibration manager. The sensitivity and spring constant of the tip during the analyses were verified to enter in the range of the tip specifics. To ensure that the surface was smooth enough to allow the data collection, initial topography mapping was performed for each sample in air, using a PNP tip in Qi mode. For the maps, the setpoint was set to 1 and the relative setpoint to 10. For the same area, the images were first collected at a pixel size of 8 × 8 and then at a pixel size of 64 × 64, for areas of 10 μm × 10 μm.

For the CFM analyses, the functionalised gold-coated tips were used. The images were taken in contact mode in Force Mapping. This mode allows creating a force-distance curve for each pixel point, which enables to calculate the adhesion force needed to disengage the tip (Hassenkam et al. 2009) (see Figure 4.2). A set force speed of 10 μm/s and a 1-second delay during the withdrawal and a relative setpoint of 0.4 were applied for all the experiments. The images were collected in 10 μm x 10 μm areas first at a pixel size of 8 × 8 and then at a pixel size of 32 × 32 or 64 × 64. Only the images taken at a pixel size of 32 × 32 were taken into account in the adhesion force measurements.

5.2.3.4. Data processing

The data were collected using the JPK software tool. To compute an automated analysis and to extract the adhesion forces and topography parameters, the raw data was extracted and processed using Python and Matlab. Topography and adhesion maps were plotted and tables with topography and adhesion forces parameters were created. The maximum value for the adhesion forces was set to 9 nN. Higher values imply that the cantilever remains attached to the surface, without registering the real adhesion force. Looking at the different force curves, 9 nN is established as a good threshold between the real and the fictitious values.

5.2.3.5. Data correlation

Once the data were collected, the rock chips were dried and carbon coated for SEM analyses. SEM images and EDX maps of the same areas analysed with the AFM were

collected. The Hitachi SU-70 FEG SEM at Durham University was used, with an operating voltage of 10 kV, a working distance of 15 mm and a magnification of 1k ×. EDX maps of the same areas were also collected at a resolution of 1024 × 884 pixels, an energy range of 20 keV and a dwell time of 250 μs. The CFM topography and adhesion maps were then compared to the SEM images and the EDX chemical maps in order to assess the differences in adhesion forces as a function of differences in mineralogy.

5.2.4. Infrared spectroscopy (IR spectroscopy)

IR spectroscopy is a technique used to have information on the vibrational bands present in a chemical compound (El-Saleh, 1996). IR spectroscopy involves the use of infrared radiation on a material. When the IR laser interacts with the material, the photons in that material are absorbed and vibrate. The molecules have different degrees of vibrational modes, meaning that every molecule can vibrate in different ways. The vibrational modes correspond to particular bond types, which are associated with specific energies and therefore frequency of the vibrations. The combination of the vibration types at specific frequencies creates a specific fingerprint for each measured compound. The possible vibrational modes are represented in Figure 4.5. The fingerprint is a function of the frequency (or wavelength) of the light absorbed. The most studied infrared region is between 4000 cm^{-1} and 400 cm^{-1}, as most of the vibrational frequencies are in that range. However, the adsorption of the electromagnetic IR radiation only occurs when the molecule presents a dipole moment, i.e. areas of partially positive and negative charge (Fifield and Kealey, 1991; Harvey, 2000; Pavia et al., 2009; Smith, 2011). In Fourier-Transform Infrared (FT-IR) analyses, after the IR source has hit the sample and excited the molecules, the vibrations will be detected in forms of frequencies by means of a photoconductive detector. The AFM-IR methodology utilises the same IR principles, but the setting and sensitivity of the instrument differ from the original FT-IR.

5.2.5. Atomic Force Microscopy combined with a nano-IR source (AFM-IR)

Prior to the analyses, four Eagle Ford rock chips from the three maturity windows (Table 5.1) were Ar-Ion polished using a Gatan precision Ion Polishing system for 5 hrs at a beam

angle 3° and 5kV. A nanoIR2 system (Anasys Instruments, Santa Barbara, CA) at Bruker, Karlsruhe, DE, was used to analyse the chemistry of the organic compounds in the samples. For the analyses, two IR tunable laser sources with different wavelength ranges were chosen. For the 2700-4000 cm^{-1} wavenumber range (high-range), a Fastspectra OPO laser was used and for wavenumbers comprised between 900 and 1900 cm^{-1} (mid-range), a PointSpectra QCL laser was used.

A gold-coated contact mode tip was used for the whole set of experiments. The metal coating allows the generation of an electric field on the tip, which intensifies the incident radiation (Dazzi and Prater, 2017). To calibrate the instrument and test the working method, a pmma (polymethyl methacrylate) test sample was first used. After the collection of the background spectra, the IR laser was tuned in 4 different spectra ranges between 900 and 1900 cm^{-1}, and in 1 spectra range for wavelengths between 2700 and 4000 cm^{-1}. This in order to provide more accurate results and to focus the laser onto the correct vibrational frequencies. As the IR sources are different, the data with the two lasers must be acquired in separate moments. The background spectra collection and the frequency tuning were performed before examining every sample. All the IR spectra were smoothed using the Savitzky-Golay algorithm with a three-point average in the Anasys instruments software Analysis studio and the two laser spectra were plotted in the same diagram normalising the frequency to the corresponding incident power. The chosen resolution was 4 cm^{-1} for the mid-range wavelength interval and 10 cm^{-1} for the high-range. For the chemical mapping of one area at a specific frequency, the 1630 cm^{-1} and the 2920 cm^{-1} wavelengths were chosen. These wavelengths correspond to the C=C aromatic vibration and to the CH_2 aliphatic stretching respectively. These absorbance bands were chosen as they are commonly found in organic compounds. The mapped areas were selected by looking at low-resolution SEM maps acquired prior to the AFM analysis using a Hitachi SU-70 FEG SEM. The maps were taken at a magnification of 200 ×, an accelerating voltage of 10 kV and a dwell time of 3 μs. The resolution was 512 × 442 pixels. The SEM maps allowed to locate the spots on the surface where different types of organic matter were present. For each sample, at least 4 areas of variable sizes presenting organic matter were analysed. To validate the results, the IR spectra point analysis was repeated two times for each different organic matter compound. Aliphatic to aromatic ratios were also calculated

using *Craddock's* method (Craddock et al., 2015); the relative the A-factor is here defined by the changes in intensities of IR absorbance bands between the aliphatic C-H and the aromatic C=C stretching vibrations at 1430 and 1600 cm^{-1} respectively.

Sample Names	Min adhesion force (nN)	Max adhesion force (nN)	Average adhesion force (nN)	R_0%	TOC (wt %)	Total Silicates (%)	Total carbonates (%)	Total I/S (%)	Total Kaolinite (%)
OW2_area1_1	0.021	9.000	1.896						
OW2_area1_2	0.000	8.718	3.349						
OW2_area1_3	0.000	2.300	0.860						
OW2_area2_2	0.016	6.528	0.785						
OW2_area2_3	0.000	5.820	0.890	0.44	2.6	8	43.2	0.8	3.9
OW2_area3_4	0.018	4.339	0.745						
OW2_area3_5	0.023	9.000	0.790						
OW2_area3_6	0.021	8.352	0.609						
OW2_area4_1	0.017	8.048	1.037						
OW2_area4_3	0.028	8.082	1.328						
GW2_area1_7	0.010	9.000	0.297						
GW2_area1_8	0.014	3.042	0.178						
GW2_area1_10	0.010	2.887	0.382						
GW2_area2_1	0.006	3.846	0.292						
GW2_area3_2	0.012	4.406	0.413						
GW2_area3_1	0.013	2.849	0.433	0.5	2.3	13.1	82.9	1.4	1.6
GW2_area3_2	0.011	3.353	0.353						
GW2_area4_2	0.016	1.772	0.155						
GW2_area4_3	0.012	3.394	0.342						
GW2_area5_4	0.009	9.000	0.327						
GW2_area5_6	0.013	9.000	0.357						
H3A4_area1_1	0.013	9.000	0.592						
H3A4_area1_2	0.000	9.000	2.883						
H3A4_area1_3	0.020	8.795	1.127						
H3A4_area1_4	0.000	7.601	1.806						
H3A4_area3_1	0.022	6.333	2.033						
H3A4_area4_1	0.009	3.040	0.360	1.2	0.7	5.4	90.7	1.4	0
H3A4_area4_2	0.011	3.010	0.560						
H3A4_area4_6	0.012	3.164	0.391						
H3A4_area4_8	0.012	3.417	0.500						
H3A4_area5_1	0.007	5.003	1.095						
H3A4_area5_3	0.009	5.427	0.900						

Sample Names	Min adhesion force (nN)	Max adhesion force (nN)	Average adhesion force (nN)	R_0%	TOC (wt %)	Total Silicates (%)	Total carbonates (%)	Total I/S (%)	Total Kaolinite (%)
H3A5_area1_9	0.090	9.000	1.162						
H3A5_area2_5	0.014	6.590	0.670						
H3A5_area3_8	0.014	6.034	0.434						
H3A5_area3_9	0.010	7.137	0.576						
H3A5_area3_10	0.012	7.993	0.416	1.2	6	10.6	50.7	21.8	1.3
H3A5_area5_7	0.012	9.000	1.051						
H3A5_area5_11	0.015	7.078	0.297						
H3A5_area6_10	0.013	9.000	0.233						
H3A5_area6_11	0.020	5.923	0.618						
H3A5_area6_12	0.010	9.000	0.320						
IM2_3_area1_1	0.000	9.000	3.938						
IM2_3_area1_2	0.006	9.000	4.113						
IM2_3_area1_3	0.155	9.000	5.297						
IM2_3_area1_4	0.335	7.665	4.263						
IM2_3_area2_1	0.161	9.000	3.887						
IM2_3_area2_2	0.104	9.000	2.470						
IM2_3_area2_4	0.235	4.126	0.666						
IM2_3_area2_5	0.289	3.123	1.236						
IM2_3_area3_1	0.026	9.000	0.099						
IM2_3_area3_2	0.157	5.120	0.459						
IM2_3_area3_3	0.059	6.773	1.658						
IM2_3_area3_4	0.569	8.633	3.459	0.5	7.9	24.2	50.1	7.2	1.8
IM2_3_area4_1	0.365	6.558	1.269						
IM2_3_area4_2	0.257	6.480	1.987						
IM2_3_area4_3	0.316	7.554	1.327						
IM2_3_area4_4	0.215	8.125	2.559						
IM2_3_area5_1	0.037	4.666	3.598						
IM2_3_area5_2	0.026	5.168	6.991						
IM2_3_area5_3	0.259	6.597	5.160						
IM2_3_area5_4	0.000	9.000	0.055						
IM2_3_area6_1	0.099	5.668	4.668						
IM2_3_area6_2	0.369	9.000	3.547						
IM2_3_area6_3	0.054	9.000	1.326						
IM2_1_area1_1	0.007	4.114	0.629						
IM2_1_area1_2	0.000	4.262	0.779						
IM2_1_area1_3	0.008	2.223	0.284						
IM2_1_area1_4	0.008	3.316	0.308						
IM2_1_area2_1	0.013	2.560	0.343	0.5	5.8	33.2	36.3	6.6	12.9
IM2_1_area2_2	0.011	3.651	0.382						
IM2_1_area2_3	0.014	2.691	0.582						
IM2_1_area2_4	0.094	3.798	0.727						
IM2_1_area2_5	0.013	6.866	1.371						
IM2_1_area2_6	0.013	6.866	1.371						

Table 5.2: List of samples used in the CFM analysis with the minimum, maximum and average adhesion force value (nN) for each 10 x 10 μm area analysed. Thermal maturity, TOC (wt %) and XRD data (%) are also listed.

5.3. Results

The samples were analysed with a suite of techniques that enabled to have a better understanding on the surface properties in relation to the mineralogy, the organic content and organic chemistry. The possibility of analysing samples at different thermal maturities is also providing insights on the evolution of the wettability of the system in relation to the evolution of the organic matter.

5.3.1. Environmental Scanning Electron Microscope (ESEM)

Freshly cleaved rock chips from an outcrop sample (OC_2, R_0 0.5%) and from three different wells were analysed using the ESEM (Table 5.1). The behaviour of the water condensed onto the surfaces of the samples can provide information on the hydrophilicity or hydrophobicity of the different mineral surfaces of the rock chips.

Three images of a foram test from an outcrop sample (OC_2, R_0 0.5%) were taken at intervals of 1 minute (Figure 5.4). The water droplets are observed to condense onto the surface and to rapidly spread, completely covering the surface of the foram (Figure 5.4 c). The sequence indicates a hydrophilic behaviour of the calcitic mineral, also seen in Figure 5.5 (sample IM2_3, R_0 0.5%). The minerals surrounding the broken chamber of the foram are not distinguishable. Figure 5.6 (sample IM2_3, R_0 0.5%) focuses on the heterogeneous matrix. At intervals of 1 minute per image, the water gradually coats most of the minerals, leaving kaolinite plates and small silt grains uncovered. The different wetting of the surfaces underlines a higher hydrophobicity of the quartz and of the kaolinite.

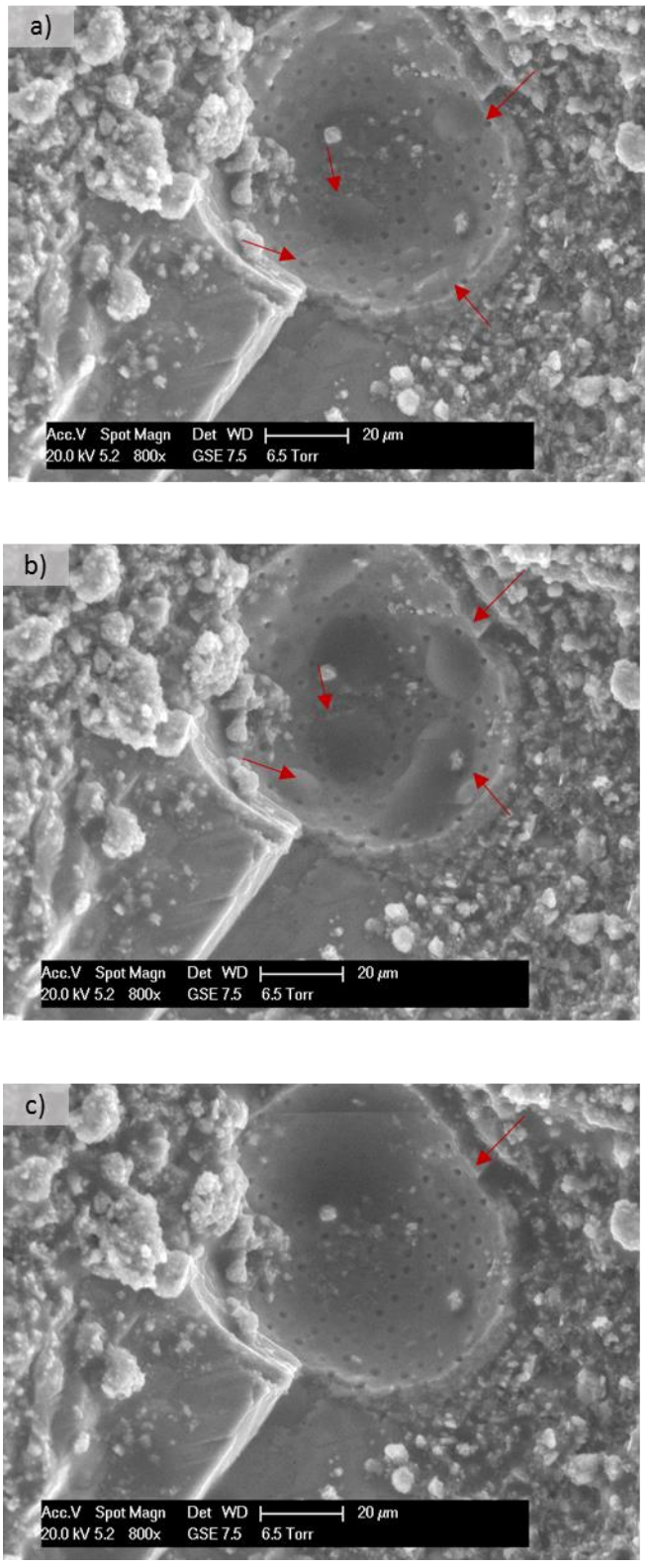

Figure 5.4: Sequence of ESEM images of a foram test in sample OC_2 (R_0 0.5%) taken at intervals of 1 minute. In a) red arrows indicate the water droplets on a smooth , concave foram test. In b) the droplets start to increase in size and spread and in c) they cover uniformly the whole foram chamber.

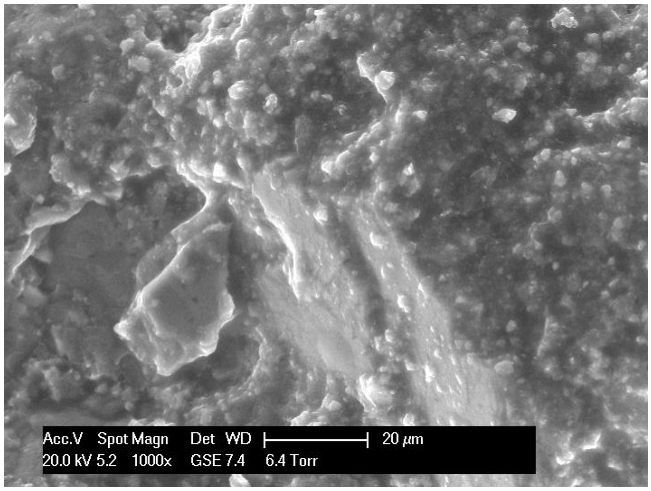

Figure 5.5: ESEM image of a calcite surface in sample IM2_3 (R_0 0.5%). The smooth surface appears to be completely covered by water.

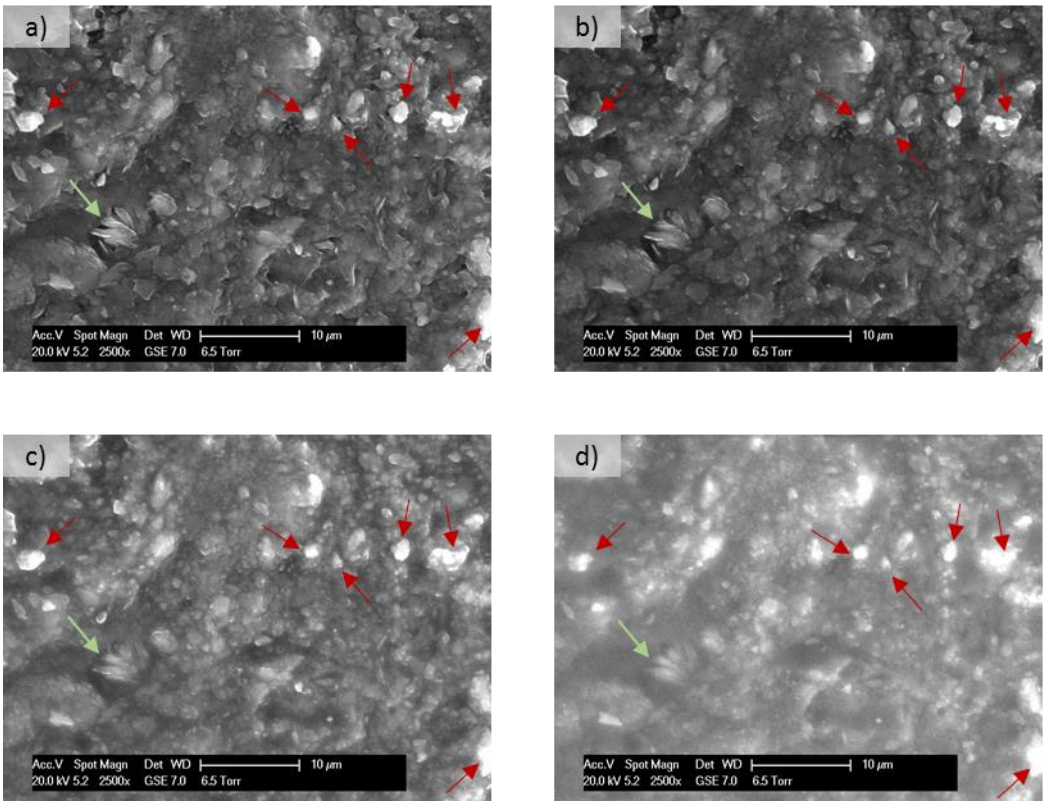

Figure 5.6: ESEM image sequence of the heterogeneous matrix in sample IM2_3 (R_0 0.5%).The silicate sub-angular grains (red arrows) and the kaolinite plates (green arrow) remain uncovered by water, indicating a more hydrophobic behaviour compared to the rest of the matrix

In Figure 5.7 (sample OW2, R_0 0.9%), within the matrix a coccolith, silicate sub-angular minerals and a pyrite framboid were identified. The coccolith results completely covered by water, whereas the silicates and the pyrite framboids remain exposed. This indicates that the pyrite and silicates have a similar hydrophobicity, whereas the carbonate material is less hydrophobic. Figure 5.7 (a) and (b) are interpreted to show large (> 50 μm) calcite cement crystal surfaces of a high maturity sample (sample GW7, R_0 1.2%). The droplets on the smooth surfaces are indicative of a more oil-wetting behaviour compared to the calcite surface in Figure 5.5 (sample IM2_3, R_0 0.5%).

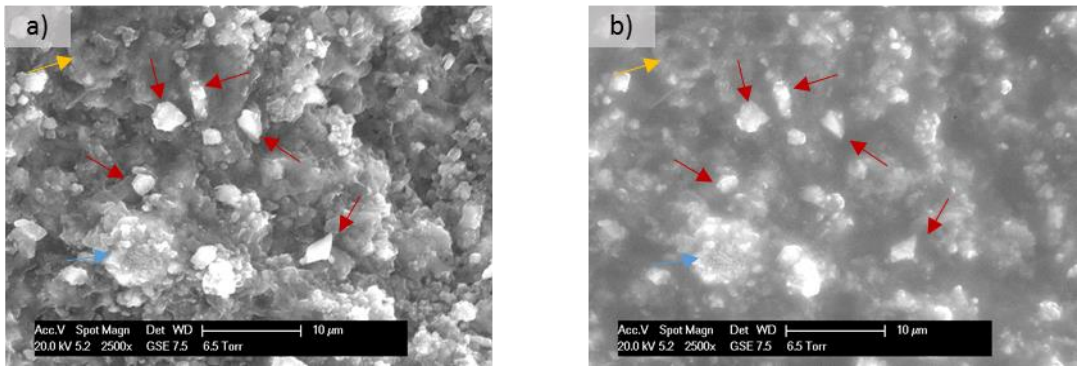

Figure 5.7: ESEM image sequence of the heterogeneous matrix in sample OW2 (R_0 0.9%).The silicate sub-angular grains (red arrows) and a pyrite framboid (blue arrow) are not covered by water unlike the rest of the matrix, indicating an hydrophobic behaviour. The coccolith (orange arrow) is instead completely covered by water, indicative of a more hydrophilic behaviour.

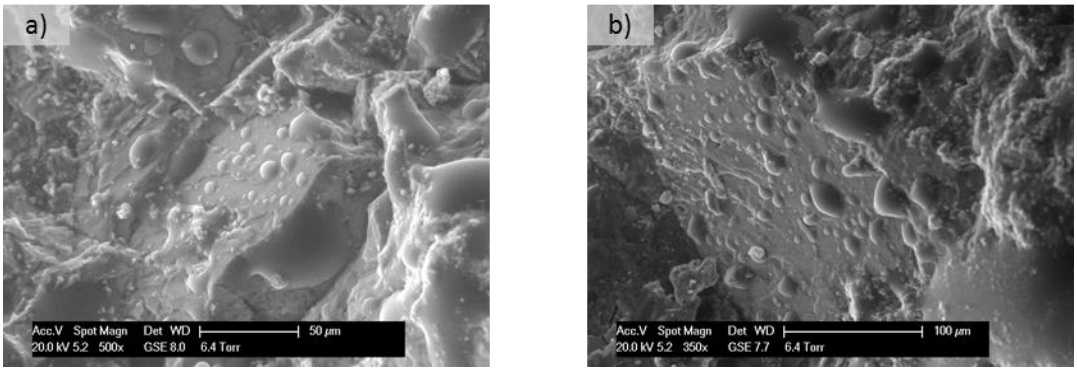

Figure 5.8: ESEM images of calcite cement surfaces in sample H3A_7 (R_0 1.2%). Both the figures show a surface with water droplets that are not spreading onto the surface, indicating a hydrophobic behaviour.

5.3.2. Chemical Force Microscopy (CFM)

Four samples from the immature window (R_0 0.44%-0.5%) and two samples from the gas window (R_0 1.2%) were analysed using the chemical force microscopy as a means to understand the wettability changes (Table 5.2). To obtain as accurate as possible analysis of natural pore surfaces, the surfaces analysed were freshly cleaved rock chips.

5.3.2.1. Overall adhesion force measurements

The overall results from the CFM experiments do not show any trend with the increase in maturity (Figure 5.9). The average adhesion values for the adhesion forces in the areas analysed range between 0.3 nN for sample GW2 to 2.3 nN in sample IM2_3. The variations in the adhesion forces within the same areas are significant (Table 5.2), whereas there is no relationship between the average adhesion forces and the maturity of the samples. This indicates that in these samples the adhesion forces depend on nanometric variations rather than on maturity differences. The TOC (wt %) values exhibit a moderate correlation (R^2=0.32) with the adhesion forces values, suggesting that the adhesion forces could be correlated to the amount of oil that has migrated within the porous network of the samples. Another possibility is that with more organic matter in the system there are more chances of analysing an adhesive organic matter phase.

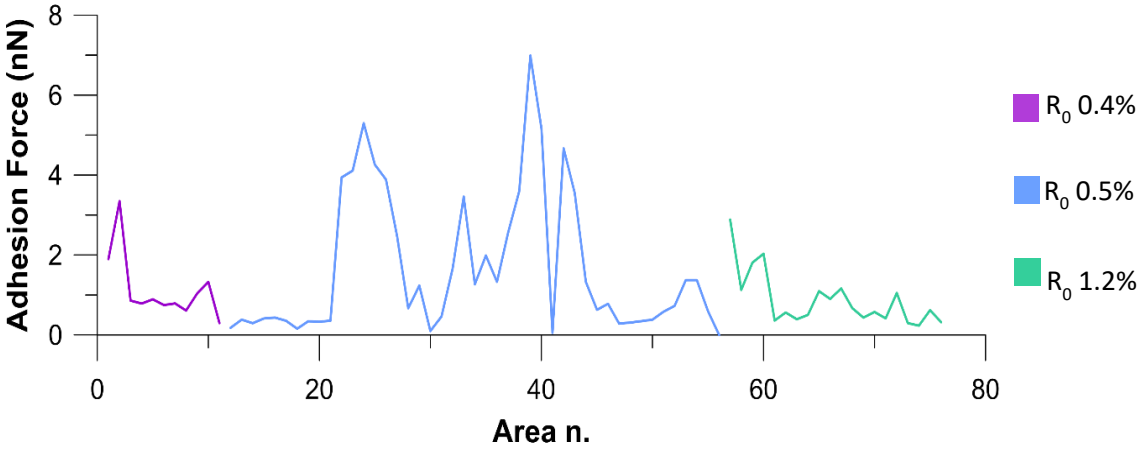

Figure 5.9: Average adhesion force for all the areas analysed, distinguished by thermal maturity. The highest average adhesion forces are found in the immature window (R_0 0.5%). There is no trend with the average adhesion forces and the increase in maturity.

5.3.2.2. Topography and adhesion forces correlation

For all the areas, a cross-correlation between the topography and the adhesion force was made. The cross-plots did not show any correlation in any of the areas analysed. In Figure 5.10, two examples of cross-plots for two of the samples analysed.

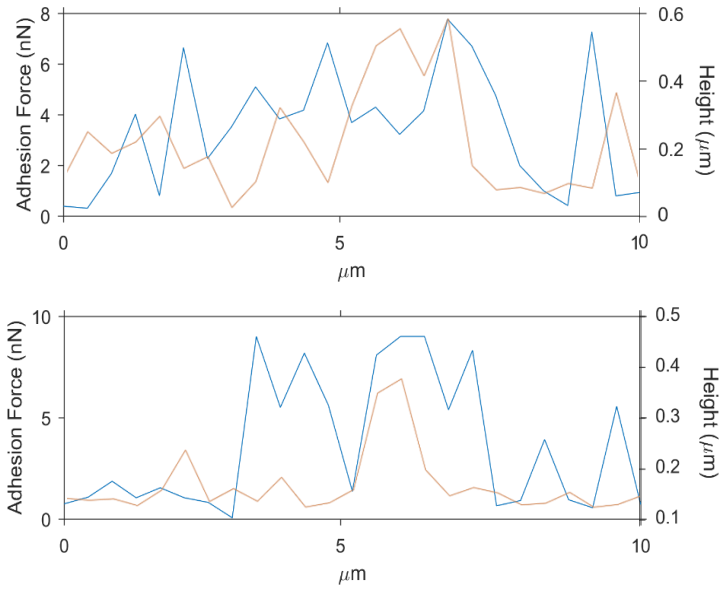

Figure 5.10: Cross-correlation between the topography (red) and the adhesion (blue) plots taken over the same line of a) sample H3A4 (area 4_6) and b) sample IM2_3 (area 1_4).

5.3.2.3. Adhesion force values and SEM maps

As mentioned in the previous paragraph, each area analysed with the chemical force microscope exhibits differences in values. To better understand whether the changes in adhesion force values are determined by mineralogical or organic constraints, CFM topography and adhesion maps were correlated with SEM and SEM-EDS chemical maps. The correlation was performed on one or two areas for each of the samples. Figure 5.11 displays a coccolith within the matrix in sample IM2_3 (R_0 0.5%). The matrix is formed by clays, quartz, pyrite and carbonate minerals and organic matter. The higher adhesion values are noticed in the lower topographic areas, i.e. within the coccolith and in the matrix, presumably in a pore throat. The higher adhesion values (4 nN) are correlated to the presence of clays (kaolinite) mixed with organic matter within the coccolith (darker colour) and to the presence of organic matter.

In Figure 5.12, two other topography lows are observed in both the CFM topography and in the SEM map. The adhesion maps report the maximum adhesion forces (3.8 nN) in the topography lows. SEM-EDS maps of the same area underline the presence of C and S, typical of organic matter, in the same areas, suggesting that the topography lows correspond to exposed pore surfaces, possibly connected to each other, containing organic carbon.

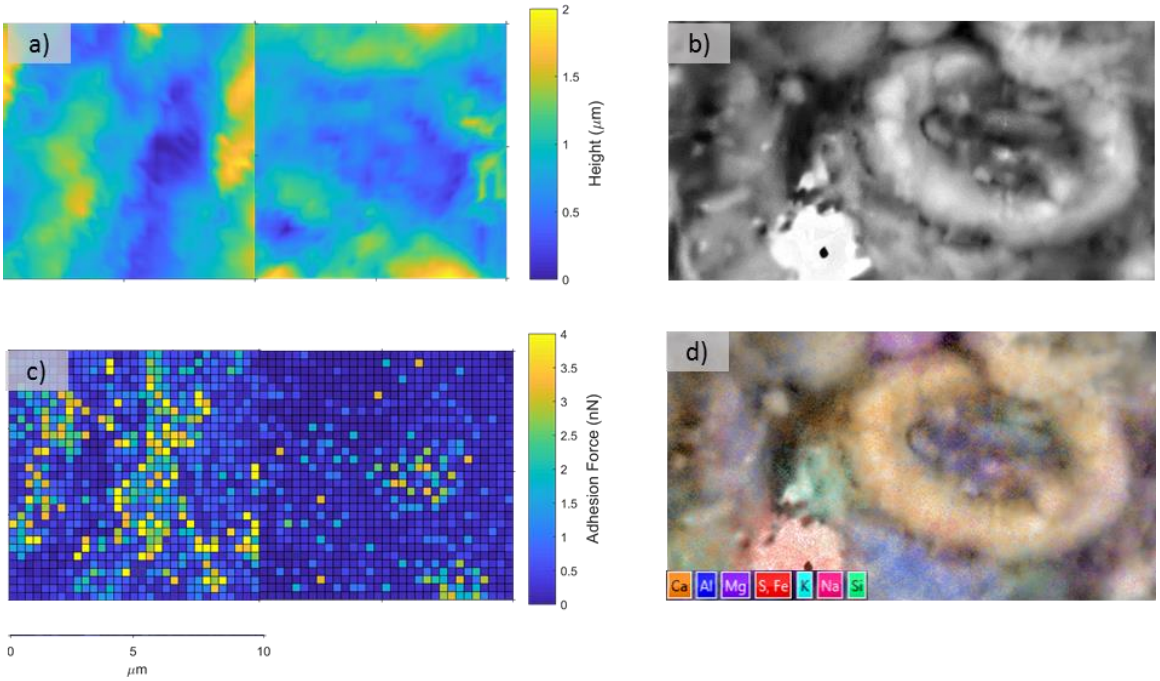

Figure 5.11: CFM rock chips experiments of sample IM2_3 (R_0 0.5%). a) is a topographic CFM map, b) is an SEM image of the corresponding area, c) is the CFM adhesion force map and d) is the SEM-EDS corresponding chemical map.

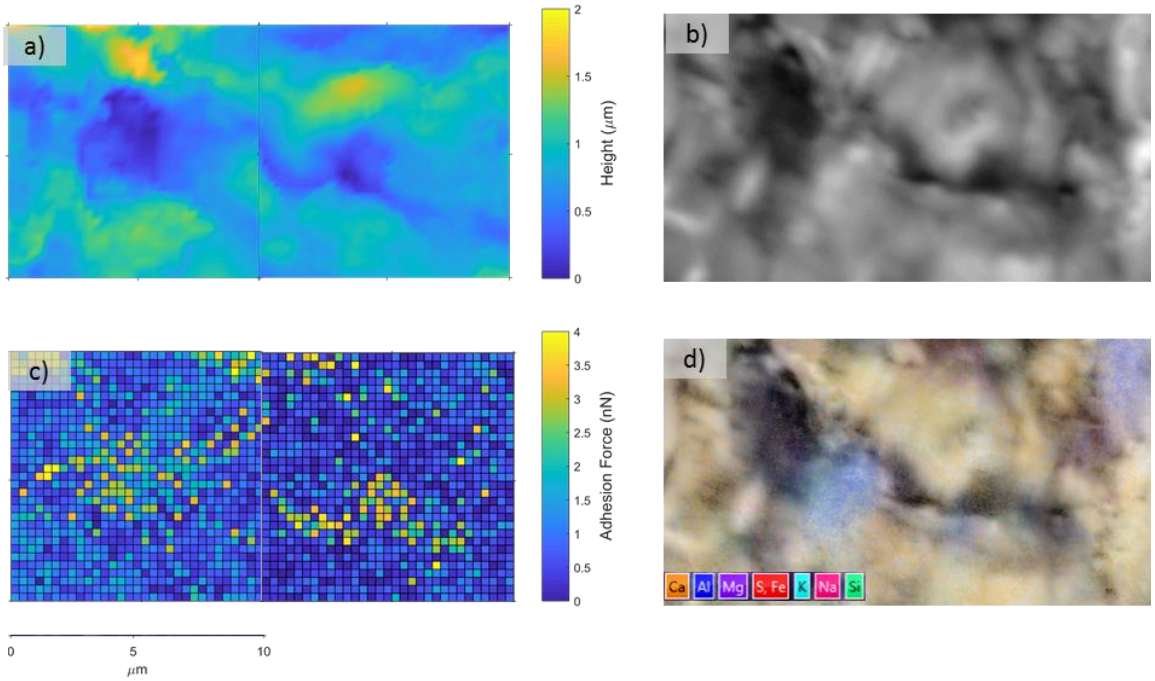

Figure 5.12: CFM rock chips experiments of sample IM2_1 (R_0 0.5%). a) is a topographic CFM map, b) is an SEM image of the corresponding area, c) is the CFM adhesion force map and d) is the SEM-EDS corresponding chemical map.

The rest of the area analysed presents adhesion values between 0 and 2.2 nN, which do not correlate to any specific mineral. Figure 5.13 (b) is an image of an area of sample H3A3 (R_0 1.2%), showing a coccolith within a heterogeneous matrix. The SEM-EDS map indicates the presence of a predominantly carbonate matrix, with traces of quartz and clay minerals. The adhesion force map shows values comprised between 0 nN and 1.5 nN in the carbonate and siliciclastic matrix, between 2 and 4 nN in areas where kaolinite and pyrite minerals are present. Within the coccolith, the high adhesion values correlate instead to the presence of a bituminous phase, indicated by the C and S in the SEM-EDS maps.

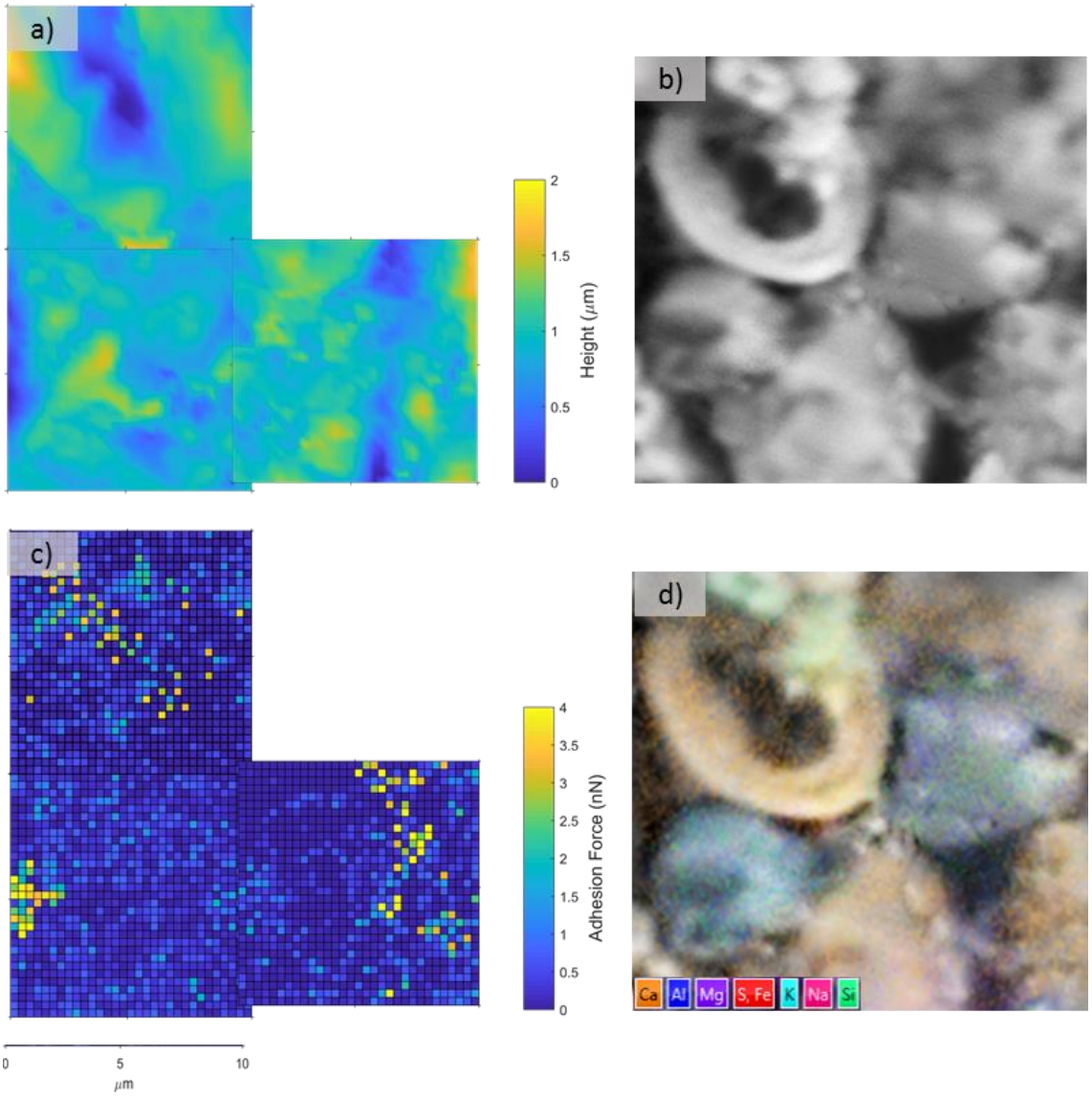

Figure 5.13: CFM rock chips experiments of sample H3A3 (R_0 1.2%). a) is a topographic CFM map, b) is an SEM image of the corresponding area, c) is the CFM adhesion force map and d) is the SEM-EDS corresponding chemical map.

The higher adhesion values on the kaolinites and pyrites compared to the carbonates are indicative of a more oil-wet behaviour of the former to the latter, as also suggested by ESEM analyses (see paragraph 5.3.1). Figure 5.14 shows the heterogeneous matrix of sample OW2 (R_0 0.44%). The adhesion values in the area vary between 0.01 and 4.3 nN. The higher adhesion values are correlated to the presence of kaolinite clays. The silicates show slightly higher (~1 nN) values compared to the carbonates. The lack of high adhesion values within the topography lows and the scarcity of concentration of C and S in the SEM-EDS maps suggest that organic carbon is not present in these areas.

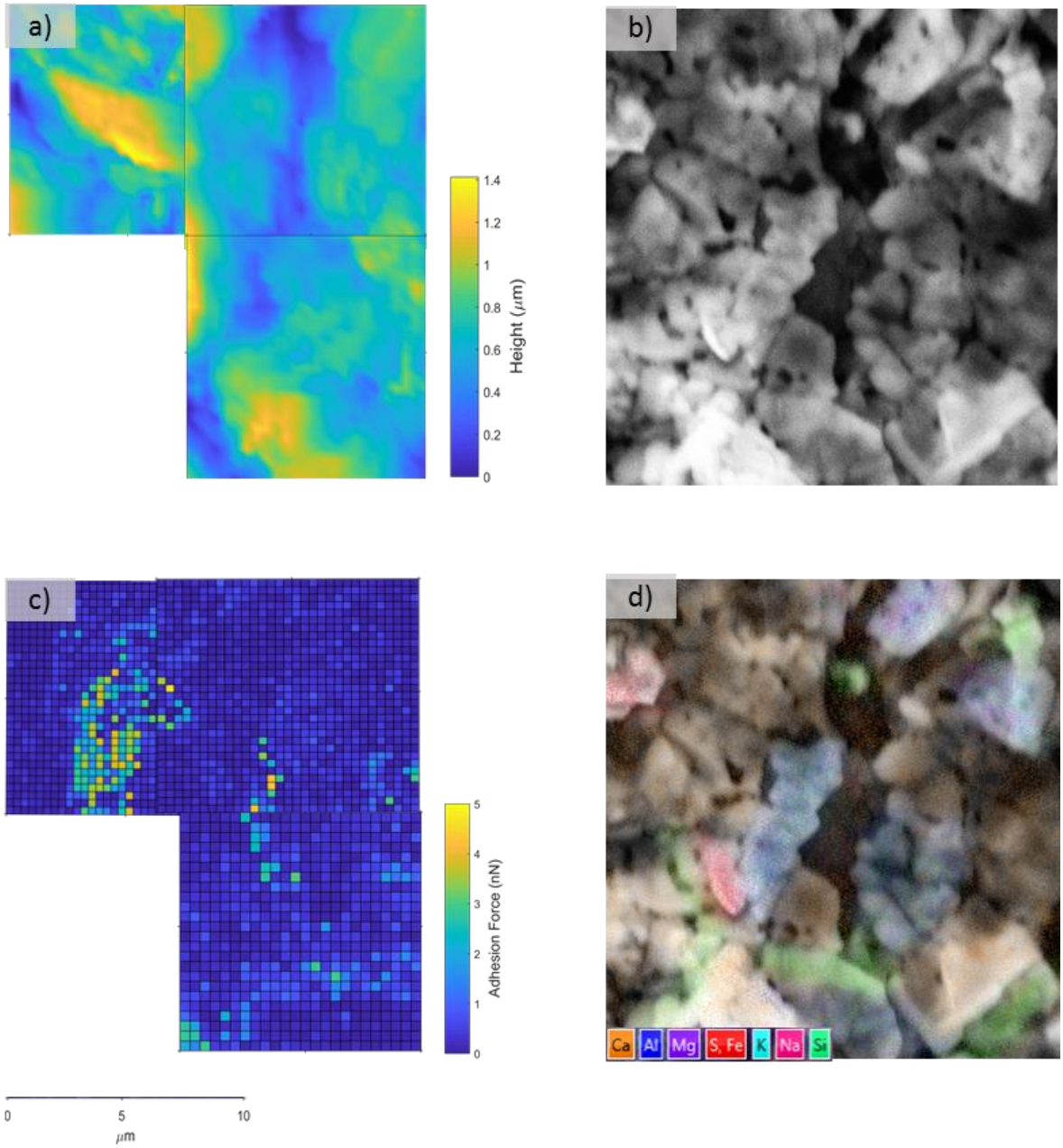

Figure 5.14: CFM rock chips experiments of sample OW2 (R_0 0.4%). a) is a topographic CFM map, b) is an SEM image of the corresponding area, c) is the CFM adhesion force map and d) is the SEM-EDS corresponding chemic

5.4. AFM-IR measurements on rock chips

In order to have an insight on which oil molecules adhere the most to the mineral phases, preliminary AFM-IR tests were performed on freshly cleaved rock chips. The same areas of the rock chips were also analysed with the SEM and SEM-EDS to correlate the mineral surfaces with the organic molecules on the surfaces.

The preliminary tests were taken on a rock chip of sample H3A5 (R_0 1.2%). The rock chip was partially polished with the same procedure as the samples analysed with the CFM method. The two topography maps (Figures 5.15 and 5.16 a) indicate an inhomogeneous, rough surface (1000 to 1200 nm). The frequency maps (Figures 5.15 and 5.16 b) were taken at a frequency of 2920 cm^{-1}, corresponding to CH_2 aliphatic stretches. The colours on the maps are representative of the relative values in the absorbance peaks. Warm colours (i.e. yellow and red) are indicative of a higher absorbance at 2920 cm^{-1}.

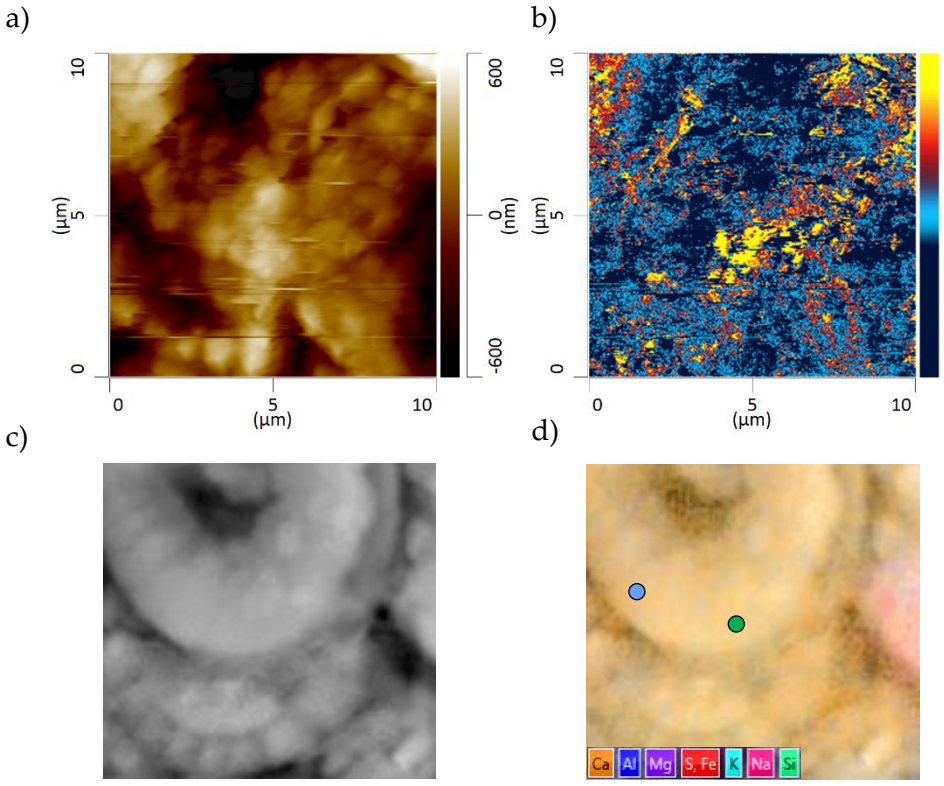

Figure 5.15: Area 1 of an AFM-IR rock chips experiment of sample H3A5 (R_0 1.2%). a) a topographic CFM map, b) is a CFM adhesion force map, c) is a BSEM image of the corresponding and d) is the SEM-EDS corresponding chemical map. The two dots in figure d) are the two locations were point-IR analyses were made (Figure 5.17).

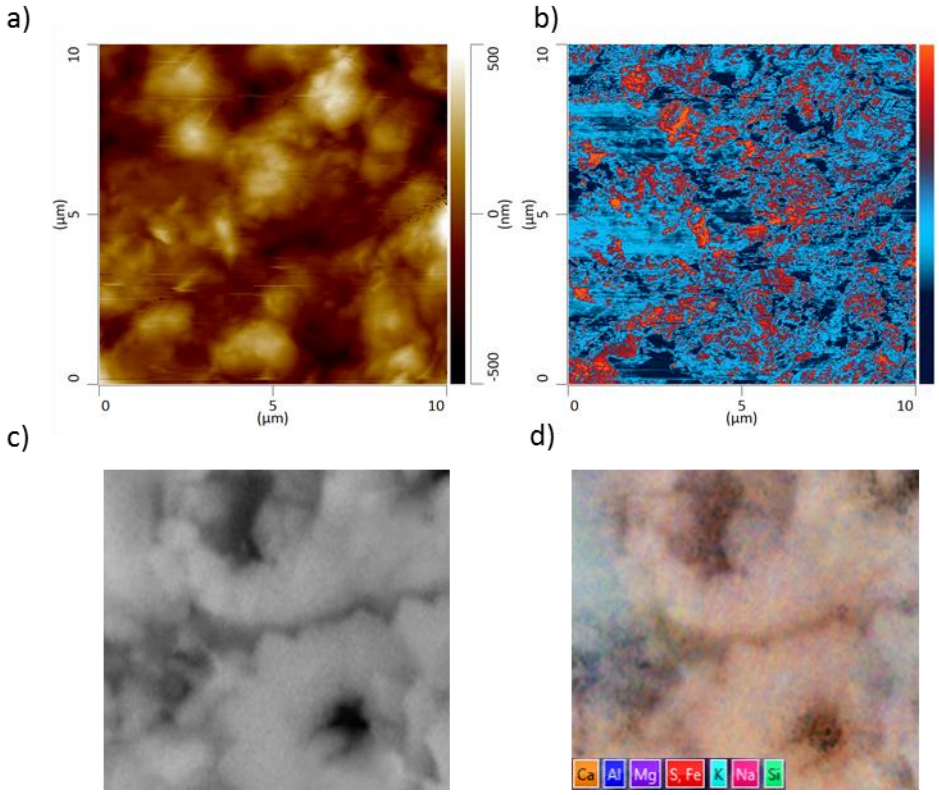

Figure 5.16: Area 2 of an AFM-IR rock chips experiment of sample H3A5 (R_0 1.2%). a) a topographic CFM map, b) is a CFM adhesion force map, c) is a BSEM image of the corresponding and d) is the SEM-EDS corresponding chemical map.

The different colours on the maps indicate a heterogeneous absorbance of the 2920 cm^{-1} frequency peak. The relative frequency value distributions do not reflect the topography, suggesting that the different values are caused by variations in the occurrence of organic molecules on the surfaces, and not by topography differences. Comparing the SEM and SEM-EDS maps of the same areas (Figures 5.15 and 5.16 c and d), little can be inferred regarding the correlation between the mineralogical distribution and the relative absorbance values, as the SEM-EDS mapping resolution is too low. It appears that the surfaces are a mixture of carbonates and I/S or kaolinite clays (Figures 5.15 and 5.16 d). Both of the point nano-IR analyses (Figure 5.17) were taken in areas that are indicated as containing carbonates in the chemical maps (Figure 5.15 d). However, the IR 2920 cm^{-1} frequency map and the spectra underline a difference in the absorbance peaks associated with organic compounds. C-O stretches at 1250 and 1710 cm^{-1} are associated with the presence of carboxyls, whereas O-H groups to hydroxyls. S-O stretches are linked to sulfonates and C-C bonds to the presence of aromatics.

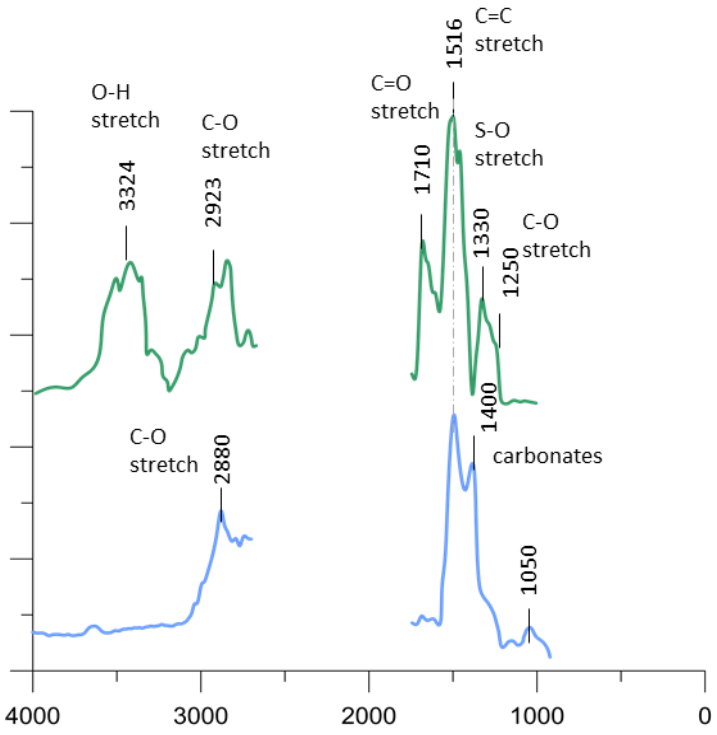

Figure 5.17: IR point spectra of two points on the surfaces of the coccolith area in sample H3A5 in figure 3.11 (R_0 1.2%). The green spectrum presents more peaks associated to organic compounds compared to the blue spectrum.

5.5. AFM-IR measurements on polished rock chips

Compared to the rock chips, the polished rocks allow to better target and visualise the different kinds of OM phases within the samples. Rock Eval analyses (Chapter 2) of the samples analysed with this technique have a different TOC (wt %) and, as they have different maturities, different hydrogen (HI) and oxygen indexes (OI) (Figure 5.18).

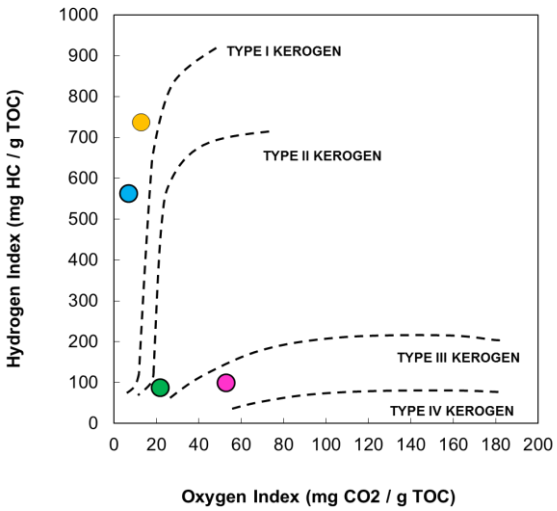

Figure 5.18: Pseudo Van Krevelen diagram for the four polished samples analysed using the AFM-IR technique. Yellow corresponds to sample IM2_3, blue to sample IM2_1, green to sample GW3 and pink to sample H3A3.

The low maturity (R_0 0.5%) samples (IM2_1, IM2_3) have a high Hydrogen Index (562 and 736 respectively) and a low Oxygen Index (7 and 13 respectively). The high maturity (R_0 1.2%) samples analysed (GW3 and H3A3) have a low Hydrogen Index (98 and 87 respectively) and a higher Oxygen Index compared to the low maturity samples (53 and 22 respectively). The most common bonds identified by observing the IR spectra are listed in Table 5.3.

IR wavenumber (cm^{-1})	**Bond**	**Type of compound**
900-1000	C=H bend	alkenes
	O-H bend	carboxyls
1040	Si-O stretch	silicates, clays
1050	C-O stretch	alcohols
	C-N stretch	amines
1110	C-N stretch	aliphatics/amines
	C-O stretch	esters, ethers, alcohols
1200-1350	C-O stretch	carboxyls
1370	S=O stretch	sulfonates
1395-1440	O-H bend	carboxyls
1400-1500	C-O stretch	carbonates
1410	C-H bend	alkene
1430	C-H bend	aliphatic
1510- 1610	C=C stretch	aromatics
1620	N-H stretch	amines
1710	C=O stretches	carboxyls
2860	C-H stretches	aliphatic
3000-3100	C-H stretches	aromatics
>3000	O-H stretches	carboxyls, hydroxyls
3360-3440	N-H stretch	amines

Table 5.3: IR wavenumbers and assigned molecular motion and functional group.

Figure 5.19 (sample IM2_3, R_0 0.5%) shows an AFM topography map (a), a frequency map at a frequency of 2920 cm^{-1} (b) and an SEM image of the same area (c). The frequency map underlines areas of higher absorbance, which correspond in the SEM maps to areas identified as bitumen infill in two foraminifera chambers and bitumen-filled microfracture. The point-IR analyses indicate a bitumen compound rich in aliphatics (C-H bend at 1490 cm^{-1} and CH_2 and CH_3 stretches at 2860 cm^{-1} and 2923 cm^{-1}). At 1050 cm^{-1}

a small absorbance peak is present, indicative of either a C-O stretch from alcohols or a C-N stretch from amine compounds.

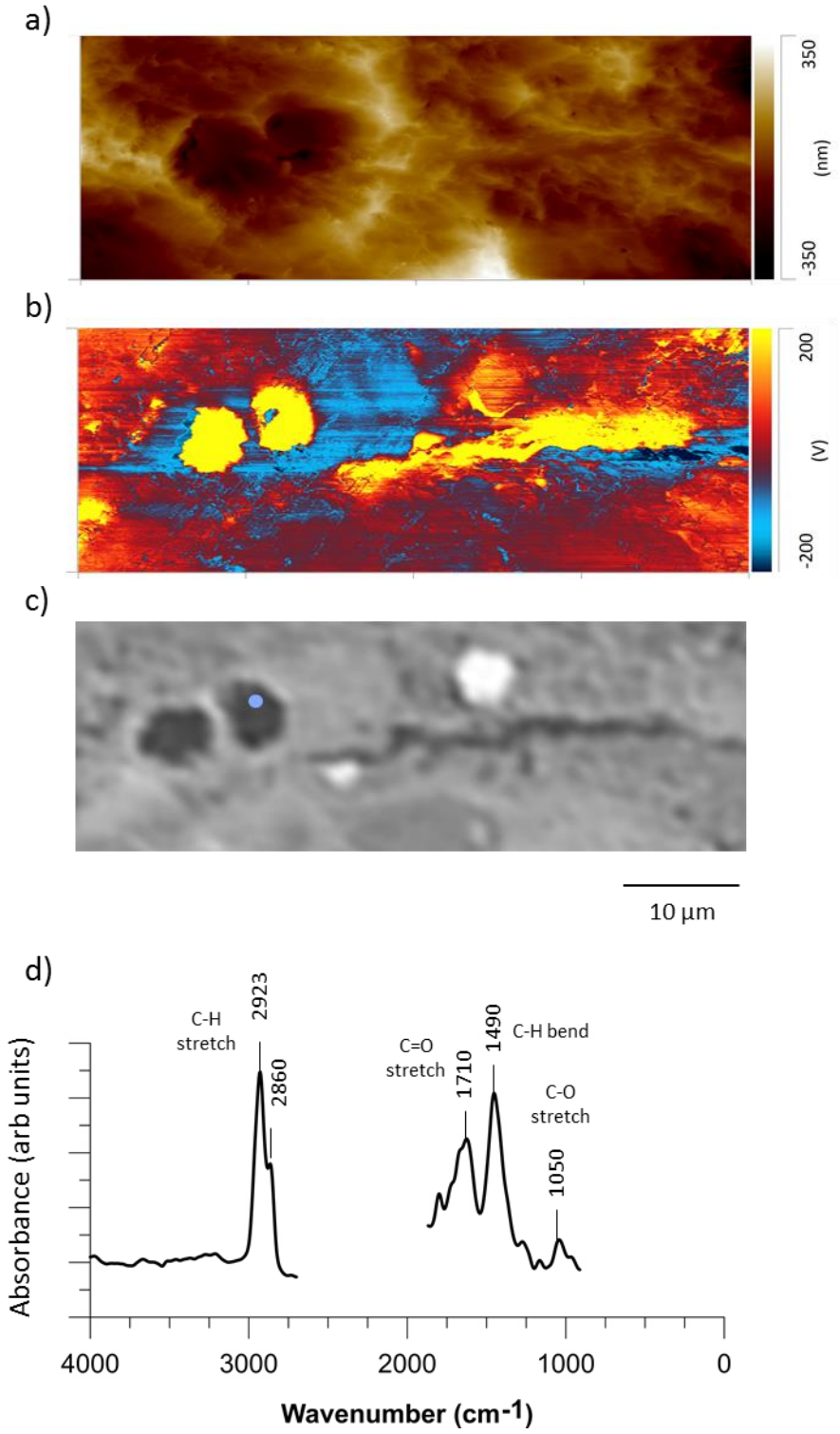

Figure 5.19: AFM-IR experiments on a polished surface of sample IM2_3 (R_0 0.5%). a) is a topographic map of the analysed are, taken simultaneously to b) which is the frequency map at the set wavenumber of 2920 cm^{-1}. c) is the corresponding area under the SEM and d) the IR spectrum of the point indicated in the SEM image. On the y axis, the absorbance values (arbitrary units). As the units vary between the lasers, an arbitrary value and different y axis were chosen for the analyses.

Figure 5.20 (sample H3A3, R_0 1.2%) is a foraminifera a with chambers infilled of bitumen. In the SEM image, it is possible to see that the bitumen presents nanoporosities, indicative of the generation of hydrocarbons. The frequency map of the same area shows frequency highs on the bitumen within the forams and on the stringer of organic matter at the top of the foram. Point analyses (Figure 5.20 d and e) indicate that both the kerogen and the bitumen present aromatics (C=C peak, 1590 cm^{-1} and 1605 cm^{-1}).

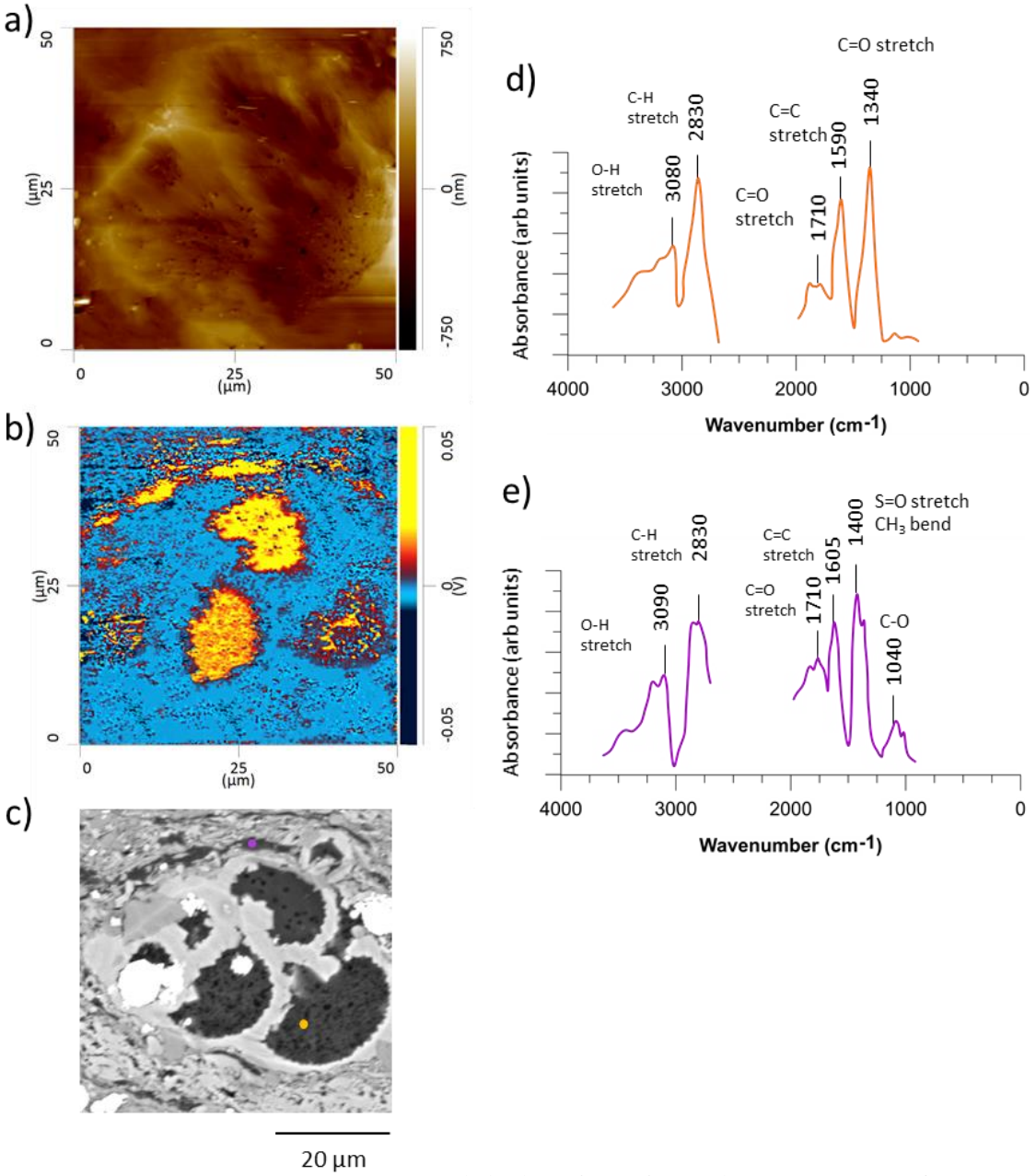

Figure 5.20: AFM-IR experiments on a polished surface of sample H3A3 (R_0 1.2%). a) is a topographic map of the analysed are, taken simultaneously to b) which is the frequency map at the set wavenumber of 2920 cm^{-1}. c) is the corresponding area under the SEM and d) the IR spectrum of bitumen, indicated in the SEM image with the colour orange and e) the IR spectrum of the kerogen, indicated in the SEM image with the colour purple.

The C-H stretch bands corresponding to the aliphatics are higher in the bitumen whereas the C=O stretches (~1040 cm^{-1} and 1710 cm^{-1}), typical of carboxylic acids, esthers or ketones are slightly higher in the kerogen. Peaks between 3180 cm^{-1} and 3390 cm^{-1} represent either O-H stretches, which represent either water or alcohols on the surface of the sample or in the bitumen and kerogen or C-H stretches in the aromatics.

In Figure 5.21 a comparison between the bitumen at low maturities (R_0 0.5%) and the bitumen at high maturities (R_0 1.2%) is shown. The main differences are noticed for the C=C aromatic stretch at 1610 cm^{-1}, which increases with the increase in maturity and the C-H bends around 1430 cm^{-1} and C-H stretches at 2920 cm^{-1}, which decrease at increasing maturities. No significant differences are noticed in the C=O carboxylic stretches.

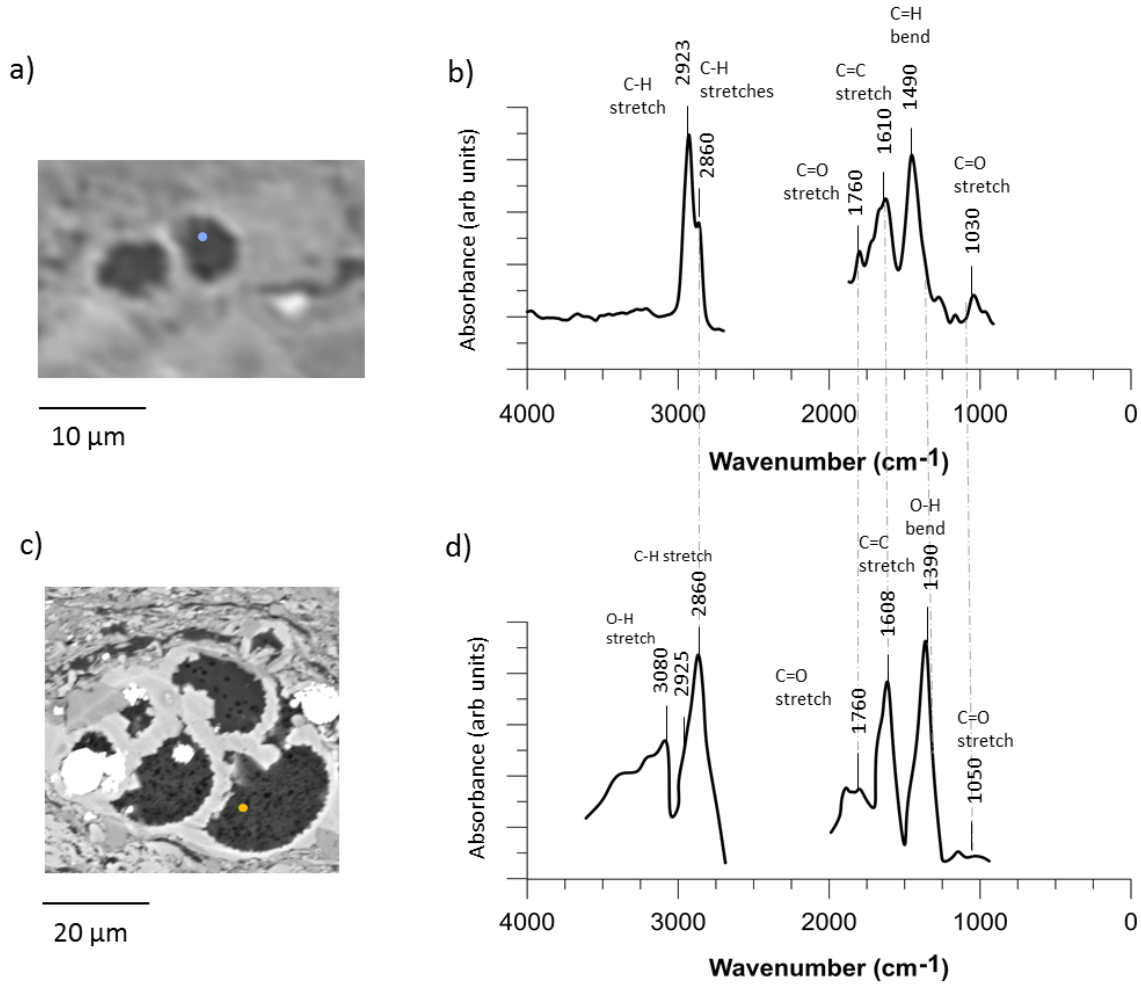

Figure 5.21: On the left, two SEM images and on the right the corresponding IR spectra of two bitumen compounds from samples a) and c) IM2_3 (R_0 0.5%) and b) and d) H3A3 (R_0 1.2%). The higher maturity bitumen has higher C=C and O-H peaks. The two dots correspond to the locations where the IR spectra were acquired.

This is consistent with the Pseudo-Van Krevelen diagram (Figure 5.18), that shows only a slight increase in the Oxygen Index between the low maturity sample (IM2_3, OI = 13) and the high maturity sample (H3A3, OI=22).

Figure 5.22 shows topographic AFM maps, frequency maps at 2920 cm^{-1} and SEM maps of an area that is interpreted as a tasmanite in sample IM2_1, R_0 0.5% and in sample H3A3 (R_0 1.2%). The frequency map highlights higher absorbance values for the organic matter compared to the surrounding matrix.

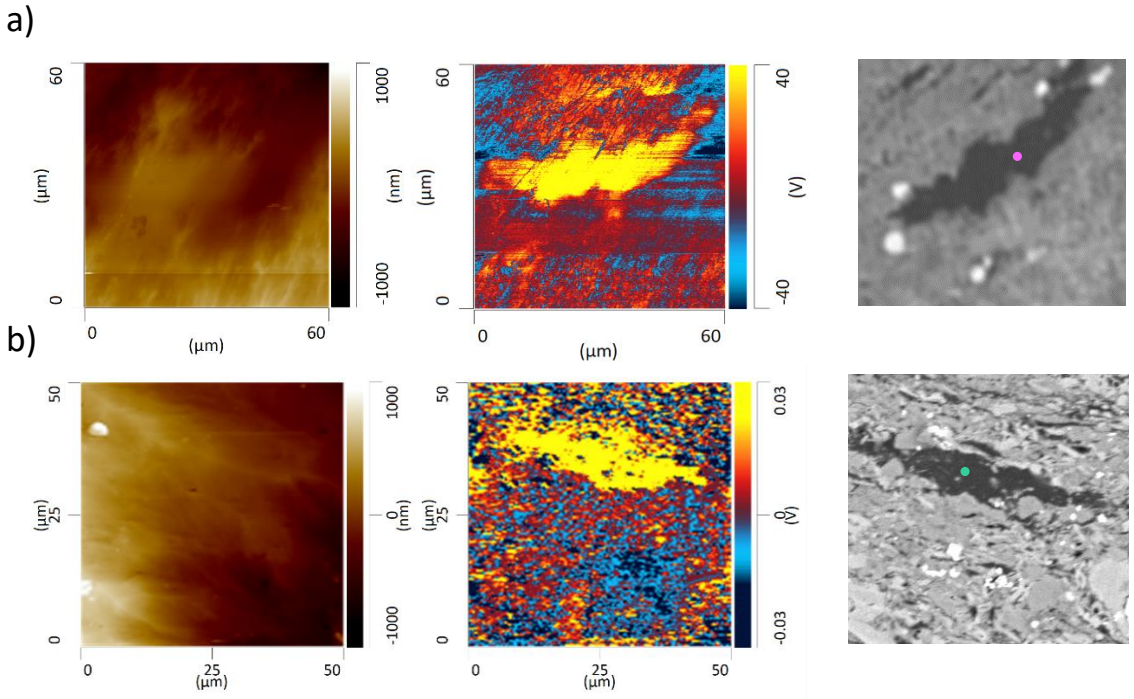

Figure 5.22: Figures of two Tasmanites in samples a) IM2_1 (R_0 0.5%) and b) H3A3 (R_0 1.2%). On the left, an AFM-IR topographic image. In the middle, a frequency map at 2920 cm-1 of the same area and on the right, the SEM images that allowed for the identification and location of the tasmanites in the AFM-IR experiments. The coloursed dots on the SEM images are the points were the IR spectra were collected.

The point IR for sample IM2_1 (Figure 5.22 a) identifies a peak at 1100 cm^{-1}, corresponding to a C-O carboxylic stretch or to a C-N stretch. The carboxyl group is also visible in the C=O stretch at 1706 cm^{-1} and the O-H stretch at 3112 cm^{-1}. An aromatic C=C stretch is present at 1630 cm^{-1}. Aliphatic C-H vibrations are also visible at 1470 cm^{-1} (bend) and 2820 cm^{-1} and 2926 cm^{-1} (stretches) for the CH_2 and CH_3 vibrational groups respectively. Point analysis on the tasmanite in sample H3A3 (R_0 1.2%) (Figure 5.22b) shows similar peaks

compared to the tasmanite in sample IM2_1 (R_0 0.5%). A C-H alkene bend is identified at 955 cm^{-1}, a C-O stretch or a C-N stretch at 1110 cm^{-1}, a S=O stretch at 1367 cm^{-1} and a C-H alkanes or aliphatics bend at 1410 cm^{-1}. At 1630 cm^{-1} the peak for the aromatic C=C stretch is present and has a higher absorbance compared to the same peak for the tasmanite in the immature window (Figure 5.23), whereas at 1710 cm^{-1} the carboxyl C=O stretch is visible but has a lower absorbance compared to the C=O stretch in the tasmanite in the immature window. At 1370 cm^{-1} peak is higher at higher maturities compared to the low maturity sample. At higher wavenumbers, the aliphatic CH_2 and CH_3 stretches are similarly present at 2830 cm^{-1} and at 2926 cm^{-1}. The O-H stretch at ~3110 cm^{-1} at high maturities is higher, signifying the presence of either water or alcohols on the surface of the sample or within the maceral moiety.

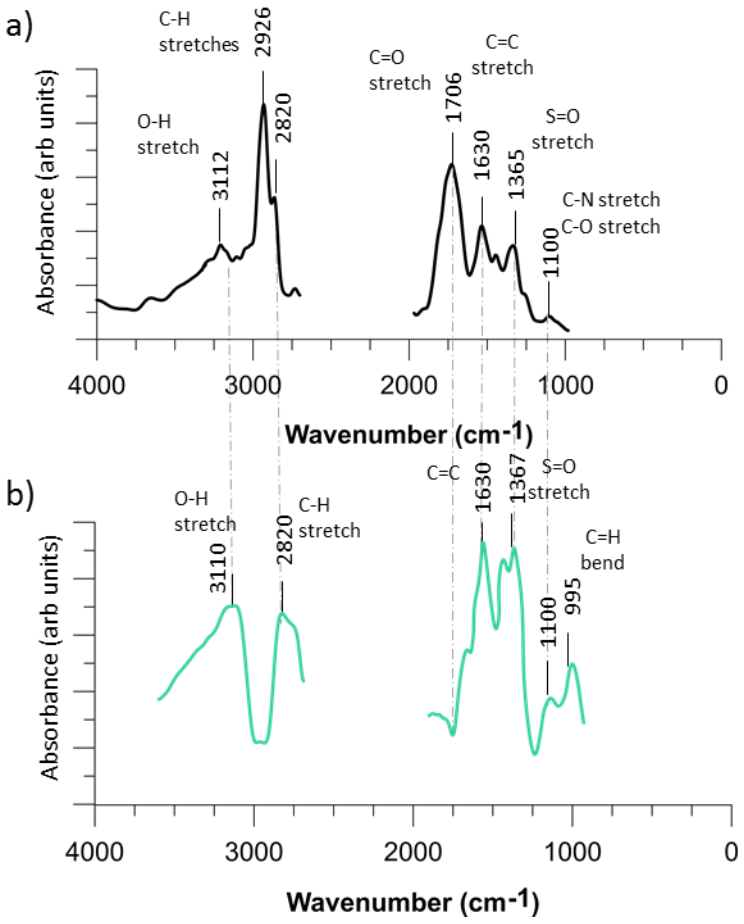

Figure 5.23: IR spectra of the Tasmanites from samples a) IM2_1 (R_0 0.5%) and b) H3A3 (R_0 1.2%). The points are indicated in the SEM maps in figure 3.16.

Figure 5.24 exhibits two types of organic matter in a high maturity sample (GW3, R_0 1.2%). The bitumen phase (Figure 5.24 b) presents peaks similar to the bitumen in sample H3A3 (Figure 5.16). The organic matter fracture infill (Figure 5.24 a) has high peaks within the carboxylic acid range (C-H bend at 1038 cm^{-1}, C=O stretch at 1754 cm^{-1} and O-H stretch at 3338 cm^{-1}).

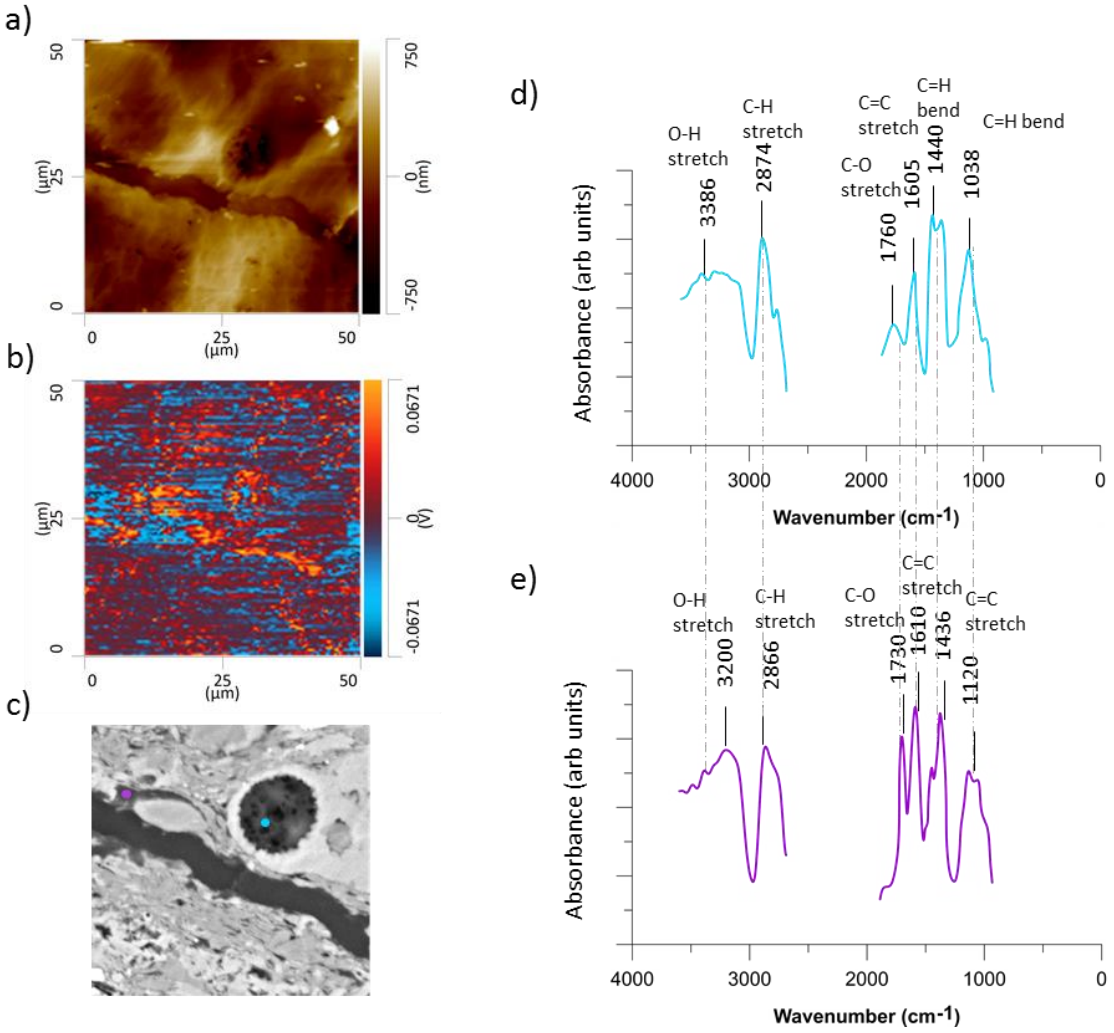

Figure 5.24: AFM-IR experiments on a polished surface of sample GW3 (R_0 1.2%). a) is a topographic map of the analysed are, taken simultaneously to b) which is the frequency map at the set wavenumber of 2920 cm^{-1}. c) is the corresponding area under the SEM and d) the IR spectrum of bitumen, indicated in the SEM image with the colour celeste and e) the IR spectrum of an inertinite, indicated in the SEM image with the colour purple. The dots on the SEM image correspond to the points where the spectra were acquired.

The inertinite (Figure 5.24 c), in comparison, shows a lower C-O absorbance at 1120 cm^{-1}, a higher C=C aromatic stretch at ~1600 cm^{-1} and a higher O-H esters stretch or C-H aromatic stretch at wavenumbers > 3000 cm^{-1}. In order to have a better understanding of the different aliphatic-aromatic present in the samples, the A factor was also calculated for all the spectra described (Table 5.4) results show that, in general, the A-factor decreases with the increase in maturity for all the maceral types (except for sample GW3). By comparing the samples at the same maturity, the A-factor is higher in the tasmanites, followed by bitumen and kerogen, meaning that tasmanites yield more aliphatics, and possibly oxygenated groups compared to the kerogen.

Sample name	**R_0 (%)**	**Maceral type**	**A-factor (aliphatic/aromatic + aliphatic)**
IM2_3	0.5	bitumen	0.46
H3A3	1.2	bitumen	0.43
H3A3	1.2	kerogen	0.44
IM2_1	0.5	tasmanites	0.59
H3A3	1.2	tasmanites	0.5
GW3	1.2	bitumen	0.47
GW3	1.2	kerogen	0.42

Table 5.4: Calculated A factor (proportional to aliphatics) for all the illustrated spectra in the samples analysed.

5.6. Discussion

The importance of wettability for petroleum reservoirs has been known for many decades (Amott, 1958; Anderson, 1986). It is well established that wettability alterations affect the productivity and the economics of a reservoir as the oil, migrating, remains trapped within the porous system. Many are the aspects that need to be taken into consideration when studying the wettability. Given the large number of properties the wettability depends on, many works on wettability in reservoirs have been performed by reducing the variabilities in play. The majority of works on reservoir wettability and wettability alterations are made on clean, smooth mineral surfaces (Al Mahri et al., 2017; Basu and Sharma, 1997; Bryant et al., 1991; Buckley and Lord, 2003; Hamouda and Karoussi, 2008; Karoussi and Hamouda, 2008).

In Chapter 4, calcite mineral surfaces were investigated to test the oil film surface coverage and to understand which are the molecules that affect the surface wettability the most. The study is in agreement with many previous works (Clementz, 1979; Cuiec, 1984), which attest the importance of asphaltenes in the oil-wetting of the surfaces. The use of clean mineral surfaces is a fundamental step into the understanding of specific aspects that modify the oil-surface interactions (i.e. brine composition, P-T conditions, oil composition). However, these experiments do not fully reflect the real mineral surface in the reservoir.

5.6.1. Environmental Scanning Electron Microscopy (ESEM) analyses

In this work, the ESEM was used to provide a qualitative assessment of the changes in wettability in relation to the composition of the samples. Despite no SEM-EDS chemical analysis was performed for these preliminary tests, from the shape and grayscale of the minerals in the ESEM pictures and the X-ray Diffraction chemical composition of the samples, it was possible to distinguish calcite cements and carbonate fossil fragments (i.e. foraminifera tests, coccolithic debris), pyrite, kaolinite and quartz. ESEM images indicate that quartz and kaolinite present a higher hydrophobicity compared to the calcite surfaces. Other works based on the ESEM technique display differences in wetting

behaviour between the different minerals; Buckman et al., (2016) released a working procedure to test the wettability of reservoir rocks, qualitatively attesting that quartz is more water-wet compared to illite and kaolinite. Deglint et al. (2017) analyse rock chip samples under the ESEM and quantitatively measure the contact angles in relation to the mineralogical complexity. The results of the study by Deglint et al. (2017) show that the measured contact angle for a K-feldspar crystal was 95^0 and for a dolomite crystal 68^0. Bennet et al. (2004), coupling core flooding experiments to environmental scanning electron microscopy (ESEM) analyses, observed that core flooding altered the wettability of the core plugs, rendering pore surfaces progressively more oil-wet. However, the study by Bennett et al. (2004), as other similar imbibition test studies performed on core plugs (Habibi et al., 2016; Lan et al., 2015; Larter et al., 2000; Standnes and Austad, 2003; Strand et al., 2007; Zolfaghari et al., 2017), did not provide any further information on wettability differences relative to mineralogy variations at the microscale. Moreover, more recent works (Deglint et al., 2017) observe that if the core plugs are not properly preserved, the core experiments will not provide adequate results. Unlike the other studies, here samples from different thermal maturities (R_0 0.5%, 0.9% and 1.2%) were considered (Figure 5.19). In this study, ESEM analyses from different thermal maturities show that comparable calcite surfaces have more oil-wet behaviour in the high-maturity sample (R_0 1.2%) compared to the low-maturity sample. This wettability change implies that wetting behaviour is not only controlled by the surface mineralogy, but also by other factors. One hypothesis is that the increase in thermal maturity also causes an increase in the oil produced, which in turn migrates along the pore network and gradually modifies the wettability of the surfaces, as it happens during the core-flooding experiments (Yuan et al., 2019). Another hypothesis could be related to the fact that, at higher maturities, the carbonate-saturated fluids are enriched in organic compounds, which become immediately adsorbed onto the carbonate surfaces (Chave, 1965; Chave and Suess, 1970). Moreover, higher maturities imply that the hydrocarbons are subject to different temperatures. Namely, at increasing maturities the organic matter generates progressively lighter composites, that migrate and are expelled. Part of the oil, however, is retained into the system and is subject to chemical composition changes (Jia et al., 2014).

These chemical composition changes, as seen in chapter 4, are responsible for different wetting behaviours.

5.6.2. CFM on rock chips

The ESEM provides important preliminary information on the wettability of the samples and allows to broadly distinguish wettability changes with changes in thermal maturity and composition. However, wettability measurements in an unconventional reservoir such as the Eagle Ford are particularly complicated by the mineralogical heterogeneity at the nanoscale and by the very small (nanometer-scale) pore system (Habibi et al., 2016; Roshan et al., 2016; Singh, 2016). Over the past decade, to study the wettability in reservoirs, authors have used the Chemical Force Microscopy technique (CFM) method (Hassenkam et al., 2009; Hilner et al., 2015; Kumar et al., 2005b; Skovbjerg et al., 2013, 2012). This method was also used in this chapter, as it allows to provide a more quantitative and detailed analysis of the rock chips. Despite the benefits of analysing the behaviour of an actual reservoir rock, working on rock chips, in general, impedes to clearly discern the factors impacting the wettability. For example, surface roughness has been proven to affect the wettability of a sample (Basu and Sharma, 1997; Morrow and Mason, 2001). Moreover, surface roughness becomes problematic while performing the CFM experiments, as the AFM instrument has limited z capacities (Habibi et al., 2016). This is why many authors use this method to test the solution salinity changes effects on quartz and mica surfaces (Hassenkam et al., 2009b; Hilner et al., 2015b; Matthiesen et al., 2016). For the sake of this work, the surface roughness of the samples was not considered in the wettability measurements and the topography issue during the experiments has been for the first time solved by partially Ar-Ion milling the surface, allowing the cantilever to reach most of the topographic lows (Figure 5.2).

5.6.3. The CFM combined with EDS analyses

The combination of CFM and SEM-EDS analyses was made in an effort to understand if the variations in the adhesion forces seen in the CFM analyses depend on mineralogy compositional changes. The cross-correlations showed that the kaolinite bears more

adhesion forces than illite-smectite clays or calcite and quartz, similarly to what observed in the ESEM experiments and by previous works; Borysenko et al. (2009) argued that illitic-smectitic mudrocks are more hydrophilic than kaolinitic mudrocks. This theory is in line with the studies by Saada, (1995) and Bantignies et al. (1997), that suggest that the Al-OH linkages present on the kaolinite surfaces play an important role in the adsorption of the hydrocarbon molecules, and argue that the Si and Al environments on the illite groups are instead insensitive to the adsorption processes. The low adhesion forces on quartz crystals could be caused by the fact that generally, quartz is hydrophilic, due to the exposure of Si and -OH groups on the surfaces. Contrarily to the ESEM analyses, no differences in adhesion forces are detected between the pyrite and the calcite surfaces, underlying a possible mixed-wetting behaviour of this mineral as suggested by Habibi et al. (2016). Calcite surfaces analysed with the CFM instead show low adhesion values. This is similar to the works by Hassenkam et al. (2009) and Skovbjerg et al. (2012), that analyse clean North Sea chalk surface properties. In their work, they also suggest that differences in adhesion forces on the coccoliths are caused by the presence of either polysaccharides remains or clay nanoparticles on the top of the calcite, which is more hydrophobic than calcite. This was also suggested by Hilner et al. (2015) examining quartz surfaces. Skovbjerg et al (2012) also validated the presence of clay nanoparticles using XRD analyses. The presence of clay nanoparticles was However, the resolution of the adhesion experiments is in the experiments performed in this thesis are too low (0.3 μm/pixel) to detect the presence of nanometric adhesion particles on the calcite surfaces as in Skovbjerg et al., (2012) and in Hassenkam et al., (2011). To detect compositional differences on the coccolith surfaces, the AFM-IR method was used. This method has the advantage of not being destructive as other techniques (i.e. XRD) and of being able to visualise the surface in-situ.

5.6.4. AFM-IR on coccolith surfaces

Here, the analysis of the surfaces of coccolith debris by means of the novel AFM-IR technique has allowed shedding light on the differences in chemical composition of the coccolith surfaces. By comparing the AFM-IR spectrum of a point with high absorbance with a spectrum of a point with fewer absorbance values, we notice that the first spectrum

presents vibrational peaks at frequencies related to organic or inorganic compound functional groups, i.e. carboxyls, sulfates and hydroxyls (Figure 5.17). These groups are also the ones that commonly characterise the polysaccharides (Fernando et al., 2017). Moreover, the peaks around 1000 cm^{-1} commonly found in clay infrared spectroscopy measurements (Madejová et al., 2017) in this case are not present. The hypothesis that the differences in adhesion forces on the coccolith surfaces are caused by the presence of polysaccharides, which attracts more oil molecules than the calcite, is a possibility. However, the high maturities and depositional processes at which these samples have been subject to render their presence unlikely. Nevertheless, the presence of nanometre-sized clays here and in other parts of the sample cannot be ruled out, analogously to the fact that the oil film is never completely homogeneous even on fresh, smooth mineral surfaces (see Chapter 4).

5.6.5. Organic matter changes with thermal maturity

AFM-IR measurements on different types of organic matter (i.e. kerogen, bitumen, tasmanites) have also testified chemical changes between the organic matter types as well as chemical changes with thermal maturity. Tasmanites contain more aliphatic compounds than bitumen, which in turn contains more aliphatic compounds than kerogen (Table 5.4) moreover, at increasing maturities the aromatic/aliphatic ratio increases in all organic matter types analysed. This is in line with previous studies on individual macerals (Birdwell and Washburn, 2015; Chen et al., 2013; Dereppe et al., 1994; DiStefano et al., 2016; Hackley et al., 2017). Although there is plenty of literature on the thermal maturation of organic matter, most of the previous studies were performed using destructive methods. Bernard et al., (2012) analysed the organic matter chemistry of a gas shale sample using a non-destructive method, the X-ray absorption near edge structure (XANES) spectra. Despite bearing a very high resolution (25 nm) compared to a traditional FT-IR method, this technique is not easily accessible as it requires the use of a synchrotron. Moreover, the study by Bernard et al. (2012) only analyses a sample from the gas maturity window. More recently, a study published by Yang et al. (2017) uses for the first time the AFM-IR technology to analyse the organic matter chemical changes in gas shale samples (Figure 5.24). Similarly to the work by Yang et al. (2017), the work that

has been carried out in this thesis analyses different organic macerals from the immature window to the gas window. Both the works show a high variation in the composition of the organic matter with an increase in maturity. The results in Yang et al. (2017) are similar to the results in this work, with the main difference being the higher resolution and spectral range of this work compared to the work by Yang et al. (2017).

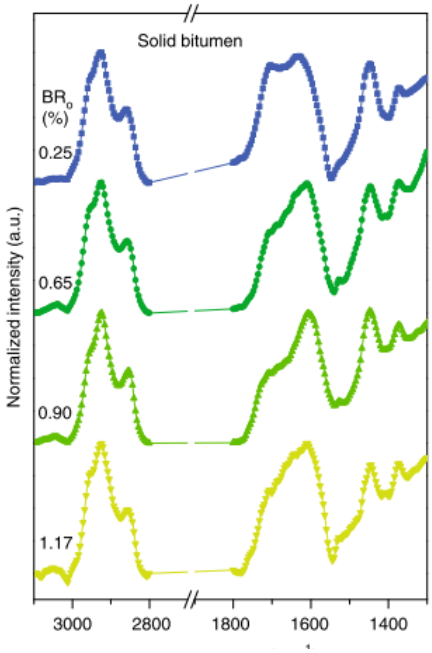

Figure 5.25: Solid bitumenIR peaks at increasing maturities (from Yang et al. (2017)).

5.7. Conclusions

Environmental Scanning Electron Microscopy (ESEM) analyses qualitatively demonstrated that the mineralogy of a reservoir rock affects the wettability behaviour. In particular, calcite is more water-wet than kaolinite and pyrite and calcite surfaces become more oil-wet with the increase in thermal maturity.

The Chemical Force Microscopy (CFM) is a powerful technique to analyse the adhesion forces changes at the nanoscale. On the rock chips analysed, at different maturities, is able to highlight high differences in the adhesion force values (0 to 9 nN) even in 10 x 10 μm areas. The locations with a high concentration of organic matter on the SEM-EDS maps correspond to points of high adhesion values relative to the surrounding points. The calcite surfaces show less adhesion compared to the quartz and to the kaolinite surfaces.

The AFM-IR tool was here used for the first time to test the surface chemistry variations on freshly cleaved rock chips. The combination of the technique with SEM-EDS maps of the same areas showed that, although the chemical mapping on coccolithic debris shows a homogeneity in the mineral chemistry, the frequency maps on the same areas exhibit molecular variations at the nanoscale. Point AFM-IR spectra collected from two points of a coccolith surface underline the chemical differences. The areas with more organic compounds on the surface suggest the presence of polysaccharides or nanometre-sized clays, which could attract hydrocarbons and render the coccolith surface more oil-wet. Although the IR peaks yield peaks common in the polysaccharides they are believed to be diagenetically unstable, rendering the clays hypothesis more valid.

The AFM-IR technique was also used to test the chemistry variations of different organic types with an increase in thermal maturity (R_0 0.5% to 1.2%). The bitumen, the tasmanites and the inertinite considered in this work show differences in the chemical composition, with the bitumen being richer in aliphatics and the kerogen in carboxylic acids. From the immature to the gas window, the bitumen and the kerogen show a decrease in aliphatics and an increase in aromatics.

The interpretation of the point IR spectra also gives an insight into the wetting behaviour of the organic molecules. The increase in aromatic molecules with the increase in maturity

is linked to a lower affinity between the organics and the water molecules and therefore increases the oil-wetting of the surfaces.

Chapter 6

Discussion and Conclusions

6.1. Summary and key findings

A combination of petrographic, physical and chemical analytical techniques has allowed the quantitative characterisation of the pore system and the pore surfaces of the Lower Eagle Ford Formation. In summary, the adoption of a multi-scale and multi-technique approach and the availability of samples from different maturities and microfacies allowed to 1) investigate the role of depositional settings and diagenesis as controls on the pore system; 2) understand how the pore system is linked to fabric and texture; 3) determine what role oil chemistry plays in surface chemistry alteration processes; 4) visualise and interpret wettability variations with nanoscale surface changes at the nanoscale and 5) investigate in situ the chemical changes in OM as a function of type and maturity and associate wettability variations to the chemical changes. This study demonstrates that a multi-disciplinary approach, although usually neglected, is necessary to fully understand the controlling factors of pore systems in unconventional reservoirs. Moreover, although being focused on a very specific case, the study is a clear example of how a multi disciplinary approach is often essential for a full comprehension of a broader range of scientific conundrums. Geologically speaking, the workflow that is presented here can also be applied to other case studies in unconventional and conventional reservoirs, as well as to more sustainable projects such as water reservoirs and carbon capture and storage applications. Nonetheless, employing several analytical techniques to chemically and physically characterise the porosities and the pore surfaces is essential

for understanding the intrinsic properties of materials in different sciences (i.e. pharmaceutical, food and nanotechnology disciplines) .

6.1.1. Microfacies

Determination of the petrographic and petrophysical characteristics of conventional and unconventional reservoirs is a standard procedure for determining reservoir quality (Aplin and Macquaker, 2011; Mathia et al., 2019; Milliken, 2014; Passey et al., 2010). However, if in conventional reservoirs mineralogical and textural variations at the micro- and nanoscale mildly affect the whole pore-system network, in unconventional reservoirs these variations, have an even higher impact, as the pore-system and the minerals are in the same scale range. This study demonstrates that in the Eagle Ford, mineralogical, fabric and textural heterogeneities exert strong controls on the pore system. Bulk mineralogy data, together with Rock-Eval and microscopy analyses, have allowed distinguishing three microfacies and their respective compositional characteristics (Figure 2.17). Laminated foraminiferal mudstones are composed of carbonates, silicates and clays. Wackestones and packstones, on the other hand, are mainly composed of carbonates (> 81%) and have undergone extensive carbonate cementation and reprecipitation. The variations between the microfacies are attributable to the different depositional environments; the laminations in the mudstones and in the wackestones are interpreted to have been formed in an intermittently dysoxic environment, whereas the massive fabric of reworked bioclasts (>20 μm) of the packstones suggests a more shallow, oxygenated environment. In the wackestone samples, pervasive carbonate dissolution and reprecipitation are here interpreted to have obliterated the original laminated fabric of the samples. Burial history interpretation, as well as mineralogy and texture variations, have important implications for the reservoir quality and the assessment of the resources; high TOC (wt %) content of type II kerogen, combined with lower amounts of cements in the laminated foraminiferal mudstones reveals a better source rock and reservoir potential compared to the wackestones and packstones microfacies. Higher TOC content, indeed, is reflective of a more connected organic pathway for the oil and gas migration

(Liu et al., 2017; Nie et al., 2018). In turn, high amounts of carbonate cementation have been linked in previous studies to porosity losses (Mathia et al., 2016; Ko et al., 2017).

6.1.2. Pore systems

Quantitative analyses on porosity loss and increase, as well as changes in pore shapes, sizes and connectivities have in this study been related to microfacies and diagenetic processes. Scanning Electron Microscopy has allowed the pores the pores to be classified in five types: interparticle matrix pores, intraparticle mineral pores, intraparticle fossil pores, intraparticle dissolution pores and organic matter pores Figure 2.21. Pore types were found to be strongly related to the microfacies type and thermal maturity of the samples Table 3.3: Pore types and corresponding microfacies and maturity. In the wackestone and packstone microfacies, the pores are mainly interparticle matrix pores (average value ~ 57%) and interpreted to be related to the rigid carbonate framework, which composes more than 80% of the overall mineral components. Intraparticle dissolution pores and organic matter pores are also present but in minor abundances. In the laminated foraminiferal mudstones, on the other hand, the pores are mainly interparticle matrix pores. In the same microfacies, in the gas window, the organic matter-related intraparticle pores increase while the intraparticle matrix pores decrease. Changes in shape factors from the immature to the gas window show that: pores become more oriented perpendicular to the burial stress, elongated and circular. A similar trend was observed in the pore shapes of other tight formations by Klaver et al., (2016) and Busch et al., (2017). Here this trend is only seen in the mudstone and wackestone samples. The packstone samples, regardless of higher maturity, display pore shapes similar to the immature laminated mudstones. Possibly, this is caused by the lack of ductile components (i.e. organic matter and clays) in the packstone samples and consequently a lack of compaction and rearrangement of the grains and pores (Milliken and Curtis, 2016). Moreover, less organic matter also translates into fewer circular nanopores as the circular nanopores are linked, similarly to other studies (Loucks et al., 2012; Valenza et al., 2013), to gas generation.

6.1.3. Pore system connectivity

Mercury Injection Porosimeter (MICP) data combined with Gas Adsorption and Focused Ion Beam (FIB) analyses have revealed that not only the pore shapes and types, but also the pore sizes and the whole connectivity of the system changes as a function of microfacies and diagenesis; in the wackestone and in the packstone samples the pore system is mainly formed by interparticle matrix pore throats and bodies between 10 and 100 nm, with high amounts of cements occupying the available primary and secondary pore spaces. In the laminated mudstone samples, the pore sizes present a bimodal distribution (< 4 nm and between 10 and 100 nm), and the average pore values register a shift towards lower values (< 10 nm) with increasing maturities. This shift is interpreted to be caused by increasing compaction and cementation processes, which occlude the interparticle and intraparticle pores associated with the mineral framework, and by the generation of organic pores, formed by the thermal maturation of the organic matter. Despite the reduction in pore sizes due to compaction and cementation, the foraminiferal laminated mudstone pore system presents well-connected pores even at high maturities. Gas adsorption and MICP analyses reveal that the pore throats are narrower (<20 nm) than the pore bodies (~20-100 nm). Combining the bulk data with SEM imaging has allowed establishing that the large pore bodies are formed by pores within the matrix, in the faecal pellets, and in the fossil cavities. The pore throats are instead formed by tighter inter- and intraparticle pores and, in the laminated foraminiferal mudstones, by the small organic matter pores. A similar pore network was suggested for other mudstones (Aplin and Moore, 2016; Clarkson et al., 2013a; Klaver et al., 2016; Mathia et al., 2019; Wang et al., 2016), with the main difference being that narrow pore throats are present at all maturities and associated with the clay-rich matrix.

6.1.4. Millimetre-centimetre scale anisotropy

Microtomography (micro-CT) analyses have revealed that laminated foraminiferal limestones present vertical heterogeneities at the microscale (Figure 2.39). High degrees of vertical heterogeneities at the microscale in mudstones can cause anisotropy in the fluid

flow and hence in the permeability of the system (Armitage et al., 2011; Chandler et al., 2016; Mullen, 2010; Philipp et al., 2017; Rutter et al., 2017; Tiab and Donaldson, 2004; Yang and Aplin, 1998). The presence of layers with more clay and organic matter alternating with layers of cemented planktonic fossils might give rise to preferential fluid flow along clay and organic-rich layers, and, when fractured, at the intersection between the more and the less competent layer. The fact that these layers can be considered as planes of weakness was also suggested by other authors (Lash and Engelder, 2005; Mckernan, 2016) and differences in vertical and horizontal fluid flow was also suggested by Yang and Aplin (2007). Although numerous fractures are seen on the thin sections, in the micro-CT experiments as well as in the SEM polished samples, caution must be taken in accounting these fractures into the pore system. Although fractures are evident planes of weaknesses occuring along bedding, they are here discounted as part of the pore network, as they could be related to mishandling or stress-release (Clarkson et al., 2012; Ramiro-Ramirez, 2016). Moreover, even if the vertical heterogeneities were quantified using micro-CT, more work needs to be done in the assessment of the anisotropy of the pore system.

6.1.5. Influence of organic matter on the pore system

Although organic pores are observed in other fine-grained reservoir studies (Loucks et al., 2009; Clarkson, Solano, et al., 2013; Chalmers and Bustin, 2015; Pommer et al., 2015; Milliken and Curtis, 2016), this reservoir presents some peculiar aspects. For instance, no decrease in organic pores is noticed between the immature and the oil window as seen in other studies (Mastalerz et al., 2013; Mathia et al., 2019). This is probably caused by the fact that oil generation and bitumen filling in these samples start occurring at $R_0 \leq 0.44\%$. Moreover, porosity decrease associated with compaction is here hindered by the rigid carbonate framework. In the gas window instead, as previously mentioned, organic matter generates porosities. Organic matter pores are typically smaller than 20 nm and on average ~ 30% of the overall pore types. This conclusion is in accordance with other works carried on in the Eagle Ford Formation (Chalmers and Bustin, 2017; Ko et al., 2017) and in other fine-grained sediments (Mastalerz et al., 2008). Nonetheless, the organic matter influence on the pore system is also related to its type and occurrence (Ko et al., 2014; Nie

et al., 2018; Valenza et al., 2013). In line with this hypothesis, previous petrographic observations on the Eagle Ford Formation showed that fusinite and inertodetrinite, for example, do not contribute to the increase in porosity even if they are accounted for in the TOC measurements (Chalmers et al., 2017; Ko et al., 2017). FIB-SEM data also reveal that in laminated foraminiferal mudstones organic matter is well connected (> 72% on all samples analysed). Organic matter connectivity has important implications for the hydrocarbons flow as it can lead to a potential migration pathway as well as to an interconnected pore pace in the organics, which favours the free gas phase flow (Loucks et al., 2009; Wang and Reed, 2009; Ambrose et al., 2010; Sondergeld et al., 2010). MICP and gas adsorption data indicate a connected pore network, underlying that organic pores are interconnected. However, in the wackestones and in the packstones the TOC values are too low (< 2.5 %) to allow high amounts of organic matter-related pores and an organic matter connected network.

6.1.6. Organic matter evolution at increasing thermal maturities

During maturation, most generated oil is expelled by organic matter migration through the pore network (Jia et al., 2014). As organic matter migrates through the pore network, pore surface molecules progressively interact more with the migrated oil. Indeed, polar oil molecules such as phenols or fatty acids have high affinities with the molecules on the mineral surfaces (Aplin and Larter, 2005; Taylor et al., 1997). The interactions are associated to C-H and O-H bonds, which interact with the cations and progressively disrupt the water films on the mineral surfaces Moreover, AFM-IR studies have underlined the presence of several oxygenated bonds like -OH and -COOH in the bitumen phase. The presence of -OH and -COOH suggests that bitumen was formed in hydrous conditions, and that water and oil were in metastable equilibrium during oil generation (Helgeson et al., 1993; Mansuy and Landais, 1995; Michels et al., 1996). Oil generation produces water-soluble polar organic compounds, which partition first into water and then onto mineral surfaces (Aplin and Larter, 2005; Taylor et al., 1997). This suggests that the wetting state of the pore system is associated to the formation of hydrophobic surfaces, which progressively attract more polar and non-polar oil

compounds rendering the pore network mixed to oil-wet (Bennett et al., 2002; Larter et al., 1997, 1996). Large scale ESEM experiments validate the hypothesis that pore mineral surfaces progressively become more hydrophobic. When oil is generated and migrates into the pore system, part of the oil is also retained in the system in various forms of bitumen (Cardott et al., 2015). Whilst the expelled oil at increasing thermal maturities generates progressively lighter composites, the retained oil is gradually enriched in aromatics and NSO compounds (Jia et al., 2014). These compounds are typically found in asphaltenes, although their chemical composition is highly variable. AFM-IR measurements on the organic phases in the Eagle Ford samples, in line with previous studies on individual macerals (Birdwell and Washburn, 2015; Chen et al., 2013; Dereppe et al., 1994; DiStefano et al., 2016; Hackley et al., 2017), have attested that, at increasing maturities, the aromatic/aliphatic ratio increases in all the OM types analysed (i.e. inertinite, bitumen, tasmanites), testifying chemical changes in the OM with increasing maturities. The asphaltenes-rich bitumens are composed of aromatic units linked by aliphatic bridges (Michels et al., 1996; Yen et al., 1961). During thermal breakdown, the aliphatic units in the asphaltenes are progressively removed giving rise to a relative enrichment in aromatics (Michels et al., 1996) and polar compounds. The key implication is that the oil-wetting state of the system will depend on the maturity of the formation as well as on the TOC (wt %) content, and that the amount of oil-wet surfaces is positively correlated to the amount of TOC (Lan et al., 2015; Siddiqui et al., 2018). As the Eagle Ford pore system is associated to the carbonates as well as to the organic matter, it is reasonable to think that the migrated bitumen, especially at high maturities, produces an overall mixed or oil-wetting behaviour.

6.1.7. Dissolution

AFM point IR at increasing maturities also indicate that the ratios of acidic compounds increase during thermal maturation. Several previous works associate the progressively higher presence of carboxylic acids at higher thermal maturities to the dissolution of minerals (Helgeson et al., 1993; Schieber et al., 2016). Petrographic evidence of the presence of a progressively higher acidic medium with increasing maturities is pressure-

solution veins and intraparticle dissolution-etched pores in carbonate and feldspar minerals. These dissolution processes are mainly present in the oil and gas maturity window, where also the acidic compound peaks measured with the AFM-IR are higher. Moreover, many studies indicate that the increase in adsorption of organic acids increases with the decrease in pH, which in turn promotes dissolution (Aksulu et al., 2012; Feng and Simpson, 2008; Madsen and Lind, 1998).

6.1.8. Pore system implications of wettability measurements

The understanding of the fluid flow behaviours and the wetting state of the pore surfaces has important implications for the relative permeability of the reservoir (Anovitz et al., 2016). As fluid thermodynamics strongly depend on rock-fluid interactions (Cole et al., 2013), it is important to analyse the pore surface chemistry as a function of pore size and type (Anovitz et al., 2016; Landrot et al., 2012; Peters, 2009). This is why here for the first-time pore system analyses have been correlated to pore chemistry analyses. As seen in the previous paragraphs, the pore system in all the microfacies is mainly associated with interparticle carbonate mineral pores and, in the laminated foraminiferal mudstone samples in the gas window, to the intraparticle organic matter pores. Chemical Force Microscopy (CFM) studies combined with Atomic Force Microscopy (AFM) - nanoIR analyses allowed to conclude that nanoscale wettability variations occur even on homogeneous calcite surfaces and that these changes are influenced by localised surface charges and by the oil chemistry. No direct relationship was determined in this study between the wettability and surface force values in contrast to previous studies (Kumar et al. 2005, Lorenz et al. 2017).

6.1.9. Asphaltenes

Data in this study show how oil fractions containing more -OH and -COOH groups have stronger interactions with calcite surfaces. The results indicate that it is asphaltene fraction of oil that most affects wettability state, rendering the pore surfaces more hydrophobic. These results are in accordance with many previous studies (Standnes and

Austad, 2003; Zhang et al., 2007; Buckley and Wang, 2002; Mahmoudvand et al., 2019; Mullins, 2011; Toulhoat et al., 1994; Buckley, 1995). Moreover, due to their large size and their affinity to be adsorbed onto porous surfaces, asphaltenes may aggregate and precipitate, causing a physical blockage of the pores (Al-Maamari and Buckley, 2003; Buckley and Wang, 2002; Sabbaghi et al., 2008; Spiecker et al., 2003). Both the alteration of the wettability and pores obstruction derived from asphaltenes precipitation are responsible to negatively affect the production phase (Davudov et al., 2018); oil-wet surfaces and the precipitation of asphaltenes into the pore throats have been associated to a reduction in pore connectivity, which leads to low reservoir permeabilities and hydrocarbon mobility (Buckley, 1998; Moghanloo et al., 2018).

6.1.10. Mineralogical controls on organic adhesion to surfaces

Chemical Force Microscopy (CFM) studies combined with Scanning Electron Microscopy (SEM) imaging have allowed inferring that 1) mineralogy influences adhesion and 2) adhesion forces vary at the nanoscale, even on the same mineral surface. In particular, adhesion forces on kaolinite surfaces are found to be higher than the adhesion forces on illite-smectite clays, calcite, pyrite or quartz. This result is in line with what observed in other studies (Bantignies et al., 1997; Borysenko et al., 2009; Skovbjerg et al., 2013) which suggest that the high adhesion on kaolinite surfaces is due to the presence of Al-OH bonds. These bonds, according to Saada, (1995) and Bantignies et al. (1997), would have high affinities with polar organic molecules.

In the Eagle Ford, the pore system is mainly associated with the carbonates and organic matter, whereas kaolinite-related pores are not abundant. Moreover, especially at high maturities, the kaolinite content is low (< 3.3 %). Nonetheless, even if the pore system is not strongly associated with clays, in this study is suggested that even low quantities of particles in the range of the nanometer can influence the whole system. In line with this hypothesis is also the fact that nanometric organic content variations measured here for the first time with the AFM-IR on coccolith surfaces could be associated to kaolinite nanometric attached on the mineral surfaces, as in Skovbjerg et al., (2012). Peters (2009)

also calculated that kaolinite, even measuring as little as 5% of the bulk mineralogy of sandstone samples, it accounted for over half of the pore-to-mineral contact area.

6.1.11. Implications for the hydrocarbons production and storage

Despite the fact that this study focuses on petrographic observations below the centimetre-scale, the findings of this work offer important implications for the understanding of the overall reservoir properties. This is because nanoscale heterogeneities and pore system properties are found to be highly correlated with the bulk mineralogy and the microfacies of the samples. Therefore, by knowing the mineralogy and the microfacies, bulk reservoir characteristics can be inferred. Firstly, it is possible to predict that wackestone and packstone samples have a lower hydrocarbon storage capacity compared to laminated foraminiferal mudstone samples. This is probably because in the laminated foraminiferal mudstones the high pore volumes are given by large macropores within the foraminifera chambers and the carbonate matrix. In the wackestone and packstone samples, these pores are instead occluded by carbonate cements, limiting the pore volumes and storage capacities. Nonetheless, in the laminated foraminiferal mudstones in the gas window, and despite mineral reprecipitation in primary pores, the organic matter in the system generates further porosity due to thermal cracking. Moreover, the organic matter is found to play a major role in the preservation of the original pores as a result of hydrocarbon expulsion and adsorption onto the mineral surfaces. Indeed, oil-wet surfaces are thought to inhibit mineral precipitation.

As pore-surfaces progressively become more oil-wet, the fluid displacement and thus the extraction of the retained oil in the pore system become more challenging (Berg et al., 2016; Sørgård et al., 2017). Fluid flow and fluid displacement are also complicated by the connectivity of the system. As previously mentioned, in the laminated foraminiferal mudstones in the gas window, the pore system is formed by very narrow (< 20 nm) pore throats. Despite the narrowness of the pores, the connectivity of the system through meso and micropores within the kerogen is thought by several authors to make a major contribution to gas flow efficiency (Chalmers et al., 2012; Chalmers and Bustin, 2008, 2007;

Clarkson and Bustin, 1996; Curtis et al., 2011; Keller et al., 2011; Larsen et al., 1995; Marsh, 1987; Mathia, 2014; Unsworth et al., 1989).

6.2. Novelties and limitations

The petrography results in this thesis are consistent with what has been previously observed in the Eagle Ford (Dawson, 1997; Mcallister, 2017; Ramiro-Ramirez, 2016; Juergen Schieber, 2013). The main difference between this and other studies is the effort to provide quantitative data to all the petrographic observations. On the other hand, these previous works have distinguished in the same area analysed other types of facies apart from the foraminiferal laminated mudstones, wackestones and packstones observed here. This draws the attention on the high heterogeneity of the samples, and to the fact that this study is unlikely to cover the whole Lower Eagle Ford section. Wackestone and packstone samples are only available from the gas window, which could be related to their absence at low maturities, but also to a lack of specimens analysed in this study. Moreover, this study is missing samples from the post-mature window ($R_0 \geq 1.4\%$), in which Mastalerz et al. (2008) detected an increase in porosity caused by a secondary cracking of bitumen. Also, more samples from the oil window could be able to provide a more robust reconstruction of pore system changes with an increase in maturity.

Considering all these limitations, however, this work is the first attempt to incorporate the surface chemistry and wettability studies in a multi-technique and multi-scale pore system characterisation. Moreover, the combination of petrographic and surface chemistry data has also allowed validating for the first time the link between the increase in dissolution with the increase in acidic compounds.

6.3. Future Work

Availability of new samples from the post-mature window (R_0 1.4%) and further samples from the oil window (R_0 0.9%) would be beneficial to understand the complete diagenesis sequence. Moreover, other samples from other microfacies at variable maturities could provide insights on the variations in depositional environments and in pore system

changes with maturity changes. In would be also useful to have a clear understanding of the facies correlation between the various wells and outcrops.

Surface chemistry studies could better be validated by testing the adhesion forces on clean calcite surfaces in distilled water saturated in calcite. This would also allow to better understand the role the brine plays in the whole wetting alteration process. As surface chemistry depends on many factors, a further study could test whether surface roughness controls the wettability on actual pore surfaces. This can be done by adopting the CFM technique on rock chip surfaces and by correlating the topography roughness values to the adhesion forces maps.

Ideally, the experiments should reflect real reservoir conditions. However, the instrumentation that was used did not allow to conduct experiments at different pressure or temperature conditions. Advancing technologies have recently allowed the assemblage of atomic force microscopes that can function at varying P-T conditions. As future work, testing how P-T conditions affect the measurements could provide valuable insights into the overall nanoscale surface chemistry changes.

Moreover, other AFM-IR work could be conducted on fresh rock chips, also by examining other mineral surfaces and by implementing a higher resolution during the analyses. Although finding the same areas in the CFM, AFM-IR and SEM-EDS is very challenging due to the different resolutions and outputs of the techniques, correlating the results from these techniques would allow to validate the interpretations and determine the best analytical workflow. Also, several authors have correlated adhesion forces and wettabilities by using specific equations (Drummond and Israelachvili, 2002; Hassenkam et al., 2009; Mirchi et al., 2014; Yang et al., 2002). In future studies, performing contact angle experiments in the same areas as adhesion measurements could be of aid in determining the right correlation between the contact angle and adhesion forces.

6.4. Conclusions

The adoption of a multi-disciplinary approach has allowed characterising the pore system and the surface chemistry of the pores in the Lower Eagle Ford Formation. In particular, it was concluded that:

1. The pore system is highly influenced by the carbonate-rich framework and by the microfacies type. Three different facies were identified: laminated foraminiferal mudstones, wackestones and packstones. In the facies, five different domains were distinguished: microfossils, matrix, faecal pellets, organic matter and mineral particles.
2. Amongst these three microfacies, in the laminated foraminiferal mudstones the microlaminations, the TOC values higher than 3% and the lower amounts of carbonates precipitates allow for a more connected pore system compared to the one in the wackestone and packstone microfacies.
3. The pores are mainly in the size of the nano (< 2 nm) and mesopores (between 2 nm and 50 nm).
4. The pore system in the laminated foraminiferal mudstones is influenced by thermal maturity changes; in the immature and oil window, the pore system is mainly associated with intraparticle and interparticle pores formed by the carbonate framework. In the gas window, the pore system is associated with the carbonate framework as well as to the pores formed within the organic matter during thermal cracking. The pores are connected at all maturities, but at high maturities the system is tighter: large interparticle and intraparticle pore bodies are mainly connected through small (< 20 nm) organic matter pore throats.
5. Chemical force microscopy studies on representative calcite crystals surfaces allowed to infer that asphaltenes are the oil fraction that alters the most the wettability of the samples. Point IR data shows high concentrations of C-O and O-H molecular groups on the oil-wet surfaces. These molecular groups have been linked to the increase in hydrophobicity and to the presence of higher amounts of carboxyls and phenol compounds in the most oil-wetting fractions.

6. Chemical force microscopy studies on real rock chips have brought to light different wetting behaviours on different minerals. Specifically, kaolinite surfaces are more hydrophobic than quartz, pyrite, illite/smectite and carbonates.
7. AFM-IR analyses on polished samples have allowed determining differences in the chemistry of different organic matter types at different maturities; in accordance to other studies, aliphatic compounds decrease progressively from tasmanites, to bitumen and kerogen. Moreover, at increasing maturities the aromaticity increases in all organic matter types analysed.
8. The presence of high -OH and -COOH absorbance values in bitumen is indicative of reactions occurring between water and oil during bitumen generation.

References

Abbott, S.T., 2000. Detached mud prism origin of highstand systems tracts from mid-Pleistocene sequences, Wanganui Basin, New Zealand. Sedimentology 47, 15–29. doi:10.1046/j.1365-3091.2000.00275.x

Abdallah, W., Buckley, J.S., Carnegie, A., Edwards, J., Herold, B., Fordham, E., Graue, A., Habashy, T., Seleznev, N., Signer, C., Hussain, H., Montaron, B., Ziauddin, M., 2007. Fundamentals of wettability. Oilf. Rev. 19, 44–61.

Abdallah, W., Gmira, A., 2014. Wettability assessment and surface compositional analysis of aged calcite treated with dynamic water, in: Energy and Fuels. pp. 1652–1663. doi:10.1021/ef401908w

Acevedo, S., Escobar, G., Gutiérrez, L., Rivas, H., 1992. Isolation and characterization of natural surfactants from extra heavy crude oils, asphaltenes and maltenes. Interpretation of their interfacial tension-pH behaviour in terms of ion pair formation. Fuel 71, 619–623. doi:10.1016/0016-2361(92)90163-I

Ahmadi, M.A., Shadizadeh, S.R., Chen, Z., 2018. Thermodynamic analysis of adsorption of a naturally derived surfactant onto shale sandstone reservoirs. Eur. Phys. J. Plus 133. doi:10.1140/epjp/i2018-12264-x

Aksulu, H., Håmsø, D., Strand, S., Puntervold, T., Austad, T., 2012. Evaluation of low-salinity enhanced oil recovery effects in sandstone: Effects of the temperature and pH gradient, in: Energy and Fuels. pp. 3497–3503. doi:10.1021/ef300162n

Al-Maamari, R.S.H., Buckley, J.S., 2003. Asphaltene precipitation and alteration of wetting: The potential for wettability changes during oil production. SPE Reserv. Eval. Eng. 6, 210–214. doi:10.2118/84938-PA

Al Mahri, M.A., Alshehhi, M., Olukan, T., Vargas, M.R., Molini, A., Alhassan, S., Chiesa, M., 2017. Surface alteration of calcite: interpreting macroscopic observations by means of AFM. Phys. Chem. Chem. Phys. 19, 25634–25642. doi:10.1039/C7CP03589F

Al Mahrouqi, D., Vinogradov, J., Jackson, M.D., 2017. Zeta potential of artificial and natural calcite in aqueous solution. Adv. Colloid Interface Sci. doi:10.1016/j.cis.2016.12.006

Alcantar-Lopez, L., Chipera, S.J., n.d. Improving Our Understanding of Porosity in Source Rock Reservoirs through Advanced Imaging Techniques.

Algré, E., Legrand, B., 2014. Design and construction of the motion mechanism of an XY micro-stage for precision positioning. Appl. Phys. Lett. 11, 1–10. doi:10.1103/PhysRevLett.56.930

Ali, S. a, Clark, W.J., Moore, W.R., Dribus, J.R., 2010. Diagenesis and Reservoir Quality. Oilf. Rev. 22, 14–27. doi:10.1080/10916466.2012.742542

Allen, N., Nykky, A., Allen, N., 2014. Pores, porosity and pore size distribution of some Draupne Formation and Colorado Group shales and kerogens.

Alvarez, J.O., Neog, A., Jais, A., Schechter, D.S., 2014. Impact of surfactants for wettability alteration in stimulation fluids and the potential for surfactant EOR in unconventional liquid reservoirs. Soc. Pet. Eng. - SPE USA Unconv. Resour. Conf. 2014 468–485. doi:10.2118/169001-MS

ALVAREZ, J.O., SCHECHTER, D.S., 2016. Application of wettability alteration in the exploitation of unconventional liquid resources. Pet. Explor. Dev. 43, 832–840. doi:10.1016/S1876-3804(16)30099-4

Ambrose, R.J., Hartman, R.C., Diaz Campos, M., Akkutlu, I.Y., Sondergeld, C., 2010. New Pore-scale Considerations for Shale Gas in Place Calculations, in: SPE-131772-MS. Society of Petroleum Engineers. doi:10.2118/131772-MS

Aminzadeh, F., Dasgupta, S.N., 2013. Geophysics for Unconventional Resources, in: Developments in Petroleum Science. Elsevier B.V., pp. 247–271. doi:10.1016/B978-0-444-50662-7.00009-3

Amott, E., 1958. Observations Relating to the Wettability of Porous Rock. Pet. Trans. AIME.

Andersen, S.I., Chandra, M.S., Chen, J., Zeng, B.Y., Zou, F., Mapolelo, M., Abdallah, W., Buiting, J.J., 2016. Detection and Impact of Carboxylic Acids at the Crude Oil-Water Interface. Energy and Fuels 30, 4475–4485. doi:10.1021/acs.energyfuels.5b02930

Anderson, W.G., 1986. Wettability Literature Survey Part 1: Rock/OiL/Brine Interactions and the Effects of Core Handling on Wettabiiity. J. Pet. Technol. 1125–1144. doi:10.2118/13932-PA

Anovitz, L.M., Cole, D.R., Swift, A., Sheets, J., Elston, H., Welch, S., Chipera, S.J., Littrell, K.C., Mildner, D.F.R., Wasbrough, M.J., 2016. Multiscale (nano to mm) porosity in the eagle ford shale: Changes as a function of maturity, in: Society of Petroleum Engineers - SPE/AAPG/SEG Unconventional Resources Technology Conference. doi:10.15530/urtec-2014-1923519

Anovitz, L.M., Cole, D.R., Swift, A.M., Sheets, J., Elston, H.W., Welch, S.A., Chipera, S.J., Littrell, K.C., Mildner, D.F.R., Wasbrough, M.J., 2014. Multiscale (nano to mm) Porosity in the Eagle Ford Shale: Changes as a Function of Maturity. Proc. 2nd

Unconv. Resour. Technol. Conf. doi:10.15530/urtec-2014-1923519

Antrett, P., Vackiner, A., Hilgers, C., Wollenberg, U., Kukla, P. a, Urai, J.L., Stollhofen, H., 2011. Nano-Scale Visualization of a Permian Tight Gas Reservoir. DGMK/ÖGEW Veranstaltung Frühjahrstagung 40821, Poster.

Aplin, A.C., Larter, S.R., 2005. Fluid Flow, Pore Pressure, Wettability, and Leakage in Mudstone Cap Rocks. Am. Assoc. Pet. Geol. Spec. Bull. Am. Assoc. Pet. Geol. Hedb. Ser. 2, 1–12. doi:10.1306/1060752H23158

Aplin, A.C., Macquaker, J.H.S., 2011. Mudstone diversity: Origin and implications for source, seal, and reservoir properties in petroleum systems. Am. Assoc. Pet. Geol. Bull. 95, 2031–2059. doi:10.1306/03281110162

Aplin, A.C., Macquaker, J.H.S., C., A.A., S., M.J.H., Aplin, A.C., Macquaker, J.H.S., 2011. Mudstone diversity: Origin and implications for source, seal, and reservoir properties in petroleum systems. Am. Assoc. Pet. Geol. Bull. 95, 2031–2059. doi:10.1306/03281110162

Aplin, A.C., Matenaar, I.F., McCarty, D.K., van der Pluijm, B.A., 2006. Influence of mechanical compaction and clay mineral diagenesis on the microfabric and pore-scale properties of deep-water Gulf of Mexico mudstones. Clays Clay Miner. 54, 500–514. doi:10.1346/CCMN.2006.0540411

Aplin, A.C., Moore, J.K.S., 2016. Observations of Pore Systems of Natural Siliciclastic Mudstones, in: Filling the Gaps – from Microscopic Pore Structures to Transport Properties in Shales. Clay Minerals Society, pp. 33–44.

Aquino Neto, F.R., Trigüis, J., Azevedo, D.A., Rodriques, R., Simoneit, B.R.T., 1992. Organic geochemistry of geographically unrelated tasmanites. Org. Geochem. 18, 791–803. doi:10.1016/0146-6380(92)90048-3

Armitage, P.J., Faulkner, D.R., Worden, R.H., Aplin, A.C., Butcher, A.R., Iliffe, J., 2011. Experimental measurement of, and controls on, permeability and permeability anisotropy of caprocks from the CO2 storage project at the Krechba Field, Algeria. J. Geophys. Res. Solid Earth. doi:10.1029/2011JB008385

Arthur, M.A., Bottjer, D.J., Dean, W.E., Fischer, A.G., Hattin, D.E., Kauffman, E.G., Pratt, L.M., Scholle, P.A., Group, R. on C.C. (R. O.C.C.., 1986. Rhythmic bedding in Upper Cretaceous pelagic carbonate sequences: Varying sedimentary response to climatic forcing. Geology 14, 153–156. doi:10.1130/0091-7613(1986)14<153:RBIUCP>2.0.CO;2

Austad, T., Milter, J., Rogaland, 1997. Spontanneous Imbibition of Water Into Low Permeable Chalk at Different Wettabilities Using Surfactants. SPE J. doi:10.2118/37236-MS

Austad, T., Rezaeidoust, A., Puntervold, T., 2010. Chemical Mechanism of Low Salinity

Water Flooding in Sandstone Reservoirs, in: SPE Improved Oil Recovery Symposium. Society of Petroleum Engineers. doi:10.2118/129767-MS

Austad, T., Strand, S., Høgnesen, E.J., Zhang, P., 2005. Seawater as IOR fluid in fractured chalk, in: Proceedings - SPE International Symposium on Oilfield Chemistry.

Awolayo, A., Sarma, H., Nghiem, L., 2018. Brine-Dependent Recovery Processes in Carbonate and Sandstone Petroleum Reservoirs: Review of Laboratory-Field Studies, Interfacial Mechanisms and Modeling Attempts. Energies 11, 3020. doi:10.3390/en11113020

Ayirala, S.C., Vijapurapu, C.S., Rao, D.N., 2006. Beneficial effects of wettability altering surfactants in oil-wet fractured reservoirs. doi:10.1016/j.petrol.2006.03.019

Bai, B., Elgmati, M., Zhang, H., Wei, M., 2013. Rock characterization of Fayetteville shale gas plays. Fuel 105, 645–652. doi:10.1016/j.fuel.2012.09.043

Bantignies, J.-L.L., Moulin, C.C.D., Dexpert, H., 1997. Wettability contrasts in kaolinite and illite clays: Characterization by infrared and x-ray absorption spectroscopies. Clays Clay Miner. 45, 184–193. doi:10.1346/CCMN.1997.0450206

Baruch, E.T., Kennedy, M.J., Löhr, S.C., Dewhurst, D.N., 2015. Feldspar dissolution-enhanced porosity in Paleoproterozoic shale reservoir facies from the Barney Creek Formation (McArthur Basin, Australia). Am. Assoc. Pet. Geol. Bull. 99, 1745–1770. doi:10.1306/04061514181

Basu, S., Sharma, M.M., 1997. Characterization of Mixed-Wettability States in Oil Reservoirs by Atomic Force Microscopy. SPE J. 2, 427–435. doi:10.2118/35572-PA

Bathurst, R.G.C., 1974. Marine Diagenesis of Shallow Water Calcium Carbonate Sediments. Annu. Rev. Earth Planet. Sci. 2, 257–274. doi:10.1146/annurev.ea.02.050174.001353

Bennett, B., Buckman, J.O., Bowler, B.F.J., Larter, S.R., Calgary, N.W., Building, D., Bennett, B., Buckman, J.O., Bowler, B.F.J., Larter, S.R., 2004. Wettability alteration in petroleum systems: The role of polar non-hydrocarbons. Pet. Geosci. 10, 271–277. doi:10.1144/1354-079303-606

Bennett, B., Larter, S.R., Bowler, B., Duin, A.C.T. Van, Winan, R., Buckman, J., Todd, A.C., 2002. Wettability alteration: the role of polar non-hydrocarbons.

Bennett, R.H.R.H., Bryant, W.R., Hulbert, M.H., 1991. Microstructure of Fine-Grained Sediments. Springer-Verlag.

Berg, R., 1999. Primary migration by oil-generation microfracturing in low-permeability source rocks: application to the Austin Chalk, Texas. archives.datapages.com.

Berg, S., Rücker, M., Ott, H., Georgiadis, A., Van Der Linde, H., Enzmann, F., Kersten, M.,

Armstrong, R.T., De With, S., Becker, J., Wiegmann, A., 2016. Connected pathway relative permeability from pore-scale imaging of imbibition. Adv. Water Resour. 90, 24–35. doi:10.1016/j.advwatres.2016.01.010

Bernard, S., Brown, L., Wirth, R., Schreiber, A., Schulz, H.-M., Horsfield, B., Aplin, A.C., Mathia, E.J., 2013a. Ch. 07: FIB-SEM and TEM Investigations of an Organic-rich Shale Maturation Series from the Lower Toarcian Posidonia Shale, Germany: Nanoscale Pore System and Fluid-rock Interactions. Electron Microsc. shale Hydrocarb. Reserv. AAPG Mem. 102 53–66. doi:10.1306/13391705M1023583

Bernard, S., Brown, L., Wirth, R., Schreiber, A., Schulz, H.-M., Horsfield, B., Aplin, A.C., Mathia, E.J., Bowen, L., 2013b. 7 FIB-SEM and TEM Investigations of an Organic-rich Shale Maturation Series from the Lower Toarcian Posidonia Shale, Germany: Nanoscale Pore System and Fluid-rock Interactions. Electron Microsc. shale Hydrocarb. Reserv. AAPG Mem. 102 53–66. doi:10.1306/13391705M1023583

Bernard, S., Horsfield, B., Schulz, H.-M., Schreiber, A., Wirth, R., Anh Vu, T.T., Perssen, F., Könitzer, S., Volk, H., Sherwood, N., Fuentes, D., 2010. Multi-scale detection of organic and inorganic signatures provides insights into gas shale properties and evolution. Chemie der Erde - Geochemistry 70, 119–133. doi:10.1016/J.CHEMER.2010.05.005

Bernard, S., Wirth, R., Schreiber, A., Schulz, H.-M., Horsfield, B., 2012a. Formation of nanoporous pyrobitumen residues during maturation of the Barnett Shale (Fort Worth Basin). Int. J. Coal Geol. 103, 3–11. doi:10.1016/j.coal.2012.04.010

Bernard, S., Wirth, R., Schreiber, A., Schulz, H.-M., Horsfield, B., Bernard, A., R., W., A., S., H.-M., S., B., H., Bernard, S., Wirth, R., Schreiber, A., Schulz, H.-M., Horsfield, B., 2012b. Formation of nanoporous pyrobitumen residues during maturation of the Barnett Shale (Fort Worth Basin). Int. J. Coal Geol. 103, 3–11. doi:10.1016/j.coal.2012.04.010

Berner, R.A., 1984. Sedimentary pyrite formation: An update. Geochim. Cosmochim. Acta 48, 605–615. doi:10.1016/0016-7037(84)90089-9

Bernhard, J.M., 1986. Characteristic assemblages and morphologies of benthic foraminifera from anoxic, organic-rich deposits; Jurassic through Holocene. J. Foraminifer. Res. 16, 207–215. doi:10.2113/gsjfr.16.3.207

Bertrand, E., Bonn, D., Broseta, D., Dobbs, H., Indekeu, J.O., Meunier, J., Ragil, K., Shahidzadeh, N., 2002. Wetting of alkanes on water. J. Pet. Sci. Eng. 33, 217–222. doi:10.1016/S0920-4105(01)00191-7

Birdwell, J.E., Washburn, K.E., 2015. Rapid Analysis of Kerogen Hydrogen-to-Carbon Ratios in Shale and Mudrocks by Laser-Induced Breakdown Spectroscopy. Energy

and Fuels 29, 6999–7004. doi:10.1021/acs.energyfuels.5b01566

Bjorlykke, K., 1998. Clay mineral diagenesis in sedimentary basins a key to the prediction of rock properties. Examples from the North Sea Basin. Clay Miner. 33, 15–34.

Bjørlykke, K., 2014. Relationships between depositional environments, burial history and rock properties. Some principal aspects of diagenetic process in sedimentary basins. Sediment. Geol. 301, 1–14. doi:10.1016/j.sedgeo.2013.12.002

Blood, D.R., Lash, G.G., 2015. Dynamic redox conditions in the Marcellus Shale as recorded by pyrite framboid size distributions.

Bondy, A.L., Kirpes, R.M., Merzel, R.L., Pratt, K.A., Banaszak Holl, M.M., Ault, A.P., 2017. Atomic Force Microscopy-Infrared Spectroscopy of Individual Atmospheric Aerosol Particles: Subdiffraction Limit Vibrational Spectroscopy and Morphological Analysis 89. doi:10.1021/acs.analchem.7b02381

Borysenko, A., Clennell, B., Sedev, R., Burgar, I., Ralston, J., Raven, M., Dewhurst, D., Liu, K., 2009. Experimental investigations of the wettability of clays and shales. J. Geophys. Res. Solid Earth 114, n/a-n/a. doi:10.1029/2008JB005928

Bovet, N., Yang, M., Javadi, M.S., Stipp, S.L.S., 2013. Interaction of alcohols with the calcite surface. J. Phys. Chem. Chem. Phys. J. Name 00, 1–3. doi:10.1039/x0xx00000x

Brady, P. V., Bryan, C.R., Thyne, G., Li, H., 2016. Altering wettability to recover more oil from tight formations. J. Unconv. Oil Gas Resour. 15, 79–83. doi:10.1016/J.JUOGR.2016.05.004

Brame, J., Griggs, C., 2016. Surface Area Analysis Using the Brunauer-Emmett-Teller (BET) Method Scientific Operating Procedure Series: SOP-C Environmental Laboratory.

Brown, R.J.S., Fatt, I., 1956. Measurements Of Fractional Wettability Of Oil Fields' Rocks By The Nuclear Magnetic Relaxation Method, in: Fall Meeting of the Petroleum Branch of AIME. Society of Petroleum Engineers. doi:10.2118/743-G

Brunauer, S., Emmett, P.H., Teller, E., 1938. Adsorption of Gases in Multimolecular Layers. J. Am. Chem. Soc. 60, 309–319. doi:10.1021/ja01269a023

Bryant, W.R., Bennett, R.H., Burkett, P.J., Rack, F.R., 1991. Microfabric and Physical Properties Characteristics of a Consolidated Clay Section: ODP Site 697, Weddell Sea. pp. 73–92. doi:10.1007/978-1-4612-4428-8_7

Bryndzia, L.T., Braunsdorf, N.R., 2014. From Source Rock to Reservoir: The Evolution of Self-Sourced Unconventional Resource Plays. Elements 10, 271–276. doi:10.2113/gselements.10.4.271

Buckley, J.S., 2001. Effective wettability of minerals exposed to crude oil, Current Opinion in Colloid and Interface Science. doi:10.1016/S1359-0294(01)00083-8

Buckley, J.S., 1998. Evaluation of Reservoir Wettability and its Effect on Oil Recovery. doi:10.2172/589685

Buckley, J S, 1998. MODIFICATION DE LA MOUILLABILIT*f* DES SURFACES SOLIDES PAR LES P*f*TROLES BRUTS ET LEURS ASPHALTéNES WETTING ALTERATION OF SOLID SURFACES BY CRUDE OILS AND THEIR ASPHALTENES 53.

Buckley, J.S., Liu, Y., Monsterleet, S., 1998. Mechanisms of Wetting Alteration by Crude Oils. SPE J. 3, 54–61. doi:10.2118/37230-PA

Buckley, J.S., Lord, D.L., 2003. Wettability and morphology of mica surfaces after exposure to crude oil. J. Pet. Sci. Eng. 39, 261–273. doi:10.1016/S0920-4105(03)00067-6

Buckley, J.S., Recovery, P., 1995. Asphaltene Precipitation and Crude Oil Wetting Crude oils can alter rock wettability with or without precipitation of asphaltenes . SPE Adv. Technol. Ser. 3, 53–59.

Buckley, J.S., Wang, J., 2002. Crude oil and asphaltene characterization for prediction of wetting alteration. J. Pet. Sci. Eng. 33, 195–202. doi:10.1016/S0920-4105(01)00189-9

Buckman, J.O., 2016. ESEM Application Note : Wettability Studies of Petroleum Reservoir Rocks. doi:10.13140/RG.2.1.1813.2246

Buckman, J.O., Polson, E.J., Todd, A.C., 2016. Measuring wettability in the environmental scanning electron microscope: a preliminary study using microinjected oil for contact angle measurement and hysteresis.

Bukar, M., 2013. Does oil emplacement stop diagenesis and quartz cementation in deeply buried sandstone reservoirs.

Burgos, W.D., Pisutpaisal, N., Mazzarese, M.C., Chorover, J., 2002. Adsorption of quinoline to kaolinite and montmorillonite. Environ. Eng. Sci. 19, 59–68. doi:10.1089/10928750252953697

Busch, A.;, Schweinar, K.;, Kampman, N., Coorn, A.; B., Pipich, V., Feoktystov, A., Leu, L., Amann-Hildenbrand, A.;, Bertier, P., Busch, A.;, Kampman, K., 2017. Determining the porosity of mudrocks using methodological pluralism. Geol. Soc. Spec. Publ. 454, 15–38. doi:10.1144/SP454.1

Bustin, R.M., Bustin, A.M.M., Cui, A., Ross, D., Pathi, V.M., 2008. Impact of Shale Properties on Pore Structure and Storage Characteristics. SPE Conf. SPE 119892. doi:10.2118/119892-MS

Canny, J., 1986. A Computational Approach to Edge Detection. IEEE Trans. Pattern Anal.

Mach. Intell. PAMI-8, 679–698. doi:10.1109/TPAMI.1986.4767851

Cao, Y., Yuan, G., Li, X., Wang, Y., Xi, K., Wang, X., Jia, Z., Yang, T., 2014. Characteristics and origin of abnormally high porosity zones in buried Paleogene clastic reservoirs in the Shengtuo area, Dongying Sag, East China. Pet. Sci. 11, 346–362. doi:10.1007/s12182-014-0349-y

Cappella, B., Dietler, G., 1999. Force-distance curves by atomic force microscopy. Surf. Sci. Rep. 34, 1–104. doi:10.1016/S0167-5729(99)00003-5

Cardott, B.J., Landis, C.R., Curtis, M.E., 2015. Post-oil solid bitumen network in the Woodford Shale, USA — A potential primary migration pathway. Int. J. Coal Geol. 139, 106–113. doi:10.1016/J.COAL.2014.08.012

Cavanaugh, T., Walls, J.D., 2015. Multi-Resolution Imaging of Shales Using Electron and Ion Microscopy, in: Proceedings of the 3rd Unconventional Resources Technology Conference. Society of Petroleum Engineers, Tulsa, OK, USA. doi:10.2118/178599-MS

Chalmers, Bustin, Power, 2012. Characterization of gas shale pore systems by porosimetry, pycnometry, surface area, and field emission scanning electron microscopy/transmission electron microscopy image analyses: Examples from the Barnett, Woodford, Haynesville, Marcellus, and Doig uni. Am. Assoc. Pet. Geol. Bull. 96, 1099–1119. doi:DOI:10.1306/10171111052

Chalmers, G.R., Bustin, R.M., Power, I.M., 2012. Characterization of gas shale pore systems by porosimetry, pycnometry, surface area, and field emission scanning electron microscopy/transmission electron microscopy image analyses: Examples from the Barnett, Woodford, Haynesville, Marcellus, and Doig uni. Am. Assoc. Pet. Geol. Bull. 96, 1099–1119. doi:DOI:10.1306/10171111052

Chalmers, G.R.L., Bustin, R.M., 2017. A multidisciplinary approach in determining the maceral (kerogen type) and mineralogical composition of Upper Cretaceous Eagle Ford Formation: Impact on pore development and pore size distribution. Int. J. Coal Geol. 171, 93–110. doi:10.1016/j.coal.2017.01.004

Chalmers, G.R.L., Bustin, R.M., 2015. Porosity and pore size distribution of deeply-buried fine-grained rocks: Influence of diagenetic and metamorphic processes on shale reservoir quality and exploration. J. Unconv. Oil Gas Resour. 12, 134–142. doi:10.1016/j.juogr.2015.09.005

Chalmers, G.R.L., Bustin, R.M., 2008. Lower Cretaceous gas shales in northeastern British Columbia, Part I: Geological controls on methane sorption capacity. Bull. Can. Pet. Geol. 56, 1–21. doi:10.2113/gscpgbull.56.1.1

Chalmers, G.R.L., Bustin, R.M., 2007. The organic matter distribution and methane capacity of the Lower Cretaceous strata of Northeastern British Columbia, Canada.

Int. J. Coal Geol. 70, 223–239. doi:10.1016/j.coal.2006.05.001

Chalmers, G.R.L., Bustin, R.M., Marc Bustin, R., Bustin, R.M., Marc Bustin, R., Bustin, R.M., Marc Bustin, R., 2017. A multidisciplinary approach in determining the maceral (kerogen type) and mineralogical composition of Upper Cretaceous Eagle Ford Formation: Impact on pore development and pore size distribution. Int. J. Coal Geol. 171, 93–110. doi:10.1016/j.coal.2017.01.004

Chandler, M.R., Meredith, P.G., Brantut, N., Crawford, B.R., 2016. Fracture toughness anisotropy in shale. J. Geophys. Res. Solid Earth. doi:10.1002/2015JB012756

Chandrasekhar, S., Mohanty, K.K., 2018. Effect of brine composition on oil-rock interaction by atomic force microscopy. J. Pet. Sci. Eng. 164, 289–301. doi:10.1016/j.petrol.2018.02.001

Chave, K.E., 1965. Carbonates: Association with organic matter in surface seawater. Science (80-.). 148, 1723–1724. doi:10.1126/science.148.3678.1723

Chave, K.E., Suess, E., 1970. CALCIUM CARBONATE SATURATION IN SEAWATER: EFFECTS OF DISSOLVED ORGANIC MATTER1. Limnol. Oceanogr. 15, 633–637. doi:10.4319/lo.1970.15.4.0633

Chen, H., Eichmann, S.L., Burnham, N.A., 2019. Understanding Calcium-Mediated Adhesion of Nanomaterials in Reservoir Fluids by Insights from Molecular Dynamics simulations. doi:10.1038/s41598-019-46999-8

Chen, J., Xiao, X., 2014. Evolution of nanoporosity in organic-rich shales during thermal maturation. Fuel 129, 173–181. doi:10.1016/j.fuel.2014.03.058

Chen, Q., Zhang, J., Tang, X., Li, W., Li, Z., 2016. Relationship between pore type and pore size of marine shale: An example from the Sinian–Cambrian formation, upper Yangtze region, South China. Int. J. Coal Geol. 158, 13–28. doi:10.1016/j.coal.2016.03.001

Chen, S., Han, Y., Fu, C., Zhang, han, Zhu, Y., Zuo, Z., 2016. Micro and nano-size pores of clay minerals in shale reservoirs: Implication for the accumulation of shale gas. Sediment. Geol. 342, 180–190. doi:10.1016/J.SEDGEO.2016.06.022

Chen, Y., Caro, L.D., Mastalerz, M., Schimmelmann, A., Blandón, A., 2013. Mapping the chemistry of resinite, funginite and associated vitrinite in coal with micro-FTIR. J. Microsc. 249, 69–81. doi:10.1111/j.1365-2818.2012.03685.x

Chilingar, G. V., Yen, T.F., 1983. Some Notes on Wettability and Relative Permeabilities of Carbonate Reservoir Rocks, II. Energy Sources 7, 67–75. doi:10.1080/00908318308908076

Cho, Y., Ozkan, E., Apaydin, O.G., 2013. Pressure-Dependent Natural-Fracture

Permeability in Shale and Its Effect on Shale-Gas Well Production. SPE Reserv. Eval. Eng. 16, 216–228. doi:10.2118/159801-PA

Chopinet, L., Formosa, C., Rols, M.P., Duval, R.E., Dague, E., 2013. Imaging living cells surface and quantifying its properties at high resolution using AFM in QI™ mode. Micron 48, 26–33. doi:10.1016/j.micron.2013.02.003

Clarkson, C.R., Bustin, R.M., 1996. Variation in micropore capacity and size distribution with composition in bituminous coal of the Western Canadian Sedimentary Basin: Implications for coalbed methane potential. Fuel 75, 1483–1498. doi:10.1016/0016-2361(96)00142-1

Clarkson, Christopher R., Solano, N., Bustin, R.M., Bustin, A.M.M., Chalmers, G.R., He, L., Melnichenko, Y.B., Radliński, A.P., Blach, T.P., 2013a. Pore structure characterization of North American shale gas reservoirs using USANS/SANS, gas adsorption, and mercury intrusion. Fuel 103, 606–616. doi:10.1016/j.fuel.2012.06.119

Clarkson, Christopher R., Solano, N., Bustin, R.M., Bustin, A.M.M., Chalmers, G.R.L., He, L., Melnichenko, Y.B., Radli Ski, A.P., Blach, T.P., 2013b. Pore structure characterization of North American shale gas reservoirs using USANS/SANS, gas adsorption, and mercury intrusion. Fuel 103, 606–616. doi:10.1016/j.fuel.2012.06.119

Clarkson, C.R., Solano, N., Bustin, R.M., Bustin, A.M.M., Chalmers, G.R.L., He, L., Melnichenko, Y.B., Radliński, A.P., Blach, T.P., 2013. Pore structure characterization of North American shale gas reservoirs using USANS/SANS, gas adsorption, and mercury intrusion. Fuel 103, 606–616. doi:10.1016/j.fuel.2012.06.119

Clarkson, C.R., Wood, J.M., Burgis, S.E., Aquino, S.D., Freeman, M., Birss, V., 2012. Nanopore Structure Analysis and Permeability Predictions for a Tight Gas / Shale Reservoir Using Low-Pressure Adsorption and Mercury Intrusion Techniques. Spe 155537 1–18. doi:10.2118/155537-MS

Clementz, D.M., 1979. Effect of oil and bitumen saturation on source rock pyrolysis. Am. Assoc. Pet. Geol. Bull.

Cole, D.R., Ok, S., Phan, A., 2013. Hydrocarbon Behavior at Nanoscale Interfaces. Artic. Rev. Mineral. Geochemistry. doi:10.2138/rmg.2013.75.16

Comisky, J.T., Santiago, M., Mccollom, B., Buddhala, A., Newsham, K.E., 2011a. Sample Size Effects on the Application of Mercury Injection Capillary Pressure for Determining the Storage Capacity of Tight Gas and Oil Shales, in: Canadian Unconventional Resources Conference. Society of Petroleum Engineers, pp. 1–23. doi:10.2118/149432-MS

Comisky, J.T., Santiago, M., Mccollom, B., Buddhala, A., Newsham, K.E., 2011b. Sample Size Effects on the Application of Mercury Injection Capillary Pressure for

Determining the Storage Capacity of Tight Gas and Oil Shales, in: Canadian Unconventional Resources Conference. Society of Petroleum Engineers, pp. 1–23. doi:10.2118/149432-MS

Craddock, P.R., Le Doan, T. Van, Bake, K., Polyakov, M., Charsky, A.M., Pomerantz, A.E., 2015. Evolution of Kerogen and Bitumen during Thermal Maturation via Semi-Open Pyrolysis Investigated by Infrared Spectroscopy. Energy & Fuels 29, 2197–2210. doi:10.1021/ef5027532

Cuiec, L., 1984. Rock/Crude-Oil Interactions and Wettability: An Attempt To Understand Their Interrelation, in: SPE Annual Technical Conference and Exhibition. Society of Petroleum Engineers. doi:10.2118/13211-MS

Curtis, M.E., Ambrose, R.J., 2011. Investigation of the relationship between organic porosity and thermal maturity in the Marcellus Shale. SPE Conf. SPE 144370, 4pp. doi:10.2118/144370-ms

Curtis, M.E., Ambrose, R.J., Sondergeld, C.H., 2010. Structural Characterization of Gas Shales on the Micro- and Nano-Scales. Can. Unconv. Resour. Int. Pet. Conf. 137693. doi:10.2118/137693-MS

Curtis, M.E., Ambrose, R.J., Sondergeld, C.H., Rai, C.S., 2011. Investigation of the Relationship Between Organic Porosity and Thermal Maturity in The Marcellus Shale, in: SPE-144370-MS. Society of Petroleum Engineers. doi:10.2118/144370-MS

Curtis, Mark E., Cardott, B.J., Sondergeld, C.H., Rai, C.S., 2012. Development of organic porosity in the Woodford Shale with increasing thermal maturity. Shale Gas Shale Oil Petrol. Petrophysics 103, 26–31. doi:10.1016/j.coal.2012.08.004

Curtis, Mark E, Sondergeld, C.H., Ambrose, R.J., Rai, C.S., 2012. Microstructural investigation of gas shales in two and three dimensions using nanometer-scale resolution imaging. Am. Assoc. Pet. Geol. Bull. 96, 665–677. doi:10.1306/08151110188

Czerniakowski, L.A., Lohmann, K.C., Wilson, J., 1984. Closed-system marine burial diagenesis: isotopic data from the Austin Chalk and its components. Sedimentology 31, 863–877. doi:10.1111/j.1365-3091.1984.tb00892.x

Davies, R.J., Mathias, S.A., Moss, J., Hustoft, S., Newport, L., 2012. Hydraulic fractures: How far can they go? Mar. Pet. Geol. 37, 1–6. doi:10.1016/j.marpetgeo.2012.04.001

Davudov, D., Moghanloo, R.G., Yuan, B., 2018. A Special Focus on Formation Damage in Unconventional Reservoirs, in: Formation Damage During Improved Oil Recovery. Elsevier, pp. 385–416. doi:10.1016/b978-0-12-813782-6.00010-5

Dawson, W.C., 2000. AAPG Datapages/Archives: Shale Microfacies: Eagle Ford Group (Cenomanian-Turonian) North-Central Texas Outcrops and Subsurface Equivalents http://archives.datapages.com/data/gcags/data/050/050001/0607.htm

Dawson, W.C., 1997. Limestone Microfacies and Sequence Stratigraphy: Eagle Ford Group (Cenomanian-Turonian)North-Central Texas Outcrops 47.

Dawson, W.C., Almon, W.M., 2010. Eagle Ford Shale Variability: Sedimentologic Influences on Source and Reservoir Character in an Unconventional Resource Unit. AAPG Datapages/Archives.

Dawson, W.C., Almon, W.R., Dempster, K., Sutton, S.J., 2008. Shale Variability in Deep-Marine Depositional Systems: Implications for Seal Character -Subsurface and Outcrop Examples*.

Dayal, A.M., 2017. Deposition and Diagenesis. Shale Gas 13–23. doi:10.1016/B978-0-12-809573-7.00002-0

Dazzi, A., Prater, C.B., 2017. AFM-IR: Technology and Applications in Nanoscale Infrared Spectroscopy and Chemical Imaging. Chem. Rev. 117, 5146–5173. doi:10.1021/acs.chemrev.6b00448

Dazzi, A., Prater, C.B., Hu, Q., Chase, D.B., Rabolt, J.F., Marcott, C., 2012. AFM-IR: Combining atomic force microscopy and infrared spectroscopy for nanoscale chemical characterization. Appl. Spectrosc. 66, 1365–1384. doi:10.1366/12-06804

Deglint, H.J., Clarkson, C.R., DeBuhr, C., Ghanizadeh, A., 2017. Live Imaging of Micro-Wettability Experiments Performed for Low-Permeability Oil Reservoirs. Sci. Rep. 7. doi:10.1038/s41598-017-04239-x

Denne, R.A., Breyer, J.A., Kosanke, T.H., Spaw, J.M., Callender, A.D., Hinote, R.E., Kariminia, M., Tur, N., Kita, Z., Kita, Z., Lees, J.A., Rowe, H.D., 2016. Biostratigraphic and geochemical constraints on the stratigraphy and depositional environments of the Eagle Ford and Woodbine groups of Texas. AAPG Mem. 110, 1–86. doi:10.1306/13541957M1103660

Denne, R.A., Hinote, R.E., Breyer, J.A., Kosanke, T.H., Lees, J.A., Engelhardt-Moore, N., Spaw, J.M., Tur, N., 2014. The Cenomanian–Turonian Eagle Ford Group of South Texas: Insights on timing and paleoceanographic conditions from geochemistry and micropaleontologic analyses. Palaeogeogr. Palaeoclimatol. Palaeoecol. 413, 2–28. doi:10.1016/j.palaeo.2014.05.029

Dereppe, J.M., Pironon, J., Moreaux, C., 1994. Characterization of the composition of fluid inclusions in minerals by 1H NMR. Am. Mineral. 79, 712–718.

Desbois, G., Urai, J.L., Houben, M., Hemes, S., Klaver, J., 2011. BIB-SEM of representative area clay structures: Insights and challenges. Unclassif. NEA/RWM/CLAYCLUB 67.

Desbois, G., Urai, J.L., Kukla, P.A., G., D., L., U.J., A., K.P., 2009. Morphology of the pore space in claystones – evidence from BIB/FIB ion beam sectioning and cryo-SEM observations. eEarth Discuss. 4, 1–19. doi:10.5194/eed-4-1-2009

Dewhurst, D.N., Aplin, A.C., Sarda, J.-P., Yang, Y., 1998. Compaction-driven evolution of porosity and permeability in natural mudstones: An experimental study. J. Geophys. Res. Solid Earth 103, 651–661. doi:10.1029/97JB02540

DiStefano, V.H., McFarlane, J., Anovitz, L.M., Stack, A.G., Gordon, A.D., Littrell, K.C., Chipera, S.J., Hunt, R.D., Lewis, S.A., Hale, R.E., Perfect, E., 2016. Extraction of organic compounds from representative shales and the effect on porosity. J. Nat. Gas Sci. Eng. 35, 646–660. doi:10.1016/j.jngse.2016.08.064

Donald E. Hattin, D.E., 1975. Petrology and Origin of Fecal Pellets in Upper Cretaceous Strata of Kansas and Saskatchewan. SEPM J. Sediment. Res. 686–696. doi:10.1306/212F6E10-2B24-11D7-8648000102C1865D

Dong, T., Harris, N.B., 2013. Ch. 08: Pore Size Distribution and Morphology in the Horn River Shale, Middle and Upper Devonian, Northeastern British Columbia, Canada. Electron Microsc. shale Hydrocarb. Reserv. AAPG Mem. 102 67–80. doi:10.1306/13391706M1023584

Donovan, A.D., Staerker, T.S., Pramudito, A., Li, W., Corbett, M.J., Lowery, C.M., Romero, A.M., Gardner, R.D., 2012. The Eagle Ford Outcrops of West Texas: A Laboratory for Understanding Heterogeneities within Unconventional Mudstone Reservoirs. Gulf Coast Assoc. Geol. Soc. J. 1, 162–185.

Driskill, B., Suurmeyer, N., Rilling-Hall, S., Govert, A., Garbowicz, A., 2009. SPE 154528 Reservoir Description Of The Subsurface Eagle Ford Formation, Maverick Basin Area, South Texas, USA.

Driskill, B., Suurmeyer, N., Rilling-Hall, S., Govert, A.M., Garbowicz, A., 2012. Reservoir Description Of The Subsurface Eagle Ford Formation, Maverick Basin Area, South Texas, USA, in: SPE Europec/EAGE Annual Conference. Society of Petroleum Engineers. doi:10.2118/154528-MS

Drummond, C., Israelachvili, J., 2002. Surface forces and wettability. J. Pet. Sci. Eng. 33, 123–133. doi:10.1016/S0920-4105(01)00180-2

Dunham, R., 1962. Classification of carbonate rocks according to depositional textures.

Edman, J.D., Pitman, J.K., 2010. Geochemistry of Eagle Ford Group source rocks and oils from the First Shot Field Area, Texas. GCAGS Trans. 60, 217–234.

El-Saleh, M., 1996. Analogy procedure for the evaluation of CO2 flooding potential for reservoirs in the Permian and Delaware basins, in: Proceedings - SPE Symposium on Improved Oil Recovery.

Elderbak, K., Leckie, R.M., Tibert, N.E., 2014. Paleoenvironmental and paleoceanographic changes across the Cenomanian–Turonian Boundary Event (Oceanic Anoxic Event 2) as indicated by foraminiferal assemblages from the eastern margin of the

Cretaceous Western Interior Sea. Palaeogeogr. Palaeoclimatol. Palaeoecol. 413, 29–48. doi:10.1016/j.palaeo.2014.07.002

Eldrett, J.S., Ma, C., Bergman, S.C., Lutz, B., Gregory, F.J., Dodsworth, P., Phipps, M., Hardas, P., Minisini, D., Ozkan, A., Ramezani, J., Bowring, S.A., Kamo, S.L., Ferguson, K., Macaulay, C., Kelly, A.E., 2015. An astronomically calibrated stratigraphy of the Cenomanian, Turonian and earliest Coniacian from the Cretaceous Western Interior Seaway, USA: Implications for global chronostratigraphy. Cretac. Res. 56, 316–344. doi:10.1016/j.cretres.2015.04.010

Eldrett, J.S., Minisini, D., Bergman, S.C., 2014. Decoupling of the carbon cycle during Ocean Anoxic Event 2. Geology 42, 567–570. doi:10.1130/G35520.1

Eoghan, D., Cook, D., Hackley, P.C., Kjoller, K., Dawson, D., Shetty, R., 2016. Investigating Oil-Prone Kerogen Conversion to Hydrocarbons Using AFM-based Infrared Spectroscopy. Am. Geophys. Union, Fall Gen. Assem. 2016, Abstr. #MR51C-2730.

Er, C., Li, Y., Zhao, J., Wang, R., Bai, Z., Han, Q., 2016. Pore formation and occurrence in the organic-rich shales of the Triassic Chang-7 Member, Yanchang Formation, Ordos Basin, China. J. Nat. Gas Geosci. 1, 435–444. doi:10.1016/j.jnggs.2016.11.013

Ergene, S.M., 2014. Lithologic heterogeneity of the Eagle Ford Formation, South Texas. Thesis.

Ese, M.-H.H., Sjöblom, J., Djuve, J., Pugh, R., 2000. An atomic force microscopy study of asphaltenes on mica surfaces. Influence of added resins and demulsifiers. Colloid Polym. Sci. 278, 532–538. doi:10.1007/s003960050551

Ezat Heydari,1 William J. Wade2, 2002. Massive recrystallization of low-Mg calcite at high temperatures in hydrocarbon source rocks: Implications for organic acids as factors in diagenesis. Am. Assoc. Pet. Geol. Bull. 86. doi:10.1306/61EEDC7E-173E-11D7-8645000102C1865D

Fabricius, I.L., 2007. Chalk: composition, diagenesis and physical properties. Bull. Geol. Soc. Denmark 55, 97–128.

Fabricius, I.L., 2003. How burial diagenesis of chalk sediments controls sonic velocity and porosity. Am. Assoc. Pet. Geol. Bull. 87, 1755–1778. doi:10.1306/06230301113

Feng, L., Xu, L., 2015. Implications of Shale Oil Compositions on Surfactant Efficacy for Wettability Alteration, in: SPE-172974-MS. Society of Petroleum Engineers, pp. 649–662. doi:10.2118/172974-MS

Feng, X., Simpson, M.J., 2008. Temperature responses of individual soil organic matter components. J. Geophys. Res. 113, G03036. doi:10.1029/2008JG000743

Fifield, F.W., Kealey, D., 1991. Principles and practice of analytical chemistry. Anal. Chim.

Acta. doi:10.1016/s0003-2670(00)82583-0

Fishman, N., Guthrie, J.M., Honarpour, M., 2014. Development of Organic and Inorganic Porosity in the Cretaceous Eagle Ford Formation, South Texas*.

Fishman, N.S., Hackley, P.C., Lowers, H.A., Hill, R.J., Egenhoff, S.O., Eberl, D.D., Blum, A.E., 2012. The nature of porosity in organic-rich mudstones of the Upper Jurassic Kimmeridge Clay Formation, North Sea, offshore United Kingdom. Int. J. Coal Geol. 103, 32–50. doi:10.1016/j.coal.2012.07.012

Flügel, E., 2004. Microfacies of carbonate rocks : analysis, interpretation and application. Springer.

Fowler, A.C., Yang, X.-S., 2003. Dissolution/precipitation mechanisms for diagenesis in sedimentary basins. J. Geophys. Res. Solid Earth 108. doi:10.1029/2002jb002269

Frébourg, G., Ruppel, S.C., Loucks, R.G., Lambert, J., 2016. Depositional controls on sediment body architecture in the Eagle Ford/Boquillas system: Insights from outcrops in west Texas, United States. Am. Assoc. Pet. Geol. Bull. 100, 657–682. doi:10.1306/12091515101

Friesen, W., Mikula, R., 1988. Mercury porosimetry of coalsPore volume distribution and compressibility. Fuel 67, 1516–1520. doi:10.1016/0016-2361(88)90069-5

Gale, J.F.W., Holder, J., 2010. Natural fractures in some US shales and their importance for gas production. Geol. Soc. London, Pet. Geol. Conf. Ser. 7, 1131–1140. doi:10.1144/0071131

Galloway, W.E., 2008. Chapter 15 Depositional Evolution of the Gulf of Mexico Sedimentary Basin, in: Miall, A.D. (Ed.), Sedimentary Basins of the World. Elsevier, pp. 505–549.

Gamero Diaz, H., Miller, C.K., Lewis, R.E., Contreras Fuentes, C., 2013. Evaluating the impact of mineralogy on reservoir quality and completion quality of organic shale plays. Search Discov. 41221, 5pp.

Ghanizadeh, A., Clarkson, C.R., Aquino, S., Ardakani, O.H., Sanei, H., 2015. Petrophysical and geomechanical characteristics of Canadian tight oil and liquid-rich gas reservoirs: I. Pore network and permeability characterization. Fuel 153, 664–681. doi:10.1016/j.fuel.2015.03.020

Giles, M.R., de Boer, R.B., 1990. Origin and significance of redistributional secondary porosity. Mar. Pet. Geol. 7, 378–397. doi:10.1016/0264-8172(90)90016-A

Gonzalez, G., Travalloni-Louvisse, A.M., 1993. Adsorption of asphaltenes and its effect on oil production. SPE Prod. Facil. 8, 91–96. doi:10.2118/21039-PA

Gorniak, K.G., 2016. Porosity evolution in the chalk: An example from the chalk-type

source rocks of the outer Carpathians (Poland). doi:10.1346/CMS-WLS-21.16

Gottardi, R., Mason, S.L., 2018. Characterization of the natural fracture system of the Eagle Ford Formation (Val Verde County, Texas). Am. Assoc. Pet. Geol. Bull. 102, 1963–1984. doi:10.1306/03151817323

Goulty, 1998. Relationships between porosity and effective stress in shales. First Break 16, 413–419. doi:10.1046/j.1365-2397.1998.00698.x

Grafton, R., Cronshaw, I., Moore, M., 2016. Risks, Rewards and Regulation of Unconventional Gas: A Global Perspective.

Gregg S. J., S.K.S.W., Gregg, S.J., Sing, K.S.W., 1982. Adsorption, surface area, and porosity. Academic Press, London; New York.

Gregg, S.J., Sing, K.S.W., Salzberg, H.W., 1967. Adsorption Surface Area and Porosity. J. Electrochem. Soc. 114, 279C-279C. doi:10.1149/1.2426447

Habibi, A., Dehghanpour, H., Binazadeh, M., Bryan, D., Uswak, G., 2016. Advances in understanding wettability of tight oil formations: A montney case study, in: SPE Reservoir Evaluation and Engineering. Society of Petroleum Engineers, pp. 583–603. doi:10.2118/175157-PA

Hackley, P.C., Cardott, B.J., 2016. Application of organic petrography in North American shale petroleum systems: A review. Int. J. Coal Geol. 163, 8–51. doi:10.1016/j.coal.2016.06.010

Hackley, P.C., Walters, C.C., Kelemen, S.R., Mastalerz, M., Lowers, H.A., 2017. Organic petrology and micro-spectroscopy of Tasmanites microfossils: Applications to kerogen transformations in the early oil window. Org. Geochem. 114, 23–44. doi:10.1016/j.orggeochem.2017.09.002

Hamouda, A.A., Karoussi, O., 2008. Effect of Temperature, Wettability and Relative Permeability on Oil Recovery from Oil-wet Chalk. Energies 1, 19–34. doi:10.3390/en1010019

Hansen, G., Hamouda, A.., Denoyel, R., 2000. The effect of pressure on contact angles and wettability in the mica/water/n-decane system and the calcite+stearic acid/water/n-decane system. Colloids Surfaces A Physicochem. Eng. Asp. 172, 7–16. doi:10.1016/S0927-7757(99)00498-7

Harbor, R.L., 2011. Facies characterization and stratigraphic architecture of organic-rich mudrocks, Upper Cretaceous Eagle Ford Formation, South Texas.

Harbor, Ruppel, 2011. Facies and lithostratigraphy of the Upper Cretaceous (Turonian-Cenomanian) Eagle Ford Formation, Central and South Texas, in: AAPG (American Association of Petroleum Geologists).

Harvey, D., 2000. Modern Analytic Chemistry, The McGraw-Hill Companies. doi:10.1136/jcp.30.1.93-a

Hassenkam, T., Andersson, M.P., Hilner, E., Matthiesen, J., Dobberschütz, S., Dalby, K.N., Bovet, N., Stipp, S.L.S., Salino, P., Reddick, C., Collins, I.R., 2016. Could Atomic-Force Microscopy Force Mapping Be a Fast Alternative to Core-Plug Tests for Optimizing Injection-Water Salinity for Enhanced Oil Recovery in Sandstone? SPE J. 21, 0720–0729. doi:10.2118/169136-PA

Hassenkam, T., Andersson, M.P., Hilner, E., Matthiesen, J., Dobberschütz, S., Dalby, K.N., Bovet, N., Stipp, S.L.S., Salino, P., Reddick, C., Collins, I.R., Dobberschu, S., Dalby, K.N., Bovet, N., 2015. Could Atomic-Force Microscopy Force Mapping Be a Fast Alternative to Core-Plug Tests for Optimizing Injection-Water Salinity for Enhanced Oil Recovery in Sandstone? SPE J. 21, 12–16. doi:10.2118/169136-PA

Hassenkam, T., Pedersen, C.S.S., Dalby, K., Austad, T., Stipp, S.L.S.L.S., 2011. Pore scale observation of low salinity effects on outcrop and oil reservoir sandstone. Colloids Surfaces A Physicochem. Eng. Asp. 390, 179–188. doi:10.1016/j.colsurfa.2011.09.025

Hassenkam, T., Skovbjerg, L.L., Stipp, S.L.S., 2009. Probing the intrinsically oil-wet surfaces of pores in North Sea chalk at subpore resolution. Proc. Natl. Acad. Sci. U. S. A. 106, 6071–6. doi:10.1073/pnas.0901051106

Heath, Jason E, Dewers, T.A., McPherson, B.J.O.L., Petrusak, R., Chidsey, T.C., Rinehart, A.J., Mozley, P.S., 2011. Pore networks in continental and marine mudstones: Characteristics and controls on sealing behavior. Geosphere 7, 429–454. doi:10.1130/GES00619.1

Heath, Jason E., Dewers, T.A., McPherson, B.J.O.L.O.L., Petrusak, R., Chidsey, T.C., Rinehart, A.J., Mozley, P.S., 2011. Pore networks in continental and marine mudstones: Characteristics and controls on sealing behavior. Geosphere 7, 429–454. doi:10.1130/GES00619.1

Hedges, J.I., Keil, R.G., 1995. Sedimentary organic matter preservation: an assessment and speculative synthesis. Mar. Chem. 49, 81–115. doi:10.1016/0304-4203(95)00008-F

Helgeson, H.C., Knox, A.M., Owens, C.E., Shock, E.L., 1993. Petroleum, oil field waters, and authigenic mineral assemblages Are they in metastable equilibrium in hydrocarbon reservoirs. Geochim. Cosmochim. Acta 57, 3295–3339. doi:10.1016/0016-7037(93)90541-4

Hemes, S., Desbois, G., Klaver, J., Urai, J.L., 2016. Microstructural characterisation of the Ypresian clays (Kallo-1) at nanometre resolution, using broad-ion beam milling and scanning electron microscopy. Netherlands J. Geosci. en Mijnb. 95–98. doi:10.1017/njg.2016.16

Hemes, S., Desbois, G., Urai, J.L., Schröppel, B., Schwarz, J.-O., 2015. Multi-scale characterization of porosity in Boom Clay (HADES-level, Mol, Belgium) using a combination of X-ray μ-CT, 2D BIB-SEM and FIB-SEM tomography. Microporous Mesoporous Mater. 208, 1–20. doi:10.1016/j.micromeso.2015.01.022

Henriksen, K., Stipp, S.L.S., Young, J.R., Marsh, M.E., 2004. Biological control on calcite crystallization; AFM investigation of coccolith polysaccharide function. Am. Mineral. 89, 1709–1716. doi:10.2138/am-2004-11-1217

Hentz, T.F., Ruppel, S.C., 2010. Regional Lithostratigraphy of the Eagle Ford Shale: Maverick Basin to East Texas Basin. AAPG Datapages/Archives.

Heydari, N., Asgari, M., Narjes, •, Kaveh, S., Fakhroueian, Z., 2018. Novel application of PEG/SDS interaction as a wettability modifier of hydrophobic carbonate surfaces. doi:10.1007/s12182-018-0260-z

Higgs, K.E., Zwingmann, H., Reyes, A.G., Funnell, R.H., 2007. Diagenesis, porosity evolution and petroleum emplacement in tght gas reservoirs, Taranaki Basin, New Zealand. J. Sediment. Res. 77, 1003–1025. doi:10.2110/jsr.2007.095

Hillier, S., 2000. Accurate quantitative analysis of clay and other minerals in sandstones by XRD: comparison of a Rietveld and a reference intensity ratio (RIR) method and the importance of sample preparation, Clay Minerals. De Gruyter. doi:10.1180/000985500546666

Hilner, E., Andersson, M.P., Hassenkam, T., Matthiesen, J., Salino, P.A., Stipp, S.L.S., 2015. The effect of ionic strength on oil adhesion in sandstone – the search for the low salinity mechanism. Sci. Rep. 5. doi:10.1038/srep09933

Hiorth, A., Cathles, L.M., Madland, M. V., 2010. The Impact of Pore Water Chemistry on Carbonate Surface Charge and Oil Wettability. Transp. Porous Media 85, 1–21. doi:10.1007/s11242-010-9543-6

Hirasaki, G.J., Zhang, D.L., 2004. Surface chemistry of oil recovery from fractured, oil-wet, carbonate formations. SPE J. 9, 151–162. doi:10.2118/88365-PA

Hoeiland, S., Barth, T., Blokhus, A.M., Skauge, A., 2001. The effect of crude oil acid fractions on wettability as studied by interfacial tension and contact angles. J. Pet. Sci. Eng. 30, 91–103. doi:10.1016/S0920-4105(01)00106-1

Holbrook, O.C., Bernard, G.G., 1958. Determination of Wettability by Dye Adsorption.

Hopkins, P.A., Omland, I., Layti, F., Strand, S., Puntervold, T., Austad, T., 2017. Crude Oil Quantity and Its Effect on Chalk Surface Wetting. Energy & Fuels 31, 4663–4669. doi:10.1021/acs.energyfuels.6b02914

Hornby, B.E., 1998. Experimental laboratory determination of the dynamic elastic

properties of wet, drained shales. J. Geophys. Res. Solid Earth. doi:10.1029/97jb02380

Horsfield, B., Disko, U., Leistner, F., 1989. The micro-scale simulation of maturation: outline of a new technique and its potential applications. Geol. Rundschau 78, 361–373. doi:10.1007/BF01988370

Houben, M., 2013. In situ characterization of the microstructure and porosity of Opalinus Clay (Mont Terri Rock Laboratory, Switzerland). Fak. für Georessourcen und Mater. Dissertati, 192.

Houben, M.E.E., Desbois, G., Urai, J.L., de Winter, D.A.M., Drury, M.R., Schwarz, J.O., 2014. No Title. doi:10.3997/2214-4609.20140020

Hsu, S., Nelson, P.P., 2002. Characterization of Eagle Ford Shale.PDF 67, 169–183.

Irwin, H., Curtis, C., Coleman, M., 1977. Isotopic evidence for source of diagenetic carbonates formed during burial of organic-rich sediments. Nature. doi:10.1038/269209a0

IUPAC, 1985. Reporting physisorption data for gas/solid systems-with special reference to the determination of surface area and porosity.

Jadhunandan, P.P., Morrow, N.R., 1991. Spontaneous imbibition of water by crude oil/brine/rock systems. Situ 15, 319–345.

Jakob, D.S., Wang, L., Wang, H., Xu, X.G., 2019. Spectro-Mechanical Characterizations of Kerogen Heterogeneity and Mechanical Properties of Source Rocks at 6 nm Spatial Resolution. Anal. Chem. 91, 8883–8890. doi:10.1021/acs.analchem.9b00264

Jarvie, D.M., Hill, R.J., Ruble, T.E., Pollastro, R.M., 2007. Unconventional shale-gas systems: The Mississippian Barnett Shale of north-central Texas as one model for thermogenic shale-gas assessment. Am. Assoc. Pet. Geol. Bull. 91, 475–499. doi:10.1306/12190606068

Javadpour, F., 2009. Nanopores and apparent permeability of gas flow in mudrocks (shales and siltstone). J. Can. Pet. Technol. 48, 16–21. doi:10.2118/09-08-16-DA

Javadpour, F., Moravvej Farshi, M., Amrein, M., Farshi, M.M., 2012. Atomic-Force Microscopy: A New Tool for Gas-Shale Characterization. J. Can. Pet. Technol. 51, 236–243. doi:10.2118/161015-PA

Jennings, D.S., Anthia, J., 2013. Electron Microscopy of Shale Hydrocarbon Reservoirs. Am. Assoc. Pet. Geol. 102, 101–113. doi:10.1306/13391708M1023586

Jennings, D.S., Antia, J., 2013. Petrographic Characterization of the Eagle Ford Shale, South Texas: Mineralogy, Common Constituents, and Distribution of Nanometer-scale Pore Types. Electron Microsc. shale Hydrocarb. Reserv. AAPG Mem. 102 101–114. doi:10.1306/13391708M1023586

Jia, W., Wang, Q., Liu, J., Peng, P., Li, B., Lu, J., 2014. The effect of oil expulsion or retention on further thermal degradation of kerogen at the high maturity stage: A pyrolysis study of type II kerogen from Pingliang shale, China. Org. Geochem. 71, 17–29. doi:10.1016/j.orggeochem.2014.03.009

Jiang, T., Rylander, E., Singer, P.M., Lewis, R.E., Sinclair, S.M., 2013. Integrated Petrophysical Interpretation of Eagle Ford Shale with 1-D and 2-D Nuclear Magnetic Resonance (NMR), in: SPWLA-2013-LL. Society of Petrophysicists and Well-Log Analysts.

Jiao, K., Yao, S., Liu, C., Gao, Y., Wu, H., Li, M., Tang, Z., 2014. The characterization and quantitative analysis of nanopores in unconventional gas reservoirs utilizing FESEM–FIB and image processing: An example from the lower Silurian Longmaxi Shale, upper Yangtze region, China. Int. J. Coal Geol. 128–129, 1–11. doi:10.1016/j.coal.2014.03.004

Jørgensen, B.B., 1982. Mineralization of organic matter in the sea bed—the role of sulphate reduction. Nature 296, 643–645. doi:10.1038/296643a0

Josh, M., Esteban, L., Delle Piane, C., Sarout, J., Dewhurst, D.N., Clennell, M.B., 2012. Laboratory characterisation of shale properties. Unconv. Hydrocarb. Explor. Prod. Challenges 88–89, 107–124. doi:10.1016/j.petrol.2012.01.023

Kakati, A., Sangwai, J.S., 2018. Wettability Alteration of Mineral Surface during Low-Salinity Water Flooding: Role of Salt Type, Pure Alkanes, and Model Oils Containing Polar Components. Energy & Fuels 32, 3127–3137. doi:10.1021/acs.energyfuels.7b03727

Karimi, M., Al-Maamari, R.S., Ayatollahi, S., Mehranbod, N., 2015. Mechanistic study of wettability alteration of oil-wet calcite: The effect of magnesium ions in the presence and absence of cationic surfactant. Colloids Surfaces A Physicochem. Eng. Asp. 482, 403–415. doi:10.1016/j.colsurfa.2015.07.001

Karoussi, O., Hamouda, A.A., 2008. Macroscopic and nanoscale study of wettability alteration of oil-wet calcite surface in presence of magnesium and sulfate ions. J. Colloid Interface Sci. 317, 26–34. doi:10.1016/J.JCIS.2007.09.045

Karoussi, O., Skovbjerg, L.L., Hassenkam, T., Stipp, S.L.S., Hamouda, A.A., 2008. AFM study of calcite surface exposed to stearic and heptanoic acids. Colloids Surfaces A Physicochem. Eng. Asp. 325, 107–114. doi:10.1016/J.COLSURFA.2008.04.039

Kasha, A., Al-Hashim, H., Abdallah, W., Taherian, R., Sauerer, B., 2015. Effect of Ca2+, Mg2+ and SO42- ions on the zeta potential of calcite and dolomite particles aged with stearic acid. Colloids Surfaces A Physicochem. Eng. Asp. 482, 290–299. doi:10.1016/j.colsurfa.2015.05.043

Kastner, M., Keene, J.B., Gieskes, J.M., 1977. Diagenesis of siliceous oozes—I. Chemical controls on the rate of opal-A to opal-CT transformation—an experimental study. Geochim. Cosmochim. Acta 41, 1041–1059. doi:10.1016/0016-7037(77)90099-0

Katsube, T.J., Williamson, M.A., 1994. Effects of diagenesis on shale nano-pore structure and implications for sealing capacity. Clay Miner. 29, 451–461.

Keller, L.M., Holzer, L., Wepf, R., Gasser, P., 2011. 3D geometry and topology of pore pathways in Opalinus clay: Implications for mass transport. Appl. Clay Sci. 52, 85–95. doi:10.1016/j.clay.2011.02.003

Kim, S., Marcano, M.C., Becker, U., 2019. Mechanistic Study of Wettability Changes on Calcite by Molecules Containing a Polar Hydroxyl Functional Group and Nonpolar Benzene Rings. doi:10.1021/acs.langmuir.8b03666

King, H.E., Eberle, A.P.R., Walters, C.C., Kliewer, C.E., Ertas, D., Huynh, C., 2015. Pore architecture and connectivity in gas shale. Energy and Fuels 29, 1375–1390. doi:10.1021/ef502402e

Klaver, J., Desbois, G., Littke, R., Urai, J.L., 2016. BIB-SEM pore characterization of mature and post mature Posidonia Shale samples from the Hils area, Germany. Int. J. Coal Geol. 158, 78–89. doi:10.1016/j.coal.2016.03.003

Klaver, Jop, Desbois, G., Littke, R., Urai, J.L., 2015. BIB-SEM characterization of pore space morphology and distribution in postmature to overmature samples from the Haynesville and Bossier Shales. Mar. Pet. Geol. 59, 451–466. doi:10.1016/j.marpetgeo.2014.09.020

Klaver, J., Desbois, G., Urai, J.L., Littke, R., 2012. BIB-SEM study of the pore space morphology in early mature Posidonia Shale from the Hils area, Germany. Int. J. Coal Geol. 103, 12–25. doi:10.1016/j.coal.2012.06.012

Klaver, J., Hemes, S., Houben, M., Desbois, G., Radi, Z., Urai, J.L., 2015a. The connectivity of pore space in mudstones: insights from high-pressure Wood's metal injection, BIB-SEM imaging, and mercury intrusion porosimetry. Geofluids 15, 577–591. doi:10.1111/gfl.12128

Klaver, J., Hemes, S., Houben, M., Desbois, G., Radi, Z., Urai, J.L., 2015b. The connectivity of pore space in mudstones: insights from high-pressure Wood's metal injection, BIB-SEM imaging, and mercury intrusion porosimetry. Geofluids 15, 577–591. doi:10.1111/GFL.12128

Ko, L.T., Loucks, R.G., Ruppel, S.C., Zhang, T., Peng, S., 2017a. Origin and characterization of Eagle Ford pore networks in the south Texas Upper Cretaceous shelf. Am. Assoc. Pet. Geol. Bull. 101, 387–418. doi:10.1306/08051616035

Ko, L.T., Loucks, R.G., Ruppel, S.C., Zhang, T., Peng, S., 2017b. Origin and

characterization of Eagle Ford pore networks in the south Texas Upper Cretaceous shelf. Am. Assoc. Pet. Geol. Bull. 101, 387–418. doi:10.1306/08051616035

Ko, L.T., Zhang, T., Loucks, R.G., Ruppel, S.C., Shao, D., 2014. Boquillas (Eagle Ford) Formation Pore Evolution Results From Laboratory Heating Experiments, in: Proceedings of the 2nd Unconventional Resources Technology Conference. American Association of Petroleum Geologists, Tulsa, OK, USA. doi:10.15530/urtec-2014-1935124

Kuila, U., 2013. Measurement and interpretation of porosity and pore-size distribution in mudrocks: the whole story of shales.

Kuila, U., McCarty, D.K., Derkowski, A., Fischer, T.B., Topór, T., Prasad, M., 2014. Nano-scale texture and porosity of organic matter and clay minerals in organic-rich mudrocks. Fuel 135, 359–373. doi:10.1016/j.fuel.2014.06.036

Kumar, K., Dao, E.K., Mohanty, K.K., 2005a. Atomic Force Microscopy Study of Wettability Alteration, in: SPE-93009-MS. Society of Petroleum Engineers. doi:10.2118/93009-MS

Kumar, K., Dao, E.K., Mohanty, K.K.K., 2005b. AFM study of mineral wettability with reservoir oils. J. Colloid Interface Sci. 289, 206–217. doi:10.1016/j.jcis.2005.03.030

Lager, A., Webb, K.J., Collins, I.R., Richmond, D.M., 2008. LoSal Enhanced Oil Recovery: Evidence of Enhanced Oil Recovery at the Reservoir Scale. Society of Petroleum Engineers. doi:10.2118/113976-MS

Lan, Q., Dehghanpour, H., Wood, J., Sanei, H., 2015. Wettability of the Montney tight gas formation. SPE Reserv. Eval. Eng. 18, 417–431. doi:10.2118/171620-PA

Landrot, G., Ajo-Franklin, J.B., Yang, L., Cabrini, S., Steefel, C.I., 2012. Measurement of accessible reactive surface area in a sandstone, with application to CO 2 mineralization. Chem. Geol. 318–319, 113–125. doi:10.1016/j.chemgeo.2012.05.010

Langevin, D., Argillier, J.F., 2016. Interfacial behavior of asphaltenes. Adv. Colloid Interface Sci. doi:10.1016/j.cis.2015.10.005

Larsen, J.W., Hall, P., Wernett, P.C., 1995. Pore Structure of the Argonne Premium Coals. Energy and Fuels 9, 324–330. doi:10.1021/ef00050a018

Larter, S., Bowler, B., Clarke, E., Wilson, C., Moffatt, B., Bennett, B., Yardley, G., Carruthers, D., 2000. An experimental investigation of geochromatography during secondary migration of petroleum performed under subsurface conditions with a real rock. Geochem. Trans. 1, 54. doi:10.1186/1467-4866-1-54

Larter, S.R., Aplin, A.C., 1995. Geological Society , London , Special Publications Reservoir geochemistry : methods , applications and opportunities service Reservoir

geochemistry : methods , applications and opportunities 5–32. doi:10.1144/GSL.SP.1995.086.01.02

Larter, S.R., Aplin, A.C., Corbett, P.W.M., Ementon, N., Chen, M., Taylor, P.N., 1997. Reservoir Geochemistry: A Link between Reservoir Geology and Engineering? SPE Reserv. Eng. (Society Pet. Eng. 12, 12–17. doi:10.2118/28849-PA

Larter, S.R., Bowler, B.F.J., Li, M., Chen, M., Brincat, D., Bennett, B., Noke, K., Donohoe, P., Simmons, D., Kohnen, M., Allan, J., Telnaes, N., Horstad, I., 1996. Molecular indicators of secondary oil migration distances. Nature 383, 593–597. doi:10.1038/383593a0

Lash, G.G., Engelder, T., 2005. An analysis of horizontal microcracking during catagenesis: Example from the Catskill delta complex. Am. Assoc. Pet. Geol. Bull. 89, 1433–1449. doi:10.1306/05250504141

Laughrey, C., Ruble, R., 2013. Dual Mineral Matrix and Organic Pore Textures in Mature Niobrara Formation, Rocky Mountains, USA – Implications for Tight-Oil Carbonate Reservoir Modeling. doi:10.3997/2214-4609.20131222

Leggett, J.K., Zuffa, G.G., 1987. Marine Clastic Sedimentology : Concepts and Case Studies. Springer Netherlands.

Lewan, M.D., 1991. Primary Oil Migration and Expulsion as Determined by Hydrous Pyrolysis.

Li, X., Jiang, Z., Wang, P., Song, Y., Li, Z., Tang, X., Li, T., Zhai, G., Bao, S., Xu, C., Wu, F., 2018. Porosity-preserving mechanisms of marine shale in Lower Cambrian of Sichuan Basin, South China. J. Nat. Gas Sci. Eng. 55, 191–205. doi:10.1016/j.jngse.2018.05.002

Liro, L.M., Dawson, W.C., Katz, B.J., Robison, V.D., 1994a. Sequence Stratigraphic Elements and Geochemical Variability within a 44.

Liro, L.M., Dawson, W.C., Katz, B.J., Robison, V.D., Robinson, V.D., 1994b. AAPG Datapages/Archives: Sequence Stratigraphic Elements and Geochemical Variability within a "Condensed Section": Eagle Ford Group, East-Central Texas [WWW Document]. Gulf Coast Assoc. Geol. Soc. Trans. URL http://archives.datapages.com/data/gcags/data/044/044001/0393.htm

Liu, 2017. Durham E-Theses Re-Os Systematics of Crude Oil and Re-Os Petroleum System Geochronology.

Liu, B., Schieber, J., Mastalerz, M., 2017. Combined SEM and reflected light petrography of organic matter in the New Albany Shale (Devonian-Mississippian) in the Illinois Basin: A perspective on organic pore development with thermal maturation. Int. J. Coal Geol. 184, 57–72. doi:10.1016/J.COAL.2017.11.002

Liu, K., Ostadhassan, M., Zhou, J., Gentzis, T., Rezaee, R., 2017. Nanoscale pore structure characterization of the Bakken shale in the USA. Fuel 209, 567–578. doi:10.1016/J.FUEL.2017.08.034

Liu, S., Sang, S., Wang, G., Ma, J., Wang, X., Wang, W., Du, Y., Wang, T., 2017. FIB-SEM and X-ray CT characterization of interconnected pores in high-rank coal formed from regional metamorphism. J. Pet. Sci. Eng. 148, 21–31. doi:10.1016/J.PETROL.2016.10.006

Löhr, S.C., Baruch, E.T., Hall, P.A., Kennedy, M.J., 2015. Is organic pore development in gas shales influenced by the primary porosity and structure of thermally immature organic matter? Org. Geochem. 87, 119–132. doi:10.1016/j.orggeochem.2015.07.010

Lønøy, A., 2006. Making sense of carbonate pore systems. Am. Assoc. Pet. Geol. Bull. 90, 1381–1405. doi:10.1306/03130605104

Lord, D.L., Buckley, J.S., 2002. An AFM study of the morphological features that affect wetting at crude oil–water–mica interfaces. Colloids Surfaces A Physicochem. Eng. Asp. 206, 531–546. doi:10.1016/S0927-7757(02)00090-0

Loucks, R.G., Reed, R.M., 2014. Scanning-Electron-Microscope Petrographic Evidence for Distinguishing Organic-Matter Pores Associated with Depositional Organic Matter versus Migrated Organic Matter in Mudrocks 64, 713.

Loucks, R.G., Reed, R.M., Ruppel, S.C., Hammes, U., 2012. Spectrum of pore types and networks in mudrocks and a descriptive classification for matrix-related mudrock pores. Am. Assoc. Pet. Geol. Bull. 96, 1071–1098. doi:10.1306/08171111061

Loucks, R.G., Reed, R.M., Ruppel, S.C., Hammes, U., 2010. Preliminary Classification of Matrix Pores in Mudrocks. Gulf Coast Assoc. Geol. Soc. Trans. 60, 435–441.

Loucks, R.G., Reed, R.M., Ruppel, S.C., Jarvie, D.M., 2009. Morphology, Genesis, and Distribution of Nanometer-Scale Pores in Siliceous Mudstones of the Mississippian Barnett Shale. J. Sediment. Res. 79, 848–861. doi:10.2110/jsr.2009.092

Loucks, R.G., Ruppel, S.C., Reed, R.M., Hammes, U., 2011. Origin and classification of pores in mudstones from shale-gas systems. Search Discov. 40855, 34pp.

Lowery, C.M., Corbett, M.J., Leckie, R.M., Watkins, D., Miceli Romero, A., Pramudito, A., 2014. Foraminiferal and nannofossil paleoecology and paleoceanography of the Cenomanian–Turonian Eagle Ford Shale of southern Texas. Palaeogeogr. Palaeoclimatol. Palaeoecol. 413, 49–65. doi:10.1016/j.palaeo.2014.07.025

Lu, Z., Klein Schaarsberg, M.H., Zhu, X., Yeo, L.Y., Lohse, D., Zhang, X., 2017. Universal nanodroplet branches from confining the Ouzo effect. Proc. Natl. Acad. Sci. U. S. A. 114, 10332–10337. doi:10.1073/pnas.1704727114

Ma, L., 2016. Multi-scale 3D imaging of the microstructure in organic-rich shales.

Ma, L., Taylor, K.G., Lee, P.D., Dobson, K.J., Dowey, P.J., Courtois, L., 2016. Novel 3D centimetre-to nano-scale quantification of an organic-rich mudstone: The Carboniferous Bowland Shale, Northern England. Mar. Pet. Geol. 72, 193–205. doi:10.1016/j.marpetgeo.2016.02.008

Ma, Y., Fan, M., Lu, Y., Guo, X., Hu, H., Chen, L., Wang, C., Liu, X., 2016. Geochemistry and sedimentology of the Lower Silurian Longmaxi mudstone in southwestern China: Implications for depositional controls on organic matter accumulation. Mar. Pet. Geol. 75, 291–309. doi:10.1016/J.MARPETGEO.2016.04.024

MacGowan, D.B., Surdam, R.C., 1993. Carboxylic acid anions in formation waters, San Joaquin Basin and Louisiana Gulf Coast, U.S.A.—Implications for clastic diagenesis. Reply to discussion by P.D. Lundegard and L.S. Land. Appl. Geochemistry 8, 301–304. doi:10.1016/0883-2927(93)90045-I

Macquaker, Gawthorpe, R.L., 1993. Mudstone Lithofacies in the Kimmeridge Clay Formation, Wessex Basin, Southern England: Implications for the Origin and Controls of the Distribution of Mudstones. SEPM J. Sediment. Res. Vol. 63, 1129–1143. doi:10.1306/D4267CC1-2B26-11D7-8648000102C1865D

Macquaker, J., 1997. The role of iron in mudstone diagenesis: Comparison of Kimmeridge Clay Formation mudstones from onshore and offshore (UKCS) localities. J. Sediment. Res. doi:10.1306/D426865D-2B26-11D7-8648000102C1865D

Macquaker, J.H.S., Bentley, S.J., Bohacs, K.M., 2010. Wave-enhanced sediment-gravity flows and mud dispersal across continental shelves: Reappraising sediment transport processes operating in ancient mudstone successions. Geology 38, 947–950. doi:10.1130/G31093.1

Macquaker, J.H.S., Bohacs, K.M., 2007. On the Accumulation of Mud. Science (80-.). 318, 1734 LP – 1735. doi:10.1126/science.1151980

Macquaker, J.H.S., Taylor, K.G., Gawthorpe, R.L., 2007. High-Resolutio facies analyses of mudstones: implications for paeleoenvironmental and sequence stratigraphic interpretations of offshore mudstone dominated successions. J. Sediment. Res. 77, 324–339. doi:10.2110/jsr.2007.029

Madejová, J., Gates, W.P., Petit, S., 2017. IR Spectra of Clay Minerals, in: Developments in Clay Science. Elsevier B.V., pp. 107–149. doi:10.1016/B978-0-08-100355-8.00005-9

Madsen, L., Lind, I., 1998. Adsorption of Carboxylic Acids on Reservoir Minerals from Organic and Aqueous Phase. SPE Reserv. Eng. (Society Pet. Eng. 1, 47–51. doi:10.2118/37292-pa

Mahmoudvand, M., Javadi, A., Pourafshary, P., 2019. Brine ions impacts on water-oil

dynamic interfacial properties considering asphaltene and maltene constituents. Colloids Surfaces A Physicochem. Eng. Asp. 579, 123665. doi:10.1016/J.COLSURFA.2019.123665

Maliva, R.G., Siever, R., 1988. Diagenetic replacement controlled by force of crystallization.

Mallon, A.J., Swarbrick, R.E., 2008. Diagenetic characteristics of low permeability, non-reservoir chalks from the Central North Sea. Mar. Pet. Geol. 25, 1097–1108. doi:10.1016/J.MARPETGEO.2007.12.001

Mansuy, L., Landais, P., 1995. Importance of the reacting medium in artificial maturation of a coal by confined pyrolysis. 2. Water and polar compounds. Energy & Fuels 9, 809–821. doi:10.1021/ef00053a012

Marsh, H., 1987. Adsorption methods to study microporosity in coals and carbons-a critique. Carbon N. Y. 25, 49–58. doi:10.1016/0008-6223(87)90039-X

Martin, R., Baihly, J., Malpani, R., Lindsay, G., Atwood, W.K., 2011. Understanding Production from Eagle Ford-Austin Chalk System. SPE Annu. Tech. … 1–28. doi:10.2118/145117-MS

Mastalerz, M., Drobniak, A., Strapoć, D., Solano Acosta, W., Rupp, J., 2008. Variations in pore characteristics in high volatile bituminous coals: Implications for coal bed gas content. Int. J. Coal Geol. doi:10.1016/j.coal.2008.07.006

Mastalerz, M., Schimmelmann, A., Drobniak, A., Chen, Y. Corporation, P., 2013. Porosity of Devonian and Mississippian New Albany Shale across a maturation gradient: Insights from organic petrology, gas adsorption, and mercury intrusion. Am. Assoc. Pet. Geol. Bull. 97, 1621–1643. doi:10.1306/04011312194

Mathia, E.J., 2014. Geological Evaluation of Posidonia and Wealden Organic-Rich Shales : Geochemical and Diagenetic Controls on Pore System Evolution.

Mathia, E.J., Bowen, L., Thomas, K.M., Aplin, A.C., 2016. Evolution of porosity and pore types in organic-rich, calcareous, Lower Toarcian Posidonia Shale. Mar. Pet. Geol. 75, 117–139. doi:10.1016/j.marpetgeo.2016.04.009

Mathia, E.J., Rexer, T.F.T., Thomas, K.M., Bowen, L., Aplin, A.C., 2019. Influence of Clay, Calcareous Microfossils, and Organic Matter on the Nature and Diagenetic Evolution of Pore Systems in Mudstones. J. Geophys. Res. Solid Earth 124, 149–174. doi:10.1029/2018JB015941

Matthiesen, J., Hassenkam, T., Bovet, N., Dalby, K.N., Stipp, S.L.S., 2016. Adsorbed Organic Material and Its Control on Wettability. doi:10.1021/acs.energyfuels.6b00627

Mcallister, R.T., 2017. Diagenetic Modifications of The Eagle Ford Formation: Implications

on Chemical and Physical Properties.

McAllister, R.T., Taylor, K.G., Garcia-Fresca, B., Hollis, C., 2015. Diagenetic Evolution of The Eagle Ford Formation, SW Texas: Impacts Upon Reservoir Quality and Rock Properties, in: Unconventional Resources Technology Conference. Unconventional Resources Technology Conference (URTEC). doi:10.2118/178536-MS

McCaffery, F.G., Mungan, N., 1970. Contact Angle And Interfacial Tension Studies of Some Hydrocarbon-Water-Solid Systems. J. Can. Pet. Technol. 9. doi:10.2118/70-03-04

McCarthy, K., Rojas, C., Niemann, M., Palmowski, M., Peters, K., Stankiewicz, A., 2011. Basic Petroleum Geochemistry for Source Rock Evaluation.

Mcgarity, H.A., 2013. Facies and Stratigraphic Framework of the Eagle Ford Shale in South Texas.

Mckernan, R., 2016. An Experimental Investigation into the Stress Dependent Fluid Transport Properties of Mudstones.

Merriman, R.J., Highley, D.E., Camero, D.G., Cameron, D.G., Camero, D.G., Cameron, D.G., Camero, D.G., Cameron, D.G., Camero, D.G., 2003. Definition and characteristics of very-fine grained sedimentary rocks: clay, mudstone, shale and slate 5, 14–15.

Michels, R., Langlois, E., Ruau, O., Mansuy, L., Elie, M., Landais, P., 1996. Evolution of Asphaltenes during Artificial Maturation: A Record of the Chemical Processes. Energy & Fuels 10, 39–48. doi:10.1021/ef9501410

Milliken, K.L., 2014. A Compositional Classification For Grain Assemblages In Fine-Grained Sediments and Sedimentary Rocks. J. Sediment. Res. 84, 1185–1199. doi:10.2110/jsr.2014.92

Milliken, K.L., Curtis, M.E., 2016. Imaging pores in sedimentary rocks: Foundation of porosity prediction. Mar. Pet. Geol. 73, 590–608. doi:10.1016/j.marpetgeo.2016.03.020

Milliken, K.L., Day-Stirrat, R.J., 2013. Cementation in mudrocks: Brief review with examples from cratonic basin mudrocks. Crit. Assess. shale Resour. Play. AAPG Mem. 103 103, 133–150. doi:10.1306/13401729H5252

Milliken, K.L., Ergene, S.M., Ozkan, A., Jones, B., 2016. Quartz types, authigenic and detrital, in the Upper Cretaceous Eagle Ford Formation, South Texas, USA. Sediment. Geol. 339, 273–288. doi:10.1016/j.sedgeo.2016.03.012

Milliken, K.L., Ko, L.T., Pommer, M., Marsaglia, K.M., 2014. Sem Petrography of Eastern Mediterranean Sapropels: Analogue Data For Assessing Organic Matter In Oil and Gas Shales. J. Sediment. Res. 84, 961–974. doi:10.2110/jsr.2014.75

Milliken, K.L., Olson, T., 2017. Silica Diagenesis, Porosity Evolution, and Mechanical Behavior In Siliceous Mudstones, Mowry Shale (Cretaceous), Rocky Mountains, U.S.A. J. Sediment. Res. 87, 366–387. doi:10.2110/jsr.2017.24

Milliken, K.L., Rudnicki, M., Awwiller, D.N., Zhang, T., 2013. Organic matter-hosted pore system, Marcellus Formation (Devonian), Pennsylvania. Am. Assoc. Pet. Geol. Bull. 97, 177–200. doi:10.1306/07231212048

Milner, M., McLin, R., Petriello, J., 2010. CSUG/SPE 138975: Imaging Texture and Porosity in Mudstones and Shales: Comparison of Secondary and Ion-Milled Backscatter SEM Methods. Can. Unconv. Resour. Int. Pet. Conf. 1–10. doi:10.2118/138975-MS

Mirchi, V., Saraji, S., Goual, L., Piri, M., 2014. Dynamic Interfacial Tensions and Contact Angles of Surfactant-in-Brine/Oil/Shale Systems: Implications to Enhanced Oil Recovery in Shale Oil Reservoirs, in: SPE Improved Oil Recovery Symposium. Society of Petroleum Engineers. doi:10.2118/169171-MS

Moghanloo, R.G., Davudov, D., Akita, E., 2018. Formation Damage by Organic Deposition, in: Formation Damage During Improved Oil Recovery. Elsevier, pp. 243–273. doi:10.1016/B978-0-12-813782-6.00006-3

Mokhtari, M., 2014. SPE-170707-MS Acoustical and Geomechanical Characterization of Eagle Ford Shale-Anisotropy, Heterogeneity and Measurement Scale.

Moore, C.H., 2001. Carbonate Reservoirs (Developments in Sedimentology).

Morrow, N.R., 1990. Wettability and its effect on oil recovery. JPT, J. Pet. Technol. 42, 1476–1484. doi:10.2118/21621-PA

Morrow, N.R., Mason, G., 2001. Recovery of oil by spontaneous imbibition. Curr. Opin. Colloid Interface Sci. 6, 321–337. doi:10.1016/S1359-0294(01)00100-5

Moussa, M.T., 1988. Zooplankton Fecal Pellets As a Source of Hydrocarbons in Chalk. J. Pet. Geol. 11, 347–354. doi:10.1126/science.212.4497.931

Mullen, J., 2010. Petrophysical Characterization of the Eagle Ford Shale in South Texas, in: Canadian Unconventional Resources and International Petroleum Conference. Society of Petroleum Engineers, pp. 19–21. doi:10.2118/138145-MS

Mullins, O.C., 2011. The Asphaltenes. Annu. Rev. Anal. Chem. 4, 393–418. doi:10.1146/annurev-anchem-061010-113849

Natarajan, A., Kuznicki, N., Harbottle, D., Masliyah, J., Zeng, H., Xu, Z., 2014. Understanding mechanisms of asphaltene adsorption from organic solvent on mica. Langmuir 30, 9370–9377. doi:10.1021/la500864h

Nie, H., Jin, Z., Zhang, J., 2018. Characteristics of three organic matter pore types in the Wufeng-Longmaxi Shale of the Sichuan Basin, Southwest China. Sci. Rep. 8.

doi:10.1038/s41598-018-25104-5

Noy, A., Vezenov, D. V., Lieber, C.M., 1997. CHEMICAL FORCE MICROSCOPY. Annu. Rev. Mater. Sci 27, 381–421. doi:10.1146/annurev.matsci.27.1.381

Odusina, E., Sondergeld, C., Rai, C., 2011. An NMR Study on Shale Wettability. Can. Unconv. Resour. Conf. 1–15. doi:10.2118/147371-MS

Ohiara, T., Taylor, K., Dowey, P., 2017. Complex Carbonate Pore Systems of the Carboniferous Hodder Mudstone Formation, Bowland Basin, UK, in: AAPG Annual Convention and Exhibition. pp. 1–6.

Ojha, S.P., Misra, S., Tinni, A., Sondergeld, C., Rai, C., Prakash Ojha, S., 2017. Pore connectivity and pore size distribution estimates for Wolfcamp and Eagle Ford shale samples from oil, gas and condensate windows using adsorption-desorption measurements. J. Pet. Sci. Eng. doi:10.1016/J.PETROL.2017.08.070

Okiongbo, K.S., Aplin, A.C., Larter, S.R., 2005. Changes in Type II Kerogen Density as a Function of Maturity: Evidence from the Kimmeridge Clay Formation. doi:10.1021/ef050194

Pahnke, P.D., 2014. Characterization of Cretaceous chalk microporosity related to depositional texture: Based upon study of the Upper Cretaceous Niobrara Formation, Denver-Julesburg Basin, Colorado and Wyoming 52.

Passey, Q.R., Bohacs, K., Esch, W.L., Klimentidis, R., Sinha, S., 2010. From Oil-Prone Source Rock to Gas-Producing Shale Reservoir - Geologic and Petrophysical Characterization of Unconventional Shale Gas Reservoirs, in: SPE-131350-MS. Society of Petroleum Engineers. doi:10.2118/131350-MS

Pathak, M., Deo, M., Craig, J., Levey, R., 2014. Geologic controls on production of shale play resources : Case of Eagle Ford , Bakken and Niobrara. URTeC 1922781, 1–8. doi:10.15530/urtec-2014-1922781

Pavia, D.L., Lampman, G.M., Kriz, G.S., 2009. Introduction to Spectroscopy: a guide for students of organic chemistry. 1979, Fort Worth, Texas. doi:10.1016/j.ehb.2012.05.003

Peltonen, C., Marcussen, Ø., Bjørlykke, K., Jahren, J., 2009. Clay mineral diagenesis and quartz cementation in mudstones: The effects of smectite to illite reaction on rock properties. Mar. Pet. Geol. 26, 887–898. doi:10.1016/J.Marpetgeo.2008.01.021

Peng, S., Yang, J., Xiao, X., Loucks, B., Ruppel, S.C., Zhang, T., 2015. An Integrated Method for Upscaling Pore-Network Characterization and Permeability Estimation: Example from the Mississippian Barnett Shale. Transp. Porous Media 109, 359–376. doi:10.1007/s11242-015-0523-8

Peng, S., Zhang, T., Ruppel, S.C., 2014. Upscaling of Pore Network and Permeability from

Micron to Millimeter Scale in Organic-Pore Dominated Mudstones*.

Penny, G.S., Zelenev, A.S., Long, W., Lett, N.L., Crafton, J.W., 2012. Laboratory and Field Evaluation of Proppants and Surfactants used in Fracturing of Hydrocarbon Rich Gas Reservoirs, in: SPE-159692-MS. Society of Petroleum Engineers. doi:10.2118/159692-MS

Peters, C.A., 2009. Accessibilities of reactive minerals in consolidated sedimentary rock: An imaging study of three sandstones. Chem. Geol. 265, 198–208. doi:10.1016/j.chemgeo.2008.11.014

Peters, K.E., Xia, X., Pomerantz, A.E., Mullins, O.C., 2015. Geochemistry Applied to Evaluation of Unconventional Resources, Unconventional Oil and Gas Resources Handbook: Evaluation and Development. doi:10.1016/B978-0-12-802238-2.00003-1

Philipp, T., Amann-Hildenbrand, A., Laurich, B., Desbois, G., Littke, R., Urai, J.L., 2017. The effect of microstructural heterogeneity on pore size distribution and permeability in Opalinus Clay (Mont Terri, Switzerland): insights from an integrated study of laboratory fluid flow and pore morphology from BIB-SEM images. doi:10.1144/SP454.3

Pommer, M., Milliken, K., 2015. Pore types and pore-size distributions across thermal maturity, Eagle Ford Formation, southern Texas. Am. Assoc. Pet. Geol. Bull. 99, 1713–1744. doi:10.1306/03051514151

Pommer, M., Milliken, K., Hayman, N., Ergene, S., Lunsford, J., Zhang, T., 2015. Pore types and pore-size distributions across thermal maturity, Eagle Ford Formation, southern Texas. Am. Assoc. Pet. Geol. Bull. 99, 1713–1744. doi:10.1306/03051514151

Pommer, M.E., 2014. Quantitative Assessment of Pore Types and Pore Size Distribution Across Thermal Maturity , Eagle Ford Formation , South Texas APPROVED BY SUPERVISING COMMITTEE :

Pommer, M.E., Milliken, K.L., Ozkan, A., 2014. Pore Types Across Thermal Maturity : Eagle-Ford Formation , South Texas. AAPG Annu. Conv. Exhib. 50987.

Porter, K.G., Robbins, E.I., 1981. Zooplankton Fecal Pellets Link Fossil Fuel and Phosphate Deposits. Science (80-.). 212, 931–933. doi:10.1126/science.212.4497.931

Potter, P.E., Maynard, J.B., Depetris, P.J. (Pedro J.., 2005. Mud and mudstones : introduction and overview. Springer.

Prabhakar, S., Melnik, R., 2017. Wettability alteration of calcite oil wells: Influence of smart water ions. Sci. Rep. 7. doi:10.1038/s41598-017-17547-z

Purswani, P., Tawfik, M.S., Karpyn, Z.T., 2017. Factors and Mechanisms Governing Wettability Alteration by Chemically Tuned Waterflooding: A Review.

doi:10.1021/acs.energyfuels.7b01067

Rabbani, H.S., Zhao, B., Juanes, R., Shokri, N., 2018. Pore geometry control of apparent wetting in porous media. Sci. Rep. 8. doi:10.1038/s41598-018-34146-8

Radke, C.J., Kovscek, A.R., Wong, H., 1992. A Pore-Level Scenario for the Development of Mixed Wettability in Oil Reservoirs, in: SPE Annual Technical Conference and Exhibition. Society of Petroleum Engineers. doi:10.2118/24880-MS

Ramirez, J.F., Aguilera, R., 2016. Factors Controlling Fluid Migration and Distribution in the Eagle Ford Shale. doi:10.2118/171626-PA

Ramiro-Ramirez, S., 2016. Petrographic and petrophysical characterization of the Eagle Ford Shale in La Salle and Gonzales counties, Gulf Coast Region, Texas. Colorado School of Mines. Arthur Lakes Library.

Rashid, F., Glover, P.W.J., Lorinczi, P., Collier, R., Lawrence, J., 2015. Porosity and permeability of tight carbonate reservoir rocks in the north of Iraq. J. Pet. Sci. Eng. 133, 147–161. doi:10.1016/j.petrol.2015.05.009

Rexer, T.F.T., Benham, M.J., Aplin, A.C., Thomas, K.M., 2013. Methane adsorption on shale under simulated geological temperature and pressure conditions. Energy and Fuels 27, 3099–3109. doi:10.1021/ef400381v

Rezaei Gomari, K.A., Denoyel, R., Hamouda, A.A., 2006. Wettability of calcite and mica modified by different long-chain fatty acids (C18 acids). J. Colloid Interface Sci. 297, 470–479. doi:10.1016/J.JCIS.2005.11.036

Rezaei, N., Firoozabadi, A., 2014. Macro- and microscale waterflooding performances of crudes which form w/o emulsions upon mixing with brines, in: Energy and Fuels. pp. 2092–2103. doi:10.1021/ef402223d

Richard M. Pollastro, P.A.S., 1986. Exploration and Development of Hydrocarbons from Low-Permeability Chalks--an Example from the Upper Cretaceous Niobrara Formation, Rocky Mountain Region 66, 129–141.

Ríos, C.A., Castellanos, O.M., Casadiego Q, E., Casadiego, E., Casadiego Q, E., 2016. Microstructural characterization of pore types in unconventional gas reservoirs utilizing FEG-SEM: An example from the Galembo Member of the Cretaceous La Luna Formation, Middle Magdalena Valley Basin (Colombia). Rev. la Acad. Colomb. Ciencias Exactas, Físicas y Nat. 40, 161–175. doi:10.18257/raccefyn.243

Robert L. Folk (2), 1959. Practical Petrographic Classification of Limestones. Am. Assoc. Pet. Geol. Bull. 43. doi:10.1306/0bda5c36-16bd-11d7-8645000102c1865d

Robison, C.R.R., 1997. Hydrocarbon source rock variability within the Austin Chalk and Eagle Ford Shale (Upper Cretaceous), East Texas, U.S.A. Int. J. Coal Geol. 34, 287–

305. doi:10.1016/S0166-5162(97)00027-X

Roshan, H., Al-Yaseri, A.Z., Sarmadivaleh, M., Iglauer, S., 2016. On wettability of shale rocks. J. Colloid Interface Sci. 475, 104–111. doi:10.1016/j.jcis.2016.04.041

Ross, D.J.K., Marc Bustin, R., 2009. The importance of shale composition and pore structure upon gas storage potential of shale gas reservoirs. Mar. Pet. Geol. 26, 916–927. doi:10.1016/j.marpetgeo.2008.06.004

Rouquerolt, J., Avnir, D., Fairbridge, C.W., Everett, D.H., Haynes, J.H., Pernicone, N., Ramsay, J.D.F., Sing, K.S.W., Unger, K.K., 1994. Recommendations for the characterization of porous solids. Pure Appl. Chem. 66, 1739–1758. doi:doi:10.1351/pac199466081739

Rutter, E., Mecklenburgh, J., Taylor, K., 2017. Geomechanical and petrophysical properties of mudrocks: introduction. Geol. Soc. London, Spec. Publ. 454, 1–13. doi:10.1144/SP454.16

Rutter, E.H., Wanten, P.H., 2000. Experimental Study of the Compaction of Phyllosilicate-Bearing Sand at Elevated Temperature and with Controlled Pore Water Pressure. J. Sediment. Res. 70, 107–116. doi:10.1306/2DC40902-0E47-11D7-8643000102C1865D

Rybacki, E., Meier, T., Dresen, G., 2016. What controls the mechanical properties of shale rocks? - Part II: Brittleness. J. Pet. Sci. Eng. doi:10.1016/j.petrol.2016.02.022

Rylander, E., Singer, P.M., Jiang, T., Lewis, R., McLin, R., Sinclair, S., 2013. NMR T2 distributions in the Eagle Ford shale: Reflections on pore size. Soc. Pet. Eng. - SPE USA Unconv. Resour. Conf. 2013 426–440. doi:10.2118/164554-MS

Saada, A., 1995. Origine des différences de propriétés de surface responsables des contrastes de mouillabilité des minéraux argileux des gisements pétroliers. http://www.theses.fr.

Sabbaghi, S., Shariaty-Niassar, M., Ayatollahi, S., Jahanmiri, A., 2008. Characterization of asphaltene structure using atomic force microscopy. J. Microsc. 231, 364–373. doi:10.1111/j.1365-2818.2008.02048.x

Saidian, M., Kuila, U., Godinez, L.J., Rivera, S., Prasad, M., 2014. A Comparative Study of Porosity Measurement in MudRocks. SEG Annu. Meet. doi:10.1190/segam2014-0426.1

Sakuma, H., Andersson, M.P., Bechgaard, K., Stipp, S.L.S., 2014. Surface Tension Alteration on Calcite, Induced by Ion Substitution. doi:10.1021/jp411151u

Salathiel, R.A., 1973. OIL RECOVERY BY SURFACE FILM DRAINAGE IN MIXED-WETTABILITY ROCKS. JPT, J. Pet. Technol. 25, 1216–1224. doi:10.2118/4104-PA

Sanaei, A., Tavassoli, S., Sepehrnoori, K., 2019. Investigation of modified Water chemistry

for improved oil recovery: Application of DLVO theory and surface complexation model. Colloids Surfaces A Physicochem. Eng. Asp. 574, 131–145. doi:10.1016/j.colsurfa.2019.04.075

Sand, K.K., Pedersen, C.S., Matthiesen, J., Dobberschütz, S., S Stipp, S.L., 2017. Controlling biomineralisation with cations. Nanoscale 9, 12925. doi:10.1039/c7nr02424j

Sand, K.K., Stipp, S.L.S., Hassenkam, T., Yang, M., Cooke, D., Makovicky, E., 2008. Ethanol adsorption on the {104} calcite surface: preliminary observations with atomic force microscopy. Mineral. Mag. 72, 353–357. doi:10.1180/minmag.2008.072.1.353

Schaiberger, A., 2016. Diagenesis in the Upper Cretaceous Eagle Ford shale, south Texas. Thesis. Colorado School of Mines. Arthur Lakes Library.

Schieber, 2013. Ch. 13: SEM Observations on Ion-milled Samples of Devonian Black Shales from Indiana and New York: The Petrographic Context of Multiple Pore Types. Electron Microsc. shale Hydrocarb. Reserv. AAPG Mem. 102 153–172. doi:10.1306/13391711M1023589

Schieber, J, 2013. SEM Observations on ion-milled samples of Devonian Black Shales from Indiana and New York: the petrographic context of multiple pore types., in: Electron Microscopy of Shale Hydrocarbon Reservoirs: American Association of Petroleum Geologists Memoir. pp. 153–171.

Schieber, Juergen, 2013. 13 SEM Observations on Ion-milled Samples of Devonian Black Shales from Indiana and New York: The Petrographic Context of Multiple Pore Types.

Schieber, J., 2011. Reverse engineering mother nature - Shale sedimentology from an experimental perspective. Sediment. Geol. 238, 1–22. doi:10.1016/j.sedgeo.2011.04.002

Schieber, J., 2010. SPE-132370 Common Themes in the Formation and Preservation of Intrinsic Porosity in Shales and Mudstones-Illustrated with Examples Across the Phanerozoic.

Schieber, J., 2003. Depositional fabric of mudstones. Encycl. Sediments Sediment. Rocks 8, 203–207.

Schieber, J., 1991. Sedimentary Structures: Textures and Depositional Settings of Shales from the Lower Belt Supergroup, Mid-Proterozoic, Montana, U.S.A. pp. 101–108. doi:10.1007/978-1-4612-4428-8_9

Schieber, J., Lazar, R., Bohacs, K., Klimentidis, R., Dumitrescu, M., Ottmann, J., Klimentidis, B., 2016. Chapter 3: An SEM Study of Porosity in the Eagle Ford Shale of Texas—Pore Types and Porosity Distribution in a Depositional and Sequence-stratigraphic Context, in: The Eagle Ford Shale: A Renaissance in U.S. Oil Production:

AAPG Memoir 110. pp. 167–186. doi:10.1306/13541961M1103589

Schieber, J., Southard, J.B., 2009. Bedload transport of mud by floccule ripples—Direct observation of ripple migration processes and their implications. Geology 37, 483–486. doi:10.1130/G25319A.1

Schieber, J., Southard, J.B., Schimmelmann, A., 2010. Lenticular shale fabrics resulting from intermittent erosion of water-rich muds - interpreting the rock record in the light of recent flume experiments. J. Sediment. Reseach 80, 119–128. doi:10.2110/jsr.2010.005

Schieber, J., Zimmerle, W., Sethi, P.S., 1998. Shales and mudstones. E. Schweizerbart, Stuttgart.

Schito, A., Romano, C., Corrado, S., Grigo, D., Poe, B., 2017. Diagenetic thermal evolution of organic matter by Raman spectroscopy. Org. Geochem. 106, 57–67. doi:10.1016/J.ORGGEOCHEM.2016.12.006

Schmitt, M., Fernandes, C.P., Da, J.A.B., Neto, C., Wolf, F.G., Dos Santos, V.S.S., 2013. Characterization of pore systems in seal rocks using Nitrogen Gas Adsorption combined with Mercury Injection Capillary Pressure techniques. Mar. Pet. Geol. 39, 138–149. doi:10.1016/j.marpetgeo.2012.09.001

Scholle, P.A., 1977. Chalk Diagenesis and Its Relation to Petroleum Exploration: Oil from Chalks, a Modern Miracle? Am. Assoc. Pet. Geol. Bull. 61. doi:10.1306/C1EA43B5-16C9-11D7-8645000102C1865D

Scotchman, I.C., 1987. Clay diagenesis in the Kimmeridge Clay Formation, onshore UK, and its relation to organic maturation. Mineral. Mag. doi:10.1180/minmag.1987.051.362.08

Sedghi, M., Piri, M., Goual, L., 2016. Atomistic Molecular Dynamics Simulations of Crude Oil/Brine Displacement in Calcite Mesopores. Langmuir 32, 3375–3384. doi:10.1021/acs.langmuir.5b04713

Seiedi, O., Rahbar, M., Nabipour, M., Emadi, M.A., Ghatee, M.H., Ayatollahi, S., 2010. Atomic Force Microscopy (AFM) Investigation on the Surfactant Wettability Alteration Mechanism of Aged Mica Mineral Surfaces. doi:10.1021/ef100699t

Shafer, J., Neasham, J., 2000. Mercury Porosimetry Protocol for Rapid Determination of Petrophysical and Reservoir Quality Properties. Int. Symp. Soc. Core Anal. 18–22.

Shanura Fernando, I.P., Asanka Sanjeewa, K.K., Samarakoon, K.W., Lee, W.W., Kim, H.S., Kim, E.A., Gunasekara, U.K., Abeytunga, D.T.U., Nanayakkara, C., De Silva, E.D., Lee, H.S., Jeon, Y.J., 2017. FTIR characterization and antioxidant activity of water soluble crude polysaccharides of Sri Lankan marine algae. Algae 32, 75–86. doi:10.4490/algae.2017.32.12.1

Shao, X., Pang, X., Li, Q., Wang, P., Chen, D., Shen, W., Zhao, Z., 2017. Pore structure and fractal characteristics of organic-rich shales: A case study of the lower Silurian Longmaxi shales in the Sichuan Basin, SW China. Mar. Pet. Geol. 80, 192–202. doi:10.1016/J.MARPETGEO.2016.11.025

Shi, C., Zhang, L., Xie, L., Lu, X., Liu, Q., Mantilla, C.A., Van Den Berg, F.G.A., Zeng, H., 2016. Interaction Mechanism of Oil-in-Water Emulsions with Asphaltenes Determined Using Droplet Probe AFM. Langmuir 32, 2302–2310. doi:10.1021/acs.langmuir.5b04392

Shim, Y.H., Atwood, K., Kok, J.C.L., Baihly, J., Ingraham, D.L., 2011. Defining Reservoir Quality for Successful Shale Gas Play Development and Exploitation, in: Canadian Unconventional Resources Conference. Society of Petroleum Engineers. doi:10.2118/147518-MS

Siddiqui, M.A.Q., Ali, S., Fei, H., Roshan, H., 2018. Current understanding of shale wettability: A review on contact angle measurements. Earth-Science Rev. 181, 1–11. doi:10.1016/J.EARSCIREV.2018.04.002

Sigal, R.F., 2009. A methodology for blank and conformance corrections for high pressure mercury porosimetry. Meas. Sci. Technol. 20, 045108. doi:10.1088/0957-0233/20/4/045108

Sing, K.S.W., 1985. Reporting physisorption data for gas/solid systems with special reference to the determination of surface area and porosity (Recommendations 1984). Pure Appl. Chem. 57, 603–619. doi:10.1351/pac198557040603

Singh, H., 2016. A critical review of water uptake by shales. J. Nat. Gas Sci. Eng. 34, 751–766. doi:10.1016/j.jngse.2016.07.003

Skauge, A., Standal, S., Boe, S.O., Skauge, T., Blokhus, A.M., 1999. Effects of Organic Acids and Bases, and Oil Composition on Wettability, in: SPE Annual Technical Conference and Exhibition. Society of Petroleum Engineers. doi:10.2118/56673-MS

Skovbjerg, L.L., Hassenkam, T., Makovicky, E., Hem, C.P., Yang, M., Bovet, N., Stipp, S.L.S., 2012. Nano sized clay detected on chalk particle surfaces. Geochim. Cosmochim. Acta 99, 57–70. doi:10.1016/j.gca.2012.05.037

Skovbjerg, L.L., Okhrimenko, D. V., Khoo, J., Dalby, K.N., Hassenkam, T., Makovicky, E., Stipp, S.L.S., 2013. Preferential adsorption of hydrocarbons to nanometer-sized clay on chalk particle surfaces. Energy and Fuels 27, 3642–3652. doi:10.1021/ef301832b

Slatt, R.M., 2011. Important geological properties of unconventional resource shales. Cent. Eur. J. Geosci. 3, 435–448. doi:10.2478/s13533-011-0042-2

Slatt, R.M., O'Brien, N.R., 2011. Pore types in the Barnett and Woodford gas shales: Contribution to understanding gas storage and migration pathways in fine-grained

rocks. Am. Assoc. Pet. Geol. Bull. 95, 2017–2030. doi:10.1306/03301110145

Slatt, R.M., O'Brien, N.R., Miceli-Romero, A., Rodriguez, H.H., 2012. Eagle Ford condensed section and its oil and gas storage and flow potential. Search Discov. 80245, 19pp.

Smith, B.C., 2011. Fundamentals of fourier transform infrared spectroscopy, second edition, Fundamentals of Fourier Transform Infrared Spectroscopy, Second Edition.

Sondergeld, C H, Ambrose, R.J., Rai, C.S., Moncrieff, J., 2010. Micro-structural studies of gas shales. Soc. Pet. Eng. Unconv. Gas Conf. SPE Pap. 131771 17. doi:10.2118/131771-MS

Sondergeld, Carl H, Ambrose, R.J., Rai, C.S., Moncrieff, J., 2010. Micro-Structural Studies of Gas Shales, in: SPE-131771-MS. Society of Petroleum Engineers. doi:10.2118/131771-MS

Sone, H., Zoback, M.D., 2013. Mechanical properties of shale-gas reservoir rocks - Part 1: Static and dynamic elastic properties and anisotropy. Geophysics.

Sørgård, H.N., Totland, C., Nerdal, W., Seland, J.G., 2017. Crude Oil Adsorbates on Calcite and Quartz Surfaces Investigated by NMR Spectroscopy. doi:10.1021/acs.jpcc.7b07125

Spain, D.R., McLin, R., 2013. SEM Characterization of Shale Gas Reservoirs Using Combined Secondary and Backscatter Electron Methods: An Example from the Haynesville Shale, Texas and Louisiana. Electron Microsc. Shale Hydrocarb. Reserv. 102, 0. doi:10.1306/13391704M102434

Spiecker, P.M., Gawrys, K.L., Kilpatrick, P.K., 2003. Aggregation and solubility behavior of asphaltenes and their subfractions. J. Colloid Interface Sci. 267, 178–193. doi:10.1016/S0021-9797(03)00641-6

Standnes, D.C., Austad, T., 2003. Wettability alteration in carbonates Interaction between cationic surfactant and carboxylates as a key factor in wettability alteration from oil-wet to water-wet conditions. doi:10.1016/S0927-7757(02)00580-0

Standnes, D.C., Austad, T., 2000. Wettability alteration in chalk 2. Mechanism for wettability alteration from oil-wet to water-wet using surfactants. J. Pet. Sci. Eng. 28, 123–143.

Stipp, S.L.S., Hochella, M.F., 1991. Structure and bonding at the calcite surface as observed with X-ray photoelectron spectroscopy (XPS) and (LEED). Geochim. Cosmochim. Acta 55, 1723–1736.

Strand, S., Hjuler, M.L., Torsvik, R., Pedersen, J.I., Madland, M. V., Austad, T., 2007. Wettability of chalk: Impact of silica, clay content and mechanical properties. Pet.

Geosci. 13, 69–80. doi:10.1144/1354-079305-696

Subramanian, D., May, N., Firoozabadi, A., 2017. Functional Molecules and the Stability of Water-in-Crude Oil Emulsions. Energy and Fuels 31, 8967–8977. doi:10.1021/acs.energyfuels.7b01039

Sun, M., Yu, B., Hu, Q., Yang, R., Zhang, Y., Li, B., 2017. Pore connectivity and tracer migration of typical shales in south China. Fuel 203, 32–46. doi:10.1016/j.fuel.2017.04.086

Sun, M., Yu, B., Hu, Q., Zhang, Y., Li, B., Yang, R., Melnichenko, Y.B., Cheng, G., 2016. Pore characteristics of Longmaxi shale gas reservoir in the Northwest of Guizhou, China: Investigations using small-angle neutron scattering (SANS), helium pycnometry, and gas sorption isotherm. Int. J. Coal Geol. 171, 61–68. doi:10.1016/j.coal.2016.12.004

Sun, X., Sun, Y., Zhang, T., Milliken, K.L., 2015. Organic geochemical evidence of redox conditions in the Eagle Ford Formation, Southwest Texas. AAPG Annu. Conv. Exhib. Denver, CO., May31-June 3, 2015 10778.

Sun, X., Zhang, T., Sun, Y., Milliken, K.L., Sun, D., 2016. Geochemical evidence of organic matter source input and depositional environments in the lower and upper Eagle Ford Formation, south Texas. Org. Geochem. 98, 66–81. doi:10.1016/j.orggeochem.2016.05.018

Taheri, S., Ghomeshi, S., Kantzas, A., Study, F., Reservoir, A., Services, Q., Oil, F.O.R.T.H.E., Industry, G.A.S., Milner, M., Mclin, R., Petriello, J., Kara-Gülbay, R., Korkmaz, S., Erdman, N., Drenzek, N., Bouska, C.K., Bash, E., 2013. Integrated Preparation and Imaging Techniques for the Microstructural and Geochemical Characterization of Shale by Scanning Electron Microscopy. Electron Microsc. shale Hydrocarb. Reserv. AAPG Mem. 102 22, 158–158. doi:10.1017/CBO9781107415324.004

Takamura, K., Chow, R.S., 1983. A Mechanism For Initiation of Bitumen Displacement From Oil Sand. J. Can. Pet. Technol. 22. doi:10.2118/83-06-01

Tang, G.Q., Morrow, N.R., 1999. Influence of brine composition and fines migration on crude oil/brine/rock interactions and oil recovery, in: Journal of Petroleum Science and Engineering. pp. 99–111. doi:10.1016/S0920-4105(99)00034-0

Tao, Z., Bhushan, B., 2006. Wetting properties of AFM probes by means of contact angle measurement. J. Phys. D Appl. Phys. Zhenhua Tao Bharat Bhushan J. Phys. D Appl. Phys. J. Phys. D Appl. Phys 39, 3858–3858. doi:10.1088/0022-3727/39/17/023

Taylor, K.G., Macquaker, J.H.H.S., Shaw, H., 2014. Diagenetic alterations in a silt- and clayrich mudstone succession: An example from the Upper Cretaceous Mancos Shale

of Utah, USA. Clay Miner. 49, 213–227. doi:10.1180/claymin.2014.049.2.05

Taylor, K.G., Macquaker, J.H.S., 2014. Diagenetic alterations in a silt- and clay-rich mudstone succession: an example from the Upper Cretaceous Mancos Shale of Utah, USA. Clay Miner. 49, 213–227. doi:10.1180/claymin.2014.049.2.05

Taylor, P., Larter, S., Jones, M., Dale, J., Horstad, I., 1997. The effect of oil-water-rock partitioning on the occurrence of alkylphenols in petroleum systems. Geochim. Cosmochim. Acta 61, 1899–1910. doi:10.1016/S0016-7037(97)00034-3

Teichmüller, M., 1986. Organic petrology of source rocks, history and state of the art. Org. Geochem. 10, 581–599. doi:10.1016/0146-6380(86)90055-0

Thommes, M., Kaneko, K., Neimark, A. V, Olivier, J.P., Rodriguez-Reinoso, F., Rouquerol, J., Sing, K.S.W., 2015. IUPAC Technical Report Physisorption of gases, with special reference to the evaluation of surface area and pore size distribution (IUPAC Technical Report). Pure Appl. Chem. doi:10.1515/pac-2014-1117

Thyberg, B., Jahren, J., 2011. Quartz cementation in mudstones: sheet-like quartz cement from clay mineral reactions during burial. doi:10.1144/1354-079310-028

Thyne, G., 2015. Wettability Alteration in the Eagle Ford: How to Design Drilling Fluids to Improve Recovery in Shale Plays*.

Tiab, D., Donaldson, E.C., 2004. Petrophysics. Elsevevier 889. doi:10.1007/s13398-014-0173-7.2

Tian, F., Wang, W., Liu, N., Jiang, J., Niu, · Congkai, Zhang, Y., Li, Y., 2018. Rock-Type Definition and Pore Characterization of Tight Carbonate Rocks Based on Thin Sections and MICP and NMR Experiments. doi:10.1007/s00723-018-0993-2

Tian, H., Pan, L., Zhang, T., Xiao, X., Meng, Z., Huang, B., 2015. Pore characterization of organic-rich Lower Cambrian shales in Qiannan Depression of Guizhou Province, Southwestern China. Mar. Pet. Geol. 62, 28–43. doi:10.1016/j.marpetgeo.2015.01.004

Tissot, B.P. (Bernard P.., Welte, D.H. (Dietrich H.., 1978. Petroleum formation and occurrence : a new approach to oil and gas exploration. Springer-Verlag.

Tölke, J., Baldwin, C., Mu, Y., Derzhi, N., Fang, Q., Grader, A., Dvorkin, J., 2010. Computer simulations of fluid flow in sediment: From images to permeability. Lead. Edge 29, 68–74. doi:10.1190/1.3284055

Torres, E.J., Slatt, R., Philp, P., Wang, T., Rodriguez, H.L., 2017. Can Fecal Pellets in Unconventional Resource Shales Generate Hydrocarbons?

Totland, C., Lewis, R.T., 2016. Mechanism of calcite wettability alteration by alkyl polyglucoside. Colloids Surfaces A Physicochem. Eng. Asp. 488, 129–137. doi:10.1016/j.colsurfa.2015.10.013

Toulhoat, H, Prayer, C., A, G.R.-C. and S., 1994, U., 1994. Characterization by atomic force microscopy of adsorbed asphaltenes. Elsevier.

Toulhoat, Herve, Prayer, C., Rouquet, G., A, G.R.-C. and S., 1994, U., 1994. Characterization by atomic force microscopy of adsorbed asphaltenes. Colloids Surfaces A Physicochem. Eng. Asp. 91, 267–283. doi:10.1016/0927-7757(94)02956-3

Tsakiroglou, C.D., Kolonis, G.B., Roumeliotis, T.C., Payatakes, A.C., 1997. Mercury Penetration and Snap-off in Lenticular Pores, JOURNAL OF COLLOID AND INTERFACE SCIENCE.

U.S. EIA, 2019. Annual Energy Outlook 2019 with projections to 2050. Annu. Energy Outlook 2019 with Proj. to 2050. doi:DOE/EIA-0383(2012) U.S.

Unsworth, J.F., Fowler, C.S., Jones, L.F., 1989. Moisture in coal. 2. Maceral effects on pore structure. Fuel 68, 18–26. doi:10.1016/0016-2361(89)90005-7

Valenza, J.J., Drenzek, N., Marques, F., Pagels, M., Mastalerz, M., 2013. Geochemical controls on shale microstructure. Geology 41, 611–614. doi:10.1130/G33639.1

van Duin, A.C.T., Larter, S.R., 2001. A computational chemical study of penetration and displacement of water films near mineral surfaces. Geochem. Trans. 2, 1–10. doi:10.1186/1467-4866-2-35

Vargas, F.M., Tavakkoli, M., 2018. Asphaltene Deposition : Fundamentals, Prediction, Prevention, and Remediation.

Walls, J.D., Sinclair, S.W., 2011. Eagle Ford shale reservoir properties from digital rock physics 29.

Wang, D., Butler, R., Zhang, J., Seright, R., 2012. Wettability survey in bakken shale with surfactant-formulation imbibition. SPE Reserv. Eval. Eng. 15, 695–705. doi:10.2118/153853-PA

Wang, F.P., Reed, R.M., 2009. Pore Networks and Fluid Flow in Gas Shales. SPE Annu. SPE 124253, 8. doi:10.2118/124253-MS

Wang, M., Yang, J., Wang, Z., Lu, S., 2015. Nanometer-Scale Pore Characteristics of Lacustrine Shale, Songliao Basin, NE China. PLoS One 10, e0135252. doi:10.1371/journal.pone.0135252

Wang, M., Yu, Q., 2017. Pore structure characterization of Carboniferous shales from the eastern Qaidam Basin, China: Combining helium expansion with low-pressure adsorption and mercury intrusion. J. Pet. Sci. Eng. doi:10.1016/j.petrol.2017.02.007

Wang, S., Javadpour, F., Feng, Q., 2016. Molecular dynamics simulations of oil transport through inorganic nanopores in shale. FUEL 171, 74–86. doi:10.1016/j.fuel.2015.12.071

Wang, S., Liu, J., Zhang, L., Masliyah, J., Xu, Z., 2010. Interaction forces between asphaltene surfaces in organic solvents. Langmuir 26, 183–190. doi:10.1021/la9020004

Wang, X., Pensini, E., Liang, Y., Xu, Z., Chandra, M.S., Andersen, S.I., Abdallah, W., Buiting, J.J., 2017. Fatty acid-asphaltene interactions at oil/water interface. Colloids Surfaces A Physicochem. Eng. Asp. 513, 168–177. doi:10.1016/j.colsurfa.2016.10.029

Wang, Y., Pu, J., Wang, L., Wang, J., Jiang, Z., Song, Y.-F., Wang, C.-C., Wang, Yanfei, Jin, C., 2016. Characterization of typical 3D pore networks of Jiulaodong formation shale using nano-transmission X-ray microscopy. Fuel 170, 84–91. doi:10.1016/j.fuel.2015.11.086

Washburn, E.W., 1921. The Dynamics of Capillary Flow. Phys. Rev. 17, 273–283. doi:10.1103/PhysRev.17.273

Wei, Q., Mather, R.R., Fotheringham, A.F., Yang, R.D., 2002. Observation of wetting behavior of polypropylene microfibers by environmental scanning electron microscope. J. Aerosol Sci. 33, 1589–1593. doi:10.1016/S0021-8502(02)00096-4

Wendler, J., Gräfe, K.-U., Willems, H., 2002. Palaeoecology of calcareous dinoflagellate cysts in the mid-Cenomanian Boreal Realm: implications for the reconstruction of palaeoceanography of the NW European shelf sea. Cretac. Res. 23, 213–229. doi:10.1006/CRES.2002.0311

Wever, P. De, Dumitrica, P., Caulet, J.P., Nigrini, C., Caridroit, M., Dumitrica, P., Caulet, J.P., Nigrini, C., Caridroit, M., 2014. Radiolarians in the Sedimentary Record. CRC Press. doi:10.1201/9781482283181

Wignall, P.B., Macquaker, J.H.S., Gawthorpe, R.L., 1994. Mudstone lithofacies in the Kimmeridge Clay Formation, Wessex Basin, southern England; implications for the origin and controls of the distribution of mudstones; discussion and reply. J. Sediment. Res. 64, 927–932. doi:10.1306/D4267F23-2B26-11D7-8648000102C1865D

Wilkinson, M., Milliken, K.L., Haszeldine, R.S., Haszeldine, & R.S., 2001. Systematic destruction of K-feldspar in deeply buried rift and passive margin sandstones, Journal of the Geological Society.

Wilson, M.J.J., Wilson, L., Shaldybin, M.V. V., 2016. Clay mineralogy and unconventional hydrocarbon shale reservoirs in the USA. II. Implications of predominantly illitic clays on the physico-chemical properties of shales. Earth-Science Rev. 158, 1–8. doi:10.1016/j.earscirev.2016.04.005

Worden, R.H., Morad, S., 2003. Clay minerals in sandstones: controls on formation, distribution and evolution, Int. Assoc. Sedimentol. Spec. Publ. doi:10.1002/9781444304336.ch1

Worden, R.H., Morad, S., 2000. Economic evaluation of a petroleum accumulation de-

mands a Quartz cementation in oil field sandstones: a review of the key controversies INTRODUCTION: WHY WORRY ABOUT QUARTZ CEMENT? Spec. Publs int. Ass. Sediment 29, 1–20.

Worden, R.H., Oxtoby, N.H., Smalley, P.C., 1998. Can oil emplacement prevent quartz cementation in sandstones? Pet. Geosci. 4, 129–137. doi:10.1144/petgeo.4.2.129

Workman, S.J., 2013. Integrating Depositional Facies and Sequence Stratigraphy in Characterizing Unconventional Reservoirs: Eagle Ford Shale, South Texas. Western Michigan University.

Wu, J., Liu, F., Yang, H., Xu, S., Xie, Q., Zhang, M., Chen, T., Hu, G., Wang, J., 2017. Effect of specific functional groups on oil adhesion from mica substrate: Implications for low salinity effect. J. Ind. Eng. Chem. 56, 342–349. doi:10.1016/j.jiec.2017.07.030

Xie, X., Weiss, W.W., Tong, Z., Morrow, N.R., 2005. Improved oil recovery from carbonate reservoirs by chemical stimulation. SPE J. 10, 276–285. doi:10.2118/89424-PA

Xin, J., Li, C., Chai, R., 2019. Effect of sulfate ions on oil detachment from calcite surface: experiments and molecular dynamics simulations. Arab. J. Geosci. 12. doi:10.1007/s12517-019-4427-8

Yang, J., Hatcherian, J., Hackley, P.C., Pomerantz, A.E., 2017. Nanoscale geochemical and geomechanical characterization of organic matter in shale. Nat. Commun. 8, 2179. doi:10.1038/s41467-017-02254-0

Yang, S.-Y.Y., Hirasaki, G.. J., Basu, S., Vaidya, R., 2002. Statistical analysis on parameters that affect wetting for the crude oil/brine/mica system. J. Pet. Sci. Eng. 33, 203–215. doi:10.1016/S0920-4105(01)00190-5

Yang, Y., Aplin, A.C., 2010. A permeability-porosity relationship for mudstones. Mar. Pet. Geol. 27, 1692–1697. doi:10.1016/j.marpetgeo.2009.07.001

Yang, Y., Aplin, A.C., 1998. Influence of lithology and compaction on the pore size distribution and modelled permeability of some mudstones from the Norwegian margin. Mar. Pet. Geol. 15, 163–175. doi:10.1016/S0264-8172(98)00008-7

Yang, Y., Wu, K., Zhang, T., Xue, M., 2015. Characterization of the pore system in an over-mature marine shale reservoir: A case study of a successful shale gas well in Southern Sichuan Basin, China. Petroleum 1, 173–186. doi:10.1016/j.petlm.2015.07.011

Yen, T.F., Erdman, J.G., Pollack, S.S., 1961. Investigation of the Structure of Petroleum Asphaltenes by X-Ray Diffraction. Anal. Chem. 33, 1587–1594. doi:10.1021/ac60179a039

Yu, L., Evje, S., Kleppe, H., Kårstad, T., Fjelde, I., Skjaeveland, S.M., 2009. Spontaneous

imbibition of seawater into preferentially oil-wet chalk cores — Experiments and simulations. J. Pet. Sci. Eng. 66, 171–179. doi:10.1016/J.PETROL.2009.02.008

Yuan, G., Cao, Y., Schulz, H.-M., Hao, F., Gluyas, J., Liu, K., Yang, T., Wang, Y., Xi, K., Li, F., 2019. A review of feldspar alteration and its geological significance in sedimentary basins: From shallow aquifers to deep hydrocarbon reservoirs. Earth-Science Rev. 191, 114–140. doi:10.1016/J.EARSCIREV.2019.02.004

Yuan, L., Dehghanpour, H., Ceccanese, A., 2019. Imbibition Oil Recovery from the Montney Core Plugs: The Interplay of Wettability, Osmotic Potential and Microemulsion Effects, in: SPE Western Regional Meeting. Society of Petroleum Engineers. doi:10.2118/195362-MS

Zhang, P., Tweheyo, M.T., Austad, T., 2007. Wettability alteration and improved oil recovery by spontaneous imbibition of seawater into chalk: Impact of the potential determining ions Ca2+, Mg2+, and SO42-. Colloids Surfaces A Physicochem. Eng. Asp. 301, 199–208. doi:10.1016/j.colsurfa.2006.12.058

Zhang, R., Somasundaran, P., 2006. Advances in adsorption of surfactants and their mixtures at solid/solution interfaces. Adv. Colloid Interface Sci. doi:10.1016/j.cis.2006.07.004

Zhou, S., Yan, G., Xue, H., Guo, W., Li, X., 2016. 2D and 3D nanopore characterization of gas shale in Longmaxi formation based on FIB-SEM. Mar. Pet. Geol. 73, 174–180. doi:10.1016/J.MARPETGEO.2016.02.033

Zolfaghari, A., Dehghanpour, H., Xu, M., 2017. Water sorption behaviour of gas shales: II. Pore size distribution. Int. J. Coal Geol. 179, 187–195. doi:10.1016/J.COAL.2017.05.009

Appendix

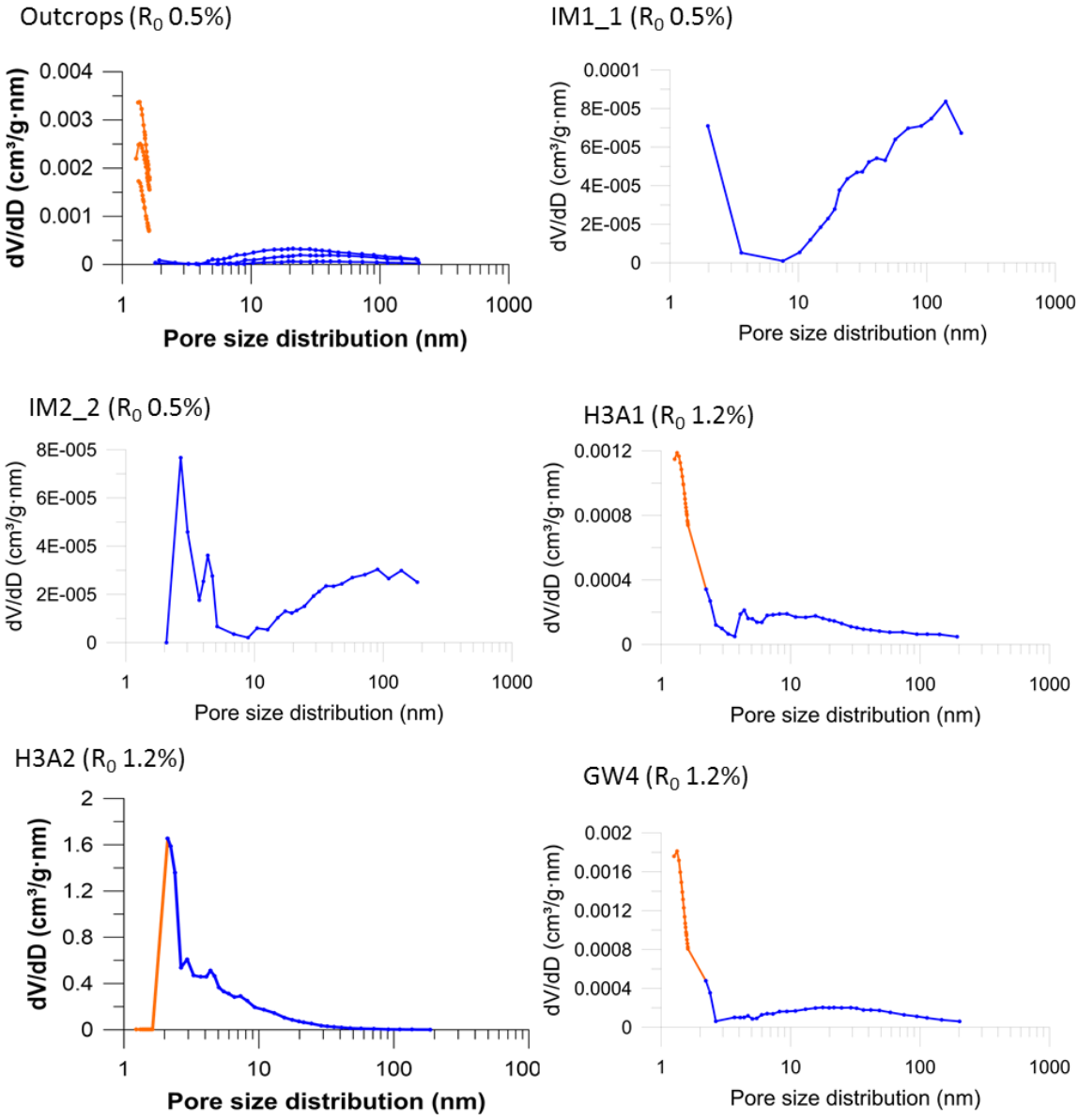

Figure A.1: CO_2 (orange) and N_2 (blue) pore size distribution graphs of the samples analysed.

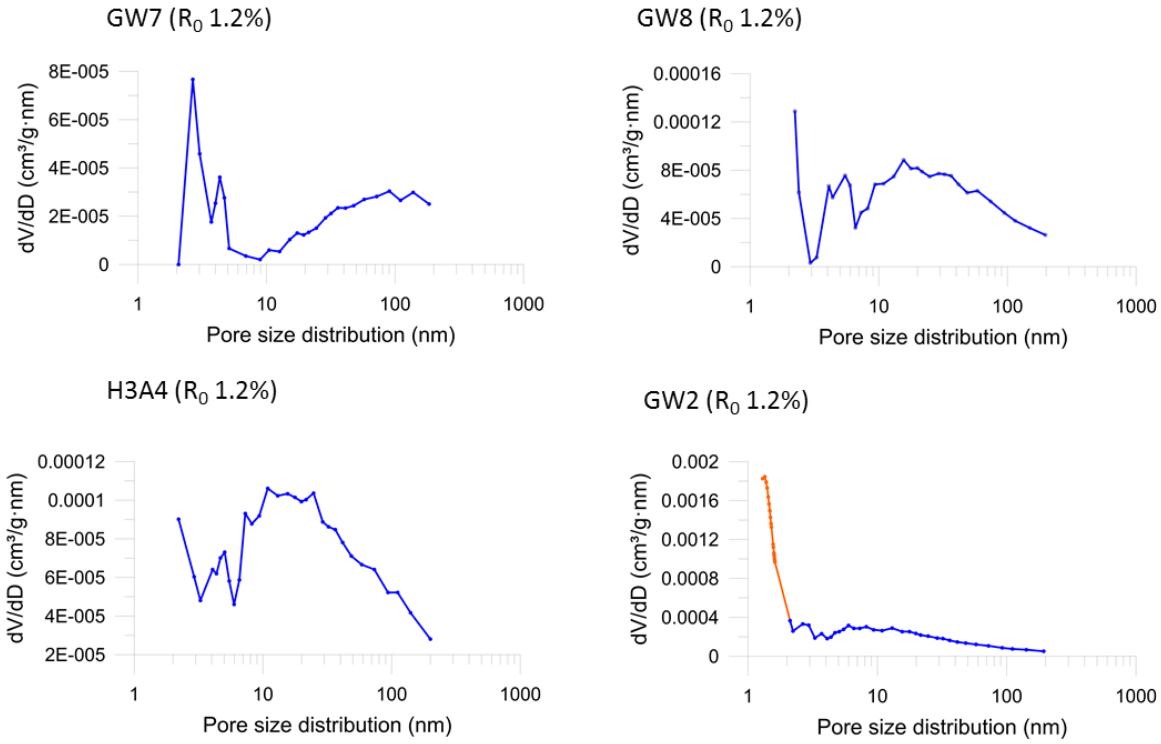

Figure A.2: CO_2 (orange) and N_2 (blue) pore size distribution graphs of the samples analysed.

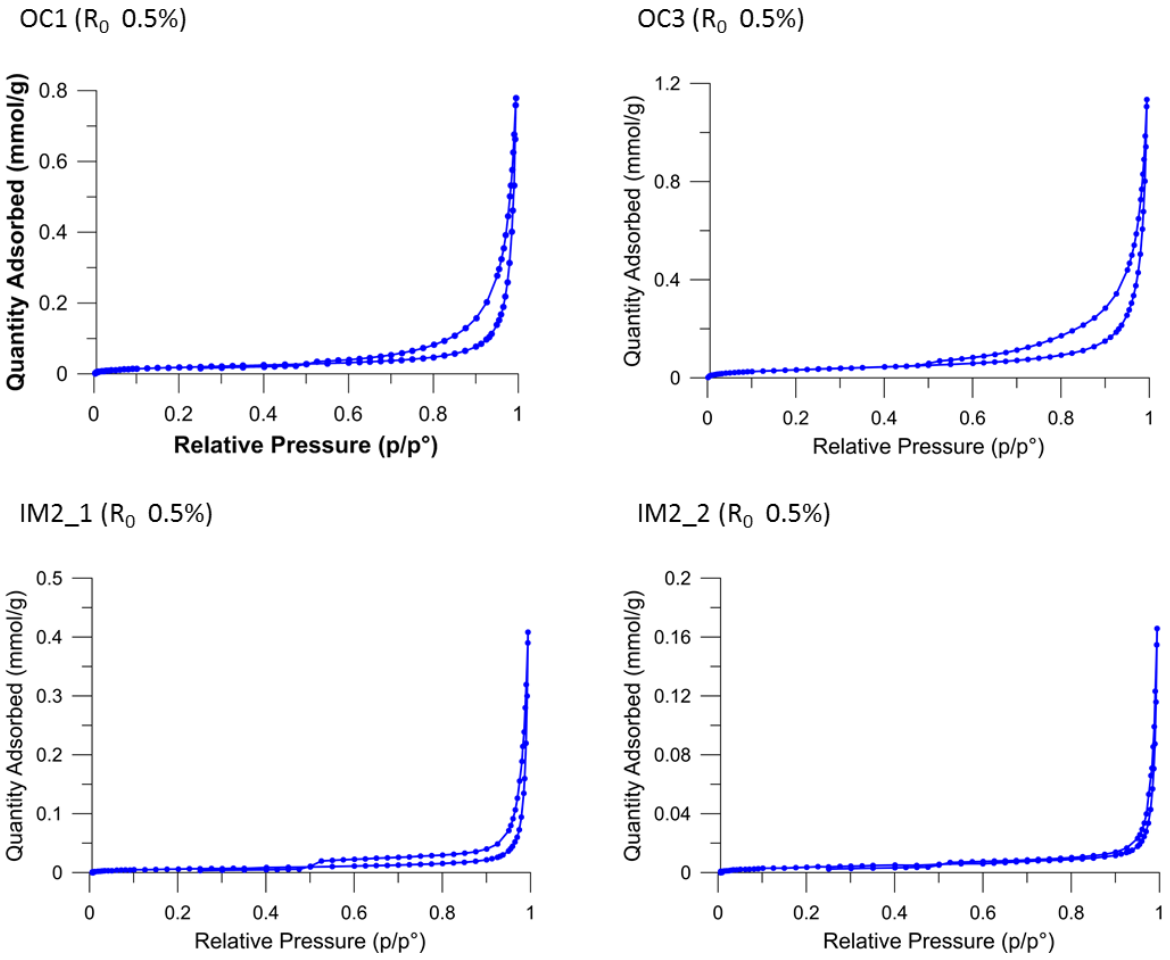

Figure A.3: Gas adsorption isotherms for the immature samples analysed. Samples OC1, OC3 and IM2_1 belong to microfacies A. Sample IM2_2 belongs to microfacies B.

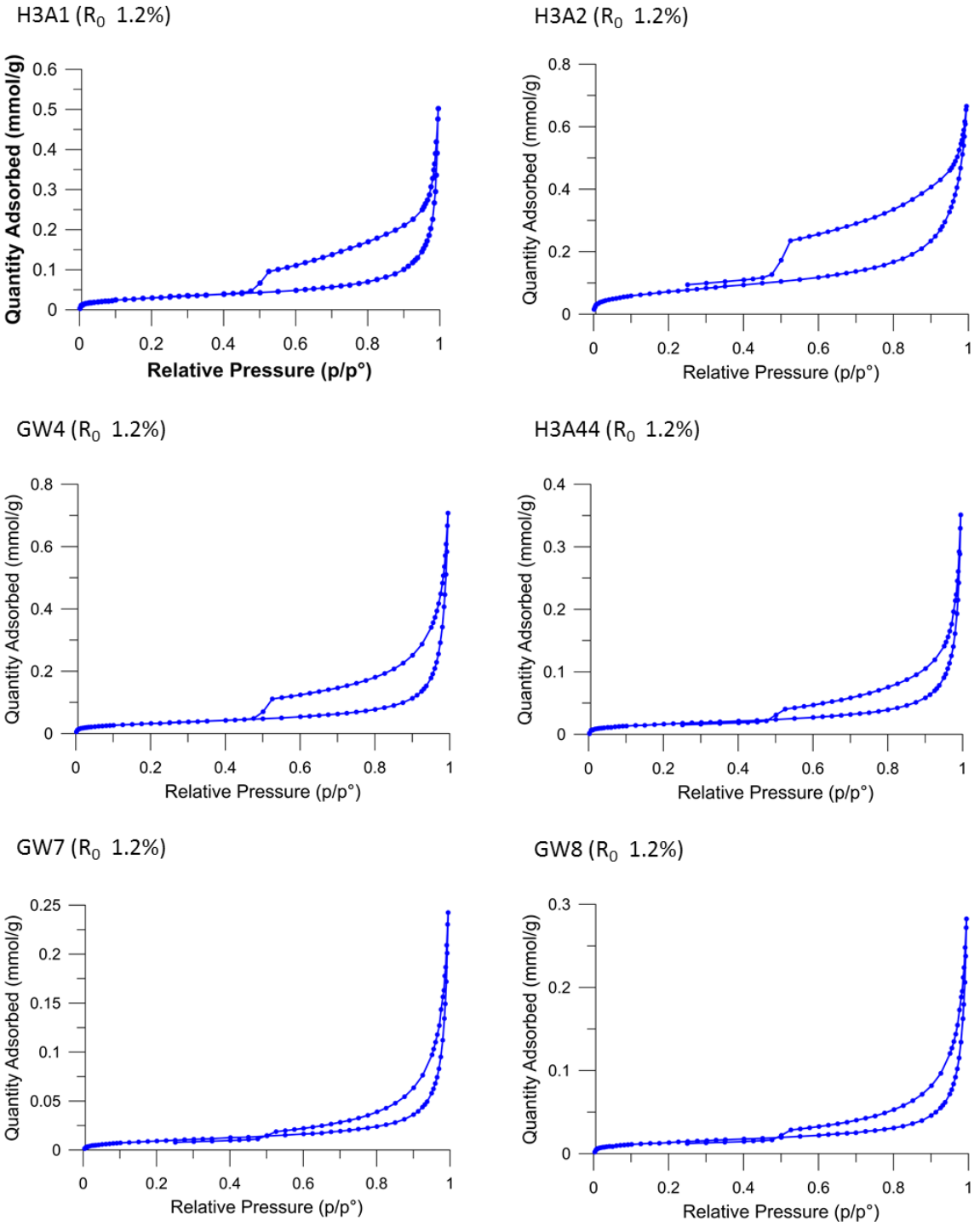

Figure A.4: Gas adsorption isotherms for the gas window samples analysed. Sample H3A2 belongs to microfacies A,samples H3A1, GW4, H3A4 belong to microfacies B. Samples GW7 and GW8 belong to microfacies C.

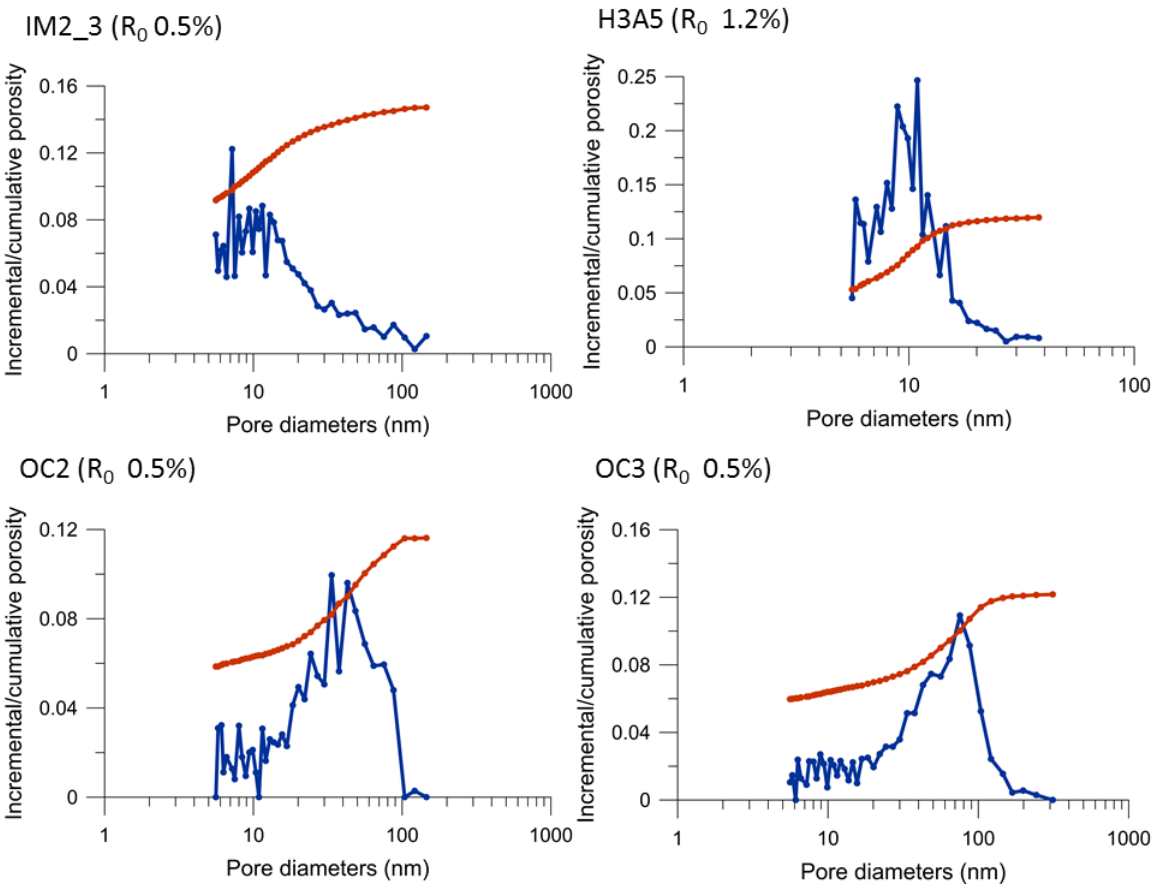

Figure A.5: Pore throat size distributions measured with the MICP technique. In red, the cumulative pore distribution. All the samples belong to microfacies A.

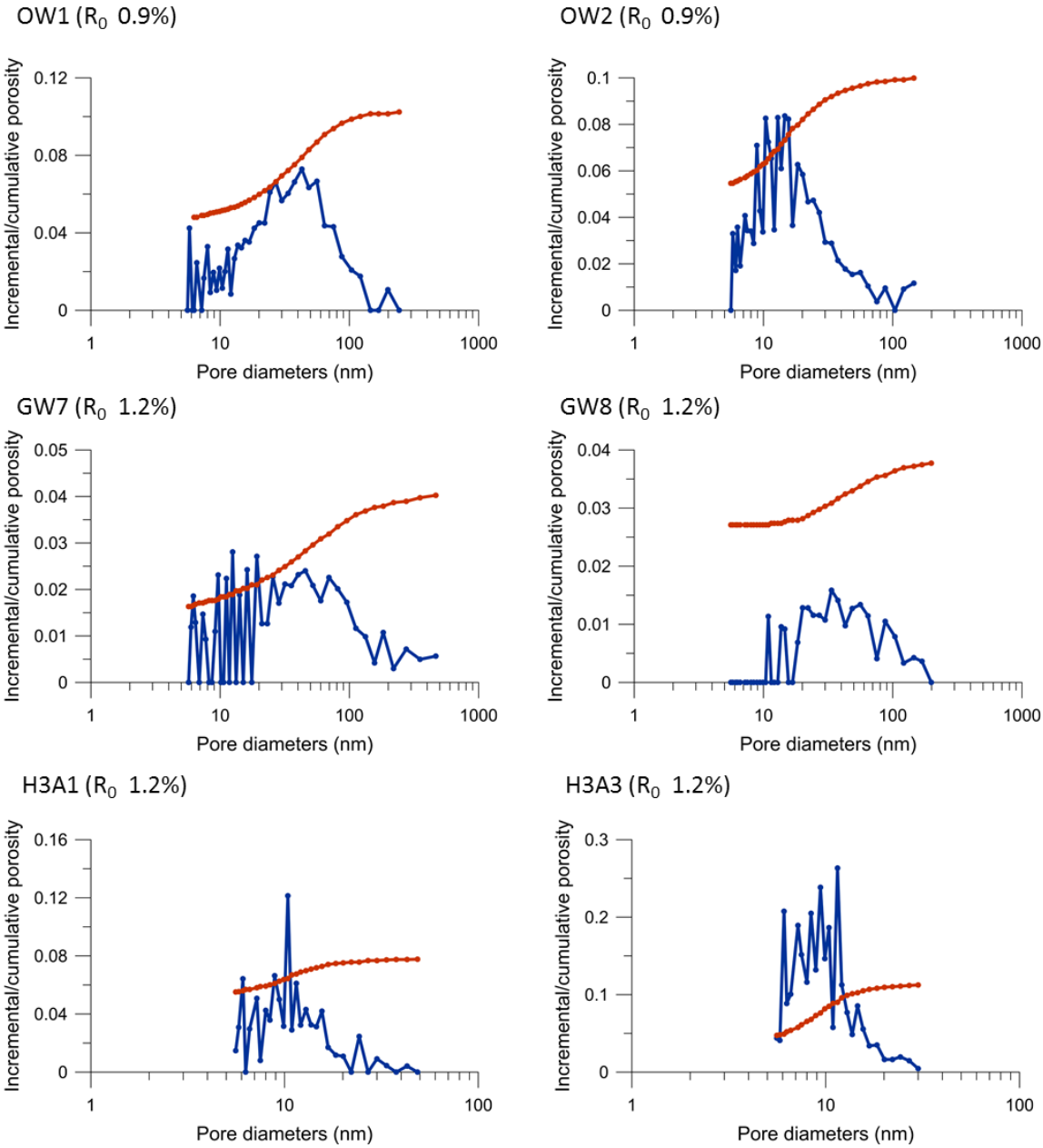

Figure A.6: Pore throat size distributions measured with the MICP technique. In red, the cumulative pore distribution. Samples OW1, OW2 and H3A3 belong to microfacies A, sample H3A1 to microfacies B and samples GW7 and GW8 to microfacies C.

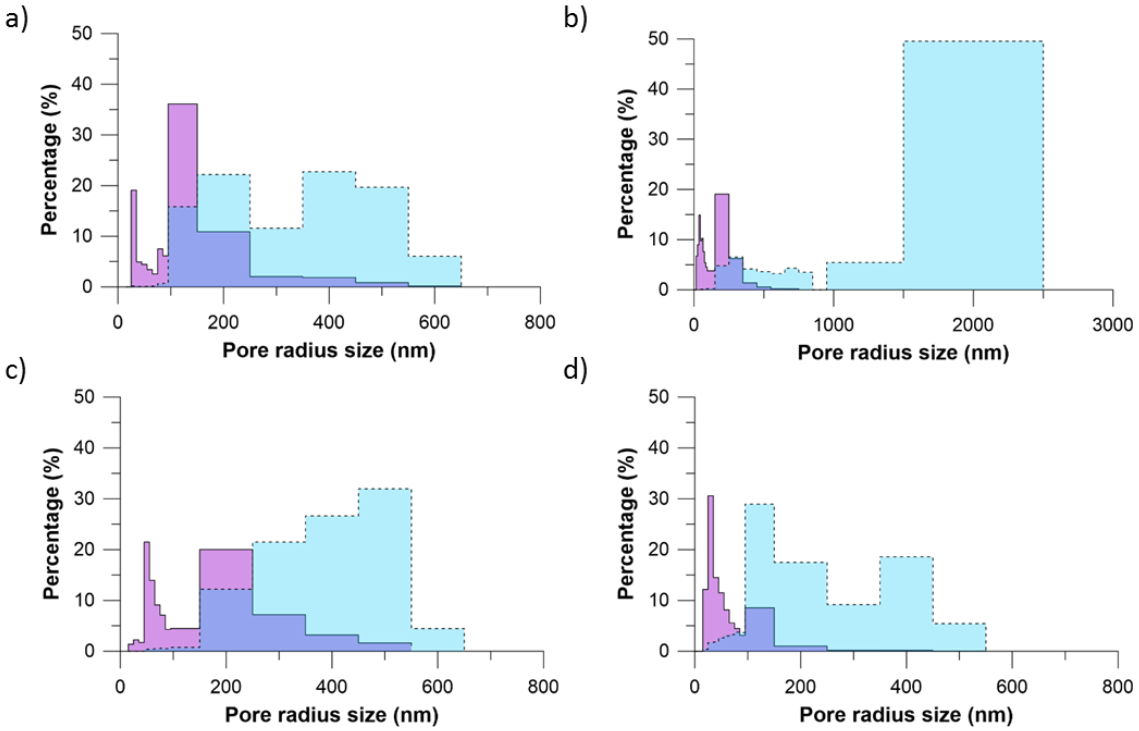

Figure A.7: Pore volume distribution (blue, dotted line) vs number of pores relative to the pore sizes (purple) for samples a) IM2_1 (R_0 0.5%) b) IM2_3 (R_0 0.5%) c) OW1 (R_0 0.9%) and d) H3A5 (R_0 1.2%).

Sample name	Min	Max	Average	n_pixels	%oil > 0.5 nm	%oil > 1 nm	%oil > 2 nm	%oil > 3 nm	%oil > 4 nm
Cal. in brine_01	0.120	0.661	0.338	25.00	3.36	0.00	0.00	0.00	0.00
Cal. in brine_02	0.101	0.327	0.136	25.00	0.00	0.00	0.00	0.00	0.00
Cal. in brine_03	0.013	0.544	0.099	25.00	0.32	0.00	0.00	0.00	0.00
Cal. in brine_04	0.019	0.565	0.123	25.00	0.32	0.00	0.00	0.00	0.00
Cal. in brine_05	0.015	0.406	0.114	25.00	0.00	0.00	0.00	0.00	0.00
Cal. in brine_06	0.012	0.437	0.085	25.00	0.00	0.00	0.00	0.00	0.00
Cal. in brine_07	0.012	0.397	0.022	25.00	0.00	0.00	0.00	0.00	0.00
Cal. in brine_08	0.012	0.402	0.024	25.00	0.00	0.00	0.00	0.00	0.00
Cal. in brine_09	0.011	0.356	0.021	25.00	0.00	0.00	0.00	0.00	0.00
Cal. in brine_10	0.012	0.147	0.021	25.00	0.00	0.00	0.00	0.00	0.00
Cal. in brine_11	0.014	0.584	0.112	25.00	0.96	0.00	0.00	0.00	0.00
Cal. in brine_12	0.016	0.672	0.144	25.00	0.48	0.00	0.00	0.00	0.00
Cal. in brine_13	0.011	0.253	0.022	25.00	0.00	0.00	0.00	0.00	0.00
Cal. in brine_14	0.011	0.277	0.026	25.00	0.00	0.00	0.00	0.00	0.00
Cal. in brine_15	0.018	0.673	0.216	25.00	1.12	0.00	0.00	0.00	0.00
Cal. in brine_16	0.012	3.600	0.460	25.00	36.64	11.36	0.96	0.32	0.00
Cal. in brine_17	0.013	4.104	0.473	25.00	37.28	11.84	1.28	0.64	0.16
Cal. in brine_18	0.012	2.389	0.346	25.00	25.76	8.32	0.48	0.00	0.00
Cal. in brine_19	0.012	3.162	0.380	25.00	28.00	9.60	1.44	0.16	0.00
Cal. in brine_20	0.011	1.929	0.189	25.00	11.04	2.72	0.00	0.00	0.00
Cal. in brine_21	0.012	2.583	0.326	25.00	23.36	5.92	0.80	0.00	0.00
Cal. in brine_22	0.010	3.504	0.264	64.00	17.04	4.54	0.24	0.02	0.00
Cal. in dodecane_01	0.146	7.028	1.704	25.00	68.48	55.84	38.88	19.04	7.20
Cal. in dodecane_02	0.113	8.113	1.882	25.00	59.68	42.72	35.36	27.04	19.36
Cal. in dodecane_03	0.000	7.806	1.638	25.00	48.16	39.68	32.00	24.64	16.48
Cal. in dodecane_04	0.014	6.633	1.746	25.00	67.20	58.40	41.44	21.92	5.76
Cal. in dodecane_05	0.105	8.149	1.342	25.00	47.52	39.04	28.48	16.96	8.32
Cal. in dodecane_06	0.146	7.028	1.704	25.00	68.48	55.84	38.88	19.04	7.20
Cal. in dodecane_07	0.000	5.145	2.072	25.00	99.84	69.60	46.88	27.36	7.52
Cal. in dodecane_08	0.019	8.327	1.549	25.00	74.72	61.92	37.60	9.44	1.60
Cal. in dodecane_09	0.017	3.728	1.247	25.00	64.80	53.76	26.88	4.16	0.00
Cal. in dodecane_10	0.017	4.456	1.309	25.00	67.52	54.08	28.00	6.88	1.12
Cal. in dodecane_11	0.015	4.395	1.155	25.00	60.64	49.60	25.12	4.48	0.16
Cal. in dodecane_12	0.014	6.203	0.529	128.0	43.71	14.32	1.27	0.22	0.10
Cal. in dodecane_13	0.017	8.452	0.670	25.00	51.04	21.44	2.56	0.32	0.16
Cal. in dodecane_14	0.021	3.306	0.612	25.00	48.96	21.28	1.92	0.16	0.00
Cal. in dodecane_15	0.020	6.791	0.550	25.00	40.48	14.88	1.92	0.64	0.48
Cal. in dodecane_16	0.019	4.501	0.222	25.00	10.88	2.88	0.80	0.16	0.16
Cal. in dodecane_17	0.018	3.099	0.396	25.00	31.20	7.84	0.16	0.16	0.00
Cal. in dodecane_18	0.017	3.075	0.246	128.0	17.89	3.64	0.05	0.01	0.00

Sample name	Min	Max	Average	n_pixels	%oil > 0.5 nm	%oil > 1 nm	%oil > 2 nm	%oil > 3 nm	%oil > 4 nm
Cal. in dodecane_19	0.015	9.000	1.242	25.00	79.04	50.56	14.88	5.76	2.08
Cal. in dodecane_20	0.026	6.304	1.185	25.00	76.64	47.52	16.16	5.76	1.76
Cal. in dodecane_21	0.020	7.197	1.384	25.00	84.80	58.72	20.00	8.00	3.36
Cal. in dodecane_22	0.014	6.203	0.529	128.0	43.71	14.32	1.27	0.22	0.10
Cal. in dodecane_23	0.006	1.339	0.267	80.00	9.25	0.09	0.00	0.00	0.00
Cal. in dodecane_24	0.004	1.588	0.164	25.00	3.84	0.32	0.00	0.00	0.00
Cal. in dodecane_25	0.008	2.976	0.174	60.00	2.06	0.53	0.11	0.00	0.00
Cal. in dodecane_26	0.006	1.332	0.270	80.00	11.97	0.08	0.00	0.00	0.00
Cal. in dodecane_27	0.006	4.107	0.301	80.00	11.58	2.28	0.92	0.16	0.02
Cal. in dodecane_28	0.006	1.339	0.267	80.00	9.25	0.09	0.00	0.00	0.00
Cal. in dodec_no brine_01	0.009	5.733	0.298	64.00	20.56	8.74	2.32	0.88	0.29
Cal. in dodec_no brine_02	0.015	0.919	0.208	25.00	5.44	0.00	0.00	0.00	0.00
Cal. in dodec_no brine_03	0.012	1.897	0.464	25.00	42.08	10.40	0.00	0.00	0.00
Cal. in dodec_no brine_04	0.011	8.205	1.098	25.00	81.76	50.40	8.96	1.92	0.32
Cal. in dodec_no brine_05	0.026	6.094	1.697	25.00	85.92	68.00	30.24	14.08	8.16
Cal. in dodec_no brine_06	0.000	6.464	1.270	64.00	71.04	49.37	20.63	9.28	3.49
Cal. in dodec_no brine_07	0.015	6.186	0.869	32.00	42.87	34.38	19.82	5.08	0.68
Cal. in dodec_no brine_08	0.000	7.638	1.019	128.0	41.39	35.39	24.38	11.99	4.08
Cal. in dodec_no brine_09	0.009	5.733	0.298	64.00	20.56	8.74	2.32	0.88	0.29
Cal. in dodec_no brine_10	0.015	1.301	0.254	128.0	5.39	0.08	0.00	0.00	0.00
Cal. in dodec_no brine_11	1.002	4.454	2.567	25.00	100.0	100.0	84.48	21.44	0.64
Cal. in dodec_no brine_12	0.958	3.954	2.396	25.00	100.0	99.84	75.04	16.00	0.00
Cal. in dodec_no brine_13	0.243	5.422	2.629	25.00	99.68	97.60	84.64	26.40	1.28
Cal. in dodec_no brine_14	0.102	5.414	1.405	128.0	98.88	78.63	14.27	1.91	0.16
Cal. in dodec_no brine_15	0.289	3.545	1.877	25.00	99.84	98.56	34.88	1.12	0.00
Cal. in dodec_no brine_16	0.015	1.301	0.254	128.0	5.39	0.08	0.00	0.00	0.00
Cal. in dodec_no brine_17	0.016	1.582	0.276	64.00	14.70	1.86	0.00	0.00	0.00
Cal. in dodec_no brine_18	0.094	6.121	0.809	25.00	81.44	25.60	0.48	0.16	0.16
Cal. in dodec_no brine_19	0.069	2.047	0.795	25.00	73.76	30.40	0.16	0.00	0.00
Cal. in dodec_no brine_20	0.113	9.000	1.844	25.00	99.36	96.48	30.56	2.08	0.80
Cal. in dodec_no brine_21	0.028	2.810	1.201	25.00	94.88	64.00	4.80	0.00	0.00
Cal. in dodec_no brine_22	0.094	1.859	0.678	25.00	65.44	16.96	0.00	0.00	0.00
Cal. in dodec_no brine_23	0.452	5.214	2.283	25.00	99.36	96.16	63.84	19.04	1.12
Cal. in dodec_no brine_24	0.094	6.121	0.809	25.00	81.44	25.60	0.48	0.16	0.16
Cal. in dodec_no brine_25	0.069	2.047	0.795	25.00	73.76	30.40	0.16	0.00	0.00
Cal. in dodec_no brine_26	0.113	9.000	1.844	25.00	99.36	96.48	30.56	2.08	0.80
Cal. in dodec_no brine_27	0.028	2.810	1.201	25.00	94.88	64.00	4.80	0.00	0.00
Cal. in dodec_no brine_28	0.094	1.859	0.678	25.00	65.44	16.96	0.00	0.00	0.00
Cal. in dodec_no brine_29	0.452	5.214	2.283	25.00	99.36	96.16	63.84	19.04	1.12
Cal. in dodec_no brine_30	0.016	1.582	0.276	64.00	14.70	1.86	0.00	0.00	0.00

Sample name	Min	Max	Average	n_pixels	%oil > 0.5 nm	%oil > 1 nm	%oil > 2 nm	%oil > 3 nm	%oil > 4 nm
Cal. in dec. acid 0.1 M_01	0.019	1.522	0.291	25.00	26.24	3.52	0.00	0.00	0.00
Cal. in dec. acid 0.1 M_02	0.021	9.000	0.337	25.00	24.96	6.08	1.12	0.64	0.48
Cal. in dec. acid 0.1 M_03	0.019	1.723	0.265	25.00	23.68	2.56	0.00	0.00	0.00
Cal. in dec. acid 0.1 M_04	0.019	1.522	0.291	25.00	26.24	3.52	0.00	0.00	0.00
Cal. in dec. acid 0.1 M_05	0.020	9.000	0.762	128.0	38.33	29.69	10.17	2.19	1.68
Cal. in dec. acid 0.1 M_06	0.107	7.272	0.636	64.00	23.71	16.28	10.67	6.08	2.83
Cal. in dec. acid 0.1 M_07	0.014	1.367	0.162	16.00	13.28	0.78	0.00	0.00	0.00
Cal. in dec. acid 0.1 M_08	0.000	8.226	0.821	25.00	32.32	23.52	13.28	7.68	4.80
Cal. in dec. acid 0.1 M_09	0.016	5.379	0.505	25.00	18.40	13.12	8.48	5.44	1.92
Cal. in dec. acid 0.1 M_10	0.021	6.862	0.593	25.00	22.40	15.84	8.32	4.16	1.76
Cal. in dec. acid 0.1 M_11	0.006	6.790	0.542	64.00	21.88	14.28	8.15	4.61	1.95
Cal. in dec. acid 0.1 M_12	0.009	7.138	0.654	64.00	30.27	21.41	11.60	5.22	2.00
Cal. in dec. acid 0.1 M_13	0.107	7.272	0.636	64.00	23.71	16.28	10.67	6.08	2.83
Cal. in dec. acid 0.1 M_14	0.006	2.922	0.195	128.0	16.93	1.31	0.12	0.00	0.00
Cal. in dec. acid 0.1 M_15	0.145	6.952	0.361	25.00	20.80	3.84	0.16	0.16	0.16
Cal. in dec. acid 0.1 M_16	0.015	2.913	0.229	25.00	13.44	2.08	0.16	0.00	0.00
Cal. in dec. acid 0.1 M_17	0.018	2.972	0.215	25.00	10.56	0.80	0.16	0.00	0.00
Cal. in dec. acid 0.1 M_18	0.015	1.363	0.185	25.00	11.20	0.48	0.00	0.00	0.00
Cal. in dec. acid 0.1 M_19	0.020	1.050	0.204	25.00	9.44	0.16	0.00	0.00	0.00
Cal. in dec. acid 0.1 M_20	0.113	2.387	0.402	64.00	32.74	8.42	0.02	0.00	0.00
Cal. in dec. acid 0.1 M_21	0.008	1.129	0.188	64.00	13.77	0.12	0.00	0.00	0.00
Cal. in dec. acid 0.1 M_22	0.006	2.922	0.195	128.0	16.93	1.31	0.12	0.00	0.00
Cal. in dec. acid 1 M_01	0.007	0.321	0.030	128.0	0.00	0.00	0.00	0.00	0.00
Cal. in dec. acid 1 M_02	0.013	3.579	0.758	25.00	28.80	22.72	15.84	11.52	0.00
Cal. in dec. acid 1 M_03	0.000	5.407	1.057	25.00	29.76	24.32	20.96	16.80	14.08
Cal. in dec. acid 1 M_04	0.000	9.000	2.323	25.00	63.36	53.76	44.48	36.00	26.40
Cal. in dec. acid 1 M_05	0.012	1.285	0.115	25.00	3.04	0.64	0.00	0.00	0.00
Cal. in dec. acid 1 M_06	0.008	0.392	0.058	25.00	0.00	0.00	0.00	0.00	0.00
Cal. in dec. acid 1 M_07	0.005	0.828	0.043	128.0	0.07	0.00	0.00	0.00	0.00
Cal. in dec. acid 1 M_08	0.003	0.634	0.032	128.0	0.03	0.00	0.00	0.00	0.00
Cal. in dec. acid 1 M_09	0.012	0.200	0.049	16.00	0.00	0.00	0.00	0.00	0.00
Cal. in dec. acid 1 M_10	0.007	0.321	0.030	128.0	0.00	0.00	0.00	0.00	0.00
Cal. in dec. acid 1 M_11	0.016	1.730	0.068	128.0	0.37	0.02	0.00	0.00	0.00
Cal. in dec. acid 1 M_12	0.000	9.000	0.197	32.00	6.05	3.52	1.07	0.68	0.39
Cal. in dec. acid 1 M_13	0.031	9.000	4.628	32.00	98.24	97.17	95.51	90.33	57.32
Cal. in dec. acid 1 M_14	0.025	6.433	0.503	32.00	33.59	20.61	1.66	0.59	0.29
Cal. in dec. acid 1 M_15	0.024	1.090	0.097	32.00	2.64	0.39	0.00	0.00	0.00
Cal. in dec. acid 1 M_16	0.012	2.571	0.068	64.00	0.59	0.02	0.02	0.00	0.00
Cal. in dec. acid 1 M_17	0.000	2.054	1.545	32.00	99.61	98.34	0.20	0.00	0.00
Cal. in dec. acid 1 M_18	0.013	1.266	0.096	64.00	1.29	0.07	0.00	0.00	0.00

Sample name	Min	Max	Average	n_pixels	%oil > 0.5 nm	%oil > 1 nm	%oil > 2 nm	%oil > 3 nm	%oil > 4 nm
Cal. in dec. acid 1 M_19	0.000	1.307	0.301	64.00	5.44	0.12	0.00	0.00	0.00
Cal. in dec. acid 1 M_20	0.023	0.922	0.062	32.00	0.78	0.00	0.00	0.00	0.00
Cal. in dec. acid 1 M_21	0.000	6.127	0.274	32.00	4.00	0.49	0.20	0.10	0.10
Cal. in dec. acid 1 M_22	0.018	1.118	0.088	64.00	0.44	0.05	0.00	0.00	0.00
Cal. in dec. acid 1 M_23	0.016	1.730	0.068	128.0	0.37	0.02	0.00	0.00	0.00
Cal. in dec. acid 1 M_24	0.005	0.947	0.129	128.0	0.70	0.00	0.00	0.00	0.00
Cal. in dec. acid 1 M_25	0.002	9.000	3.019	25.00	94.40	92.32	77.28	49.92	13.44
Cal. in dec. acid 1 M_26	0.000	4.679	2.372	25.00	99.20	96.48	83.36	9.12	0.32
Cal. in dec. acid 1 M_27	0.120	3.900	3.024	25.00	98.72	97.92	94.24	62.24	0.00
Cal. in dec. acid 1 M_28	0.039	9.000	5.852	25.00	94.88	93.28	85.12	82.88	81.44
Cal. in maltene C5_ 01	0.083	7.341	2.674	25.00	91.52	39.52	36.00	34.88	34.88
Cal. in maltene C5_ 02	0.074	3.097	0.781	25.00	76.48	22.08	1.60	0.16	0.00
Cal. in maltene C5_ 03	0.035	4.907	0.844	25.00	74.72	28.00	3.68	0.64	0.16
Cal. in maltene C5_ 04	0.040	2.251	0.538	25.00	46.08	7.68	0.16	0.00	0.00
Cal. in maltene C5_ 05	0.052	4.672	0.550	25.00	40.80	9.44	1.60	0.16	0.16
Cal. in maltene C5_ 06	0.000	5.268	1.168	25.00	89.44	51.04	9.12	3.20	1.28
Cal. in maltene C5_ 07	0.011	7.898	0.883	25.00	79.20	32.32	3.04	0.80	0.32
Cal. in maltene C5_ 08	0.031	5.927	0.947	25.00	83.36	33.12	3.68	1.28	0.32
Cal. in maltene C5_ 09	0.004	0.828	0.117	25.00	1.44	0.00	0.00	0.00	0.00
Cal. in maltene C5_ 10	0.005	0.947	0.129	128.0	0.70	0.00	0.00	0.00	0.00
Cal. in maltene C5_ 11	0.015	3.912	1.973	25.00	94.08	88.32	53.44	6.40	0.00
Cal. in maltene C5_ 12	0.022	9.000	2.319	25.00	82.72	76.96	59.36	33.76	13.92
Cal. in maltene C5_ 13	0.020	5.814	1.703	25.00	70.56	62.40	42.40	25.76	1.28
Cal. in maltene C5_ 14	0.651	9.000	4.514	25.00	100.0	99.68	98.56	91.36	70.24
Cal. in maltene C5_ 15	0.037	9.000	3.206	25.00	97.92	95.68	82.40	56.16	22.72
Cal. in maltene C5_ 16	0.016	9.000	4.644	128.0	97.72	97.01	94.15	85.94	68.27
Cal. in maltene C5_ 17	0.022	8.422	1.187	25.00	36.64	29.44	23.36	16.96	10.56
Cal. in maltene C5_ 18	0.067	9.000	1.600	25.00	76.96	57.44	30.08	15.20	5.92
Cal. in maltene C5_ 19	0.014	3.540	1.030	25.00	40.48	15.10	10.50	2.60	0.00
Cal. in maltene C5_ 20	0.000	7.729	3.143	25.00	68.80	63.84	56.80	51.36	41.44
Cal. in maltene C5_ 21	0.000	7.956	2.984	25.00	82.24	71.84	56.80	42.72	33.12
Cal. in maltene C5_ 22	0.000	7.439	3.373	25.00	88.32	83.68	73.44	65.28	51.68
Cal. in maltene C5_ 23	0.000	9.000	2.084	25.00	50.24	38.56	31.52	26.88	22.72
Cal. in maltene C5_ 24	0.000	8.568	6.170	25.00	92.16	87.52	82.56	79.04	75.20
Cal. in maltene C5_ 25	0.000	7.892	4.444	25.00	85.92	79.84	72.80	68.48	63.52
Cal. in maltene C5_ 26	0.014	9.000	1.564	25.00	72.16	54.08	27.20	13.28	6.40
Cal. in maltene C5_ 27	0.067	9.000	1.600	25.00	76.96	57.44	30.08	15.20	5.92
Cal. in asphaltene_01	0.000	9.000	1.540	25.00	19.84	13.44	7.68	4.96	3.52
Cal. in asphaltene_02	0.052	9.000	2.722	25.00	72.64	64.96	52.80	36.16	24.48
Cal. in asphaltene_03	0.000	9.000	7.919	25.00	95.04	94.08	92.32	90.88	89.60

Sample name	Min	Max	Average	n_pixels	%oil > 0.5 nm	%oil > 1 nm	%oil > 2 nm	%oil > 3 nm	%oil > 4 nm
Cal. in asphaltene_04	0.000	9.000	7.769	25.00	88.80	88.48	87.84	87.04	86.08
Cal. in asphaltene_05	0.000	9.000	4.072	25.00	51.36	50.56	49.28	48.00	46.88
Cal. in asphaltene_06	0.000	9.000	7.331	25.00	88.64	87.84	85.12	83.68	81.44
Cal. in asphaltene_07	0.000	9.000	7.497	25.00	90.72	89.92	89.28	87.36	84.64
Cal. in asphaltene_08	0.014	9.000	4.756	25.00	87.04	80.00	65.60	59.84	52.00
Cal. in asphaltene_09	0.000	9.000	4.371	25.00	83.52	81.12	76.32	60.48	40.80
Cal. in asphaltene_10	0.019	8.150	1.457	25.00	47.36	38.56	24.48	17.28	12.96
Cal. in asphaltene_11	0.029	8.887	4.531	25.00	97.76	95.84	87.20	64.80	51.20
Cal. in asphaltene_12	0.000	9.000	1.908	25.00	64.32	49.76	34.40	26.40	18.56
Cal. in asphaltene_13	0.000	9.000	1.617	25.00	70.88	54.40	21.44	11.04	9.28
Cal. in asphaltene_14	0.000	9.000	7.183	25.00	96.16	93.92	89.12	85.60	80.16
Cal. in asphaltene_15	0.056	8.948	1.826	25.00	93.12	71.36	38.56	10.24	3.20
Cal. in oil_01	0.008	8.381	3.799	25.00	83.36	75.68	64.80	56.96	47.36
Cal. in oil_02	0.034	9.000	2.737	25.00	92.00	79.20	57.44	35.68	24.16
Cal. in oil_03	0.024	9.000	1.451	25.00	87.84	51.52	13.12	8.16	6.88
Cal. in oil_04	0.016	3.847	0.945	25.00	61.76	43.20	9.76	0.32	0.00
Cal. in oil_05	0.014	9.000	0.991	25.00	77.28	47.36	3.20	0.80	0.16
Cal. in oil_06	0.000	7.135	1.184	25.00	78.72	49.44	15.52	5.92	2.24
Cal. in oil_07	0.016	7.414	1.901	25.00	83.68	66.40	28.00	17.60	13.60
Cal. in oil_08	0.015	9.000	3.268	25.00	73.28	66.72	54.40	45.44	34.88
Cal. in oil_09	0.013	9.000	1.615	25.00	52.32	38.08	27.20	22.72	16.00
Cal. in oil_10	0.000	9.000	5.151	25.00	85.92	77.60	67.20	60.64	57.12
Cal. in oil_11	0.000	9.000	2.309	25.00	47.84	44.48	37.92	29.28	24.48
Cal. in oil_12	0.000	9.000	2.455	25.00	58.24	48.32	38.24	31.36	26.24
Cal. in oil_13	0.000	9.000	2.818	25.00	52.96	48.00	37.44	33.28	28.48
Cal. in oil_14	0.000	9.000	2.267	25.00	63.68	56.64	43.36	28.00	19.04
Cal. in oil_15	0.000	9.000	3.875	25.00	60.96	56.96	49.76	44.96	42.40
Cal. in oil_16	0.013	9.000	1.615	25.00	52.32	38.08	27.20	22.72	16.00
Cal. in oil_17	0.015	9.000	3.268	25.00	73.28	66.72	54.40	45.44	34.88

Table A.1: Table of all the CFM experiments on calcite surfaces described in chapter 4.

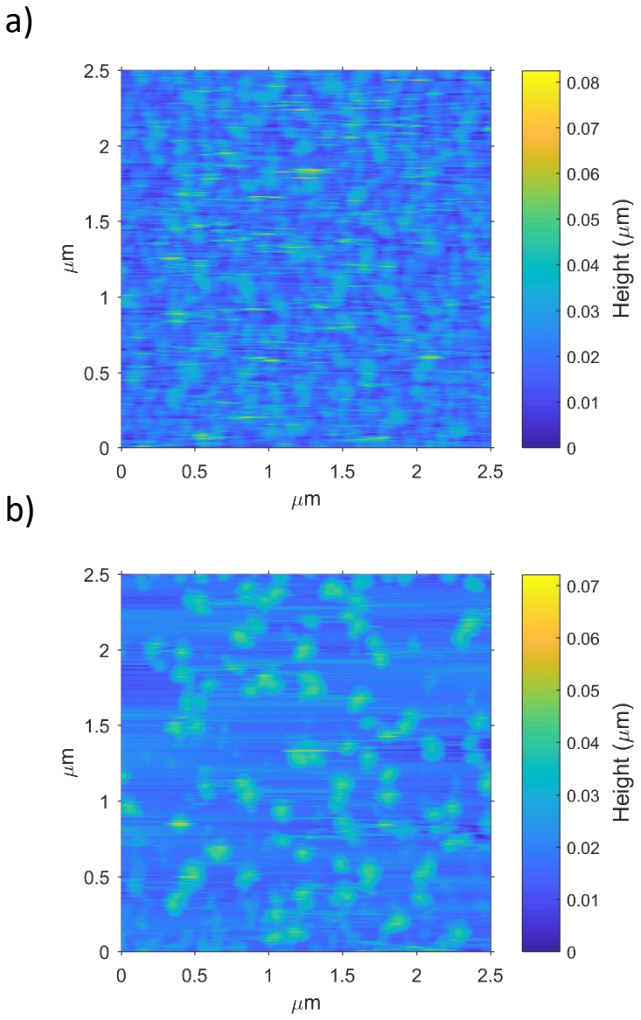

Figure A.8: a) CFM scan of a 2.5 x 2.5 μm² area of a calcite surface aged in maltene C_8. b) is the same area, scanned for the second time at a setpoint value of 1.